



Ricerca di Sistema elettrico

Development of best estimate numerical tools for LFR design and safety analysis

A. Del Nevo, A. Cervone, G. Grasso, M. Tarantino
T. Barani, A. Cammi, M. Cerini, S. Cervino, L. Cognini,
L. De Luca, L. Luzzi, M. Giola, E. Macerata, M. Mariani,
S. Lorenzi, D. Pizzocri
R. Bonifetto, D. Caron, S. Dulla, P. Ravetto, L. Savoldi,
R. Zanino

L. Chirco, R. Da Vià, S. Manservigi
G. Caruso, M. Frullini, F. Giannetti, V. Narcisi, A. Subioli
M. Angelucci, G. Barone, N. Forgione, R. Lo Frano,
A. Pesetti, C. Ulissi



DEVELOPMENT OF BEST ESTIMATE NUMERICAL TOOLS FOR LFR DESIGN AND SAFETY ANALYSIS

A. Del Nevo, A. Cervone, G. Grasso, M. Tarantino (ENEA)

T. Barani, A. Cammi, M. Cerini, S. Cervino, L. Cognini, L. De Luca, L. Luzzi, M. Giola, E. Macerata, M. Mariani, S. Lorenzi, D. Pizzocri (POLIMI)

R. Bonifetto, D. Caron, S. Dulla, P. Ravetto, L. Savoldi, R. Zanino (POLITO)

L. Chirco, R. Da Vià, S. Manservigi (UNIBO)

G. Caruso, M. Frullini, F. Giannetti, V. Narcisi, A. Subioli (UNIROMA1)

M. Angelucci, G. Barone, N. Forgiione, R. Lo Frano, A. Pesetti, C. Ulissi (UNIFI)

Settembre 2017

Report Ricerca di Sistema Elettrico

Accordo di Programma Ministero dello Sviluppo Economico - ENEA

Piano Annuale di Realizzazione 2016

Area: Generazione di Energia Elettrica con Basse Emissioni di Carbonio

Progetto: Sviluppo competenze scientifiche nel campo della sicurezza nucleare e collaborazione ai programmi internazionali per il nucleare di IV Generazione.

Linea: Collaborazione ai programmi internazionali per il nucleare di IV Generazione

Obiettivo: Progettazione di sistema e analisi di sicurezza

Responsabile del Progetto: Mariano Tarantino, ENEA

Il presente documento descrive le attività di ricerca svolte all'interno dell'Accordo di collaborazione "Sviluppo competenze scientifiche nel campo della sicurezza nucleare e collaborazione ai programmi internazionali per il nucleare di IV Generazione"

Responsabile scientifico ENEA: Mariano Tarantino

Responsabile scientifico CIRTEN: Marco Ricotti

Titolo

Development of best estimate numerical tools for LFR design and safety analysis

Descrittori

Tipologia del documento: Rapporto Tecnico
Collocazione contrattuale: Accordo di programma ENEA-MSE su sicurezza nucleare e Reattori di IV generazione
Argomenti trattati: Reattori Nucleari Veloci, Termoidraulica dei reattori nucleari
 Sicurezza nucleare, Analisi incidentale

Sommario

Nell'ambito della linea LP2, sono state condotte attività di ricerca al fine di sviluppare, aggiornare e convalidare codici di calcolo e modelli numerici per sostenere la progettazione ed effettuare analisi di sicurezza di un reattore veloce refrigerato a metallo liquido. Nell'ambito del PAR 2016, sono state messe in atto delle azioni al fine di integrare e coordinare tali attività. Si sono, pertanto, definite le aree di simulazione e le interconnessioni rilevanti per la progettazione e sicurezza di reattori Gen-IV. Ognuna di queste aree di simulazione è coperta da uno o più codici e simula un set di fenomeni multi-fisica e multi-scala rilevanti, e.g. termoidraulica di sistema, di contenimento, di sotto-canale, fluidodinamica tridimensionale, termo-meccanica della barretta di combustibile, del fuel assembly e di componenti, generazione di sezioni d'urto e sviluppo di metodi di aggiustamento delle stesse mediante utilizzo di dati sperimentali, dinamica neutronica tridimensionale, rilascio e trasporto di prodotti di fissione, etc. Tale attività servirà come base di partenza per un'azione di sviluppo e convalida di una piattaforma di calcolo per sistemi nucleari innovativi, che si protrarrà nel PT2015- 2017 (e successivi). Pertanto, si propone di procedere con l'attività secondo la seguente logica:

- definire le aree di simulazione e le interconnessioni rilevanti per la progettazione e sicurezza di reattori Gen-IV;
- definire i codici e la piattaforma di accoppiamento e identificare le necessità di sviluppo e lo stato di convalida;
- procedere con l'attività di sviluppo, convalida e applicazione in continuità con quanto fatto negli ultimi anni.

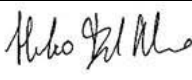
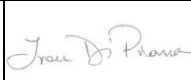

Relativamente a sviluppo e convalida, riportate nella parte 2 del presente report, sono state effettuate attività relative a:

1. termo-meccanica della barretta di combustibile – supporto allo sviluppo del codice TRANSURANUS.
2. accoppiamento codici CFD/SYS-TH e loro validazione a fronte delle campagne sperimentali TALL e CIRCE
3. termoidraulica di sistema – supporto alla validazione del codice REALP5-3D per applicazione ai sistemi a piscina
4. dinamica accoppiata neutronica-termoidraulica tridimensionale - sviluppo e applicazione codice FRENETIC
5. modellazione multifisica neutronica – termoidraulica - accoppiamento OpenFoam-Serpent
6. dinamica molecolare per lo studio di fenomeni di diffusione nella interazione combustibile refrigerante
7. termoidraulica multifluid/multiphase e analisi di incidenti severi – supporto allo sviluppo e alla validazione del codice SIMMER-III e -IV

Note: --


Autori: A. Del Nevo, A. Cervone, G. Grasso, M. Tarantino (ENEA); T. Barani, A. Cammi, M. Cerini, S. Cervino, L. Cognini, L. De Luca, L. Luzzi, M. Giola E. Macerata, M. Mariani, S. Lorenzi, D. Pizzocri (POLIMI); R. Bonifetto, D. Caron, S. Dulla, P. Ravetto, L. Savoldi, R. Zanino (POLITO); L. Chirco, R. Da Vià, S. Manservigi (UNIBO); G. Caruso, M. Frullini, F. Giannetti, V. Narcisi, A. Subioli (UNIROMA1) M. Angelucci, G. Barone, N. Forgiione, R. Lo Frano, A. Pesetti, C. Ulissi (UNIFI)


Copia n.
In carico a:

1			NOME			
			FIRMA			
0	EMISSIONE	12/12/2017	NOME	A. Del Nevo	I. Di Piazza	M. Tarantino
			FIRMA			
REV.	DESCRIZIONE	DATA	REDAZIONE	CONVALIDA	APPROVAZIONE	

(Page intentionally left blank)


(

 RICERCA SISTEMA ELETTRICO	<u>Title:</u> Development of BE numerical tools for LFR design and safety analysis – Part 1 <u>Project:</u> ADP ENEA-MSE PAR 2016	<u>Distribution</u> PUBLIC	<u>Issue Date</u> 12.12.2017	<u>Pag.</u> 3 di 300
		<u>Ref.</u> ADPFISS-LP2-144	Rev. 0	

LIST OF REVISIONS


Revision	Date	Scope of revision	Page
0	12/12/2017	First issue	300



 RICERCA SISTEMA ELETTRICO	<u>Title:</u> Development of BE numerical tools for LFR design and safety analysis – Part 1 <u>Project:</u> ADP ENEA-MSE PAR 2016	<u>Distribution</u> PUBLIC	<u>Issue Date</u> 12.12.2017	<u>Pag.</u> 4 di 300
		<u>Ref.</u> ADPFISS-LP2-144	Rev. 0	

(Page intentionally left blank)




 RICERCA SISTEMA ELETTRICO	<u>Title:</u> Development of BE numerical tools for LFR design and safety analysis – Part 1 <u>Project:</u> ADP ENEA-MSE PAR 2016	<u>Distribution</u> PUBLIC	<u>Issue Date</u> 12.12.2017	<u>Pag.</u> 5 di 300
		<u>Ref.</u> ADPFISS-LP2-144	Rev. 0	

DEVELOPMENT OF BEST ESTIMATE NUMERICAL TOOLS FOR LFR DESIGN AND SAFETY ANALYSIS


Part 1: General aspects



 RICERCA SISTEMA ELETTRICO	<u>Title:</u> Development of BE numerical tools for LFR design and safety analysis – Part 1 <u>Project:</u> ADP ENEA-MSE PAR 2016	<u>Distribution</u> PUBLIC	<u>Issue Date</u> 12.12.2017	<u>Pag.</u> 6 di 300
		<u>Ref.</u> ADPFISS-LP2-144	Rev. 0	

(Page intentionally left blank)




 RICERCA SISTEMA ELETTRICO	<u>Title:</u> Development of BE numerical tools for LFR design and safety analysis – Part 1	<u>Distribution</u> PUBLIC	<u>Issue Date</u> 12.12.2017	<u>Pag.</u>
	<u>Project:</u> ADP ENEA-MSE PAR 2016	<u>Ref.</u> ADPFISS-LP2-144	Rev. 0	7 di 300

LIST OF CONTENTS

LIST OF REVISIONS	3
LIST OF FIGURES	9
LIST OF TABLES	10
LIST OF ABBREVIATIONS	11
1 INTRODUCTORY REMARKS	13
1.1 Objectives.....	13
2 DESIGN AND SAFETY ANALYSIS AREAS IN SUPPORT OF LEAD-COOLED FAST REACTOR DEVELOPMENT	15
3 CHARACTERIZATION OF THE MODELING NEEDS FOR THE SELECTED AREAS	17
3.1 Core Design.....	20
3.1.1 Thermal-hydraulics	21
3.1.2 Thermo-mechanics	22
3.1.3 Neutronics	23
3.1.4 A possible platform layout (limited to core design activities).....	24
3.2 Primary system design R&D development needs	25
3.2.1 Identification of the key topics for the LFR development.....	25
3.2.2 LFR material studies and coolant physical-chemistry.....	25
3.2.3 LFR studies of Core integrity, moving mechanisms, instrumentation, maintenance, in service inspection and repair.....	28
3.2.4 Steam Generator functionality and safety experimental studies.....	29
3.2.5 Thermal hydraulics.....	31
3.2.6 HLM pump and corrosion/erosion studies	33
3.2.7 Instrumentations	33
3.2.8 Fuel and Irradiation Testing	35
3.2.9 Hot laboratories capabilities and needs	37
3.2.10 Neutronics	38
3.3 Auxiliary and ancillary systems design.....	39
3.3.1 Decay heat removal system.....	39
3.3.2 Fuel handling system for core assembly loading and unloading, irradiated fuel cooling during transfer and transport to the irradiated fuel pool	40
3.3.3 Other auxiliary systems	40
3.4 Instrumentation and control design	41
3.5 Probabilistic Safety Analysis.....	43
3.5.1 PSA levels	43




 RICERCA SISTEMA ELETTRICO	<u>Title:</u> Development of BE numerical tools for LFR design and safety analysis – Part 1	<u>Distribution</u> PUBLIC	<u>Issue Date</u> 12.12.2017	<u>Pag.</u> 8 di 300
	<u>Project:</u> ADP ENEA-MSE PAR 2016	<u>Ref.</u> ADPFISS-LP2-144	Rev. 0	

3.5.2	Complements for the PSA application in a safety analysis	44
3.5.3	PSA application in preliminary safety analysis	44
3.5.4	ISAM methodology	44
3.5.5	PSA modelling needs	45
3.6	Deterministic Safety Analysis	45

4 OVERVIEW OF THE MODELING ACTIVITIES IN 2016 (PART 2) 55

LIST OF REFERENCES 57




 RICERCA SISTEMA ELETTRICO	<u>Title:</u> Development of BE numerical tools for LFR design and safety analysis – Part 1	<u>Distribution</u> PUBLIC	<u>Issue Date</u> 12.12.2017	<u>Pag.</u>
	<u>Project:</u> ADP ENEA-MSE PAR 2016	<u>Ref.</u> ADPFISS-LP2-144	Rev. 0	9 di 300

LIST OF FIGURES

<i>Fig. 1 – 3D cut view of the ALFRED reactor.....</i>	<i>14</i>
<i>Fig. 2 – Iterative process of reactor configuration development.....</i>	<i>16</i>
<i>Fig. 3 – Hypothetical relation between complexity and accuracy of a model.....</i>	<i>50</i>
<i>Fig. 4 – LFR core design process with the main physical interconnections highlighted.</i>	<i>50</i>
<i>Fig. 5 – List of candidate codes for the aimed core design/verification platform.....</i>	<i>51</i>
<i>Fig. 6 – Simplified coupling scheme for thermal-hydraulics feedback evaluation in design.</i>	<i>51</i>
<i>Fig. 7 – Detailed coupling scheme for thermal-hydraulics feedback evaluation in design.</i>	<i>51</i>
<i>Fig. 8 – Detailed coupling scheme for thermal-hydraulics feedback evaluation in verification.</i>	<i>52</i>
<i>Fig. 9 – Platform utilization in the case of core restraint design.....</i>	<i>52</i>
<i>Fig. 10 – Configuration of the operational control system in terms of functions (please note the connection with protection and limitation systems^[18].....</i>	<i>53</i>
<i>Fig. 11 – Control strategy road map.....</i>	<i>53</i>
<i>Fig. 12 – Different approaches in modelling, 0D/1D modelling (control-oriented) vs 3D modelling (design-oriented).....</i>	<i>54</i>
<i>Fig. 13 – ISAM methodology representation [23].....</i>	<i>54</i>




 RICERCA SISTEMA ELETTRICO	<u>Title:</u> Development of BE numerical tools for LFR design and safety analysis – Part 1	<u>Distribution</u> PUBLIC	<u>Issue Date</u> 12.12.2017	<u>Pag.</u>
	<u>Project:</u> ADP ENEA-MSE PAR 2016	<u>Ref.</u> ADPFISS-LP2-144	Rev. 0	10 di 300

LIST OF TABLES

<i>Tab. 1 – ALFRED specifications.</i>	14
<i>Tab. 2 – Aspects encompassed in the design and verification of main reactor sub-systems (N: Neutronics; TH: Thermal-Hydraulics; TM: Thermo-Mechanics; C: Chemistry; E: Electronics).</i>	16
<i>Tab. 3 – Aspects encompassed in the design of core components(N: Neutronics; TH: Thermal-Hydraulics; TM: Thermo-Mechanics)..</i>	48
<i>Tab. 4 – Main features and differences between causal and acausal approach.</i>	48
<i>Tab. 5 – Summary of available instrumentations.</i>	48
<i>Tab. 6 – Summary of the European zero power reactors.</i>	49
<i>Tab. 7 – EUR Design Basis Category.</i>	49
<i>Tab. 8 – Options for Combination of a Computer Code and Input Data^[32].</i>	49
<i>Tab. 9 – Development, validation and application of computational tools: summary of the activity performed in the framework of PAR-2016.</i>	55




 RICERCA SISTEMA ELETTRICO	<u>Title:</u> Development of BE numerical tools for LFR design and safety analysis – Part 1	<u>Distribution</u> PUBLIC	<u>Issue Date</u> 12.12.2017	<u>Pag.</u>
	<u>Project:</u> ADP ENEA-MSE PAR 2016	<u>Ref.</u> ADPFISS-LP2-144	Rev. 0	11 di 300

LIST OF ABBREVIATIONS


AdP	Accordo di Programma
ALFRED	Advanced Lead Fast Reactor European Demonstrator
ATHENA	Advanced Thermal Hydraulic Experiment for Nuclear Application
BE	Best Estimate
BEPU	Best Estimate Plus Uncertainty
BoP	Balance of Plant
BoT	Beginning of Transient
CEA	Commissariat a l'Energie Atomique et aux Energies Alternatives
CFD	Computational Fluid Dynamics
CIRCE	Circolazione Eutettico
CIRTEN	Interuniversity Consortium for Technological Nuclear Research
CHEOPEIII	Chemistry Operation III Facility
CR	Control Rod
DBA	Design Base Accident
DHR	Decay Heat Removal
DHRS	Decay Heat Removal System
DOC	Design-Oriented Code
DSA	Deterministic Safety Analysis
ESFRI	European Strategy Forum on Research Infrastructures
EoT	End of Transient
FA	Fuel Assembly
FALCON	Fostering ALFRED Construction
FPC	Fuel Performace Code
FR	Fast Reactor
GIORDI	Grid to Rod fretting facility
HBS	High Burnup Structure
HELENA	Heavy Liquid Metal Experimental Loop for Advanced Nuclear Applications
HLM	Heavy Liquid Metal
HX or HEX	Heat Exchanger
I&C	Instrumentation and Control
LBE	Lead Bismuth Eutectic
LECOR	Lead Corrosion Loop
LEADER	Lead-cooled Advanced Demonstration Reactor
LIFUS5	Lead-Lithium for Fusion Facility (5)
LFR	Lead Fast Reactor
LM	Liquid Metal
LMR	Liquid Metal Reactor
LWR	Light Water Reactor
MA	Minor Actinide
MABB	Minor Actinides Bearing Blankets
MOX	(U-Pu) Mixed Oxide
NACIE	Natural Circulation Experiment Loop
NPPs	Nuclear Power Plants
O&M	Operation and Maintenance
OPEX	Operating EXperience
PAR	Piani Annuali di Realizzazione
PID	Proportional-Integral-Derivative controllers
PLD	Pulsed Laser Deposition



 RICERCA SISTEMA ELETTRICO	<u>Title:</u> Development of BE numerical tools for LFR design and safety analysis – Part 1	<u>Distribution</u> PUBLIC	<u>Issue Date</u> 12.12.2017	<u>Pag.</u>
	<u>Project:</u> ADP ENEA-MSE PAR 2016	<u>Ref.</u> ADPFISS-LP2-144	Rev. 0	12 di 300

POLIMI	Politecnico di Milano
POLITO	Politecnico di Torino
PP	Primary Pump
PSA	Probabilistic Safety Analysis
RACHELE	Reactions and Advanced chemistry for Lead
RSE	Ricerca Sistema Elettrico
RV	Reactor Vessel
RVACS	Reactor Vessel Air-Cooling System
SA	Safety Analysis
SET-PLAN	Strategic Energy Technology Plan
SG	Steam Generator
SGTR	Steam Generator Tube Rupture
SISO	Single Input Single Output
SYS	System
SYS-TH	System- ThermalHydraulics
TH	Thermal-Hydraulics
TKE	Turbulent Kinetic Energy
TRL	Technological Readiness Level
TSO	Technical Safety Organization
ULOF	Unprotected Loss of Flow
UNIBO	Università di Bologna
UNIPI	Università di Pisa
UNIROMA1	Università di Roma - Sapienza
VOC	Verification-Oriented Code
V&V	Verification & Validation



 RICERCA SISTEMA ELETRICO	<u>Title:</u> Development of BE numerical tools for LFR design and safety analysis – Part 1	<u>Distribution</u> PUBLIC	<u>Issue Date</u> 12.12.2017	<u>Pag.</u>
	<u>Project:</u> ADP ENEA-MSE PAR 2016	<u>Ref.</u> ADPFISS-LP2-144	Rev. 0	13 di 300

1 INTRODUCTORY REMARKS

The Lead-cooled Fast Reactor (LFR) technology brings about the possibility of fully complying with all the Generation IV requirements^[1]. This capability being more and more acknowledged in international fora, the LFR is gathering a continuously increasing interest, with new industrial actors committing on LFR-related initiatives.

In this context, the Italian nuclear community evaluates strategic to continue elevating the competences and capabilities, with the perspective of extending the support to the design and safety analysis of future LFR systems.

The most appropriate framework for this advancement is the Accordo di Programma (AdP), within which ENEA and CIRTEN (the consortium gathering all Italian universities engaged in nuclear education, training and research) are already cooperating on the LFR technology since 2006, along with national industry as main stakeholder.

Within the AdP, the LFR system chosen as reference for all studies and investigations is ALFRED, the Advanced Lead-cooled Fast Reactor European Demonstrator [2]. As a demonstration reactor, indeed, it was reckoned as the system best fitting with the research and development (R&D) nature of the activities performed in the AdP, being demonstration the step that logically follows R&D in the advancement of the LFR technology by readiness levels. Moreover, ALFRED is envisaged as the key facility of a distributed research infrastructure of pan-European interest [3], open to scientists and technologists for relevant experiments to be performed on a fully LFR-representative and integral environment, with the long-term perspective of supporting to the safe and sustainable operation of future LFRs, thereby fulfilling the general objectives of the AdP itself.


The collaborative spirit behind the development of ALFRED is an inherent trademark of the project since its very beginning. As a matter of facts, it was originally conceived and initially developed within the LEADER (Lead-cooled European Advanced Demonstration Reactor) collaborative research project [4], co-funded by the European Commission through the 7th EURATOM Framework Programme. After the conclusion of the LEADER project, the Fostering ALFRED Construction (FALCON) International Consortium was signed between Ansaldo Nucleare, ENEA and the Romanian research organization RATEN-ICN with the twofold objective of further developing the ALFRED design and of performing all the strategic, managerial, and financial activities required to set the consortium prepared for the realization of ALFRED in Romania [5].

A view of the ALFRED reactor block layout, and the main parameters of the reactor, as resulting at the conclusion of the LEADER project, are shown in Fig. 1 and Tab. 1, respectively.

1.1 Objectives

In the wide spectrum of possible activities to support the further development of the LFR technology, and exploiting the specific expertise acquired by the universities in the past years, within the scope of the 2016 Piano Annuale di Realizzazione (PAR) it was decided to focus the cooperative efforts shared between ENEA and CIRTEN towards the development of an **best estimate computational tools supporting the various stages of design and safety analyses of LFR systems**, so to increase – or help in viewing how to fill the gaps – the modeling capabilities.



 RICERCA SISTEMA ELETTRICO	<u>Title:</u> Development of BE numerical tools for LFR design and safety analysis – Part 1	<u>Distribution</u> PUBLIC	<u>Issue Date</u> 12.12.2017	<u>Pag.</u>
	<u>Project:</u> ADP ENEA-MSE PAR 2016	<u>Ref.</u> ADPFISS-LP2-144	Rev. 0	14 di 300

The first step in this process, which is also the objective planned for the first year of activity and accordingly included in the PAR2016, is thus to define what are the most important modelling needs and fundamental features that the desired platform and its tools should possess. This will permit, on one hand, to derive guidelines for the selection of tools to be embedded in the platform (should they exist), or for their development wherever a remarkable gap is found between the codes in the present landscape and those envisaged for the platform; on the other, to retrieve guidelines for the development of the integration platform hosting and managing the execution of the identified tools.

Reactor specification	
Thermal power (MW)	300
Fuel residence time (years)	5
Coolant inlet temperature (°C)	400
Average coolant outlet temperature (°C)	480
Coolant mass flow rate (kg s ⁻¹)	≈ 25700
Average coolant velocity (m s ⁻¹)	≈ 1.4

Tab. 1 – ALFRED specifications.

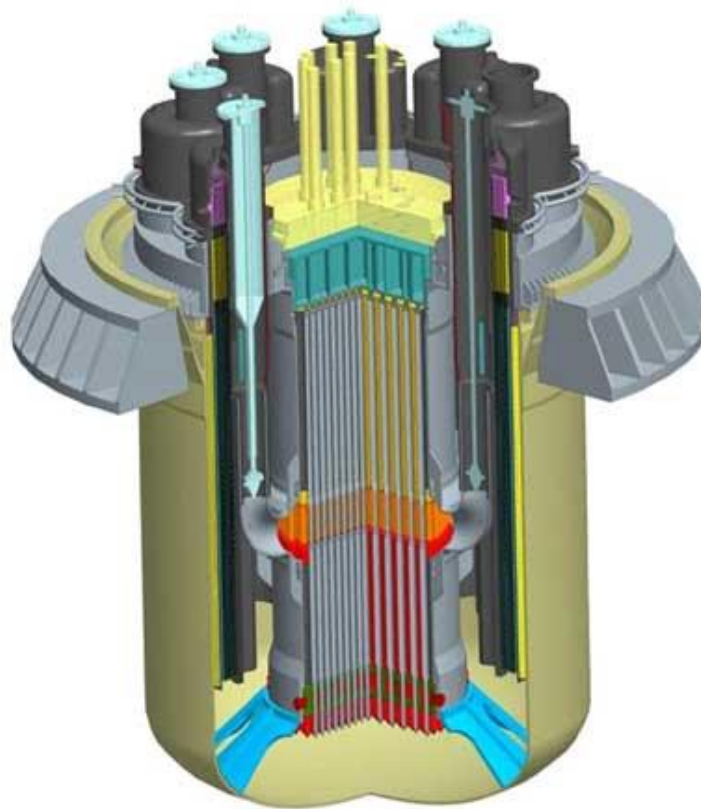



Fig. 1 – 3D cut view of the ALFRED reactor.



 RICERCA SISTEMA ELETTRICO	<u>Title:</u> Development of BE numerical tools for LFR design and safety analysis – Part 1	<u>Distribution</u> PUBLIC	<u>Issue Date</u> 12.12.2017	<u>Pag.</u>
	<u>Project:</u> ADP ENEA-MSE PAR 2016	<u>Ref.</u> ADPFISS-LP2-144	Rev. 0	15 di 300

2 DESIGN AND SAFETY ANALYSIS AREAS IN SUPPORT OF LEAD-COOLED FAST REACTOR DEVELOPMENT

Design is, very generally, the discipline aiming at determining the main parameters which unequivocally define a reactor configuration providing the desired performances while targeting all the desired performances and complying with all the constraints, both in nominal and accidental conditions. Given the very different nature of the performances and constraints, and the multidisciplinary essence of the task, reactor design is principally an art of engineering compromise and harmonization.

Conversely, verification is the discipline aiming at determining the actual behavior of a reactor configuration, both in nominal and accidental conditions, so as to evaluate the extent to which performances have been achieved and constraints respected. Given the relevance of verification, notably when addressing the safety aspects of a reactor, the confidence on the obtained results is the principal objective of this task.


Generally speaking, design and verification are the two sides of the same coin: while design translates target performances and constraints into a reactor configuration, verification analyzes the latter to retrieve the actual performances expressed, and constraints respected, by the configuration, eventually providing feedbacks to the design stage for optimization. In developing a reactor configuration (Fig. 2), these two activities are therefore iteratively performed until convergence is reached, with the final reactor configuration performing as desired and fulfilling all the imposed constraints.

The apparent symmetry between design and verification is broken by the interface with safety authorities, for the certification of the reactor configuration obtained at the end of the iterative process. Licensing has indeed so strict rules, and is so a fundamental objective, to practically impose all verification activities during the iterative process to be performed with the same rules, and possibly codes, of the certification phase (the only possible most notable difference being the quality assurance requirements needed for fully complying with the safety authority demands during the licensing process, both from a software and analysis management procedures point of views). Design instead moves in a more free domain, thereby remaining the sole phase, in the development of a new reactor configuration, where actions to optimize the iterative process can be deployed.

The development of new LFR systems must fulfill all the objectives put forward by the GIF ^[1]. Extending the Generation IV safety philosophy also to the other areas (economics, sustainability, proliferation resistance and physical protection), provisions are to be “built in” the design, rather than “added to” configurations not yet scoring as aimed. As a matter of facts, this approach not only guarantees the fulfillment of the goals, but also top-scoring effectiveness and robustness, along with design simplicity, which is an asset for reliability and economics itself. For provisions to be built in, all the aimed performances and constraints are to be considered from early design stages, which is compatible with the degree of freedom of the design phase mentioned above.

Practically, this implies achieving the target objectives by a proper combination of materials and design, in which the latter comes in aid when the former ends. In the specific case of LFRs such a process involves the examination of all lead properties so that all weaknesses are coped with, while all advantages are exploited. The design is then set orienting choices so to take profit of inherent features, thus making it more robust and the chosen configuration either directly target-embedding, or compatible with the achievement of the goals; finally, should any objective be not fulfilled, complementing engineering provisions can be easily foreseen. These general considerations define the first requirement for design and safety analysis.



 RICERCA SISTEMA ELETTRICO	<u>Title:</u> Development of BE numerical tools for LFR design and safety analysis – Part 1	<u>Distribution</u> PUBLIC	<u>Issue Date</u> 12.12.2017	<u>Pag.</u> 16 di 300
	<u>Project:</u> ADP ENEA-MSE PAR 2016	<u>Ref.</u> ADPFISS-LP2-144	Rev. 0	

The second main aspect defining the requirements for design and safety analysis is the complexity of a reactor. Like a human body, it is indeed a complex system, made of several sub-systems (apparatuses), in turn made of several components (organs); all these components and sub-systems differ in nature, but are altogether strictly interfaced and interdependent: the design and verification of a reactor, therefore, has to take into account the performances and constraints not only of every single component by itself, nor just of the single sub-systems, but also of the entire reactor as a whole. Moreover, for each component – and even more so for each sub-system – a number of analyses (during both design and verification) are required on different fields. In Tab. 2, an overview of the aspects encompassed in the design and verification of the main reactor sub-systems is presented.

Reactor		Encompassed aspect				
		N	TH	TM	C	E
Sub-system	Core system	×	×	×		
	Primary system		×	×		
	Auxiliary and Ancillary systems		×	×	×	
	Instrumentation and control systems					×
	Reactor (integration)	×	×	×	×	×

Tab. 2 – Aspects encompassed in the design and verification of main reactor sub-systems (N: Neutronics; TH: Thermal-Hydraulics; TM: Thermo-Mechanics; C: Chemistry; E: Electronics).

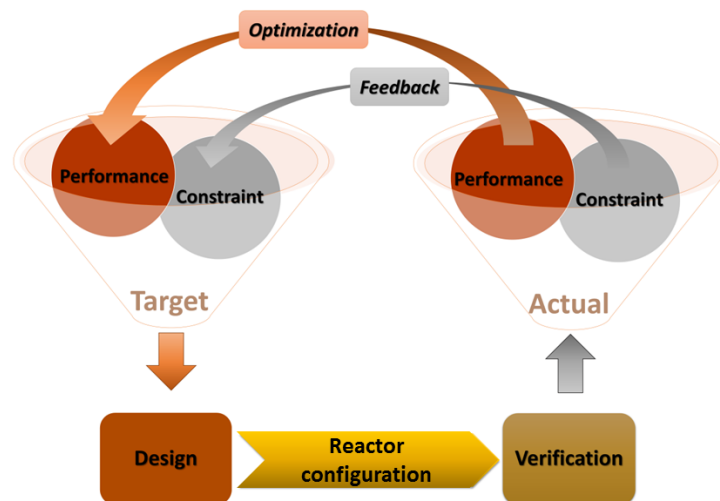



Fig. 2 – Iterative process of reactor configuration development



 RICERCA SISTEMA ELETTRICO	<u>Title:</u> Development of BE numerical tools for LFR design and safety analysis – Part 1	<u>Distribution</u> PUBLIC	<u>Issue Date</u> 12.12.2017	<u>Pag.</u>
	<u>Project:</u> ADP ENEA-MSE PAR 2016	<u>Ref.</u> ADPFISS-LP2-144	Rev. 0	17 di 300

3 CHARACTERIZATION OF THE MODELING NEEDS FOR THE SELECTED AREAS

The primary characteristic of the aimed platform is to effectively support the decision-making process. In practical terms, this can be translated in bringing to fruition the benefits of a rationale design or verification approach – logically the opposite of the trial-and-error one. Appropriate tools should be developed for each component or sub-system, and differentiated, wherever appropriate, depending on their application during the design or verification phase. It is worth stressing the fact that differentiating design- and verification-oriented tools – besides the trivial benefit of optimizing each for the aimed purpose – has also the additional benefit of domain separation, that allows a double, independent check of the design aspects, which is in line with all safety recommendations and best practices.

The last statement also defines the general philosophy for the development of the aimed platform in response to the modeling needs. Whilst specific requirements will be addressed in the following subsections, the general needs for tools of analysis in support to the design and verification, according to the specificities of these phases, are introduced.

Design-Oriented Tools

During the design phase, little or no information is available on the object itself of the design. Several scoping analyses are usually performed to down-select (*screening*) candidate options among all the possible ones. Corrective actions are often required to account for the impact of some aspects – related to one or more parameters – on the other parameters.

All these things put together, a computational tool effectively supporting the design process has to possess a number of instrumental features like:

- equilibrium,
- low computational times and
- a clear application domain.


A code satisfying these prerequisites is called a Design-Oriented Code (DOC)^[6]. It is also worth mentioning that these characteristics are synergistic, in the sense that they point in the same direction and, as such, they can effectively be met together. In the following, each of the mentioned features of a DOC will be discussed in more detail.

Equilibrium

With equilibrium it is intended a good balance between the ability of the code in reproducing experimental data on one side, and, on the other, the complexity of the implemented models and overall structure so to maintain a clear relationship among the various system parameters. It should therefore represent an clear improvement over analytical methods for what concerns accuracy and possibilities, while still keeping their clarity in relating constraints/performances to core parameters. This objective is believed to be crucial, since a very complex tool would hinder the user's understanding of the system under study, while an inaccurate one would render unusable or less significant the results, reducing the confidence of the user in utilizing them.

To better illustrate this concept, it can be assumed that the curve relating accuracy with model complexity – in the form of degree of completeness of the phenomena description – has the form reported in Fig. 2; the code general structure should therefore be placed on the point of optimal trade-off, where the minimum degree of complexity allows a satisfactory accuracy.



 RICERCA SISTEMA ELETRICO	<u>Title:</u> Development of BE numerical tools for LFR design and safety analysis – Part 1	<u>Distribution</u> PUBLIC	<u>Issue Date</u> 12.12.2017	<u>Pag.</u>
	<u>Project:</u> ADP ENEA-MSE PAR 2016	<u>Ref.</u> ADPFISS-LP2-144	Rev. 0	18 di 300

Even if vaguely introduced, the term “satisfactory accuracy” has actually a precise meaning. Equilibrium, indeed, also means that the various sources, contributing to the overall uncertainties, are balanced so to avoid excessive efforts to increase accuracy on terms that are already poorly contributing to the uncertainty on the final results. The terms in questions can be essentially divided in three categories:

1. input data
in terms of quality (and quantity) of the available input parameters; a DOC should indeed require a level of input detail fitting with the current design stage. Many input values are often not yet known and only a rough first estimate is usable in the early design stages; for such kind of parameters an extremely accurate (and thus complex) tool would be oversized, besides hindering the understanding of the relation between performances/constraints and configuration.
2. material properties
in terms of the only approximate knowledge stemming from measurement campaigns or the difficulty in reproducing particular conditions (e.g., irradiation effects, modification of the chemical environment). Depending on the specific physical field covered by the DOC under development, material properties can contribute significantly to the final uncertainties.
3. models
in terms of modeling errors; is the one directly under control of the DOC developer. Reducing this error, as previously discussed (see Fig. 3 – Hypothetical relation between complexity and accuracy of a model.
4.), implies a stronger modeling effort and thus code complexity. The contribution of this term should then be balanced with the effect of the other two so to avoid the coupling of a very refined and time consuming model with poor material properties or input data. This will enforce code homogeneity and modeling efficiency, both helping in keeping clear the link between performances/constraints and the resulting configuration.


Low computational times

While it is true that a DOC can help in understanding the features of the system being designed, due the non-bijective relation between the geometric configuration and the performances/constraints, a complete knowledge can never be achieved. This means that a DOC can help in rationally orienting choices for setting up a coherent configuration, but such a process would remain tentative in nature. Due to this, it could be desirable to test a number of configuration options and, as such, a DOC should be fast running with a low computational burden. Moreover, a sensitivity analysis could be performed to span the operational phase-space looking for quantitative correlations substantiating intuitive optimization strategies or for understanding safety margins in key parameters; since these are all generally time consuming tasks, short computational times must be pursued.

Clear application domain

To enhance confidence in the DOC results, simplifying their interpretation phase – necessary in a rational design process –, to facilitate Verification and Validation (V&V) activities, and to enable a clear comprehension of the calculation flow by the user, the application and validity domain must be openly stated. To carry this concept to the extreme, the application domain can be decided beforehand, so that it is unequivocally known, and equations and models derived accordingly. The idea is therefore, not to solve a set of equations and models and to see a posteriori their validity range – the approach historically followed –, but to select the equations and models in order to be consistent with an a priori decided application range. This will maximize efficiency in code development and simplify V&V activities.



 RICERCA SISTEMA ELETTRICO	<u>Title:</u> Development of BE numerical tools for LFR design and safety analysis – Part 1	<u>Distribution</u> PUBLIC	<u>Issue Date</u> 12.12.2017	<u>Pag.</u>
	<u>Project:</u> ADP ENEA-MSE PAR 2016	<u>Ref.</u> ADPFISS-LP2-144	Rev. 0	19 di 300

If the path of an a priori selection of the application range is not fully followed, the developer should at least make any effort engineeringly possible to make it as clear as possible.

Verification-Oriented Tools

During the verification phase, detailed information is available on the designed object. Single simulations are sufficient to evaluate each and every specific aspect whose knowledge is required. High-fidelity results are mandatory in response to the simulations, notably concerning safety-related aspects.

All these things put together, and proceeding in parallel with the previously discussed DOC characteristics, a computational tool effectively supporting the verification process has to possess a number of instrumental features like:

- accuracy,
- reasonable computational times and
- quality assurance.

A code satisfying these prerequisites is called a verification-Oriented Code (VOC)^[6]. In the following, each of the mentioned features of a VOC will be discussed in more detail.

Accuracy

The equilibrium requirement, for a VOC, is substituted by accuracy; a VOC indeed is meant at affording a higher degree of complexity (see Fig. 3) and at losing clarity in the name of accuracy. During the verification stage the system is fully characterized by the previous design phase and with the maximum degree of input information available; the real hindrance towards accuracy are bound to be material properties.

Reasonable computational times

Computational times, similarly to a DOC, should be as low as possible. Again in the name of accuracy, however, the increase of computational times can be afforded if this entails an increased precision. Compatibly with the available resources, and for those physical fields in which achieving considerable accuracy would require prohibitive computational times, techniques for refining only the more complex regions of the system while modeling in a simplified way their interconnections could be exploited.

Quality assurance


A point which is diriment for VOCs used in safety analysis for licensing purposes is the Software Quality Assurance (SQA). SQA is ideally important also for DOCs, but becomes mandatory for VOCs which produce results to be submitted to the safety authorities. When developing a VOC, therefore, all the best practices for managing the SQA must be put forward, significantly increasing the development effort as a whole; this is a strong incentive in moving towards already available qualified tools which, unfortunately, are generally not open source.

SQA plays also an indirect role when, during development, a strong level of accuracy is pursued, as this almost certainly increases code complexity. Indeed, SQA becomes increasingly more difficult to manage for complex software, making the development process more expensive in term of human resources. This can be another consideration to take into account when performing a weighted decision for selecting an already existing code or starting development from scratch.

Integration platform

Finally, focusing on the platform meant for hosting all the tools (DOCs and VOCs) required for the aimed integrated system supporting LFR systems' design and safety assessment, the following wish-list of features can be drafted:



 RICERCA SISTEMA ELETTRICO	<u>Title:</u> Development of BE numerical tools for LFR design and safety analysis – Part 1	<u>Distribution</u> PUBLIC	<u>Issue Date</u> 12.12.2017	<u>Pag.</u>
	<u>Project:</u> ADP ENEA-MSE PAR 2016	<u>Ref.</u> ADPFISS-LP2-144	Rev. 0	20 di 300

- A. to tackle the multi-physics, multi-scale and heterogeneous nature of the problem at hand, the platform must include a variety of codes, each responsible for one specific physical aspect and scale; ideally, even for the same aspect, different levels of modeling and computational complexity should be present so to make the platform more ductile relatively to the user needs;
- B. versatility must be pursued, meaning the ability to move from the necessities of a user design-oriented to the ones of a user verification-oriented so to support in full the LFR development chain;
- C. similarly to the previous requirement, inside the specific domain, be it design or verification, the possibility of freely and selectively (as much as physically and engineeringly possible) linking the available tools should be present, enabling the user to carry out specific tasks using the desired amount of complexity, from a physical, modeling and computational resources point of view;
- D. the flow of information between codes, handled by the platform, should be as efficient and clear as possible, to simplify the user understanding of the problem and aiding the final results interpretation phase, of the utmost importance in any rational endeavor;
- E. adding tools to the platform should be as easy as possible, helping in reducing the interface development time for any new tool to be added;
- F. to increase system portability and appeal, reliance on open software must be pursued as much as practicable. This requirement can battle with the need for qualified software accepted by safety authorities in the case of licensing applications, making the selection of codes and points A and C of this list non-trivial tasks.

3.1 Core Design


The design of the core is typically the first step in the process of developing a new reactor configuration. For the core, all the general arguments discussed in Sect. 2 hold; are anyhow worth mentioning, to complete the picture of this discipline, the heavily multi-physics, multi-scale and strongly heterogeneous aspects involved in this specific task.

Due to the central role of core design, the philosophy adopted by the Italian research community gravitates around the concept of “holistic design approach”, somehow anticipated in Sect. 2, that is: the inclusion of all the target constraints and performances deeply within the process, so as to set a final configuration fulfilling all these goals by-design. This approach permits also to develop approaches adjusted so as to permit the optimization of the iterative process, even accounting for the strict verification rules.

Due to the strong complexity of the problem, however, this simple statement to be put in practice requires mastering the process of translation of all the aforementioned constraints and performances – a priori known – in relations among the geometric, material and physical parameters defining a core configuration. As a matter of facts, the perfect, quantitative knowledge of these relations is the only key for the designer to properly setting-up a system configuration complying with all the requirements. Such relations can sometimes originate from experience or from the use of simple physical/empirical correlations; due however to the heavy interdependence among the many multi-physical, multi-scale and very different aspects encompassed in the core design, dedicated tools suitably developed as DOCs can be of great aid.

Before substantiating the modeling needs deriving from this approach, according to the general scheme presented in Sect. 2, an overview of the components to be designed and aspects to be considered for each of the latter is presented. In fact, being the core a system-in-the-system, a number of elementary components can be identified, each with its specificities and thus requiring a dedicated approach for its design. The “core” entry in Tab. 2 can therefore be exploded as shown in Tab. 3.



 RICERCA SISTEMA ELETTRICO	<u>Title:</u> Development of BE numerical tools for LFR design and safety analysis – Part 1	<u>Distribution</u> PUBLIC	<u>Issue Date</u> 12.12.2017	<u>Pag.</u>
	<u>Project:</u> ADP ENEA-MSE PAR 2016	<u>Ref.</u> ADPFISS-LP2-144	Rev. 0	21 di 300

The logical scheme of the process of core design according to the holistic approach is also shown in Fig. 4 specifically for the case of an LFR.

The aspects encompassed in core design, along with examples of their application to the core components and proposed tools meant for inclusion in the simulation platform for supporting their design, are briefly discussed in the following subsections.

3.1.1 Thermal-hydraulics

Elementary cell

The elementary cell design is heavily guided by thermal-hydraulics considerations: apart from the minimum operating temperature which is fixed by the margin to coolant freezing, all the upper bounds are actually established by the ability of the steel structures to safely operate in a lead environment, meaning to limit corrosion processes to acceptable levels. The elementary cell must therefore be sized to guarantee the respect of the clad temperature constraint – allowing also for uncertainty margins – and to limit coolant velocity and the consequent erosion dynamics. Another important, safety-related objective is to assure the onset of natural circulation at affordable temperatures; this is particularly important in the case of a Loss Of Flow (LOF) accident (notably under Unprotected conditions – ULOF) in order to avoid excessive cladding temperatures and the risk of a short time creep failure or even melting. To achieve this, low pressure drops through the fuel bundle are necessary; and a suitable dimensioning of the elementary cell must therefore be pursued.

Proposed software:

To aid the designer in this process, simplified codes able to simulate the dynamic behavior of the core in supposed transients can be used. The **BELLA** code^[7] is an existing tool possibly fitting this role, especially for the safety-related part, since it features the DOC characteristics, being able to simplify the problem description while preserving the salient relationship between the physical quantities of interest. Indeed it is a simplified tool acting as a bridge with system codes and so naturally suited for implementing the safety-informed design approach mandatory for Gen-IV systems.

For the verification phase, no specific code is required for the elementary cell, as its analysis is included in general system studies.


Sub-assembly (S/A)

The main objective during the S/A thermal-hydraulic sizing is to guarantee a uniform radial profile of the coolant temperature and adequate cooling for all the pins in the bundle. This is important, especially, for enclosed Fuel Assembly (FA) concepts. The primary objective is to avoid local hot spots, cold by-passes and to reduce thermal gradients which could create unwanted mechanical stresses. The pressure drops through the main components of the S/A such as spacers, foot and any other relevant area change or narrow paths must also be such that the benefits of a wide elementary cell are not overshadowed by excessive pressure losses in other S/A components. From the safety point of view, the threat of a flow blockage due to cooling channel plugging via corrosion/erosion products sedimentation, coolant solidification or any foreseeable occlusion agent must be prevented as much as practicable, or mitigated in the residual cases.

Proposed software:

To this aim the sub-channel code **ANTEO+**^[8] could be efficiently used, since it has been specifically developed following the guidelines of a DOC as discussed in Sect. 3. ANTEO+ has also been extensively validated making its use during the design phase even more meaningful with the concrete possibility of assessing uncertainties on the main quantity of interest so to allow for sufficient margins.



 RICERCA SISTEMA ELETTRICO	<u>Title:</u> Development of BE numerical tools for LFR design and safety analysis – Part 1	<u>Distribution</u> PUBLIC	<u>Issue Date</u> 12.12.2017	<u>Pag.</u>
	<u>Project:</u> ADP ENEA-MSE PAR 2016	<u>Ref.</u> ADPFISS-LP2-144	Rev. 0	22 di 300

For validation purposes, the punctual analysis of specific aspects can be investigated by means of Computational Fluid Dynamics (CFD) codes as FLUENT^[9] (or any other commercial code) or OpenFOAM^[10], the former having the robustness and maturity of commercial codes, the latter the openness to modifications as required, being open-source.

Core

The core thermal-hydraulic design is, in a way, similar to the FA one; cold by-passes must be avoided, especially in the case closed FAs are used, but, at the same time, excessive thermal gradients among opposite faces of the FA ducts prevented. This means assuring a suitable coolant flow outside the FAs themselves, which has to be determined according to the inter-assemblies gap, established by the thermo-mechanical design. If a wrapped FA is used, the possibility of gagging arises, giving an extra degree of freedom to the designer for actually leveling thermal gradients at the FA outlet. During the core thermal-hydraulic design, the amount of pressure drops necessary to balance the coolant flow with the FA power must be calculated and a gagging zoning proposed so to achieve a lifetime optimum configuration, while still keeping low fabrication costs.

Proposed software:

No DOCs are available in the open literature to support the thermal-hydraulic design of an LFR core. For the by-pass problem, the development of a specifically dedicated tool has already been planned. For the gagging problem, due to the relevant connection with the FA and by-pass problems, it is sought a coupling between the future by-pass DOC with ANTEO+ to perform all the needed analyses.

For the validation of the by-pass, the same CFD tools presented for the FA problem can be envisaged. Concerning the gagging problem, as for the elementary cell case, no specific tool is required, the analysis being part of general system studies.

3.1.2 Thermo-mechanics

Pin

The pin thermo-mechanic design is aimed at ensuring on one hand that the fuel temperature be lower than the melting one, allowing margins for uncertainties, in nominal and accidental conditions (with particular regard to the Unprotected Transient of Over-Power – UTOP); on the other hand, at assuring the integrity of the cladding via its ability to withstand both the internal pin pressure, arising from gas release due to fission (in fuel pins) or boron captures (in absorber pins), and pellet-clad mechanical interactions stemming from swelling, thermal expansion and cracking of the pellet. Being in particular the fuel pin cladding the first engineered barrier against the dispersion of radioactivity, ensuring its integrity is of paramount importance in the overall design process.

Proposed software:


To what concerns the pin design, the TEMIDE code^[6] can be employed on the platform, since it has been specifically developed for fuel pins following the DOC guidelines discussed in Sect. 3, and is also undergoing a preliminary validation.

For validation purposes, no available code has undergone the requested extensive validation, as experimental information on pins irradiated in fast spectrum are not so abundant in the open literature. However, sophisticated codes such as TRANSURANUS^[11] can be chosen for the purpose of fuel pins thermos-mechanic verification.

Sub-assembly

The S/A is a complicated system from the thermo-mechanical standpoint, chiefly for the enclosed concepts. Any interaction among pins and between the pins and the wrapper, due to differential swelling and thermal



 RICERCA SISTEMA ELETTRICO	<u>Title:</u> Development of BE numerical tools for LFR design and safety analysis – Part 1	<u>Distribution</u> PUBLIC	<u>Issue Date</u> 12.12.2017	<u>Pag.</u>
	<u>Project:</u> ADP ENEA-MSE PAR 2016	<u>Ref.</u> ADPFISS-LP2-144	Rev. 0	23 di 300

bowing, must be avoided or at least limited to acceptable values; this also includes the spacing means used to form the bundle, which have to restrain the pins while preventing (or reducing below the threshold for significant fretting) flow-induced vibrations. The structural skeleton of the S/A also has to provide the stiffness required for core stability and safe handling.

Proposed software:

This particular field is presently poorly covered and no DOC is available for inclusion in the platform; this suggests that for further advancing LFR projects development, work on this sector should be a priority. Due to the very peculiar nature of the phenomena to be accounted for, it is questionable that existing codes for thermo-mechanic analysis (such as ANSYS^[12]) can be applied to the extent required for validation purposes.

Core

The mechanical core design is strongly related to the mechanical design of the S/A. The collective behavior of the S/As under the actions of differential bowing can generate forces to be managed to ensure core integrity and the possibility of S/A handling; conversely, if gaps are allowed between the S/As to avoid contact forces, the possibility for positive reactivity insertion due to compaction appears, which is to be avoided or reduced to manageable values. The restraint of the core is achieved by properly designing the S/A support structures (upper and lower core plates, where present), the S/A structural skeleton and the structure perimetering the core (barrel).

Proposed software:

In complete analogy to the previous paragraph, no DOC is actually available, nor VOC fully applicable, for such tasks and competences in this field should be strengthened in the Italian framework.

3.1.3 Neutronics

Core


The main purposes of the core neutronic design involve i) the definition of the fuel enrichment and/or enrichment zoning which guarantee the operability of the reactor for the foreseen time span, respecting all the constraints on the maximum burn-up along with requirements on the cladding and fuel temperatures; ii) the sizing and positioning of redundant, diverse and independent banks of control and safety rods, able to manage any reactivity excursion during normal operation (from startup/shutdown to criticality swing and power excursions) and emergency. On the fringes of the core neutronic design, there is the evaluation of the core reactivity coefficients so to allow safety analysis and dynamic studies to be performed. Although LFRs, thanks to the huge margins offered by the coolant, usually present a very forgiving behavior in accidental conditions, it could be the case that the optimization of the reactivity coefficients enters the core design process, mainly at the level of neutronics (even if also thermo-mechanics and thermal-hydraulics play important roles).

Proposed software:

To achieve all the mentioned objectives the code ERANOS^[13] could be used, since specifically developed for fast reactors and with intentions going in the direction of a DOC. Moreover, the two-steps approach – with cells and core calculations – is still the most suited (in many cases) for preliminary design evaluations. The main limitation of ERANOS is its non-open-source nature; an alternative in this sense could be the DRAGON/DONJON suite^[14]. These tools, although not strictly DOCs nor powerful as ERANOS, are one rare example of open-source software in the deterministic neutronics field.

For validation purposes, Monte Carlo codes are usually chosen because of their superior capability at modeling the system than deterministic ones. Among the most advanced Monte Carlo codes available,



 RICERCA SISTEMA ELETTRICO	<u>Title:</u> Development of BE numerical tools for LFR design and safety analysis – Part 1	<u>Distribution</u> PUBLIC	<u>Issue Date</u> 12.12.2017	<u>Pag.</u>
	<u>Project:</u> ADP ENEA-MSE PAR 2016	<u>Ref.</u> ADPFISS-LP2-144	Rev. 0	24 di 300

MCNP^[15] outstands for the level of development and validation, even though its use is restricted by export control rules. Alternatively, Serpent^[16], although less mature, can be considered as open-source code.

Shielding

Shielding analysis, mostly dealing with neutronics (or better, radiation transport), has the twofold objective of i) ensuring that the radiation-induced damage to the reactor structures remains below acceptable limits; ii) ensuring that the radiation levels in all the premises of the reactor (especially if human access is considered) remain below the limits set for radiation protection.

Proposed software:

Shielding analysis is an activity for which design and verification phases typically merge together. For close-to-the-core analyses (e.g., structural damage), coupled deterministic and Monte Carlo codes can be used, to facilitate the latter in defining effective variance reduction approaches; for analyses far from the active zone (e.g., radiation protection), Monte Carlo codes by themselves are typically used. All the codes listed in the previous paragraph can be used as well for the purpose of shielding.

3.1.4 A possible platform layout (limited to core design activities)

Putting together all the requirements for the complete design and verification of the reactor core, and considering the codes available or to be developed to fill emerged gaps that were listed in the previous subsections, it is possible to draft a preliminary layout of the aimed platform, at least for what concerns the core. The general layout of the platform to what concerns core design/verification is shown in Fig. 5.

According to the presented taxonomy, some possible utilizations of the platform are qualitatively illustrated in the following.

Neutronic analysis with thermal-hydraulic feedback


The impact of the temperature field on the core neutronics, meaning criticality and power distribution, plays a non-negligible role, and has to be investigated to understand how much the power flattening effect resulting from the thermal feedback can help in reducing gradients and hot spots inside the core.

In the supposed platform, the problem could be tackled in a variety of ways, each with an increasing level of detail or focusing on a particular facet of the problem at hand. Having as reference Fig. 5, the following calculation schemes and interconnections could be exploited for design purposes:

1. As depicted in Fig. 6 a simplified approach based on a cell code (ECCO or DRAGON) and the core code FRENETIC^[17] can be elaborated. The cell code is used to compute the macroscopic cross sections for a particular thermal state; these information are then passed to FRENETIC which computes the overall power distribution and, on this basis, a lumped-values the temperature field in the fuel, structures and coolant. At this point the new thermal state at each S/A level is passed back to the cell code to update the cross sections matrix. The process is repeated until convergence.
2. A more elaborate and complete scheme could also be used by switching from FRENETIC to the core analysis modules in ERANOS/DONJON, and including the thermal-hydraulic feedback at sub-channel, rather than S/A, level, by means of the ANTEO+ code. For even more accurate information the thermo-mechanic feedback at pin level can be included by means of the TEMIDE code. The mentioned coupling process is reported in Fig. 7.

The platform also allows to perform the same analysis with verification purpose: in this case, the most detailed coupling scheme is used, as the one shown in the previous case, with all DOCs replaced by VOCs



 RICERCA SISTEMA ELETRICO	<u>Title:</u> Development of BE numerical tools for LFR design and safety analysis – Part 1	<u>Distribution</u> PUBLIC	<u>Issue Date</u> 12.12.2017	<u>Pag.</u>
	<u>Project:</u> ADP ENEA-MSE PAR 2016	<u>Ref.</u> ADPFISS-LP2-144	Rev. 0	25 di 300

and respectively: from ECCO/ERANOS or DRAGON/DONJON to MCNP or Serpent for the transport solution, from ANTEO+ to Fluent or OpenFOAM for the thermal field in the coolant, and from TEMIDE to TRANSURANUS for the thermal field in the fuel, obtaining the new, equivalent scheme shown in Fig. 8.

Core restrain system design

To present the power of such a platform, one of the most complex calculation schemes is here presented, concerning the design of the core radial restraint, as it encompasses the neutronic, mechanic and thermal-hydraulic fields. A possible code correlation is shown in Fig. 9: the power distribution computed by the neutronic DOC is given to thermal-hydraulic tools at both sub-channel and by-pass level in order to retrieve the main temperature field in the whole core; this information is then used by the thermo-mechanic codes at pin, S/A and core level to understand the radial and axial deformations of the components in order to provide relevant information to properly design the restraining system.

3.2 Primary system design R&D development needs

3.2.1 Identification of the key topics for the LFR development

R&D efforts are necessary for completing the design, support the pre-licensing and starting with the construction of such systems. Such activities require the identification of the technological gaps, which are design dependent, and the key topics for LFR developments. The LFR technological issues have been divided into the following main topics^{[25]-[31]}:

- Material studies and coolant physical-chemistry;
- Studies of core integrity, moving mechanisms, instrumentation, maintenance, in service inspection and repair;
- Steam Generator functionality and safety experimental studies;
- Thermal-hydraulics;
- HLM pump reliability;
- Instrumentations;
- Advanced fuels and Irradiation Testing;
- Neutronics;

3.2.2 LFR material studies and coolant physical-chemistry


Corrosion by liquid metal

Corrosion of structural materials in lead is the main issue for the design of LFR. The topic is related to lifetime limits and circuit design. The following sub-issues are considered:

- Corrosion in Lead of
 - ✓ fuel cladding,
 - ✓ vessel,
 - ✓ reactor internals,
 - ✓ components, and
 - ✓ heat exchangers;
- Corrosion at high temperatures (related to development for long term perspectives);
- Corrosion of pump impeller materials;
- Corrosion inhibitors development (i.e. coating);

Efforts have been devoted to short / medium term corrosion experiments in stagnant and flowing LBE. Few experiments were carried out in pure Lead (i.e. CHEOPE III at ENEA). Research activities are still needed



 RICERCA SISTEMA ELETRICO	<u>Title:</u> Development of BE numerical tools for LFR design and safety analysis – Part 1	<u>Distribution</u> PUBLIC	<u>Issue Date</u> 12.12.2017	<u>Pag.</u>
	<u>Project:</u> ADP ENEA-MSE PAR 2016	<u>Ref.</u> ADPFISS-LP2-144	Rev. 0	26 di 300

on medium/long term corrosion behaviour in flowing lead. The following list of facilities is available for investigating heavy liquid metals corrosion at ENEA:

- LECOR (ENEA), $T_{max}= 500^{\circ}\text{C}$, $v_{max}= 1 \text{ m/s}$, fluid Pb
- HELENA (ENEA), $T_{max}= 500^{\circ}\text{C}$, $v_{max}= 2 \text{ m/s}$, fluid Pb

A specific Pb loop able to achieve higher temperature (at least 650°C) and 2 m/s is still missing and is identified as potential required infrastructure to cover long term development of the technology as well as to perform specific tests under particular conditions (i.e. DBA).

Embrittlement and degradation of structures by liquid metal

The condition represents the lower bound of mechanical properties of liquid metal exposed materials. It consists in the reduction of fracture toughness and of ductility of un-irradiated materials after long term exposure to lead.

It is necessary to experience and to standardize (in order to be reproduced with a typical standard procedure) tests with respect to:

- LME,
- fatigue,
- creep,
- stress corrosion cracking, and
- fretting in HLM.

These experiments are necessary and must be conducted in testing machines where the specimens are exposed to the liquid metal effect, both static and flowing tests. There is only one facility available at ENEA for investigating fretting of structures by liquid metal:

- GIORDI (ENEA), $T_{max}=550^{\circ}\text{C}$, Pb and LBE

Pb facilities devoted to the investigation of embrittlement, fatigue, creep SCC up to 650°C in liquid metal, under oxygen control are still missing and represent required infrastructures.

High temperature materials for long term perspectives


Full development of GEN IV programmes foresees the future increase of reactors operating temperatures (beyond 550°C). This evolution is aimed to enhance the thermodynamic efficiency and to allow the association of side energy production efficient processes. This challenging goal requires, to test:

- “new” materials such as ODS steels, refractory alloys, SiC composites, “MAX” phase materials;
- coated materials as developed by GESA treatment, PLD (@IIT), CVD-Ta.

The testing conditions are:

- $650\text{-}800^{\circ}\text{C}$ lead temperature,
- 1 – 2 m/s lead velocity.



 RICERCA SISTEMA ELETTRICO	<u>Title:</u> Development of BE numerical tools for LFR design and safety analysis – Part 1	<u>Distribution</u> PUBLIC	<u>Issue Date</u> 12.12.2017	<u>Pag.</u>
	<u>Project:</u> ADP ENEA-MSE PAR 2016	<u>Ref.</u> ADPFISS-LP2-144	Rev. 0	27 di 300

Currently test can be performed by the RACHELE laboratory (ENEA) with these conditions in stagnant HLM. Since the existing facilities for corrosion testing are not able to achieve 650-800°C in flowing lead, new infrastructures are necessary to meet these requirements.

Irradiation effects on materials

The reactor pressure vessel, the structural materials, the internals and the fuel cladding are subjected, with different extent, to several degradation mechanisms such as neutron irradiation, thermal ageing and corrosion. In case of HLM systems, research activities are generally aiming at understanding, quantifying and predicting such effects on critical components of a nuclear power plant. Focus is given on the performances of the materials in terms of (neutron irradiation induced) embrittlement, on the behavior of stress corrosion, as well as neutron irradiation induced effects such as creep and swelling. The main objective is to determine whether or not irradiation will promote embrittlement and corrosion attack by HLM.

The current status of knowledge is not completely addressed, and more experimental investigations are needed, providing high quality data on the material behavior. It is expected that assessments of fuel cladding and structural core materials, subjected to both high temperature in a lead environment and fast flux, are critical issues.

Summarizing the following main issues on irradiation performance of candidate materials are of primarily importance for LFR systems development:

- Corrosion in HLM under irradiation (coated and uncoated material);
- Irradiation embrittlement of selected materials;
- Irradiation creep;
- Swelling.

The effects of irradiation on materials is a critical issues for LFR system development. The experimental infrastructure needed to address these issues are currently available irradiation machines and research reactors.

Impeller pump materials

The relatively high speed between structural material and HLM implies that the pump impellers are subjected to severe corrosion-erosion conditions that might not be sustained in the long term. Tests are planned on specimens of materials. The materials of the pump impeller have to satisfy a couple of demanding requirements which deserve specific experimental installation:


- capability to withstand to an exposure to high temperature lead (up to 480°C, and higher for long term perspective);
- capability to withstand to corrosion/erosion effects due to high relative coolant velocity (10 m/s, and up to 20m/s);
- demonstration of reliability and performances of the pump for a long term application.

A new infrastructure is under operation in ENEA: HELENA loop. It is aimed at investigating the issue above, testing the prototypical pump impeller (i.e. geometry and material).

Coolant chemistry control

Chemistry control of the coolant and cover gas is a critical issue of operating HLM systems. It is essential to control the concentrations of impurities, because of the potential for activation and also because of the possible effect on corrosion, mass transfer and scale formation at heat transfer surfaces. Therefore, coolant



 RICERCA SISTEMA ELETTRICO	<u>Title:</u> Development of BE numerical tools for LFR design and safety analysis – Part 1	<u>Distribution</u> PUBLIC	<u>Issue Date</u> 12.12.2017	<u>Pag.</u>
	<u>Project:</u> ADP ENEA-MSE PAR 2016	<u>Ref.</u> ADPFISS-LP2-144	Rev. 0	28 di 300

chemistry control includes oxygen, but also pollution source term studies, mass transport and filtering and capturing techniques. The following specific issues are considered:

- Coolant control and purification during operation (i.e. oxygen control, oxygen sensor reliability, coolant filtering, HLM purification, HLM cleaning from components);
- Cover gas control (i.e. radiotoxicity assessment of different elements, migration flow path into cover gas, removal and gettering).

Currently test related to oxygen control issues can be performed by the RACHELE laboratory (ENEA). Facility aiming to study metal evaporation is missing in ENEA. Other facilities are under design or planned to cover topics, such as the HLM purification. In this connection, it should be noted that specific issues, such as testing of filtering systems or corrosion products source term and transport, can be addressed in facility already available constructed for other purposes (i.e HELENA, NACIE, CIRCE).

3.2.3 LFR studies of Core integrity, moving mechanisms, instrumentation, maintenance, in service inspection and repair

Fuel manipulator

The fuel manipulator (or handling) system is used for the purpose of controlling the reactor power distribution (by off-line shuffling). The system is also in charge of storing and handling the fuel assemblies during its overall lifetime (i.e. from the arrival up to the storage of spent fuel). In current LFR design, refuelling and shuffling are performed remotely. The design and the operation of such machine, has to be tested before the installation in the reactor, for demonstrating its capability to fulfil his functions in reliable and safe way. This requires the assessment in an experimental facility of the prototype machine as well of its component for qualification purposes. On this regard, the following sample experimental activities are considered:

- cold testing of components (in air);
- testing of submerged components;
- reliability of fuel handler components;
- integral test, including fuel recovery strategy and in core rescue strategy.


In this frame CIRCE facility might be in principle suitable for addressing the issues, thanks it high flexibility. Nevertheless, considering the time schedule for testing the current designs, an new experimental infrastructure is compulsory for LFR development.

Fuel assembly structure and support

The fuel channel assemblies support and locate the fuel within the reactor core, facilitate the cooling of the fuel and provide shielding from radiation streaming from the core. Therefore, different issues need to be experimentally tested to verify the suitability of the design features, including ensure the structural integrity of the fuel assembly. The following list can be considered:

- mechanical and structural integrity of fuel assembly, in connection with
 - ✓ fuel loading procedure,
 - ✓ wide range of operating conditions;
- flow induced vibrations;
- spacer grids fuel pin interactions.



 RICERCA SISTEMA ELETRICO	<u>Title:</u> Development of BE numerical tools for LFR design and safety analysis – Part 1	<u>Distribution</u> PUBLIC	<u>Issue Date</u> 12.12.2017	<u>Pag.</u>
	<u>Project:</u> ADP ENEA-MSE PAR 2016	<u>Ref.</u> ADPFISS-LP2-144	Rev. 0	29 di 300

The topics of investigations above are considered as part of the studies discussed in the previous section and in section related with fuel assembly hydro-dynamics.

Core arrangement integrity and safety systems (control rods)

The bases for the core design need to be investigated in connection with the influence of the neutronics on regulating and shutdown systems, which are designed to meet requirements set for the normal and abnormal (accident) conditions. The areas of investigations related to neutronics and reactor kinetic are described later. On the contrary, the present section consider all topics related to the issues, which involve the core cool-ability, integrity and the behavior of the safety systems (i.e. control rods). The following areas of investigations are considered:

- loss of core cool-ability and integrity
 - ✓ identification of the initiating events, including connections with control rods mechanisms design (e.g. control rod withdrawal and ejection) and integral tests;
 - ✓ fuel coolant interaction,
 - ✓ fuel degradation mechanisms and its behavior (up to its release in the primary system),
 - ✓ dispersion and relocation of fuel in primary system,
 - ✓ impact of seismic loads and sloshing;
- control rod(s) design and mechanisms
 - ✓ testing of control rods mechanisms operation and performance,
 - ✓ reliability of control rods mechanisms and components,
 - ✓ impact of seismic loads and sloshing: demonstration that the system is qualified to Design Basis Earthquake to permit shutoff rods to drop into the core.

The experimental infrastructures suitable to investigate the topics is the multipurpose facility CIRCE. This facility does not cover all issues connected with the LFR design development.

In particular, instrumented hot cells are mandatory to address fuel-coolant interaction, fuel degradation, fuel dispersion and fuel relocation.

Therefore, the availability of new facility is considered necessary for supporting the LFR system development. These infrastructures shall be devoted primarily to the study of the sources of core damage events including the assessment of severe accident, the investigation of the fuel coolant interaction, the testing of the control rods operation, the consequences of the seismic loads on core structures and the fuel dispersion in primary system.


3.2.4 Steam Generator functionality and safety experimental studies

LEAD-water interaction

LFR designs are pool type reactors, which have the steam generators (or the heat exchangers) inside the reactor vessel. This implies that the interaction between the secondary side coolant and the HLM may occur. Thus, the primary to secondary leak (e.g. steam generator tube rupture) shall be considered as a safety issue in the design, but also in the preliminary safety analysis, of these reactor types. Two are the topics of investigation in case of Steam Generator Tube Rupture (SGTR) postulated event: to understand the phenomena involved in the accident scenario, and to study how to prevent or mitigate the consequences of the event, reducing the primary system pressurization. In synthesis, areas of investigation are:

- Phenomena /processes:
 - ✓ pressure wave propagation across the primary system,
 - ✓ sloshing,



 RICERCA SISTEMA ELETTRICO	<u>Title:</u> Development of BE numerical tools for LFR design and safety analysis – Part 1	<u>Distribution</u> PUBLIC	<u>Issue Date</u> 12.12.2017	<u>Pag.</u>
	<u>Project:</u> ADP ENEA-MSE PAR 2016	<u>Ref.</u> ADPFISS-LP2-144	Rev. 0	30 di 300

- ✓ steam transport in primary system,
- ✓ steam entrainment into the core,
- ✓ LEAD-water interface phenomena;
- Rupture/leakage detection systems;
- Tube rupture mitigation countermeasure.

The existing facilities addressing the topic is LIFUS 5. Recently, experiments related to LBE/LEAD-water interaction were executed in LIFUS 5 facility. The tests are performed for understanding the phenomena and for developing and validating the numerical models at small scale. The results of the experiments, due to scaling effects, cannot be directly extrapolated to reactor scale. Analogously, the models developed and implemented in the computer codes require implicit assumption that they have the capabilities to scale up the phenomenon from test facility to full scale plant conditions: this is not ensured a priori.

A new European infrastructure having larger scale is necessary in view of the construction of LFR systems. The facility (i.e. ATHENA) will permit: a) reliable representation of safety parameters at reactor scale, b) to improve the knowledge of the phenomena / processes, in geometrical and operating conditions more representative of the real reactor, and, c) to address the scaling issue in connection with code applications for design and safety analysis purposes.

Steam generator

The steam generator has to be installed directly in the HLM pool. This solution implies the simplification of the design: nor loops in primary system, neither intermediate loops (such as in sodium fast reactor designs). For these reasons, the SG is of overall importance and deserves accurate studies and evaluations to be qualified. The main qualification studies regard:

- design validation;
- unit isolation on demand;
- pressure drop characteristics;
- component behaviour in
 - ✓ normal operation (e.g. forced, mixed and natural convection);
 - ✓ operational transients and accident conditions.

The existing CIRCE facility (ENEA) is suitable for the tests, provided that enough safety is granted towards tube rupture, such as in case of double tube heat exchange. The DHR, with a double tube exchanger, has already been tested at 800 kW power.


Adequate testing and qualification in lead (LFR) requires a new infrastructure, because CIRCE is operated with LBE and cannot deal with the tests involving the tube rupture risks of steam generator (at secondary side pressures typical of LFR design). For economic reasons, the issue connected with the steam generator qualification and the investigations on steam generator tube rupture might be carried out in a single complex facility, having a large scale (i.e. large volume like ATHENA).

Auxiliary nuclear systems

Apart from the steam generator, in a reactor there are several auxiliary systems which need to be qualified for nuclear applications. The following systems are mentioned:

- Decay heat removal system (DHR);
- Dip-coolers and isolation condenser;
- Reactor vessel auxiliary cooling system (RVACS);



 RICERCA SISTEMA ELETTRICO	<u>Title:</u> Development of BE numerical tools for LFR design and safety analysis – Part 1	<u>Distribution</u> PUBLIC	<u>Issue Date</u> 12.12.2017	<u>Pag.</u>
	<u>Project:</u> ADP ENEA-MSE PAR 2016	<u>Ref.</u> ADPFISS-LP2-144	Rev. 0	31 di 300

- Fuel assembly transport system;
- Spent fuel element transport and cooling system.

The only facility identified to test and qualify the systems above is CIRCE (ENEA), but its application is undergone the availability of suitable test sections and instrumentation. Anyway it is mandatory to outline that due to the planned experiments, CIRCE will be not available to be used for investigating the auxiliary systems of LFR design. A new large scale multipurpose facility it seems mandatory.

3.2.5 Thermal hydraulics

HLM pool thermal-hydraulics

Since several years, the research on heavy liquid metals thermal-hydraulics has been conducted in Italy and in Europe. Nevertheless, open issues are still pending for HLM system development.

The objectives of the activities in relation to pool thermal-hydraulics is twofold: 1) gathering experimental data in geometry and with boundary conditions which may improve the knowledge of phenomena/processes at component and system levels; 2) generating databases for supporting the development and demonstrating the capability of computer codes to predict phenomena/processes relevant for the design and safety. The following not exhaustive list of topics is identified as relevant at component and system levels:


- flow patterns in forced convection, including
 - ✓ mixing,
 - ✓ stratification (inducing thermal stresses),
 - ✓ stagnant zones,
 - ✓ surface level oscillations;
- transition to buoyancy driven flow;
- natural convection flow
 - ✓ pressure drop
 - ✓ surface level oscillations
- fluid structure interaction,
- thermal fatigue issue; and
- sloshing due to seismic event tests.

In Italy the only facility suitable to address the topics of investigations above, assuming that a suitable instrumentation is installed, is CIRCE (ENEA). Anyway the refurbishment and upgrade of the CIRCE facilities is not sufficient and a new facility has to be envisaged for pool thermal hydraulics. Regarding the seismic testing, existing earthquake vibrating platforms (e.g. in ENEA) are suitable to investigate the fluid motion in scaled down vessel filled with heavy liquid metal. A dedicated infrastructure addressing the issue might be required. In conclusion, the need of investigating issues connected with the pool thermal-hydraulics is considered a necessary prerequisite for developing LFR/ADS systems.

Fuel Assembly thermal-hydraulics

Thermal-hydraulic of nuclear fuel assemblies has the objective to develop such geometry of the assembly with spacers, which will provide optimal conditions for heat transfer between fuel rods and coolant. Moreover, the fuel assembly should demonstrate the capability to withstand to irradiation, high temperatures, mechanical loads and corrosion environment with minimal changes in stiffness characteristics and geometry. The areas of investigations include the fuel assembly thermal-hydraulics and hydrodynamics for a wide range of operating conditions. The objectives of the activities in relation to fuel assembly thermal-hydraulics and hydrodynamics is: 1) gathering experimental data for geometries and boundary conditions consistent with the design prototype; 2) generating databases for computer code development and validation.



 RICERCA SISTEMA ELETTRICO	<u>Title:</u> Development of BE numerical tools for LFR design and safety analysis – Part 1	<u>Distribution</u> PUBLIC	<u>Issue Date</u> 12.12.2017	<u>Pag.</u>
	<u>Project:</u> ADP ENEA-MSE PAR 2016	<u>Ref.</u> ADPFISS-LP2-144	Rev. 0	32 di 300

For design purposes, it is important to test the fuel assembly on the basis of thermal-hydraulics parameters (i.e. pressure losses, flow distribution, velocity field, clad wall temperature distribution, etc.) and the geometrical features, such as: rod bundle lattice, sub-channel geometry, spacer grids.

The following not exhaustive list of topics should be experimentally investigated for supporting LFR systems development:

- heat transfer in forced and natural convection (including transition);
- sub-channel flow distribution;
- cladding temperature distribution and hot spot;
- pressure drop;
- fluid structure interaction;
- ✓ flow induced vibrations;
- grid-to-rod fretting;
- fuel assembly bow

The topics of investigations involve also the study of the sources and the consequences of core damage. No facility is available for investigating this issue. Moreover, some of the topics above are connected and already mentioned in section related to “Fuel assembly structure and support”.

In ENEA three facilities are currently operated (i.e. CIRCE, NACIE and HELENA). These experimental infrastructures are suitable for investigating the issues above reported. On the basis of the fuel assembly design, specific test sections can be developed and installed in these facilities.

Integral tests


Integral tests data are, in principle, applicable to full scale nuclear plant conditions. Nevertheless, the data can be extrapolated to full scale, if the test facilities and the initial and boundary conditions of experiments are properly scaled, i.e. the scaling will not affect the evolution of physical processes important for the postulated accident scenario. This evaluation determines whether the data may be used in nuclear plant safety analyses.

On the other side, integral tests are fundamental for supporting the development and demonstrating the reliability of computer codes in simulating the behavior of a NPP, during a postulated accident scenario: in general, this is a regulatory requirement. Applications of computer codes to accident analyses require the implicit assumptions that these codes have the capabilities to scale up phenomena and processes from test facilities to full scale plant conditions. However, the different scale, in terms of geometry, characterizing any facility and a nuclear plant does not ensure a priori that a code, which is able to reproduce a generic transient in a scaled facility, is also able to calculate with the same accuracy the same transient in NPP.

These considerations implies that integral tests are unavoidable and complex activities, which involve the following objective and areas of investigations:

- phenomena and processes of interest at system level and connected with design, safety and operation issues;
- simulations and analyses of a broad spectrum of accident scenarios;
- accident management procedures;
- component testing;
- scaling issue;



 RICERCA SISTEMA ELETTRICO	<u>Title:</u> Development of BE numerical tools for LFR design and safety analysis – Part 1	<u>Distribution</u> PUBLIC	<u>Issue Date</u> 12.12.2017	<u>Pag.</u>
	<u>Project:</u> ADP ENEA-MSE PAR 2016	<u>Ref.</u> ADPFISS-LP2-144	Rev. 0	33 di 300

- generating databases for supporting licensing process;
- codes assessment and validation.

At present, only CIRCE facility is available and suitable to perform, with some extent, integral tests. Another experimental facility under design (i.e. ATHENA), for investigating the steam generator issues, has features suitable to perform successfully integral tests, if the necessary investments will be performed. The availability of these experimental facilities above has been evaluated satisfactory to address the issues connected with the integral testing.

3.2.6 HLM pump and corrosion/erosion studies

Main pumps

The main pump is a critical component for the LFR/ADS development. The reasons are connected with the characteristics of the coolant, which flows in the system, and with the relevance of the component in relation with the reactor safety. Indeed, the main coolant pumps in nuclear technology are nuclear grade components. It refers to a process of rigorous manufacturing quality assurance for those components that are especially critical to reactor safety. Notwithstanding this, postulated initiating events in safety analysis and licensing refers to malfunction of main coolant pumps (e.g. single or multiple main coolant pump failure, locked rotor and shaft seizure).

It implies that experimental investigations are needed on materials, characterizations of the mechanical parts (i.e. impeller, bearings and housing), performances tests and reliability of the component. The R&D activities related to the pump impeller material have been already outlined. Other activities are connected with

- bearing characterization tests;
- integral pump tests addressing
 - ✓ pump performances, and
 - ✓ long term reliability.

Among the available facilities, only CIRCE appears adequate to perform tests related to the topics above, following a specific adaptation and upgrade. Another facility is under design, i.e. ATHENA, similar to CIRCE but with a volume about ten times bigger.


3.2.7 Instrumentations

Concerning instrumentations, HLM reactor, have higher requirements, due to the higher thermal loads, higher temperatures, high fast neutron flux, corrosion effects and the opacity of liquid metals. The main problems that reduce the choice significantly, however, are the harsh environmental conditions of reactors. Even higher than operational temperatures must be detected and recorded reliably in case of anomalies up to accident conditions.

A common need for HLM nuclear reactor designs is therefore the understanding and development of materials and structures capable of functioning reliably for a long time in an environment described above. Moreover the position of instruments in a system have influence on their performance.

Hereafter is reported a qualitative overview of available instrumentations for LFR/ADS (see Tab. 5). A green “OK” means “fit for purpose” and a red “OK” states that the technology is available, but R&D activities are necessary for adaptation and/or improvement to meet the specific needs. A red question mark “?” is an indication, that a lack of proven technology exists or that other limitation hinders application to reactor



 RICERCA SISTEMA ELETTRICO	<u>Title:</u> Development of BE numerical tools for LFR design and safety analysis – Part 1	<u>Distribution</u> PUBLIC	<u>Issue Date</u> 12.12.2017	<u>Pag.</u>
	<u>Project:</u> ADP ENEA-MSE PAR 2016	<u>Ref.</u> ADPFISS-LP2-144	Rev. 0	34 di 300

application, or which has not yet been addressed. Three dashes “---“ indicate that no information are available in literature.

As can be noted for most of the issued to be measured technical solutions exists for out-of-pile conditions or are presently in the status of improvement and qualification. For in-pile situations, the improvement and qualification has to be initiated and promoted, especially with respect to aging and size.

Another issue is the very wide operational range required for in-core instrumentation for neutron sensors as well as for safety related instrumentation for the reactor protection system (RPS). Safety related instrumentation is focused on core monitoring and detecting early deviation from normal operation and/or local abnormal states, e.g. pin failure, local coolant voiding, sub assembly blockages, unintended control rod movements. These needs are on top of normal operational.

For the understanding of the actual instrumentations available, and thus to plan R&D activities on this issue, the following items would be considered: Diversity, Uncertainty, Applicability, Robustness, Response Time and Required Space (in-core).

For **Diversity** the possibilities are two: no diverse system available, and the sensing device is unique, or diverse system(s) available. The ongoing research on nuclear safety has shown that the safety gain by redundancy alone may be insufficient because of a possible common cause failure. Diversification is needed. **Uncertainty** includes the sensor error, errors during data processing and erroneous measurement due to integration. The available instrumentations can be classified as:

- Low uncertainty (< 2 % normal operation and <5% accidental situations)
- High uncertainty (only acceptable if no other system is usable)

Instrumentations with high uncertainty would be avoided as much as possible.

Applicability gives information whether this device can be applied to in-core situations with high neutron and Gamma fluxes. So far, four different fields of operation have been identified for critical nuclear systems:


1. normal operation,
2. accidental situations,
3. normal inspection and maintenance (fuel handling),
4. exceptional inspection and repair.

The used instrumentations for in-core application would be qualified for any fields of operations.

Robustness is the capability of the instrumentation to survive operation limit exceeding and/or to survive mechanical, thermal or electrical loads on the device. This is important for in-core instrumentation, since the ISI&R capabilities of HLM reactors are limited. Robust instrumentation is a key issue for safety requirements.

Response time is the time delay between the physical signal at the sensor position and the response of the I/C system in the control room. There are different reasons for delay times such as, high thermal inertia, travelling time due to large distances to the sensor (sampling lines), sampling time to improve statistics, and computational time (tomographic sensors). The response time can vary between tenths to tens of seconds.



 RICERCA SISTEMA ELETTRICO	<u>Title:</u> Development of BE numerical tools for LFR design and safety analysis – Part 1	<u>Distribution</u> PUBLIC	<u>Issue Date</u> 12.12.2017	<u>Pag.</u>
	<u>Project:</u> ADP ENEA-MSE PAR 2016	<u>Ref.</u> ADPFISS-LP2-144	Rev. 0	35 di 300

Required space is easy to explain: two thermocouples (TC) as flow sensor require less space than an electromagnetic, a vortex or an orifice flow meter. The required space includes mounting, housing, supply, extra space for inlet conditions, cables, etc. This example shows that it is difficult to quantify the required space generally.

Another issue to be considered is the **interference/integration** with the system in term of fluid dynamic, electrical signal (LM), neutronic, and mechanical arrangement.

To gain a full qualification for the in-core innovative instrumentations, which were not applied to any nuclear system, need basic qualification in prototypic reactors.

This is a critical step in the definition of a roadmap: in-vessel instrumentation and moreover core instrumentation, has to be qualified in two steps:

1. under well defined conditions covering the whole operational spectrum to get the accuracy and
2. together with different (diverse) instrumentation in a prototypic environment(e.g. temperature sensors at S/A exit, flow sensors at S/A entrance.)

3.2.8 Fuel and Irradiation Testing

Concerning LFR development has been already outlined that structural materials qualification under irradiation and the qualification of advanced fuel are an open issues. For the assessment of such issues, material testing reactors, transient testing reactors and hot labs are needed. In the follow are outlined the R&D needs for LFR development. The fuel is standard FBR MOX fuel clad by 15-15 Ti Steel with coating, (T91 as alternative)

Irradiation effects on cladding material

It is necessary to complement the database on irradiation performance of candidate materials:

- Coolant clad interaction
 - Corrosion in Lead under irradiation
 - behaviour of degraded cladding
 - Irradiation embrittlement of selected materials (e.g. T91, 15-15 Ti, AISI316L)
- Irradiation creep (mechanical load, fission gas) (in principle covered by the use of proven technology excepts for the coating)
- Irradiation swelling (in principle covered by the use of proven technology excepts for the coating)
- Coating coolant interaction
- Coating integrity


A facility able to perform these tests is in Dimitrovgrad (Russia): BOR 60 reactor.

Recently, irradiation with heavy ions have been widely used for preliminary/screening tests. Relevant neutronic irradiation are however still needed for the licensing assessment.

Fuel R&D and qualification is considered to be fulfilled by existing sodium databases (since standard MOX has been adopted) with some adjustments due to the use of lead and of a different pin design geometry.

These steps have been identified:



 RICERCA SISTEMA ELETTRICO	<u>Title:</u> Development of BE numerical tools for LFR design and safety analysis – Part 1	<u>Distribution</u> PUBLIC	<u>Issue Date</u> 12.12.2017	<u>Pag.</u>
	<u>Project:</u> ADP ENEA-MSE PAR 2016	<u>Ref.</u> ADPFISS-LP2-144	Rev. 0	36 di 300

Screening:

- Coolant-clad interaction (to be investigated)
- Coating integrity (to be investigated)
- Clad Irradiation tests (to be experienced)
- Clad-fuel interaction (already proved for 15-15 Ti up to 100dpa, not relevant for ferritic/martensitic steels such as T91)
- Fuel coolant interaction (to be investigated)
- Fabrication: France, Japan, Russia,...?

Pre-qualification: to be done in laboratory scale

Qualification approach: to be performed by a prototype in representative conditions

Demonstration: to be done in Demo (innovative coolant & cladding)

Feedback from sodium reactors & FBR R&D (Phénix, SNR, Monju, Superphénix):

- Database on normal MOX fuel pin behaviour
 - Fission product release, fuel restructuring, and swelling
 - Clad swelling, irradiation embrittlement, corrosion (only fuel side), clad-FP interaction, clad fatigue, elongation (creep)
 - Fuel & clad evolution
- Failure margin assessment
 - Limit to clad deterioration and failure in case of local hot spots, affordable fuel swelling, clad swelling, transient rate, start-up rates after scram, EOL embrittlement, ... (to be adapted to the new geometry)
- Establish envelope conditions for fuel
 - Normal operation conditions,
 - Anticipated operational occurrences
 - Postulated accidents in a regulatory context

Additional R&D required


- Clad-coolant interaction
- Clad-coolant-fuel interaction
- Corium-coolant interaction
 - Fuel dispersion and relocation in coolant
 - Chemical stability of corium
- Failed fuel pin behaviour
 - insufficient previous experience
 - database on subassembly behaviour in case of small and large coolant flow blockage;
- maximum acceptable damage in the subassembly

For “advanced” fuels (MA mixed MOX fuel, nitride fuel, carbide fuel) all aspects related to fuel need to be redone

A survey of the existing reactors within the EU for material and fuel performance testing, including their main experimental devices, is in the following:

- OSIRIS (CEA-Saclay, France)
- HFR (Petten, The Netherlands)
- BR2 (SCK•CEN, Mol, Belgium)
- LVR-15 (CV Rez, Czech Republic)



 RICERCA SISTEMA ELETTRICO	<u>Title:</u> Development of BE numerical tools for LFR design and safety analysis – Part 1	<u>Distribution</u> PUBLIC	<u>Issue Date</u> 12.12.2017	<u>Pag.</u>
	<u>Project:</u> ADP ENEA-MSE PAR 2016	<u>Ref.</u> ADPFISS-LP2-144	Rev. 0	37 di 300

- TRIGA-SSR (INR, Pitesti, Romania)
- BRR (KFKI AEKI, Budapest, Hungary)

For safety studies, two facilities are available: the TRIGA-ACPR (INR, Pitesti, Romania) and CABRI (IRSN-CEA, France). Other facilities are available worldwide (e.g. BOR-60 in Russia and CEFR in China), and other facilities have been planned in EU like JHR, ASTRID, MYRRHA. It should be noted that alternative facilities outside EU can be considered to help solving most of the R&D needs: e.g. HFIR, ATR (USA); JOYO, MONJU (Japan); BOR60, BN600 (Russia); FBTR (India); CEFR (China). By the way, BOR60 is actually being used for material testing campaigns in the framework of the LFR/MYRRHA research (at a cost of about 0.5 M€ per one year campaign). However, their degree of suitability and their availability has to be checked on case to case basis. BOR60, for example, has a quite compact core, resulting in limited irradiation capabilities in terms of volume. Currently Japan has no fast neutron irradiation capabilities available, and access to Chinese installations is not straightforward. Moreover, the issues of transport authorization (mainly for irradiated material, but even for non-irradiated fuel samples) and insurance need to be clarified.

Concerning the study of the mechanical behaviour under irradiation of structural materials for components, circuits and cladding, the tests should be performed at elevated temperatures. For most tests the integrated fluence (or the dpa level) is the main parameter, so the exact value of the fast flux is not crucial, but it should anyway be at least of the order of 10^{14} n/cm²s to reach the required fluence on a reasonable time scale. For some research aspects (corrosion, cladding-coolant interactions,..) irradiation in relevant coolant conditions is a must.


3.2.9 Hot laboratories capabilities and needs

Whereas our understanding of the behaviour of GenII/GenIII reactor fuels has reached a reasonable (yet not complete) level and such fuels have been qualified for GenII and GenIII operation limits, fuel operating conditions in the GenIV fast reactor systems will include much higher temperatures and fast-neutron flux. Most importantly, the objectives of improved safety combined with high burn-up targets up to 20% must rely on the development of new fuel types and high performance materials. In order to establish fuel and cladding operational and safety related properties and to improve the basic understanding of fuel behaviour under such conditions, a multidisciplinary scientific and technological programme has to be developed. This is especially true for the fuels for advanced recycling schemes in fast reactor systems (in heterogeneous or homogeneous minor actinides (MA) recycling strategies). Major fabrication and characterization R&D efforts are required to develop reliable, safe and viable fabrication routes and to assess the thermo-chemical, thermo-physical and thermo-mechanical properties of the new materials. Such information will help to validate models for fuel performance prediction under the conditions expected for Gen IV fast reactors. These issues will require the upgrade and/or construction of suitable hot laboratories for both sample fabrication and PIE testing of advanced nuclear fuels.

Within this context, this task focuses on the analysis of future developments in facilities for experimental fuel sample fabrication and characterisation as well as post irradiation experiments (PIE). For LFR development is needed:

- development/characterization of mixed U-Pu fuels with novel designs as driver fuel for prototypes
- safety of Minor Actinides (MA) oxide bearing fuels and associated recycling processes (treatment, refabrication) for MA recycling modes (heterogeneous and homogeneous),
- preparation/characterization of dense fuels (carbide, and possibly also nitride or metal) and associated recycling processes (treatment, partitioning, refabrication) to be qualified in a



 RICERCA SISTEMA ELETTRICO	<u>Title:</u> Development of BE numerical tools for LFR design and safety analysis – Part 1	<u>Distribution</u> PUBLIC	<u>Issue Date</u> 12.12.2017	<u>Pag.</u>
	<u>Project:</u> ADP ENEA-MSE PAR 2016	<u>Ref.</u> ADPFISS-LP2-144	Rev. 0	38 di 300

second phase of operation of the LFR prototype as alternative fuels for this type of reactor featuring enhanced safety

In the short-term, an essential goal is to confirm that ready-to-use technical solutions exist (with uranium-plutonium MOX without minor actinides as the main candidate), so that fuel can be provided in timing with the ALFRED operation. Existing experience in MOX fabrication indicates that fuel with 15-35 wt% enrichment in reactor grade plutonium in pellets of 90-97% of theoretical density can be produced. Such fuel was indeed fabricated, qualified and used in a number liquid metal fast reactors and experimental fast reactors cooled by sodium.

In the mid-term, the possibility of using advanced MA (Minor Actinide) bearing fuels as well as of achieving high fuel burn-ups have to be assessed. New fuels with 2.5-5 at% and later even 10-20 at% of MA in heavy metal will have to be developed; nitride fuels are considered as an option for this purpose.

In the long term, the potential for industrial deployment of advanced MA-bearing fuels and the possibility of using fuels that can withstand high temperatures to exploit the advantage of the high boiling point of lead will have to be investigated.

3.2.10 Neutronics

In the following specific topics concerning neutronic issue related to LFR/ADS development, are reported.

Validation measurements for nuclear data improvement

- Threshold processes : (n,n') and (n, xn) reactions
- MA cross-sections

Validation measurements for licensing & operation

- Uncertainty reduction on cross-sections (Pb-MA-241Pu, 242Pu, in high energy range <1 MeV)
- Determination of flux gradients in fast spectrum
- Reactivity effects (voiding of HLM coolant in MOX core, secondary scram system)

The above areas and topics were identified for zero power reactor experiments.


European zero power reactors are shown in Tab. 6. A simple relevance for SFR, LFR and GFR was included, based mainly on the spectrum and equipment.

Additional reactors in the world, which could be considered for the SFR, LFR and GRF in case of future deficiencies. The list includes:

1. BFS-2 (Russia)
2. FBR-L (Russia)
3. SPR-2 (USA)
4. ZPR FAST (China)
5. FCA (Japan)

All above-mentioned reactors have fast spectrum with thermal power up to 5kW and fast flux up to 10^{11} n/cm²s. The above areas and topics were identified mainly for zero power reactor experiments. Concerning data libraries and neutronic code validation, the task includes experiments producing benchmarking data for problematic materials:



 RICERCA SISTEMA ELETTRICO	<u>Title:</u> Development of BE numerical tools for LFR design and safety analysis – Part 1	<u>Distribution</u> PUBLIC	<u>Issue Date</u> 12.12.2017	<u>Pag.</u>
	<u>Project:</u> ADP ENEA-MSE PAR 2016	<u>Ref.</u> ADPFISS-LP2-144	Rev. 0	39 di 300

- minor actinides cross sections validation and improving
- non elastic neutron scattering thresholds
- libraries for innovative materials (SiC, ZrC, Zr₃Si₂, ...)

At this aim the following facilities can be used:

1. MASURCA (FRANCE)
2. VENUS (BELGIUM)
3. TAPIRO (ITALY)
4. LR 0 (Czech)
5. PROTEUS (SWITZERLAND)

Concerning the operational and control issues

- determination of flux peaks and gradients
- absorber and reflector worth
- degraded geometry studies

the following facilities can be used:

1. MASURCA (FRANCE)
2. VENUS (BELGIUM)
3. LR 0 (Czech)
4. PROTEUS (SWITZERLAND)

3.3 Auxiliary and ancillary systems design

3.3.1 Decay heat removal system


As DHR system, isolation condenser system is foreseen for ALFRED. The removal system uses the 8 SGs connected to the 8 isolation condensers. Each isolation condenser subsystem is composed of:

1. An heat exchanger (Isolation Condenser, IC), constituted by a vertical tube bundle with an upper and lower header;
2. A water pool, where the IC is immersed; the amount of water contained in the pool is sufficient to guarantee three incidental operation days;
3. A condensate isolation valve (to meet the single failure criteria this function shall be performed at least by two parallel valves).

As it has been said, each IC is connected to a steam generator where: the main steam line of a steam generator is connected to the upper header of the isolation condenser, and the lower header of the isolation condenser is connected to the main feed water line of a steam generator. This connection includes a condensate isolation valve which isolates the isolation condenser from the secondary system (isolation valve is full closed during normal operation).

Isolation condenser solution is viable for all points of view, except for the diversification. A redundant, but diversified DHR is required to fully respect the safety rules. An experimental demonstration of system self-regulation capability, to avoid lead freezing, is needed. A second DHR type will be developed and tested in near future. Two possible concept, completely diversified respect the Isolation Condenser are:



 RICERCA SISTEMA ELETRICO	<u>Title:</u> Development of BE numerical tools for LFR design and safety analysis – Part 1	<u>Distribution</u> PUBLIC	<u>Issue Date</u> 12.12.2017	<u>Pag.</u>
	<u>Project:</u> ADP ENEA-MSE PAR 2016	<u>Ref.</u> ADPFISS-LP2-144	Rev. 0	40 di 300

- Dip Coolers;
- Reactor Vessel Air-Cooling System (RVACS).

The two solutions are not fully analyzed and some drawbacks are known.

For the dip cooler, natural convection into the pool, for ALFRED geometry, should be demonstrated and quantified; an additional water inventory into the pool is added and the containment function of the vessel should be guaranteed. For the RVACS, the pool dimension is a constrain for the heat transfer surface and, for this, experimental analysis for the validation of the concept is needed. An option for the dip cooler could be the radiative-based passive system proposed in FP7-LEADER^[22].

3.3.2 Fuel handling system for core assembly loading and unloading, irradiated fuel cooling during transfer and transport to the irradiated fuel pool


This system is fundamental and not completely defined in this phase of the design. This system could be modify the design of the vessel head and the upper part of FA. The detailed design of Reactor vessel upper part will be taken into account the components suitable for sustaining main reactor vessel components (Inner vessel, Steam generators, Primary pumps, eventual DHR deep coolers, etc.). To allowing the operation of the fuel loading/unloading machine, actual solution is probably feasible but the ballast needed for each FA needs an accurate seismic analysis. An alternative solution could be probably with rotating plugs.

3.3.3 Other auxiliary systems

Other system needs in a LFR plant are listed below:

1. Irradiated fuel pool with coolant cleaning and cooling system
2. Lead leakage protection systems: guard reactor vessel or stainless steel liner on the reactor vessel cavity, holding possible lead leakage, preventing in-vessel DHR heat exchangers uncover
3. Instrumentation and control system
4. Heating system to avoid lead freezing
5. Insulation and cooling system beyond the stainless steel protection of the cavity (if this is the chosen solution), in order to prevent concrete damage
6. Lead filling and draining system
7. Lead purification system (regarding oxygen control and possible radioactive isotopes not gaseous and trapped in the covering gas)
8. Monitoring and sampling systems in the reactor building
9. Dedicated post severe accident management systems
10. Storage, filling, purification, radioactive isotopes handling, cooling, recovery system for lead covering gas
11. Seismic isolation system and other systems in support of civil works
12. Conventional auxiliary systems including (the BOP is not taken into account in this list):
 - a. HVAC in the reactor building, in the spent fuel building, in the control room, etc.
 - b. Closed circuit water cooling system, with safety grade components for duty required by components relevant to safety (irradiated fuel coolant HX, Etc.)
 - c. Essential Service water system, with safety grade components for duty required by components relevant to safety
 - d. Electric generation (including Emergency diesel generators) and distribution systems, with appropriate safety level design
 - e. Various monitoring systems, with appropriate safety level design



 RICERCA SISTEMA ELETTRICO	<u>Title:</u> Development of BE numerical tools for LFR design and safety analysis – Part 1	<u>Distribution</u> PUBLIC	<u>Issue Date</u> 12.12.2017	<u>Pag.</u>
	<u>Project:</u> ADP ENEA-MSE PAR 2016	<u>Ref.</u> ADPFISS-LP2-144	Rev. 0	41 di 300

3.4 Instrumentation and control design

The basic purpose of Nuclear Power Plants (NPPs), i.e., the generation of electrical power as cheaply as possible while ensuring the safety of the public and the operating staff, determines the requirements to be fulfilled in the development of control (and instrumentation) design. In particular, the objectives of control system are to i) assist the operator in controlling the plant consistently with specified economic, safety and pollution purposes; ii) monitor the plant and warn of divergences from normal; iii) provide independent safety and control actions (and shutdown actions if required); iv) prevent further undesirable consequences of an accident for a significant time (at least 30 min) without operator intervention and then provide appropriate facilities for whatever action is necessary^[18]. On one hand, the control design includes all the open loop and closed loop controllers which are not related to the "safety-grade" components and process control during operational transients. Control systems are designed to maintain the reactor within operational limits for effective power generation and these limits are kept sufficiently below plant safety limits to ensure safety during power demand variations or anticipated operational disturbances (Fig. 10). On the other hand, safety actuation systems are designed to shut the reactor down, keep it shutdown and ensure core and system cooling if plant parameters exceed plant safety limits. As a measure of defense in depth, safety limits are set below calculated allowable limits to ensure that any unanticipated delays in protection system response will not cause unacceptable consequences. The introduction of digital systems in place of analog systems in some areas of the protection systems has simplified surveillance testing and reduced the duration of plant shutdown for testing.

In the specific context of Lead-cooled Fast Reactor, the need to investigate in the I&C field arises from two main reasons:

- the new technological issues brought by the use of lead as coolant^[19] do not make possible the adoption of the classic approaches retrieved from Light Water and Sodium Fast Reactor concepts since the different features result in different constraints on control and controlled variables and on the instrumentations (e.g., the spatial dependence plays a relevant role in the dynamics evolution, both in neutronics and in thermal-hydraulics environment).
- the need of improving the plant availability and the present energy production situation require constantly enhanced performance for Nuclear Power Plants (NPPs), along with a more and more ability to follow grid demands^[18].


Modelling needs in Dynamics and Control area

The definition of the control design for a nuclear reactor is a multi-phase and multidisciplinary process whose final result is the implementation of dedicated instrumentation and controllers (Fig. 11).

As shown in the Fig. 11, before starting to build up the control system and to implement controllers and devices, it is fundamental to have an exhaustive knowledge of the system being governed, i.e., characterizing the **dynamics** of the system. For this reason, during the development of nuclear reactor control design, a relevant role is played by the plant simulator whose purpose is: (i) to obtain detailed information on the **dynamic behaviour**; and (ii) to help the I&C system implementation for both its realization, validation and testing. This holds particularly true in the case of the LFR reactor concept for which no notable operational experience is available. In this sense, simulation-based choices, both in the control and in the instrumentation field, may help. Only after this preliminary stage, having characterized the governing dynamics of the system, it is possible to develop the control system and in particular on the:

- **pairing selection**, i.e., which are the variable to be control and select which are the control variables;



 RICERCA SISTEMA ELETTRICO	<u>Title:</u> Development of BE numerical tools for LFR design and safety analysis – Part 1	<u>Distribution</u> PUBLIC	<u>Issue Date</u> 12.12.2017	<u>Pag.</u>
	<u>Project:</u> ADP ENEA-MSE PAR 2016	<u>Ref.</u> ADPFISS-LP2-144	Rev. 0	42 di 300


- **control scheme implementation**, i.e., the selection of the control scheme and the implementation of the controllers;
- **definition of the operational modes**, i.e., the definition of the behavior of the control devices during the different phases of the reactor operation (i.e., full power, startup, shutdown, ...);
- **master control scheme design**, i.e. the design of the supervisory control system which coordinate the several operational modes.

As for the dynamics and control, two main modelling need can be identified, namely the **development of a power plant simulator** and the **improvement of the classic control-oriented modelling approach**.

The first modelling need identified is then a **power plant simulator** specifically devoted to the control system development which can be used to represent the entire behavior of the power plant, Balance of Plant included. Besides control purposes, the latter can be useful for diagnostics and fault detection during operational transients[20] and safety insights as well. Differently from a system code for safety study, such a simulation tool has to fulfill some requirements. In particular, fast-running simulations, a comprehensive representation of the entire plant behaviour, and the possibility to couple the plant dynamics simulator with the control system model are the main requests. These goals could be accomplished by using an Object-oriented modelling in order to take advantage from the hierarchical structure, the abstraction and the encapsulation features. By adopting this approach, the developed model could achieve the requirements of modularity, openness and efficiency that are required for a power plant simulator oriented to the control. In addition, the modelling approach used for the description of the power plant simulator should feature the so-called acausal modelling, i.e., the direct use of equations without imposing the classic input/output declaration, enabling a more flexible and efficient data flow. In this way, models would be much easier to write and reuse since the burden of determining the actual sequence of computations required for the simulation can be left to the compiler. The main features and differences between causal and acausal approach are listed in Tab. 4.

The second modelling need is related to the modelling approach used to represent the system. A poor detailed modelling precludes the possibility to exploit all the potentialities of the advanced control schemes and techniques. In particular, these techniques should adopt a detailed modelling in order to provide the control system design with spatial information regarding neutron flux, temperature, pressure, and mass flow rate. The control system usually adopted in nuclear reactors is based on Proportional-Integral-Derivative controllers (PID) in decentralized control scheme, which ensure simplicity in the implementation and robustness towards malfunctioning of single control loops, favoring the Operation and Maintenance (O&M)^[21]. The choice of simple Single Input Single Output (SISO) control laws has brought to the development of simulators that implement simple models (zero-dimensional) for the description of the main physics of a nuclear reactor (e.g., the point kinetics for the neutronics). The classic control-oriented approach based on 0D/1D modelling is appropriate whether the spatial effects are not relevant and only the estimation of integral quantities is required as for the SISO control laws. On the opposite side, the 3D modelling is usually devoted to design purposes having a high level of detail but extremely expensive from a computational point of view (Fig. 12). In the light of the previous considerations, the research efforts should be devoted to combine **a high-detail modelling featuring spatial capabilities** (e.g., 3D modelling) with the requirements demanded for a control-oriented tool, firstly the computational efficiency. The high accuracy guaranteed by the adoption of high-detail modelling can allow solving some control issues related to modelling aspects, in particular the spatial ones, which otherwise could not be managed by means of the classic control-oriented approach. The practical application could be the improvement of a control-oriented simulator of an LFR plant, i.e., substituting some components based on zero-dimensional approach with high-detailed models ensuring a high level of accuracy and a better physical description without increasing the computational burden. The use of advanced modelling in the control-oriented simulation tools may allow adopting innovative control strategies, whose feasibility in the nuclear field cannot be adequately studied by



 RICERCA SISTEMA ELETTRICO	<u>Title:</u> Development of BE numerical tools for LFR design and safety analysis – Part 1	<u>Distribution</u> PUBLIC	<u>Issue Date</u> 12.12.2017	<u>Pag.</u>
	<u>Project:</u> ADP ENEA-MSE PAR 2016	<u>Ref.</u> ADPFISS-LP2-144	Rev. 0	43 di 300

means of a zero-dimensional model and providing, at the same time, some safety insights. For instance, with a spatial neutronics model, an optimal control of the Control Rods (CRs) movement that minimizes the perturbation on the neutron flux can be assessed, since the model allows for the flux distortion due to the CR insertion. Another possible application involves the instrumentation in the reactor pool (e.g., for the oxygen control).

3.5 Probabilistic Safety Analysis

Three general safety objectives would be guarantee in Generation IV nuclear energy systems:

1. in all conditions, reactor operations will excel in safety and reliability;
2. to have a very low possibility and degree of reactor core damage;
3. to eliminate the need for offsite emergency response, also in case of severe accident.

The basic points for the GEN IV safety, as the GEN III+ LWR, are:

- defence in depth;
- “risk-informed” approach, starting from the design phase.

In addition to prototyping and demonstration, modelling and simulation for should play a fundamental role in principle during the design and in near future during the assessment.

Probabilistic Safety Analysis (PSA) offers a consistent and integrated framework for safety related decision-making. Furthermore, PSA is a conceptual tool for deriving numerical estimates of risk for nuclear plants and industrial installations in general and also for evaluating the uncertainties in these estimates. PSA differs from traditional deterministic safety analysis in that it provides a methodological approach to identifying accident sequences issued from a broad range of initiating events, and it includes the systematic and realistic determination of accident frequencies and consequences.

In GEN III/III+ reactors, at the present time, a PSA is used:

- during the design process of new nuclear plants, complementary to the deterministic approach;
- for periodic safety reviews;
- in the decision process of plant specific changes to the current licensing process.

Specific objectives and corresponding uses of PSA for the objective of assessing plant safety to assist plant operation are:


- evaluation of plant technical specifications and limiting conditions of operations;
- prioritization of inspection/testing activities;
- evaluation of operating experience;
- accident management.

Its role is to study the accident sequences with multiple failures and to verify target values given by the designer or by the safety authorities. The targets internationally recommended for LWR are a core melt frequency of $10^{-5}/(\text{reactor} \cdot \text{year})$ including external events and a frequency of high release of fission product of $10^{-6}/(\text{reactor} \cdot \text{year})$.

3.5.1 PSA levels

The Probabilistic safety analysis, also for fast reactors, is divided in three levels:



 RICERCA SISTEMA ELETTRICO	<u>Title:</u> Development of BE numerical tools for LFR design and safety analysis – Part 1	<u>Distribution</u> PUBLIC	<u>Issue Date</u> 12.12.2017	<u>Pag.</u>
	<u>Project:</u> ADP ENEA-MSE PAR 2016	<u>Ref.</u> ADPFISS-LP2-144	Rev. 0	44 di 300

- 1) The assessment of plant failure leading to the determination of “core damage frequency”
- 2) The assessment of containment response leading; together with level 1 results, to the determination of containment release frequency.
- 3) The assessment of off-site consequences leading, together with the results of Level 2 analysis, to estimate the public risk.

Level 1 deterministic analysis in support to PSA was carried out in past EU projects and this is a solid base for future steps, and level 3 is similar to LWR plants. Instead, for Level 2 PSA, no computer programs are available for a detailed analysis. R&D for a tool able to make deterministic safety analysis in lead and the validation of this is required. This would be a fundamental step needed in the LFR technology development roadmap.

3.5.2 Complements for the PSA application in a safety analysis

For the application of PSA into a licensing processing, a complete regulation and rules are needed. In particular, is needed to define:

- Design Basis Category
- Acceptance criteria
- Safety category

The starting point is from the EUR (Tab. 7).

3.5.3 PSA application in preliminary safety analysis

The safety analysis will be a fundamental point for the project development. The analysis performed in past projects are a good starting point, but a detailed Probabilistic Safety Analysis (PSA) following the state-of-the-art approach for advanced reactors will be carried out.

The PSA complement deterministic safety studies because DSA:

- do not have quantitative risk assessment of severe accidents;
- do not analyze complex sequences of accidents;
- do not necessarily process the interdependencies of support systems (instrumentation, power supply, etc).


The PSA, like any model (thermo-hydraulic , neutronic and others) includes uncertainties especially in the degraded mode of operation (e.g. addressed through sensitivity analysis), and on the estimation of reliability ratios (addressed through distribution of random variable), which are incorporated in the calculations. This should allow modulating the decisions based on the results.

One difficulty for safety is the inability to control statistically the predictions accidents with very low probability. This does not allow to completely validate the studies, the overall results such as "practically eliminated" (deterministic approach), or probabilities such as 10^{-7} per reactor year (PSA approach) are either not demonstrable in the mathematical way.

3.5.4 ISAM methodology

ISAM methodology [23] should be used for the full development of the new systems and components. In this approach, all design aspects are safety oriented. This approach is needed into the developing of new systems or components, and for the upgrading of safety features for the existent systems. Thanks to this additional



 RICERCA SISTEMA ELETTRICO	<u>Title:</u> Development of BE numerical tools for LFR design and safety analysis – Part 1	<u>Distribution</u> PUBLIC	<u>Issue Date</u> 12.12.2017	<u>Pag.</u>
	<u>Project:</u> ADP ENEA-MSE PAR 2016	<u>Ref.</u> ADPFISS-LP2-144	Rev. 0	45 di 300

step, the iterations during the final safety analysis are reduced and the time spent in this phase is recovered in next steps of design.

The ISAM tools, described also in [24], are the following:

1. Qualitative Safety Features Review (QSR)
2. Phenomena Identification and Ranking Table (PIRT)
3. Objective Provision Tree (OPT)
4. Deterministic and Phenomenological Analyses (DPA)
5. Probabilistic Safety Analysis (PSA)

3.5.5 PSA modelling needs

PSA will be developed and enriched by successive stages throughout the development of future reactors, they bring:

- Assistance in the design of safety systems: a comparison of technical solutions, impacts of redundancy, diversification, separation, etc.
- The evaluation of the gain, with respect to safety, provided by the provisions in the event of a severe accident,
- The participation in the demonstration that situations which may lead to early and large releases are "practically eliminated"
- The comparison of the safety level versus reactors in operation or other reactors under development.

The needs for a PSA applied to LFR are focalized in level 2 PSA modeling, where it is necessary to develop a tool for calculating the source term. For the phenomenology side, not equal in comparison to LWR reactor, new aspects will have to be taken into account, as steam ingress into the core, flow blockage, and others.

3.6 Deterministic Safety Analysis


Within the defense in depth concept, the DSA (or accident analysis)^[32] is a tool for assessing the adequacy and the efficiency of provisions for the safety of a nuclear installation. This tool is employed to demonstrate that fundamental safety functions of the nuclear installations^[33] (i.e. control of reactivity, removal of heat from the fuel, confinement of radioactive materials and control of operational discharges, as well as limitation of accidental releases) are achieved in operational states and accidental conditions^[34]. Therefore, a list of initiating events is established to bound the possibilities for the loss and/or degradation of fundamental safety function. The identification of initiating events is challenging and requires the use of OPEX, engineering judgement, PSA studies and deterministic analysis of accidents. Accident analysis is applied to determine the course and the consequences of the event and to evaluate the capability of the plant and its personnel to control or to accommodate such conditions.

The initiating events are typically grouped into categories, based on

- Principal effect on potential degradation of fundamental safety functions^[35],
- Principal cause of the initiating event,
- Frequency and potential consequences of the event (i.e. Tab. 7),
- Relation of the event to the original NPP design).

Acceptance criteria^[36] are used to evaluate^[37] the acceptability of the results of the safety analyses. They are applied to licensing calculations, and to the results of severe accident analyses. For instance, Acceptance



 RICERCA SISTEMA ELETTRICO	<u>Title:</u> Development of BE numerical tools for LFR design and safety analysis – Part 1	<u>Distribution</u> PUBLIC	<u>Issue Date</u> 12.12.2017	<u>Pag.</u>
	<u>Project:</u> ADP ENEA-MSE PAR 2016	<u>Ref.</u> ADPFISS-LP2-144	Rev. 0	46 di 300


Criteria for each Plant Condition are defined on the basis of NRC Standard Review Plan and of 10CFR50, Appendix A, General Design Criteria^[38]. The acceptance criteria are anyway dependent by the jurisdiction where the nuclear installation is constructed. In general, the Acceptance Criteria depend by the frequency of the initiating event, the reactor design and the plant conditions. Higher probability of occurrence implies more stringent criteria.

The verification of the acceptance criteria can be demonstrated with different approaches: from conservative to best estimate approaches. These approaches (Tab. 8) have been tailored by the national regulations thus different options and applications are possible. Present regulations^[39] permit the use of best estimate codes^[42], but requires conservative input assumptions, sensitivity studies or uncertainty studies^[43]. Applications of BE codes is broadly accepted around the world: an extensive database exists for nearly all power reactor designs and best estimate plant calculations are well documented. In case of new designs, such as the LFR, it is important to consider the applicability of the code models, developed for LWR technology, and their associated uncertainties.

DSA has different applications and the results are used at different project stages (from preliminary design to decommissioning) with different scopes^[32]. They are:

- **Design analysis.** Design analysis is used in the design of a new plant or in modifications to the design of an existing plant. It is done to assist in setting: 1) equipment sizing, including those safety related; 2) approximate determination of set point values (e.g. Ref. [40]); 3) assessment of dose to the public.
- **Licensing analysis.** It is used in the design of a new plant, or in modification of the design of an existing plant (e.g. SG replacement, power up-rate, etc.), to provide evidence to the regulatory body that the design is safe.
- **Validation of emergency operating procedures and plant simulators.** The development and validation of EOPs are carried out by using computer codes. They can be performed using best estimate code, models, data and assumptions. The development consists in analyses and sensitivities for assessing time margins and the optimization of procedures. Then, the validation confirm that the actions specified in the procedures could be followed in the appropriate time and manner by a trained operator and that the expected response of the system is achievable, resulting in the final safe state of the reactor system.
- **Analysis related to probabilistic safety analysis.** DSA related to PSA is relevant 1) to give an accurate measure of the risks associated with different scenarios; 2) to assist in the development of EOPs; 3) to determine whether an event sequence is successful or not.
- **Support for accident management and emergency planning.** Analysis of accidents for supporting accident management (e.g. Ref. [41]) describes the plant behaviour in conditions for BDBAs. Operator actions are normally accounted for in the assessment of BDBAs. The results from analyses of BDBAs are used to develop operator strategy, the main goals being to prevent severe core damage and to mitigate the consequences of an accident in the event of core damage. On the basis of such analyses, guidelines for accident management could also be developed.
- **Analysis of operational event.** Accident analysis is frequently used as a tool for a full understanding of events occurring during the operation of NPPs, as part of the feedback of operational experience.
- **Regulatory audit analysis.** Analyses used by regulatory bodies 1) for performing an independent verification of DBAs; 2) for supplementing the task of reviewing and assessing the design and operation of NPPs; 3) for checking the completeness and consistency of accident analyses submitted for licensing purposes.




 RICERCA SISTEMA ELETTRICO	<u>Title:</u> Development of BE numerical tools for LFR design and safety analysis – Part 1	<u>Distribution</u> PUBLIC	<u>Issue Date</u> 12.12.2017	<u>Pag.</u>
	<u>Project:</u> ADP ENEA-MSE PAR 2016	<u>Ref.</u> ADPFISS-LP2-144	Rev. 0	47 di 300

DSA is performed using different types of computer codes, ranging from specialized reactor physics codes to coupled codes. BE computer codes have various levels of qualification: this depends by the availability of experimental data or NPP data, and the extent of independent assessment. Experimental data are fundamental for supporting the development and demonstrating the reliability of computer codes in simulating the behavior of an NPP during a postulated accident scenario: in general, this is a regulatory requirement^[44]. However, the user always has the responsibility of the appropriate use of such codes. The following main categories of codes for BE analyses are identified

- (a) Core physics codes;
- (b) Component specific or phenomenon specific codes
 - a. Fuel behaviour codes;
 - b. Sub-channel codes;
 - c. Porous media codes;
 - d. Containment analysis codes, with features for the transport of radioactive materials;
 - e. Atmospheric dispersion and dose codes;
 - f. Structural analysis codes
- (c) System thermohydraulic codes
- (d) CFD
- (e) Coupled codes

Validation and verification are essential steps in qualifying any computational method and are the primary means of assessing the accuracy of computational simulations.



 RICERCA SISTEMA ELETTRICO	<u>Title:</u> Development of BE numerical tools for LFR design and safety analysis – Part 1	<u>Distribution</u> PUBLIC	<u>Issue Date</u> 12.12.2017	<u>Pag.</u>
	<u>Project:</u> ADP ENEA-MSE PAR 2016	<u>Ref.</u> ADPFISS-LP2-144	Rev. 0	48 di 300

Core		Encompassed aspect		
		N	TH	TM
Component	Pin (fuel, absorber, shield, etc.)			×
	Cell (fuel, absorber, shield, etc.)		×	
	Sub-assembly (fuel, absorber, shield, etc.)		×	×
	Restraint system			×
	Shield (thermal, radiological)	×	×	×
	Core (integration)	×	×	×

Tab. 3 – Aspects encompassed in the design of core components(N: Neutronics; TH: Thermal-Hydraulics; TM: Thermo-Mechanics)..


Causal approach	Acausal approach
System input and output variables have to be established at the beginning	It is not necessary to establish <i>a priori</i> input and output variables
Equations have to be rewritten for each specific application in state space representation	Causality remains unspecified as long as equations are solved
Low flexibility in changing the model configuration	More realistic description of components and modularity
Low reusability of previous work. Problem formulation in a series of operations must be performed by the user, according to the particular applicative context	Possibility of easily reusing previously developed models. Models of components are defined independently of their potential connections
Block diagram representation (physics-oriented)	Plant representation (component-oriented)
Integration algorithm for ordinary differential equations (lower computational cost)	Integration algorithm for differential algebraic equations (higher computational cost)
Low order modelling, easy to linearize (stability analyses)	Potentially high number of equations involved

Tab. 4 – Main features and differences between causal and acausal approach.

	LFR
Neutronics and Gamma	OK
Pin Failure Detection	OK
Thermal Hydraulic Data	OK
Fluid Chemistry Control	OK
Displacements / Vibrations	OK
Leak detection of primary/secondary system	OK
In vessel structure topology	?
ISI&R	OK
Remote Handling	OK

Tab. 5 – Summary of available instrumentations.



 RICERCA SISTEMA ELETTRICO	<u>Title:</u> Development of BE numerical tools for LFR design and safety analysis – Part 1	<u>Distribution</u> PUBLIC	<u>Issue Date</u> 12.12.2017	<u>Pag.</u> 49 di 300
	<u>Project:</u> ADP ENEA-MSE PAR 2016	<u>Ref.</u> ADPFISS-LP2-144	Rev. 0	

Facility	Brief characteristics	Availability	GIF Relevance
EOLE	Thermal reactor for studying moderated lattices	?	Low
MINERVE	Reactor with both thermal and fast lattices – measurements on various actinides and absorbers	?	Med
MASURCA	Fast reactor for fast lattice measurements – reactivity feedbacks, compact shielding and reflectors,	2017	High
VENUS	Fast reactor optionally driven by accelerator for mock-ups of SFR, LFR and ADS	2011	High
LR-0	Thermal VVER reactor with multi-zone configurations including fast spectrum zones	Now	Med
VR-1	Thermal training reactor with two vessels (possibility to implement accelerator driven system)	Now	Low
TAPIRO	Fast reactor used for fast neutron dosimetry and shielding studies	Now	High
PROTEUS	Thermal reactor with multi-zone capability	?	Med

Tab. 6 – Summary of the European zero power reactors.

Design Basis Category	Definition	Frequency of initiating event (per year)
1	Normal Operation	
2	Incidents	$f > 10^{-2}$
3	Accidents (low frequency)	$10^{-2} > f > 10^{-4}$
4	Accidents (very low frequency)	$10^{-4} > f > 10^{-6}$

Tab. 7 – EUR Design Basis Category.

#	Option	Computer code	Availability of systems	Initial and boundary conditions
1	Conservative	Conservative	Conservative assumptions	Conservative input data
2	Combined	Best Estimate	Conservative assumptions	Conservative input data
3	Best Estimate	Best Estimate	Conservative assumptions	Realistic plus uncertainty; partly most unfavourable conditions
4	Risk informed	Best Estimate	Derived from PSA	Realistic plus uncertainty ^(a)

^(a)Realistic input data are used only if the uncertainties or their probabilistic distributions are known. For those parameters whose uncertainties are not quantifiable with a high level of confidence, conservative values should be used

Tab. 8 – Options for Combination of a Computer Code and Input Data^[32].



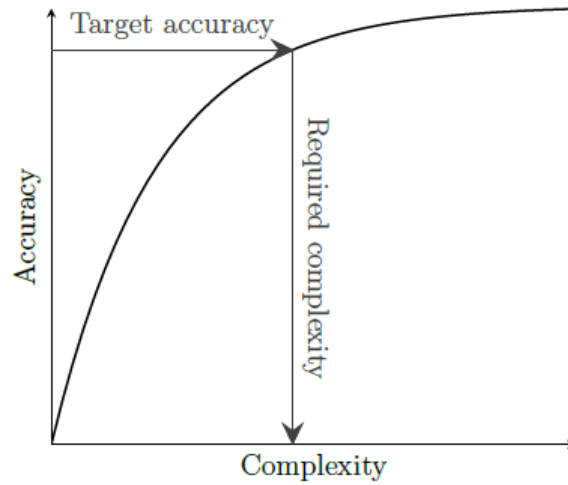


Fig. 3 – Hypothetical relation between complexity and accuracy of a model.

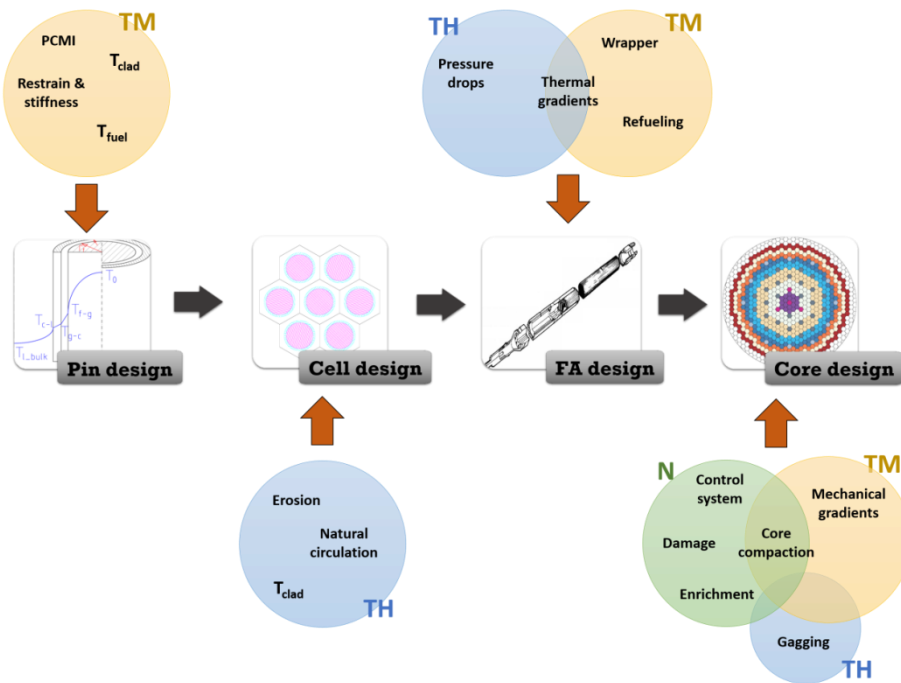



Fig. 4 – LFR core design process with the main physical interconnections highlighted.



 RICERCA SISTEMA ELETTRICO	<u>Title:</u> Development of BE numerical tools for LFR design and safety analysis – Part 1	<u>Distribution</u> PUBLIC	<u>Issue Date</u> 12.12.2017	<u>Pag.</u> 51 di 300
	<u>Project:</u> ADP ENEA-MSE PAR 2016	<u>Ref.</u> ADPFISS-LP2-144	Rev. 0	

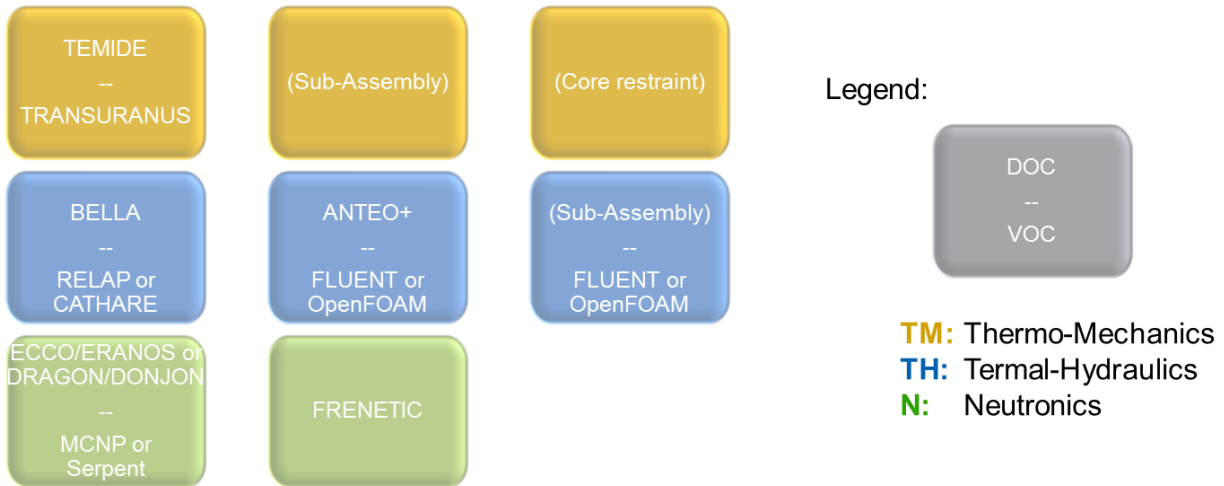


Fig. 5 – List of candidate codes for the aimed core design/verification platform.

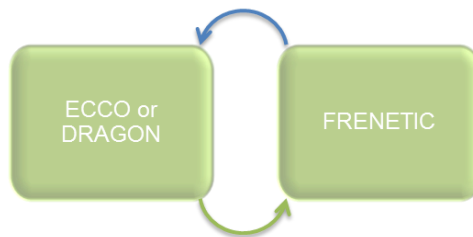



Fig. 6 – Simplified coupling scheme for thermal-hydraulics feedback evaluation in design.



Fig. 7 – Detailed coupling scheme for thermal-hydraulics feedback evaluation in design.



 RICERCA SISTEMA ELETTRICO	<u>Title:</u> Development of BE numerical tools for LFR design and safety analysis – Part 1	<u>Distribution</u> PUBLIC	<u>Issue Date</u> 12.12.2017	<u>Pag.</u>
	<u>Project:</u> ADP ENEA-MSE PAR 2016	<u>Ref.</u> ADPFISS-LP2-144	Rev. 0	52 di 300

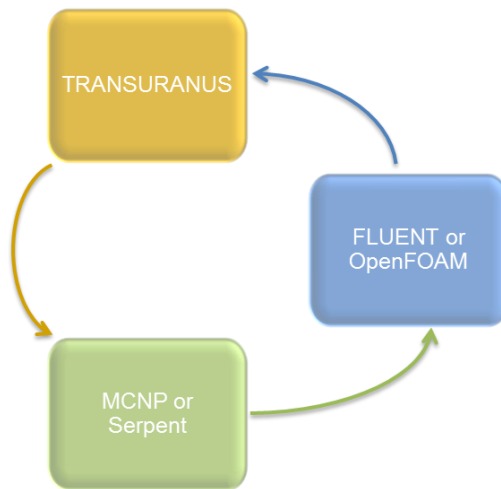


Fig. 8 – Detailed coupling scheme for thermal-hydraulics feedback evaluation in verification.

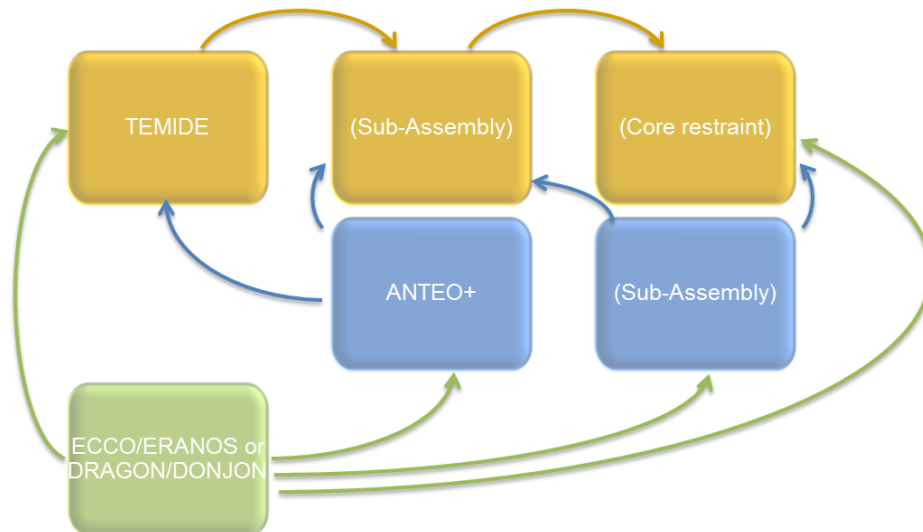


Fig. 9 – Platform utilization in the case of core restraint design.



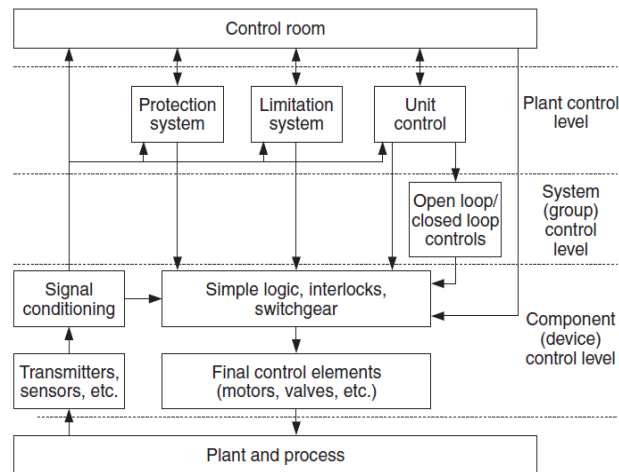


Fig. 10 – Configuration of the operational control system in terms of functions (please note the connection with protection and limitation systems)^[18]

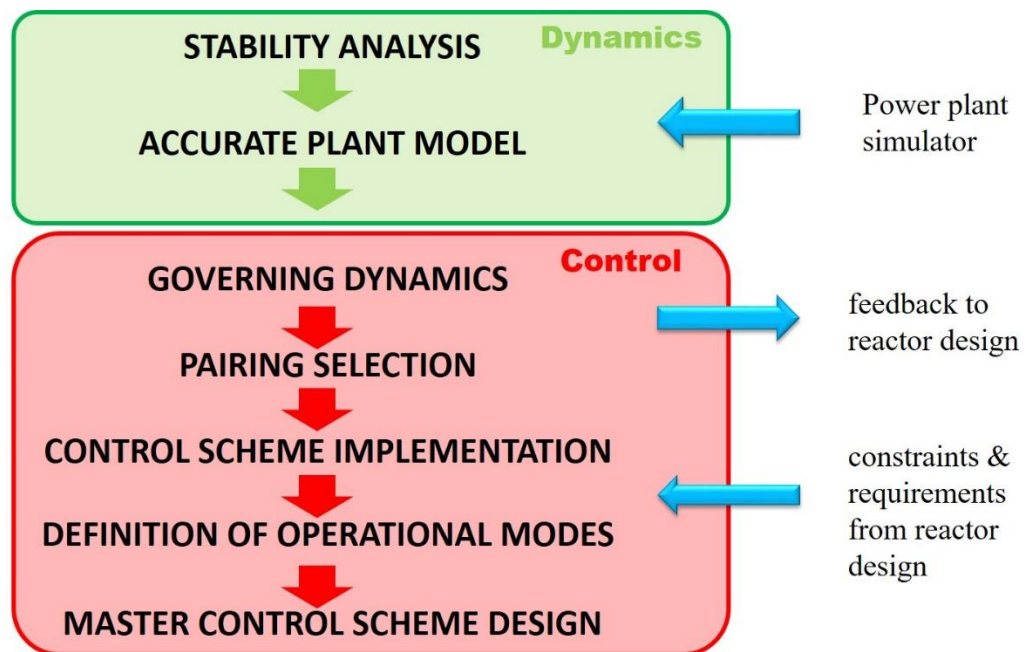



Fig. 11 – Control strategy road map.



 RICERCA SISTEMA ELETTRICO	<u>Title:</u> Development of BE numerical tools for LFR design and safety analysis – Part 1	<u>Distribution</u> PUBLIC	<u>Issue Date</u> 12.12.2017	<u>Pag.</u> 54 di 300
	<u>Project:</u> ADP ENEA-MSE PAR 2016	<u>Ref.</u> ADPFISS-LP2-144	Rev. 0	

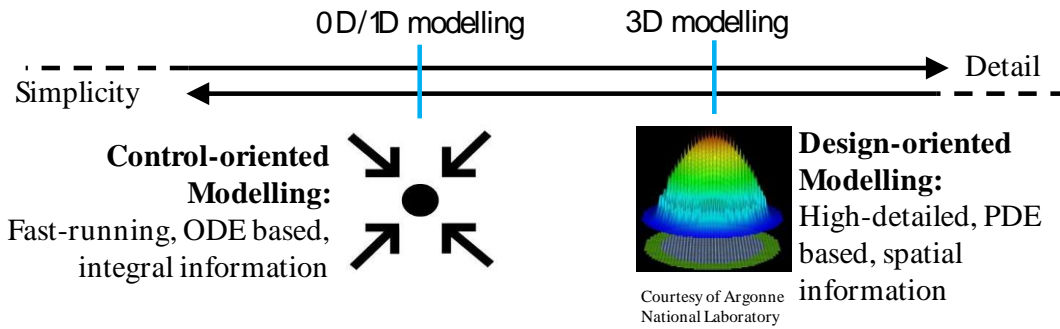


Fig. 12 – Different approaches in modelling, 0D/1D modelling (control-oriented) vs 3D modelling (design-oriented).

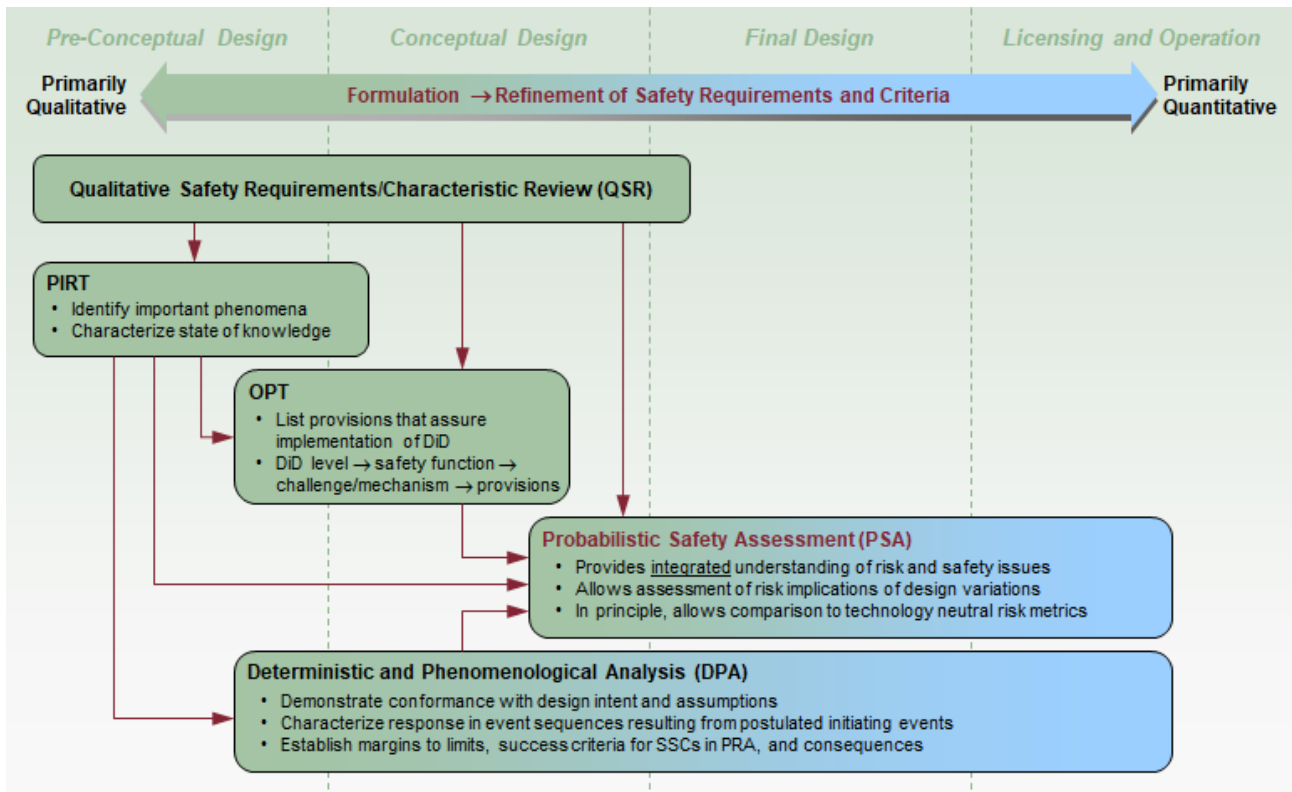



Fig. 13 – ISAM methodology representation [23]




 RICERCA SISTEMA ELETTRICO	<u>Title:</u> Development of BE numerical tools for LFR design and safety analysis – Part 1	<u>Distribution</u> PUBLIC	<u>Issue Date</u> 12.12.2017	<u>Pag.</u>
	<u>Project:</u> ADP ENEA-MSE PAR 2016	<u>Ref.</u> ADPFISS-LP2-144	Rev. 0	55 di 300

4 OVERVIEW OF THE MODELING ACTIVITIES IN 2016 (PART 2)

Category	Type	Code	Section
Core physics	Continuous Cross Section Databases	--	--
	Problem-dependent Multigroup XSecs	--	--
	Fuel Assembly Transport Calculations & XSec Libraries Generation	--	--
	Burn-up Calculations	--	--
	3D NK	--	--
	Spent Fuel Disposal – Criticality & Shielding	--	--
Component specific or phenomenon specific	Fuel behavior	TRANSURANUS	Section 1
	Sub-channel	--	--
	Porous media	--	--
	Containment analysis	--	--
	Atmospheric dispersion and dose codes	--	--
	Structural analysis	--	--
	Material molecular dynamics	CALPHAD method	Section 6
	Multi-fluid / Severe accident	SIMMER-III	Section 9
System thermohydraulic	--	RELAP5-3D	Section 2 Section 5
CFD	--	--	--
Coupled codes	3D NK – SYS/TH		
	neutronics, fluid dynamics, heat transfer, and thermal expansions	COMSOL Multiphysics SERPENT	Section 8
	3D NK – sub-assembly/TH	FRENETIC	Section 7
	SYS-TH - CFD	FEM-LCORE/CATHARE RELAP5/Mod3.3–Fluent	Section 2 Section 4


Tab. 9 – Development, validation and application of computational tools: summary of the activity performed in the framework of PAR-2016.



 RICERCA SISTEMA ELETTRICO	<u>Title:</u> Development of BE numerical tools for LFR design and safety analysis – Part 1 <u>Project:</u> ADP ENEA-MSE PAR 2016	<u>Distribution</u> PUBLIC	<u>Issue Date</u> 12.12.2017	<u>Pag.</u> 56 di 300
		<u>Ref.</u> ADPFISS-LP2-144	Rev. 0	

(Page intentionally left blank)




 RICERCA SISTEMA ELETRICO	<u>Title:</u> Development of BE numerical tools for LFR design and safety analysis – Part 1	<u>Distribution</u> PUBLIC	<u>Issue Date</u> 12.12.2017	<u>Pag.</u>
	<u>Project:</u> ADP ENEA-MSE PAR 2016	<u>Ref.</u> ADPFISS-LP2-144	Rev. 0	57 di 300

LIST OF REFERENCES


- [1] U.S. Department Of Energy Nuclear Energy Research Advisory Committee and Generation IV International Forum, *A Technology Roadmap for Generation IV Nuclear Energy Systems*, Technical Report GIF (2002), <http://www.gen-4.org/Technology/roadmap.htm>.
- [2] A. Alemberti et al., *The European Lead Fast Reactor strategy and the roadmap for the demonstrator ALFRED*, Proc. of *Int. Conf. on Fast Reactors and Related Fuel Cycles: Safe Technologies and Sustainable Scenarios (FR13)*, Paris, France, March 4-7, 2013.
- [3] A. A. Alemberti et al., *ALFRED and the lead technology research infrastructure*, Proc. of *European Research Reactor Conference (RRFM2015)*, Bucharest, Romania, April 19-23, 2015.
- [4] D. De Bruyn et al., *Main achievements of the FP7-LEADER collaborative project of the European Commission regarding the design of a Lead-cooled Fast Reactor*. In *Proceedings of 2013 International Congress on Advances in Nuclear Power Plants (ICAPP '13)*, Jeju Island, Korea, April 14-18, 2013.
- [5] A. Alemberti et al. *The FALCON Consortium*. In *Proceedings of 12th WEC Central & Eastern Europe regional energy forum (FOREN 2014)*, Bucharest, Romania, June 22-26, 2014.
- [6] F. Lodi. *Development of core design methods and tools for Gen-IV Heavy Liquid Metal cooled Reactors*. PhD Thesis, UniBO, 2017.
- [7] S. Bortot et al. *BELLA: a multi-point dynamics code for safety-informed design of fast reactors*. *Ann. Nucl. Energy* **85**:228-235 (2015).
- [8] F. Lodi et al. *ANTEO+: A subchannel code for thermal-hydraulic analysis of liquid metal cooled systems*. *Nucl. Eng. Des.* **301**:128-152 (2016).
- [9] ANSYS, *FLUENT Theory Guide*. ANSYS, Inc. (2017).
- [10] OpenFOAM v5 User Guide. OpenFOAM Foundation (2017).
- [11] K. Lassmann. *TRANSURANUS: a fuel rod analysis code ready for use*. *J. Nucl. Mater.* **188**:295-302 (1992).
- [12] ANSYS Mechanical User's Guide. ANSYS, Inc. (2017).
- [13] G. Rimpault et al. *The ERANOS Code and Data System for Fast Reactor Neutronic Analyses*. Proc. of *Int. Conf. on the New Frontiers of Nuclear Technology: Reactor Physics, Safety and High-Performance Computing (PHYSOR 2002)*, Seoul, Korea, October 7-10, 2002.
- [14] A. Hébert. *DRAGON5 and DONJON5, the contribution of École Polytechnique de Montréal to the SALOME platform*. *Ann. Nucl. Energy* **87**(1):12-20 (2016).
- [15] MCNP6 User's Manual - Code Version 6.1.1beta. Technical Report LA-CP-14-00745, Los Alamos Nuclear Laboratories (2014).
- [16] J. Leppänen et al. *The Serpent Monte Carlo code: Status, development and applications in 2013*. *Ann. Nucl. Energy* **82**:142-150 (2015).
- [17] R. Bonifetto et al. *A full-core coupled neutronic/thermal-hydraulic code for the modeling of lead-cooled nuclear fast reactors*. *Nucl. Eng. Des.* **261**:85-94 (2013).
- [18] IAEA, *Modern Instrumentation and Control for Nuclear Power Plants: A Guidebook*, Technical Reports Series No. 387, Vienna, 1999.



 RICERCA SISTEMA ELETRICO	<u>Title:</u> Development of BE numerical tools for LFR design and safety analysis – Part 1	<u>Distribution</u> PUBLIC	<u>Issue Date</u> 12.12.2017	<u>Pag.</u>
	<u>Project:</u> ADP ENEA-MSE PAR 2016	<u>Ref.</u> ADPFISS-LP2-144	Rev. 0	58 di 300


- [19] Tucek, K., Carlsson, J., Wider, H., *Comparison of sodium and lead-cooled fast reactors regarding reactor physics aspects, severe safety and economical issues*, Nuclear Engineering and Design, 236, 1589–1598, 2006.
- [20] IAEA, *Implementing Digital Instrumentation and Control Systems in the Modernization of Nuclear Power Plants*, IAEA Nuclear Energy Series NP-T-1.4, , Vienna, 2009.
- [21] Levine, W. S., *The Control Handbook*, IEEE Press, 1996.
- [22] F. Manni et al., *Innovative DHR for the ALFRED reactor*, LEADER TEC-DOC 72
- [23] Risk and Safety Working Group (RSWG), *An Integrated Safety Assessment Methodology (ISAM) for Generation IV Nuclear Systems*, GIF/RSWG/2010/002/Rev 1.
- [24] IAEA, *Basic Safety Principles for Nuclear Power Plants*, 75-INSAG-3 Rev. 1 (INSAG-12) STI/PUB/1082, Vienna, 1999.
- [25] L. Vála, C. Latgé, P. Agostini, C. Poette, W Hering, L. Vermeeren, V. Juříček, J Prah, *Evaluation of existing research infrastructure for long-term vision of sustainable energy*, Deliverable D8.2, ADRIANA Project, EURATOM FP7 Grant Agreement no.249687.
- [26] G.I. Toshinsky, O.G. Komlev, I.V. Tormyshev, *Effect of Potential Energy Stored in Reactor Facility Coolant on NPP Safety and Economic Parameters*, ICAPP 2011, Paper 11465.
- [27] L. Cinotti, M. Tarantino, D. Rozzia, *Lead-cooled Fast Reactor development Gaps*, IAEA Technical Meeting on to Identify Innovative Fast Neutron Systems Development Gaps, IAEA Headquarters, 29 February – 02 March 2012, Vienna, Austria. (<http://www.iaea.org/NuclearPower/FR/>).
- [28] P. Agostini, A. Del Nevo, *Report on future needs and for clear infrastructure road map supporting LFR system development*, Deliverable D3.2, ADRIANA Project, EURATOM FP7 Grant Agreement no.249687.
- [29] [W. Hering, M. Schyns, T.C. Boersma, L.Vermeeren, *Infrastructure road map and future needs for innovative systems development focused on instrumentation, diagnostics and experimental devices*, Deliverable D5.2, ADRIANA Project, EURATOM FP7 Grant Agreement no.249687.
- [30] L. Vermeeren, M. Rini, C. Roth, S. Knol, M. Marek, N. Girault, A. Horvath, *Report on future needs and infrastructure road map supporting irradiation facilities and hot labs development*, Deliverable D6.2, ADRIANA Project, EURATOM FP7 Grant Agreement no.249687.
- [31] V. Juricek, L. Vermeeren, A. Kochetkov, A. Santagata, *Report on future needs and infrastructure road map supporting Zero Power Reactors development*, Deliverable D7.2, ADRIANA Project, EURATOM FP7 Grant Agreement no.249687.
- [32] IAEA, *Accident Analysis for Nuclear Power Plants*, Safety Reports Series No. 23, Vienna, 2002.
- [33] IAEA, *The Safety of Nuclear Installations*, Safety Series No. 110, IAEA, Vienna (1993).
- [34] IAEA, *Safety of Nuclear Power Plants: Design*, IAEA Safety Standards Series No. NS-R-1, IAEA, Vienna (2000).
- [35] US NRC, *Standard Format and Content of Safety Analysis Reports for Nuclear Power Plants (LWR Edition)*, Regulatory Guide 1.70, US Govt Printing Office, Washington, DC (1979).
- [36] ANSI N18.2; *Nuclear Safety Criteria For The Design Of Stationary PWR Plants*; 1973.
- [37] NUREG-0800; *Standard Review Plan For The Review Of Safety Analysis Reports For Nuclear Power Plants*; U.S. Nuclear Commission; July, 1981.



 RICERCA SISTEMA ELETTRICO	<u>Title:</u> Development of BE numerical tools for LFR design and safety analysis – Part 1	<u>Distribution</u> PUBLIC	<u>Issue Date</u> 12.12.2017	<u>Pag.</u>
	<u>Project:</u> ADP ENEA-MSE PAR 2016	<u>Ref.</u> ADPFISS-LP2-144	Rev. 0	59 di 300


- [38] Westinghouse Electric Co.; *API1000 Design Control Document*; APP-GW-GL-700, Revision 2; April 29, 2002.
- [39] NEA/CSNI, *CSNI Status Summary on Utilization of Best-Estimate Methodology in Safety Analysis and Licensing*, NEA/CSNI/R (1996) 19, OECD Nuclear Energy Agency, Paris (1996).
- [40] N. Muellner, A. Del Nevo, M. Cherubini, F. D’Auria, O. Mazzantini, *Optimizing the Initial Pressure of Accumulators for the Atucha2 NPP Using an Optimization Method*, Proc. of 17th Int. Conf. on Nuc. Eng., (ICONE-17), Brussels, Belgium, July 12–16, 2009.
- [41] F. D’Auria, O. Melikhov, V. Melikhov, I. Elkin, A. Suslov, M. Bykov, A. Del Nevo, D. Araneo, N. Muellner, M. Cherubini, W. Giannotti, *Accident Management Technology in VVER-1000*, Industrie Grafiche Pacini Editore, ISBN 88-902189-1-6 (2 Vol.), pp 0-1440, Pisa, June 2006.
- [42] F. D’Auria, A. Bousbia-Salah, A. Petruzzi, A. Del Nevo, *State of the Art in Using Best Estimate Calculation Tools in Nuclear Technology*, Nuclear Engineering and Technology, Vol. 38, No. 1, Feb. 2006, pp 11-32
- [43] M. Perez, et. Al., *Uncertainty and sensitivity analysis of a LBLOCA in a PWR Nuclear Power Plant: Results of the Phase V of the BEMUSE programme*, Nucl. Eng. Des. 241 (2011) 4206–4222.
- [44] K. Umminger, A. Del Nevo, *Integral Test Facilities and Thermal-Hydraulic System Codes in Nuclear Safety Analysis*, Special issue: Science and Technology of Nuclear Installations, vol. 2012, Article ID 826732, 3 pages, 2012.



 RICERCA SISTEMA ELETTRICO	<u>Title:</u> Development of BE numerical tools for LFR design and safety analysis – Part 1 <u>Project:</u> ADP ENEA-MSE PAR 2016	<u>Distribution</u> PUBLIC	<u>Issue Date</u> 12.12.2017	<u>Pag.</u> 60 di 300
		<u>Ref.</u> ADPFISS-LP2-144	Rev. 0	

(Page intentionally left blank)




 RICERCA SISTEMA ELETTRICO	<u>Title:</u> Development of BE numerical tools for LFR design and safety analysis – Part 2	<u>Distribution</u> PUBLIC	<u>Issue Date</u> 12.12.2017	<u>Pag.</u>
	<u>Project:</u> ADP ENEA-MSE PAR 2016	<u>Ref.</u> ADPFISS-LP2-144	Rev. 0	61 di 300

DEVELOPMENT OF BEST ESTIMATE NUMERICAL TOOLS FOR LFR DESIGN AND SAFETY ANALYSIS


Part 2: Ongoing activities on development, validation and application of computational tools



 RICERCA SISTEMA ELETTRICO	<u>Title:</u> Development of BE numerical tools for LFR design and safety analysis – Part 2	<u>Distribution</u> PUBLIC	<u>Issue Date</u> 12.12.2017	<u>Pag.</u>
	<u>Project:</u> ADP ENEA-MSE PAR 2016	<u>Ref.</u> ADPFISS-LP2-144	Rev. 0	62 di 300

(Page intentionally left blank)



 RICERCA SISTEMA ELETRICO	<u>Title:</u> Development of BE numerical tools for LFR design and safety analysis – Part 2	<u>Distribution</u> PUBLIC	<u>Issue Date</u> 12.12.2017	<u>Pag.</u>
	<u>Project:</u> ADP ENEA-MSE PAR 2016	<u>Ref.</u> ADPFISS-LP2-144	Rev. 0	63 di 300

LIST OF CONTENTS

LIST OF FIGURES 67

LIST OF TABLES 75

LIST OF ABBREVIATIONS 77

1 DEVELOPMENT/ASSESSMENT OF MODELS DESCRIBING THE INERT GAS BEHAVIOR IN THE FUEL FOR APPLICATION TO THE TRANSURANUS FUEL PIN THERMO-MECHANICAL CODE 79

- 1.1 Background and references 81
 - 1.1.1 Helium diffusivity 81
 - 1.1.2 High burnup structure porosity 82
- 1.2 Body of the report concerning the ongoing activities 82
 - 1.2.1 Helium diffusivity 82
 - 1.2.2 High burnup structure porosity 84
- 1.3 Role of the activity, general goals and future development 87
- 1.4 List of References 95


2 VALIDATION OF FEM-LCORE/CATHARE BY TALL 3D EXPERIMENTAL TESTS 99

- 2.1 Background and references 101
 - 2.1.1 The multiscale / multiphysics platform 101
- 2.2 Validation of the FEMLCORE-CATHARE coupling model by Tall-3D facility experimental tests 101
 - 2.2.1 TALL-3D facility and 1D-CATHARE system model 101
 - 2.2.2 TALL-3D test section in FEMLCORE simulation 103
 - 2.2.3 Problem coupling on FEMLCORE-SALOME-CATHARE platform 107
- 2.3 Role of the activity, general goals and future development 110
- 2.4 List of References 135

3 VALIDATION OF RELAP5-3D BY CIRCE-ICE EXPERIMENTAL TESTS 137


- 3.1 Background and references 139
- 3.2 CIRCE-ICE facility 139
- 3.3 Simulation results 141
- 3.4 List of References 159



 RICERCA SISTEMA ELETRICO	<u>Title:</u> Development of BE numerical tools for LFR design and safety analysis – Part 2	<u>Distribution</u> PUBLIC	<u>Issue Date</u> 12.12.2017	<u>Pag.</u>
	<u>Project:</u> ADP ENEA-MSE PAR 2016	<u>Ref.</u> ADPFISS-LP2-144	Rev. 0	64 di 300

4 APPLICATION OF RELAP5/MOD3.3–FLUENT COUPLING CODES TO CIRCE-HERO	161
4.1 Background and references	163
4.2 Body of the report concerning the ongoing activities	164
4.2.1 CFD preliminary analysis	164
4.2.2 Adopted coupling procedure and obtained results	167
4.2.3 Conclusions	169
4.3 Role of the activity, general goals and future development.....	170
4.4 List of References	185
5 APPLICATION OF RELAP5-3D ON PHENIX EXPERIMENTAL TESTS.....	187
5.1 Background and references	189
5.2 Assessment of RELAP5-3D code in the framework of PHENIX dissymmetric tests....	189
5.2.1 Brief description of PHENIX	189
5.2.2 The dissymmetric tests	190
5.2.3 RELAP5-3D nodalization	190
5.2.4 Synthesis of blind results.....	192
5.3 Conclusive remarks and follow-up	193
5.4 List of References	209
6 FUEL-COOLANT CHEMICAL INTERACTION.....	211
6.1 Introduction.....	213
6.2 Computational activities	213
6.2.1 Implementation of the thermochemical database	213
6.2.2 Thermodynamic predictions by CALPHAD method	214
6.3 Experimental activities.....	215
6.4 Conclusions and future work	216
6.5 List of References	220
7 DEVELOPMENT AND VALIDATION OF DECAY HEAT MODELS INTO THE FRENETIC CODE.....	223
7.1 Background and references	225
7.1.1 Neutronic module	225
7.1.2 Thermal-hydraulic module	226
7.1.3 Modules coupling and feedback models	227
7.2 Body of the report concerning the ongoing activities	228
7.2.1 Introduction	228
7.2.2 Adaptive selection of the shape time steps	229
7.2.3 Adaptive selection of the reactivity time steps.....	232
7.2.4 Representative results.....	233
7.2.5 Conclusions and future work on time step adaptiveness.....	235
7.3 Role of the activity, general goals and future development.....	235



 RICERCA SISTEMA ELETTRICO	<u>Title:</u> Development of BE numerical tools for LFR design and safety analysis – Part 2	<u>Distribution</u> PUBLIC	<u>Issue Date</u> 12.12.2017	<u>Pag.</u>
	<u>Project:</u> ADP ENEA-MSE PAR 2016	<u>Ref.</u> ADPFISS-LP2-144	Rev. 0	65 di 300

7.3.1	Role of the activity and general goals	235
7.3.2	Future development	236
7.4	List of References	243


8 DEVELOPMENT OF MULTI-PHYSIC CODE FOR LEAD-COOLED FAST REACTOR 245

8.1	Background and references	247
8.1.1	Multiphysics modelling	247
8.2	Body of the report concerning the ongoing activities	247
8.2.1	Multi-physics modelling approach	248
8.2.2	Verification of the multi-physics neutronic model	253
8.2.3	Results and discussion	255
8.2.4	Nomenclature	256
8.3	Role of the activity, general goals and future development	257
8.4	List of References	268

9 VALIDATION OF SIMMER CODE AGAINST EXPERIMENTAL DATA 269


9.1	Background and references	271
9.2	Body of the report concerning the ongoing activities	271
9.2.1	LIFUS5/Mod2 facility	271
9.2.2	Instrumentation, control and data acquisition systems	273
9.2.3	Test matrix	274
9.2.4	SIMMER-III model	274
9.2.5	SIMMER-III results	275
9.2.6	Test T#1	275
9.2.7	Test T#2	276
9.2.8	Test T#3	277
9.2.9	Test T#4	278
9.2.10	Conclusions	280
9.3	Role of the activity, general goals and future development	281
9.4	List of References	299



 RICERCA SISTEMA ELETTRICO	<u>Title:</u> Development of BE numerical tools for LFR design and safety analysis – Part 2	<u>Distribution</u> PUBLIC	<u>Issue Date</u> 12.12.2017	<u>Pag.</u>
	<u>Project:</u> ADP ENEA-MSE PAR 2016	<u>Ref.</u> ADPFISS-LP2-144	Rev. 0	66 di 300

(Page intentionally left blank)



 RICERCA SISTEMA ELETTRICO	<u>Title:</u> Development of BE numerical tools for LFR design and safety analysis – Part 2	<u>Distribution</u> PUBLIC	<u>Issue Date</u> 12.12.2017	<u>Pag.</u>
	<u>Project:</u> ADP ENEA-MSE PAR 2016	<u>Ref.</u> ADPFISS-LP2-144	Rev. 0	67 di 300

LIST OF FIGURES

<i>Fig. 1.1 – Plot of the experimental helium diffusivity in oxide fuel obtained via the infusion technique.</i>	91
<i>Fig. 1.2 – Plot of the experimental helium diffusivity in oxide fuel obtained via the ion</i>	91
<i>Fig. 1.3 – Plot of the experimental helium diffusivity in oxide fuel obtained via the doping technique.</i>	92
<i>Fig. 1.4 – Plot of the experimental helium diffusivity in oxide fuel. The measurements performed via the infusion technique (green) are clustered in the lower part of the plot, whereas in the upper part emerges a cluster of those measurements performed via the ion implantation (blue) and doping (red) technique. This clustering is ascribed to the different level of lattice damage caused to the sample by the different experimental techniques. Each cluster is fitted by a distinct correlation (magenta and light green).</i>	92
<i>Fig. 1.5 – Comparison between the pore density obtained from experimental data and the model prediction.</i>	93
<i>Fig. 1.6 – Comparison between the pore volume values obtained from experimental data and the model prediction.</i>	93
<i>Fig. 1.7 – Comparison between the porosity measured by image analysis and the model prediction.</i>	94
<i>Fig. 2.1 - Possible multiphysics-multiscale code combinations on SALOME platform.</i>	113
<i>Fig. 2.2 - TALL-3D facility (left) with geometric dimensions (right).</i>	113
<i>Fig. 2.3 - One-dimensional CATHARE model for the TALL-3D facility (left) and point of interests S1-S2 of the left leg (on the right), S3-S4 of the central leg and S5-S6 of the right vertical leg.</i>	114
<i>Fig. 2.4 - Left, central and right vertical leg (from left to right) in 1D system model with 3D test section.</i>	114
<i>Fig. 2.5 - Bottom and top leg (from left to right) in 1D CATHARE system model (bottom) and experimental test section (top).</i>	115
<i>Fig. 2.6 - Computed temperature at points S1-S2 of the left leg (on the left) and at S3-S4 of the central leg (on the right) as a function of time t.</i>	116
<i>Fig. 2.7 - Computed temperature at the points S5-S6 of the right leg (on the left) and fluid flow rate at S1 (left), S3 (central) and S6 (right leg) (on the right) as a function of time t.</i>	116
<i>Fig. 2.8 - Experimental and computed mass flowrate on different legs (FM1, FM2, FM3).</i>	116
<i>Fig. 2.9 - Experimental and computed temperature at the thermocouple points TC3_4490, TC3_5615 along the left vertical leg (left), at TC1_0346, TC1_1740 on the right vertical leg (center) and at the thermocouple points TC_1211, TC2_2111 along the central vertical leg (left).</i>	117
<i>Fig. 2.10 - Geometry and dimensions of the three-dimensional test section.</i>	118
<i>Fig. 2.11 - Initial steady state for non-turbulent flow.</i>	119
<i>Fig. 2.12 - Average temperature over the outlet HG (A-B) and inlet boundary AB (C) over the iteration numbers for the laminar (A) and the turbulent case (B-C).</i>	119
<i>Fig. 2.13 - Initial steady state for turbulent flow model case (κ-ω) and turbulent viscosity ν_t with turbulent thermal diffusivity α_t.</i>	120





 RICERCA SISTEMA ELETTRICO	<u>Title:</u> Development of BE numerical tools for LFR design and safety analysis – Part 2	<u>Distribution</u> PUBLIC	<u>Issue Date</u> 12.12.2017	<u>Pag.</u>
	<u>Project:</u> ADP ENEA-MSE PAR 2016	<u>Ref.</u> ADPFISS-LP2-144	Rev. 0	68 di 300

Fig. 2.14 - TALL-3D facility at reference point 2 (RESERVE4, leg 1), temperature (left) and mass flow (right) for Case AB, ACF and ADE (from top to bottom).	121
Fig. 2.15 - TALL-3D facility at reference point 3 (BELOW3D25, central leg), temperature (left) and mass flow (right) for Case AB, ACF and ADE (from top to bottom).	122
Fig. 2.16 - TALL-3D facility at reference point 4 (ABOVE3D3, central leg), temperature (left) and mass flow (right) for Case AB, ACF and ADE (from top to bottom).	123
Fig. 2.17 - TALL-3D facility at reference point 5 (LINUP4, leg 3), temperature (left) and mass flow (right) for Case AB, ACF and ADE (from top to bottom).	124
Fig. 2.18 - TALL-3D facility at reference point 6 (PUMP0, leg 3), temperature (left) and mass flow (right) for Case AB, ACF and ADE (from top to bottom).	125
Fig. 2.19 - Temperature and streamline profiles over the 3D test component at $t = 10$ and 20 s for case B (non turbulent natural convection) and constant turbulent Prandtl number.	126
Fig. 2.20 - Temperature and streamline profiles over the 3D test component at $t = 30, 50, 100, 150, 200, 250, 500$ and 1000 s for case B (non turbulent natural convection) and constant turbulent Prandtl number.	127
Fig. 2.21 - Temperature and streamline profiles over the 3D test component at $t = 1500$ and 2000 s for case B (non turbulent natural convection) and constant turbulent Pr number.	128
Fig. 2.22 - Temperature and streamline profiles over the 3D test component at $t=10, 20, 30$ and 50 s for $\kappa-\omega$ turbulence case and Kays turbulent Pr number model for heat exchange.	128
Fig. 2.23 - Temperature and streamline profiles over the three-dimensional test component at $t=100, 150, 200, 250, 500, 1000, 1500$ and 2000 s, for $\kappa-\omega$ turbulence case and Kays turbulent Prandtl number model for heat exchange.	129
Fig. 2.24 - Temperature and streamline profiles over the three-dimensional test component at $t = 3000, 4000, 5000$ and 6000 s, for $\kappa-\omega$ turbulence case and Kays turbulent Prandtl number model for heat exchange.	130
Fig. 2.25 - Turbulent kinetic energy κ and streamline profiles over the three-dimensional test component at $t = 10, 20$ s, for $\kappa-\omega$ turbulence case and Kays turbulent Pr number model for heat exchange.	131
Fig. 2.26 - Turbulent kinetic energy κ and streamline profiles over the three-dimensional test component at $t=30, 50, 100, 150, 200, 250, 500$ and 1000 s, for $\kappa-\omega$ turbulence case and Kays turbulent Prandtl number model for heat exchange.	132
Fig. 2.27 - Turbulent kinetic energy κ and streamline profiles over the three-dimensional test component at $t=1500, 2000s, 3000s, 4000s, 5000s$ and 6000 s, for $\kappa-\omega$ turbulence case and Kays turbulent Prandtl number model for heat exchange.	133
Fig. 2.28 - Points of interest in the 1D overlapping mesh.	133
Fig. 2.29 - Mass flow rate (right) and temperature (left) as boundary conditions from CATHARE to FEMLCORE as a function of time.	134
Fig. 2.30 - Temperature and pressure imposed to CATHARE by FEMLCORE at point 4 as a function of time.	134
Fig. 3.1 - CIRCE isometric view.	146



 RICERCA SISTEMA ELETRICO	<u>Title:</u> Development of BE numerical tools for LFR design and safety analysis – Part 2	<u>Distribution</u> PUBLIC	<u>Issue Date</u> 12.12.2017	<u>Pag.</u>
	<u>Project:</u> ADP ENEA-MSE PAR 2016	<u>Ref.</u> ADPFISS-LP2-144	Rev. 0	69 di 300

<i>Fig. 3.2 - ICE test section.</i>	146
<i>Fig. 3.3 - ICE test section: primary flow path.</i>	147
<i>Fig. 3.4 - FPS cross section.</i>	147
<i>Fig. 3.5 - HX bayonet tube.</i>	148
<i>Fig. 3.6 - CIRCE instrumentation: FPS (1).</i>	148
<i>Fig. 3.7 - CIRCE instrumentation: FPS (2).</i>	149
<i>Fig. 3.8 - CIRCE instrumentation: pool.</i>	150
<i>Fig. 3.9 - CIRCE-ICE nodalizzation scheme: first version.</i>	151
<i>Fig. 3.10 - Nodalizzation scheme: Region 1.</i>	152
<i>Fig. 3.11 - Nodalizzation scheme: Region 2.</i>	152
<i>Fig. 3.12 - TEST I: LBE mass flow rate.</i>	153
<i>Fig. 3.13 - TEST I: HX removed power.</i>	153
<i>Fig. 3.14 - TEST I: FPS inlet/outlet temperatures.</i>	153
<i>Fig. 3.15 - TEST I: HX inlet/outlet temperatures.</i>	153
<i>Fig. 3.16 - FPS nodalizzation scheme.</i>	153
<i>Fig. 3.17 - Power supplied.</i>	154
<i>Fig. 3.18 - Feed-water mass flow rate.</i>	154
<i>Fig. 3.19 - Argon injection.</i>	154
<i>Fig. 3.20 - LBE mass flow rate.</i>	154
<i>Fig. 3.21 - HX inlet/outlet temperature.</i>	154
<i>Fig. 3.22 - FPS inlet/outlet temperature.</i>	154
<i>Fig. 3.23 - FPS temperature.</i>	154
<i>Fig. 3.24 - TS and MC: 2000 s.</i>	155
<i>Fig. 3.25 - TS and MC: 3000 s.</i>	155
<i>Fig. 3.26 - TS and MC: 5000 s.</i>	156
<i>Fig. 3.27 - TS and MC: 12000 s.</i>	156
<i>Fig. 3.28 - TS and MC: end of simulation.</i>	157
<i>Fig. 3.29 - LBE temperature into the pool.</i>	158
<i>Fig. 4.1 - HERO periodic geometrical domain: overall geometry (a), initial (b) and final (c) region.</i>	172
<i>Fig. 4.2 - HERO periodic transversal section.</i>	172
<i>Fig. 4.3 - LBE side spatial discretization.</i>	173
<i>Fig. 4.4 - HERO tubes spatial discretization.</i>	173
<i>Fig. 4.5 - Boundary walls.</i>	173




 RICERCA SISTEMA ELETRICO	<u>Title:</u> Development of BE numerical tools for LFR design and safety analysis – Part 2	<u>Distribution</u> PUBLIC	<u>Issue Date</u> 12.12.2017	<u>Pag.</u>
	<u>Project:</u> ADP ENEA-MSE PAR 2016	<u>Ref.</u> ADPFISS-LP2-144	Rev. 0	70 di 300

Fig. 4.6 - LBE temperature comparison between the three turbulence models: RNG $k-\varepsilon$ Model (a), Realizable $k-\varepsilon$ Model (b) and SST $k-\omega$ Model (c).....	174
Fig. 4.7 - LBE velocity magnitude comparison between the three turbulence models: RNG $k-\varepsilon$ Model (a), Realizable $k-\varepsilon$ Model (b) and SST $k-\omega$ Model (c).....	175
Fig. 4.8 - LBE turbulent kinetic energy comparison between the three turbulence models: RNG $k-\varepsilon$ Model (a), Realizable $k-\varepsilon$ Model (b) and SST $k-\omega$ Model (c).....	176
Fig. 4.9 - Brown line on the transversal section of the LBE domain, where calculation results were extracted.....	177
Fig. 4.10 - LBE temperature (a), velocity (b) and turbulent kinetic energy (c) profiles.	177
Fig. 4.11 - Temperature (a), velocity (b) and turbulent kinetic energy (c) profiles changing the turbulent Prandtl number.	178
Fig. 4.12 - Simplified sketch of the coupling technique adopted for HERO.....	179
Fig. 4.13 - Trend of temperatures obtained with the coupling procedure in the central pipe (Wall 3).	179
Fig. 4.14 - Trend of temperatures obtained with the coupling procedure in the lateral pipes (Wall 2).	180
Fig. 4.15 - Trend of temperatures obtained with the coupling procedure in the lateral pipes (Wall 2).	180
Fig. 4.16 - Comparison of the axial trend of HTC - water side.	181
Fig. 4.17 - Comparison of the axial trend of HTC - LBE side.	181
Fig. 4.18 - Comparison of the axial trend of wall the heat flux in the central pipe (Wall 3).	182
Fig. 4.19 - Comparison the axial trend of the wall heat flux in the lateral pipes (Wall 2).	182
Fig. 4.20 - LBE temperature distribution at $z=1.5975$ m (a) and $z= 4.0975$ m (b).....	183
Fig. 4.21 - LBE velocity at $z=1.5975$ m (a) and $z=4.0975$ m (b).	184
Fig. 5.1 - General overview of PHENIX reactor.....	197
Fig. 5.2 – PHENIX SA configuration.	198
Fig. 5.3 – PHENIX nodalization: layout of IHXs and PPs top view (PHENIX) and azimuthal meshes (RELAP5-3D©).....	198
Fig. 5.4 – PHENIX nodalization: MULTID component schematization.....	199
Fig. 5.5 – Blind results: MCPs pipe coolant temperature top position.....	199
Fig. 5.6 – Blind results: IHXs outlet coolant temperature bundle zone.....	200
Fig. 5.7 – Blind results: IHXs inlet coolant temperature annular zone.....	200
Fig. 5.8 – Blind results: diagrid inlet coolant temperature and average.....	201
Fig. 5.9 – Blind results: average SA coolant temperature, ranks 1 to 10.	201
Fig. 5.10 – Blind results: MCPs mass flow rate.....	202
Fig. 5.11 – Blind results: SA outlet coolant temperature ranks 1 to 7.....	202
Fig. 5.12 – Blind results: IHXs power.....	203
Fig. 5.13 – Blind results: screenshots of temperature trends, cylindrical slices through each MCPs and IHXs.	206




 RICERCA SISTEMA ELETTRICO	<u>Title:</u> Development of BE numerical tools for LFR design and safety analysis – Part 2	<u>Distribution</u> PUBLIC	<u>Issue Date</u> 12.12.2017	<u>Pag.</u>
	<u>Project:</u> ADP ENEA-MSE PAR 2016	<u>Ref.</u> ADPFISS-LP2-144	Rev. 0	71 di 300

Fig. 5.14 – Blind results: screenshots of temperature trends, vertical slices from center (core region) to IHX 1 A.208

Fig. 6.1 – Comparison between the heat capacity value calculated from DFT-GGA simulations and the values obtained from the Neumann-Kopp and Dulong-Petit laws.....218

Fig. 6.2 – Schematical composition of irradiated fuel and species distribution.218

Fig. 6.3 – Manual press and furnace inside the glove box operating under inert atmosphere.....219

Fig. 6.4 – Some of the samples obtained from the interaction experiments.219

Fig. 7.1 – FRENETIC steady-state solution algorithm.239

Fig. 7.2 – FRENETIC transient solution algorithm.240

Fig. 7.3 – Algorithm for shape time step selection [7.13].240

Fig. 7.4 – Algorithm for reactivity time step selection.241

Fig. 7.5 – Geometry of the system considered for the spatial transient [7.13].241

Fig. 7.6 – Error estimate and shape step size as a function of time, of the quantity regulated and of the tolerance for the continuous insertion of reactivity transient [7.13].242

Fig. 8.1 – Explicit Operator Splitting approach in multi-physics modelling.260

Fig. 8.2 – Implicit iterative approach in multi-physics modelling.260

Fig. 8.3 – Implicit fully coupled (or monolithic) approach in multi-physics modelling.....260

Fig. 8.4 – (a) Analysed fuel pin and surrounding lead. Radial sizes at nominal conditions (room temperature), expressed in mm. (b) Longitudinal (r; z) view of the modelled geometry.261

Fig. 8.5 – (a) Main boundary conditions applied for the neutronic model. (b) Main boundary conditions applied for the thermal-fluid dynamic model.261

Fig. 8.6 – Meshed geometry.261

Fig. 8.7 – (a) Fuel macroscopic capture cross-section versus temperature of energy group 3. (b) Fuel macroscopic capture cross-section versus density of energy group 3.262

Fig. 8.8 – (a) Lead macroscopic capture cross-section versus temperature of energy group 3. (b) Lead macroscopic capture cross-section versus density of energy group 3.262

Fig. 8.9 – k_{eff} estimate versus fuel temperature. SERPENT: bullets, COMSOL: lines.262

Fig. 8.10 – (a) k_{eff} estimate versus relative fuel axial expansion. SERPENT: bullets, COMSOL: lines. (b) k_{eff} estimate versus lead density variation. SERPENT: bullets, COMSOL: lines.263

Fig. 8.11 – (a) Axial neutron flux profiles within the active height. SERPENT: bullets, COMSOL: lines. (b) Relative difference between axial neutron fluxes computed by COMSOL and SERPENT.263

Fig. 8.12 – (a) Channel temperature field at nominal power conditions. (b) Cladding outer temperature and lead bulk temperature versus the z-coordinate, at nominal power conditions.264

Fig. 8.13 – (a) Velocity field inside the fluid domain. (b) Outer fuel radius and inner cladding radius, as a function of the axial coordinate, at nominal power conditions and at room temperature conditions.264




 RICERCA SISTEMA ELETTRICO	<u>Title:</u> Development of BE numerical tools for LFR design and safety analysis – Part 2	<u>Distribution</u> PUBLIC	<u>Issue Date</u> 12.12.2017	<u>Pag.</u>
	<u>Project:</u> ADP ENEA-MSE PAR 2016	<u>Ref.</u> ADPFISS-LP2-144	Rev. 0	72 di 300

Fig. 8.14 – (a) Total pin power during the transient case study with a reactivity insertion of 150 pcm. (b) Average fuel temperature during the transient case study with a reactivity insertion of 150 pcm.....	265
Fig. 8.15 – (a) Fuel axial expansion during the transient case study with a reactivity insertion of 150 pcm. (b) Average gap size during the transient case study with a reactivity insertion of 150 pcm.....	265
Fig. 8.16 – Axial profile of the cladding outer surface temperature during the transient case study with a reactivity insertion of 150 pcm.....	266
Fig. 8.17 – (a) Total pin power during the transient case study with inlet lead temperature increase of 20 °C. (b) Average fuel temperature during the transient case study with inlet lead temperature increase of 20 °C.....	266
Fig. 8.18 – Axial profile of the cladding outer surface temperature during the transient case study with inlet lead temperature increase of 20 °C.....	267
Fig. 9.1 – LIFUS5/Mod2 overall sketch (from [9.4]).....	284
Fig. 9.2 – LIFUS5/Mod2 facility, S1 and injection system (from [9.4]).	284
Fig. 9.3 – Support structure of the thermocouples in S1 (from [9.4]).....	285
Fig. 9.4 – Detailed view of the TCs’ support structure (from [9.4]).....	285
Fig. 9.5 – View of the protective cap “A” and injection orifice “B” (from [9.4]).....	286
Fig. 9.6 – P&ID of LIFUS5/Mod2 facility, acquisition and control systems (from [9.4]).....	286
Fig. 9.7 – Implemented instrumentation on the support structure and reaction tank S1 (from [9.4]).....	287
Fig. 9.8 – Control and regulation systems (from [9.4]).....	287
Fig. 9.9 – SIMMER-III geometrical model.....	288
Fig. 9.10 – SIMMER-III geometrical model injecting water from the cap orifice.....	288
Fig. 9.11 – Calculated and experimental pressure time trends of the test T#1.....	289
Fig. 9.12 – Calculated and experimental pressure time trends of the test T#1, without vacuum region in the injection line.....	289
Fig. 9.13 – LBE volume fraction and vapour bubble evolution during the water interaction phase, calculated by SIMMER-III code.....	290
Fig. 9.14 – Water kinetic energy time trends in the cover gas and LBE regions, T#1.....	290
Fig. 9.15 – Calculated and experimental pressure time trends of the test T#2.....	291
Fig. 9.16 – LBE volume fraction and vapour bubble evolution during the water interaction phase, calculated by SIMMER III code.....	291
Fig. 9.17 – Water kinetic energy time trends in the cover gas and LBE regions, T#2.....	292
Fig. 9.18 – Calculated and experimental pressure time trends of the test T#3.....	292
Fig. 9.19 – LBE volume fraction and vapour bubble evolution during the water interaction phase, calculated by SIMMER III code.....	293
Fig. 9.20 – Water kinetic energy time trends in the cover gas and LBE regions, T#3.....	293




 RICERCA SISTEMA ELETTRICO	<u>Title:</u> Development of BE numerical tools for LFR design and safety analysis – Part 2	<u>Distribution</u> PUBLIC	<u>Issue Date</u> 12.12.2017	<u>Pag.</u>
	<u>Project:</u> ADP ENEA-MSE PAR 2016	<u>Ref.</u> ADPFISS-LP2-144	Rev. 0	73 di 300

Fig. 9.21 – Calculated and experimental pressure time trends of the test T#4.294

Fig. 9.22 – LBE volume fraction and vapour bubble evolution during the water interaction phase, calculated by SIMMER-III code.....294

Fig. 9.23 – Water kinetic energy time trends in the cover gas and LBE regions, T#4.295

Fig. 9.24 – Calculated and experimental pressure time trends of the test T#4, with two-phase flow multiplier.....295

Fig. 9.25 – Calculated and experimental pressure time trends of the test T#4, with modified two-phase flow multiplier.....296


Fig. 9.26 – Experimental and calculated temperature time trends in the Level 1 of the test T#4.296

Fig. 9.27 – Experimental and calculated temperature time trends in the Level 2 of the test T#4.297

Fig. 9.28 – Experimental and calculated temperature time trends in the Level 3 of the test T#4.297


Fig. 9.29 – Experimental and calculated temperature time trends in the Level 4 of the test T#4.298



 RICERCA SISTEMA ELETTRICO	<u>Title:</u> Development of BE numerical tools for LFR design and safety analysis – Part 2	<u>Distribution</u> PUBLIC	<u>Issue Date</u> 12.12.2017	<u>Pag.</u>
	<u>Project:</u> ADP ENEA-MSE PAR 2016	<u>Ref.</u> ADPFISS-LP2-144	Rev. 0	74 di 300

(Page intentionally left blank)




 RICERCA SISTEMA ELETTTRICO	<u>Title:</u> Development of BE numerical tools for LFR design and safety analysis – Part 2	<u>Distribution</u> PUBLIC	<u>Issue Date</u> 12.12.2017	<u>Pag.</u>
	<u>Project:</u> ADP ENEA-MSE PAR 2016	<u>Ref.</u> ADPFISS-LP2-144	Rev. 0	75 di 300

LIST OF TABLES

<i>Tab. 1.1 – Summary of the experimental helium diffusivities in oxide fuel obtained via the infusion technique.</i>	89
<i>Tab. 1.2 – Summary of the experimental helium diffusivities in oxide and mixed oxide fuel obtained via the ion implantation technique.</i>	89
<i>Tab. 1.3 – Summary of the experimental helium diffusivities in oxide and mixed oxide fuel obtained via the doping technique.</i>	89
<i>Tab. 1.4 – Summary of the information concerning the fit of correlations.</i>	90
<i>Tab. 1.5 – List of parameters used in the HBS porosity model.</i>	90
<i>Tab. 2.1 - Initial state condition for the one-dimensional Problem C. The initial condition satisfies the steady state equation.</i>	112
<i>Tab. 2.2 – Final state condition for the one-dimensional code (CATHARE) solved without coupling.</i>	112
<i>Tab. 2.3 – Numerical stabilization and turbulence models used for all the simulated cases. Case A refers to Cathare standalone.</i>	112
<i>Tab. 3.1 - CIRCE S100 main parameters.</i>	145
<i>Tab. 3.2 - TEST I main parameters.</i>	145
<i>Tab. 4.1 - Mesh statistics.</i>	171
<i>Tab. 4.2 - AISI-304 steel thermal properties.</i>	171
<i>Tab. 4.3 - AISI-316 powder thermal properties.</i>	171
<i>Tab. 4.4 - Reference boundary conditions.</i>	171
<i>Tab. 4.5 - Reference boundary conditions for Fluent CFD Code.</i>	171
<i>Tab. 4.6 - Reference boundary conditions for RELAP5 System Code.</i>	171
<i>Tab. 5.1 – PHENIX end of life tests.</i>	194
<i>Tab. 5.2 – PHENIX dissymmetrical test: imposed sequence of main events.</i>	194
<i>Tab. 5.3 – PHENIX nodalization: adopted code resources.</i>	194
<i>Tab. 5.4 – Steady state results.</i>	195
<i>Tab. 5.5 – Pressure drops in primary system.</i>	196
<i>Tab. 7.1 – Amplitudes, relative to the initial value, as a function of the time and of the tolerance on the maximum allowed variation of the integral kinetics parameters with respect to their mean value on the reactivity time step for the point-like transient [7.13].</i>	237
<i>Tab. 7.2 – Number of reactivity time steps as a function of the time and of the tolerance on the maximum allowed variation of the integral kinetics parameters with respect to their mean value on the reactivity time step for the point-like transient [7.13]; N_p: cumulative number of reactivity time steps; ΔN_p: differential number of reactivity time steps.</i>	237
<i>Tab. 7.3 – Total power, relative to the initial value, as a function of time, of the quantity regulated and of the tolerance imposed on the variation of the error metric on the shape time step for the</i>	



 RICERCA SISTEMA ELETTRICO	<u>Title:</u> Development of BE numerical tools for LFR design and safety analysis – Part 2	<u>Distribution</u> PUBLIC	<u>Issue Date</u> 12.12.2017	<u>Pag.</u>
	<u>Project:</u> ADP ENEA-MSE PAR 2016	<u>Ref.</u> ADPFISS-LP2-144	Rev. 0	76 di 300

spatial transient [7.13]; NA: reference solution not computed for the entire duration of the transient.238

Tab. 7.4 – . Number of shape time steps as a function of time, of the quantity regulated and of the tolerance imposed on the variation of the error metric on the shape time step for the spatial transient [7.13]; N_{ψ} : cumulative number of shape time steps; N_{ψ}^R : cumulative number of rejected shape time steps.....239

Tab. 8.1 – Main parameters of the analysed core single-channel [8.10].....259

Tab. 8.2 – Energy structure adopted in multi-group neutron diffusion.....259

Tab. 8.3 – Segregated groups employed in the numerical solution.....259

Tab. 8.4 – Isotopic composition of the SERPENT input materials.....259

Tab. 9.1 – LIFUS5/Mod2 main features of components (from [9.4]).282

Tab. 9.2 – Experimental campaign test matrix (from [9.4]).282


Tab. 9.3 – Computational-BIC of test T#1.283

Tab. 9.4 – Computational-BIC of test T#2.283

Tab. 9.5 – Computational-BIC of test T#3.283

Tab. 9.6 – Computational-BIC of test T#4.283




 RICERCA SISTEMA ELETTRICO	<u>Title:</u> Development of BE numerical tools for LFR design and safety analysis – Part 2	<u>Distribution</u> PUBLIC	<u>Issue Date</u> 12.12.2017	<u>Pag.</u>
	<u>Project:</u> ADP ENEA-MSE PAR 2016	<u>Ref.</u> ADPFISS-LP2-144	Rev. 0	77 di 300

LIST OF ABBREVIATIONS


AdP	Accordo di Programma
ALFRED	Advanced Lead Fast Reactor European Demonstrator
ATHENA	Advanced Thermal Hydraulic Experiment for Nuclear Application
BE	Best Estimate
BEPU	Best Estimate Plus Uncertainty
BoP	Balance of Plant
BoT	Beginning of Transient
CEA	Commissariat a l'Energie Atomique et aux Energies Alternatives
CFD	Computational Fluid Dynamics
CIRCE	Circolazione Eutettico
CIRTEN	Interuniversity Consortium for Technological Nuclear Research
CHEOPEIII	Chemistry Operation III Facility
CR	Control Rod
DBA	Design Base Accident
DHR	Decay Heat Removal
DHRS	Decay Heat Removal System
DOC	Design-Oriented Code
DSA	Deterministic Safety Analysis
ESFRI	European Strategy Forum on Research Infrastructures
EoT	End of Transient
FA	Fuel Assembly
FALCON	Fostering ALFRED Construction
FPC	Fuel Performace Code
FR	Fast Reactor
GIORDI	Grid to Rod fretting facility
HBS	High Burnup Structure
HELENA	Heavy Liquid Metal Experimental Loop for Advanced Nuclear Applications
HLM	Heavy Liquid Metal
HX or HEX	Heat Exchanger
I&C	Instrumentation and Control
LBE	Lead Bismuth Eutectic
LECOR	Lead Corrosion Loop
LEADER	Lead-cooled Advanced Demonstration Reactor
LIFUS5	Lead-Lithium for Fusion Facility (5)
LFR	Lead Fast Reactor
LM	Liquid Metal
LMR	Liquid Metal Reactor
LWR	Light Water Reactor
MA	Minor Actinide
MABB	Minor Actinides Bearing Blankets
MOX	(U-Pu) Mixed Oxide
NACIE	Natural Circulation Experiment Loop
NPPs	Nuclear Power Plants
O&M	Operation and Maintenance
PAR	Piani Annuali di Realizzazione
PID	Proportional-Integral-Derivative controllers
PLD	Pulsed Laser Deposition
POLIMI	Politecnico di Milano



 RICERCA SISTEMA ELETTRICO	<u>Title:</u> Development of BE numerical tools for LFR design and safety analysis – Part 2	<u>Distribution</u> PUBLIC	<u>Issue Date</u> 12.12.2017	<u>Pag.</u>
	<u>Project:</u> ADP ENEA-MSE PAR 2016	<u>Ref.</u> ADPFISS-LP2-144	Rev. 0	78 di 300

POLITO	Politecnico di Torino
PP	Primary Pump
PSA	Probabilistic Safety Analysis
RACHELE	Reactions and Advanced chemistry for Lead
RSE	Ricerca Sistema Elettrico
RV	Reactor Vessel
RVACS	Reactor Vessel Air-Cooling System
SA	Safety Analysis
SET-PLAN	Strategic Energy Technology Plan
SG	Steam Generator
SGTR	Steam Generator Tube Rupture
SISO	Single Input Single Output
SYS	System
SYS-TH	System- ThermalHydraulics
TH	Thermal-Hydraulics
TKE	Turbulent Kinetic Energy
TRL	Technological Readiness Level
TSO	Technical Safety Organization
ULOF	Unprotected Loss of Flow
UNIBO	Università di Bologna
UNIPI	Università di Pisa
UNIROMA1	Università di Roma - Sapienza
VOC	Verification-Oriented Code
V&V	Verification & Validation



 RICERCA SISTEMA ELETTRICO	<u>Title:</u> Development of BE numerical tools for LFR design and safety analysis – Part 2	<u>Distribution</u> PUBLIC	<u>Issue Date</u> 12.12.2017	<u>Pag.</u>
	<u>Project:</u> ADP ENEA-MSE PAR 2016	<u>Ref.</u> ADPFISS-LP2-144	Rev. 0	79 di 300


1 DEVELOPMENT/ASSESSMENT OF MODELS DESCRIBING THE INERT GAS BEHAVIOR IN THE FUEL FOR APPLICATION TO THE TRANSURANUS FUEL PIN THERMO-MECHANICAL CODE

L. Luzzi, D. Pizzocri, T. Barani, L. Cognini




POLITECNICO
MILANO 1863



 RICERCA SISTEMA ELETTRICO	<u>Title:</u> Development of BE numerical tools for LFR design and safety analysis – Part 2	<u>Distribution</u> PUBLIC	<u>Issue Date</u> 12.12.2017	<u>Pag.</u> 80 di 300
	<u>Project:</u> ADP ENEA-MSE PAR 2016	<u>Ref.</u> ADPFISS-LP2-144	Rev. 0	

(Page intentionally left blank)



 RICERCA SISTEMA ELETTRICO	<u>Title:</u> Development of BE numerical tools for LFR design and safety analysis – Part 2	<u>Distribution</u> PUBLIC	<u>Issue Date</u> 12.12.2017	<u>Pag.</u>
	<u>Project:</u> ADP ENEA-MSE PAR 2016	<u>Ref.</u> ADPFISS-LP2-144	Rev. 0	81 di 300

1.1 Background and references

This activity is twofold: first, we present the derivation of two new correlations based on available literature data for helium diffusivity in oxide nuclear fuel; second, we present a model describing the evolution of the high burnup structure porosity observed in oxide nuclear fuel. Both these contributions are intended for implementation and use in the TRANSURANUS fuel performance code, in particular for its application to fast reactors.

1.1.1 Helium diffusivity

The knowledge of helium behavior in nuclear fuel is of fundamental importance for its safe operation and storage^{[1.1], [1.2]}. This is true irrespectively of the particular fuel cycle strategy adopted. In fact, both open and closed fuel cycles tend towards operating nuclear fuel to higher burnups (i.e., keeping the fuel in the reactor for a longer time to extract more specific energy from it), thus implying higher accumulation of helium in the fuel rods themselves^[1.3]. Moreover, considering open fuel cycles foreseeing the disposal of spent fuel, the helium production rate in the spent nuclear fuel is positively correlated with the burnup at discharge, and the production of helium (by α -decay of minor actinides) progresses during storage of spent fuel^{[1.4], [1.5]}. On the other hand, closed fuel cycles imply the use of fuels with higher concentrations of minor actinides (e.g., minor actinides bearing blankets, MABB), thus being characterized by higher helium production rates during operation^[1.6].


Helium is produced in nuclear fuel by ternary fissions, (n, α)-reactions and α -decay^{[1.7], [1.8], [1.9]}. After its production, it precipitates into intra- and inter-granular bubbles and can be absorbed/released from/to the nuclear fuel rod free volume^{[1.10], [1.11]}. Helium thus contributes to the fuel swelling (and eventually to the stress in the cladding after mechanical contact is established), to the pressure in the fuel rod free volume, and to the gap conductance (giving feedback to the fuel temperature)^[1.12].

Among the several properties governing the behavior of helium in nuclear fuel, its diffusivity and solubility govern the transport and absorption/release mechanisms^{[1.13], [1.14], [1.15]}. Compared to xenon and krypton, helium presents both a higher solubility and a higher diffusivity in oxide nuclear fuel^{[1.16], [1.17], [1.18]}. A considerable amount of experiments has been performed with the goal of determining the diffusivity and solubility of helium in nuclear fuel^{[1.13]-[1.16], [1.19]-[1.28]}. In particular, several measurements have been made to determine the helium diffusivity as a function of temperature^{[1.14]-[1.16], [1.20]-[1.28]}, whereas few experiments are available to characterize the Henry's constant^{[1.13]-[1.16], [1.19]-[1.21], [1.29]}.

The experimental procedures available for measuring helium diffusivity differ mainly in the way in which the helium is introduced in the fuel samples. In particular, three introduction techniques are used: (i) infusion^{[1.14], [1.16], [1.20], [1.21]}, in which the sample is kept in a pressurized helium atmosphere for a certain infusion time, (ii) ionic implantation^{[1.22]-[1.24], [1.26]-[1.28]}, in which a beam of $^3\text{He}^+$ hits and penetrates the sample, and (iii) doping^{[1.15], [1.25]}, in which α -decaying elements are introduced in the sample, resulting in an internal source of helium. These introduction techniques originate in the samples different helium spatial distributions and induce different levels of damage to the crystal lattice of the sample^{[1.15], [1.30]}.

In the light of the profound differences in experimental techniques and in microstructure of the samples, the correlations derived from rough data fitting must be critically analyzed. In fact, the spread of available diffusivities is extremely large. Nevertheless, the correlations for the helium diffusivity currently implemented in the TRANSURANUS code, as well as those available in the open literature, are derived from rough data fitting^{[1.14], [1.15], [1.24], [1.25], [1.28]} or are intended to be upper/lower boundaries enveloping the data^{[1.7], [1.25]}.



 RICERCA SISTEMA ELETTRICO	<u>Title:</u> Development of BE numerical tools for LFR design and safety analysis – Part 2	<u>Distribution</u> PUBLIC	<u>Issue Date</u> 12.12.2017	<u>Pag.</u>
	<u>Project:</u> ADP ENEA-MSE PAR 2016	<u>Ref.</u> ADPFISS-LP2-144	Rev. 0	82 di 300

1.1.2 High burnup structure porosity

In the peripheral region of light water reactor (LWR) UO₂ fuel pellets and in fast reactor MOX fuel as well, when the local burnup exceeds 50-60 GWd/tHM, a microstructural transformation starts to take place, as a consequence of enhanced accumulation of radiation damage, fission products and inhibited thermal recovery (temperature < 1273 K)^[1.31]. The newly formed structure is commonly named High Burnup Structure (HBS)^[1.32]. One of the main characteristics of the HBS is the large increase in local porosity, which can exceed the pellet average porosity by a factor 2-3^[1.33]. The newly formed micron-size inter-granular pores are surrounded by fine-grains (with average size 1·10⁻⁷-3·10⁻⁷ m), which give them a faceted appearance^{[1.33], [1.34]}. These spherical pores trap most of the created fission gas depleted from the fuel matrix^[1.31]. The HBS pores largely contribute to fuel swelling at high burnup and act as a thermal barrier, which contrasts the increase of lattice thermal conductivity following the reduction of point defect concentration inside the grains^{[1.35], [1.36]}. The gaseous fuel swelling increases the stresses on the cladding^[1.37], whereas a degradation of the fuel thermal conductivity, due to the poor thermal conductivity of fission gas bubbles, could result in enhanced fission gas release^[1.38]. The fission gas accumulation in the HBS region has therefore relevant implications to fuel performance^[1.39], and should be taken into account in fuel performance codes^[1.40].

At present, the TRANSURANUS code contains a model for the depletion of fission products^[1.32] in the HBS, and a separate model that describes the porosity increase in the HBS linearly dependent on burnup^[1.40]. Here, a first step is taken to describe the evolution of both phenomena in a more consistent manner. The modelling approach is based on a compromise between a physics-based treatment and a semi-empirical one to obtain a level of complexity suitable for future application to integral fuel performance codes.

1.2 Body of the report concerning the ongoing activities

Sect. 1.2.1 provides a complete overview of all the experimental results obtained for helium diffusivity in oxide nuclear fuel. The experimental results are classified according to the helium introduction technique used. At last, we derive empirical correlations and recommend the most suitable values of the helium diffusivity in the main cases of interest (e.g., in-pile, storage or annealing condition). The derivation of empirical correlations is complemented by an uncertainty analysis.

Sect. 1.2.2 describes a model for the evolution of high burnup structure porosity. This model extends the model for the formation of the high burnup developed as part of the POLIMI activities for the PAR 2015. The model presented here is preliminary validated against experimental data.


1.2.1 Helium diffusivity

Early measurements of the helium diffusivity in oxide nuclear fuel have been performed since the 1960s. The growing interest in determining helium behavior in nuclear fuel to assess its performance in storage conditions translated in several new experiments performed in the last twenty years.

Helium can be introduced into oxide nuclear fuel sample by infusion^{[1.14], [1.17], [1.21]}, ion implantation^{[1.22]-[1.24], [1.26]-[1.28]} or by doping the matrix with short-lived α -emitters^{[1.15], [1.25]}. Fig. 1.1 shows a sketch of the different experimental techniques herein considered. Depending on the helium introduction technique, the crystalline lattice suffers different levels of damage. Crystalline lattices with different damage levels show different helium behavior. Moreover, each technique used to introduce the helium in the sample has a corresponding specific technique to measure the amount of helium introduced.

Belle^[1.16] first studied the diffusivity of helium in a UO₂ powder. After his work, the helium diffusivity in oxide nuclear fuels was estimated by Rufe^{[1.17], [1.20]} and Sung^[1.21] using UO₂ samples (some in powder form and some single-crystals) with helium introduced through the infusion technique.



 RICERCA SISTEMA ELETRICO	<u>Title:</u> Development of BE numerical tools for LFR design and safety analysis – Part 2	<u>Distribution</u> PUBLIC	<u>Issue Date</u> 12.12.2017	<u>Pag.</u>
	<u>Project:</u> ADP ENEA-MSE PAR 2016	<u>Ref.</u> ADPFISS-LP2-144	Rev. 0	83 di 300

In a more recent study, Trocellier et al.^[1.22] measured the thermal diffusivity of ³He implanted in different nuclear materials. Subsequently, also Guilbert et al.^[1.23] and Roudil et al.^[1.24] performed similar experiments in similar temperature ranges (around 1173–1373 K), both using samples of polycrystalline UO₂. Ronchi and Hiernaut^[1.25] focused their activity on the mixed oxide fuel (U_{0.9},²³⁸Pu_{0.1})O₂, exploiting the plutonium content as a doping of the sample itself (²³⁸Pu is a convenient α -emitter). This is the first experimental work about helium diffusivity in mixed oxide fuel. Martin et al.^[1.26] measured helium concentrations in disks of polycrystalline UO₂, using the implantation technique. Pipon et al.^[1.27] applied the implantation technique to determine the diffusivity of mixed oxide samples with stoichiometry (U_{0.75},²³⁹Pu_{0.25})O₂.

Furthermore, Nakajima et al.^[1.14] determined the helium diffusivity in single-crystal UO₂ samples. They adopted the infusion technique and measured the helium infused concentration through a Knudsen–effusion mass-spectrometric method (KEMS). Garcia et al.^[1.28] measured the helium diffusivity in samples of polycrystalline UO₂ implanted at a fluence of 10²⁰ ³He·m⁻². They also estimated the diffusivity of helium at grain boundaries by comparing their results to those obtained from single crystals sample. Talip et al.^[1.15] used ²³⁸Pu-doped UO₂ samples. They measured the helium release rate as a function of the annealing temperature and used this information to derive the diffusivity of helium single atoms and of helium bubbles as well^[1.15]. Moreover, this study leveraged on the TEM technique, employed to obtain images of the sample before and after the introduction of helium. TEM provides additional qualitative and quantitative information, which is very useful for the interpretation of the outcome of the experiment (e.g., the amount of helium that precipitates into bubbles, the size of these bubbles and their location)^[1.15].

A recent study by Talip et al.^[1.41] investigated the diffusivity of helium in non-stoichiometric UO₂ fuel samples. This is of major interest because the fuel gradually transitions into a hyper-stoichiometric composition during storage^[1.5], and during operation if high burnups are achieved^[1.42]. The results of this work indicated that the diffusivity of helium is higher in non-stoichiometric samples compared to the diffusivity in stoichiometric ones, for both single-crystals and polycrystalline microstructures^[1.43].


Ending this brief overview, it is worth mentioning the important contribution to these studies arising from molecular dynamics (MD) calculations^{[1.26], [1.44]}. In particular, Yakub et al.^[1.44] investigated both hypo- and hyper-stoichiometric UO₂. They concluded that small deviations from stoichiometry significantly accelerate helium diffusion, in agreement with the experimental results for hyper-stoichiometric samples^[1.45]. The strength of this effect appears to be more pronounced in the hypo-stoichiometric domain^{[1.44], [1.46]}.

Tab. 1.1 to Tab. 1.3 and Fig. 1.1 to Fig. 1.3 collect all the diffusivity data discussed in this overview.

Considering the two clusters observed in the relevant experimental data (see Fig. 1.4), we propose two distinct empirical correlations for the helium diffusivity: one based on the data for infused samples and another one based on the data for implanted and doped samples. This implies that one correlation is suited for applications with no (or very limited) lattice damage, whereas the other is more suited for applications with significant lattice damage.

The proposed correlations for the diffusion coefficient D (m² s⁻¹) are in the form $D = D_0 \exp[-Q/kT]$. Tab. 1.4 collects the derived fitting parameters and the uncertainties related to each fitting parameter and to the diffusivity prediction as well. We can notice that the parameters for the correlation for ion implantation and doping data is affected by high uncertainty, related to the wide spread of the experimental data. Every comparison between the two correlations, in terms of activation energy Q (eV) and pre-exponential factor D_0 (m² s⁻¹), represents an indication of a tendency. In fact, the available data are not sufficient to statistically support conclusions. On the other hand, since we included all the available data in the fitting procedure, these correlations are the best available at this time.



 RICERCA SISTEMA ELETTRICO	<u>Title:</u> Development of BE numerical tools for LFR design and safety analysis – Part 2	<u>Distribution</u> PUBLIC	<u>Issue Date</u> 12.12.2017	<u>Pag.</u>
	<u>Project:</u> ADP ENEA-MSE PAR 2016	<u>Ref.</u> ADPFISS-LP2-144	Rev. 0	84 di 300

By fitting separately the two clusters of data (i.e., data from samples with no or very limited lattice damage and with significant lattice damage, respectively), we obtain an improved fitting quality. In fact, if data clustering is disregarded, the fit of all the data has a coefficient of determination of the linear regression $R^2 = 0.43$.

The best estimate correlation for the cluster of data with no or very limited lattice damage is

$$D = 2.0 \cdot 10^{-10} \exp[-2.12/kT] \quad (1.1)$$

whereas for the cluster of data with significant lattice damage we get

$$D = 3.3 \cdot 10^{-10} \exp[-1.64/kT] \quad (1.2)$$

We calculated the uncertainty on the prediction of the diffusivity by propagating the uncertainty of each fitting parameter. The resulting uncertainty is of the order of a factor of ten (x10) for the correlation relative to no or very limited lattice damage (Eq. 1.1) and of a factor of one thousand (x1,000) for the correlation relative to significant lattice damage (Eq. 1.2). For comparison, the uncertainty of the fit made with all the data is a factor of ten thousands (x10,000). The proposed categorization therefore allows for a reduction of uncertainties of a factor of one thousand/ten, respectively.

Fig. 1.4 collects the experimental results shown in Fig. 1.1-Fig. 1.3. The overall range of temperature covered by the available data is 968–2110 K. The range of the diffusivity itself is roughly five (5) orders of magnitude.

The experimental diffusivities are categorized depending on the technique used to introduce the helium in the samples (i.e., infusion, ion implantation and doping, with the color code green, blue and red, respectively). With this categorization, two clusters of data become evident: the measurements performed via the infusion technique are in the lower region of the diffusivity range, whereas the measurements performed via the ion implantation and doping techniques lie in the upper region.


We ascribe this major clustering of the data to the different level of lattice damage induced by the different experimental techniques used to introduce helium in the samples. In particular, ion implantation and doping introduce additional defects in the crystal lattice of the sample^[1.41], enhancing diffusion. This conclusion is in line with the studies showing enhanced diffusion in hypo- and hyper-stoichiometric samples^{[1.41], [1.44]}, i.e., in samples characterized by somewhat damaged crystal lattices. Fig. 1.4 reports two distinct correlations fitting each cluster of data.

1.2.2 High burnup structure porosity

According to the model for the fission gas depletion presented in Ref. [1.47], the average grain size in the HBS reduces exponentially with the local effective burnup¹. The increase in the concentration gradient within the fuel grains results in a depletion of fission gas from the grain interior. During the grain subdivision, it is assumed that pores are formed proportionally to the increase in the grain surface-to-volume ratio, namely:

¹ The local effective burnup is defined as the local burnup integrated below 1273 K^[1.61].



 RICERCA SISTEMA ELETTRICO	<u>Title:</u> Development of BE numerical tools for LFR design and safety analysis – Part 2	<u>Distribution</u> PUBLIC	<u>Issue Date</u> 12.12.2017	<u>Pag.</u>
	<u>Project:</u> ADP ENEA-MSE PAR 2016	<u>Ref.</u> ADPFISS-LP2-144	Rev. 0	85 di 300

$$\frac{dN_v}{dt} = K \cdot \frac{d}{dt} \left(\frac{S}{V} \right) \quad (1.3)$$

where N_v (m^{-3}) is the pore number density, t (s) is the time, S (m^2) is the grain surface, V (m^3) is the grain volume, and K (m^{-2}) is an empirical constant, chosen to fit the experimental data.

In agreement with the experimental observations, the gas depleted from the fuel matrix precipitates in the pores via grain boundary diffusion. The diffusion towards the pores is based on a cell model without source term^[1.48]. Each pore is assumed to be the center of a spherical Wigner-Seitz cell. Every pore is characterized by a spherical shape and radius R_p , whereas the unit cell has an equivalent radius R_c depending on the pore number density.

The diffusion proceeds in the spherical cell according to the following:

$$\begin{aligned} \frac{\partial c}{\partial t} &= \frac{D_{gb}}{r^2} \frac{\partial}{\partial r} \left(r^2 \frac{\partial c}{\partial r} \right) \\ \text{IC} \quad c(r, t_0) &= 0 \\ \text{BC} \quad c(R_p, t) &= 0 \\ &[\partial c / \partial r]_{R_c} = 0 \end{aligned} \quad (1.4)$$

where c (wt%) is the inter-granular gas concentration, D_{gb} ($\text{m}^2 \text{s}^{-1}$) is the grain boundary diffusion coefficient, R_p and R_c (m) the pore and cell radius, respectively.

The HBS is characterized by large values of porosity and pore density. At high density of trapping sites, competition between sinks should be taken into account. The effective rate constant k for gas precipitation in the HBS pores (e.g., see Ref. [1.48] for the complete set of equations considered in the cell model without source term) is written according to the work from Gösele^[1.49]:

$$k = 4\pi D_{gb} R_p (1 + 1.8P^{1/3}) \quad (1.5)$$

where D_{gb} , R_p have the same meaning as before and P (/) is the porosity calculated as:

$$P = N_v \frac{4}{3} \pi R_p^3 \quad (1.6)$$

The accumulation of fission gas in the pores causes pore pressurization. The pore overpressure is given by:


$$\Delta p = p - \left(\frac{2\gamma}{R_p} - p_h \right) \quad (1.7)$$

where γ (J m^{-2}) is the specific surface energy at the interface UO_2 and pore surface, set equal to^[1.50] 1 J m^{-2} , and p_h (Pa) represents the external hydrostatic pressure.

The pore pressure p (Pa) is calculated according to the Van der Waals gas law:

$$p(V_p - n_g \omega) = n_g k_b T \quad (1.8)$$



 RICERCA SISTEMA ELETTICO	<u>Title:</u> Development of BE numerical tools for LFR design and safety analysis – Part 2	<u>Distribution</u> PUBLIC	<u>Issue Date</u> 12.12.2017	<u>Pag.</u>
	<u>Project:</u> ADP ENEA-MSE PAR 2016	<u>Ref.</u> ADPFISS-LP2-144	Rev. 0	86 di 300

where n_g (/) is the number of gas atoms per pore, ω (m^3) is the is the xenon Van der Waals atomic volume equal to $8.50 \cdot 10^{-29} \text{ m}^3$, k (J K^{-1}) the Boltzmann's constant, T (K) the temperature, and V_p (m^3) the pore volume, given by:

$$V_p = n_v \Omega \quad (1.9)$$

where n_v (/) is the number of vacancies per pore and Ω (m^3) is the vacancy volume in the pore, assumed equal to^[1.23] $4.09 \cdot 10^{-29} \text{ m}^3$.

The model of Speight and Beere^[1.51] describes the growth (or shrinkage) of bubbles as proceeding by absorption (or emission) of vacancies in grain boundaries, induced by the bubble overpressure. The model of Speight and Beere was adapted to a spherical geometry to obtain the vacancy absorption/emission rate at a bubble:

$$\frac{dn_v}{dt} = \frac{2\pi D_v R_c}{k_b T F} \Delta p \quad (1.10)$$

where D_v ($\text{m}^2 \text{ s}^{-1}$) is the vacancy diffusion coefficient and F (/) is calculated as:

$$F = \frac{10\varphi(1 + \varphi^3)}{-\varphi^6 + 5\varphi^2 - 9\varphi + 5} \quad (1.11)$$

The inflow of vacancies causes a variation in the pore growth given by:

$$\left. \frac{dV_p}{dt} \right|_g = \frac{dn_v \Omega}{dt} \quad (1.12)$$

It was shown by Torquato et al.^[1.52] that for a system of random penetrable spheres (i.e., Poisson distributed), sphere contact can occur at volume fractions above 0.085. Since in the HBS porosity fractions can exceed such value, possible coalescence by geometric interference of the growing pores is considered in the model^[1.53]. In the coalescence event, the volume of the interacting pores is conserved as assumed in Ref. [1.50]. Following the same argument as in Ref. [1.50], the pore growth and coalescence leads to a decrease in pore number density which in 3D is:


$$\frac{dn_p}{dt} = - \frac{4n_p^2}{1 + 4n_p V_p} \frac{dV_p}{dt} \quad (1.13)$$

The rate change of the pore volume accounts both for the growth contribution and a contribution due to the coalescence^[1.50]:

$$\frac{dV_p}{dt} = \left(\frac{dV_p}{dt} \right)_g + \left(\frac{dV_p}{dt} \right)_c \quad (1.14)$$

The additional term owing to solely coalescence is:



 RICERCA SISTEMA ELETRICO	<u>Title:</u> Development of BE numerical tools for LFR design and safety analysis – Part 2	<u>Distribution</u> PUBLIC	<u>Issue Date</u> 12.12.2017	<u>Pag.</u>
	<u>Project:</u> ADP ENEA-MSE PAR 2016	<u>Ref.</u> ADPFISS-LP2-144	Rev. 0	87 di 300

$$\left(\frac{dV_p}{dt}\right)_c = -\frac{V_p}{n_p} \frac{dn_p}{dt} \quad (1.15)$$

No release from the HBS is considered in this model, according to experimental evidence that support that most of the gas is retained in the HBS.

The model for the fission gas depletion presented in Ref. [1.47] and the model for the pore growth introduced above were coded as stand-alone computer program. All the relevant information about fuel fabrication data (e.g., initial porosity P_0 and fabrication grain size a_0), local fission density, temperature and hydrostatic stress are given as input. The model parameters used are listed in Tab. 1.5.

For the grain boundary diffusion coefficient of the gas, the model by Turnbull^[1.54] was used, based on the values reported by Matzke^[1.55]:

$$D_{gb} = 10^{-8} \exp\left(-\frac{4.8 \cdot 10^{-19}}{k_b T}\right) + 5.64 \cdot 10^{-25} \sqrt{\dot{F}} \exp\left(-\frac{1.9 \cdot 10^{-19}}{k_b T}\right) + 10^{-39} \dot{F} \quad (1.16)$$

For the vacancy diffusion coefficient, the expression is^{[1.53], [1.56]}:

$$D_v = 8.86 \cdot 10^{-6} \exp\left(-\frac{5.75 \cdot 10^{-19}}{k_b T}\right) + 10^{-39} \dot{F} \quad (1.17)$$


In Fig. 1.5 to Fig. 1.7, the model predictions are compared to the experimental data from Refs. [1.57] and [1.58]. The pore growth model correctly predicts the pore density drop starting at approximately 100 GWd/tHM (Fig. 1.5), but the pore density decrease is largely underestimate. The increase in the pore volume is underestimated (Fig. 1.6). As a consequence of the first two, the porosity is largely overestimated (Fig. 1.7). In particular, the model fails in reproducing the change in slope in the porosity increase rate experimentally seen^{[1.57], [1.58]} from ≈ 110 GWd/tHM, resulting in a large over-estimation of the porosity. This is likely due to an underestimation of the diffusion coefficient in the HBS, thus leading to an underestimation of the rate of precipitation of gas and vacancies. On the other side, it has to be mentioned that the model does not account for the pore size distribution, rather the pores are assumed to be monodispersed with characteristic size R_p . This assumption might not be suitable for burnups above 150 GWd/tHM, at which the pore size distribution is very poly-disperse, and might influence the coalescence rate. Further development in the coalescence model seems necessary.

1.3 Role of the activity, general goals and future development

The activity represents an ideal continuation of previous efforts carried out in modeling the impact of inert gas behavior on the thermo-mechanical performance of oxide nuclear fuels and for the advancement of available numerical tools for the simulation of oxide fuel in LFR conditions^{[1.59], [1.60]}. In this picture, helium diffusivity plays a fundamental role in determining oxide fuel swelling and fuel rod pressurization, thus affecting its thermo-mechanical behavior under both normal operation and transient conditions. Moreover, since high burnups are attractive from an economical perspective, modeling the formation of the high burnup structure and its peculiar thermo-mechanical behavior is of the utter relevance to the safe operation of oxide-fueled rods in LFR systems.

The exposed advancements in the modeling of helium diffusivity and HBS behavior represent two mandatory steps in the enhancements of the available numerical tools, and contribute to overcome the




 RICERCA SISTEMA ELETTRICO	<u>Title:</u> Development of BE numerical tools for LFR design and safety analysis – Part 2	<u>Distribution</u> PUBLIC	<u>Issue Date</u> 12.12.2017	<u>Pag.</u>
	<u>Project:</u> ADP ENEA-MSE PAR 2016	<u>Ref.</u> ADPFISS-LP2-144	Rev. 0	88 di 300

substantial limitations in the state-of-the-art fuel performance codes for the analysis of the inert gas behavior in oxide nuclear fuel in fast reactor conditions.

Near-term efforts will be devoted to further improvements of the description of helium behavior. In particular, an analysis of intra-granular helium solubility in the mixed U-Pu oxide matrix is envisaged, aimed at deriving new and accurate correlations for the Henry's constant of helium. The latter aspect will complete the here begun characterization of intra-granular helium behavior, and paves the way to the development of a complete, physically-based model for intra-granular helium behavior. This calls for a dedicated numerical tool to be included in the available fuel performance codes. In fact, in contiguity to the work done in the past years^[1,60], the development of a new numerical method to efficiently solve the mathematical problem represented by helium intra-granular model is of interest.



 RICERCA SISTEMA ELETTICO	<u>Title:</u> Development of BE numerical tools for LFR design and safety analysis – Part 2	<u>Distribution</u> PUBLIC	<u>Issue Date</u> 12.12.2017	<u>Pag.</u> 89 di 300
	<u>Project:</u> ADP ENEA-MSE PAR 2016	<u>Ref.</u> ADPFISS-LP2-144	Rev. 0	

	Sample	Diffusivity ($\text{m}^2 \text{s}^{-1}$)	Temperature (K)
Belle[1.16]	UO ₂ powder (0.16 μm)	$9.05 \cdot 10^{-22}$	968
Belle[1.16]	UO ₂ powder (0.16 μm)	$1.01 \cdot 10^{-20}$	1070
Belle[1.16]	UO ₂ powder (0.16 μm)	$4.08 \cdot 10^{-20}$	1166
Belle[1.16]	UO ₂ powder (0.16 μm)	$1.86 \cdot 10^{-19}$	1268
Rufeh[1.20] Rufeh et al.[1.17]	UO ₂ powder (4 μm)	$1.5 \cdot 10^{-17}$	1473
Sung[1.21]	UO ₂ single-crystal (1 μm)	$6.14 \cdot 10^{-18}$	1473
Sung[1.21]	UO ₂ single-crystal (1 μm)	$9.15 \cdot 10^{-18}$	1623
Sung[1.21]	UO ₂ single-crystal (1 μm)	$12.57 \cdot 10^{-18}$	1773
Nakajima et al.[1.14]	UO ₂ single-crystal (18 μm)	$9.50 \cdot 10^{-10} \exp[-2.05/kT]$	range 1170–2110
Nakajima et al.[1.14]	UO ₂ single-crystal (18 μm)	$4.88 \cdot 10^{-10} \exp[-1.93/kT]$	range 1390–2070

Tab. 1.1 – Summary of the experimental helium diffusivities in oxide fuel obtained via the infusion technique.


	Sample	Diffusivity ($\text{m}^2 \text{s}^{-1}$)	Temperature (K)
Trocellier et al.[1.22]	UO ₂ poly-crystal	$(3.7 \pm 0.74) \cdot 10^{-18}$	1273
Guilbert et al.[1.23]	UO ₂ poly-crystal (8 μm)	$6 \cdot 10^{-17}$	1373
Roudil et al.[1.24]	UO ₂ poly-crystal (10 μm)	$8 \cdot 10^{-9} \exp[-(2 \pm 0.1)/kT]$	range 1123–1273
Roudil et al.[1.24]	UO ₂ poly-crystal (10 μm)	$4 \cdot 10^{-10} \exp[-(2 \pm 0.1)/kT]$	range 1123–1273
Martin et al.[1.26]	UO ₂ poly-crystal (24 μm)	$2.25 \cdot 10^{-17}$	1073
Martin et al.[1.26]	UO ₂ poly-crystal (24 μm)	$7.6 \cdot 10^{-17}$	1373
Pipon et al.[1.27]	(U _{0.75} , ²³⁹ Pu _{0.25})O ₂ poly-crystal	$9.2 \cdot 10^{-18}$	1123
Pipon et al.[1.27]	(U _{0.75} , ²³⁹ Pu _{0.25})O ₂ poly-crystal	$1.6 \cdot 10^{-16}$	1273
Garcia et al.[1.28]	UO ₂ poly-crystal	$5 \cdot 10^{-10} \exp[-(1.4 \pm 0.2)/kT]$	range 973–1373

Tab. 1.2 – Summary of the experimental helium diffusivities in oxide and mixed oxide fuel obtained via the ion implantation technique.

	Sample	Diffusivity ($\text{m}^2 \text{s}^{-1}$)	Temperature (K)
Ronchi and Hiernaut[1.25]	(U _{0.9} , ²³⁸ Pu _{0.1})O ₂ poly-crystal	$(8 \pm 2) \cdot 10^{-7} \exp[-(2.00 \pm 0.02)/kT]$	N/A
Talip et al. [1.15]	(U _{0.999} , ²³⁸ Pu _{0.001})O ₂ poly-crystal (10 μm)	$10^{-7} \exp[-2.59/kT]$	range 1320–1800

Tab. 1.3 – Summary of the experimental helium diffusivities in oxide and mixed oxide fuel obtained via the doping technique.



 RICERCA SISTEMA ELETTRICO	<u>Title:</u> Development of BE numerical tools for LFR design and safety analysis – Part 2	<u>Distribution</u> PUBLIC	<u>Issue Date</u> 12.12.2017	<u>Pag.</u> 90 di 300
	<u>Project:</u> ADP ENEA-MSE PAR 2016	<u>Ref.</u> ADPFISS-LP2-144	Rev. 0	

Data	Log D_0 (m ² s ⁻¹)	Q (eV)	Range (K)	R^2
Infusion [1.14], [1.16], [1.17], [1.20], [1.21]	-9.7 (-11, -8.4)	2.12 (1.77, 2.56)	968–2110	0.93
Ion implantation [1.22]-[1.24], [1.26]-[1.28] and doping [1.15],[1.25]	-9.5 (-13, -5.8)	1.64 (0.74, 2.56)	973–1800	0.52

Tab. 1.4 – Summary of the information concerning the fit of correlations.

Parameter	Value	Reference
K	$2.9 \cdot 10^{10} \text{ m}^{-2}$	[1.57]
R_{p0}	$0.25 \cdot 10^{-6} \text{ m}$	[1.57]
\dot{F}	$10^{19} \text{ m}^3 \text{ s}^{-1}$	[1.56]
T	900.15 K	This work
p_h	-20 MPa	This work
a_0	$13.5 \cdot 10^{-6} \text{ m}$	This work
P_0	0.04	[1.58]

Tab. 1.5 – List of parameters used in the HBS porosity model.



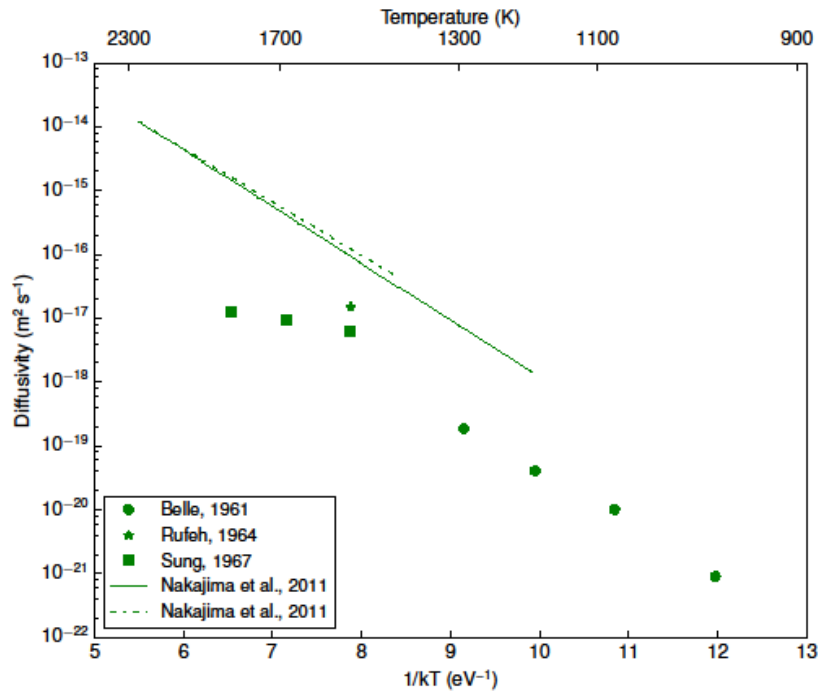


Fig. 1.1 – Plot of the experimental helium diffusivity in oxide fuel obtained via the infusion technique.

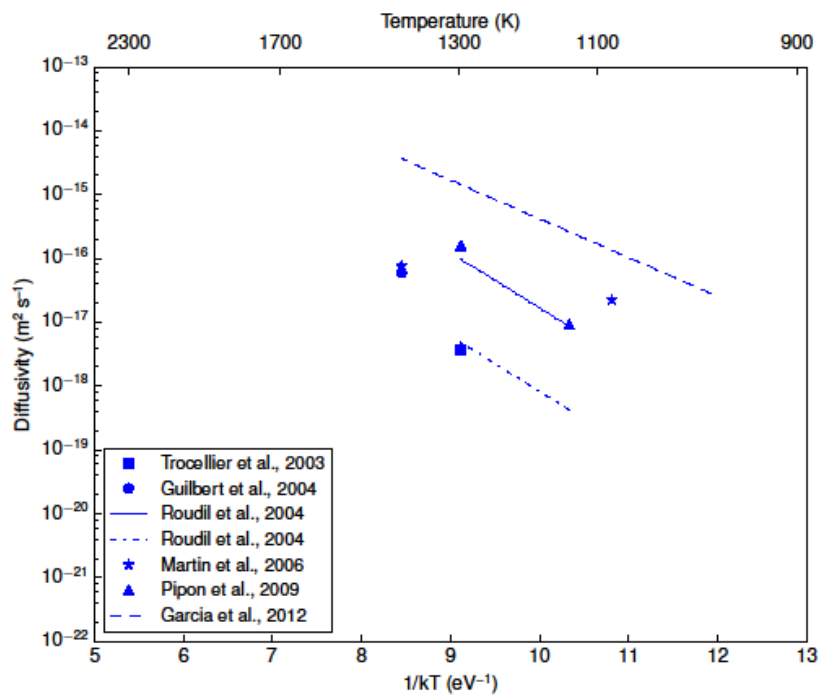


Fig. 1.2 – Plot of the experimental helium diffusivity in oxide fuel obtained via the ion technique.



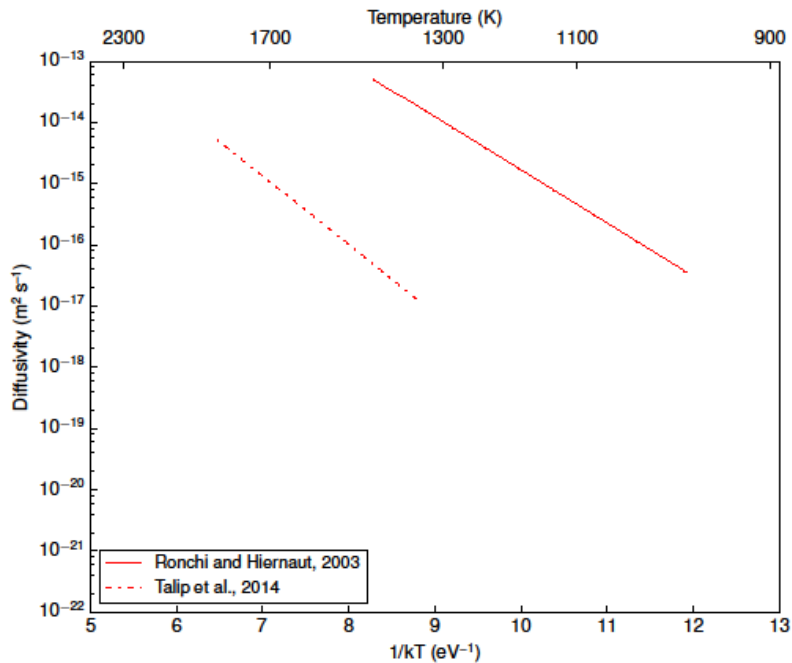


Fig. 1.3 – Plot of the experimental helium diffusivity in oxide fuel obtained via the doping technique.

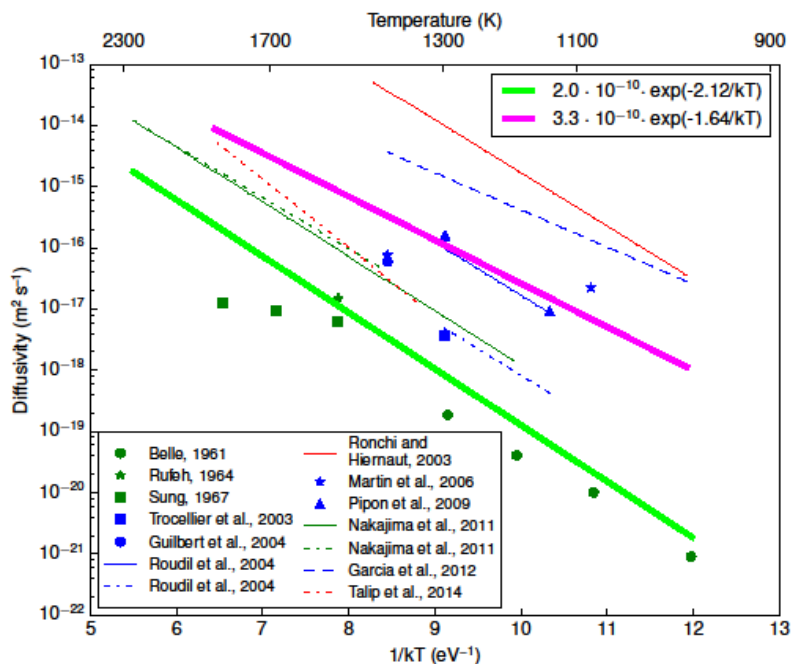


Fig. 1.4 – Plot of the experimental helium diffusivity in oxide fuel. The measurements performed via the infusion technique (green) are clustered in the lower part of the plot, whereas in the upper part emerges a cluster of those measurements performed via the ion implantation (blue) and doping (red) technique. This clustering is ascribed to the different level of lattice damage caused to the sample by the different experimental techniques. Each cluster is fitted by a distinct correlation (magenta and light green).



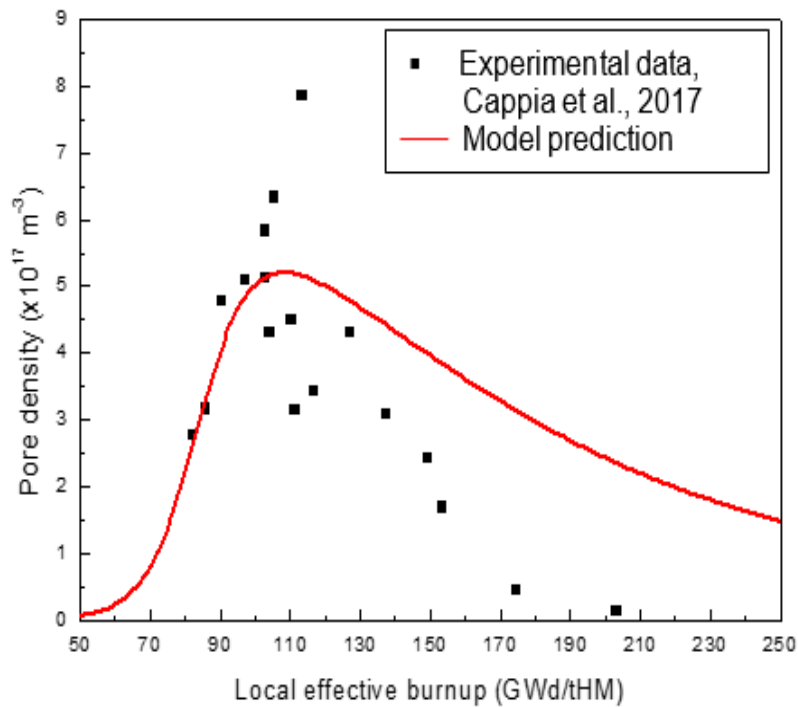


Fig. 1.5 – Comparison between the pore density obtained from experimental data and the model prediction.

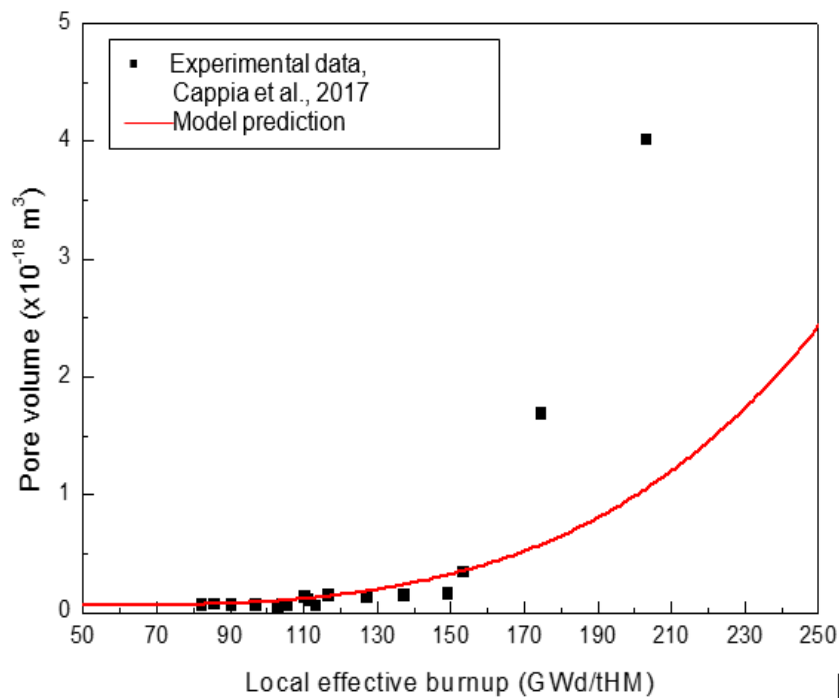


Fig. 1.6 – Comparison between the pore volume values obtained from experimental data and the model prediction.



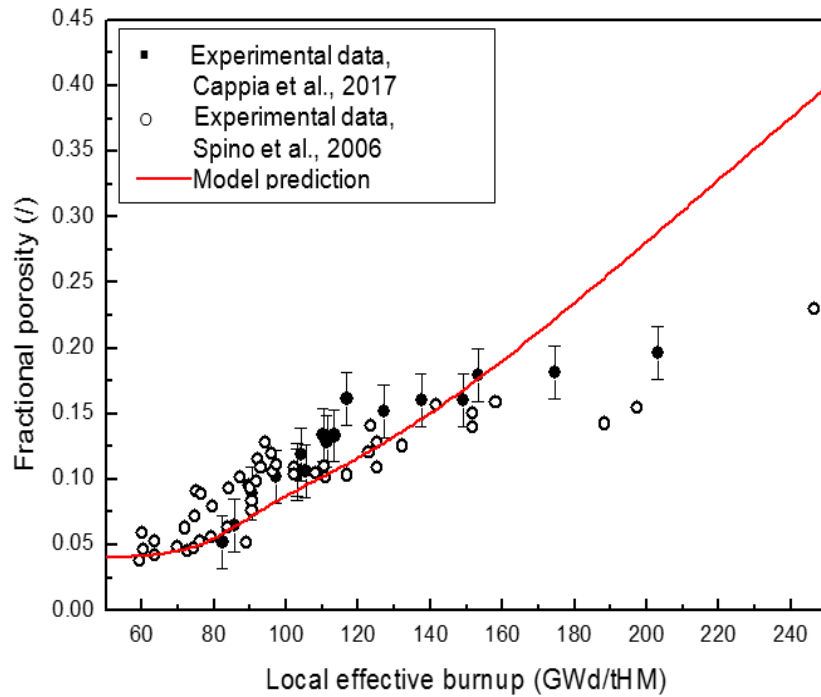



Fig. 1.7 – Comparison between the porosity measured by image analysis and the model prediction.




 RICERCA SISTEMA ELETTRICO	<u>Title:</u> Development of BE numerical tools for LFR design and safety analysis – Part 2	<u>Distribution</u> PUBLIC	<u>Issue Date</u> 12.12.2017	<u>Pag.</u>
	<u>Project:</u> ADP ENEA-MSE PAR 2016	<u>Ref.</u> ADPFISS-LP2-144	Rev. 0	95 di 300

1.4 List of References


- [1.1] G. Rossiter, Understanding and modelling fuel behaviour under irradiation, in: I. Crossland (Ed.), Nucl. Fuel Cycle Sci. Eng., Woodhead Publishing Limited, 2012: pp. 396–426.
- [1.2] D.R. Olander, Fundamental Aspects of Nuclear Reactor Fuel Elements Fundamental Aspects of Nuclear Reactor Fuel Elements, 1976. doi:10.1016/0022-3115(77)90226-4.
- [1.3] V.V. Rondinella, T. Wiss, J. Cobos, H. Hiernaut, Studies on spent fuel alterations during storage and radiolysis effects on corrosion behaviour using alpha-doped UO₂, in: 9th Conf. Radioact. Waste Manag. Environ. Remediat., 2003: p. 4593.
- [1.4] I. Crossland, Nuclear fuel cycle science and engineering, Woodhead Publishing Limited, 2012.
- [1.5] T. Wiss, J.P. Hiernaut, D. Roudil, J.Y. Colle, E. Maugeri, Z. Talip, A. Janssen, V. Rondinella, R.J.M. Konings, H.J. Matzke, W.J. Weber, Evolution of spent nuclear fuel in dry storage conditions for millennia and beyond, J. Nucl. Mater. 451 (2014) 198–206. doi:10.1016/j.jnucmat.2014.03.055.
- [1.6] I. Crossland, Nuclear fuel cycle science and engineering, Woodhead Publishing Limited, 2012.
- [1.7] E. Federici, A. Courcelle, P. Blanpain, H. Cognon, Helium production and behavior in nuclear oxide fuels during irradiation in LWR, Proc. Int. LWR Fuel Perform. Meet. San Fr. Calif. (2007) 664–673.
- [1.8] P. Botazzoli, Helium Production and Behaviour in LWR Oxide Nuclear Fuels, PhD Thesis, Politec. Di Milano, Italy. (2011).
- [1.9] R.C. Ewing, W.J. Weber, F.W. Clinard, Radiation effects in nuclear waste forms for high-level radioactive waste, Prog. Nucl. Energy. 29 (1995) 63–127. doi:10.1016/0149-1970(94)00016-Y.
- [1.10] H. Matzke, Gas release mechanisms in UO₂ - A critical review, Radiat. Eff. 53 (1980) 219–242.
- [1.11] A.H. Booth, A method of calculating fission gas diffusion from UO₂ fuel and its application to the X-2-f loop test, At. Energy Canada Ltd. Chalk River Proj. Res. Dev. Rep. AECL-496. (1957) 1–23.
- [1.12] J. Piron, J. P.; Pelletier, M.; Pavageau, Fission gas behaviour in water reactor fuels, OECD/NEA. (2000).
https://books.google.co.jp/books/about/Fission_gas_behaviour_in_water_reactor_f.html?id=iYdTAA AAMA AJ&pgis=1.
- [1.13] E. Maugeri, T. Wiss, J.P. Hiernaut, K. Desai, C. Thiriet, V. V. Rondinella, J.Y. Colle, R.J.M. Konings, Helium solubility and behaviour in uranium dioxide, J. Nucl. Mater. 385 (2009) 461–466. doi:10.1016/j.jnucmat.2008.12.033.
- [1.14] K. Nakajima, H. Serizawa, N. Shirasu, Y. Haga, Y. Arai, The solubility and diffusion coefficient of helium in uranium dioxide, J. Nucl. Mater. 419 (2011) 272–280. doi:10.1016/j.jnucmat.2011.08.045.
- [1.15] Z. Talip, T. Wiss, V. Di Marcello, A. Janssen, J.Y. Colle, P. Van Uffelen, P. Raison, R.J.M. Konings, Thermal diffusion of helium in 238Pu-doped UO₂, J. Nucl. Mater. 445 (2014) 117–127. doi:10.1016/j.jnucmat.2013.10.066.
- [1.16] J. Belle, Uranium Dioxide: properties and nuclear applications, Library (Lond). (1961) 569–589.
- [1.17] T.H. Ruffe, F; Olander, D R; Pigford, The solubility of helium in uranium dioxide, Nucl. Sci. Eng. (1965).
- [1.18] [18] T. Petit, M. Freyss, P. Garcia, P. Martin, M. Ripert, J.P. Crocombette, F. Jollet, Molecular modelling of transmutation fuels and targets, J. Nucl. Mater. 320 (2003) 133–137. doi:10.1016/S0022-3115(03)00179-X.



 RICERCA SISTEMA ELETTRICO	<u>Title:</u> Development of BE numerical tools for LFR design and safety analysis – Part 2	<u>Distribution</u> PUBLIC	<u>Issue Date</u> 12.12.2017	<u>Pag.</u>
	<u>Project:</u> ADP ENEA-MSE PAR 2016	<u>Ref.</u> ADPFISS-LP2-144	Rev. 0	96 di 300


- [1.19] S. Hasko, R. Szwarc, Noble gas solubility and diffusion in UO₂, AEC, Div. React. Dev. Washingt. (1963).
- [1.20] F. Rufeh, Solubility of helium in uranium dioxide, M. S. Thesis, Univ. Calif. (1964).
- [1.21] P. Sung, Equilibrium solubility and diffusivity of helium in single-crystal uranium dioxide, PhD Thesis, Univ. Washingt. (1967).
- [1.22] P. Trocellier, D. Gosset, D. Simeone, J.M. Costantini, X. Deschanel, D. Roudil, Y. Serruys, R. Grynszpan, S.E. Saudé, M. Beauvy, Application of nuclear reaction geometry for ³He depth profiling in nuclear ceramics, Nucl. Instruments Methods Phys. Res. Sect. B Beam Interact. with Mater. Atoms. 206 (2003) 1077–1082. doi:10.1016/S0168-583X(03)00914-5.
- [1.23] S. Guilbert, T. Sauvage, P. Garcia, G. Carlot, M.F. Barthe, P. Desgardin, G. Blondiaux, C. Corbel, J.P. Piron, J.M. Gras, He migration in implanted UO₂ sintered disks, J. Nucl. Mater. 327 (2004) 88–96. doi:10.1016/j.jnucmat.2004.01.024.
- [1.24] D. Roudil, X. Deschanel, P. Trocellier, C. Jégou, S. Peugeot, J.M. Bart, Helium thermal diffusion in a uranium dioxide matrix, J. Nucl. Mater. 325 (2004) 148–158. doi:10.1016/j.jnucmat.2003.11.012.
- [1.25] C. Ronchi, J.P. Hiernaut, Helium diffusion in uranium and plutonium oxides, J. Nucl. Mater. 325 (2004) 1–12. doi:10.1016/j.jnucmat.2003.10.006.
- [1.26] G. Martin, P. Garcia, H. Labrim, T. Sauvage, G. Carlot, P. Desgardin, M.F. Barthe, J.P. Piron, A NRA study of temperature and heavy ion irradiation effects on helium migration in sintered uranium dioxide, J. Nucl. Mater. 357 (2006) 198–205. doi:10.1016/j.jnucmat.2006.06.021.
- [1.27] Y. Pipon, C. Raepsaet, D. Roudil, H. Khodja, The use of NRA to study thermal diffusion of helium in (U, Pu)O₂, Nucl. Instruments Methods. 267 (2009) 2250–2254. doi:10.1016/j.nimb.2009.03.025.
- [1.28] P. Garcia, G. Martin, P. Desgardin, G. Carlot, T. Sauvage, C. Sabathier, E. Castellier, H. Khodja, M.F. Barthe, A study of helium mobility in polycrystalline uranium dioxide, J. Nucl. Mater. 430 (2012) 156–165. doi:10.1016/j.jnucmat.2012.06.001.
- [1.29] K. Blanpain, P. Lippens, M.; Schut, H., Federov, A. V., Bakker, The HARLEM Project, Helium solubility in UO₂, Work. MMSNF-5, Nice, Fr. (2006).
- [1.30] [H. Labrim, M.F. Barthe, P. Desgardin, T. Sauvage, C. Corbel, G. Blondiaux, J.P. Piron, Thermal evolution of the vacancy defects distribution in 1 MeV helium implanted sintered UO₂, Nucl. Instruments Methods Phys. Res. Sect. B Beam Interact. with Mater. Atoms. 261 (2007) 883–887. doi:10.1016/j.nimb.2007.04.059.
- [1.31] V. V. Rondinella, T. Wiss, The high burn-up structure in nuclear fuel, Mater. Today. 13 (2010) 24–32. doi:10.1016/S1369-7021(10)70221-2.
- [1.32] K. Lassmann, C.T. Walker, J. van de Laar, F. Lindström, Modelling the high burnup UO₂ structure in LWR fuel, J. Nucl. Mater. 226 (1995) 1–8. doi:10.1016/0022-3115(95)00116-6.
- [1.33] J. Spino, K. Vennix, M. Coquerelle, Detailed characterisation of the rim microstructure in PWR fuels in the burn-up range 40-67 GWd/tM, J. Nucl. Mater. 231 (1996) 179–190. doi:10.1016/0022-3115(96)00374-1.
- [1.34] C.T. Walker, T. Kameyama, S. Kitajima, M. Kinoshita, Concerning the microstructure changes that occur at the surface of UO₂ pellets on irradiation to high burnup, J. Nucl. Mater. 188 (1992) 73–79. doi:10.1016/0022-3115(92)90456-U.



 RICERCA SISTEMA ELETRICO	<u>Title:</u> Development of BE numerical tools for LFR design and safety analysis – Part 2	<u>Distribution</u> PUBLIC	<u>Issue Date</u> 12.12.2017	<u>Pag.</u>
	<u>Project:</u> ADP ENEA-MSE PAR 2016	<u>Ref.</u> ADPFISS-LP2-144	Rev. 0	97 di 300


- [1.35] C. Ronchi, M. Sheindlin, D. Staicu, M. Kinoshita, Effect of burn-up on the thermal conductivity of uranium dioxide up to 100.000 MWdt-1, *J. Nucl. Mater.* 327 (2004) 58–76. doi:10.1016/j.jnucmat.2004.01.018.
- [1.36] X.M. Bai, M.R. Tonks, Y. Zhang, J.D. Hales, Multiscale modeling of thermal conductivity of high burnup structures in UO₂ fuels, *J. Nucl. Mater.* 470 (2016) 208–215. doi:10.1016/j.jnucmat.2015.12.028.
- [1.37] P. Van Uffelen, M. Sheindlin, V.V. Rondinella, C. Ronchi, On the relations between the fission gas behaviour and the pellet-cladding mechanical interaction in LWR fuel rods, in: *Pellet-Cladding Interact. Water React. Fuels*, 2004: pp. 213–228.
- [1.38] D. Olander, Swelling due to fission gases, in: *Fundam. Asp. Nucl. React. Fuel Elem.*, 1976: pp. 210–213.
- [1.39] Very High Burn-ups in Light Water Reactors, 2006.
- [1.40] K. Lassmann, A. Schubert, J. van de Laar, Recent developments of the TRANSURANUS code with emphasis on high burnup phenomena, in: *Nucl. Fuel Behav. Model. High Burn. Its Exp. Support*, 2001: pp. 387–405.
- [1.41] Z. Talip, T. Wiss, E.A. Maugeri, J.Y. Colle, P.E. Raison, E. Gilabert, M. Ernstberger, D. Staicu, R.J.M. Konings, Helium behaviour in stoichiometric and hyper-stoichiometric UO₂, *J. Eur. Ceram. Soc.* 34 (2014) 1265–1277. doi:10.1016/j.jeurceramsoc.2013.11.032.
- [1.42] B.J. Lewis, W.T. Thompson, F.C. Iglesias, Fission product chemistry in oxide fuels, in: R.J.M. Konings (Ed.), *Compr. Nucl. Mater.*, Elsevier Inc., 2012: pp. 515–546. doi:10.1016/B978-0-08-056033-5.00042-2.
- [1.43] J.-P. Crocombette, Ab initio energetics of some fission products (Kr, I, Cs, Sr and He) in uranium dioxide, *J. Nucl. Mater.* 305 (2002) 29–36. doi:10.1016/S0022-3115(02)00907-8.
- [1.44] E. Yakub, C. Ronchi, D. Staicu, Diffusion of helium in non-stoichiometric uranium dioxide, *J. Nucl. Mater.* 400 (2010) 189–195. doi:10.1016/j.jnucmat.2010.03.002.
- [1.45] E. Yakub, C. Ronchi, D. Staicu, Computer simulation of defects formation and equilibrium in non-stoichiometric uranium dioxide, *J. Nucl. Mater.* 389 (2009) 119–126. doi:10.1016/j.jnucmat.2009.01.029.
- [1.46] K. Govers, S. Lemehov, M. Hou, M. Verwerft, Molecular dynamics simulation of helium and oxygen diffusion in UO_{2±x}, *J. Nucl. Mater.* 395 (2009) 131–139. doi:10.1016/j.jnucmat.2009.10.043.
- [1.47] D. Pizzocri, F. Cappia, L. Luzzi, G. Pastore, V.V. Rondinella, P. Van Uffelen, A semi-empirical model for the formation and the depletion of the high burnup structure in UO₂ fuel, *J. Nucl. Mater.* (n.d.) 1–20.
- [1.48] P. Van Uffelen, Contribution to the modelling of fission gas release in Light Water Reactor fuel, Université de Liège, 2002.
- [1.49] U. Gösele, Concentration dependence of rate constants for diffusion- or reaction-controlled void-point-defect reactions, *J. Nucl. Mater.* 78 (1978) 83–95. doi:10.1016/0022-3115(78)90507-X.
- [1.50] G. Pastore, L. Luzzi, V. Di Marcello, P. Van Uffelen, Physics-based modelling of fission gas swelling and release in UO₂ applied to integral fuel rod analysis, *Nucl. Eng. Des.* 256 (2013) 75–86. doi:10.1016/j.nucengdes.2012.12.002.



 RICERCA SISTEMA ELETTRICO	<u>Title:</u> Development of BE numerical tools for LFR design and safety analysis – Part 2	<u>Distribution</u> PUBLIC	<u>Issue Date</u> 12.12.2017	<u>Pag.</u>
	<u>Project:</u> ADP ENEA-MSE PAR 2016	<u>Ref.</u> ADPFISS-LP2-144	Rev. 0	98 di 300

- [1.51] M.V. Speight, W. Beere, Vacancy potential and void growth on grain boundaries, *Met. Sci.* 9 (1975) 190–191.
- [1.52] S. Torquato, B. Lu, J. Rubinstein, Nearest-neighbor distribution functions in many-body systems, *Phys. Rev. A.* 41 (1990) 2059–2075.
- [1.53] R.J. White, The development of grain-face porosity in irradiated oxide fuel, *J. Nucl. Mater.* 325 (2004) 61–77. doi:10.1016/j.jnucmat.2003.10.008.
- [1.54] J.A. Turnbull, C.A. Friskney, J.R. Findlay, F.A. Johnson, A.J. Walter, The diffusion coefficients of gaseous and volatile species during the irradiation of uranium dioxide, *J. Nucl. Mater.* 107 (1982) 168–184. doi:10.1016/0022-3115(82)90419-6.
- [1.55] H. Matzke, Gas release mechanisms in UO₂ - a critical review, *Radiat. Eff.* 53 (1980) 219–242.
- [1.56] P. Blair, Modelling of fission gas behaviour in high burnup nuclear fuel, 4084 (2008) 188.
- [1.57] F. Cappia, D. Pizzocri, A. Schubert, P. Van Uffelen, G. Paperini, D. Pellottiero, R. Macian-Juan, V. V. Rondinella, Critical assessment of the pore size distribution in the rim region of high burnup UO₂ fuels, *J. Nucl. Mater.* 480 (2016) 138–149.
- [1.58] J. Spino, A.D. Stalios, H. Santa Cruz, D. Baron, Stereological evolution of the rim structure in PWR-fuels at prolonged irradiation: Dependencies with burn-up and temperature, *J. Nucl. Mater.* 354 (2006) 66–84. doi:10.1016/j.jnucmat.2006.02.095.
- [1.59] L. Luzzi, G. Pastore, P. Botazzoli, Modelli di rilascio dei gas di fissione per combustibili MOX ad elevato burnup, ENEA, Report RDS/2013/022, 2013.
- [1.60] L. Luzzi, T. Barani, E. Bruschi, D. Pizzocri, D. Rozzia, A. Del Nevo, Advancement in FGR modeling for transient analysis of FR fuel, ENEA, ADPFISS-LP2-118, 2016.
- [1.61] L. Holt, A. Schubert, P. Van Uffelen, C.T. Walker, E. Fridman, T. Sonoda, Sensitivity study on Xe depletion in the high burn-up structure of UO₂, *J. Nucl. Mater.* 452 (2014) 166–172. doi:10.1016/j.jnucmat.2014.05.009.




 RICERCA SISTEMA ELETTRICO	<u>Title:</u> Development of BE numerical tools for LFR design and safety analysis – Part 2	<u>Distribution</u> PUBLIC	<u>Issue Date</u> 12.12.2017	<u>Pag.</u>
	<u>Project:</u> ADP ENEA-MSE PAR 2016	<u>Ref.</u> ADPFISS-LP2-144	Rev. 0	99 di 300

2 VALIDATION OF FEM-LCORE/CATHARE BY TALL 3D EXPERIMENTAL TESTS


R. Da Vià, L. Chirco, A. Cervone, S. Manservigi



 RICERCA SISTEMA ELETTRICO	<u>Title:</u> Development of BE numerical tools for LFR design and safety analysis – Part 2	<u>Distribution</u> PUBLIC	<u>Issue Date</u> 12.12.2017	<u>Pag.</u>
	<u>Project:</u> ADP ENEA-MSE PAR 2016	<u>Ref.</u> ADPFISS-LP2-144	Rev. 0	100 di 300

(Page intentionally left blank)



 RICERCA SISTEMA ELETTRICO	<u>Title:</u> Development of BE numerical tools for LFR design and safety analysis – Part 2	<u>Distribution</u> PUBLIC	<u>Issue Date</u> 12.12.2017	<u>Pag.</u>
	<u>Project:</u> ADP ENEA-MSE PAR 2016	<u>Ref.</u> ADPFISS-LP2-144	Rev. 0	101 di 300

2.1 Background and references

In this report we develop and validate the multiscale software FEMLCORE-CATHARE in the framework of the open-source SALOME platform. In particular we develop the 1D-3D coupling software and simulate the evolution of an unprotected loss of flow going from forced to natural circulation flow in the experimental TALL-3D facility. In this unprotected loss of flow the system is initially in fully working conditions, then the pump stops while the supplied power is not switched off. We consider, by using a defective coupling algorithm with overlapping meshes, a one-dimensional circuit and a three-dimensional test section. In order to evaluate the behavior of the coupling system we have studied the system by using up-wind and supg algorithms in laminar natural convection regime or by introducing simple momentum ($\kappa\omega$) and energy turbulent models (with constant and non-constant turbulent Prandtl number).

2.1.1 The multiscale / multiphysics platform

An open-source multiscale and multiphysics platform has been developed with joint effort between ENEA and UNIBO. This platform is capable of 1D-3D multiscale coupling between open, research and commercial codes. The developed software is used in this report to study the TALL-3D facility. This platform mimics for Lead-cooled Fast Reactors (LFR) an existing numerical platform, the NURES SAFE platform, developed by the CEA for coupling different codes in the study of a new design of light water reactors (LWR). The CEA software is not open source but it is based on SALOME platform, which is indeed an open-source software [2.1]. Inside this well known framework we have used the open-software platform to add new codes and develop coupling interface compatible with open and closed source codes. The SALOME platform brings several tools: KERNEL, GUI, GEOM, SMESH, MED and Paravis module. The KERNEL module provides a common shell for all components, which can be integrated into the SALOME platform. The GUI module provides visual representation with basic widgets and the GEOM module draws and optimizes geometrical models using a wide range of CAD functions. The SMESH module generates meshes on geometrical models previously created or imported by the GEOM component, ParaVis performs data visualization and post processing and finally MED allows to work with highly compressed files. Over this platform several codes may be installed as suggested in Fig. 2.1.


2.2 Validation of the FEMLCORE-CATHARE coupling model by Tall-3D facility experimental tests

2.2.1 TALL-3D facility and 1D-CATHARE system model

The experimental facility. The experimental TALL-3D facility is reported in Fig. 2.2 on the left with its geometrical dimensions on the right. The facility operates with Lead-Bismuth Eutectic (LBE) (melting point 125° C) which is optimal with high temperature sensitive instrumentation. The facility consists of a LBE-cooled primary (on the left) and an oil-cooled secondary loop (on the right). The primary loop consists of the sump tank used to store, melt and supply LBE into the main loop, 3 vertical legs and 2 connecting horizontal sections. The secondary loop is used to control heat balance in the primary loop. The primary loop is rather complex and consists of three legs. For details on TALL-3D facility the interested reader can see Refs from [2.2] to [2.7].

The total electric power is about 80 kW, with 27 kW in the Main Heater section (MH) and 15 kW in the 3D-test section heater. The maximum measurable LBE flow velocity is 5 kg/s in forced circulation and 0.6 kg in natural circulation in the Heat Exchanger (HX) leg. The maximum LBE temperature is 460 °C in the hot side and 350 °C in the cold side. The secondary loop can be operated at temperatures in the range of 50-300 °C. Maximum temperature difference across the heat exchanger can be 90 °C. The static pressure at the top is 1.3 bar while at the bottom can reach 7.8 bar. The maximum hydrostatic head from the EPM pump is therefore 2 bar.



 RICERCA SISTEMA ELETTRICO	<u>Title:</u> Development of BE numerical tools for LFR design and safety analysis – Part 2	<u>Distribution</u> PUBLIC	<u>Issue Date</u> 12.12.2017	<u>Pag.</u>
	<u>Project:</u> ADP ENEA-MSE PAR 2016	<u>Ref.</u> ADPFISS-LP2-144	Rev. 0	102 di 300

The thermal-hydraulics system code model facility. Thermal-hydraulics of this primary loop is the main subject of the numerical test for the 3D-1D coupling and validation of the code interfaces. The one-dimensional system code computation model is shown in Fig. 2.3. For this one-dimensional simulation of the whole system we propose CATHARE 2.5 code^{[2.8], [2.9], [2.10]}. The 1D model of the left vertical legs is shown in Fig. 2.4 on the left. This leg consists of the main heater and it is connected on the top to the main tank and on the bottom to the sump tank. The Main Heater (labeled with MH) is a rod-like electric heating element. Its maximum electric power is 27 kW. The 1D model of the central vertical leg is shown in Fig. 2.4 in the center. This leg is the key part of the circuit for our test since this contains the 3D test section. It consists of three AXIALS: the ABOVE3D, BELOW3D and 3DPIPE module. TALL-3D test section is an axisymmetric cylindrical stainless steel vessel with an inlet at the bottom and an outlet at the top. The upper part of the test section is equipped with two 7.5 kW line heaters rolled jointly around the circumference. The heaters enhance the development of thermal stratification in the LBE pool. Simulations predict that the pool is fully mixed at 0.7 kg/s LBE flow rate and stratified at 0.3 kg/s LBE flow rate. For details on TALL-3D facility the interested reader can see Refs from [2.2] to [2.7].


As one can see in Fig. 2.3 on the right we consider six reference points labeled by S1, S2, S3, S4, S5 and S6. The points S1 and S2 are located along the left vertical leg. The point S1 is in the COR module at the element mesh 3. We denote such point with COR3 or S1. The point S2 is inside the RESERVE module at the element mesh 4. We denote such point with RESERVE4. The points S3 and S4 are located in the central vertical leg. The point S3 is in the BELOW3D module at the element mesh 25. The point S4 is inside the ABOVE3D module at the element mesh 8. We denote such points with BELOW3D24 and ABOVE3D8, respectively. Finally the points S5 and S6 are located along the right vertical leg. The point S5 is in the LINUP2 module at the element mesh 14. The point S6 is in the PUMP module at the element mesh 0. In a similar way, we denote such points with LINUP14 and PUMP, respectively.

During loop operation temperatures up to 500 °C, pressures up to 0.7 MPa and flow rates up to about 5 kg/s, which corresponds to a flow velocity of approx. 1.7 m/s, can be achieved in HX leg. Oxygen control system is implemented to monitor chemical potential of the LBE dissolved oxygen. It is required to stay within 1.5e-7 and 1.85e-5 wt% to stabilize the protective oxide layer on the LBE wet components. The sensor is YSZ membrane with oxygen saturated Bi reference. The minimal operation temperature is determined by the membrane permeability which becomes active at 360 °C, though the recommended temperature interval is 400-450 °C.

The top horizontal part of the LBE circuit is shown in Fig. 2.5 and modeled in one-dimensional coordinate geometry. It consists of the main expansion tank (labeled with TANK), two AXIALS (LINUP1, LINUP2) and a volume that links this part of the top LBE circuit to the central vertical leg with the three-dimensional test section. The TANK volume and the LINUP2 are connected with the left (with the MH) and right vertical leg (with HX), respectively. The expansion tank is used to monitor the LBE level in the loop and maintain loop pressure during temperature induced deformation along the loop components. The bottom horizontal part of the LBE circuit, shown in Fig. 2.5 on the bottom and modeled with 1D coordinate geometry, consists of 2 axial modules (LINDOWN, DOWNPUMP) and a volume module (VOLDDOWN) which links the bottom to the central vertical leg with the three-dimensional test section.

Initial state of the one-dimensional system code. In order to set the initial conditions we need to compute an initial state that satisfies the one-dimensional equation. Then we consider the Unprotected Loss of Flow (ULOF) test (labeled T01.09) which reproduces a forced to natural circulation transient. A solution of this high nonlinear system is computed for the mono-dimensional model in its steady state. We start with inlet temperature for the PIPE3D set to 241.35 °C. The flow rate is set to 4.275 Kg/s with density $\rho = 10448$



 RICERCA SISTEMA ELETRICO	<u>Title:</u> Development of BE numerical tools for LFR design and safety analysis – Part 2	<u>Distribution</u> PUBLIC	<u>Issue Date</u> 12.12.2017	<u>Pag.</u>
	<u>Project:</u> ADP ENEA-MSE PAR 2016	<u>Ref.</u> ADPFISS-LP2-144	Rev. 0	103 di 300

Kg/m³. The one-dimensional code has a variable time step. We start with $dt = 0.01$ and allow maximal value of 1s. After 1500 s the temperature reaches the steady value reported in Tab. 2.1.

ID-CATHARE simulation and experimental results. We simulate the evolution of an Unprotected Loss of Flow going from forced to natural circulation flow. We consider the system at $t = 0^-$ in fully working conditions. At $t = 1$ the pump stops working while the power supplied through the rod in MH leg and 3D vessel heater are not switched off. As explained in the previous section the main initial conditions in forced circulation are obtained as a steady state and they are shown in Tab. 2.1. The test is characterized by almost constant boundary conditions, also during the transient phase. To approach the correct heat transfer conditions with LBE in the secondary side, the initial LBE temperature of 206 °C is reduced to 199 °C in the first 10 s of transient. The mass flow rate, kept constant during the test, is set to 1.752 kg/s. Due to the lack of secondary side mass flow rate measurement, the oil flow rate has been calculated starting from the loss of enthalpy in the primary side, then with a thermal balance in the secondary side. The flow rate evolutions in the three legs are presented in Fig. 2.6 and Fig. 2.7. Here we do not report the experimental data which can be found in Refs from [2.2] to [2.7].

Differences between the simulations and experimental data can be observed. The magnitude and frequency of the external mass flow rate oscillations, in which the left and the right leg reach the reverse flow conditions, are well captured. The following oscillations are a little bit ahead of time in frequency and underestimated in terms of amplitude. During the initial transient phase, a discrepancy in the heat exchanging condition is evident, even though the thermal balances are reliable only in steady-state conditions. The facility heat losses during the transient are almost constant at about 2.2 kW. The lower heat exchange affects the temperature evolutions as can be seen in the pictures. The experimental inlet temperature increases during the reverse flow phase due to mixing effects in 3D vessel. This behavior cannot be caught by system codes. The differential pressure, which are not reported, shows a quite good agreement between the experimental values and the simulations. The final conditions are reported in the table on the right of Tab. 2.2.


Finally we report the experimental results. These are shown with a previous CATHARE model which is the same we used in the rest of the report. Mass flowrate from experimental data is shown in Fig. 2.8 on different legs (FM1, FM2, FM3). The experimental data are labelled with OFFSET. The left, central and right vertical legs are labeled with FM1, FM2 and FM3, respectively. In Fig. 2.9 the experimental data for temperatures at the thermocouple points TC3_4490 and TC3_5615 along the left vertical leg (left), at TC1_0346 and TC1_1740 on the right vertical leg (right) and at TC_1211 and TC2_2111 along the central vertical leg (left) are shown. Detailed experimental data are reported in Refs from [2.2] to [2.7].

2.2.2 TALL-3D test section in FEMLCORE simulation

Mesh and geometry. TALL-3D test section is an axisymmetric cylindrical stainless steel vessel with an inlet at the bottom and an outlet at the top. The upper part of the test section is equipped with two 7.5 kW heaters which promote the development of thermal stratification in the LBE pool. The dimensions of the test section and thermal insulation are provided in Fig. 2.10. Note that the internal diameter (ID) of the inlet pipe is smaller than the ID of the pipes throughout the rest of the loop. According to the nomenclature the segment AB is the inlet region of the domain, the segment HG is the outlet zone of the domain and finally the segment AH is the symmetry axis of the geometry.

3D-FEMLCORE momentum conservation equations. For three-dimensional simulations the code FEMLCORE is used. This is an open-source code developed at UNIBO that is able to solve multiphysics problems^{[2.11]-[2.14]}. Since the motion is driven by natural convection we have to solve only the conservation equations if we consider the laminar case, while, if the flow is turbulent, we have to add a turbulence model. In order to understand the numerical tests we briefly summarize the mathematical model that is solved.



 RICERCA SISTEMA ELETTRICO	<u>Title:</u> Development of BE numerical tools for LFR design and safety analysis – Part 2	<u>Distribution</u> PUBLIC	<u>Issue Date</u> 12.12.2017	<u>Pag.</u>
	<u>Project:</u> ADP ENEA-MSE PAR 2016	<u>Ref.</u> ADPFISS-LP2-144	Rev. 0	104 di 300

Let (\mathbf{v}, p) be the state of the fluid flow that enters the domain Ω , with boundary Γ , defined by the velocity and pressure solution of the following Navier-Stokes equations

$$\frac{\partial \rho}{\partial t} + \nabla \cdot \mathbf{v} = 0 \quad (2.1)$$

$$\frac{\partial \rho \mathbf{v}}{\partial t} + \nabla \cdot (\rho \mathbf{v} \mathbf{v}) = -\nabla p + \nabla \cdot \boldsymbol{\tau} + \rho \mathbf{g} \quad (2.2)$$

The fluid can be considered incompressible, while the density may be assumed only to be slightly variable as a function of temperature, with a given law $\rho = \rho(T)$. $\boldsymbol{\tau}$ is the viscous tensor and Re is the Reynolds number. For high Reynolds numbers the turbulence model can be defined by splitting the velocity vector into a resolved-scale field $\bar{\mathbf{v}}$ and a subgrid-scale field \mathbf{v}' as $\mathbf{v} = \bar{\mathbf{v}} + \mathbf{v}'$. The filtered equations are developed from the incompressible Navier-Stokes equations of motion. By substituting $\mathbf{v} = \bar{\mathbf{v}} + \mathbf{v}'$ and $p = \bar{p} + p'$ in the decomposition and then filtering the resulting equation we write the equations of motion for the average fields $\bar{\mathbf{v}}$ and \bar{p} as

$$\frac{\partial \rho \bar{\mathbf{v}}}{\partial t} + \nabla \cdot (\rho \bar{\mathbf{v}} \bar{\mathbf{v}}) = -\nabla \bar{p} + \nabla \cdot \bar{\boldsymbol{\tau}} + \rho \mathbf{g} \quad (2.3)$$

We assume $\bar{\tau}_{ij} = \bar{v}_i \bar{v}_j - \overline{v'_i v'_j}$. Boussinesq hypothesis allows us to calculate the deviatoric part of the stress tensor using $\boldsymbol{\tau} = \frac{1}{3} \tau_{kk} \boldsymbol{\delta}_{ij} - 2 \mu_t \bar{\mathcal{S}}_{ij}$ where $\bar{\mathcal{S}}_{ij}$ is the rate-of-strain tensor for the resolved scale and μ_t is the subgrid-scale turbulent viscosity. Finally, we have

$$\frac{\partial \rho \mathbf{v}}{\partial t} + \nabla \cdot (\rho \mathbf{v} \mathbf{v}) = -\nabla p + \nabla \cdot [(\mathbf{v} + \mathbf{v}_t) \nabla \mathbf{v}] + \rho \mathbf{g} \quad (2.4)$$

where we have used the incompressibility constraint to simplify the equation and the pressure is now modified to include the trace term $\tau_{kk} \boldsymbol{\delta}_{ij} / 3$. In the rest of this report we drop the average notation $\bar{\mathbf{v}}$ and \bar{p} to use the standard notation \mathbf{v} and p . With this notation this approximation model results in the average Navier-Stokes equations


$$\frac{\partial \rho}{\partial t} + \nabla \cdot \mathbf{v} = 0 \quad (2.5)$$

$$\frac{\partial \rho \mathbf{v}}{\partial t} + \nabla \cdot (\rho \mathbf{v} \mathbf{v}) = -\nabla p + \nabla \cdot \boldsymbol{\tau} + \rho \mathbf{g} \quad (2.6)$$

identical to the (2.1-2.2) for the average fields $(\bar{\mathbf{v}}, \bar{p})$ but a modified viscous stress tensor should be considered in the form $\bar{\boldsymbol{\tau}} = 2(\boldsymbol{\mu} + \rho \mathbf{v}_t) \mathcal{D}(\mathbf{v})$. The function \mathbf{v}_t is called turbulent viscosity and must be computed by solving other transport equations, referred to as *turbulence models*. In the rest of this section we introduce different turbulence models that can be used to compute the turbulent viscosity \mathbf{v}_t and therefore close the Navier-Stokes system. In particular in the FEM-LCORE code the following four models are available: LES, κ - ϵ , κ - ω , SST- κ - ω . Some of these models are still basic and need improvement.

In the κ - ϵ turbulence model the turbulent viscosity μ_t is modeled as $\mu_t = \rho \nu_t = \rho C_\mu \kappa^2 / \epsilon$. The turbulent kinetic energy κ and the turbulent dissipation energy ϵ satisfy the following equations



 RICERCA SISTEMA ELETTRICO	<u>Title:</u> Development of BE numerical tools for LFR design and safety analysis – Part 2	<u>Distribution</u> PUBLIC	<u>Issue Date</u> 12.12.2017	<u>Pag.</u>
	<u>Project:</u> ADP ENEA-MSE PAR 2016	<u>Ref.</u> ADPFISS-LP2-144	Rev. 0	105 di 300

$$\frac{\partial \rho \kappa}{\partial t} + \nabla \cdot \rho \mathbf{v} \kappa = \nabla \cdot \left[\left(\frac{\mu_t}{\sigma_k} + \mu \right) \nabla \kappa \right] - \rho \beta_k^\epsilon + \rho \gamma_k^\epsilon S^2 + P_b \quad (2.7)$$

$$\frac{\partial \rho \epsilon}{\partial t} + \nabla \cdot \rho \mathbf{v} \epsilon = \nabla \cdot \left[\left(\frac{\mu_t}{\sigma_\epsilon} + \mu \right) \nabla \epsilon \right] - \rho \beta_\epsilon + \rho \gamma_\epsilon S^2 + \frac{\epsilon}{\kappa} C_{1\epsilon} C_{3\epsilon} P_b \quad (2.8)$$

where γ_k^ϵ is the production coefficient of κ and P_b the buoyancy term. The coefficient β_k^ϵ in the standard model can be assumed unitary. The $\gamma_\epsilon = C_\mu C_{1\epsilon} \kappa$ is the coefficient for the turbulent dissipation energy source and $\beta_\epsilon = C_{2\epsilon} \kappa$ the coefficient of the dissipation term for the same equation. We remark that in this formulation γ_ϵ and β_ϵ depend of turbulent kinetic energy κ . The model constants are $C_{1\epsilon} = 1.44$, $C_{2\epsilon} = 1.92$, $C_\mu = 0.09$, $\sigma_k = 1.0$, and $\sigma_\epsilon = 1.3$. The production P_κ of κ is defined as $P_\kappa = -\overline{v_i' v_j'} \frac{\partial v_j}{\partial x_i} = \mathbf{v}_t S^2$, where S is the modulus of the mean rate-of-strain tensor, defined as

$$S \equiv \sqrt{2S_{ij}S_{ij}} = \frac{1}{2} |\nabla \mathbf{v} + \nabla \mathbf{v}^T| \quad (2.9)$$

The effect of buoyancy P_b is given by $P_b = \frac{\alpha_t \mu_t}{Pr_t} \mathbf{g} \cdot \nabla T$, where Pr_t is the turbulent Prandtl number for energy and \mathbf{g} is the gravity vector. For the standard and realizable models, the default value of $Pr_t = 0.85$. The coefficient α_t is the thermal expansion coefficient.

In the κ - ω model, where κ is the turbulent kinetic energy and ω the specific dissipation rate, the turbulent viscosity μ_t is defined as $\mu_t = \rho \kappa / \omega$. The standard κ - ω system is defined by

$$\frac{\partial \rho \kappa}{\partial t} + \nabla \cdot \rho \mathbf{v} \kappa = \nabla \cdot \left[\left(\frac{\mu_t}{\sigma_k} + \mu \right) \nabla \kappa \right] - \rho \beta_\kappa + \rho \gamma_\kappa S^2 + P_b \quad (2.10)$$

$$\frac{\partial \rho \omega}{\partial t} + \nabla \cdot \rho \mathbf{v} \omega = \nabla \cdot \left[\left(\frac{\mu_t}{\sigma_\omega} + \mu \right) \nabla \omega \right] - \rho \beta_\omega + \rho \gamma_\omega S^2 \quad (2.11)$$

with $\beta_\kappa = \beta^* = \frac{9}{100}$, $\gamma_\kappa = \mu_t$, $\beta_\omega = \frac{5}{9}$, $\gamma_\omega = \alpha = \frac{3}{40}$, $\sigma_k = 2$ and $\sigma_\omega = 2$.

3D-FEMLCORE energy conservation equation. The evolution of the system is described by the solution $\mathbf{e} = \mathbf{e}(T, \mathbf{v})$, where e represents the total energy $e \equiv C_v T + \frac{v^2}{2}$, of the following equation


$$\frac{\partial \rho e}{\partial t} + \nabla \cdot (\rho \mathbf{v} e) = \Phi + \nabla \cdot \mathbf{q} + \dot{Q} \quad (2.12)$$

The heat flux, \mathbf{q} , is given by Fourier's law

$$\mathbf{q} = -\lambda \nabla T \equiv -\frac{C_p \mu}{Pr} \nabla T. \quad (2.13)$$

The laminar Prandtl Pr and the Péclet Pe numbers are defined by $Pr = \frac{C_p \mu}{\lambda}$ and $Pe = Re Pr$, respectively. The fluid can be considered incompressible and the density slightly variable as a function of temperature, in this case we set $\rho = a + \gamma T$, where a and γ are constant. The quantity C_v is the volume specific heat and λ



 RICERCA SISTEMA ELETRICO	<u>Title:</u> Development of BE numerical tools for LFR design and safety analysis – Part 2	<u>Distribution</u> PUBLIC	<u>Issue Date</u> 12.12.2017	<u>Pag.</u>
	<u>Project:</u> ADP ENEA-MSE PAR 2016	<u>Ref.</u> ADPFISS-LP2-144	Rev. 0	106 di 300

the heat conductivity. The quantity \dot{Q} is the volume heat source and Φ the dissipative heat term. The equation is completed with these data and appropriate boundary conditions.

For high Reynolds numbers again we decompose the velocity and temperature fields into a resolved scale field and a subgrid-scale field. With usual notation these approximation models result in the same equations as (2.12)

$$\frac{\partial \rho C_p T}{\partial t} + \nabla \cdot (\rho \mathbf{v} C_p T) = \Phi + \nabla \cdot \mathbf{q} + \dot{Q} \quad (2.14)$$

for the average fields ($T = \bar{T}$) and in a modified heat flux \mathbf{q} as follows

$$\mathbf{q} = -C_p \left(\frac{\mu}{Pr} + \frac{\rho \mathbf{v}_t}{Pr_t} \right) \nabla T. \quad (2.15)$$

The function Pr_t is called turbulent Prandtl number. The computation of Pr_t determines the turbulence contribution. We have implemented two models: the constant turbulent Prandtl number model and the $\kappa - \epsilon - \kappa_t - \epsilon_t$ turbulence model. The second model is still in progress and it is available only for development studies. For preliminary applications of the four parameters turbulence model and for its modifications, the interested reader can refer to Refs. [2.15], [2.16] and [2.17]. For many fluids Pr_t can be assumed to be constant, and its values range from 0.85 to 0.95. In a more advanced model the turbulent Prandtl number may be defined as

$$Pr_t = Pr_{t0} [B(\mathbf{v}, \mathbf{v}_t, Pr, R) + 1] C_\alpha (R + C_\gamma) / (2R), \quad (2.16)$$

where $R = \frac{\kappa_t \epsilon}{\epsilon_t \kappa}$ and C_α, C_γ are constants. The function $B(\mathbf{v}, \mathbf{v}_t, Pr, R)$ can take several forms. The equation for the *averaged temperature squared fluctuations* is defined by the following transport equation

$$\frac{\partial \kappa_t}{\partial t} + \mathbf{u}_i \frac{\partial \kappa_t}{\partial x_i} = \frac{\partial}{\partial x_i} \left(\alpha + \frac{\alpha_t}{\sigma_{\kappa_t}} \right) \frac{\partial \kappa_t}{\partial x_i} + P_t - \epsilon_t, \quad (2.17)$$

where

$$P_t \equiv -\overline{u_i' T'} \frac{\partial T}{\partial x_i} = \frac{\mathbf{v}_t}{Pr_t} \left(\frac{\partial T}{\partial x_i} \right)^2. \quad (2.18)$$


In a similar way an equation for ϵ_t can be written as

$$\frac{\partial \epsilon_t}{\partial t} + \mathbf{u}_i \frac{\partial \epsilon_t}{\partial x_i} = \frac{\partial}{\partial x_i} \left[\left(\alpha + \frac{\alpha_t}{\sigma_{\kappa_t}} \right) \frac{\partial \epsilon_t}{\partial x_i} \right] + \frac{\epsilon_t}{\kappa} (C_{p1} P_t - C_{d1} \epsilon_t) + \frac{\epsilon_t}{\kappa} (C_{d1} P_\kappa - C_{d2} \epsilon), \quad (2.19)$$

where P_κ is defined by

$$P_\kappa \equiv -\overline{u_i' u_j' T'} \frac{\partial u_i}{\partial x_j} = \mathbf{v}_t \left(\frac{\partial u_i}{\partial x_j} + \frac{\partial u_j}{\partial x_i} \right) \frac{\partial u_i}{\partial x_j}. \quad (2.20)$$



 RICERCA SISTEMA ELETTRICO	<u>Title:</u> Development of BE numerical tools for LFR design and safety analysis – Part 2	<u>Distribution</u> PUBLIC	<u>Issue Date</u> 12.12.2017	<u>Pag.</u>
	<u>Project:</u> ADP ENEA-MSE PAR 2016	<u>Ref.</u> ADPFISS-LP2-144	Rev. 0	107 di 300

The coefficients can be considered as constants, with values $C_{p1} = 1$, $C_{p2} = 0.60$, $C_{d1} = 1$ and $C_{d2} = 0.9$ or as model functions. An approximation of this model can be obtained by assuming the Kays approximation $Pr_t = 0.85 + 1.5 / (1 + \nu_t / \nu)$.

Initial conditions for CFD in 3D-section: laminar and turbulent steady condition. The coupling between the system code and the three-dimensional problem is achieved by a mutual exchange of boundary conditions between the problems. In order to obtain a stable coupling between the two problems both the systems must reach the same thermodynamical working conditions. For this reason we do not couple the system code and the three-dimensional problem from the beginning of the simulation, but instead we first find the nominal steady state working condition for the one-dimensional system and then we perform several uncoupled stabilization iterations in the 3D problem. Concerning the boundary conditions for the energy balance equation we impose the temperature evaluated by the system code on the surface AB, an inhomogeneous Neumann condition on EO and a homogeneous Neumann boundary conditions on the remaining surfaces. The thermal heat flux imposed on EO is 45785 W/m^2 . Concerning boundary conditions for the axial component of the momentum balance equation, we impose the flow rate evaluated by the system code on the surface AB, a vanishing Neumann condition on the axis ANUIH and the no-slip condition on the other surfaces. The velocity on AB is multiplied by a factor of $48/37$ to compensate for the flat profile set by the mono-dimensional boundary conditions. The normal component of the velocity field is set to zero on all the wall boundaries of the domain. The initial condition for the stabilization process is a constant temperature field with $T = 260^\circ\text{C}$ and a vanishing velocity in all the domain.


The temperature evolution and the steady state fields obtained after stabilization are shown in Fig. 2.11 and Fig. 2.13 for the laminar and turbulent case, respectively. In Fig. 2.12, the trends of different average temperatures over the iteration numbers are shown. We indicated the temperature on the outlet boundary (HG) for the laminar case with label A and for the turbulent case with label B. The trend line labeled with C refers to the inlet boundary (AB) for the turbulent case. We remark that the stabilization process is used as the initial condition for the coupling of the one and three-dimensional problems.

2.2.3 Problem coupling on FEMLCORE-SALOME-CATHARE platform

Coupling on FEMLCORE-SALOME-CATHARE platform. We use the defective coupling algorithm with overlapping meshes. The one-dimensional mesh is defined over the entire domain and a three-dimensional mesh is defined only in the three-dimensional test region. We solve at the same time the three-dimensional code and the one-dimensional system code over the overlapping domain. On the right of Fig. 2.3, six reference points are shown with red circles. They are labeled with 1-2 (COR3-RESERVE4) on the left vertical leg, 3-4 (BELOW3D25-ABOVE3D3) in the central vertical leg) and 5-6 (PUMP0-LINUP14) on the right vertical leg. The point 3 (BELOW3D25) is the 1D/3D matching interface for the inlet section of the three-dimensional domain. The point 4 (ABOVE3D3) is the 3D/1D matching interface for the outlet section of the three-dimensional domain. The meshes are generated with GUTHARE for the one-dimensional case and with SALOME GEOM and MESH modules for the three-dimensional one. The coupling algorithm can be schematized as follows:

- a) Problem 3D Initialization (FEMLCORE);
- b) Problem 1D Initialization (CATHARE);
- c) Stabilization with matching of the state variables for the 1D and 3D Initialization (CATHARE-FEMLCORE);
- d) Set up coupled transient;
- e) For each time step:
 - 1) Defective correction from 3D near the outlet of the TALL3D component and one step solution for the one-dimensional code;



 RICERCA SISTEMA ELETRICO	<u>Title:</u> Development of BE numerical tools for LFR design and safety analysis – Part 2	<u>Distribution</u> PUBLIC	<u>Issue Date</u> 12.12.2017	<u>Pag.</u>
	<u>Project:</u> ADP ENEA-MSE PAR 2016	<u>Ref.</u> ADPFISS-LP2-144	Rev. 0	108 di 300

- 2) Boundary conditions from 1D at the inlet section of 3D geometry one step solution for the three-dimensional code;
- f) Repeat to end time.

The step a) initializes the three-dimensional Problem P and the 1D/3D and 3D/1D interfaces. After the initialization of the Problem class we create the 1D/3D and 3D/1D interfaces: these are four interfaces from the three-dimensional mesh generated over sub-meshes (called groups). The group 21 defines the inlet sub-mesh of the 3D test section while the group 22 defines the sub-mesh of the outlet region. For each sub-mesh we use two different representations and the corresponding mapping: the MED and code format. Both the system and CFD codes can read and map the MED format into its own format and vice versa. It is necessary to create one interface function for each state variable. We impose the boundary conditions in velocity and temperature at the inlet from the system code and extract the value at the outlet to impose on the system code. We set the initial condition to the Problem P and compute the pressure at the inlet and outlet to determine the pressure losses. We compute mean integral values of the surface variables in order to pass them to the one-dimensional code.

In step b) of the algorithm we define as point1 and point2 the 27-th element of the BELOW3D module and the 3-rd element of the ABOVE3D module, respectively. The Problem class for the one-dimensional code is set and initialized. The pressure from the CATHARE code is extracted at point1 and point2. The momentum equation source DPLEXT controls the pressure variable. In the defective mode algorithm the pressure at the specified locations is controlled by a control feedback technique. Finally, also the density, which is a function of temperature, is extracted at point1.


In step c), after the initialization of the Problems P and C, the evolution transient should be solved. The transient loop is determined by a pass-fail time step for the one-dimensional code. The logical variables Stop and Ok are evaluated to determine the convergence of the nonlinear system. The time step ends the iterations when Ok is *true*. The algorithm ends when Stop is *true*. The time step is the same for both the codes. Since we cannot restart the one-dimensional code during the coupling, the stabilization is performed before the coupling during the first 1500 s. This interval of time is sufficient to reach a steady state condition that will be the initial condition for the transient phase. The transient starts after 1500 s when the coupling becomes active and the pump is turned off (total time 1501 s).

In step e1), during the transient for each time step, the state value (\dot{m} , T , p) are solved, where \dot{m} is the fluid flow rate, T the temperature and p the pressure. For one-dimensional system liquid flow rate substitutes the knowledge of the velocity field ($\mathbf{v} = \dot{m} / A \rho$). The state (\dot{m} , T , p) is extracted from the one-dimensional simulation at point1 and point2 to determine the source needed for the correction in the mass, momentum and energy equations.

The energy correction is obtained by computing $ENTLEXT = h_{43} - \alpha C_p (t_{43} - T_{out})$ where h_{43} , t_{43} are the entalpy and the temperature at point2. T_{out} is the average temperature at the outlet of the 3D test section which has been computed after the FEMLCORE time step. The constant α is the feedback constant. The higher the value of α , the faster the coupling brings the two solution to match. The momentum correction is obtained by computing DPLEXT as $DPLEXT = dp_{100} - \beta (dp_{3d} - dp_{1d})$. Here $dp_{3d} = (P_{in3D} - P_{out3D}) - \rho_{3d} H_{3D} g$ and $dp_{1d} = (P_{in1D} - P_{out1D}) - \rho_{1d} H_{1D} g$, where H_{3D} is the total height of the 3D simulation domain, g is the gravity constant.

Therefore, dp_{3d} and dp_{1d} are the pressure losses of the three- and one-dimensional 3D test-section when the gravity contribution is subtracted. The value dp_{100} is the old value of DPLEXT and is directly read from the one-dimensional code. The constant β is the feedback constant. As before, the higher the value of β , the



 RICERCA SISTEMA ELETTTRICO	<u>Title:</u> Development of BE numerical tools for LFR design and safety analysis – Part 2	<u>Distribution</u> PUBLIC	<u>Issue Date</u> 12.12.2017	<u>Pag.</u>
	<u>Project:</u> ADP ENEA-MSE PAR 2016	<u>Ref.</u> ADPFISS-LP2-144	Rev. 0	109 di 300

faster the matching is achieved. If the 3d pressure losses dp_{3d} are higher than the the one-dimensional one dp_{1d} the source *DPLEXT* increases the one-dimensional pressure losses. When $dp_{3d} = dp_{1d}$ the momentum equation source *DPLEXT* reaches a stationary value.

In step e2) the FEMLCORE time step is computed by setting the inlet state with boundary condition from the one-dimensional code. The temperature T_3 , obtained by CATHARE, is imposed to interface 11 (inlet) in analytical form. In addition, the liquid flow is imposed from the one-dimensional code to the three-dimensional inlet. After solving the FEMLCORE time step the pressure, the temperature and the velocity fields are available. We compute and average the pressures at the inlet and at the outlet to compute the pressure losses. We compute several averaged quantities, as the pressures, at inlet and outlet section of 3D geometry, and the temperature at 3D outlet section, in order to calculate the source correction terms for the system code.


Simulation results. The solution of the coupled system are reported for the one- and three-dimensional code for three computational cases: laminar natural circulation (case AB), turbulent $\kappa\text{-}\omega$ with SUPG regularization (case ACF) and standard up-wind regularization (case ADE) for the advection term. Inside each case, we have simulated two different turbulent heat exchange models. In one model (case C and D), we have set constant turbulent Prandtl number, namely the turbulent thermal diffusivity is proportional to the turbulent viscosity. In the second case (case F and E), we have used variable Prandtl turbulent number as discussed in the previous section. For the one-dimensional code, the results are shown in Fig. 2.14-Fig. 2.18 and Fig. 2.3, where the reference points are defined.

The points 2 (RESERVE4), 3 (BELO3D25), 4 (ABOVE3D3), 5 (LINUP5) and 6 (PUMP0) are reported one in each figure. We can find the temperature (on the left) and the mass flow (on the right) for the case AB, case ACF and case ADE. The A case is the CATHARE standalone simulation. The properties of each simulated case, namely numerical stabilization of advection term and adopted turbulence models, are reported in Tab. 2.3. We compare the coupled computation with the uncoupled one by keeping the case A in all the figures. One of the advantages of the coupled simulation is the availability of the three-dimensional fields on the 3D test section. The solutions are reported for two computational cases: laminar natural circulation (case B) with constant turbulent Prandtl number and turbulent $\kappa\text{-}\omega$ model with Kays model for the definition of the heat turbulent heat transfer. Temperature and streamline profiles for the velocity field over the three-dimensional test component for case B are shown in Fig. 2.19-Fig. 2.21. In Fig. 2.19 we show the profiles for $t = 10 - 20$ s, in Fig. 2.20 for $t = 30 - 1000$ s and in Fig. 2.20 for $t = 1500 - 2000$ s. The temperature is on the left side of the test component while the streamlines are on the right.

Temperature, turbulent kinetic energy and velocity streamline profiles over the three-dimensional test component for the turbulent case are shown in Fig. 2.22 - Fig. 2.27. In particular temperature and streamline profiles over the three-dimensional test component for $t=100 - 2000$ s, with the $\kappa\text{-}\omega$ turbulence case and Kays turbulent Prandtl number model for heat exchange are shown in Fig. 2.22 - Fig. 2.24. Fig. 2.25 - Fig. 2.27 report turbulent kinetic energy and velocity streamline profiles for $t = 100 - 2000$ s.

Defective coupling over overlapping meshes for FEMLCORE-CATHARE codes. As described in the previous sections, in order to couple the three- and one-dimensional codes we use a defective algorithm which is based on feedback control to impose the boundary conditions^{[2.18][2.19][2.20]}. The points where the boundary conditions are evaluated or imposed are defined in Fig. 2.28. At the point 3 the liquid flow and temperature values of the one-dimensional code are imposed as inlet boundary conditions. In Fig. 2.29, one can see the liquid flow rate at the inlet (right) and the temperature (left). Since the mesh are overlapping and no flow may exit from the test section, there can be no error in the mass balance equation.



 RICERCA SISTEMA ELETTRICO	<u>Title:</u> Development of BE numerical tools for LFR design and safety analysis – Part 2	<u>Distribution</u> PUBLIC	<u>Issue Date</u> 12.12.2017	<u>Pag.</u>
	<u>Project:</u> ADP ENEA-MSE PAR 2016	<u>Ref.</u> ADPFISS-LP2-144	Rev. 0	110 di 300

The temperatures of 1D and 3D simulation at the point 4 are shown in Fig. 2.30 on the left. The energy correction is obtained by computing $ENTLEXT = h_{43} - \alpha C_p (t_{43} - T_{3D})$, where h_{43} are the entalpy and the temperature at point 2. T_{3D} is the average temperature at the outlet of the 3D test section which has been computed after the FEMLCORE time step. The constant α is set to 0.1. As one can see, the matching is almost perfect at each time step. The momentum correction is obtained by computing DPLEXT as $DPLEXT = DPLEXT_o - \beta (\Delta p_{3D} - \Delta p_{1D})$, where Δp_{3D} and Δp_{1D} are the pressure losses, when the gravity contribution is subtracted, of the three- and one-dimensional 3D test-section. The value $DPLEXT_o$ is the old value of DPLEXT that is directly read from the one-dimensional code. The constant β is set to 1. The pressure at the point 4 in the 3D/1D interface is shown in Fig. 2.30 on the right.

2.3 Role of the activity, general goals and future development

The LFR technology is very important in many fields but in particular in the production of electricity. In the framework of the Generation IV International Forum (GIF), nuclear experts formulated the requirements for a fourth generation of nuclear systems that could respond to the world future energy needs and reduce the huge demand for electricity with the corresponding emissions from fossil fuels. The main aims of the GIF are five: making efficient use of uranium natural resources, minimizing waste production, satisfying economic competitiveness, maintaining stringent standards of safety and proliferation resistance.


Initial development on the LF reactors was focused on two pool-type reactors: Small Secure Transportable Autonomous Reactor (SSTAR) of 20 MWe in USA and the European Lead-cooled SYstem (ELSY) of 600 MWe in Europe. The SSTAR core is one meter high and 1.2 m in diameter. The ELSY project was led by Ansaldo Nucleare from Italy and was financed by Euratom. The 600 MWe design was nearly complete in 2008 and a small-scale demonstration facility was planned. This prototype runs on MOX fuel at 480 °C with liquid lead pumped to eight steam generators with decay heat removal by convection. However, the ALFRED reactor superseded this design.

The goal of this activity is to develop a multiscale and multiphysics computational platform, based on open-source software SALOME, in a strict collaboration between the University of Bologna and ENEA, with the purpose of studying issues of LFR technology^{[2.21], [2.22]}. The platform developed during these years should be flexible enough to allow design, development and verification of the available experimental data. The platform should be able to couple research, in-house and commercial codes in a way that the new and old development in this field will not be lost.

In previous reports we have studied multiscale and multiphysics simulation where the main component was a reactor while the primary loop was a simplified circuit^{[2.23], [2.24]}. Now in order to show the flexibility of this platform we studied the TALL3D plant where the three-dimensional component is simple and the mono dimensional loop is rather complex. The model for TALL-3D has been developed in the previous report^[2.25] and coupling simulations with laminar natural convection has been studied for different configurations. In this work, we improved existing interfaces for FEMLCORE and CATHARE coupling^[2.22]. During the analysis of this lead-cooled facility three-dimensional effects cannot be ignored and its features cannot be modeled by simple volumetric balances of energy, momentum and mass. The coupling techniques between system and three-dimensional codes give a good opportunity to explore problems that are more complex but great difficulties are added from combining multi-dimensional and overlapping meshes together. In this work we have investigated the use of turbulence models that are implemented on the platform^[2.14] with the aim to improve the three-dimensional coupling.

We try to use simple turbulence model for the momentum and for energy equation. The dynamic coupling between a one-dimensional code and a three-dimensional one with a turbulent model leads to problems that




 RICERCA SISTEMA ELETTRICO	<u>Title:</u> Development of BE numerical tools for LFR design and safety analysis – Part 2	<u>Distribution</u> PUBLIC	<u>Issue Date</u> 12.12.2017	<u>Pag.</u>
	<u>Project:</u> ADP ENEA-MSE PAR 2016	<u>Ref.</u> ADPFISS-LP2-144	Rev. 0	111 di 300

are more complex since the turbulent quantities should be passed as boundary conditions. The one-dimensional flow does not have dimensionality and the dimensional turbulence effects are not taken into account in a very accurate way. The turbulent kinetic energy and its dissipation rate at the boundary are fundamental and therefore it is necessary to develop appropriate models that can lead to improved coupling. The use of this model in a trivial manner can even lead to less accurate simulations than the standalone case. In this report we have simulated the TALL-3D facility by using the FEMLCORE and CATHARE code coupled through the SALOME platform.

We computed the one-dimensional circuit and the three-dimensional test section by using a defective coupling algorithm on overlapping meshes in order to correct the one-dimensional simulation. We have reported the results of the evolution of an unprotected loss of flow going from forced to natural circulation flow. The system is initially considered to be in fully working conditions. The one-dimensional system code standalone has produced temperature oscillations that were shifted in phase and smaller in term of amplitude. However, the use of the turbulence model has not improved the matching with the experimental results showing that the turbulence boundary conditions taken from the one-dimensional circuit need to be enforced correctly by modeling appropriately such a coupling. In future works we plan to study in more details different aspects of turbulence by coupling other codes with more specialized implementations. For example in open-source codes like OpenFOAM and CODE_SATURNE very sophisticated turbulent models have been implemented. We plan to bring into our platform such codes by developing appropriate interfaces and model appropriately the 1D/3D interfaces with turbulent state.



	<u>Title:</u> Development of BE numerical tools for LFR design and safety analysis – Part 2	<u>Distribution</u> PUBLIC	<u>Issue Date</u> 12.12.2017	<u>Pag.</u> 112 di 300
	<u>Project:</u> ADP ENEA-MSE PAR 2016	<u>Ref.</u> ADPFISS-LP2-144	Rev. 0	

	Initial Condition	Unit
T BELOW3D	241.45	°C
T ABOVE3D	259.81	°C
T LINUP2	251.76	°C
T PUMP	242.38	°C
T COR	244.16	°C
T RESERVE	248.33	°C
MH rod power	2578	W
3D vessel power	4833	W
LBE mass flowrate	4.2750	kg/s
Oil inlet temperature	61.1	°C
Oil outlet temperature	82.6	°C
Oil mass flowrate	0.1435	[kg/s]

Tab. 2.1 - Initial state condition for the one-dimensional Problem C. The initial condition satisfies the steady state equation.

	Final Condition	Unit
T BELOW3D	218.01	°C
T ABOVE3D	314.93	°C
T LINUP2	299.41	°C
T PUMP	223.53	°C
T COR	241.89	°C
T RESERVE	298.58	°C
MH rod power	2578	W
3D vessel power	4833	W
LBE mass flowrate	0.53054	kg/s
Oil inlet temperature	61.2	°C
Oil outlet temperature	80.6	°C
Oil mass flowrate	0.1404	kg/s

Tab. 2.2 – Final state condition for the one-dimensional code (CATHARE) solved without coupling.

	A	B	C	D	E	F
Stabilization	-	SUPG	SUPG	Upwind	Upwind	SUPG
Dynamic Turbulence model	-	-	$k-\omega$	$k-\omega$	$k-\omega$	$k-\omega$
Thermal Turbulence model	-	-	Constant Pr_t	Constant Pr_t	Kays Pr_t	Kays Pr_t

Tab. 2.3 – Numerical stabilization and turbulence models used for all the simulated cases. Case A refers to Cathare standalone.



physics/multiscale	CFD scale	system scale
Thermalhydraulics	CFD-porous 3D	system 1D
open-src CEA-EDF open-src	FEMLCORE (FEM) MC/TRIOCFD OPENFOAM (FV) ?	FEMuS (FEM) CATHARE OPENFOAM (FV) ?
Neutronics	Trasport	2-5 group diffusion
open-src CEA-EDF	DRAGON (assembly)	DONJON (reactor) APOLLO
Structural	3D structural	1D beam
open-src CEA-EDF open-src	FEMuS (FEM) Code_Aster Code_Aster	FEMuS (FEM) Code_Aster Code_Aster
Two-phase	interface	two-fluid model
open-src CEA-EDF open-src	VOF multilevel TRIOU NEPTUNE OPENFOAM (FV) ?	FEMuS (FEM) CATHARE

Fig. 2.1 - Possible multiphysics-multiscale code combinations on SALOME platform.

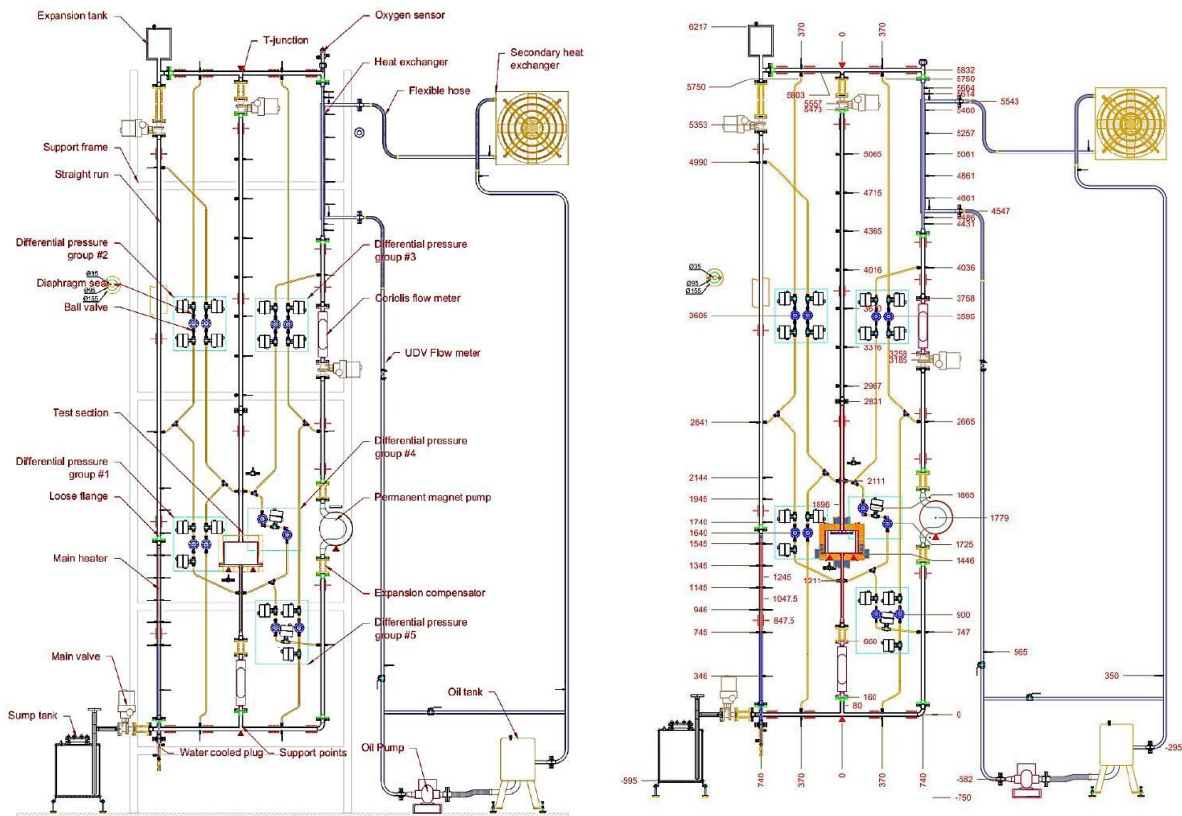


Fig. 2.2 - TALL-3D facility (left) with geometric dimensions (right).



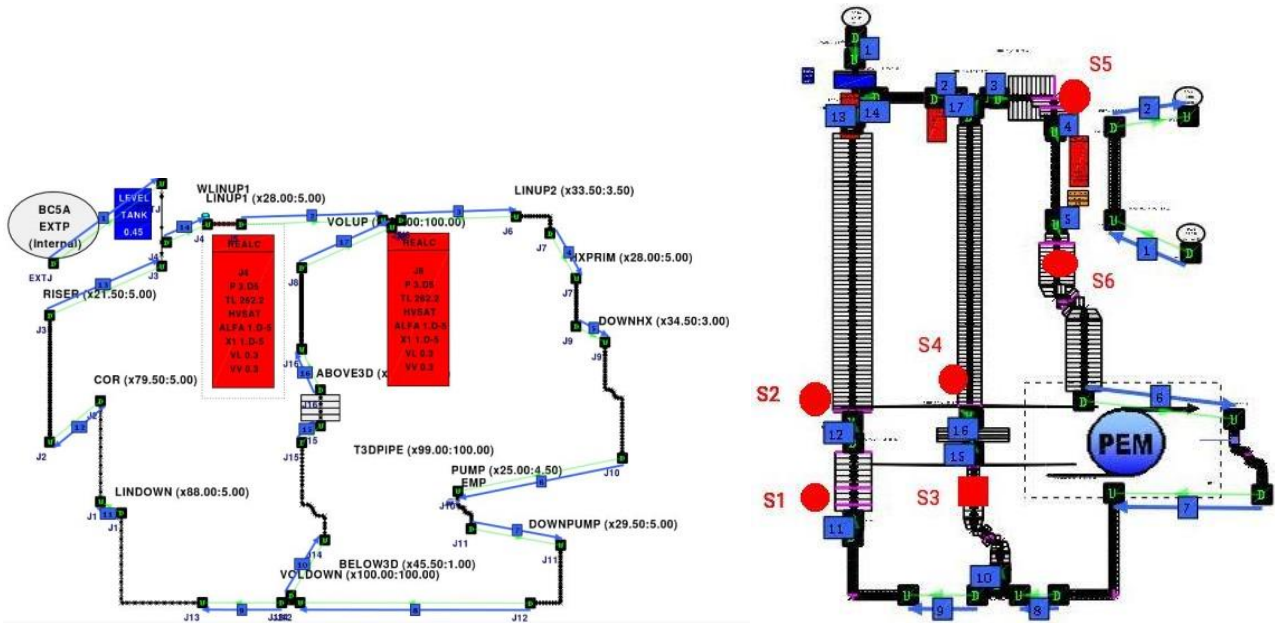


Fig. 2.3 - One-dimensional CATHARE model for the TALL-3D facility (left) and point of interests S1-S2 of the left leg (on the right), S3-S4 of the central leg and S5-S6 of the right vertical leg.

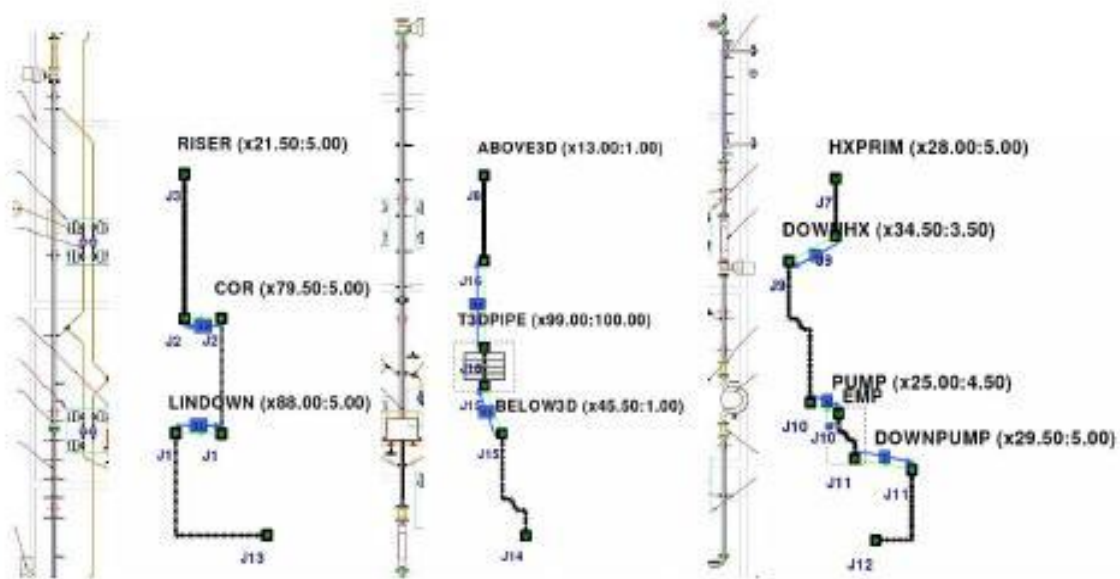


Fig. 2.4 - Left, central and right vertical leg (from left to right) in 1D system model with 3D test section.

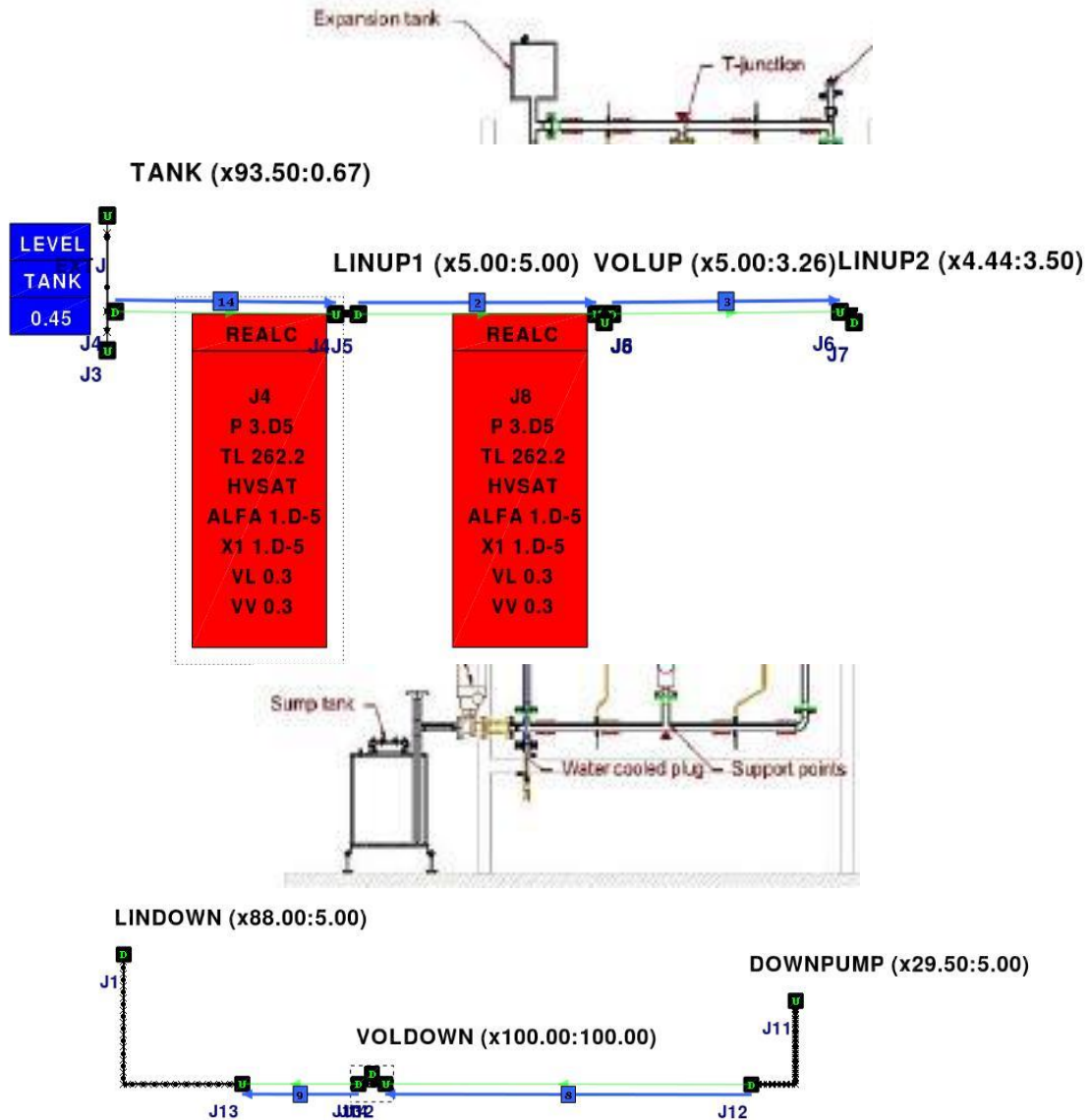


Fig. 2.5 - Bottom and top leg (from left to right) in 1D CATHARE system model (bottom) and experimental test section (top).

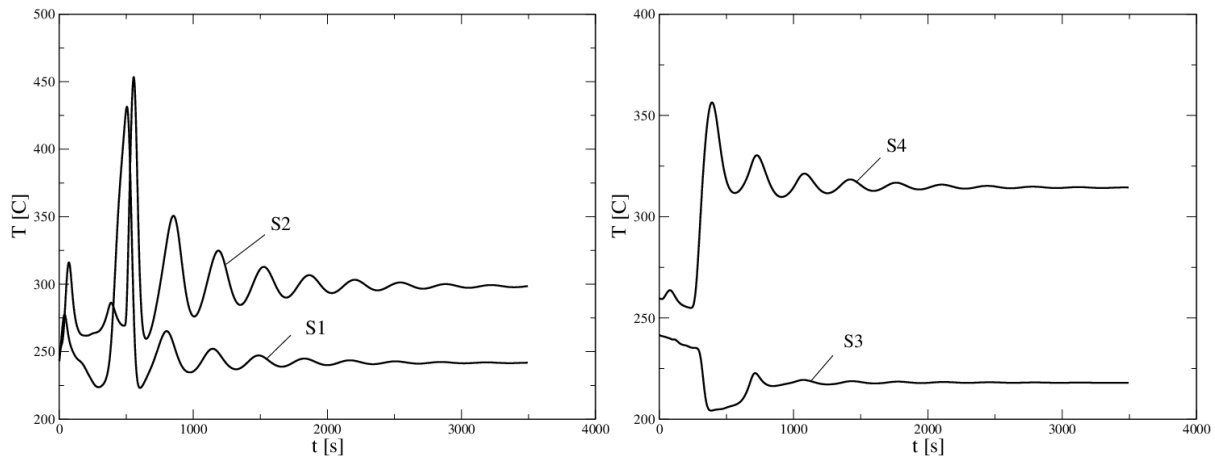


Fig. 2.6 - Computed temperature at points S1-S2 of the left leg (on the left) and at S3-S4 of the central leg (on the right) as a function of time t.

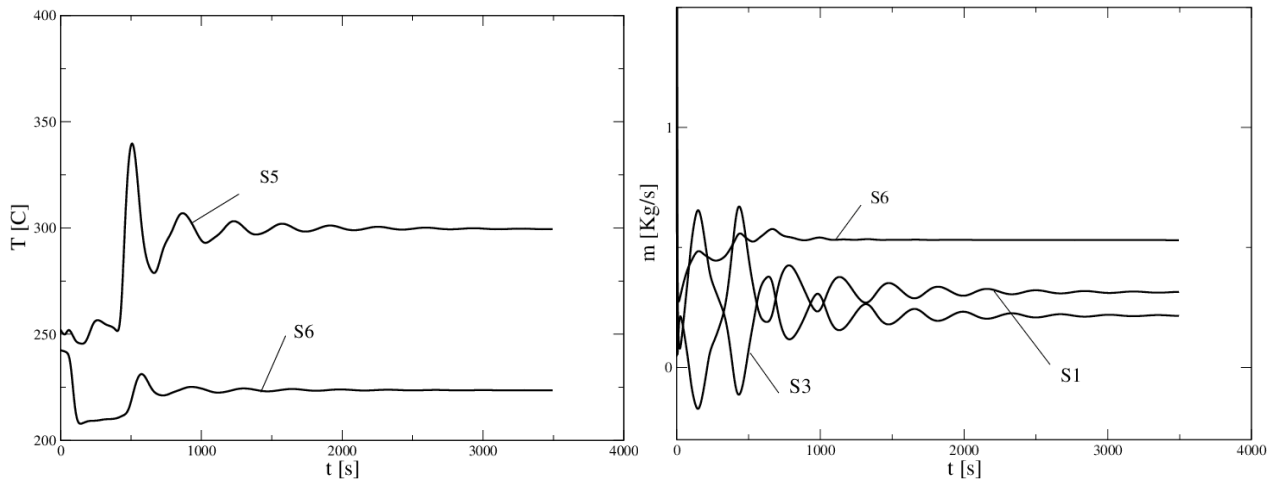


Fig. 2.7 - Computed temperature at the points S5-S6 of the right leg (on the left) and fluid flow rate at S1 (left), S3 (central) and S6 (right leg) (on the right) as a function of time t.

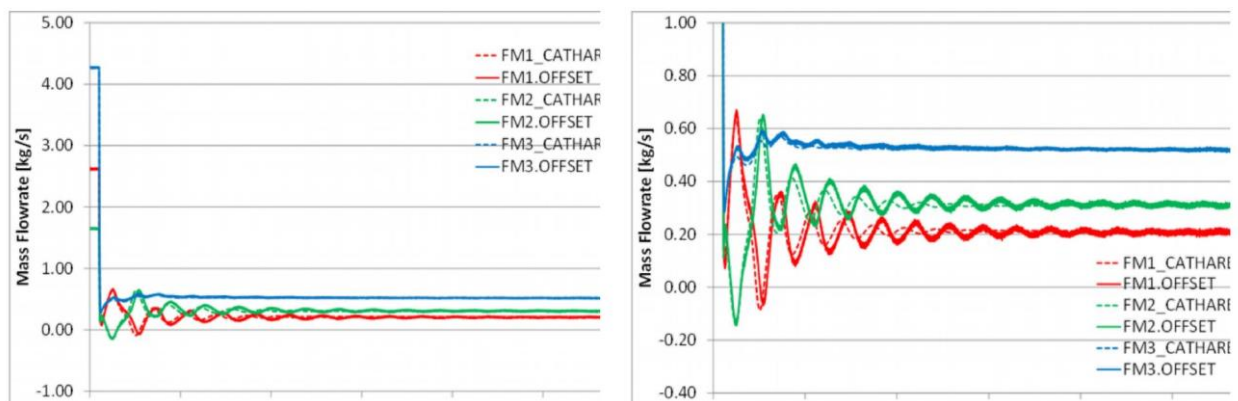


Fig. 2.8 - Experimental and computed mass flowrate on different legs (FM1, FM2, FM3).

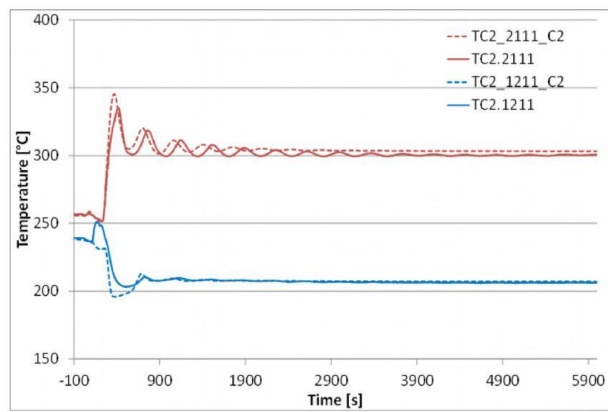
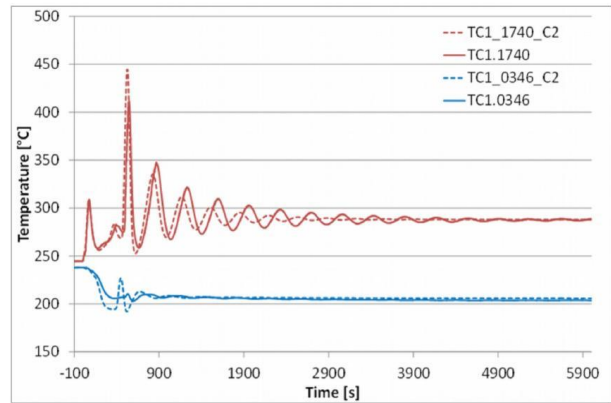
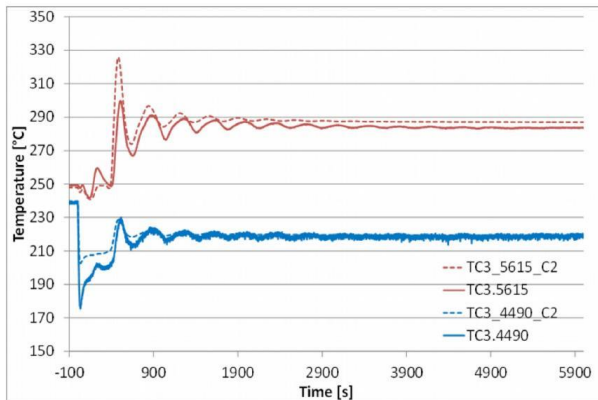
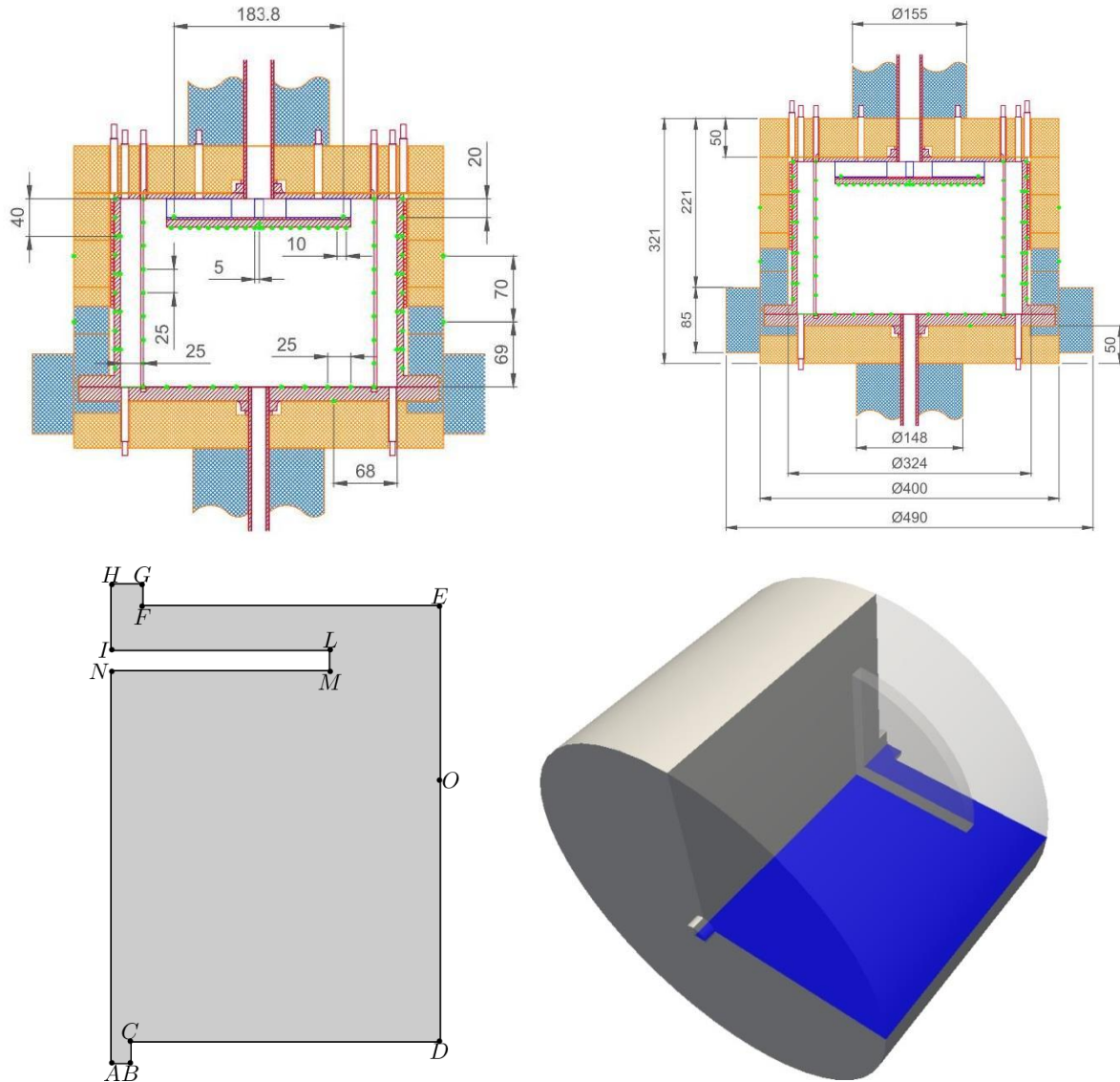


Fig. 2.9 - Experimental and computed temperature at the thermocouple points TC3_4490, TC3_5615 along the left vertical leg (left), at TC1_0346, TC1_1740 on the right vertical leg (center) and at the thermocouple points TC_1211, TC2_2111 along the central vertical leg (left).





Point	x	y	Point	x	y	Point	x	y
A	0	-0.01	B	0.0085	-0.01	C	0.0085	0.
D	0.15	0.	E	0.15	0.2	F	0.0139	0.2
G	0.0139	0.21	H	0.	0.21	G	0.0139	0.21
H	0.	0.21	I	0.	0.18	L	0.1	0.18
M	0.1	0.17	N	0.	0.17	O	0.15	0.0904118

Fig. 2.10 - Geometry and dimensions of the three-dimensional test section.

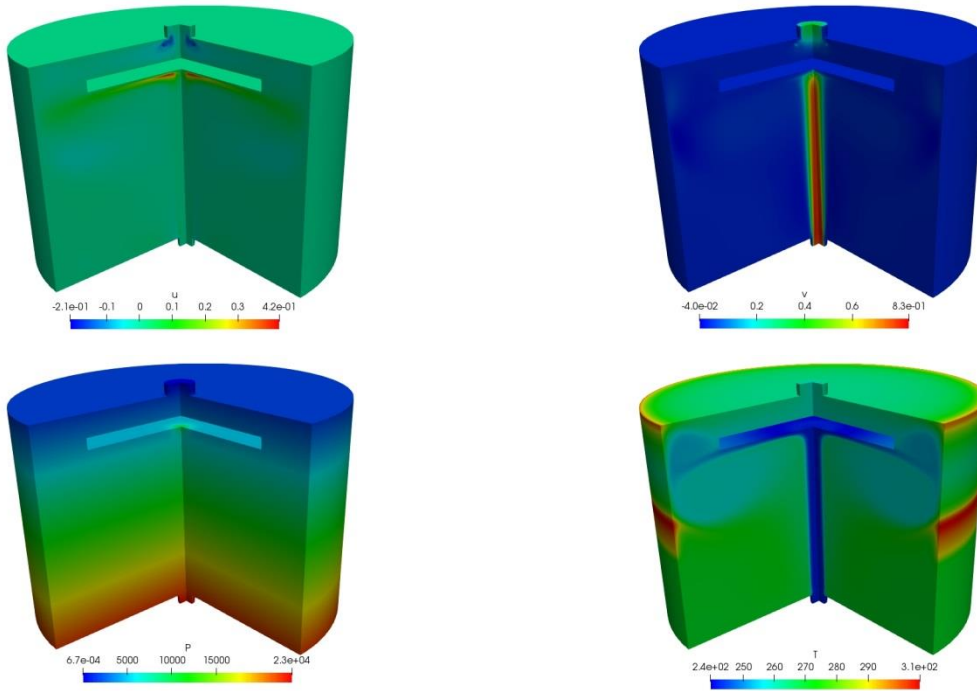


Fig. 2.11 - Initial steady state for non-turbulent flow.

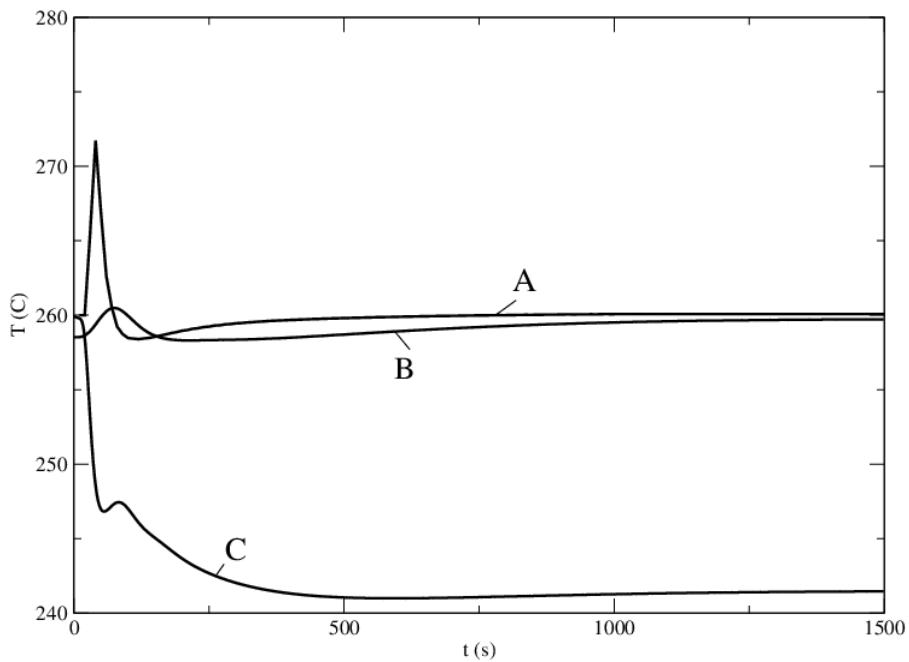


Fig. 2.12 - Average temperature over the outlet HG (A-B) and inlet boundary AB (C) over the iteration numbers for the laminar (A) and the turbulent case (B-C).

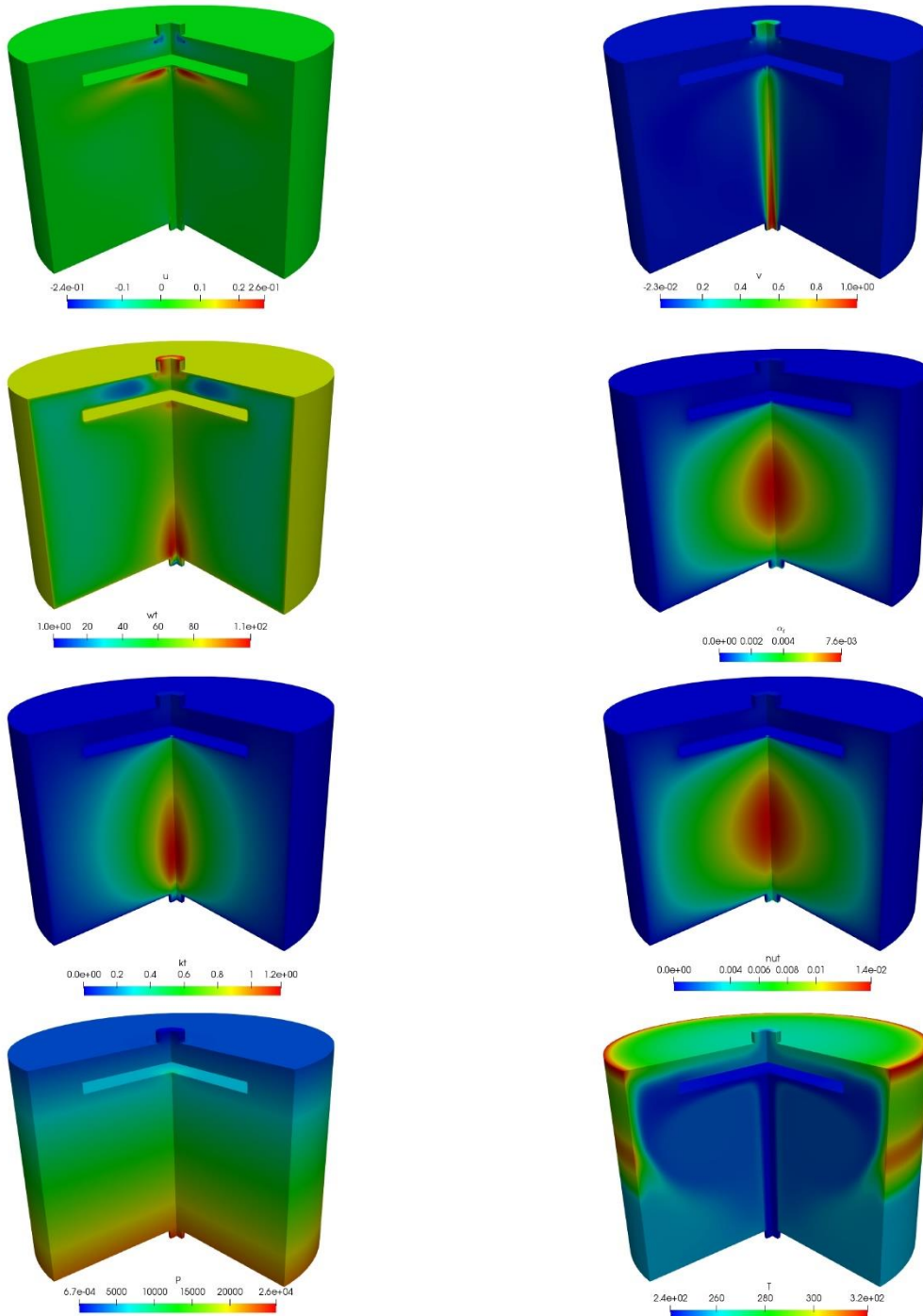


Fig. 2.13 - Initial steady state for turbulent flow model case (κ - ω) and turbulent viscosity ν_t with turbulent thermal diffusivity α_t .

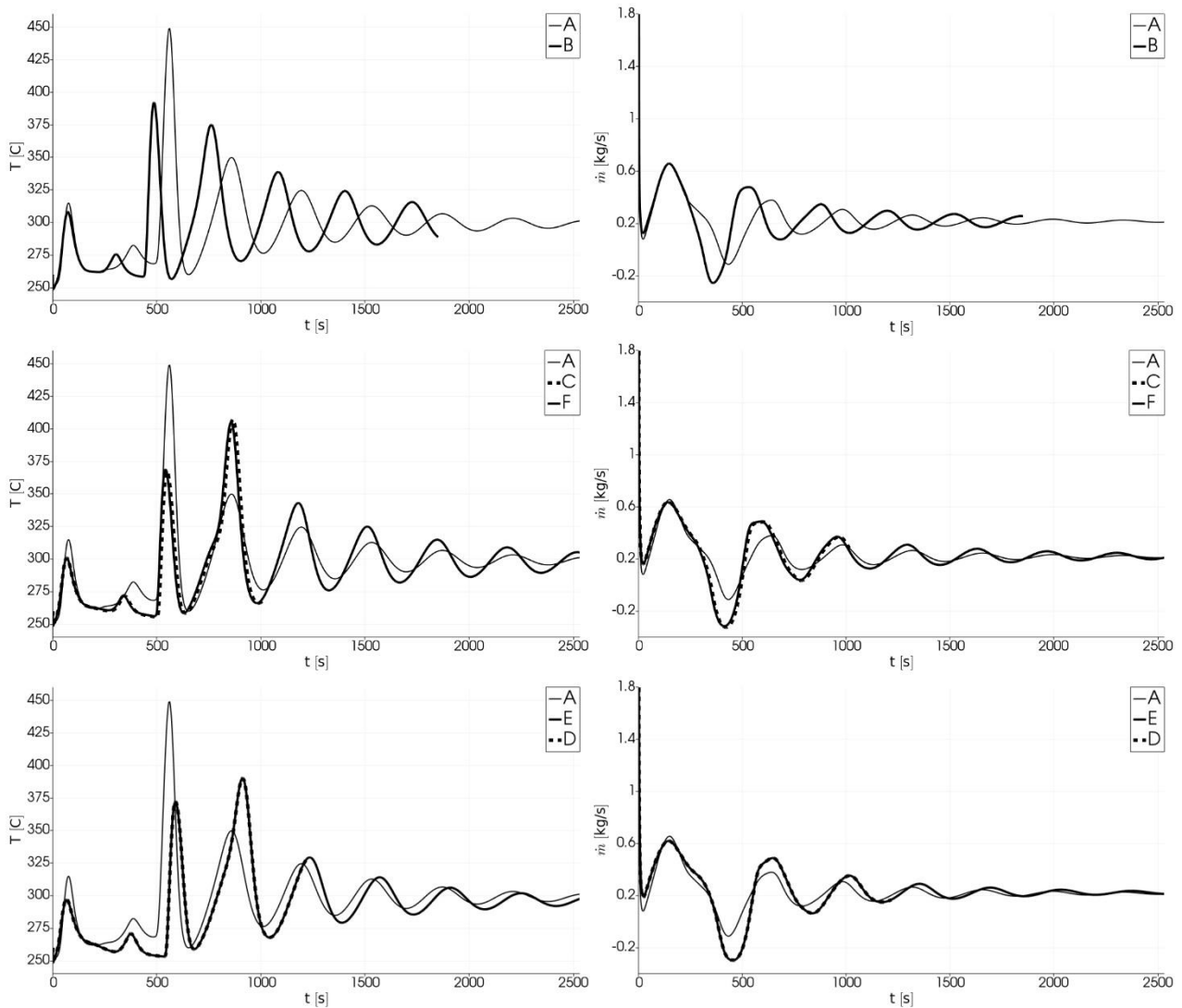


Fig. 2.14 - TALL-3D facility at reference point 2 (RESERVE4, leg 1), temperature (left) and mass flow (right) for Case AB, ACF and ADE (from top to bottom).



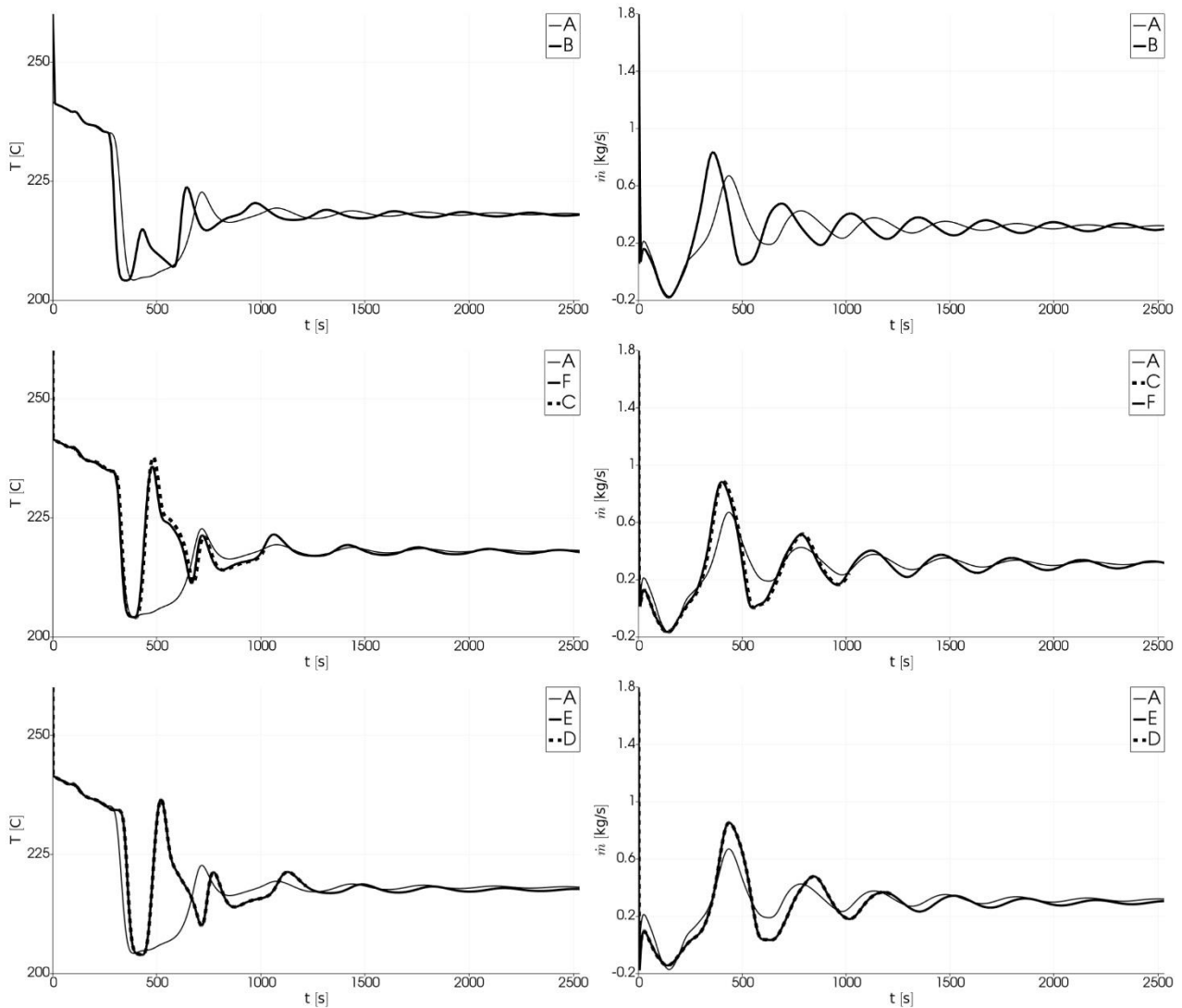


Fig. 2.15 - TALL-3D facility at reference point 3 (BELOW3D25, central leg), temperature (left) and mass flow (right) for Case AB, ACF and ADE (from top to bottom).



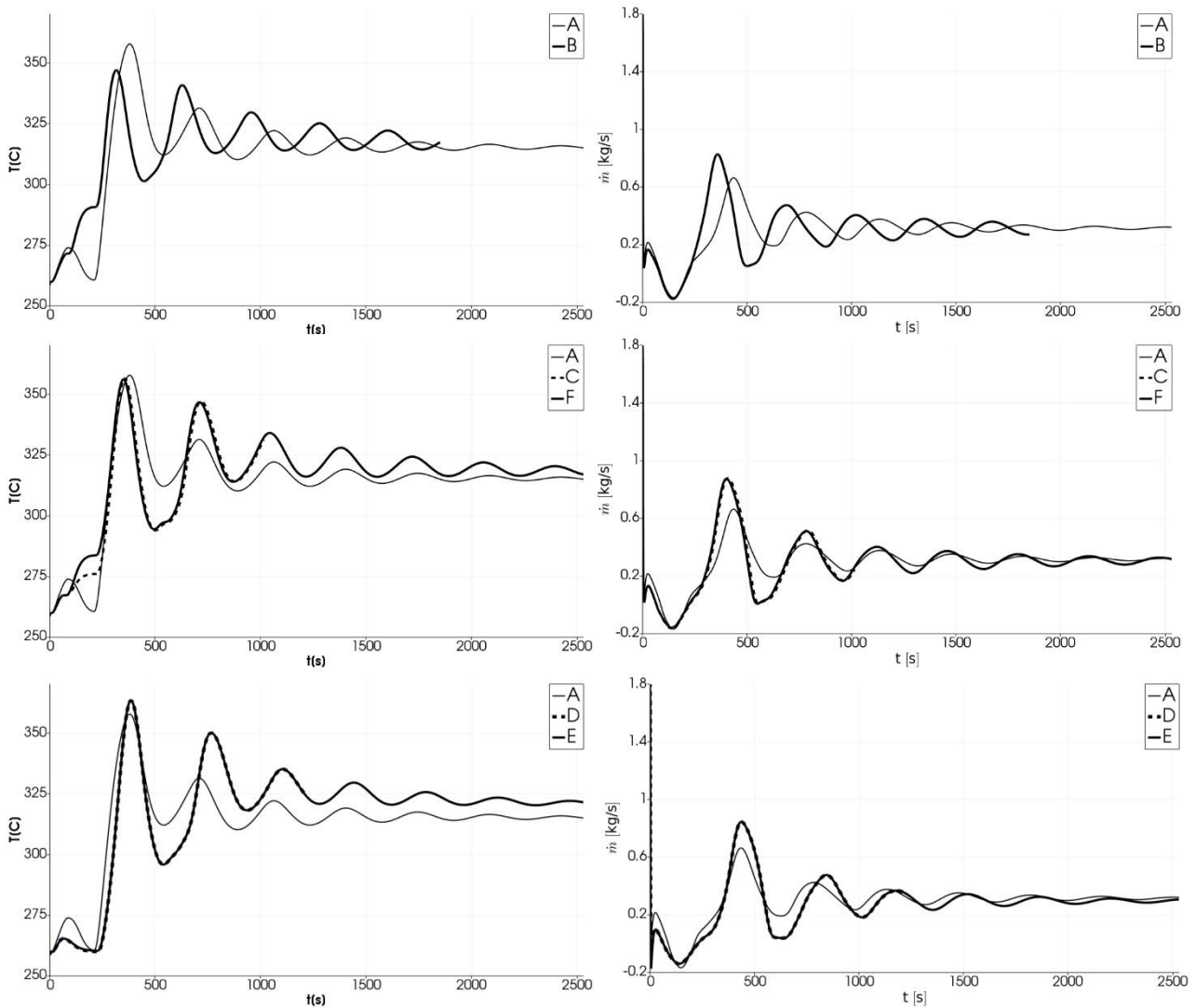


Fig. 2.16 - TALL-3D facility at reference point 4 (ABOVE3D3, central leg), temperature (left) and mass flow (right) for Case AB, ACF and ADE (from top to bottom).



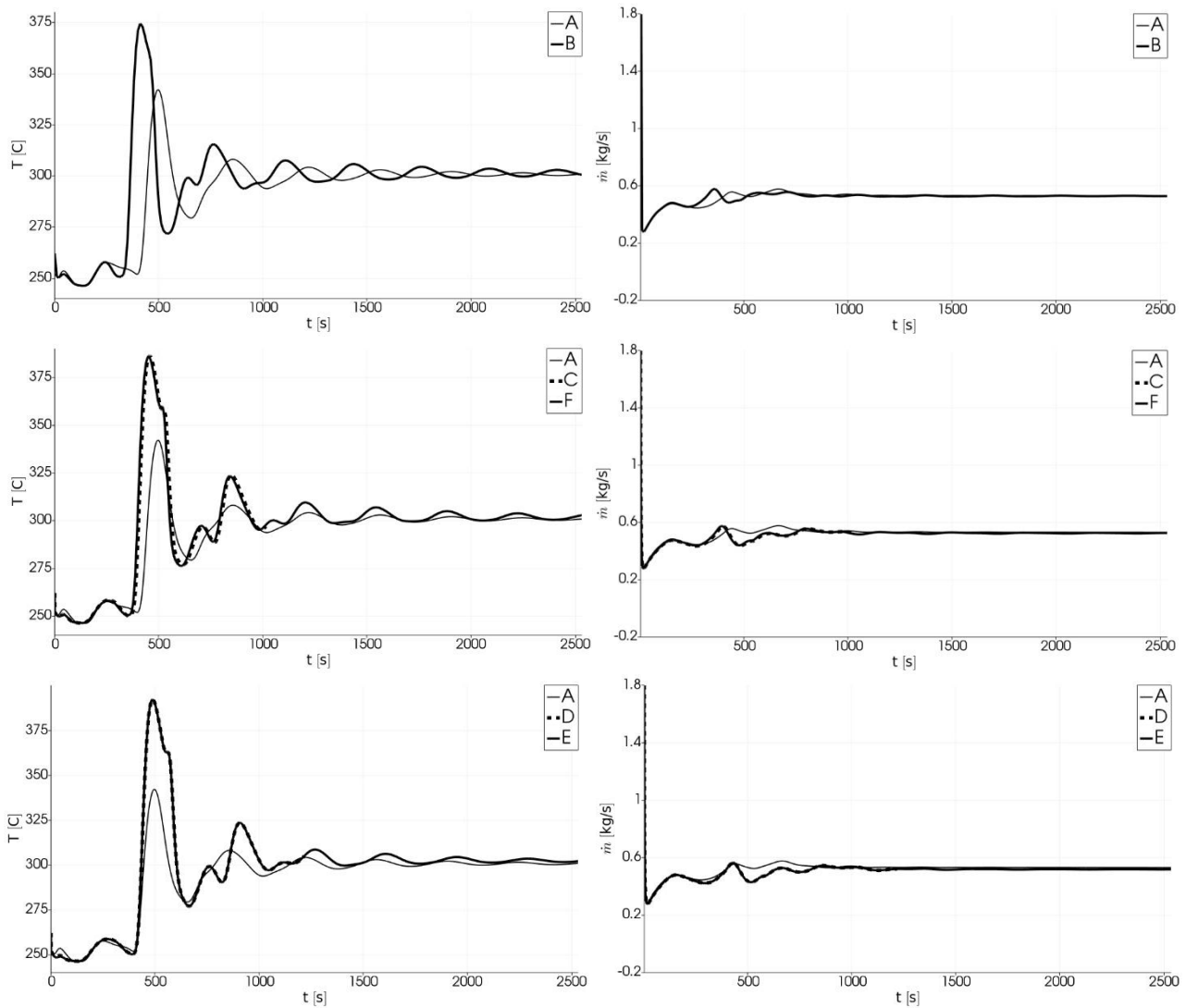


Fig. 2.17 - TALL-3D facility at reference point 5 (LINUP4, leg 3), temperature (left) and mass flow (right) for Case AB, AC and AD (from top to bottom).



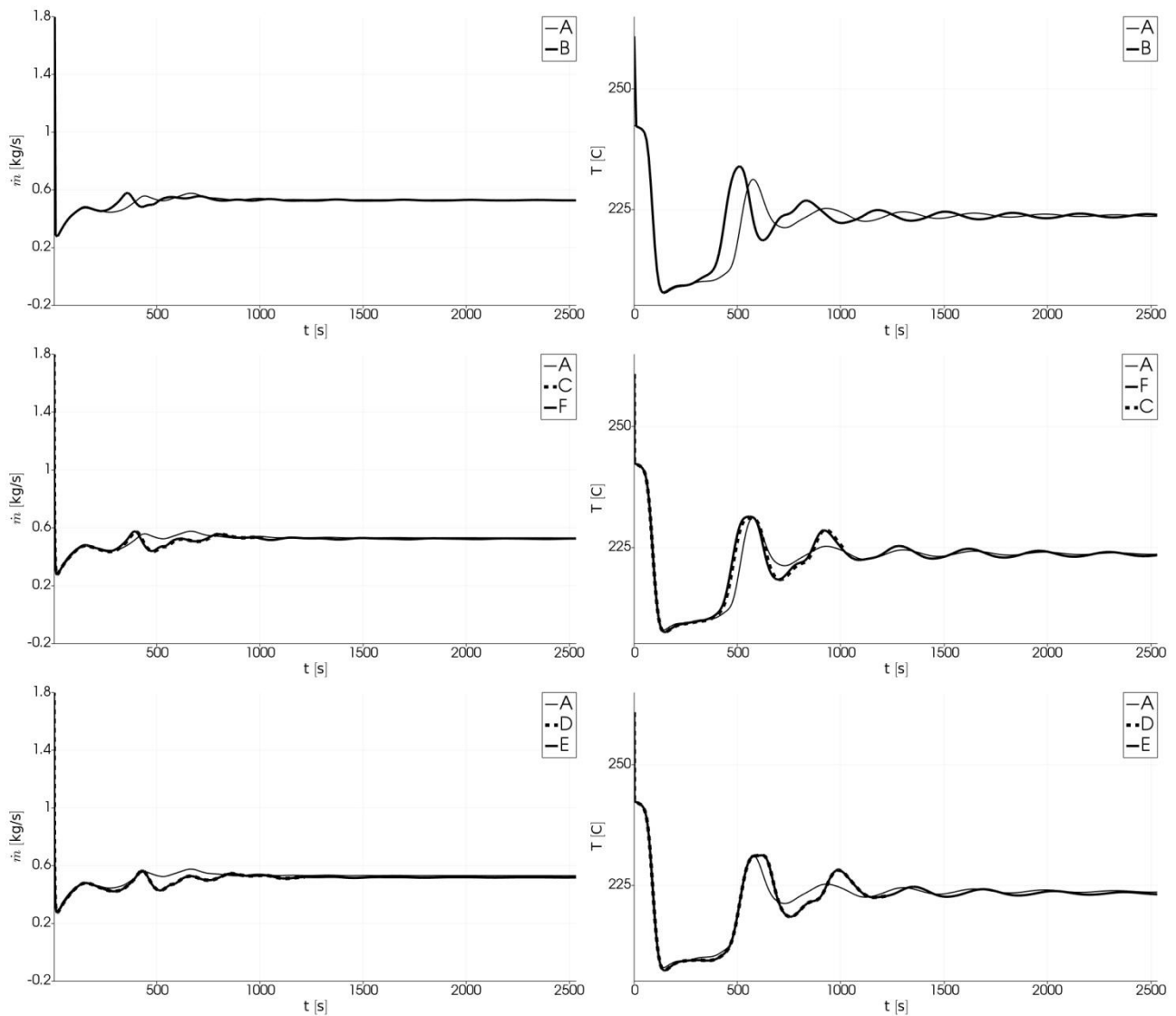



Fig. 2.18 - TALL-3D facility at reference point 6 (PUMP0, leg 3), temperature (left) and mass flow (right) for Case AB, ACF and ADE (from top to bottom).



 RICERCA SISTEMA ELETTRICO	<u>Title:</u> Development of BE numerical tools for LFR design and safety analysis – Part 2	<u>Distribution</u> PUBLIC	<u>Issue Date</u> 12.12.2017	<u>Pag.</u> 126 di 300
	<u>Project:</u> ADP ENEA-MSE PAR 2016	<u>Ref.</u> ADPFISS-LP2-144	Rev. 0	

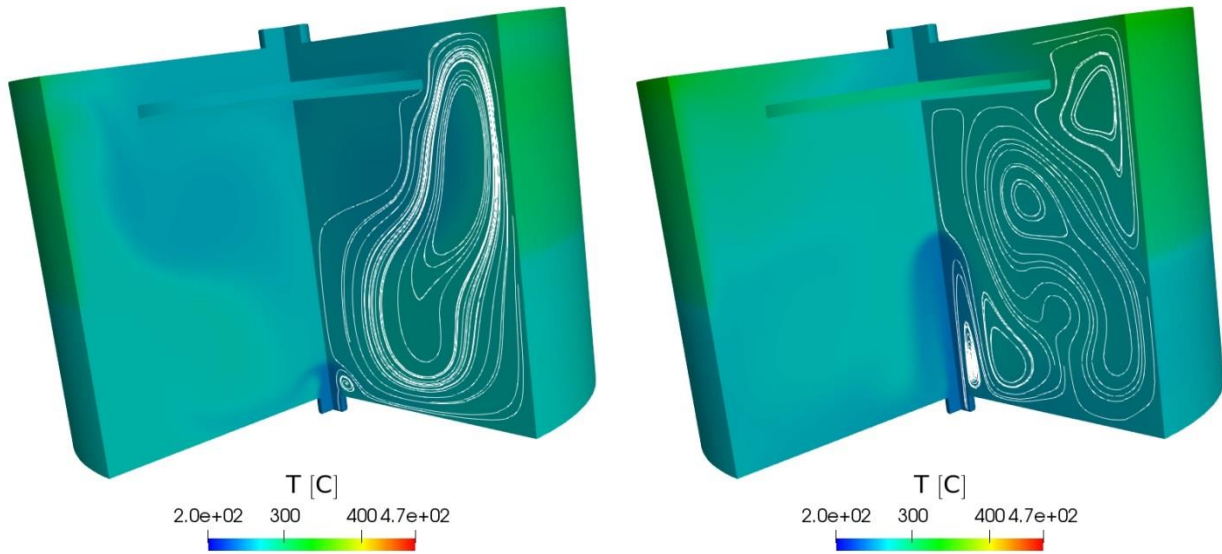


Fig. 2.19 - Temperature and streamline profiles over the 3D test component at $t = 10$ and 20 s for case B (non turbulent natural convection) and constant turbulent Prandtl number.



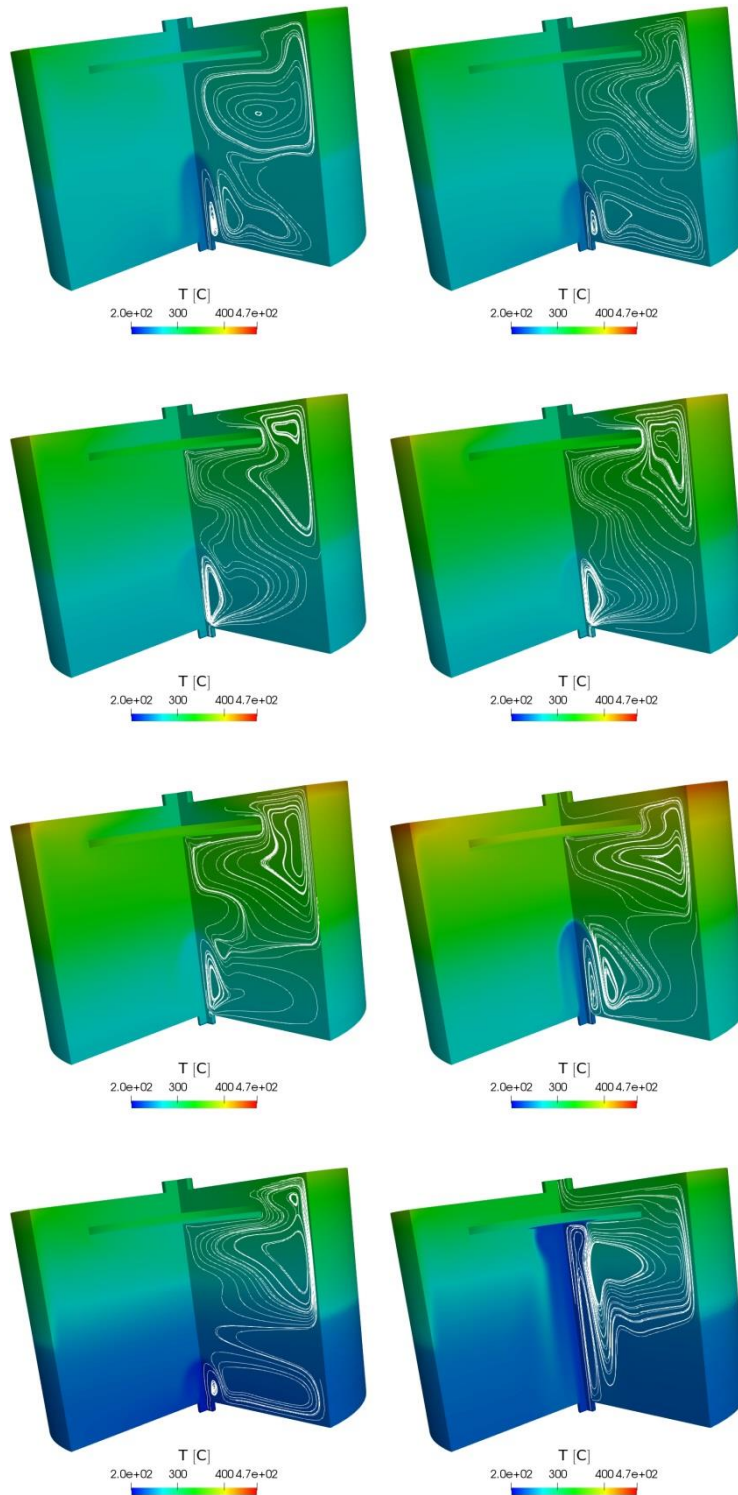


Fig. 2.20 - Temperature and streamline profiles over the 3D test component at $t = 30, 50, 100, 150, 200, 250, 500$ and 1000 s for case B (non turbulent natural convection) and constant turbulent Prandtl number.



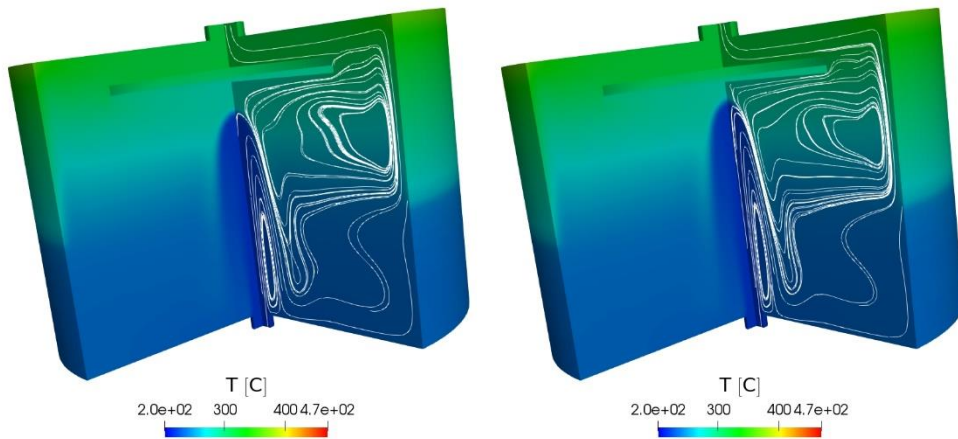


Fig. 2.21 - Temperature and streamline profiles over the 3Dtest component at $t = 1500$ and 2000 s for case B (non turbulent natural convection) and constant turbulent Pr number.

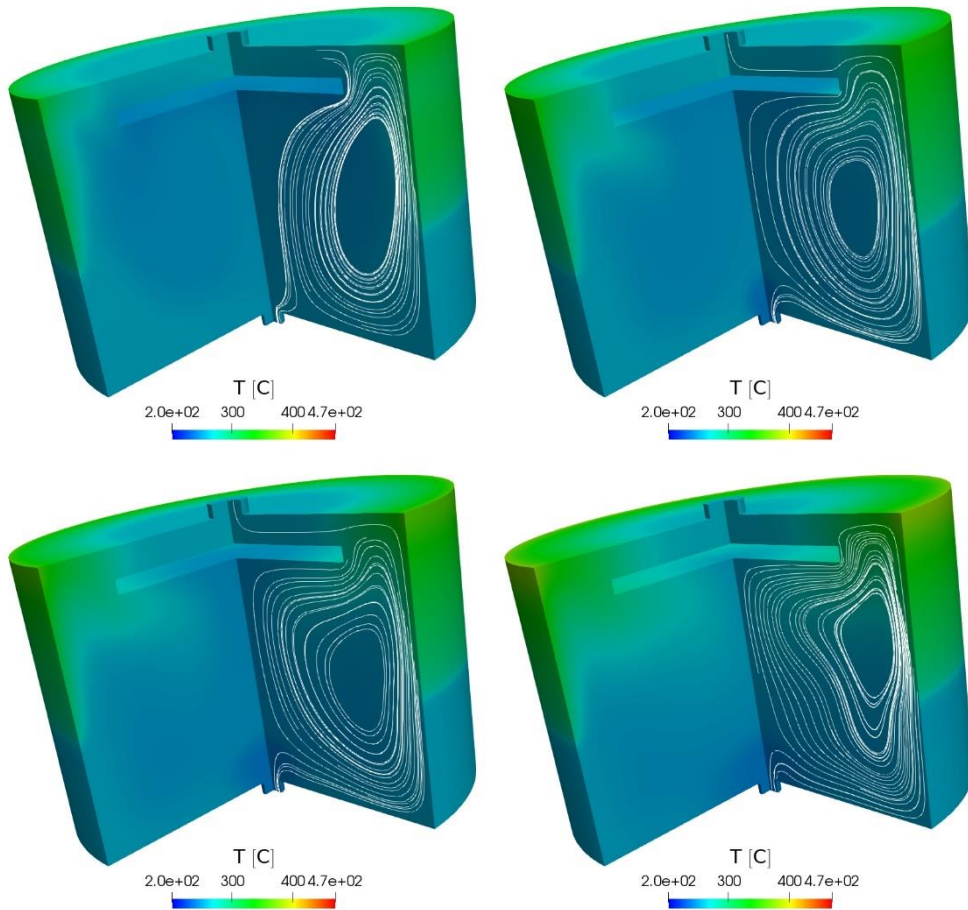


Fig. 2.22 - Temperature and streamline profiles over the 3D test component at $t=10, 20, 30$ and 50 s for $\kappa\text{-}\omega$ turbulence case and Kays turbulent Pr number model for heat exchange.

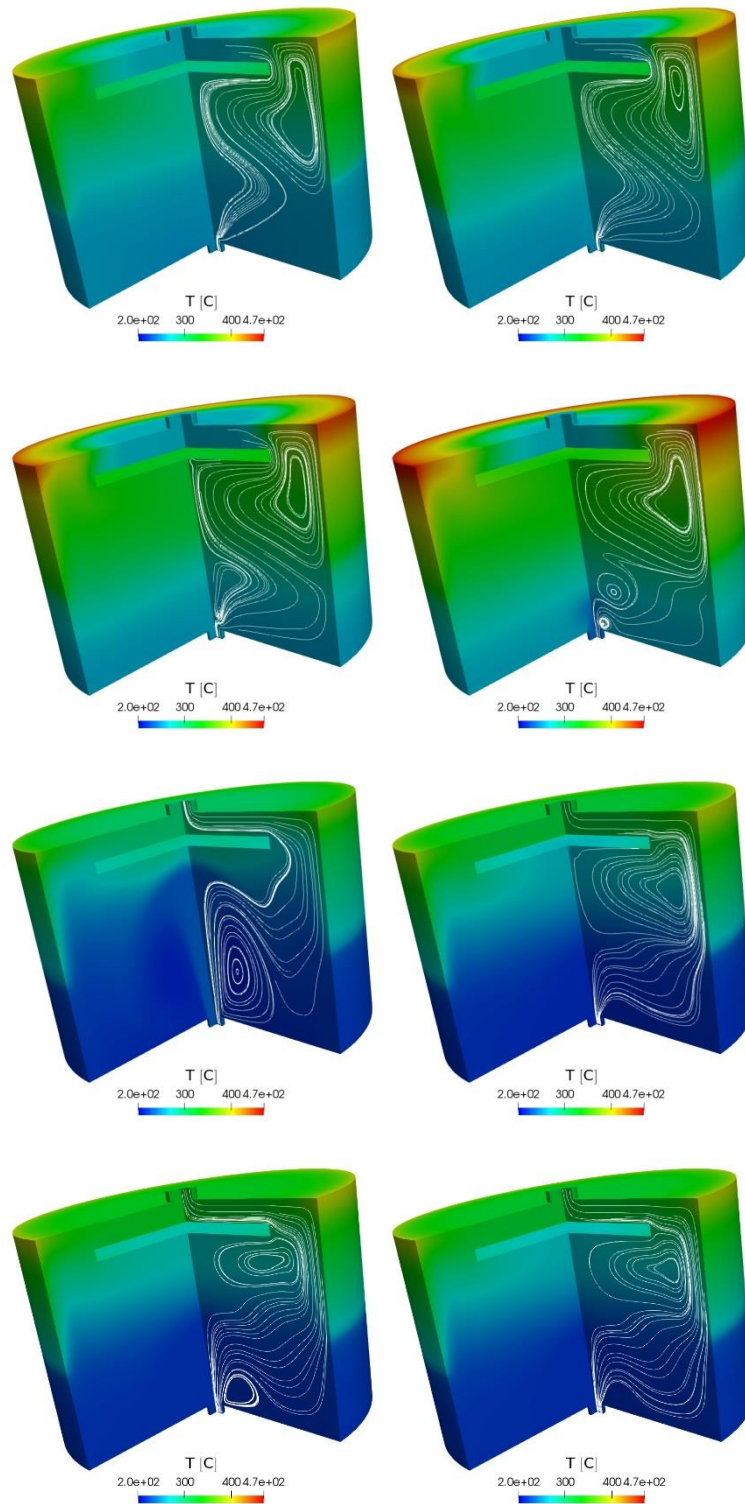


Fig. 2.23 - Temperature and streamline profiles over the three-dimensional test component at $t=100, 150, 200, 250, 500, 1000, 1500$ and 2000 s, for $\kappa\text{-}\omega$ turbulence case and Kays turbulent Prandtl number model for heat exchange.



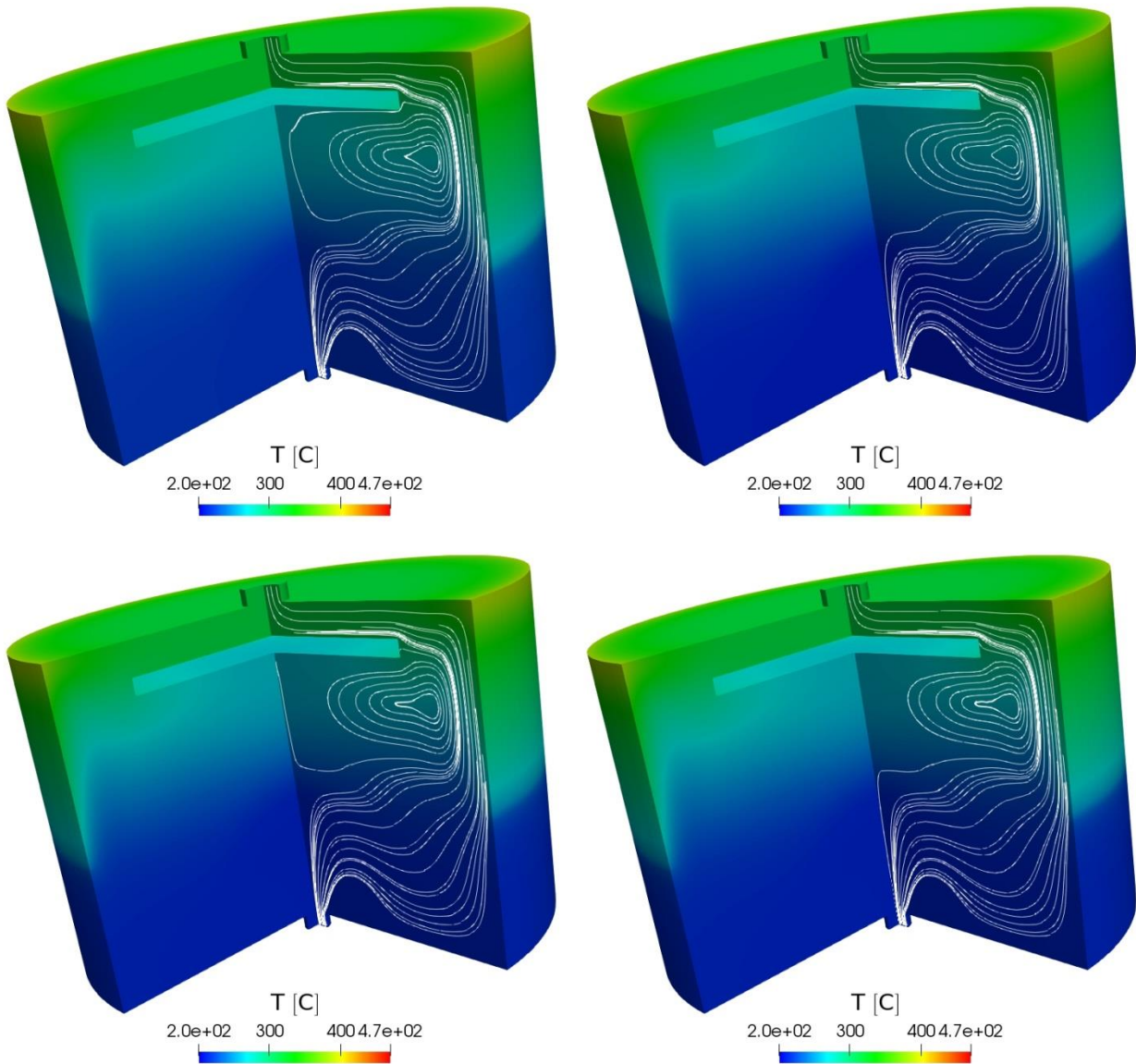



Fig. 2.24 - Temperature and streamline profiles over the three-dimensional test component at $t = 3000, 4000, 5000$ and 6000 s, for κ - ω turbulence case and Kays turbulent Prandtl number model for heat exchange.

 RICERCA SISTEMA ELETTRICO	<u>Title:</u> Development of BE numerical tools for LFR design and safety analysis – Part 2	<u>Distribution</u> PUBLIC	<u>Issue Date</u> 12.12.2017	<u>Pag.</u> 131 di 300
	<u>Project:</u> ADP ENEA-MSE PAR 2016	<u>Ref.</u> ADPFISS-LP2-144	Rev. 0	

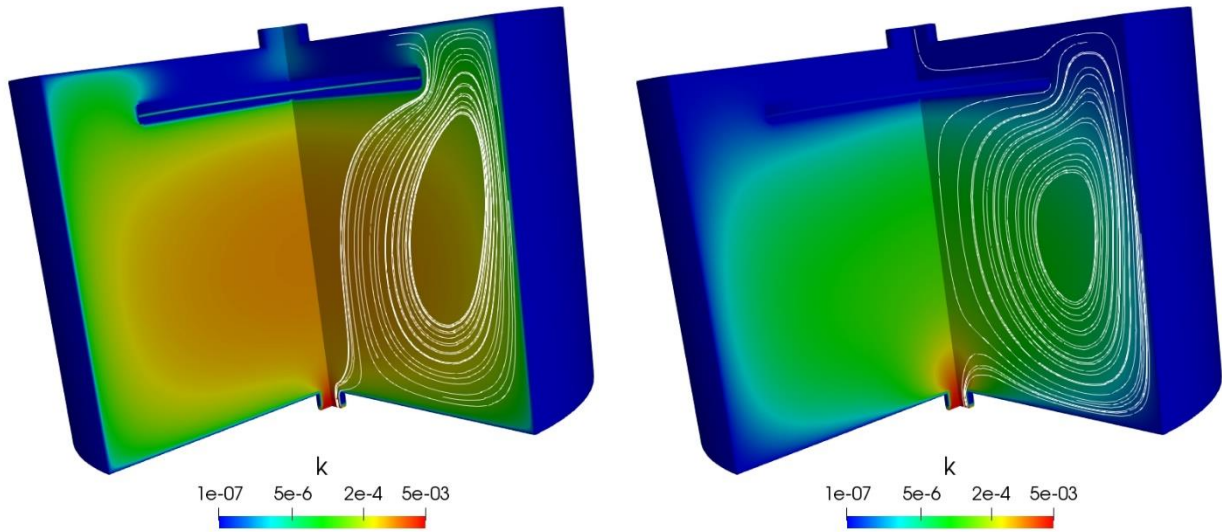


Fig. 2.25 - Turbulent kinetic energy κ and streamline profiles over the three-dimensional test component at $t = 10, 20$ s, for κ - ω turbulence case and Kays turbulent Pr number model for heat exchange.



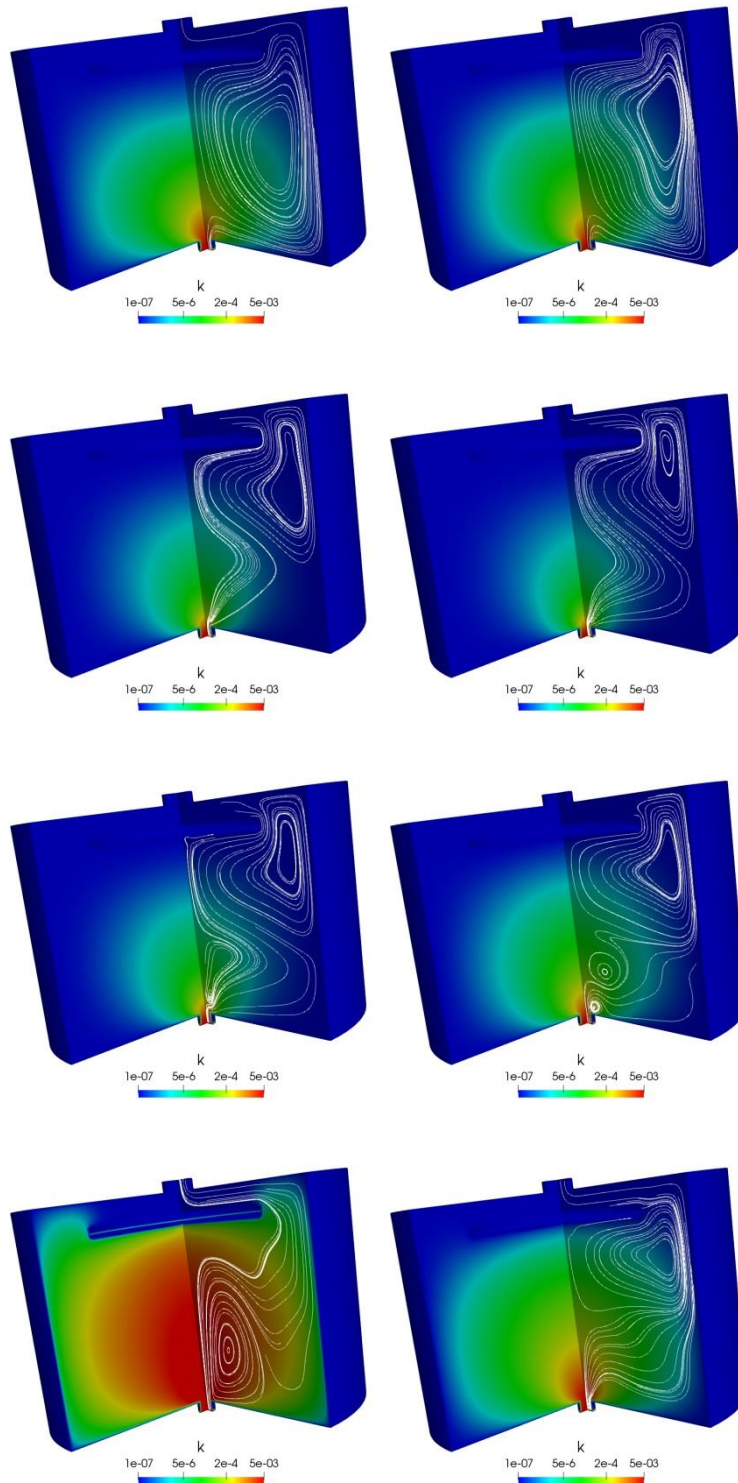


Fig. 2.26 - Turbulent kinetic energy κ and streamline profiles over the three-dimensional test component at $t=30, 50, 100, 150, 200, 250, 500$ and 1000 s, for $\kappa-\omega$ turbulence case and Kays turbulent Prandtl number model for heat exchange.

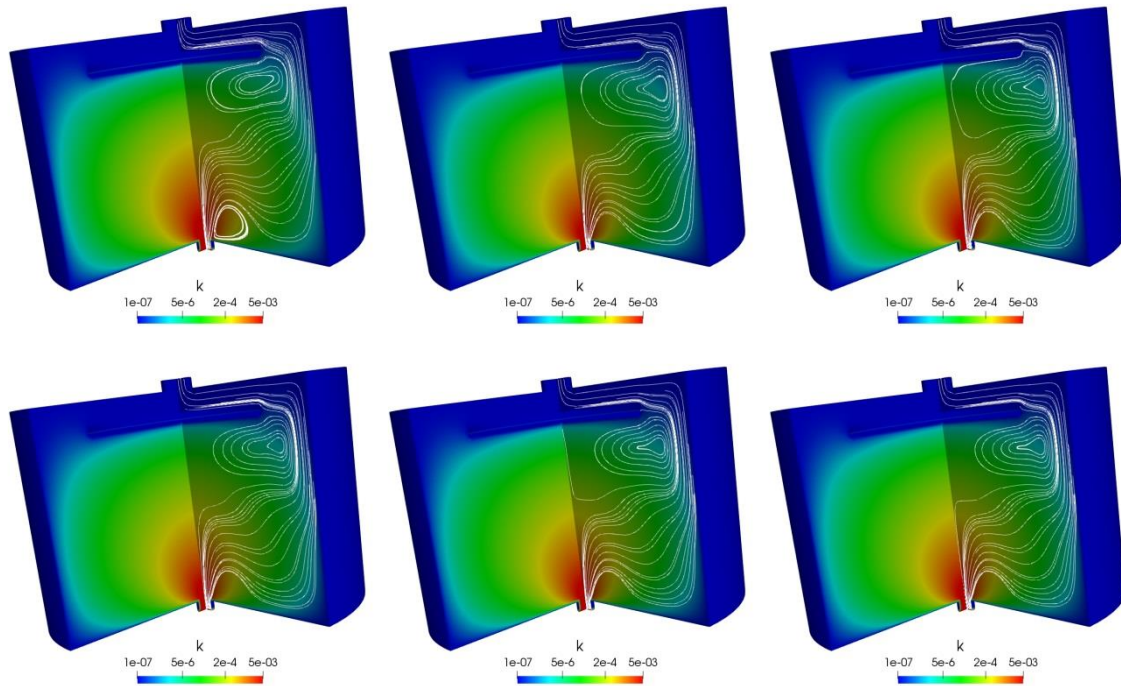


Fig. 2.27 - Turbulent kinetic energy κ and streamline profiles over the three-dimensional test component at $t=1500, 2000s, 3000s, 4000s, 5000s$ and $6000 s$, for $\kappa-\omega$ turbulence case and Kays turbulent Prandtl number model for heat exchange.

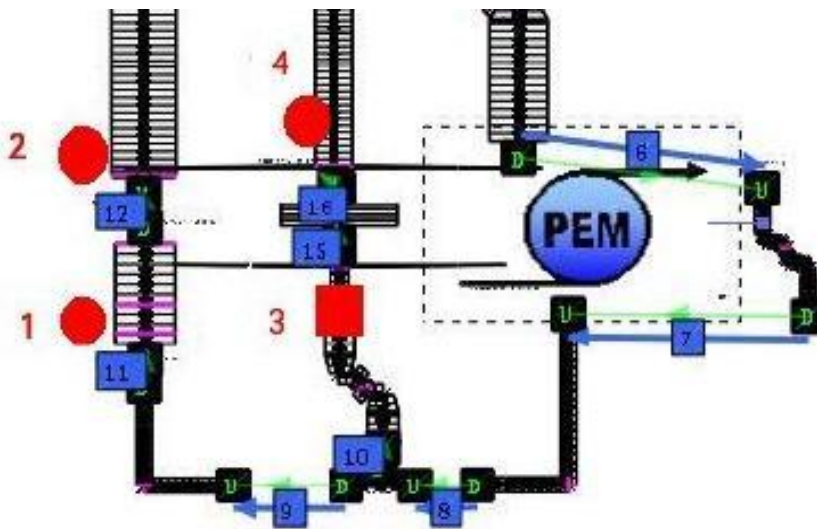


Fig. 2.28 - Points of interest in the 1D overlapping mesh.

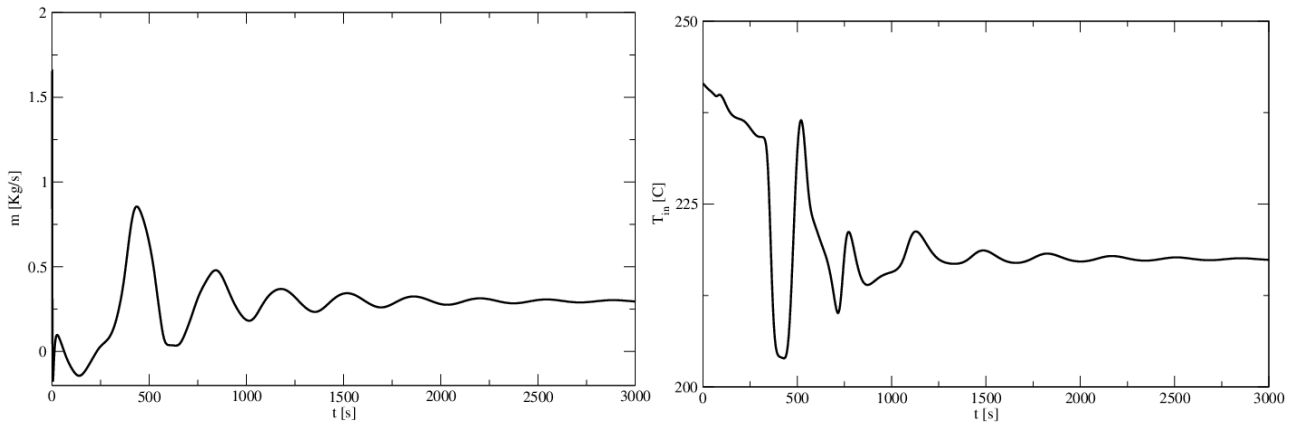


Fig. 2.29 - Mass flow rate (right) and temperature (left) as boundary conditions from CATHARE to FEMLCORE as a function of time.

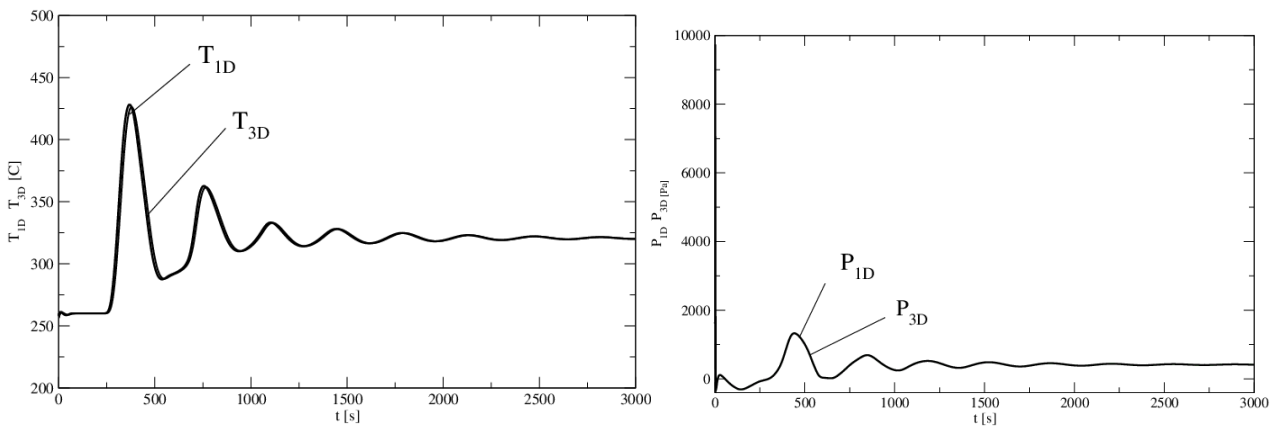



Fig. 2.30 - Temperature and pressure imposed to CATHARE by FEMLCORE at point 4 as a function of time.




 RICERCA SISTEMA ELETRICO	<u>Title:</u> Development of BE numerical tools for LFR design and safety analysis – Part 2	<u>Distribution</u> PUBLIC	<u>Issue Date</u> 12.12.2017	<u>Pag.</u>
	<u>Project:</u> ADP ENEA-MSE PAR 2016	<u>Ref.</u> ADPFISS-LP2-144	Rev. 0	135 di 300

2.4 List of References


- [2.1] A. Ribes and C. Caremoli, “Salome platform component model for numerical simulation,” (2007), pp.553–564.
- [2.2] M. Jeltsov, K. Koop, D. Grishchenko, A. Karbojian, W. Villanueva, and P. Kudinov, “Development of tall-3d facility design for validation of coupled sth and cfd codes,” (2012).
- [2.3] D. Grishchenko, M. Jeltsov, K. Koop, A. Karbojian, W. Villanueva, and P. Kudinov, “Design and commissioning tests of the tall-3d experimental facility for validation of coupled sth and cfd codes,” (2014).
- [2.4] D. Grishchenko, M. Jeltsov, K. Koop, A. Karbojian, W. Villanueva, and P. Kudinov, Nuclear Engineering and Design 290, 144–153 (2015).
- [2.5] F. Cadinu and P. Kudinov, “Development of a “coupling-by-closure” approach between cfd and system thermal-hydraulics codes,” (2009).
- [2.6] M. Jeltsov, F. Cadinu, W. Villanueva, A. Karbojian, K. Koop, and P. Kudinov, “An approach to validation of coupled cfd and system thermal-hydraulics codes,” (2011).
- [2.7] M. Jeltsov, K. Koop, P. Kudinov, and W. Villanueva, “Development of a domain overlapping coupling methodology for sth/cfd analysis of heavy liquid metal thermal-hydraulics,” (2013).
- [2.8] F. Barre and M. Bernard, Nuclear Engineering and Design 124, 257–284 (1990).
- [2.9] M. Robert, M. Farvacque, M. Parent, and B. Faydide, “Cathare 2 v2.5: a fully validated cathare version for various applications,” Tech. Rep. (2003).
- [2.10] G. Geffraye, O. Antoni, M. Farvacque, D. Kadri, G. Lavialle, B. Rameau, and A. Ruby, Nuclear Engineering and Design 241, 4456–4463 (2011).
- [2.11] A. Cervone and S. Manservigi, “A three-dimensional cfd program for the simulation of the thermohydraulic behavior of an open core liquid metal reactor,” Tech. Rep. lin-thrg 108 (2008).
- [2.12] S. Bnà, S. Manservigi, and O. L. Bot, “Simulation of the thermal-hydraulic behavior of liquid metal reactors using a three-dimensional finite element model,” Tech. Rep. (2010).
- [2.13] G. Bornia, M. Finelli, S. Manservigi, V. Mikhin, M. Polidori, and K. Voukelatou, “Development and validation of femlcore code for the thermal hydraulics of open cores,” Tech. Rep. (2011).
- [2.14] G. Bornia, D. Cerroni, S. Manservigi, M. Polidori, and F. Donato, “Femlcore code: parallelization, turbulence models and code integration,” Tech. Rep. (2012).
- [2.15] S. Manservigi and F. Menghini, Nuclear Engineering and Design 273, 251 – 270 (2014).
- [2.16] S. Manservigi and F. Menghini, Nuclear Engineering and Design 295, 251 – 260 (2015).
- [2.17] R. Da Vià, S. Manservigi, and F. Menghini, International Journal of Heat and Mass Transfer 101, 1030–1041 (2016).
- [2.18] R. Bavière, N. Tauveron, F. Perdu, E. Garré, and S. Li, Nuclear Engineering and Design 277, 124–37 (2014).
- [2.19] T. P. Grunloh and A. Manera, Annals of Nuclear Energy 90, 422–32 (2016).
- [2.20] A. Chierici, L. Chirco, R. D. Vià, S. Manservigi, and R. Scardovelli, “Multiscale numerical algorithm for heat transfer simulation between multidimensional cfd and monodimensional system codes,” (2017).



 RICERCA SISTEMA ELETTRICO	<u>Title:</u> Development of BE numerical tools for LFR design and safety analysis – Part 2	<u>Distribution</u> PUBLIC	<u>Issue Date</u> 12.12.2017	<u>Pag.</u>
	<u>Project:</u> ADP ENEA-MSE PAR 2016	<u>Ref.</u> ADPFISS-LP2-144	Rev. 0	136 di 300

- [2.21] D. Cerroni, R. D. Vià, S. Manservisi, F. Menghini, and G. Pozzetti, “Integration of the femlcore code in the salome platform,” Tech. Rep. (2014).
- [2.22] A. Attavino, D. Cerroni, A.Cervone, L. Fancellu, and S. Manservisi, “Femlcore-cathare coupling on salome platform,” Tech. Rep. RL 1361/CERSE-UNIBO (2015).
- [2.23] F. Bassenghi, G. Borna, L. Deon, and S. Manservisi, “Implementation and validation of the nurisp platform,” Tech. Rep. (2011).
- [2.24] D. Cerroni, S. Manservisi, and E. Vincenzi, “Developing multiscale transient simulations with femlcore code,” Tech. Rep. (2013).
- [2.25] R. Da Vià, D. Cerroni, A.Cervone, and S. Manservisi, “Validation of the femlcore-cathare coupling model of the tall-3d facility,” Tech. Rep. RL 1362/CERSE-UNIBO (2016). A. Ribes and C. Caremoli, “Salome platform component model for numerical simulation,” (2007), pp.553–564.




 RICERCA SISTEMA ELETTRICO	<u>Title:</u> Development of BE numerical tools for LFR design and safety analysis – Part 2	<u>Distribution</u> PUBLIC	<u>Issue Date</u> 12.12.2017	<u>Pag.</u>
	<u>Project:</u> ADP ENEA-MSE PAR 2016	<u>Ref.</u> ADPFISS-LP2-144	Rev. 0	137 di 300

3 VALIDATION OF RELAP5-3D BY CIRCE-ICE EXPERIMENTAL TESTS


V. Narcisi, F. Giannetti, G. Caruso, M. Frullini



 RICERCA SISTEMA ELETTRICO	<u>Title:</u> Development of BE numerical tools for LFR design and safety analysis – Part 2	<u>Distribution</u> PUBLIC	<u>Issue Date</u> 12.12.2017	<u>Pag.</u>
	<u>Project:</u> ADP ENEA-MSE PAR 2016	<u>Ref.</u> ADPFISS-LP2-144	Rev. 0	138 di 300

(Page intentionally left blank)



 RICERCA SISTEMA ELETRICO	<u>Title:</u> Development of BE numerical tools for LFR design and safety analysis – Part 2	<u>Distribution</u> PUBLIC	<u>Issue Date</u> 12.12.2017	<u>Pag.</u>
	<u>Project:</u> ADP ENEA-MSE PAR 2016	<u>Ref.</u> ADPFISS-LP2-144	Rev. 0	139 di 300

3.1 Background and references

The Fukushima Daiichi nuclear power plant (NPP) accident, happened on March 11, 2011, highlighted the need of NPP capability to assure residual heat removal for long periods and to limit significant off-site releases after the occurrence of a severe accident.

The lesson was acknowledged by Generation IV International Forum (GIF) and established the requirement of highest level of safety for innovative nuclear systems.

The GIF was founded on January 2000 by 9 Countries (Argentina, Brazil, Canada, France, Japan, the Republic of Korea, the Republic of South Africa, the United Kingdom and the United States), becoming 13 in the following years (Switzerland, Euratom, Peoples Republic of China and Russian Federation). The goal of the GIF is to develop innovative nuclear energy systems in order to help meet the world's future energy needs. The new system will have to satisfy the main goals of a generation IV system: sustainability, economics, safety & reliability and proliferation resistance & physical protection. A generation IV nuclear system will have to provide a sustainable energy generation assuring a long-term availability of the system and the effective fuel utilization and reducing the production of nuclear waste. The operation of a GEN IV reactor will have to excel in safety and reliability; it will have a very low likelihood and degree of reactor core damage and it will eliminate the need for offsite emergency response^[3.1].


Lead-cooled fast reactor (LFR) belong to the six concepts selected by GIF as Generation IV systems and includes lead and lead-bismuth eutectic alloy (LBE) technologies; both coolants are chemically inert and they offer other attractive characteristics in terms of interaction with structural materials and thermodynamic features. LFR systems also well respond to lesson of Fukushima accident allowing natural circulation both in nominal and accident conditions. This feature offers considerable grace time in order to cope with unprotected loss of flow transient and permits to introduce fully passive decay heat removal system (DHR), assuring very high safety features over long periods without need for operator actions, combined with active systems.

In the frame of the development of the LFR system, several R&D activities are promoted in the UE. At this purpose, the CIRCE pool facility (CIRColazione Eutettico) at ENEA Brasimone research center, was refurbished in order to host the test section ICE (Integral Circulation Experiment) which aims to simulate the thermal-hydraulic behavior of the primary system in a HLM cooled pool reactor. The test section consists of a fuel pin simulator (FPS), which electrically simulates the core of the facility, the heat exchanger (HX) and the DHR system, immersed in the upper part of the pool. LBE circulation into the main flow path is enhanced by the injection of argon at the inlet section of the riser^[3.2]. The main goals of the experimental campaign conducted on CIRCE-ICE test facility are to investigate mixing convection and thermal stratification phenomena in a HLM pool and to provide experimental data for the validation of analytical codes.

3.2 CIRCE-ICE facility

CIRCE is a multipurpose pool facility designed to host different test sections welded to and hung from bolted vessel heads for the investigation of thermal-hydraulic aspects related to the HLM pool system. The facility consists of a main vessel, earmarked for containing test section and filled with about 70 tons of molten LBE, two auxiliary tanks, dedicated to store LBE during maintenance phases and to transfer liquid metal during loading and drainage phases, and data acquisition system. The main vessel (S100) is characterized by the outer diameter of 1200 mm and the height of 8500 mm. The Fig. 3.1 depicts the isometric view of the facility and the main parameters are summarized in Tab. 3.1.



 RICERCA SISTEMA ELETTRICO	<u>Title:</u> Development of BE numerical tools for LFR design and safety analysis – Part 2	<u>Distribution</u> PUBLIC	<u>Issue Date</u> 12.12.2017	<u>Pag.</u>
	<u>Project:</u> ADP ENEA-MSE PAR 2016	<u>Ref.</u> ADPFISS-LP2-144	Rev. 0	140 di 300

The experimental campaign is conducted on ICE test section, installed into the main vessel. ICE aims to simulate the primary system of a HLM pool type reactor and the main objectives of the experimental campaign were to investigate thermal stratification and mixing convection phenomena into the pool and to provide experimental data for the validation of analytical codes. These are two of the main topics for the development of LFR system: the thermal stratification could induce thermo-mechanical stress on the structure and the validation of TH (Thermal Hydraulics) codes against the experimental data is a fundamental step in order to justify their use in the design phase for improving safety aspects.


The principal components and the primary main flow path of the test section are depicted in Fig. 3.2 and Fig. 3.3; the inlet section consists of the feeding conduit, which allows the hydraulic connection between the lower plenum of the pool and the fuel pin simulator (FPS). The value of the LBE mass flow rate entering the FPS is measured by a Venturi-nozzle flow meter, installed into the feeding conduit. The fuel pin simulator represents the heat source of the unit. It consists of an electrical pin bundle with a nominal thermal power of 800 kW and an active length of 1000 mm. The bundle is composed of 37 electrically heated pins arranged in a wrapped hexagonal lattice and characterized by a pitch to diameter ratio equal to 1.8 (Fig. 3.4); the relative position between the pin bundle and the external wrapper is fixed by three spacer grids, located along the heat source, and the unit rests to the lower grid, placed at the inlet section of the FPS. Each pin has an outer diameter of 8.2 mm, a thermal power of 25 kW and a heat flux at the pin wall of 1 MW/m². The hot fluid exits the core and it is introduced into the fitting volume, which allows the connection between the fuel pin simulator and the riser, double wall insulated pipe connecting the fitting volume and the separator. At the inlet section of the riser, a nozzle is installed allowing the injection of argon in order to promote the circulation of the primary coolant. The mixture flows upward and collects inside the separator, where the separation of LBE and Ar occurs (LBE enters the heat exchanger while Ar flows upward into the gas plenum through the free surface). The HX (heat exchanger) is made of 91 bayonet tubes, characterized by an active length of 3462 mm, contained into a cylindrical shell. The relative position between the tubes and the external shell is fixed by only one grid at the outlet section of the HX. The Fig. 3.5 shows a sketch of the bayonet element which consists of three concentric tubes. The feed-water flows downward into the inner tube and then upward into the annular riser between inner and middle tube, where the change of phase take place; the double physical separation is obtained with the second and the third tube and the LBE flows downwards outside the tubes.

The volume between middle and outer tube is filled by pressurized helium to detect any leakage. Exiting the HX, primary coolant flows through the downcomer reaching the lower plenum. The DHR system is located in the upper zone of the pool, as shown in Fig. 3.2. It consists of only one bayonet tube and the decay power is removed by forced circulation of air. The tube is located inside a double wall shell with a thin air insulation gap to thermally decouple the DHR from the external LBE pool. Hot LBE enters the DHR by the upper inlet section, it flows downward decreasing the temperature and it exits the component in the downcomer^[3,2].

The test section is equipped with several thermocouples to investigate the thermal behavior of the LBE. The primary coolant temperature inside the FPS is measured by 36 TCs (thermocouples), arranged at 7 different axial levels. Two series of penetration are obtained at the inlet and outlet section of the active zone, as shown in Fig. 3.6. In addition, along the HS active length, four different sections are monitored as depicted in Fig. 3.7, investigating the temperature of the LBE along three characteristic sub-channels and the pin clads.

Several TCs are also installed inside the pool in order to investigate mixing convection and thermal stratification phenomena. 119 thermocouples are installed in 17 axial levels and 9 different azimuthal positions, as shown in Fig. 3.8.



 RICERCA SISTEMA ELETTTRICO	<u>Title:</u> Development of BE numerical tools for LFR design and safety analysis – Part 2	<u>Distribution</u> PUBLIC	<u>Issue Date</u> 12.12.2017	<u>Pag.</u>
	<u>Project:</u> ADP ENEA-MSE PAR 2016	<u>Ref.</u> ADPFISS-LP2-144	Rev. 0	141 di 300

3.3 Simulation results

The nodalization scheme of the test facility is obtained with RELAP5-3D[®] ver. 4.3.4 (R5-3D). RELAP5 is a light water reactor transient analysis code developed by the U.S. Nuclear Regulatory Commission (NRC) for use in rulemaking, licensing audit calculations, evaluation of operator guidelines and as a basis for a nuclear plant analyzer. It is a generic code that, in addition to calculating the behaviour of a reactor coolant system during a transient, can be used for simulation of a wide variety of hydraulic and thermal transients in both nuclear and non-nuclear systems involving mixtures of steam, water, non-condensable and solute. R5-3D is the last version of the series of RELAP5 code and contains several improvements; the two most enhancements from the previous versions are the multi-dimensional thermal-hydraulic capability and the addition of new working fluids, including heavy liquid metals^[3.3].

Starting from the technical design of each components, provided by ENEA research center of Brasimone, the first version of the nodalization scheme of the facility was carried out at the beginning of the activity. The global test facility was simulated with a mono-dimensional model (Fig. 3.9) consisting of 253 control volumes and 255 junctions. The scheme included the primary main flow path, the secondary system of the HX and the DHR. The volume between the main vessel and the internal components was simulated only by a single pipe (in light blue). Several heat structures were adopted to simulate thermal behavior of the global facility. The mono-dimensional scheme well reproduced the data measured across the main flow path, but it was not able to reproduce the convective motions of the LBE into the pool.

The next step was to adopt a three-dimensional component to simulate the pool of the facility. The new model was divided in two macro-regions: the region number 1 reproduced the primary main flow path, the secondary system of the HX and the DHR system (Fig. 3.10) and the region number 2 model the pool of the facility (Fig. 3.11, the internals are depicted only to highlights the volume occupied by each components).


The 1-D scheme reproduced all components described in previous section. The HS was simulated by a single equivalent pipe and one heat structure, which reproduced the 37 electrical pins. In R5-3D, for the evaluation of the heat transfer coefficient (HTC) on heavy liquid metals, Todreas & Kazimi correlation^[3.4] is implemented. Previous simulation of HLM system showed that this correlation underestimates the Nusselt number for pitch-to-diameter ratio greater than 1.3^[3.5]. Additionally, R5-3D does not permit a pitch-to-diameter ratio of 1.8 and the p/d of the pin bundle was set to the maximum allowed value of 1.6. In order to improve the HTC according to Ushakov correlation^[3.6] (more accurate in this case) and to correct the heat exchange to experimental p/d value, an artificial fouling factor of 0.86, evaluated as the ratio between the two correlations in nominal flow conditions, was applied to the HTC. Upstream the FPS, the pressure drop of the Venturi nozzle was simulated by a concentrated pressure loss coefficient K, dependent on the flow conditions, according to the equation:

$$K_{Venturi} = 10.5 Re^{-0.014}$$

The argon injection at the inlet section of the riser was simulated by the boundary conditions: the time dependent volume set gas inlet conditions and the time dependent junction adjusted the mass flow rate injection. An additional time dependent volume set the pressure of the gas plenum of the facility.

The HX primary side was simulated by a single equivalent pipe and one heat structure, which thermally couples the primary and the secondary side. A calibrated fouling factor of 1.02 was evaluated as the ratio between Ushakov and Todreas & Kazimi correlation and it was applied on the LBE side to increase the HTC. The bayonet tubes are modelled by only two pipes in order to simulate the descending and ascending side of water/steam tubes and one heat structure to model heat dispersion between the two pipes.



 RICERCA SISTEMA ELETTRICO	<u>Title:</u> Development of BE numerical tools for LFR design and safety analysis – Part 2	<u>Distribution</u> PUBLIC	<u>Issue Date</u> 12.12.2017	<u>Pag.</u>
	<u>Project:</u> ADP ENEA-MSE PAR 2016	<u>Ref.</u> ADPFISS-LP2-144	Rev. 0	142 di 300

The pressure losses due to grids installed into FPS and heat exchanger are calculated by the Rheme correlation^[3.7]:

$$\Delta p_{grid} = C_v \cdot \varepsilon^2 \cdot 0.5 \cdot \rho \cdot v^2$$

where ρ and v are respectively the density and the velocity of the fluid while ε represents the blockage factor of the grids, calculated as:

$$\varepsilon = \frac{A_{grid}}{A_{flow}}$$

The C_v parameter is a modified drag coefficient and it is calculated as:

$$C_v = MIN \left[3.5 + \frac{73.14}{Re^{0.264}} + \frac{2.79 \cdot 10^{10}}{Re^{2.79}}, \frac{2.6}{\varepsilon^2} \right]$$

The bayonet tube of the DHR system was also simulated and it was composed of one pipe for the LBE channel and two pipes to model the descending and ascending air side.

The region number 2 was the 3D component which simulated the volume between the main vessel and the internals. The nodalization scheme was obtained to compare the LBE temperature in the exact position of the Thermocouples into the pool, in order to investigate the capability of the code to reproduce thermal stratification and mixing convection phenomena. The model consisted of 51 axial levels, 4 radial meshes and 8 azimuthal intervals. The mono-dimensional model and the 3D component was hydraulically coupled with 12 junctions and the heat dispersions through the internals and the main vessel were evaluated with several heat structures.


The global model was composed of 1929 control volumes, 4856 junctions and 15353 heat transfer nodes.

The nodalization scheme previous described was used to reproduce the full power operation of the experimental TEST I^[3.2]; the main parameters of the test are summarized in Tab. 3.2:

The simulation analysis was carried out using default thermophysical properties correlations of R5-3D and repeated using the most recent correlations for LBE^[3.8], implemented in R5-3D as described in Ref. [3.9].

The LBE mass flow rate, measured by the Venturi-nozzle, is represented in Fig. 3.12. The strong oscillations, during first phase of the experimental test, are due to the volumetric blowers used to inject argon into the riser and, after 13000 seconds, they are dumped by installing a check valve into the gas injection system^[3.2]. The experimental data are compared to the simulated values, calculated with default correlations of R5-3D and Nuclear Energy Agency (NEA) recommended correlations. Unless the fluctuations, Fig. 3.12 highlights that both calculated values well reproduce the experimental data, reaching a value of about 55 kg/s. According to Ref. [3.9], the simulation with default correlations underestimates the LBE mass flow of about 1%, because the smaller value of the natural driving force, depending on temperature drop across the core and the heat exchanger. The experimental trend of the LBE temperature at the inlet and outlet sections of the FPS, both represented by the average value measured by three thermocouples, is compared in Fig. 3.14



 RICERCA SISTEMA ELETTRICO	<u>Title:</u> Development of BE numerical tools for LFR design and safety analysis – Part 2	<u>Distribution</u> PUBLIC	<u>Issue Date</u> 12.12.2017	<u>Pag.</u>
	<u>Project:</u> ADP ENEA-MSE PAR 2016	<u>Ref.</u> ADPFISS-LP2-144	Rev. 0	143 di 300

with the calculated values. The numerical results well predict the experimental trend. In particular the simulation with NEA correlations highlights a higher temperature drop of about 3% (mainly due to the different specific heat capacity) and, as a consequence, a slight overestimation of the experimental data.

Fig. 3.15 depicts the comparison of the LBE temperature at the heat exchanger inlet and outlet sections, obtained averaging respectively the values of three and six thermocouples. The temperature at inlet section is lower than the value at the outlet of the FPS, due to the heat losses through the hot leg (towards the pool), which are well predicted by the simulations. The difference between the experimental and calculated temperature at the outlet of the HX depends on the relative positioning between the thermocouples and the volume control, arranged 45 mm upstream. The use of the NEA correlations results an increment of about 4% in the temperature drop, and a better agreement with the experimental data.

Fig. 3.13 shows the comparison of the thermal power removed by the heat exchanger. The calculated values are essentially the same and they both slightly overestimate the experimental data, probably due to the fouling which is not considered during the simulations.

In order to analyze the FPS sub-channel by sub-channel, the last upgrading was introduced into the model. The fuel pin simulator was reproduced with 72 parallel pipes which simulate the sub-channels. Each pipe was composed of 15 control volumes and was coupled with near pipes with a total of 1536 cross junctions. The power supplied by the HS was simulated by 5760 heat structure nodes and other 1728 nodes reproduced the heat dispersion through the hexagonal wrapper. the nodalization scheme (Fig. 3.16) was obtained in prder to compare the LBE temperature in the exact position of the several TCs into the unit.


The experimental campaign was reproduced with the upgraded model only with the most recent thermophysical correlations properties. Fig. 3.17, Fig. 3.18 and Fig. 3.19 highlight the comparing between experimental and simulated boundary conditions. In particular, the power supplied by the HS was reduced of 5% of the nominal value to take into account the dissipations which occur in the cables and connectors of the outer circuits, which does not contribute to the thermal power supplied.

According to previous simulations, the code well predicts the LBE mass flow rate (Fig. 3.20) and the temperature drop across the primary side of the HX (Fig. 3.21). The Fig. 3.22 depicts the temperature drop across the FPS and the Fig. 3.23 highlights the LBE temperature sub-channel by sub-channel in five most representative section. As shown in Fig. 3.23, the temperature at the inlet section of the unit is quickly uniform and in Fig. 3.22 the average value of the simulated temperature at the inlet is compared with the average value of the three TCs positioned at the entrance of the FPS. Flowing upward across the HS, the LBE temperature assumes the typical profile shown in Fig. 3.23. In Fig. 3.22 the temperature measured by the TCs 34 and 36 (positioned in two most representative sub-channels at the end of the active length) are compared with the simulated value in the exact position, highlighted the good prediction of the code.

The next figures (i.e. from Fig. 3.24 to Fig. 3.27) shown the comparison between experimental and simulated LBE temperature in the pool in different instants. The plots depicts the LBE temperature versus the axial level in four azimuthal position: the plot (a) compare the simulated temperature of the control volume between the HX and the DHR with the average value of the temperatures measured by 5 TCs arranged in the azimuthal positions A, B, C, D and E; the plots (b) compare the simulated temperature with the average value of the measurement of the TCs F and G and the plots (c) and (d) compare the simulated temperature with the value measured respectively by thermocouples H and I.

The simulation results, according to the experimental data, highlights that the LBE temperature is rather homogenous at each level. At the beginning of the test, after 2000 s, the code well predicts the axial trend,




 RICERCA SISTEMA ELETTRICO	<u>Title:</u> Development of BE numerical tools for LFR design and safety analysis – Part 2	<u>Distribution</u> PUBLIC	<u>Issue Date</u> 12.12.2017	<u>Pag.</u>
	<u>Project:</u> ADP ENEA-MSE PAR 2016	<u>Ref.</u> ADPFISS-LP2-144	Rev. 0	144 di 300

showing the thermal stratification at about 4 m from the bottom of the main vessel. During the test, the discrepancy between the simulated values and the experimental data increases and the thermal stratification is predicted at about 1 m above the experimental data at the end of the simulation (see Fig. 3.28). the temporal evolution of the LBE temperature into the pool is depicted in Fig. 3.29 which represent the LBE conditions in the most relevant section which includes the FPS and the HX.

In conclusion, the experimental campaign conducted on CIRCE-ICE test facility offered additional data for the validation of RELAP5-3D in the frame of HLM system. The nodalization scheme of the facility well reproduces the thermal-hydraulics of the primary flow path and the implementation of the most recent thermophysical properties correlations allow a better estimation of the LBE conditions. About the thermal-hydraulic phenomena into a HLM pool, the activity highlights the prospect to reproduce the thermal stratification with RELAP5-3D, provided that the discrepancy of the comparison will be decreased. At this purpose, further investigations are needed, in particular about a detailed characterization of the heat losses which could improve the goodness of the simulations. The CIRCE-HERO experimental campaign could provide an important contribution in this framework.



 RICERCA SISTEMA ELETTRICO	<u>Title:</u> Development of BE numerical tools for LFR design and safety analysis – Part 2	<u>Distribution</u> PUBLIC	<u>Issue Date</u> 12.12.2017	<u>Pag.</u> 145 di 300
	<u>Project:</u> ADP ENEA-MSE PAR 2016	<u>Ref.</u> ADPFISS-LP2-144	Rev. 0	

Parameters	Value
Outside diameter (mm)	1200
Wall thickness (mm)	15
Material	AISI 316L
Max LBE inventory (ton)	90
Temperature range (K)	473 to 773

Tab. 3.1 - CIRCE S100 main parameters.

Parameters	Value
Duration (h)	7
Electical power supplied (kW)	720
Average LBE initial temperature (K)	600
LBE mass flow rate at full power (kg/s)	55
Feed-water mass flow rate (kg/s)	0.65

Tab. 3.2 - TEST I main parameters.



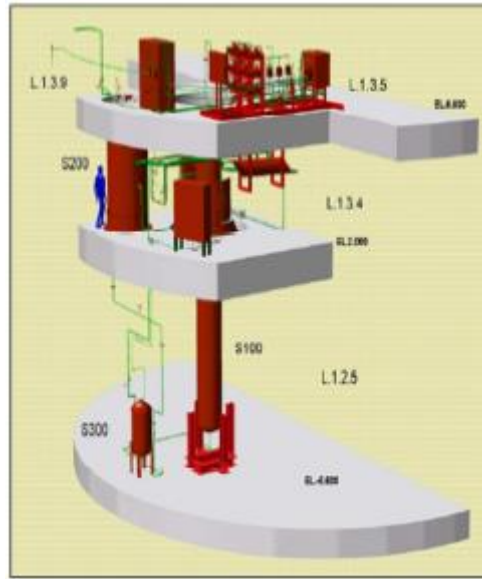


Fig. 3.1 - CIRCE isometric view.

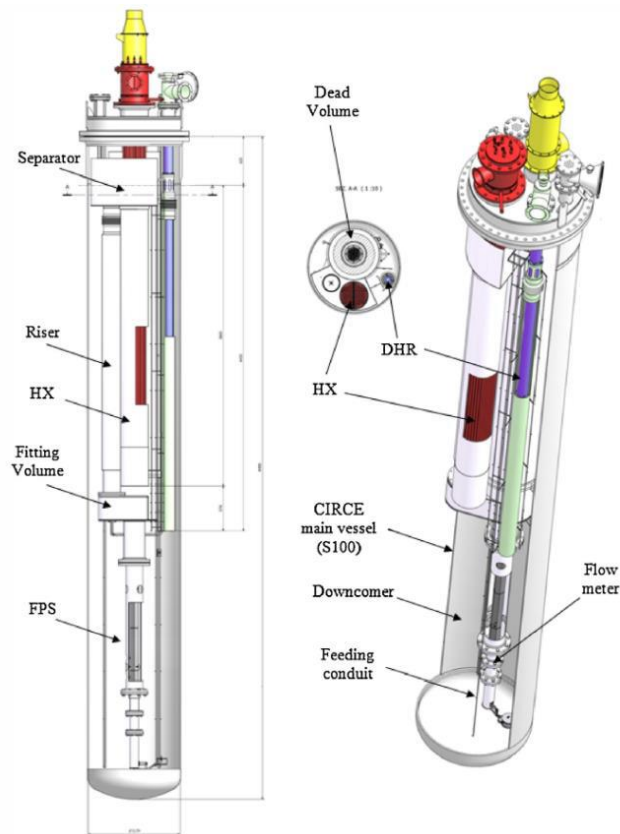


Fig. 3.2 - ICE test section.



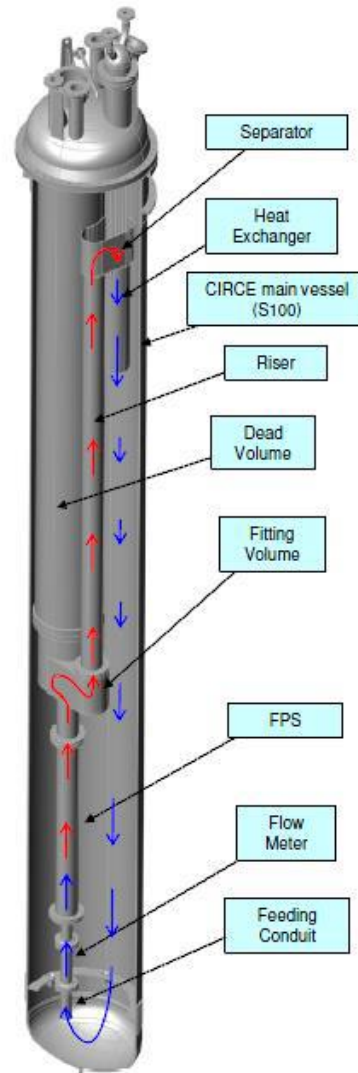


Fig. 3.3 - ICE test section: primary flow path.

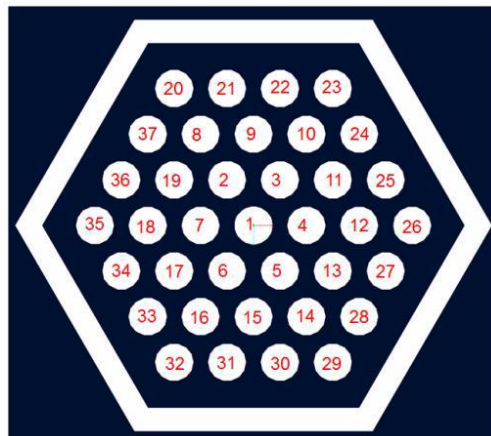


Fig. 3.4 - FPS cross section.

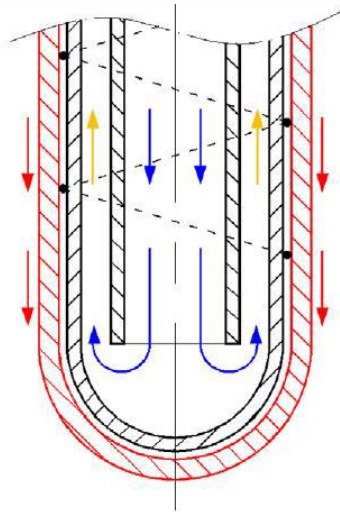


Fig. 3.5 - HX bayonet tube.

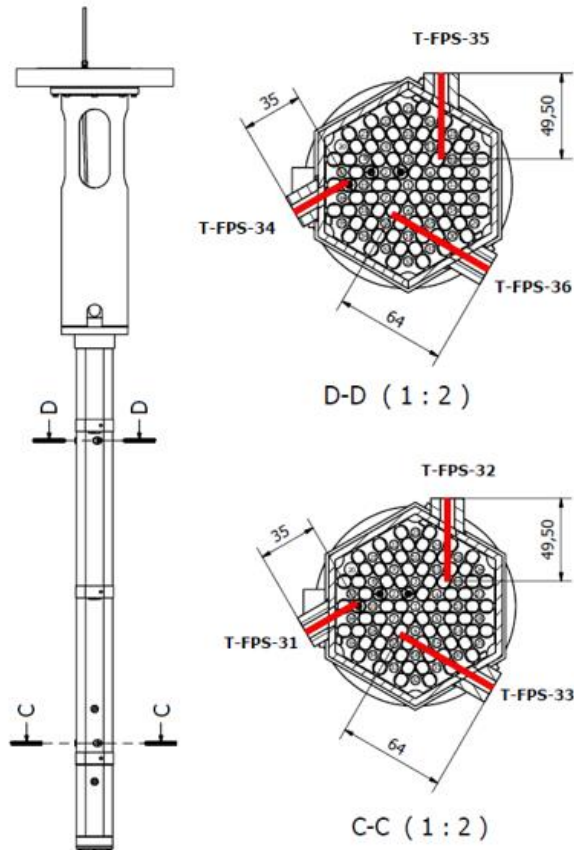


Fig. 3.6 - CIRCE instrumentation: FPS (1).

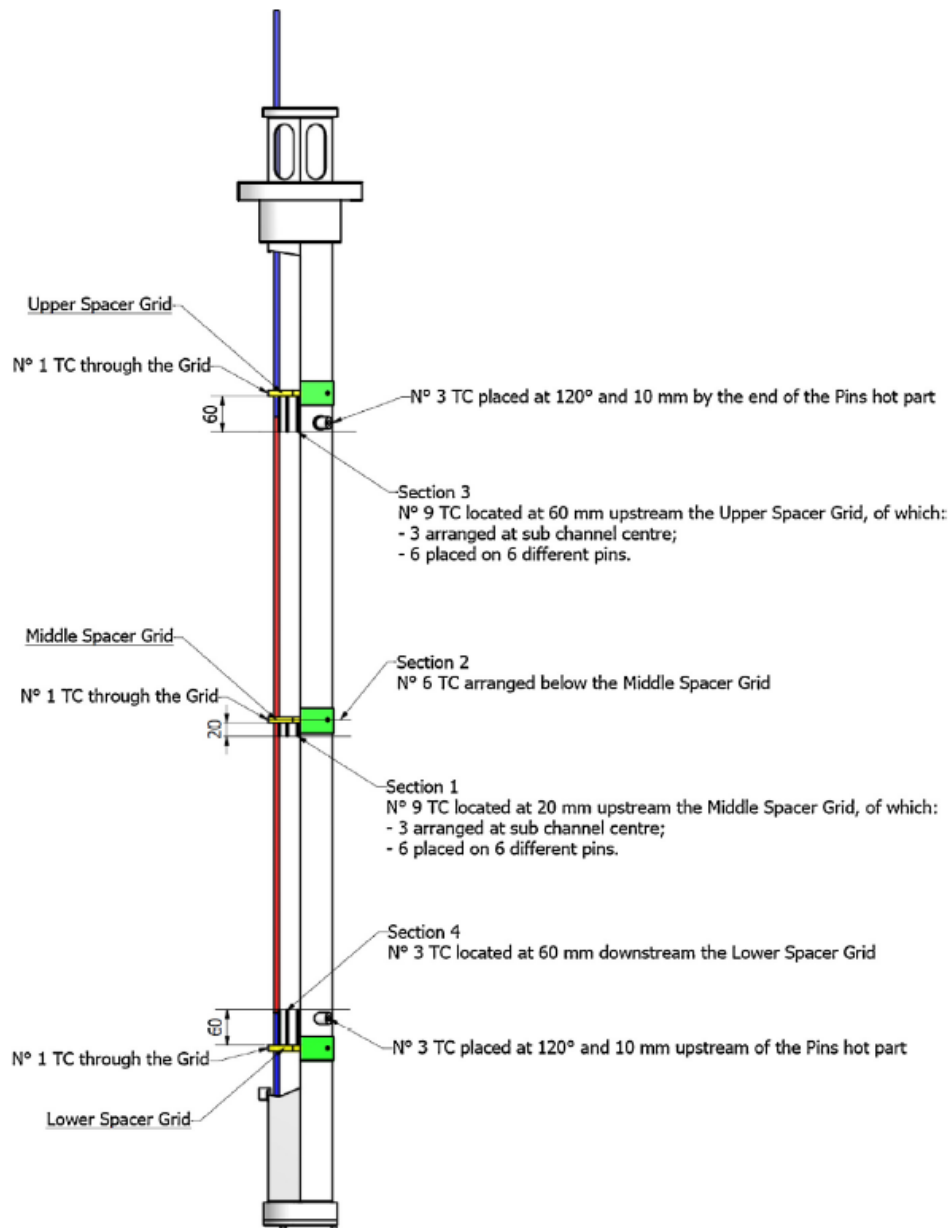


Fig. 3.7 - CIRCE instrumentation: FPS (2).



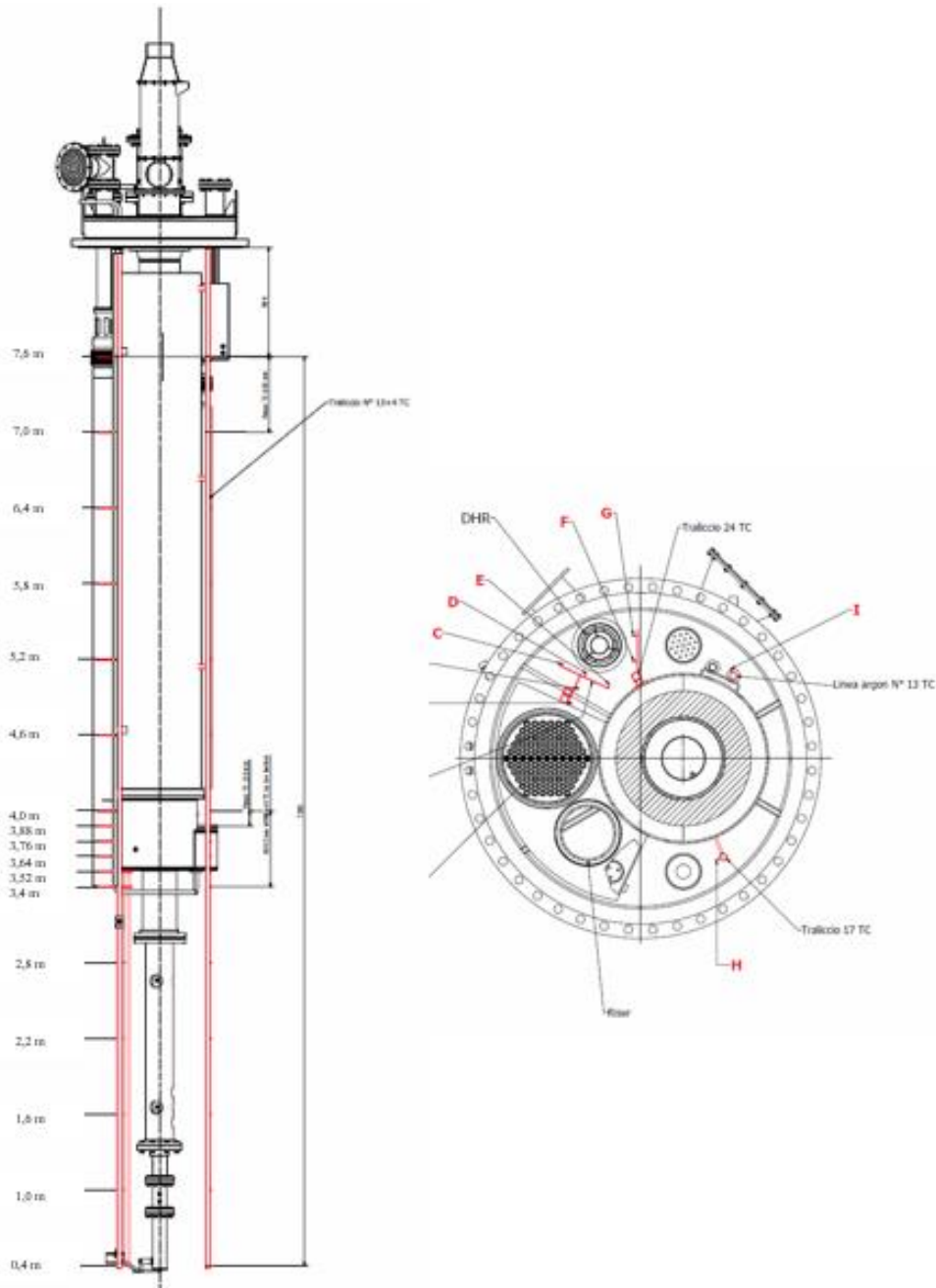


Fig. 3.8 - CIRCE instrumentation: pool.

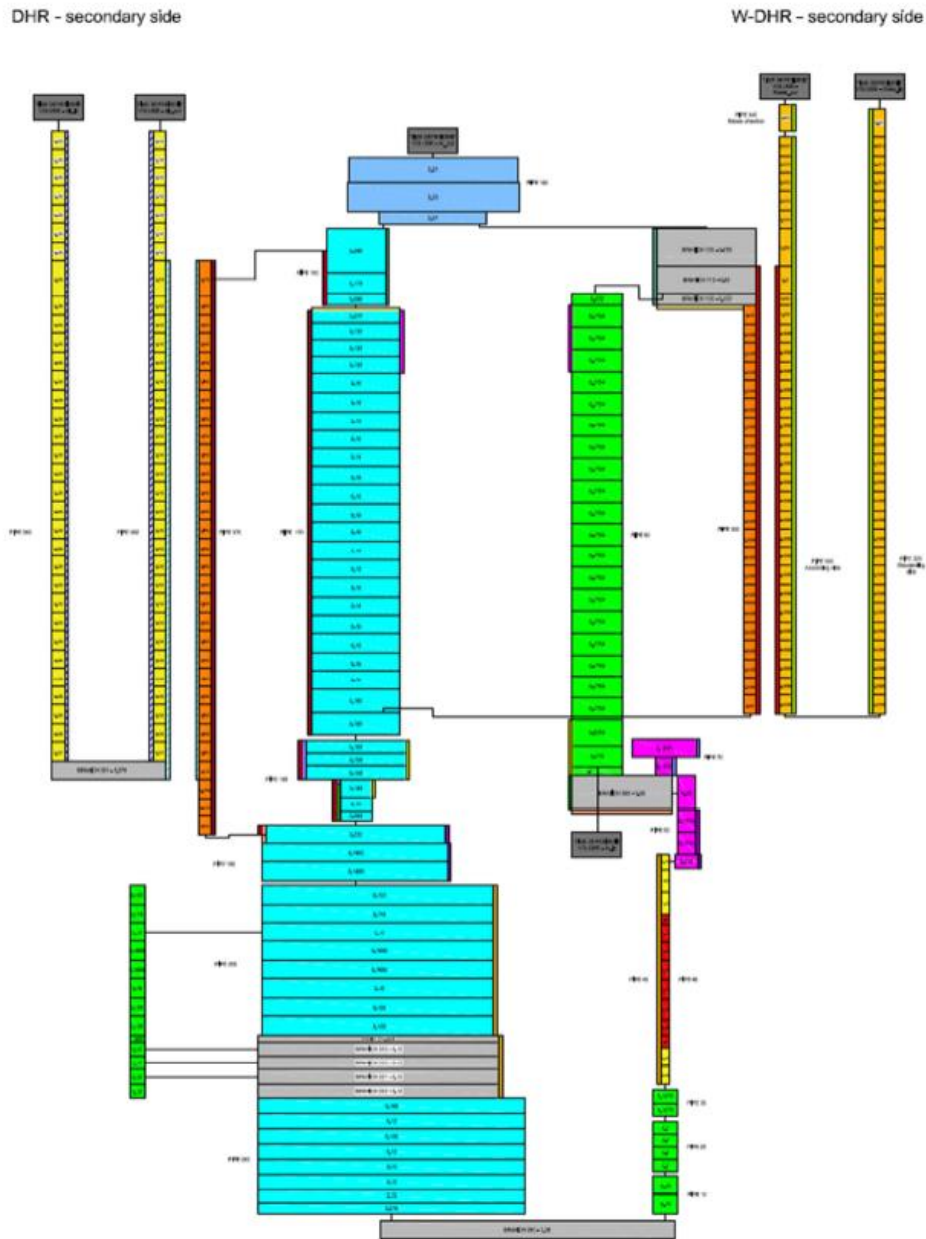


Fig. 3.9 - CIRCE-ICE nodalization scheme: first version.



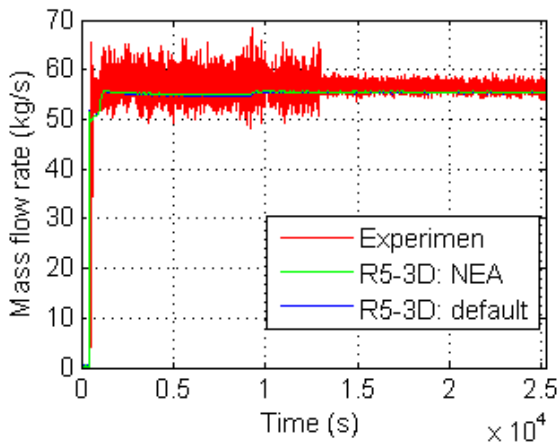


Fig. 3.12 - TEST I: LBE mass flow rate.

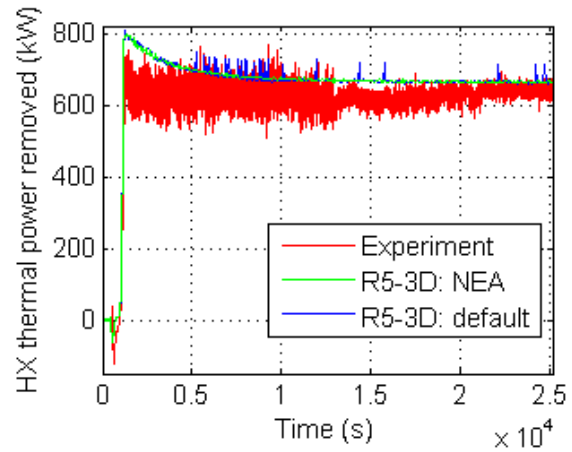


Fig. 3.13 - TEST I: HX removed power.

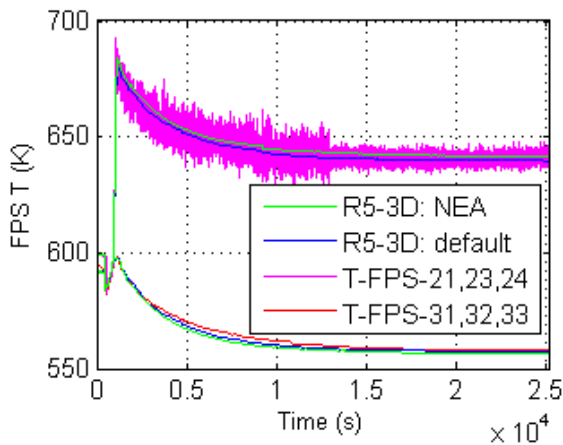


Fig. 3.14 - TEST I: FPS inlet/outlet temperatures.

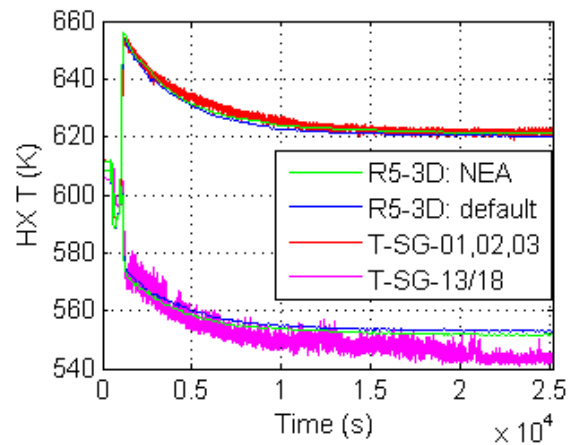


Fig. 3.15 - TEST I: HX inlet/outlet temperatures.

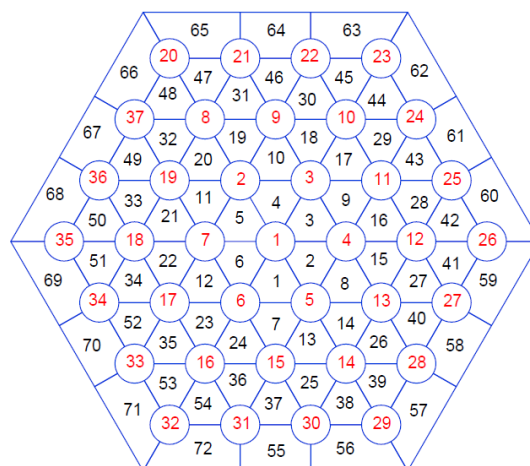


Fig. 3.16 - FPS nodalization scheme.



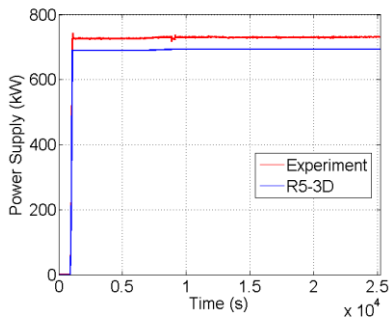


Fig. 3.17 - Power supplied.

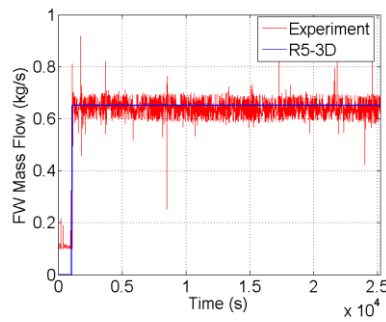


Fig. 3.18 - Feed-water mass flow rate.

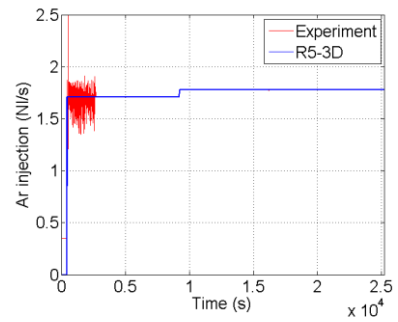


Fig. 3.19 - Argon injection.

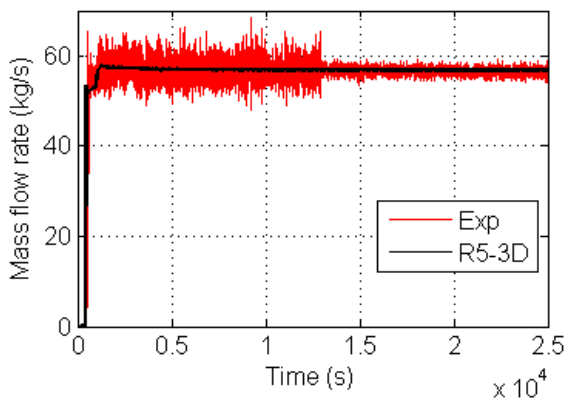


Fig. 3.20 - LBE mass flow rate.

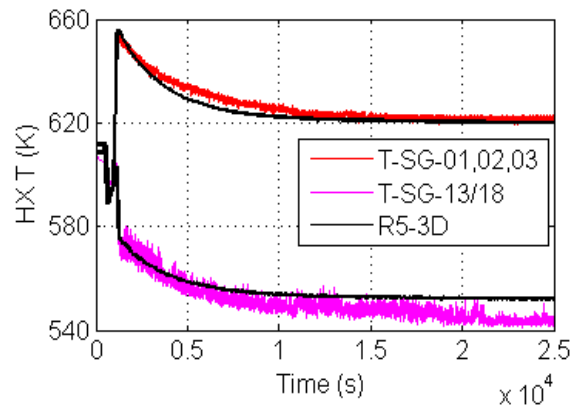


Fig. 3.21 - HX inlet/outlet temperature.

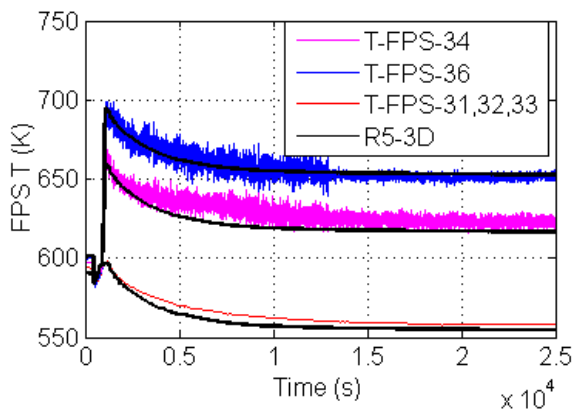


Fig. 3.22 - FPS inlet/outlet temperature.

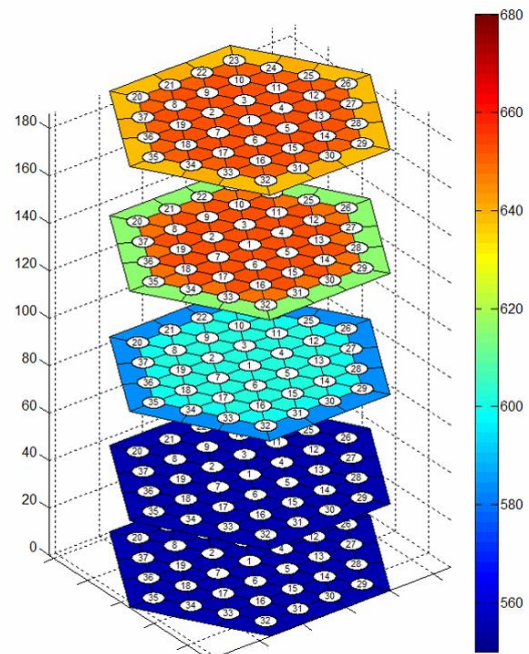
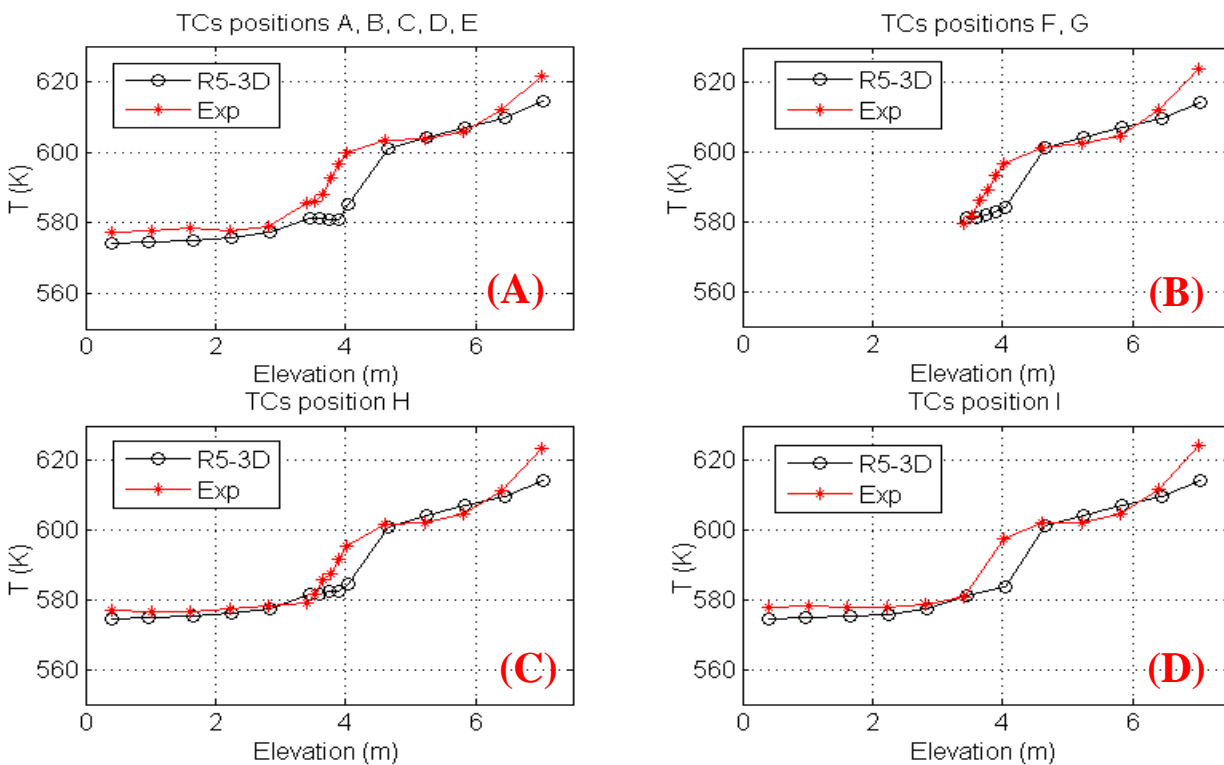
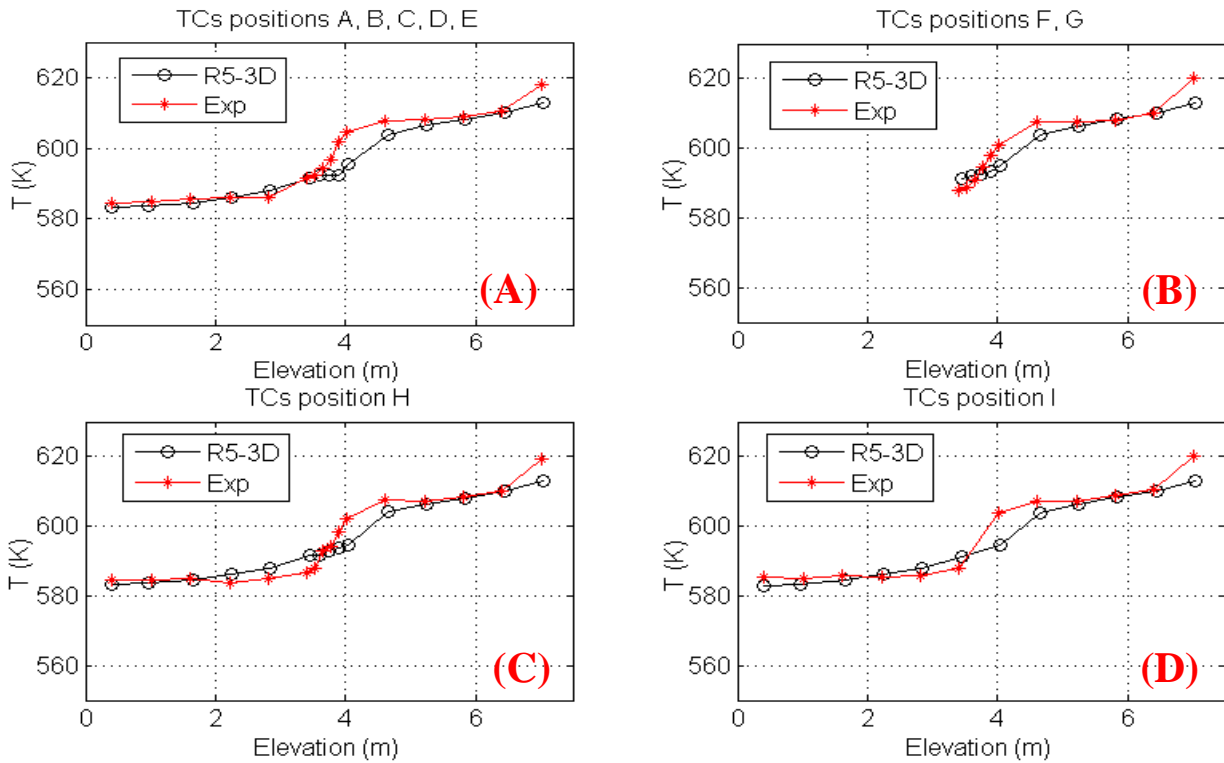
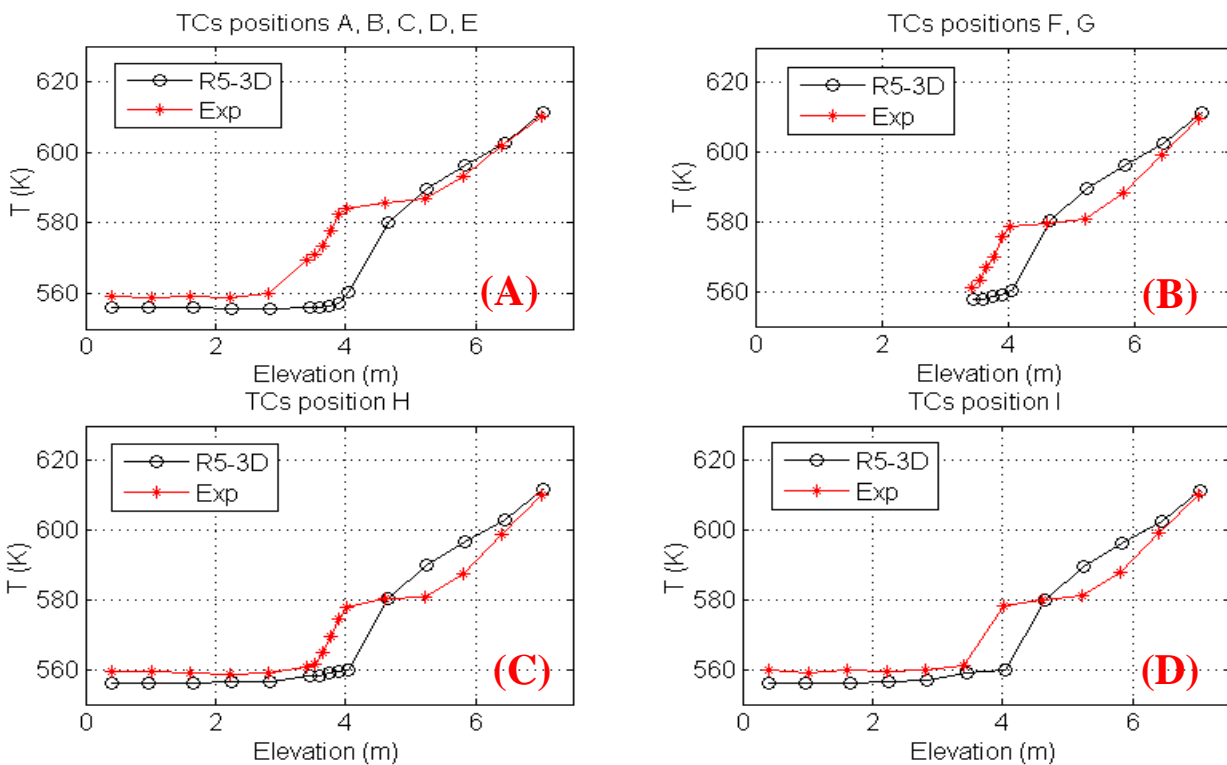
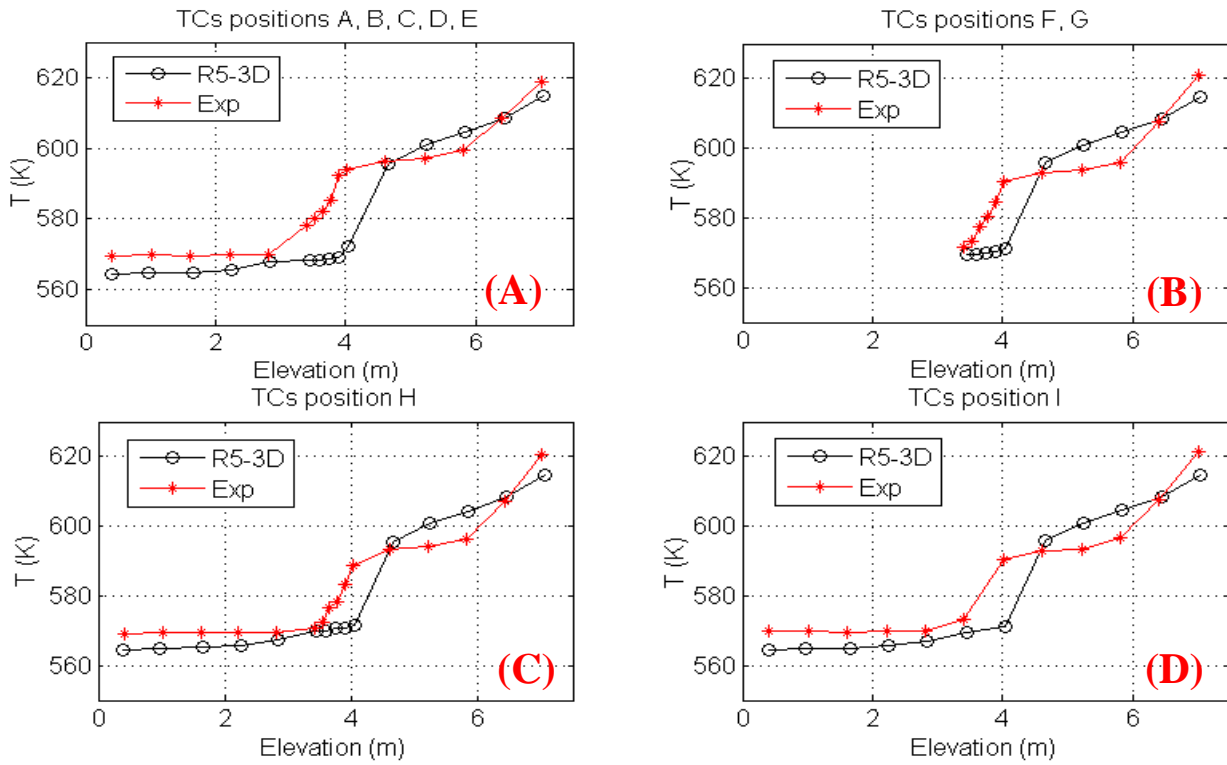


Fig. 3.23 - FPS temperature.





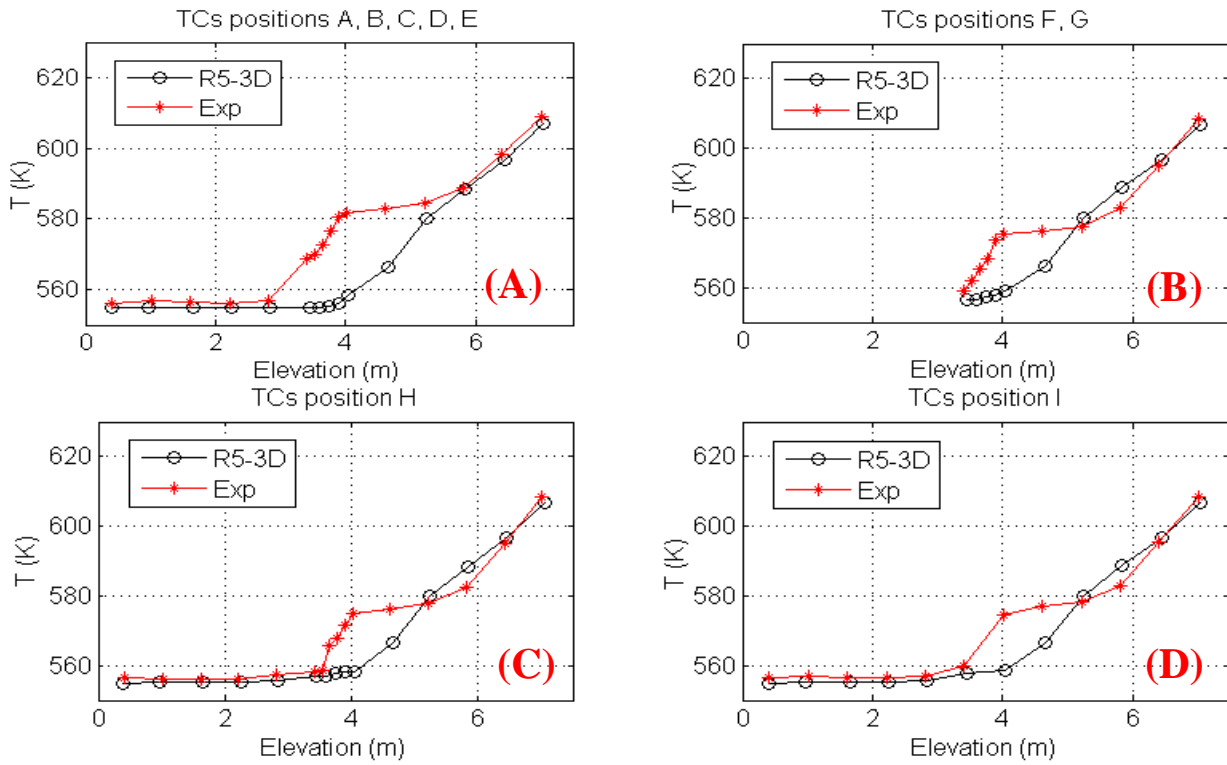


Fig. 3.28 - TS and MC: end of simulation.



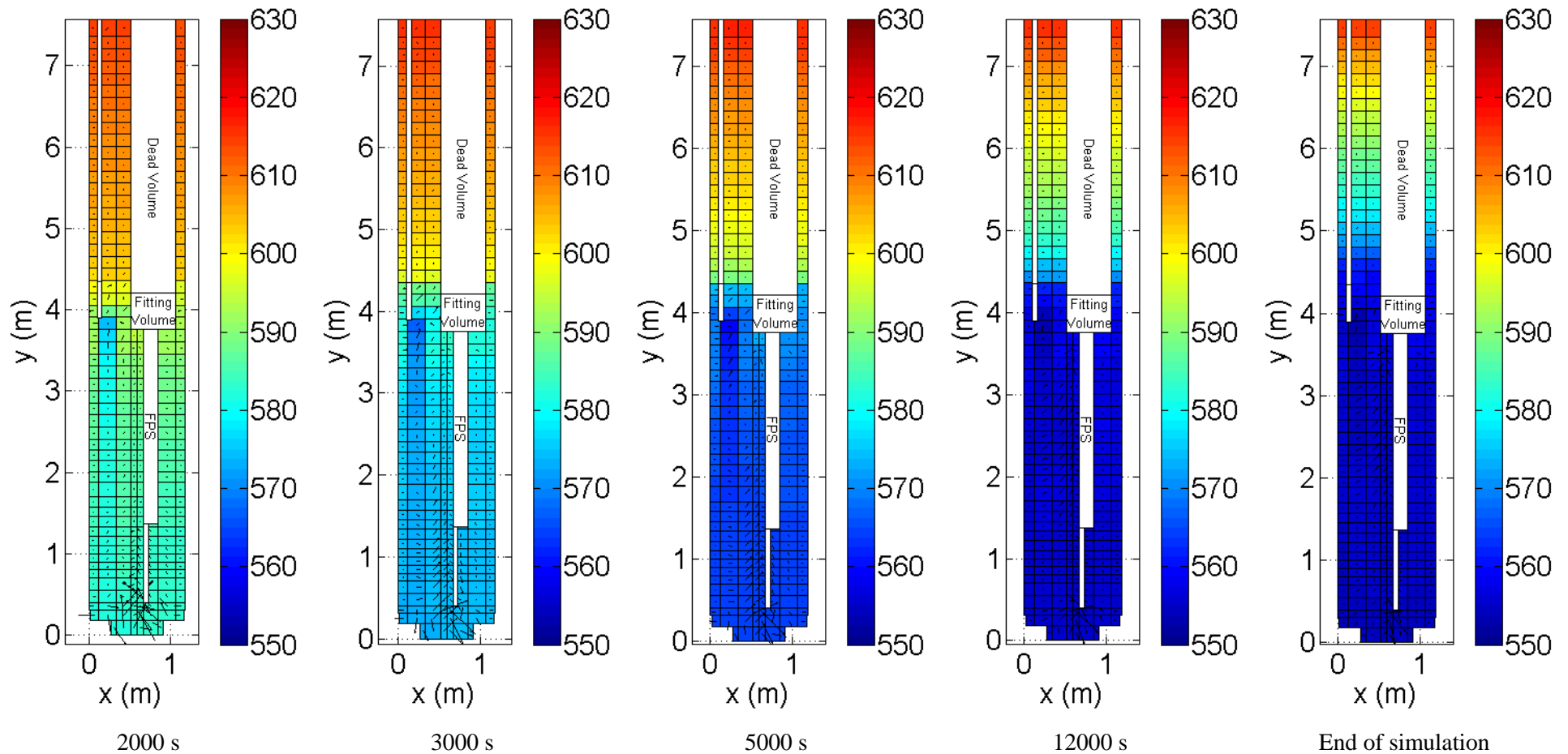



Fig. 3.29 - LBE temperature into the pool.




 RICERCA SISTEMA ELETTRICO	<u>Title:</u> Development of BE numerical tools for LFR design and safety analysis – Part 2	<u>Distribution</u> PUBLIC	<u>Issue Date</u> 12.12.2017	<u>Pag.</u>
	<u>Project:</u> ADP ENEA-MSE PAR 2016	<u>Ref.</u> ADPFISS-LP2-144	Rev. 0	159 di 300

3.4 List of References


- [3.1] NEA, *Technology Roadmap Update for Generation IV Nuclear Energy Systems*. 2014
- [3.2] M. Tarantino, D. Martelli, G. Barone, I. Di Piazza, N. Forgiione, *Mixed convection and stratification phenomena in a heavy liquid metal pool*. Nuclear Engineering and Design, 286 261-77, 2015
- [3.3] Team T R C D, *RELAP5/MOD4.3 CODE MANUAL*.
- [3.4] N. E. Todreas, M. S. Kazimi, Schlumberger, Maersk, Imo, N. Giordano, R. J. Brogan, F. Ahlgren, M. E. Mondejar, M. Genrup and M. Thern, *Nuclear System I – Thermal Hydraulic Fundamentals*. Taylor Fr. Publ., 2015
- [3.5] F. Giannetti, D. Vitale Di Maio, A. Naviglio, G. Caruso, *Thermal-hydraulic analysis of an innovative decay heat removal system for lead-cooled fast reactors*. Nuclear Engineering and Design, 305 168-78, 2016
- [3.6] P. A. Ushakov, A. V. Zhukov, N. M. Matyukhin, *Heat transfer to liquid metals in regular arrays of fuel elements*. 1977
- [3.7] M. Schikorr, E. Bubelis, L. Mansani, K. Litfin, *Proposal for pressure drop prediction for a fuel bundle with grid spacers using Rehme pressure drop correlations*. Nuclear Engineering and Design, 240 1830-42, 2010
- [3.8] NEA, *Handbook on lead-bismuth eutectic alloy and lead properties, materials compatibility, thermal-hydraulics and technologies*. 2015
- [3.9] P. Balestra, F. Giannetti, G. Caruso, A. Alfonsi, *New RELAP5-3D lead and LBE thermophysical properties implementation for safety analysis of Gen IV reactors*. Science Technology of Nuclear Installation, 2016



 RICERCA SISTEMA ELETTRICO	<u>Title:</u> Development of BE numerical tools for LFR design and safety analysis – Part 2	<u>Distribution</u> PUBLIC	<u>Issue Date</u> 12.12.2017	<u>Pag.</u> 160 di 300
	<u>Project:</u> ADP ENEA-MSE PAR 2016	<u>Ref.</u> ADPFISS-LP2-144	Rev. 0	

(Page intentionally left blank)




 RICERCA SISTEMA ELETTRICO	<u>Title:</u> Development of BE numerical tools for LFR design and safety analysis – Part 2	<u>Distribution</u> PUBLIC	<u>Issue Date</u> 12.12.2017	<u>Pag.</u>
	<u>Project:</u> ADP ENEA-MSE PAR 2016	<u>Ref.</u> ADPFISS-LP2-144	Rev. 0	161 di 300

4 APPLICATION OF RELAP5/MOD3.3–FLUENT COUPLING CODES TO CIRCE-HERO


C. Ulissi, M. Angelucci, G. Barone, R. Lo Frano, N. Forgone



 RICERCA SISTEMA ELETTRICO	<u>Title:</u> Development of BE numerical tools for LFR design and safety analysis – Part 2 <u>Project:</u> ADP ENEA-MSE PAR 2016	<u>Distribution</u> PUBLIC	<u>Issue Date</u> 12.12.2017	<u>Pag.</u> 162 di 300
		<u>Ref.</u> ADPFISS-LP2-144	Rev. 0	

(Page intentionally left blank)



 RICERCA SISTEMA ELETTRICO	<u>Title:</u> Development of BE numerical tools for LFR design and safety analysis – Part 2	<u>Distribution</u> PUBLIC	<u>Issue Date</u> 12.12.2017	<u>Pag.</u>
	<u>Project:</u> ADP ENEA-MSE PAR 2016	<u>Ref.</u> ADPFISS-LP2-144	Rev. 0	163 di 300

4.1 Background and references

The University of Pisa (UniPi), from the early 2000, has been involved in the implementation of a dedicated version of the RELAP5 STH code, capable to simulate liquid metals cooled systems. More specifically, UniPi, in collaboration with ANSALDO and ENEA, performed several simulations on the Accelerator Driven System (ADS) cooled by heavy liquid metal using the RELAP5/Mod3.2 code. The code was modified to simulate the thermo-hydraulics of Pb and LBE cooled systems. Therefore, the thermodynamic and thermo-physical properties of these specific working fluids had to be implemented in the code, together with an upgrade of the heat exchange models and specific correlations for liquid metals. Both the self-standing version of the code and a version coupled with PARCS multigroup reactor kinetics code were qualified^[4.1]. Subsequently, a modified version of PARCS neutronic code, to treat subcritical system with the presence of a spallation sources, was implemented and qualified. The qualification procedure confirmed that the new PARCS version maintained the coupling capability with RELAP5/Mod.3^[4.2]. Previously, the thermodynamic properties of Pb and LBE were implemented in RELAP5/Mod.3.2 by ANSALDO using the soft-sphere EOS model^[4.3].

In 2001, UniPi was involved (TRASCO research program) in a code benchmark^[4.4] on the core configuration of an ADS using a version of RELAP5/PARCS coupled code specially adapted to treat LBE cooled subcritical systems with external source. The coupling between neutronics and thermal-hydraulics was verified comparing the obtained results with those achieved by ENEA and Politecnico di Torino using the NILO in-house code.


In 2002, the version of RELAP5/Mod.3.2, modified to account for LBE properties, was used in a post-test validation process. Experiments were conducted on CHEOPE, loop located at ENEA (Brasimone), designed to study the LBE chemical and technological aspects. The comparison^[4.5] between experimental and numerical results showed a reasonable agreement and assessed the code capabilities in simulating LBE in natural circulation regime.

In 2006, an experimental campaign was performed on a LBE cooled facility, named CIRCE, located at ENEA Brasimone, where gas-injection enhanced circulation tests were carried out. The experimental data were compared with the outcomes of the post-test simulations made by the modified RELAP5/Mod.3.2 code (in the frame of TRASCO)^[4.6], and showed a good agreement with the experimental data. The code was able to reproduce friction losses along the flow path and the void buoyancy in the riser. However, the code was unable to reproduce the 3-D characteristics of the injection jet influencing the slip ratio and the void distribution near the injection nozzle.

In 2007, UniPi implemented the thermodynamic properties of Pb and LBE in RELAP5/Mod.3.3 stand-alone code version, in the same way as performed by ANSALDO for RELAP5/Mod3.2, adding the updated properties for viscosity, thermal conductivity and surface tension. The code difficulties in treating liquid metal with the presence of non-condensable gas was solved by properly modifying some FORTRAN subroutines. Simulations made to assess the coupling performances between RELAP5/Mod.3.3 code and PARCS neutronic code, provided results in accordance with the physics of the problem, and in perfect agreement with the results obtained from the previous version of the code^[4.7].

Subsequently, this upgraded version of RELEP5/Mod.3.3 code was extensively employed in support of the experimental activities performed at ENEA (Brasimone) in the field of HLM nuclear system. In particular, two main LBE facilities, NACIE (loop type)^{[4.8], [4.9], [4.10]} and CIRCE (pool type)^{[4.11], [4.12]}, were reproduced in order to investigate the related thermal-hydraulic phenomenology in both nominal conditions (gas enhanced



 RICERCA SISTEMA ELETTRICO	<u>Title:</u> Development of BE numerical tools for LFR design and safety analysis – Part 2	<u>Distribution</u> PUBLIC	<u>Issue Date</u> 12.12.2017	<u>Pag.</u>
	<u>Project:</u> ADP ENEA-MSE PAR 2016	<u>Ref.</u> ADPFISS-LP2-144	Rev. 0	164 di 300

circulation) and transient conditions (e.g. transition to natural circulation, ULOF). A pre-test analysis on operational transients of the HELENA lead facility was carried out as well^[4.13].

A further task employed RELAP5 to simulate the ALFRED lead cooled nuclear reactor. A well-defined model was generated to analyze the dynamic response of ALFRED in case of accidental scenarios^[4.14]. The simulations were carried out considering the reactivity feedbacks provided by the RELAP reactor kinetic model.

In 2012 UniPi started a research activity on the development of a coupling tool between the modified RELAP5/Mod3.3 code and the CFD Fluent code^[4.15]. In 2013, in order to perform this activity in a rational way, the last revised liquid metal thermodynamic properties were assigned to RELAP5/Mod3.3, for Sodium, Pb and LBE^[4.10]. In particular, the upgraded transport properties (thermal conductivity, dynamic viscosity and surface tension) were implemented directly in the FORTRAN source file, while the other thermodynamic properties were used to generate the external properties file for the specific working fluid (file tpfpb and tpfbbi). These properties were taken from Sobolev database^[4.16]. In addition, specific convective heat transfer correlations (e.g. Mikitiuk and Ushakov for bundles) for LMs were also implemented in RELAP5/Mod3.3. Since 2012 up to now, different approaches have been investigated (e.g., implicit and explicit numerical schemes, etc.) improving the method efficiency in terms of CPU time consuming, computational stability and consistency of the results. The coupling tool validation procedure^{[4.17]-[4.21]} involved both NACIE and CIRCE facilities, by comparing the outcomes with both the experimental data and RELAP standalone outcomes.

More recently (2015), RELAP5/Mod3.3 was used to support the design of a 2.5 MW, LBE cooled, facility (CLEAR-S) currently under construction in China. In particular, the activities focused on the thermo-hydraulic characterization of the Main Heat Exchanger^[4.22] and the secondary side operational transients procedures^[4.23]. Moreover, a full model of CLEAR-S facility was generated to analyze the global system response^[4.24].

4.2 Body of the report concerning the ongoing activities

The ongoing activity is finalized to analyze the heat transfer performance of HERO SGBT (Heavy liquid metal – pResurized water cOoled Steam Generator Bayonet Tube), which is composed by seven double-walls bayonet tubes with stainless steel powder filling gap. The unit consists of a hexagonal wrap (6795mm in length) whose inner and outer transversal heights are, respectively, 126mm and 132mm. Six slots are realized in the wrap at the top of the active length (6000 mm) to feed the liquid metal side of the SGBT unit^[4.25].


This evaluation is accomplished using RELAP5 system code coupled with CFD ANSYS Fluent code. This coupling approach allows to give updated and more realistic heat transfer boundary conditions to the CFD model and to obtain more accurate information on heat transfer for this component with, in particular, a detailed distribution of the LBE temperature inside the hexagonal wrapper.

The adopted methodology for the computational domain is “non-overlapping”. Indeed, the primary side of the heat exchanger and the heat structure are simulated with the CFD code, while the secondary side (which contains water-vapour two-phase flow) is modelled with the RELAP5 system code.

4.2.1 CFD preliminary analysis

The CFD preliminary analysis was carried out by ANSYS Fluent solver. The code is based on a finite volume method, and the numerical algorithm consists of the following steps:



 RICERCA SISTEMA ELETTRICO	<u>Title:</u> Development of BE numerical tools for LFR design and safety analysis – Part 2	<u>Distribution</u> PUBLIC	<u>Issue Date</u> 12.12.2017	<u>Pag.</u>
	<u>Project:</u> ADP ENEA-MSE PAR 2016	<u>Ref.</u> ADPFISS-LP2-144	Rev. 0	165 di 300

- integration of the governing equations of fluid flow over all the finite control volumes of the domain;
- discretization – conversion of the resulting equations into a system of algebraic equations;
- solution of the algebraic equations by an iterative method.

Before to begin the CFD analysis, it was necessary to define the geometry of the region of interest (computational domain). For this purpose, a 3D model of the LBE side and of the HX solid structures was built and the mesh was created using the native tool of ANSYS Workbench. Actually, the computational domain is one sixth of the entire geometry in the transversal section, exploiting the symmetry of the section, in order to reduce the number of elements and the required computational time. Fig. 4.1 (a) shows the overall geometry used in CFD code calculation while the details of initial and final regions are displayed respectively Fig. 4.1 (b) and (c). Fig. 4.2 illustrates the transversal section.

In the 3D model, the LBE part is in blue color, while the solid structures of AISI-304 steel are depicted in red (the one in contact with LBE side) and green (the one in contact with water side). The AISI-316 powder between the two steel tubes is colored in orange. The LBE lateral inlet section is represented in yellow in Fig. 4.1 (a), which simulates one of the six entrance slots of the HERO test section.


Instead, the total length was considered including also a LBE zone below the end of the seven water tubes, which was mainly modeled to avoid the “reversed flow” occurrence at the “pressure outlet” boundary condition. This zone is noticeable in the final part of the geometry in Fig. 4.1 (c). The spatial discretization, displayed in Fig. 4.3 and Fig. 4.4, is characterized by primarily structured hexahedral elements, for a total of 731454 nodes and 688213 elements; additional mesh statistics are reported in Tab. 4.1.

The Fluent code needs to set up the material properties (LBE and steel) and the appropriate boundary conditions. The LBE properties, such as the density, the molecular viscosity, the thermal conductivity and the specific heat, were taken into account as polynomial functions of the temperature in agreement with OECD/NEA Handbook of 2007 [4.26]. For AISI-304 steel and AISI-316 powder, the Fluent steel default values of density and specific heat were chosen, whereas the thermal conductivity of the AISI-304 steel was changed using a polynomial function of the temperature. A constant lower value of 3.41 W/(m K), was used for the AISI-316 powder, according to Ref. [4.27]. The thermal properties of solid structures materials are summarized in Tab. 4.2 and Tab. 4.3.

To model heat transfer, the energy equation was activated and the “Convection” condition was fixed on the pipe walls. The axial profile of the water side heat transfer coefficient and the two-phase fluid bulk temperature were imposed as thermal wall boundary conditions. This specific kind of boundary parameters was chosen in view of the application to coupled simulations, which will be described in sect. 4.2.2. These boundary conditions were obtained from a RELAP5 stand-alone simulation. The thermal wall boundary conditions were applied at the inner walls of the ascending water pipes, which were named Wall 1, Wall 2 and Wall 3, as shown in Fig. 4.5. Differentiated wall boundary conditions between the central pipe (Wall 3) and the lateral pipes (Wall 1 and Wall 2) were adopted, with the aim to obtain more realistic results (especially when applied to the coupled simulations).

In Fig. 4.5, Wall 4 is also shown, which represents the hexagonal wrapper, where no slip and adiabatic conditions were applied. In addition, the LBE mass flow rate and temperature were imposed at the inlet section, while a zero gauge pressure value was fixed at the outlet section. The inlet LBE mass flow rate was set obviously to one sixth of the nominal inlet LBE mass flow rate.



 RICERCA SISTEMA ELETTRICO	<u>Title:</u> Development of BE numerical tools for LFR design and safety analysis – Part 2	<u>Distribution</u> PUBLIC	<u>Issue Date</u> 12.12.2017	<u>Pag.</u>
	<u>Project:</u> ADP ENEA-MSE PAR 2016	<u>Ref.</u> ADPFISS-LP2-144	Rev. 0	166 di 300

In order to simulate the turbulence effects, Fluent requires activating a turbulence model and the selection of a near-wall modeling approach. For the first element close to the wall, a $y^+ > 30$ approach was adopted in which the viscosity-affected inner region is not resolved and wall functions are used to describe the viscous sublayer and buffer layer. The use of the wall function permits to reduce the computational time required for the calculations. To choose the turbulence model, three different models were attempted:

- RNG k- ϵ Model;
- Realizable k- ϵ Model;
- SST k- ω Model.

The parameters set to carry out the simulations are summarized in Tab. 4.4.

Once the calculation has converged, the field of the LBE temperature, velocity and turbulent kinetic energy (TKE) were plotted; the results are reported in Fig. 4.6, Fig. 4.7 and Fig. 4.8, respectively. The contours depict the variables in a transversal plane of about $z=4.1$ m, where the flow is fully developed and the variables are not affected by entrance region effects.

For further comparison, the profiles of the LBE temperature, velocity magnitude and turbulent kinetic energy of the simulations with the different turbulence models were extracted from a line on the transversal section at axial coordinate of about $z = 4.1$ m. The line where the results were extracted is depicted in brown, in Fig. 4.9. The results of the LBE temperature, velocity magnitude and turbulent kinetic energy profiles are shown respectively in Fig. 4.10 (a), (b), and (c).

From Fig. 4.6, Fig. 4.7, Fig. 4.8 and Fig. 4.10, it can be observed that LBE temperature, velocity and turbulent kinetic energy (TKE) distributions are not highly influenced by the turbulence model. In the temperature and velocity profiles, the RNG and Realizable k- ϵ Models show a similar trend while the SST k- ω Model results are slightly lower. Instead, the TKE profiles display a more noticeable difference among the models, especially in the SST k- ω Model, which generally estimated smaller turbulent parameters. Nevertheless, in absence of reference data, the choice of the model was based on the comparison of the residual behavior of the different turbulence models. The model that shows lowest residuals is the Realizable k- ϵ model.


Since the turbulent Prandtl number is one of the major parameters affecting sensitively the turbulent heat transfer behavior in Liquid Metal, additional CFD calculations with Realizable k- ϵ model were carried out using different turbulent Prandtl number values: 0.85, 1, 1.5 and 2. Changing the turbulent Prandtl number, the LBE temperature profile is slightly different, as shown in Fig. 4.11. In particular, higher turbulent Prandtl number gave higher LBE temperature profile over the chosen line.

In absence of experimental data to compare the numerical results and to decide which turbulent Prandtl number is the most appropriate, the choice was based on the following correlation [4.28]:

$$Pr_t = \begin{cases} 1.5 & Pe \leq 2000 \\ 2.5 - 0.0005 Pe & 2000 \leq Pe \leq 3000 \\ 1.0 & Pe \geq 3000 \end{cases}$$

In our test cases, the Péclet number is generally smaller than 2000, then a $Pr_t = 1.5$ was chosen for the CFD-STH coupled code simulations reported in the next section.



 RICERCA SISTEMA ELETTRICO	<u>Title:</u> Development of BE numerical tools for LFR design and safety analysis – Part 2	<u>Distribution</u> PUBLIC	<u>Issue Date</u> 12.12.2017	<u>Pag.</u>
	<u>Project:</u> ADP ENEA-MSE PAR 2016	<u>Ref.</u> ADPFISS-LP2-144	Rev. 0	167 di 300

4.2.2 Adopted coupling procedure and obtained results

The scheme used for the coupling model is represented in Fig. 4.12. It highlights the thermodynamic variables exchanged at the interfaces between the two domains. Basically, the exchange of the variables takes place at the walls of the ascending water pipes along the entire tube length. As already explained, exchanged data are differentiated for the central and the lateral pipes. This differentiation is shown in Fig. 4.12, where the RELAP5 nodalization of the HERO secondary side is reported: the components from 420 to 452 are representative of the central pipe, whereas components from 520 to 552 represent the six lateral tubes. This separation of the central pipe from the lateral ones allows to obtain differentiated boundary conditions on the pipes wall from the detailed temperature distribution in the primary side of the HX (LBE side), calculated by the CFD code. In the RELAP5 model, the water is injected through the time-dependent junction 415 inside the inlet plenum 418 and then redistributes inside the two pipes (420 and 520).

For post-processing purpose, 60 artificial surfaces have been created on each boundary wall of the CFD domain, in order to exchange data with the system code. The height of these surfaces is equivalent to the respective volume length of pipes 442 (542) and part of pipes 448 (548) of RELAP5. Actually, the division are operated on the Wall 2 (the division of Wall 1 is not necessary for symmetry) and Wall 3 because these boundaries are located where the data exchange is carried out between CFD and STH codes. The schematic representation of the artificial subdivision for the data exchange is showed in Fig. 4.12. At each iteration, wall temperature results from Fluent are averaged over the tubes surface (axially and azimuthally) in the 60 above-mentioned zones; then these data are transferred to RELAP5. In turn, RELAP5 gives back 60 data points, which are used to build an axial profile (with linear trend between two consecutive points) of both the two-phase water mixture bulk temperature and the heat transfer coefficient (HTC), which are given to Fluent as boundary conditions.

The adopted numerical method for the coupled simulation is the semi-implicit scheme. At each step, for both outer and inner iterations, the variables exchanged between the boundaries of the two codes are:

- the bulk temperatures;
- the heat transfer coefficient at the pipes wall of the ascending water;
- the wall temperature of the ascending water (in two-phase flow).


The convergence is obtained when the difference (as a percentage) between the value of each variable at two consecutive steps goes below a preset value. More detailed information on the coupling numerical algorithm can be found in Ref. [4.29].

Different boundary conditions were adopted for the Fluent CFD code (HERO primary side) and RELAP5 system code (HERO secondary side), which are reported respectively in Tab. 4.5 and Tab. 4.6.

The results of coupled calculation have been compared with the RELAP5 stand-alone results in order to demonstrate, not only that this methodology brings to realistic results, but also that it can provide more detailed flow and heat transfer information. Fig. 4.13 and Fig. 4.14 show the trend of temperatures along the HERO test section obtained by coupling calculation respectively in central pipe (442) and lateral pipes (542). displays the analogous trends obtained with the RELAP5 stand-alone calculation, for comparison. It should be mentioned that in the RELAP5 stand-alone calculation the seven tubes of the HERO test section were simulated with only one tube, which has a total flow area equal to the sum of the individual tube areas.

The temperature profiles reported in the above-mentioned figures are referred to the LBE temperature, the wall temperature on LBE side, the wall temperature on water side and the water temperature in the ascending



 RICERCA SISTEMA ELETRICO	<u>Title:</u> Development of BE numerical tools for LFR design and safety analysis – Part 2	<u>Distribution</u> PUBLIC	<u>Issue Date</u> 12.12.2017	<u>Pag.</u>
	<u>Project:</u> ADP ENEA-MSE PAR 2016	<u>Ref.</u> ADPFISS-LP2-144	Rev. 0	168 di 300

and descending tubes. In Fig. 4.13, Fig. 4.14 and Fig. 4.15, the temperature range is the same for a better comparison of the obtained results. At first sight, it can be noticed that the trends of the temperatures of the central and lateral pipes are similar and there are not evident differences with the RELAP5 stand-alone calculation.

In the LBE entrance region ($z \approx 0$ m), the descending trend of both the LBE temperature and the LBE side wall temperature have a greater slope meaning that the heat transfer is more efficient in this area. In correspondence of this area, the secondary side water flows upwards towards the tubes annular region (counter-current flow) in a two-phase regime, at constant temperature (saturation point). In such conditions, the HTC-water side is very high, enhancing the heat transfer between the fluids. The trend of the water side HTC is shown in Fig. 4.16, which reports the comparison of the results achieved with the coupled calculation (both in central and lateral pipes) and the those obtained from the RELAP5 stand-alone simulation. The trend of the three curves is very similar; however, the change in slope occurs in slight different axial positions. In particular, it occurs closer to the entrance region in the central pipe than the lateral ones, showing that the differentiation of pipes can lead to more accurate information on heat transfer.

Concerning the HTC in the LBE side, the trend obtained in the coupled calculation is extracted from the Fluent domain, using the following relationship:


$$HTC_{LBE}(z) = \frac{q''_{wall}(z)}{\bar{T}_{wall}(z) - T_b(z)} \quad (1)$$

where q''_{wall} is the wall heat flux, \bar{T}_{wall} is the wall temperature LBE side and T_b is the LBE bulk temperature. These values are extracted from artificial axial planes specifically created in the CFD domain. In each plane, the q''_{wall} and the \bar{T}_{wall} are averaged over the total perimeter of both central and lateral walls, while T_b is the mass-weighted average temperature. In Fig. 4.17, the obtained curve is compared with the LBE side HTC from the RELAP5 stand-alone simulation. In RELAP5 stand-alone, the LBE side HTC is computed using one of the two correlations implemented in the code for fuel bundles convective heat transfer; in this case, the Ushakov correlation was chosen.

The difference between the two trends is caused by a more accurate information on LBE heat transfer obtained using a CFD code in the coupled procedure. In particular, thanks to the CFD calculation it is possible to compute a more detailed variation along the axial coordinate. Further, the initial sharp trend of the curve obtained from the CFD is related to the entrance region, where the flow and the temperature profile are not completely established and the difference between the average wall temperature \bar{T}_{wall} and the bulk temperature T_b is small.

Since in the coupled simulation the imposed conditions are the water side wall temperature for the RELAP domain and the water side heat transfer coefficient and the two-phase fluid bulk temperature for the CFD domain, the continuity of the heat flux on boundary walls (Wall 2 and Wall 3), computed by the two codes, must be guaranteed. In Fig. 4.18 and Fig. 4.19, it can be seen that the heat flux extracted from Fluent and RELAP5 domains in the coupling simulation are practically coincident and have also a similar trend with respect to the curve obtained from the RELAP5 stand-alone computation. The initial descending trend of heat fluxes is a direct consequence of greater heat exchange efficiency in the entrance region.



 RICERCA SISTEMA ELETRICO	<u>Title:</u> Development of BE numerical tools for LFR design and safety analysis – Part 2	<u>Distribution</u> PUBLIC	<u>Issue Date</u> 12.12.2017	<u>Pag.</u>
	<u>Project:</u> ADP ENEA-MSE PAR 2016	<u>Ref.</u> ADPFISS-LP2-144	Rev. 0	169 di 300

The heat flux (Fig. 4.18 and Fig. 4.19) and HTC (Fig. 4.16) curves obtained with the coupling procedure display a decreasing trend for z below zero: the reason of this behavior is that above the LBE entrance region there is LBE stagnation.

As advantage of the coupled calculation, there is the possibility to analyze in the detail the flow in the portion of the domain modelled by the CFD code. In this work, the temperature and velocity fields in the LBE side of the HX were obtained from the CFD simulation and are illustrated in Fig. 4.20 and Fig. 4.21. The profiles are extracted at the end of the coupled simulation, when the steady state condition was reached. The LBE contour plots are reported in two different planes, respectively at about $z=1.6$ m and $z=4.1$ m. For a better comparison, the same scale was used for Fig. 4.20 (a) and (b) and for Fig. 4.21 (a) and (b). The LBE temperature is quite colder in the outer region, between the lateral pipes and the hexagonal wrapper (Wall 4) because the heat transfer area is relatively smaller in that narrow gap; further, the LBE velocity is smaller. The velocity field in Fig. 4.21 (a) appears slightly different with respect to the contour in Fig. 4.21 (b), despite the flow is fully developed in both sections. The different LBE velocity distribution at $z=1.6$ m is related to a density effect, since in this section the average temperature is colder than that in $z=4.1$ m.

4.2.3 Conclusions

The present work consists of two main parts, aimed at contributing to the development and improvement of a coupling methodology between CFD code and system code in order to analyze the heat transfer performance of the HERO test section.

In the first part of the work, CFD simulations were realized in order to investigate the thermal hydraulic phenomena in the heat exchanger and, consequently, to choose the most suitable models to perform the simulations. For this purpose, a symmetrical 3D CFD model of the LBE side and of the HX solid structures was build.


To accomplish the CFD calculation, the energy and turbulent models were selected. After a sensitivity analysis, the appropriate boundary conditions, obtained from a previous RELAP5 standalone calculation, were imposed. In particular, the thermal wall boundary conditions were applied at the inner walls of the ascending water pipes in view of the coupling applications, since this is the location where the data exchange between the CFD code and RELAP5 code occurs.

In the second part of the work, the coupled methodology was applied to the entire HERO section: the primary LBE side and the pipe structures were modelled with the CFD Fluent code whereas the water side was modelled with the STH code RELAP5. The coupling procedure was verified by comparing the obtained results with the analogous ones achieved with the RELAP5 standalone calculation. Similar temperature, heat flux and HTC trends were obtained with the two calculations, proving that the developed coupling methodology is reliable. Further, the coupled simulation allows to obtain more accurate information on the LBE flow and on the heat transfer performance for this component.

As next step, this methodology could be adopted to analyse the efficiency of the HERO component in several operating conditions (by varying the water side operating pressure, LBE and/or water inlet mass flow rates and temperatures).

In the future, once the experimental tests on CIRCE-HERO will be performed and detailed experimental data will be available, the computational results will be critically compared with the experimental data to verify the ability of the Fluent/RELAP5 coupled codes in predicts the involved phenomena.



 RICERCA SISTEMA ELETTRICO	<u>Title:</u> Development of BE numerical tools for LFR design and safety analysis – Part 2	<u>Distribution</u> PUBLIC	<u>Issue Date</u> 12.12.2017	<u>Pag.</u>
	<u>Project:</u> ADP ENEA-MSE PAR 2016	<u>Ref.</u> ADPFISS-LP2-144	Rev. 0	170 di 300

4.3 Role of the activity, general goals and future development


Since 2012, University of Pisa has been involved in the development of a coupling tool between a modified version of RELAP5/Mod3.3 and the CFD ANSYS Fluent code. Indeed, the interest in coupling techniques between existing codes is emerging worldwide with the aim to model the interaction of multidisciplinary physical phenomena. For thermal-hydraulic analysis purposes, the coupling between STH and CFD codes allows to model multi-scale phenomena, at different level of detail. The CFD code should be used to analyse a smaller part of the domain where 3D effects are significant and/or detailed flow information is demanded. The STH code should be applied to the portions of the system characterized by 1D components (i.e. pipes) and to model multi-phase and/or multi-component flow.

During these years, the coupling numerical algorithm was improved from the explicit scheme to semi-implicit one, where "inner-cycles" are repeated until specified convergence criteria are satisfied. The technique to handle the synchronization of the codes and the exchange of data was also enhanced, bringing an advantage in terms of global computational time required. Regarding the coupled code applications, the first developed tool was verified with NACIE experimental data. Successive application concerned the pool configuration (i.e. CIRCE-ICE) with simulation of isothermal and accidental transient tests.

The last task of UniPi regarded the use of the coupling tool for the new CIRCE configuration with the prototypical component HERO. For this purpose, a new methodology, with the coupling at the thermal boundaries, was setup and used for the analysis of the HERO component (the pool, as well as the test section where HERO will be installed, were not simulated). The ongoing activity and next step is to model the complete CIRCE-HERO facility with STH-CFD coupled codes. Actually, a STH-CFD model has been already completed and some isothermal coupled calculations are ongoing. Once the CIRCE-HERO coupled model has been tested, the simulation of accidental transient, with active heat source and heat sink, will be performed.

As future development, the University of Pisa is considering the feasibility to couple the RELAP/Mod3.3 thermal-hydraulic system code with the SIMMER code. SIMMER (developed in both 2D and 3D versions) is a three-velocity-field, multiphase, multicomponent, fluid-dynamics code coupled with a space- and energy-dependent neutron kinetics model, which also allows to solve mass, momentum and energy balance equations for multi-fluid systems. The University of Pisa gained great experience in the use of the SIMMER code and has recently modified its FORTRAN source file to implement a chemical model for the Water-PbLi exothermic reaction. The development of this new coupling tool could allow the simulation of new complex system, such as the WCLL+PHTS foreseen in fusion nuclear reactors, extending the application of coupled calculation to fusion systems.



 RICERCA SISTEMA ELETTRICO	<u>Title:</u> Development of BE numerical tools for LFR design and safety analysis – Part 2	<u>Distribution</u> PUBLIC	<u>Issue Date</u> 12.12.2017	<u>Pag.</u>
	<u>Project:</u> ADP ENEA-MSE PAR 2016	<u>Ref.</u> ADPFISS-LP2-144	Rev. 0	171 di 300

Nodes	731454
Elements	688213
Max Aspect Ratio	38.94
Max Skewness	0.79
Min Orthogonal Quality	0.999
Avg Orthogonal Quality	0.983

Tab. 4.1 - Mesh statistics.

Density [kg/m ³]	8030
Specific heat [J/(kg K)]	502.48
Thermal conductivity [W/(m K)]	9.437+0.0154 T

Tab. 4.2 - AISI-304 steel thermal properties.

Density [kg/m ³]	8030
Specific heat [J/(kg K)]	502.48
Thermal conductivity [W/(m K)]	3.41

Tab. 4.3 - AISI-316 powder thermal properties.

Inlet LBE mass flow rate [kg/s]	6.225
Outlet gauge pressure [Pa]	0
Inlet LBE temperature [°C]	480

Tab. 4.4 - Reference boundary conditions.

LBE inlet mass flow rate [kg/s]	1.5
Outlet gauge pressure [Pa]	0
LBE inlet temperature [°C]	480

Tab. 4.5 - Reference boundary conditions for Fluent CFD Code.

Water mass flow rate [kg/s]	0.33
Water inlet temperature [°C]	335
HERO outlet pressure [bar]	180

Tab. 4.6 - Reference boundary conditions for RELAP5 System Code.



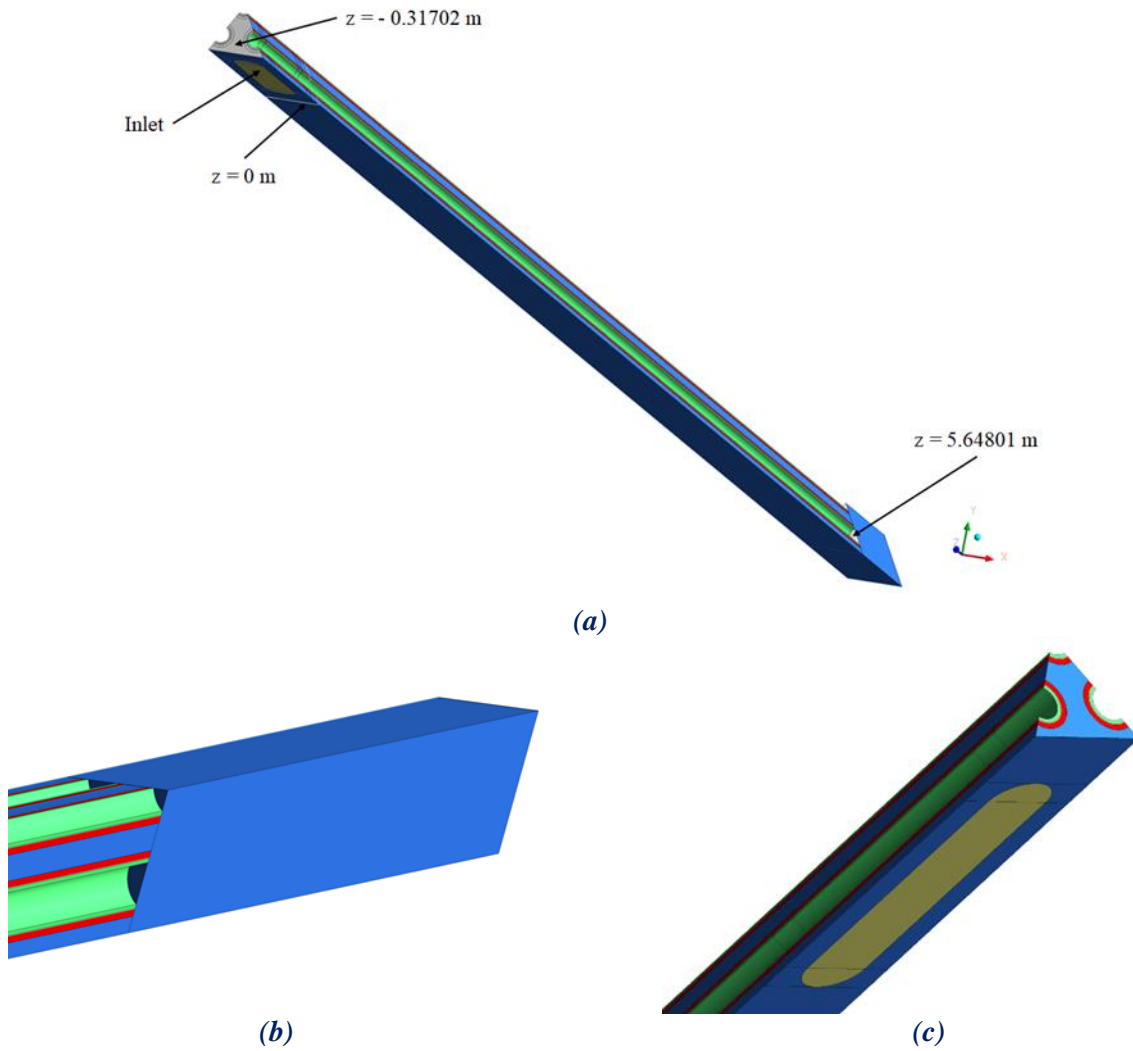


Fig. 4.1 - HERO periodic geometrical domain: overall geometry (a), initial (b) and final (c) region.

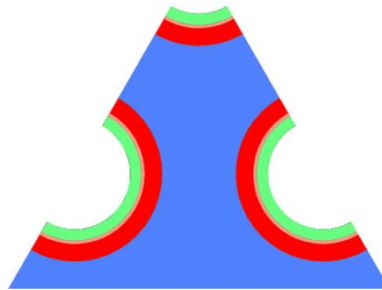


Fig. 4.2 - HERO periodic transversal section.

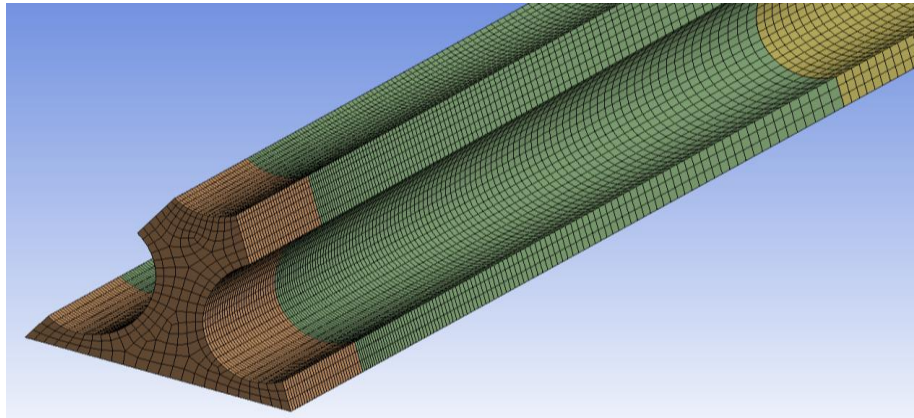


Fig. 4.3 - LBE side spatial discretization.

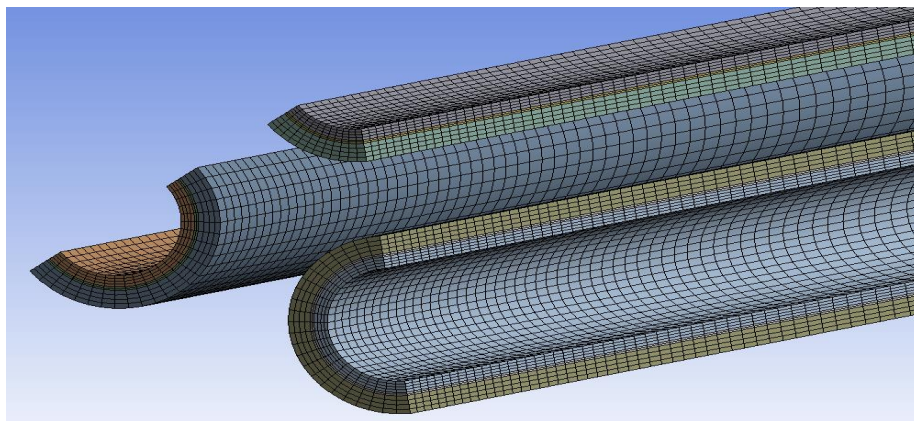


Fig. 4.4 - HERO tubes spatial discretization.

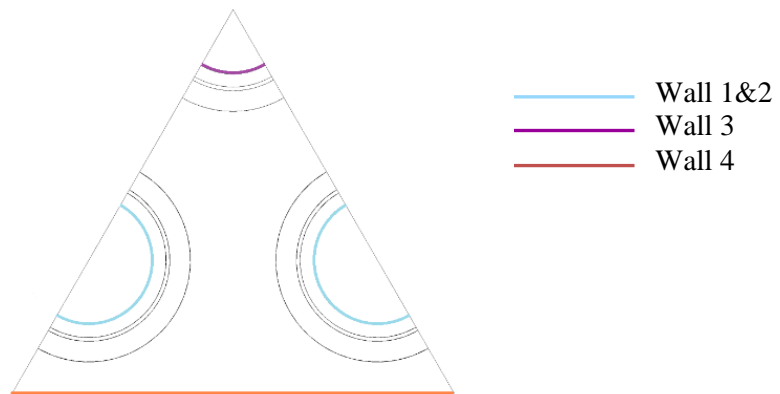
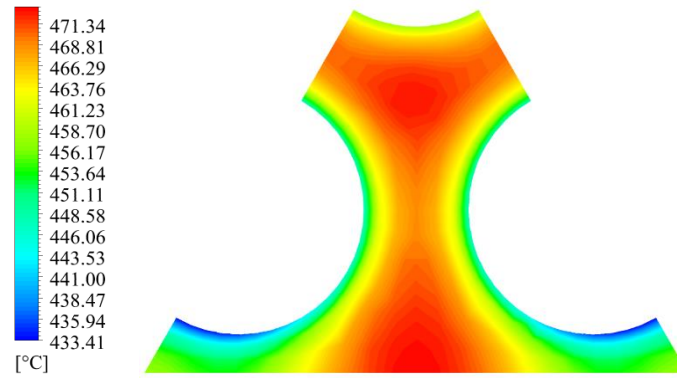
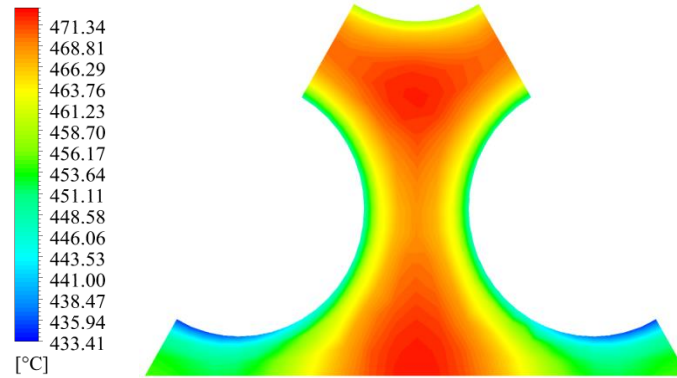


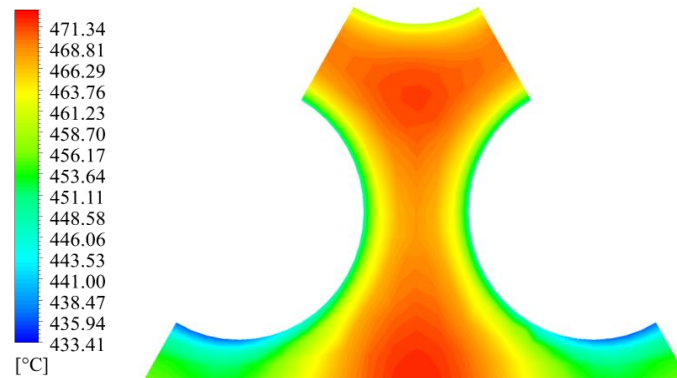
Fig. 4.5 - Boundary walls.



(a)



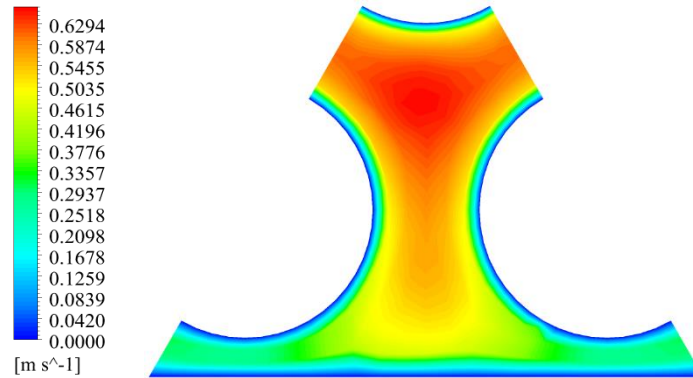
(b)



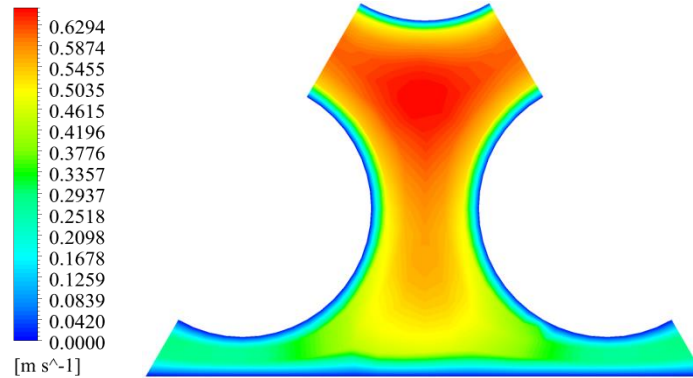
(c)

Fig. 4.6 - LBE temperature comparison between the three turbulence models: RNG $k-\varepsilon$ Model (a), Realizable $k-\varepsilon$ Model (b) and SST $k-\omega$ Model (c).

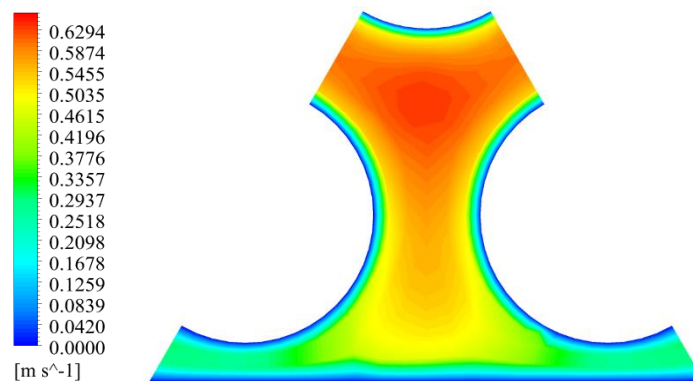




(a)



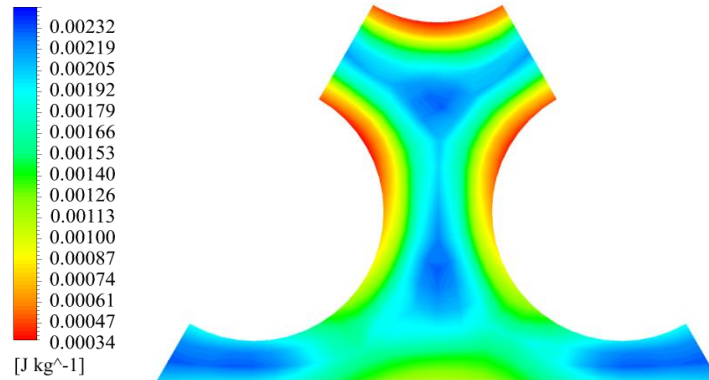
(b)



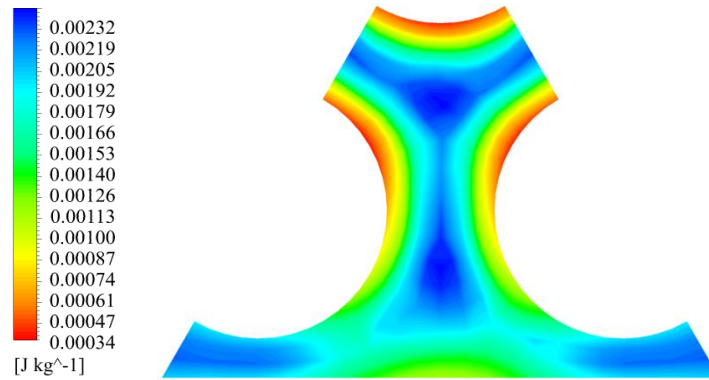
(c)

Fig. 4.7 - LBE velocity magnitude comparison between the three turbulence models: RNG $k-\epsilon$ Model (a), Realizable $k-\epsilon$ Model (b) and SST $k-\omega$ Model (c).

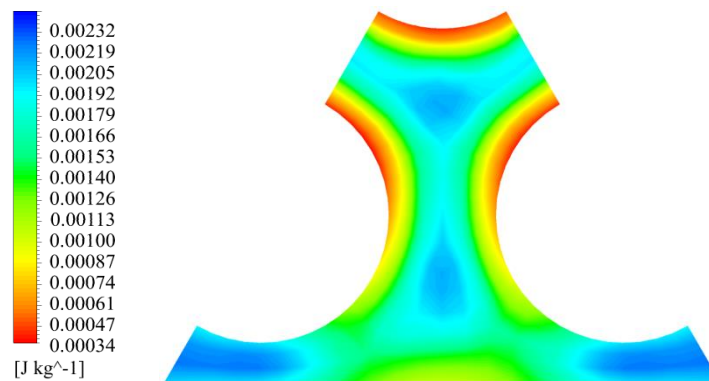




(a)



(b)



(c)

Fig. 4.8 - LBE turbulent kinetic energy comparison between the three turbulence models: RNG $k-\epsilon$ Model (a), Realizable $k-\epsilon$ Model (b) and SST $k-\omega$ Model (c).

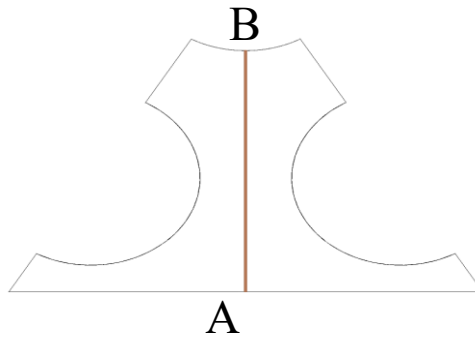


Fig. 4.9 - Brown line on the transversal section of the LBE domain, where calculation results were extracted.

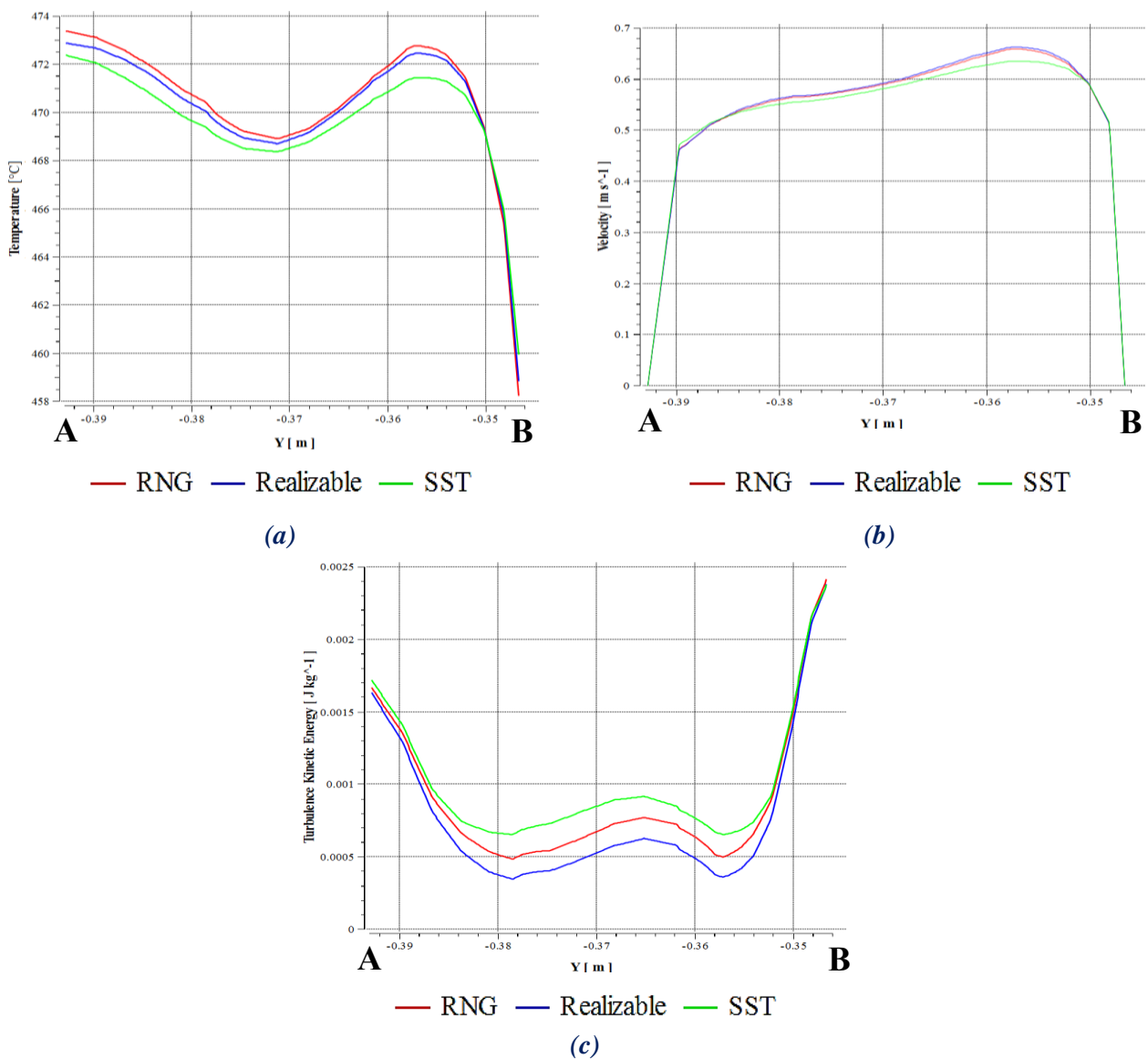


Fig. 4.10 - LBE temperature (a), velocity (b) and turbulent kinetic energy (c) profiles.



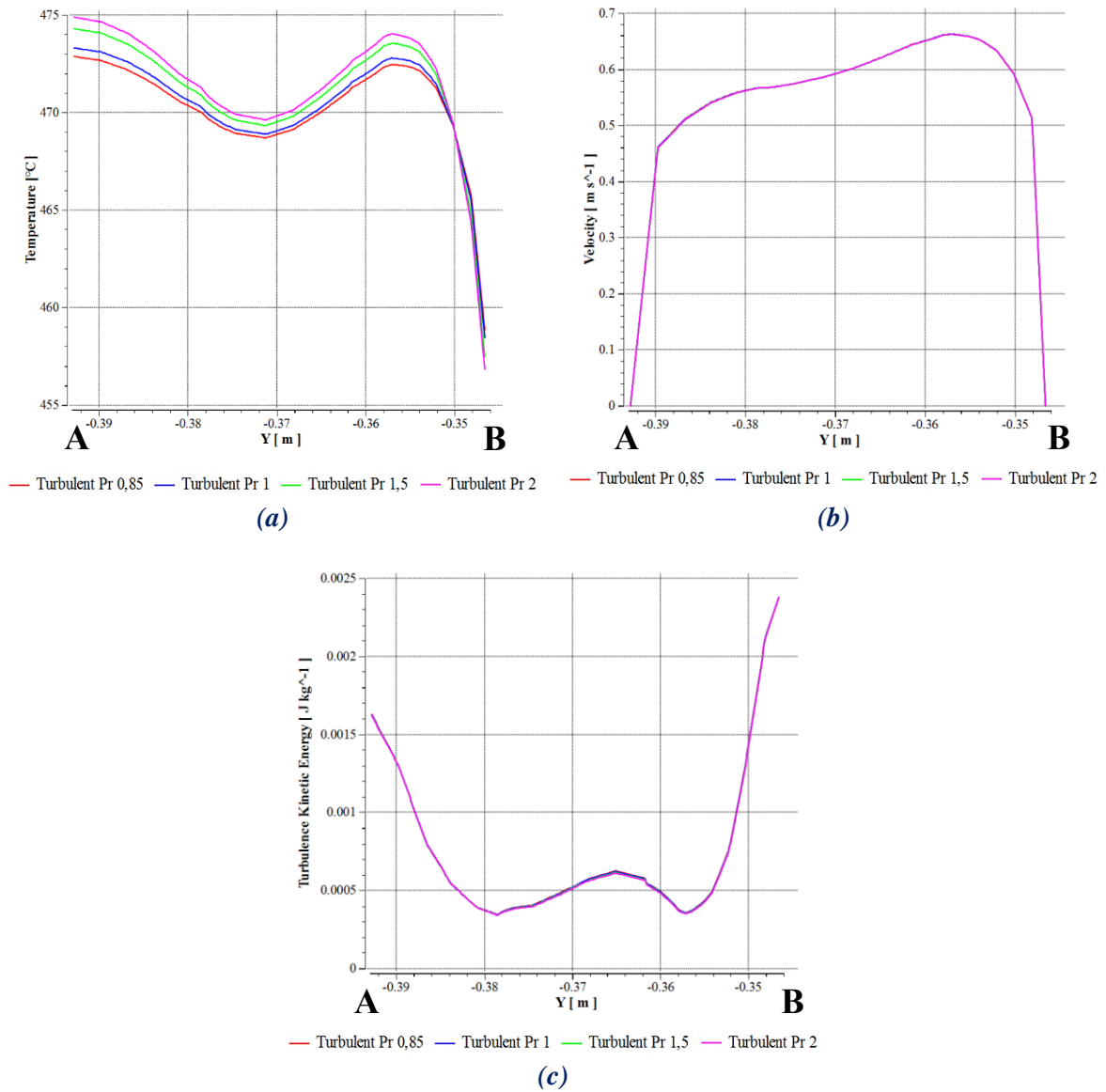


Fig. 4.11 - Temperature (a), velocity (b) and turbulent kinetic energy (c) profiles changing the turbulent Prandtl number.



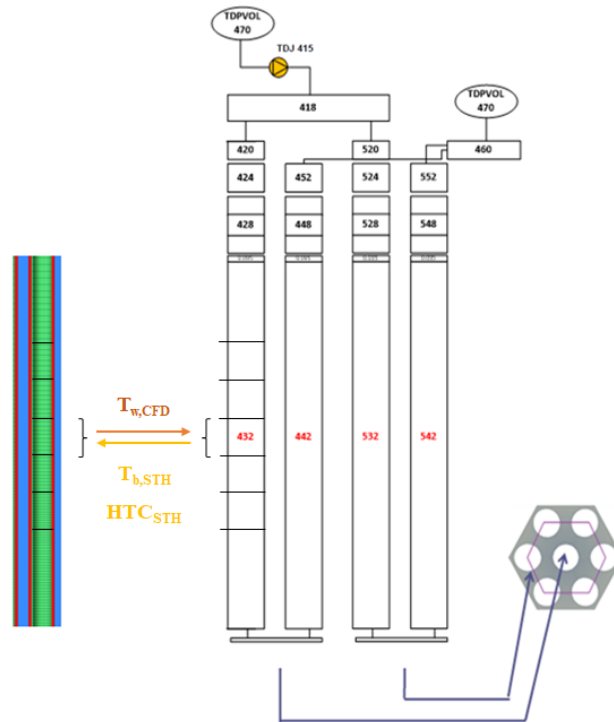


Fig. 4.12 - Simplified sketch of the coupling technique adopted for HERO.

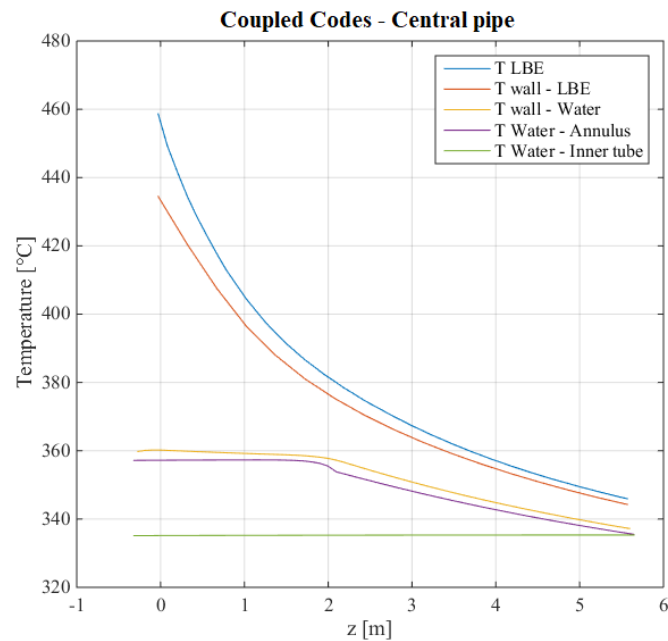


Fig. 4.13 - Trend of temperatures obtained with the coupling procedure in the central pipe (Wall 3).

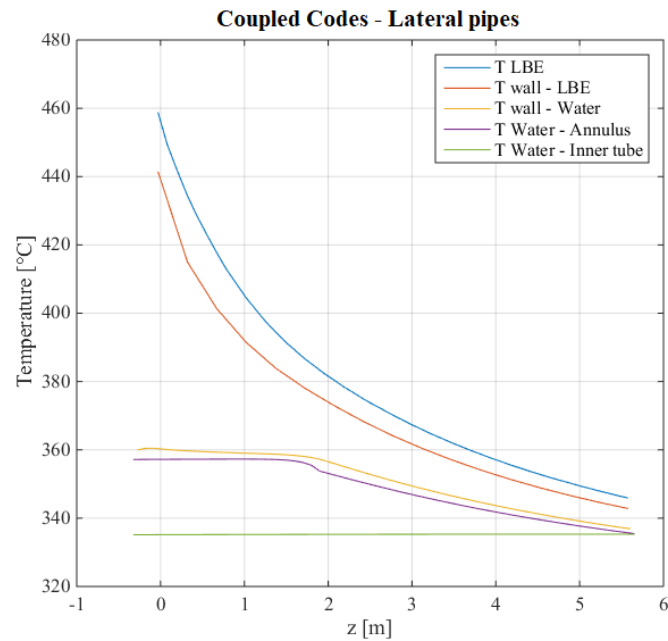


Fig. 4.14 - Trend of temperatures obtained with the coupling procedure in the lateral pipes (Wall 2).

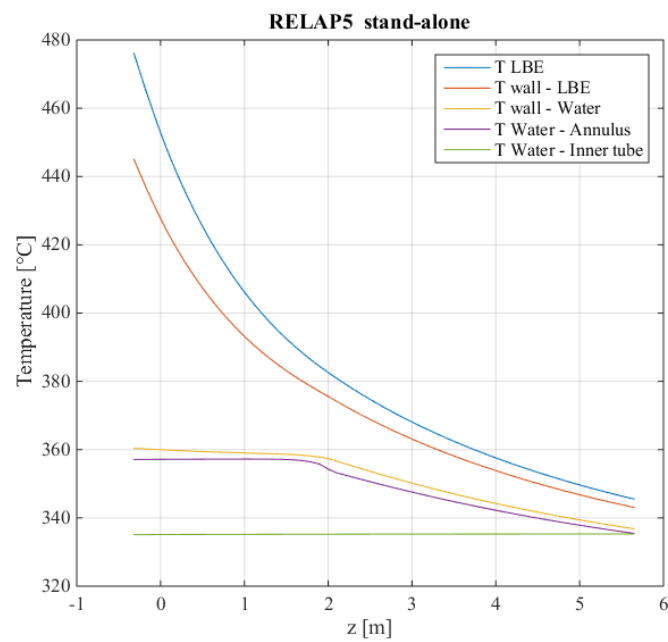


Fig. 4.15 - Trend of temperatures obtained with the coupling procedure in the lateral pipes (Wall 2).



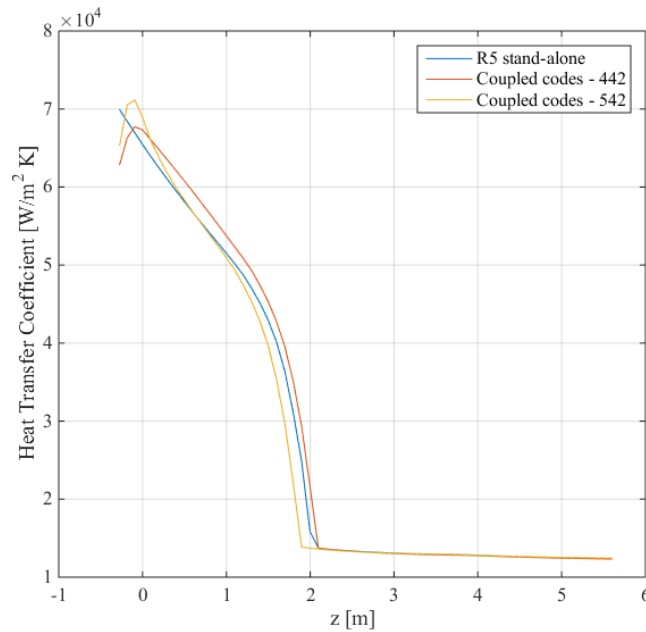


Fig. 4.16 - Comparison of the axial trend of HTC - water side.

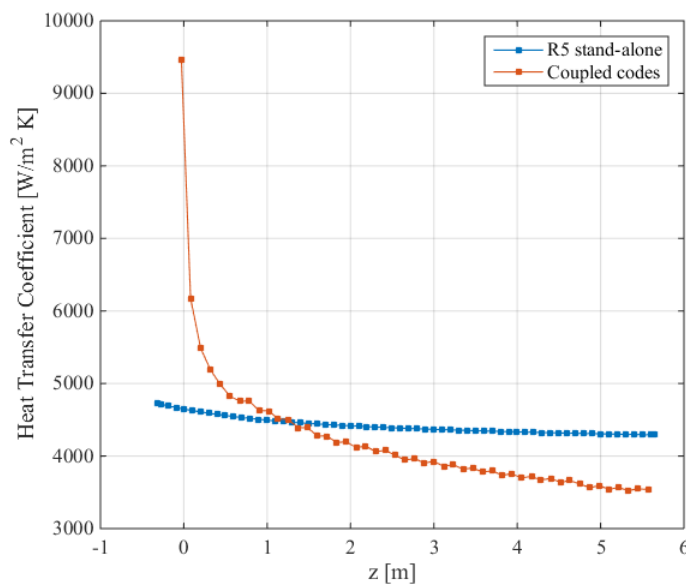


Fig. 4.17 - Comparison of the axial trend of HTC - LBE side.



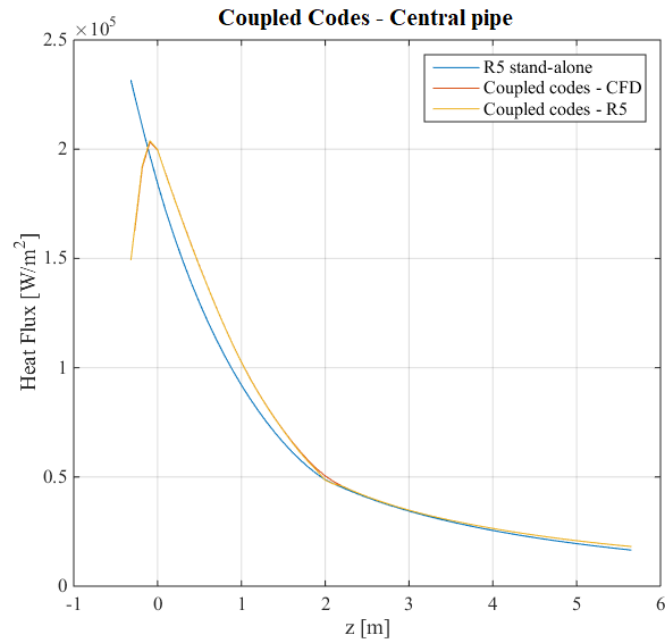


Fig. 4.18 - Comparison of the axial trend of wall the heat flux in the central pipe (Wall 3).

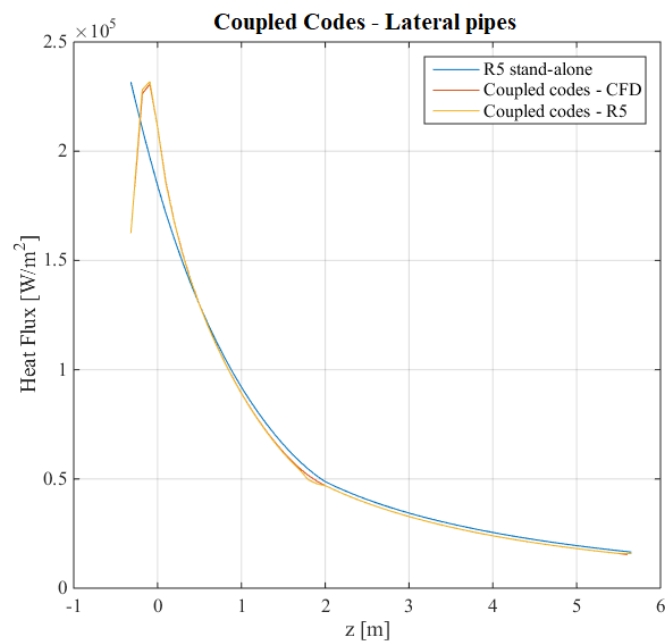

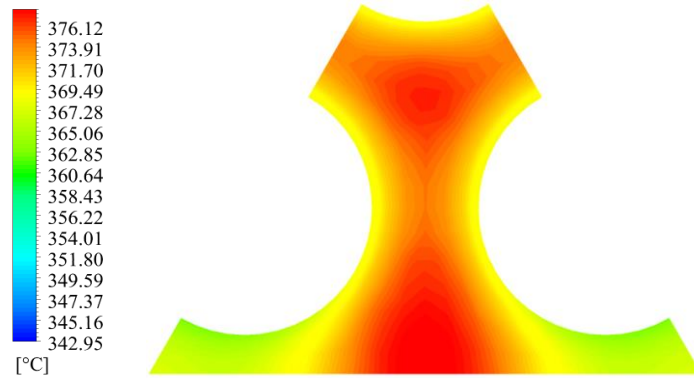


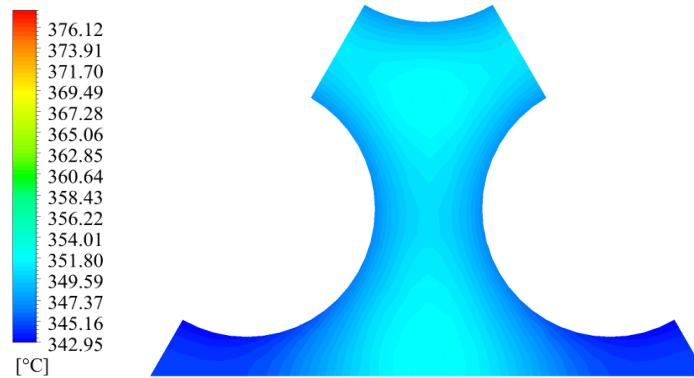
Fig. 4.19 - Comparison the axial trend of the wall heat flux in the lateral pipes (Wall 2).



 RICERCA SISTEMA ELETTRICO	<u>Title:</u> Development of BE numerical tools for LFR design and safety analysis – Part 2	<u>Distribution</u> PUBLIC	<u>Issue Date</u> 12.12.2017	<u>Pag.</u> 183 di 300
	<u>Project:</u> ADP ENEA-MSE PAR 2016	<u>Ref.</u> ADPFISS-LP2-144	Rev. 0	



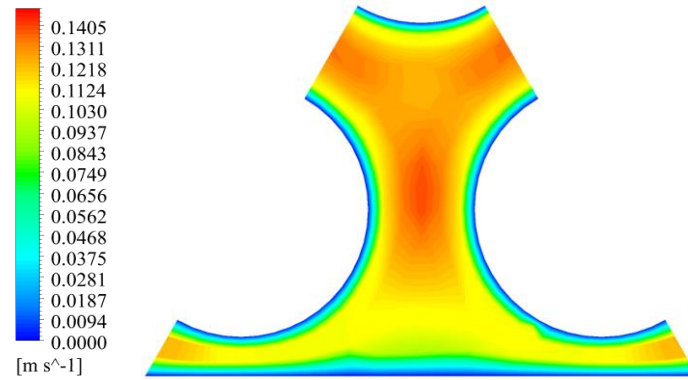
(a)



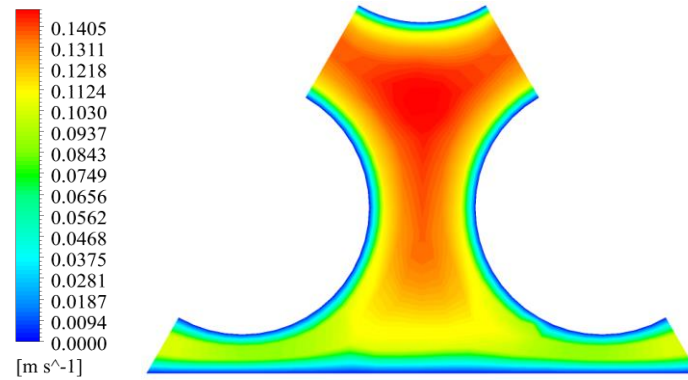
(b)

Fig. 4.20 - LBE temperature distribution at $z=1.5975$ m (a) and $z= 4.0975$ m (b).






(a)



(b)


Fig. 4.21 - LBE velocity at $z=1.5975$ m (a) and $z=4.0975$ m (b).

 RICERCA SISTEMA ELETTRICO	<u>Title:</u> Development of BE numerical tools for LFR design and safety analysis – Part 2	<u>Distribution</u> PUBLIC	<u>Issue Date</u> 12.12.2017	<u>Pag.</u>
	<u>Project:</u> ADP ENEA-MSE PAR 2016	<u>Ref.</u> ADPFISS-LP2-144	Rev. 0	185 di 300

4.4 List of References


- [4.1] F. Oriolo, A. De Varti, G. Fruttuoso, M. Leonardi, S. Bocci, G. Forassassi, **“Modifiche del Codice RELAP5 versione MOD3.2 β per la Simulazione di Sistemi Refrigerati con leghe di Pb o Pb-Bi”**, RL 031/00, Università di Pisa, novembre 2000.
- [4.2] W. Ambrosini, F. Oriolo, S. Bocci, G. Fruttuoso, G. Forassassi, **“Modifica e messa a punto del codice di neutronica 3-D PARCS per Analisi Termoidraulich di Bes-Estimate di Sistemi sottocritici con Sorgente di Spallazione”**, RL 029/00, Università di Pisa, novembre 2000.
- [4.3] R. Lobello, F. de Angelis, A. Alamberti, **“RELAP5 Code Modifications for ADS Demonstration Facility Simulation”**, ANSALDO Technical Report ADS 1 TRIX 0243, Genova, marzo 2000.
- [4.4] G. Bianchini, S. Bocci, M. Carta, G. Forassassi, G. Fruttuoso, F. Mattioda, F. Oriolo, **“Calcoli di Benchmark su Nocciolo ADS. Confronto tra i Risultati della Versione Integrata del codice RELAP5/PARCS Modificata per la Trattazione di Sistemi Sottocritici con Sorgente Refrigerati a Pb-Bi e i Risultati del codice NILO”**, RL 032/01, Università di Pisa, aprile 2001.
- [4.5] P. Agostini, G. Bertacci, G. Gherardi, F. Bianchi, P. Meloni, D. Nicolini, W. Ambrosini, N. Forgone, G. Fruttuoso, F. Oriolo, **“Natural Circulation of Lead-Bismuth in a One-dimensional Loop: Experiments and Code Predictions”**, ICONE10, Arlington, April 2002.
- [4.6] W. Ambrosini, G. Beneamati, S. Carnevali, C. Foletti, N. Forgone, F. Oriolo, G. Scadozzo, M. Tarantino, **“Experiments on Gas Injection Enhanced Circulation in a Pool-type Liquid Metal Apparatus”**, UIT, Napoli, giugno 2006.
- [4.7] W. Ambrosini, N. Forgone, F. Oriolo, **“Limiti di applicabilità dell'accoppiamento tra il codice RELAP5 Mod. 3.3 e il codice PARCS multigruppo alla simulazione di sistemi sottocritici raffreddati a metalli liquidi pesanti”**, RL 1162, Università di Pisa, settembre 2007.
- [4.8] G. Coccoluto, P. Gaggini, V. Labanti, M. Tarantino, W. Ambrosini, N. Forgone, A. Napoli, F. Oriolo, **“Heavy liquid metal natural circulation in a one-dimensional loop”**, Nuclear Engineering and Design 241 (2011) 1301–1309.
- [4.9] G. Barone, N. Forgone, D. Martelli, A. Del Nevo, **“Pre-test analysis of thermal-hydraulic behavior of the NACIE facility for the characterization of a fuel pin bundle”**, CIRTEN-University of Pisa, August, 2012.
- [4.10] G. Barone, N. Forgone, D. Martelli, W. Ambrosini, **“System codes and CFD codes applied to loop- and pool-type experimental facilities”**, RL 1530/2013, CIRTEN Technical Report, University of Pisa, 2013.
- [4.11] G. Barone, N. Forgone, F. Oriolo, **“Thermal-hydraulic post-test analysis of the transition from forced to natural circulation in ICE test section”**, CIRTEN-University of Pisa, August 2011.
- [4.12] M. Tarantino, P. Gaggini, I. Di Piazza, P. Agostini, N. Forgone, D. Martelli, G. Barone, **“Circe experimental report”**, ENEA-Ricerca Sistema Elettrico, ADPFISS-LP2-027, settembre 2013.
- [4.13] Forgone, F. Oriolo, S. Palazzo, **“RELAP5 Pre-Test Analysis on the HELENA Facility for Operational Transient”**, CIRTEN-University of Pisa, RL-1076, 2010.
- [4.14] G. Barone, M. Cherubini, N. Forgone, **“Thermal-hydraulic analysis of a single primary pump trip in ALFRED Reactor”**, CIRTEN-University of Pisa, February 2013.



 RICERCA SISTEMA ELETTRICO	<u>Title:</u> Development of BE numerical tools for LFR design and safety analysis – Part 2	<u>Distribution</u> PUBLIC	<u>Issue Date</u> 12.12.2017	<u>Pag.</u>
	<u>Project:</u> ADP ENEA-MSE PAR 2016	<u>Ref.</u> ADPFISS-LP2-144	Rev. 0	186 di 300

- [4.15] D. Martelli, N. Forgione, G. Barone, I. di Piazza, **“Coupled simulations of the NACIE facility using RELAP5 and ANSYS FLUENT codes”**, Annals of Nuclear Energy 101 (2017) 408–418.
- [4.16] V. Sobolev, **“Database of thermophysical properties of liquid metal coolants for GEN-IV”**, SCK-CEN Scientific Report, December 2011.
- [4.17] D. Martelli, N. Forgione, G. Barone, W. Ambrosini, **“Validation of the coupled calculation between RELAP5 STH code and Ansys FLUENT CFD code”**, CIRTEN-UNIFI, RL 1536, settembre 2014.
- [4.18] F. Andreoli, G. Damiani, D. Martelli, N. Forgione, W. Ambrosini, **“Verifica e validazione preliminare sull'accoppiamento del codice di calcolo RELAP5/Mod.3.3 e il codice di fluidodinamica computazionale ANSYS Fluent”**, CERSE-UNIFI RL-1545, 2015.
- [4.19] N. Forgione, M. Angelucci, D. Martelli, D. Rozzia, F. D'Auria, W. Ambrosini, **“Verifica e Validazione sull'Accoppiamento del Codice di Sistema RELAP5 e il Codice di Fluidodinamica Computazionale Fluent applicato su Sistemi a Piscina”**, CERSE-UNIFI RL 1547, 2016.
- [4.20] M. Angelucci, D. Martelli, N. Forgione, M. Tarantino, **“RELAP5 STH And Fluent CFD Coupled Calculations of a PLOHS + LOF Tansient in the HLM Experimental Facility CIRCE”**, ICONE25-67278, Shanghai, May 2016.
- [4.21] M. Angelucci, D. Martelli, D. Rozzia, F. D'auria, A. Giovinazzi, W. Ambrosini, N. Forgione, **“Vericifation and Validation of RELAP5 STH and FLUENT CFD Coupled Codes Applied to Pool Systems”**, CERSE-UNIFI, RL 1545, September 2016.
- [4.22] D. Rozzia, **“Conceptual design of the CLEAR-S Heat Exchanger”**, ENEA-UTIS, internal report, LR-D-S-144, 2016.
- [4.23] G. Barone, **“CLEAR-S Secondary Loop System operational assessment”**, ENEA-UTIS, internal report, LR-D-S-283, 2017.
- [4.24] G. Morresi, G. Barone, N. Forgione, **“Preliminary Thermal-Hydraulics Analysis of CLEAR-S Nuclear Facility using RELAP5 code”**, Internal Report, University of Pisa, 2015.
- [4.25] D. Rozzia, A. Del Nevo, M. Tarantino, **“HERO-CIRCE CONFIGURATION”**, Report ENEA CI-I-R-166.
- [4.26] OECD/NEA, **“Handbook on Lead-bismuth Eutectic Alloy and Lead Properties, Materials Compatibility, Thermal-hydraulics and Technologies”**, 2007.
- [4.27] ENEA, 2016. Private communication.
- [4.28] X. Cheng, N.I. Tak, **“CFD analysis of thermal–hydraulic behavior of heavy liquid metals in sub-channels”**, Nucl. Eng. Des. 236, pp. 1874-1885, 2006
- [4.29] M. Angelucci, D. Martelli, G. Barone, I. Di Piazza, N. Forgione, “STH-CFD codes coupled calculations applied to HLM loop and pool systems”, article In Press, No 1936894, pre-print version available on <https://www.hindawi.com/journals/stni/aip/1936894/>, Science and Technology of Nuclear Installations, 2017.**




 RICERCA SISTEMA ELETTRICO	<u>Title:</u> Development of BE numerical tools for LFR design and safety analysis – Part 2	<u>Distribution</u> PUBLIC	<u>Issue Date</u> 12.12.2017	<u>Pag.</u>
	<u>Project:</u> ADP ENEA-MSE PAR 2016	<u>Ref.</u> ADPFISS-LP2-144	Rev. 0	187 di 300

5 APPLICATION OF RELAP5-3D ON PHENIX EXPERIMENTAL TESTS


A. Del Nevo, A. Subioli, V. Narcisi, F. Giannetti



 RICERCA SISTEMA ELETTRICO	<u>Title:</u> Development of BE numerical tools for LFR design and safety analysis – Part 2	<u>Distribution</u> PUBLIC	<u>Issue Date</u> 12.12.2017	<u>Pag.</u>
	<u>Project:</u> ADP ENEA-MSE PAR 2016	<u>Ref.</u> ADPFISS-LP2-144	Rev. 0	188 di 300

(Page intentionally left blank)



 RICERCA SISTEMA ELETTRICO	<u>Title:</u> Development of BE numerical tools for LFR design and safety analysis – Part 2	<u>Distribution</u> PUBLIC	<u>Issue Date</u> 12.12.2017	<u>Pag.</u>
	<u>Project:</u> ADP ENEA-MSE PAR 2016	<u>Ref.</u> ADPFISS-LP2-144	Rev. 0	189 di 300

5.1 Background and references

Assessment of nuclear power plant performances during transient conditions is the main issue of safety research. Until recent years, most of the safety analyses were successfully performed using thermal-hydraulics system codes. However, these codes have limitations for conditions where complex feedback exists between core neutronics and thermalhydraulics or when multidimensional phenomena are involved.

The ESNII fast reactor projects, and in particular the LFR, rely on a pool type designs. The design and safety analysis of these reactor types require 3D thermal-hydraulic capabilities and multiphysics approaches based on codes' coupling.

Being the application of CFD codes in DSA limited by the long calculation time and difficulties in predicting the transient behavior at system level, current generation of system codes with three-dimensional capabilities may represent an option. Moreover, the accuracy of the simulations can benefit by modeling directly the interaction between the neutron kinetics and the thermal-hydraulics using already available code features or the coupled codes calculation methods.

In view of this, validation and benchmark activities based on experimental data were carried out with main focus on three-dimensional nodalization of the primary system (see sect. 3) and the full representation of the reactor core (Refs. [5.1] and [5.2]) for neutron kinetic or FPC coupling^[5.3].

This activity, in synergy with H2020 SESAME project (<http://sesame-h2020.eu/>), is aimed at validating RELAP5-3D and at improving analytical and numerical capabilities in fast reactor design and analysis thanks the availability of PHENIX experimental data. Specific objectives are:

- to assess RELAP5-3D code against nuclear reactor scale data
- to master the code limitations and developing modelling approaches
- to develop a reliable approach for SYS analysis of new gen. FR systems, including coupling with NK and FPC

5.2 Assessment of RELAP5-3D code in the framework of PHENIX dissymmetric tests

5.2.1 Brief description of PHENIX


Before the definitive shutdown of the prototype pool-type sodium-cooled fast reactor PHENIX, occurred in the year 2009, the CEA decided to carry out a final set of experimental tests, in order to gather data and additional knowledge on relevant aspects of the operation of sodium fast reactors (SFR). Ten different tests of four types were performed (Tab. 5.1).

PHENIX is a pool-type fast breeder reactor cooled with liquid sodium, located at the Marcoule nuclear site, near Orange, France. Its construction began in November 1968 and the first connection to the French national electricity grid was in December 1973. It was stopped in 2009.

PHENIX plant^{[5.4], [5.5], [5.6]} generated a thermal power of 563 MW(th), with an electric output of approximately 250MW(e) until 1993, then it was operated at a reduced power of 350 MW(th) (140 MW(e)).

The reactor block is of the suspended type (see Fig.1). The upper cover slab supports all the vessels, ensures biological protection, and allows the passage of components. The main vessel has a diameter of 11.8 m and contains about 800 tons of primary sodium. It is attached to the upper slab by 21 suspension hangers and it is



 RICERCA SISTEMA ELETTRICO	<u>Title:</u> Development of BE numerical tools for LFR design and safety analysis – Part 2	<u>Distribution</u> PUBLIC	<u>Issue Date</u> 12.12.2017	<u>Pag.</u>
	<u>Project:</u> ADP ENEA-MSE PAR 2016	<u>Ref.</u> ADPFISS-LP2-144	Rev. 0	190 di 300

closed by means of a flat roof, featuring penetrations for the components. The double-envelope vessel, welded to the upper part of the main vessel, has the task of containing any possible sodium leaks. The roof and the double envelope vessel are thermally isolated. A third vessel, the primary containment vessel, is welded to the slab's underside, and attached to the reactor pit. The role of this vessel is to contain radioactive products, in the event of a severe accident. It carries the final emergency cooling system, welded onto its outside, which has the purpose of maintaining the reactor pit concrete at ambient temperature, and ensuring decay heat removal, in the event of a loss of normal cooling systems.

The strongback has the function of supporting the core and it carries about the 10% of operating flow to the vessel cooling system. The diagrid, connected to primary pumps, has the function of positioning, supporting and supplying sodium to core SA. A conical shell, welded to the main vessel, guarantees, together with the strongback and the diagrid, the completely support for the core.

The core consists of an array of hexagonal assemblies, with a width across flats of 127 mm, for an overall length of 4.3 m. The fuel is mixed uranium–plutonium oxide. The central fissile zone is divided in two regions, that have different enrichment values, and it is surrounded by annular fertile zones, and further out by steel reflectors, and lateral neutron shielding rods. Reactor control was ensured by means of 6 control rods and 1 safety rod (see Fig. 5.2).

The hot pool and the cold pool are separated by the primary vessel, which features a conical baffle. Three vertical-axis primary pumps ensure sodium circulation, taking sodium by the cold pool, and discharging sodium into the diagrid by means of three connector pipes. Six intermediate heat exchangers (straight tube types), connected in pairs to the three secondary loops, remove the heat generated by the core. Primary sodium circulates along the shell side (along the outside of the tubes). From 1993 until the stopping of the reactor, the secondary loop two didn't work and the two corresponding heat exchangers was plugged.

5.2.2 The dissymmetric tests

The dissymmetrical test is used to support LMR plant design and to demonstrate effectiveness of natural circulation cooling characteristics.

The test started with PHENIX in nominal steady state conditions, thus at full power and flow. The initiating event was the trip of the secondary coolant pump (on one loop), thus the rotation speed was reduced from 700 to 100 rpm in about 13 s. This caused azimuthal and axial dissymmetries in the cold plenum.

The lack of cooling created an hot shock in the cold plenum of the primary vessel at the outlet of the two intermediate heat exchangers connected to the corresponding secondary system.


After 5 seconds from the BoT there was: the automatic shutdown (the control rods were inserted at velocity of 1.4 mm/s in 45 s.), the turbine trip, the trip of the secondary coolant pump (in the active loop): the MCP velocity was reduced from 700 to 110 rpm in about 60 s.

After 48 seconds from the started the reactor was instantaneously scrammed. The test stopped after 1800 seconds. The sequence of the events is summarized in Tab. 5.2.

5.2.3 RELAP5-3D nodalization

The nodalization has been developed using the same criteria of Ref. [5.2]. The main features of PHENIX RELAP5-3D© nodalization^[5.7] are:



 RICERCA SISTEMA ELETRICO	<u>Title:</u> Development of BE numerical tools for LFR design and safety analysis – Part 2	<u>Distribution</u> PUBLIC	<u>Issue Date</u> 12.12.2017	<u>Pag.</u>
	<u>Project:</u> ADP ENEA-MSE PAR 2016	<u>Ref.</u> ADPFISS-LP2-144	Rev. 0	191 di 300

- Recommended common rules involving characteristic dimensions, flow path area, elevations, heat structures and capacities have been taken into account from the data package for PHENIX dissymmetric test benchmark.
- Bypass is modeled according to geometric specifications and mass flow data in steady state.
- A sliced approach is applied at all systems (i.e. coolant system, reactor core).
- The relevant elevations of the different parts of the plant are maintained in the nodalization, with minor exceptions due to modeling constraints.
- Dimension of nodes is set-up according with the expected spatial temperature gradients, relevant geometrical features of the systems and measurement points constraints.
- The node to node ratio is kept uniform, as much as possible, with reference maximum ratio of 1.2 between adjacent sub-volumes.
- The roughness is set 3.2^{-5} m with the exception of the core region where is set 1.0^{-6} m.
- The standard RELAP5 wall friction correlations (i.e. laminar and turbulent regions) are modified with Cheng and Todreas formulations to represent wire wrapped rod bundle^[5,8]. The model applies in laminar, turbulence and transition flows. Transition zone is limited to 2200 and 3000 in RELAP5, on the opposite it has larger range of Re numbers in the correlation.
- K-loss coefficients in junctions have been evaluated or estimated on the basis of geometries, when available.
- Westinghouse heat transfer correlation^[5,9] is used in bundle regions, Seban –Shimazaki correlation^[5,9] is used everywhere.

Adopted code resources are summarized in Tab. 5.3. The nodalization is composed by:

- 1 MULTID component modelling large part of the primary system, and
- 1D components in charge of representing the zones where a predominant 1D flow is expected (i.e. hexagonal fuel assemblies; heat exchangers; pump suction and feeding conduit, VCS, and gas plenum).

The MULTID component (Fig. 5.3) models the diagrid, the core bypass, the hot pool and the cold pool. It is composed by 35 axial lengths, 6 radial rings and 12 azimuthal sectors.


The number of azimuthal meshes is chosen on the basis of the geometrical positions of the MCPs and IHXs (Fig. 5.3 – PHENIX nodalization: layout of IHXs and PPs top view (PHENIX) and azimuthal meshes (RELAP5-3D©).

). The axial mesh lengths of the cold and hot pool regions and of the other components (reactor zone, skirt and MCPs pipes, IHX, and VCS) are consistent with the vertical sliced approach.

The fuel SAs are modelled with 1D pipes and exchange power with the corresponding MULTID zone modelling the bypass zone through the hexagonal wrapper.

The reactor core is divided into three main parts: 1) the assemblies of the inner core and the outer core regions, the first 7 rows, modeled one by one, according to the geometrical specifications; 2) the blanket zone rows 8 to 10 modeled with 36 equivalent PIPE components, with the radial blanket, the ARA and the ASA assemblies grouped separately, according to the azimuthal configuration; and 3) the reflector zone where the SA (i.e. ARA, ASA, storage and B4C) are also distributed along the twelve azimuthal meshes. The axial nodes have lengths equal or sub-multiple with respect of the meshes of the 3D component.



 RICERCA SISTEMA ELETTRICO	<u>Title:</u> Development of BE numerical tools for LFR design and safety analysis – Part 2	<u>Distribution</u> PUBLIC	<u>Issue Date</u> 12.12.2017	<u>Pag.</u>
	<u>Project:</u> ADP ENEA-MSE PAR 2016	<u>Ref.</u> ADPFISS-LP2-144	Rev. 0	192 di 300

The model of each subassembly in the core regions is rather detailed to represent the relevant geometric characteristics. Fuel assembly orifices have been set up based on mass flow rate data and overall dynamic pressure drops in the nominal steady state. No geometrical details of the subassemblies orifices or form loss coefficients as function of Re were delivered to the benchmark participants.

Each component is placed according with the 3-D geometry geometrical specifications and relevant elevations are preserved. Porosity factors are used in the MULTID component to model the geometry and the flow paths.

The four IHX primary sides are modelled separately with PIPE components connected upstream and downstream with the MULTID component.

The four IHX secondary sides are modelled separately with PIPE components from an inlet and outlet collectors (dummy) and fed with imposed boundary conditions.

Primary and secondary sides of DOTE components are modelled and idle. The connections between the IHXs #2 are closed to prevent the primary mass flow rate passing through. Primary-to-secondary heat structures modelled using ferritic-martensitic EM10 steel.

The pumps and connected conduits are modeled separately with proper PUMP and PIPE components. These are connected upstream with the cold pool and downstream with the pressure chamber hydraulic volume feeding the SA accounting for the real 3D representation. The homologous curves are The homologous curves have set-up using PHENIX reference data.

The vessel cooling system and the strongback are modelled with an PIPE component connected up-stream with the pressure chamber hydraulic volume feeding the SA, on the top with gas plena, and downstream with the corresponding regions of cold pool.

5.2.4 Synthesis of blind results

The blind calculation was run with a personal computer equipped with a Intel I7-6700 CPU @ 3.4 GHz having 16 GB of RAM. The operative system is Windows 10. The transient (1800s) required 17 hours of computational time.


Steady state conditions are achieved by running the code with the transient option for 1000s (only the last 50s are reported in the figures).

Tab. 5.4 summarizes the values achieved at the end of the steady state. The results of the dynamic pressure drops in the primary system is reported in Tab. 5.5.

The results reported bring the considerations hereafter summarized.

- The relevant initial and boundary conditions of the test are, in general, acceptable.
- The calculated time trends are stable with the exception of the temperatures in the DOTE IHXs. This is anyway considered not relevant for the transient results.
- Imposed core power is larger than the corresponding calculated thermal balance. This is confirmed by the power removed by the secondary side.
- Overall MCP mass flow rate is in good agreement with the estimated test specifications. Nevertheless the core mass flow rate is underestimated of about 3.3%.



 RICERCA SISTEMA ELETTRICO	<u>Title:</u> Development of BE numerical tools for LFR design and safety analysis – Part 2	<u>Distribution</u> PUBLIC	<u>Issue Date</u> 12.12.2017	<u>Pag.</u>
	<u>Project:</u> ADP ENEA-MSE PAR 2016	<u>Ref.</u> ADPFISS-LP2-144	Rev. 0	193 di 300

- The calculated core outlet temperature is referred to the averaged value of the SA ranks from 1 to 10. This value is larger than the test specification of about 10°C. This difference is explained with the lower mass flow rate (about 4 °C), the temperature increase across the MCP (about 2 °C), the larger core power with respect to the thermal balance (2 °C). The remaining difference is smaller than the uncertainty of the datum reported in the test specification. It should be noted that this difference has a negligible influence in the hot pool temperature (because the large mass inventory) and, thus, in the IHX inlet temperature.
- MCPs pressure head needed to achieve the overall mass flow rate, highlights an overestimation of the pressure drops in the primary system. Beside the diagrid, this overestimation is placed in the zones where no datum is provided by the test specification. This also explains the reason why the MCPs velocity is set to an higher value with respect to the reference.

The transient results are hereafter reported by means of the time trends of selected parameters from Fig. 5.5 to Fig. 5.12.

Screenshots of the coolant temperature profiles in the system sections are reported in Fig. 5.13 and Fig. 5.14. These provide the temperature distributions each 10 seconds during the first 200s of the transient. It should be noted that the screenshots in Fig. 5.14 include the temperature of selected SA channels (according with the nodalization approach) belonging to the corresponding section (i.e. azimuthal sector). They are: one selected SA per each rank from 1 to 7, one SA per type (three) for the ranks 8 – 10, and one SA per type (three) for the ranks >10. This last group experiences higher coolant temperatures after the core SCRAM because they are blind channels, thus not fed by the MCP.


5.3 Conclusive remarks and follow-up

The nodalization of PHENIX by REALP53D© is available.

- Configuration dissymmetrical configuration test is completed.
- Nodalization is detailed and suitable for 3D NK coupling.
- Preliminary test run demonstrates satisfactory computing time and robustness of the nodalization.
- Additional checks and improvements are needed to complete the qualification process. These are:
 - Geometrical checks in terms of coolant and structure volumes, heat transfer surfaces,
 - DP in primary system are slightly overestimated (about 10%), but should not affect the overall transient performances because the primary pumps remains in operation at the initial velocity.

The qualification of the nodalization in transient conditions and the sensitivity analyses will be carried out in 2018, when the experimental data will be available.



 RICERCA SISTEMA ELETTRICO	<u>Title:</u> Development of BE numerical tools for LFR design and safety analysis – Part 2	<u>Distribution</u> PUBLIC	<u>Issue Date</u> 12.12.2017	<u>Pag.</u>
	<u>Project:</u> ADP ENEA-MSE PAR 2016	<u>Ref.</u> ADPFISS-LP2-144	Rev. 0	194 di 300

THERMAL HYDRAULICS TESTS	FUEL TEST
1. Dissymmetrical transient 2. Natural convection	8. Partial fuel melting
CORE PHYSICS TESTS	NEGATIVE REACTIVITY TRANSIENT INVESTIGATION TESTS
3. Decay heat 4. Control rod offsetting 5. Subassembly reactivity worth 6. Control rod worth 7. Sodium void	9. Experimental carrier/Blankets interactions 10. Core flowering

Tab. 5.1 – PHENIX end of life tests.


#	Event	TIME (s)
1	Secondary pump trip (on one loop): speed reduced from 700 to 100 rpm in about 13 s.	0
2	Automatic shutdown: insertion of the control rods (1.4 mm/s) in 45 s. Turbine trip. Secondary pump speed reduced (on the other loop) from 700 to 110 rpm in about 60 s.	5
3	Scram.	48
4	End of benchmark test.	1800

Tab. 5.2 – PHENIX dissymmetrical test: imposed sequence of main events.

#	QUANTITY	Value
1	# of HYDR volumes	7492
2	# of HYDR junctions	12419
3	# of HEAT structures	8100
4	# of HEAT structures mesh points	45054

Tab. 5.3 – PHENIX nodalization: adopted code resources.




 RICERCA SISTEMA ELETTRICO	<u>Title:</u> Development of BE numerical tools for LFR design and safety analysis – Part 2	<u>Distribution</u> PUBLIC	<u>Issue Date</u> 12.12.2017	<u>Pag.</u> 195 di 300
	<u>Project:</u> ADP ENEA-MSE PAR 2016	<u>Ref.</u> ADPFISS-LP2-144	Rev. 0	

#	QUANTITY	Unit	PHENIX	R5-3D	Note
				<small>r10</small>	
1.1	Primary circuit balance	MW	351.7	351.7	Imposed
1.2	Secondary circuit balance	MW	--	346.5	
2.1	T - Core inlet	°C	385.0	387.5	
2.2	T - Core outlet	°C	525.0	535.3	Avg. between ranks 1 to 10
2.3	T - primary system IHX inlet	°C	525.0	520.8	IHX 1A
2.4	T - primary system IHX outlet	°C	385.0	381.5	IHX 1A
2.5	T - secondary system IHX inlet	°C	320.0	320.1	
2.6	T - secondary system IHX outlet	°C	525.0	515.1	
2.7	T - Gas plenum temperature	°C	--	523.947	
3.1	MF - Total MCP	kg/s	2216.6	2200.4	
3.2	MF - Total core	kg/s	1988.0	1923.1	
3.3	MF - Core bypass	kg/s	29.8	37.4	Assumed 1.5% of core MF
3.4	MF - VCS	kg/s	198.8	220.1	10% of core MF
3.5	MF - Control plug	kg/s	33.2	--	1.5% of nominal flow rate
3.6	MF - IHX primary system (1)	kg/s	497.0	498.3	IHX 1A
3.7	MF - IHX secondary system (1)	kg/s	345.0	340.9	Imposed
4.1	Speed of primary MCP	rpm	540	565	
4.2	Speed of secondary pump	rpm	700	--	Not modelled
5.1	Lvl of hot pool	m	2.061	1.853	
5.2	Lvl of cold pool	m	1.325	1.0101	
5.3	Lvl of VCS	m	1.54	1.029	
6.1	DP - core SA	kPa	195.50	198.31	
6.2	DP - dyagrid	kPa	3.04	0.26	
6.3	DP - IHX tube bundle	kPa	5.65	5.19	
6.4	DP - LIPOSO (MCP-dyagrid)	kPa	4.94	4.12	
6.5	DP - MCP	kPa	209.01	239.61	
6.6	DP - VCS reversal	kPa	2.19	--	
7.1	MCP head	kPa	209.01	239.61	MCP1
8.1	Enthalpy @ 658.2	J/kg	5.88E+05	5.88E+05	R5-3D Na proprieties
8.2	Enthalpy @ 798.2	J/kg	7.66E+05	7.66E+05	R5-3D Na proprieties
8.3	Calculated core power	W	3.54E+05	3.42E+05	Calculated on the basis of specifications

Tab. 5.4 –Steady state results.



 RICERCA SISTEMA ELETTRICO	<u>Title:</u> Development of BE numerical tools for LFR design and safety analysis – Part 2 <u>Project:</u> ADP ENEA-MSE PAR 2016	<u>Distribution</u> PUBLIC	<u>Issue Date</u> 12.12.2017	<u>Pag.</u> 196 di 300
		<u>Ref.</u> ADPFISS-LP2-144	Rev. 0	

DP vs Length										
#	From	H [m]	From CV	#	To	H [m]	To CV	DeltaH [m]	DP [kPa]	cntrlvar
1	MCP out	6.022	604010000	2	Dyagrid in	2.255	604260000	3.767	4.12	CV185
2	Dyagrid in	2.255	604260000	3	Dyagrid cntr	2.255	900101015	0.000	3.60	CV186
3	Dyagrid cntr	2.255	900101015	4	SA in	1.994	2010000	0.261	11.85	CV189
4	SA in	1.994	2010000	5	SA wire wrapped in	3.266	2060000	1.273	2.26	CV192
5	SA wire wrapped in	3.266	2060000	6	SA wire wrapped out	4.674	2150000	1.408	157.53	CV195
6	SA wire wrapped out	4.674	2150000	7	SA end	6.022	2200000	1.348	44.68	CV198
7	SA end	6.022	2200000	8	HP in	6.304	900101195	0.282	1.63	CV300
8	HP in	6.304	900101195	9	HP out	8.562	900611276	2.258	2.41	CV302
9	HP out	8.562	900611276	10	IHX bundle in	10.095	402070000	1.533	0.85	CV305
10	IHX bundle in	10.095	402070000	11	IHX bundle out	4.904	402260000	5.191	6.96	CV254
11	IHX bundle out	4.904	402260000	12	CP in	4.904	900611144	0.000	0.39	CV306
12	CP in	4.904	900611144	13	CP out	3.472	900612056	1.432	0.00	CV310
13	CP out	3.472	900612056	14	MCP skirt in	3.640	602010000	0.168	0.39	CV314
14	MCP skirt in	3.640	602010000	15	MCP in	8.280	602310000	4.640	6.65	CV317
15	MCP in	8.280		1	MCP out	6.022		2.258	7.38	CV182
--	MCP head		239.6 kPa	Total DP (calculated)			242.9 kPa			

Tab. 5.5 – Pressure drops in primary system.



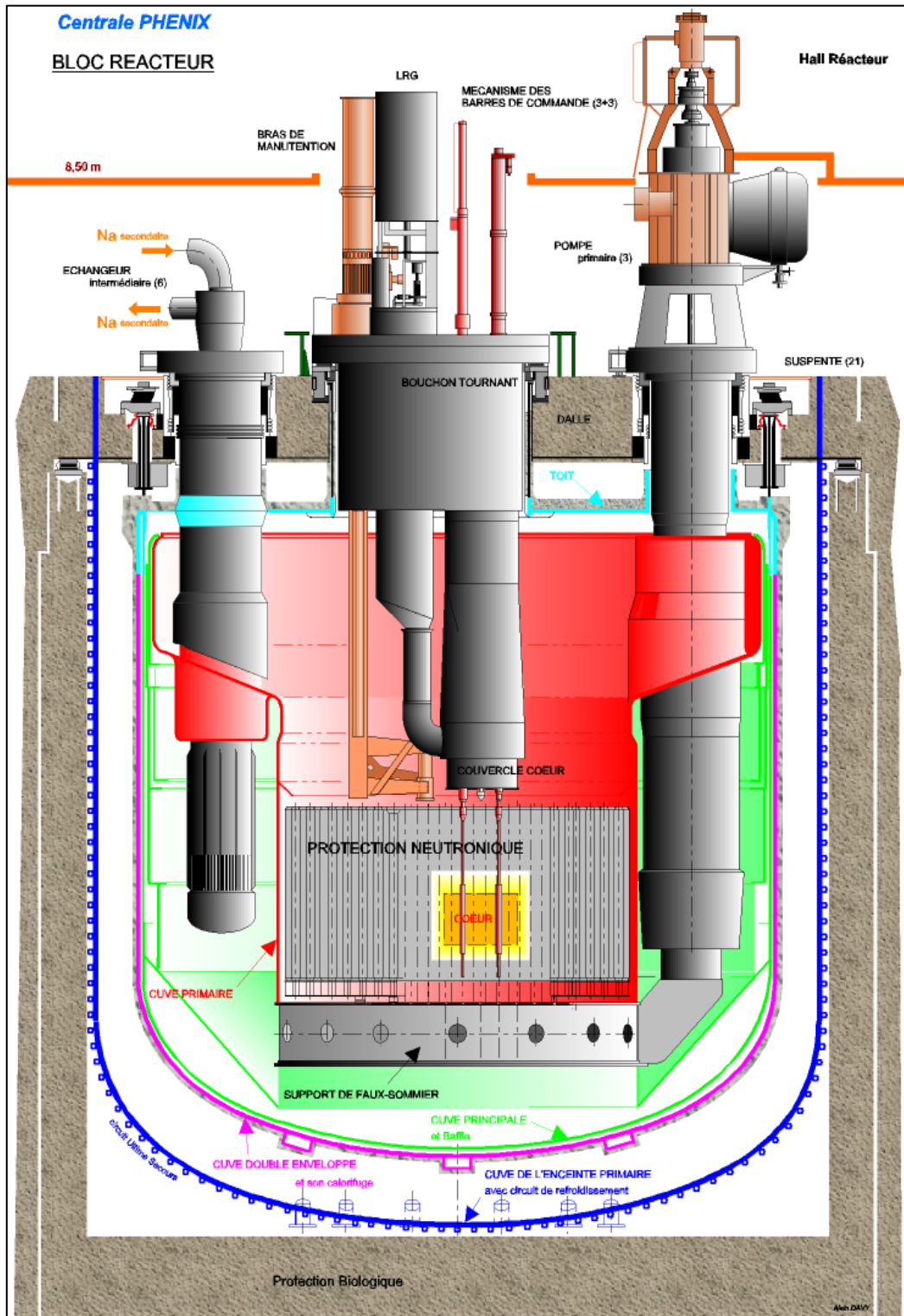


Fig. 5.1 - General overview of PHENIX reactor.



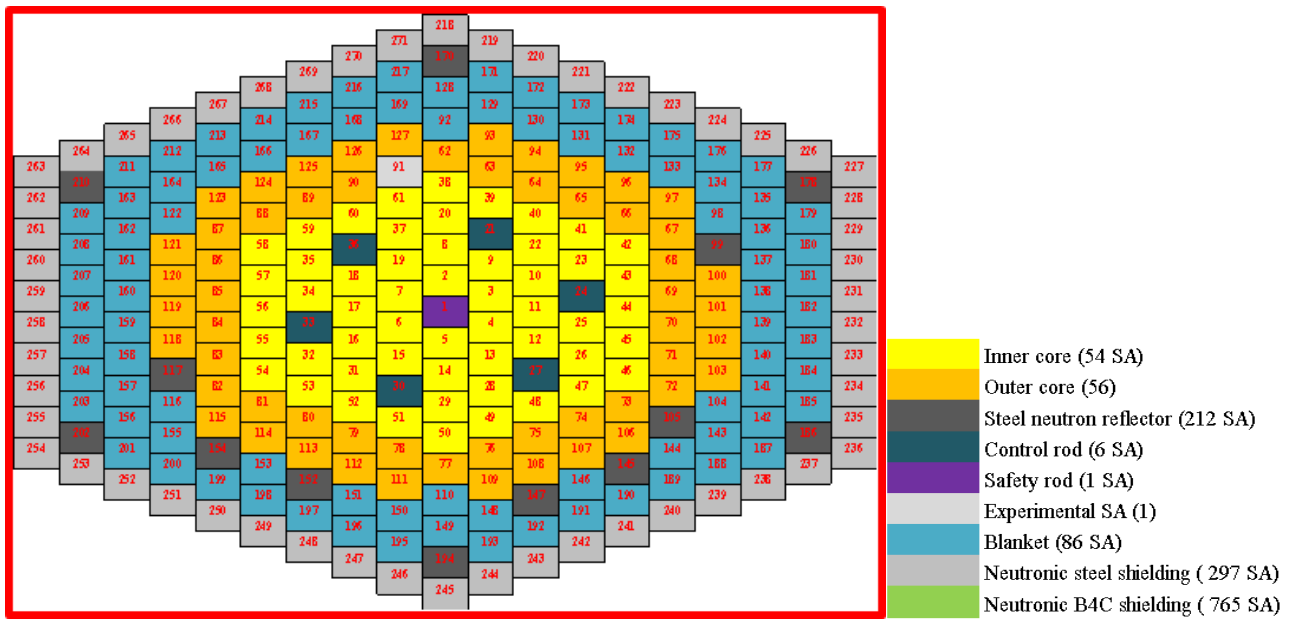


Fig. 5.2 – PHENIX SA configuration.

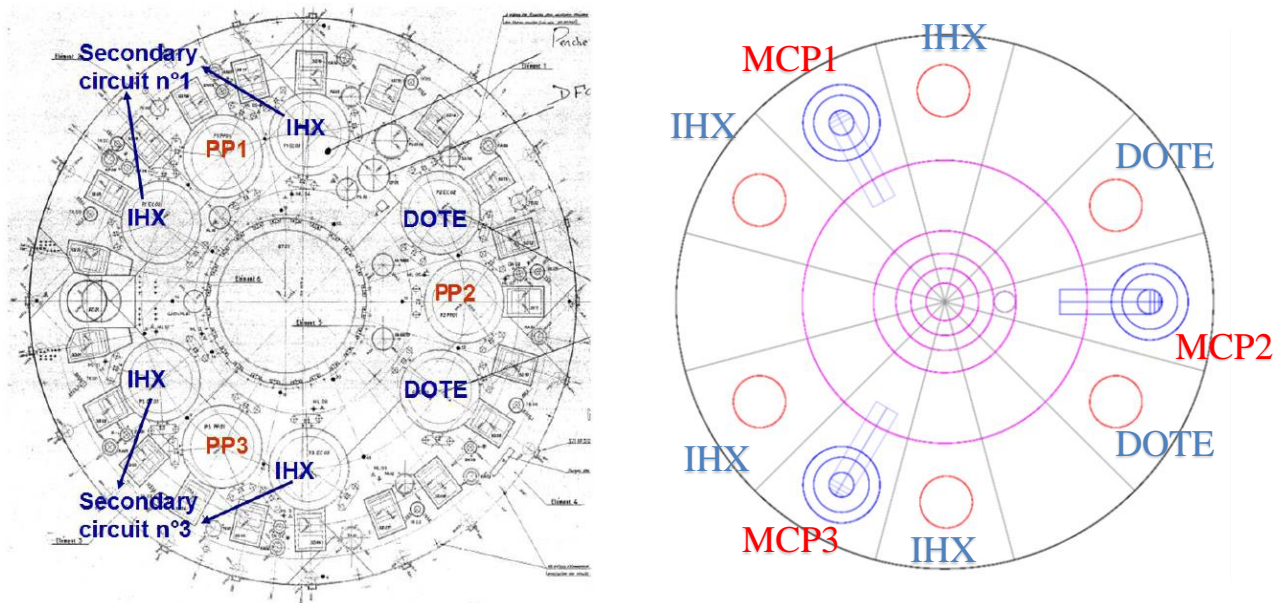


Fig. 5.3 – PHENIX nodalization: layout of IHXs and PPs top view (PHENIX) and azimuthal meshes (RELAP5-3D).

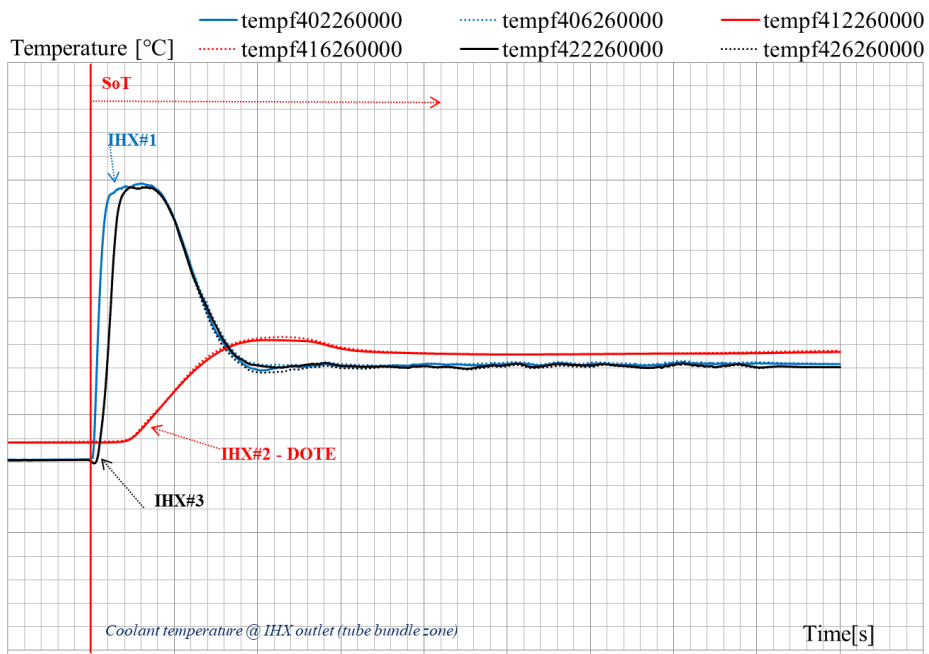


Fig. 5.6 – Blind results: IHXs outlet coolant temperature bundle zone.

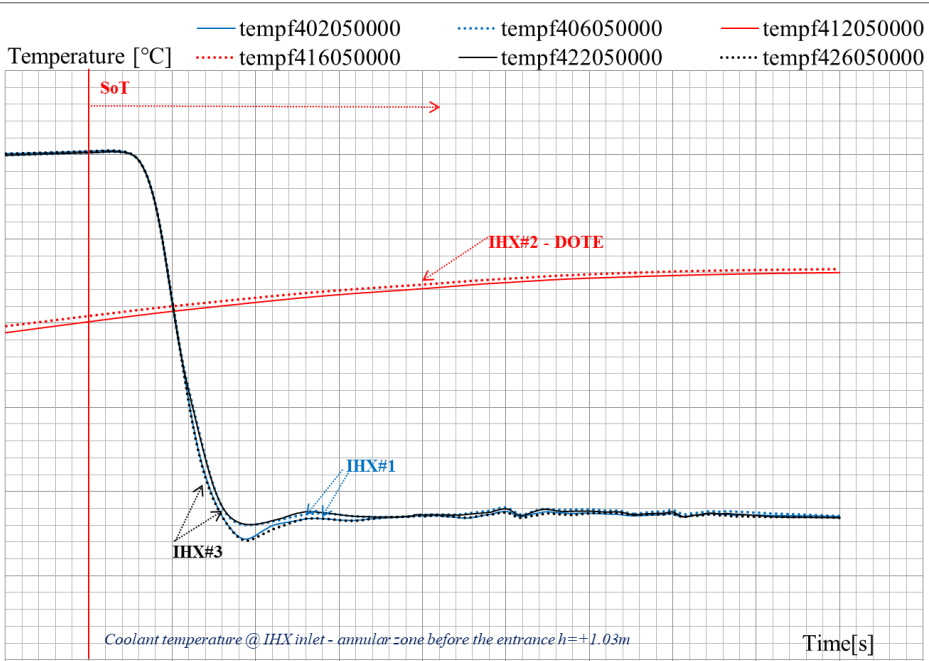


Fig. 5.7 – Blind results: IHXs inlet coolant temperature annular zone.



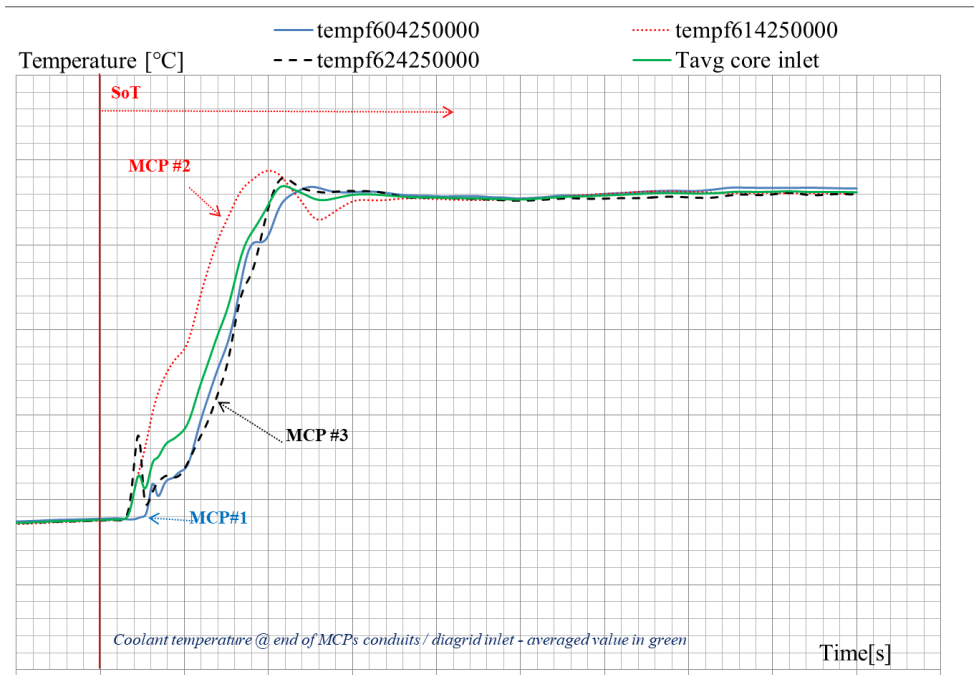


Fig. 5.8 – Blind results: diagrid inlet coolant temperature and average.

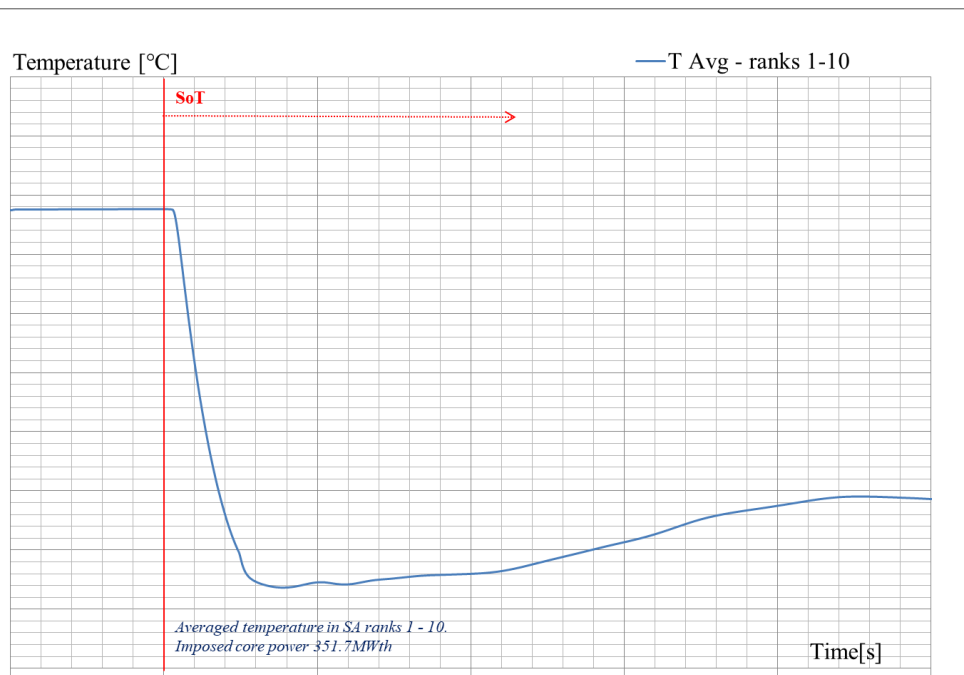


Fig. 5.9 – Blind results: average SA coolant temperature, ranks 1 to 10.



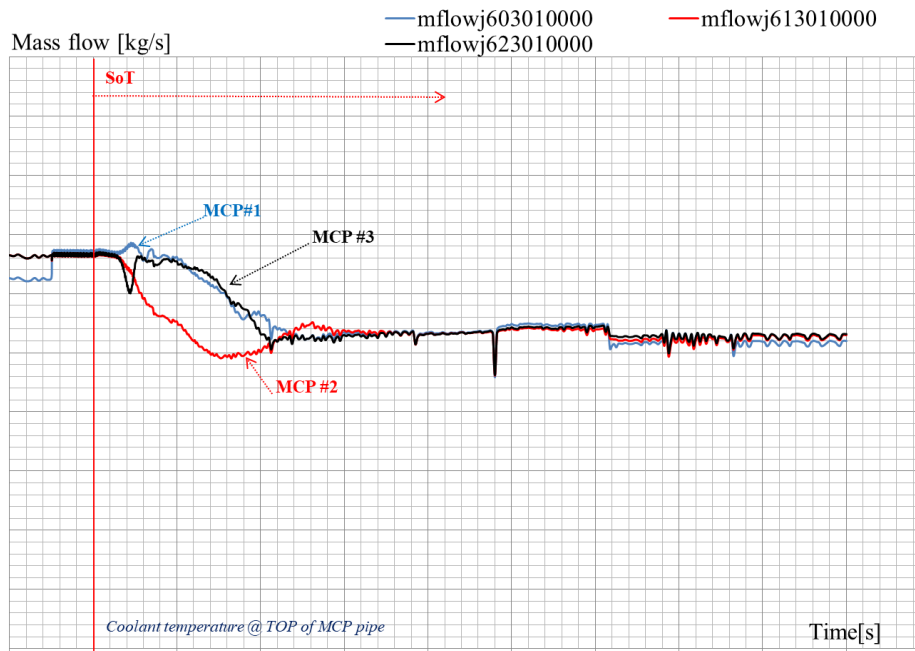


Fig. 5.10 – Blind results: MCPs mass flow rate.

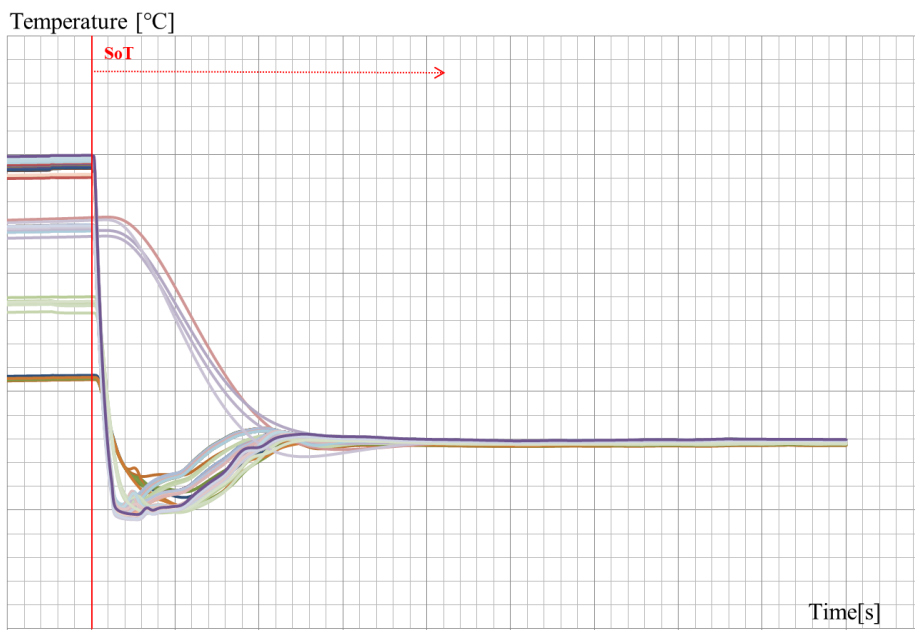


Fig. 5.11 – Blind results: SA outlet coolant temperature ranks 1 to 7.



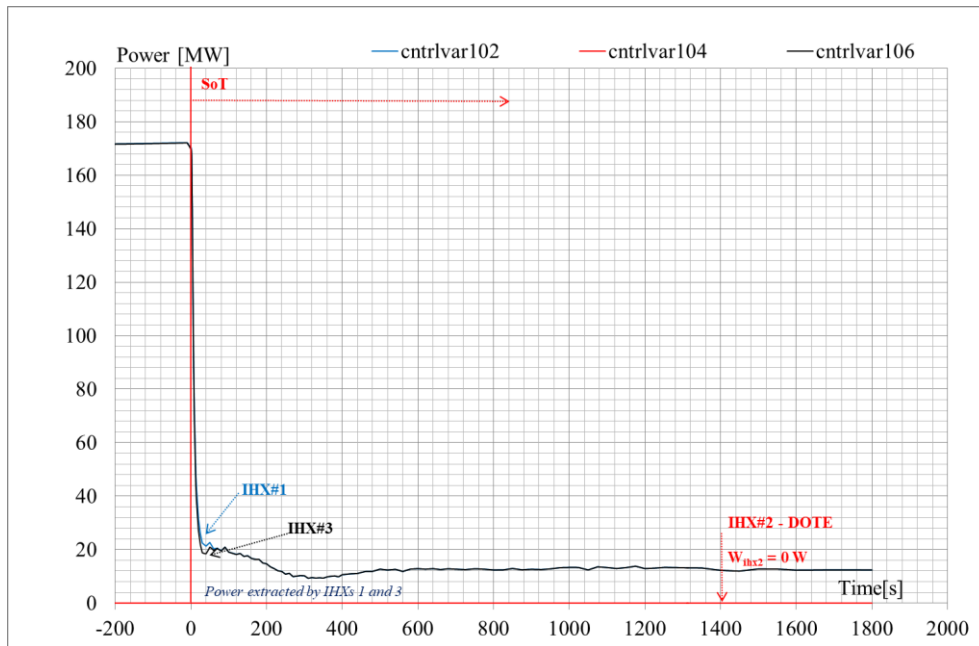
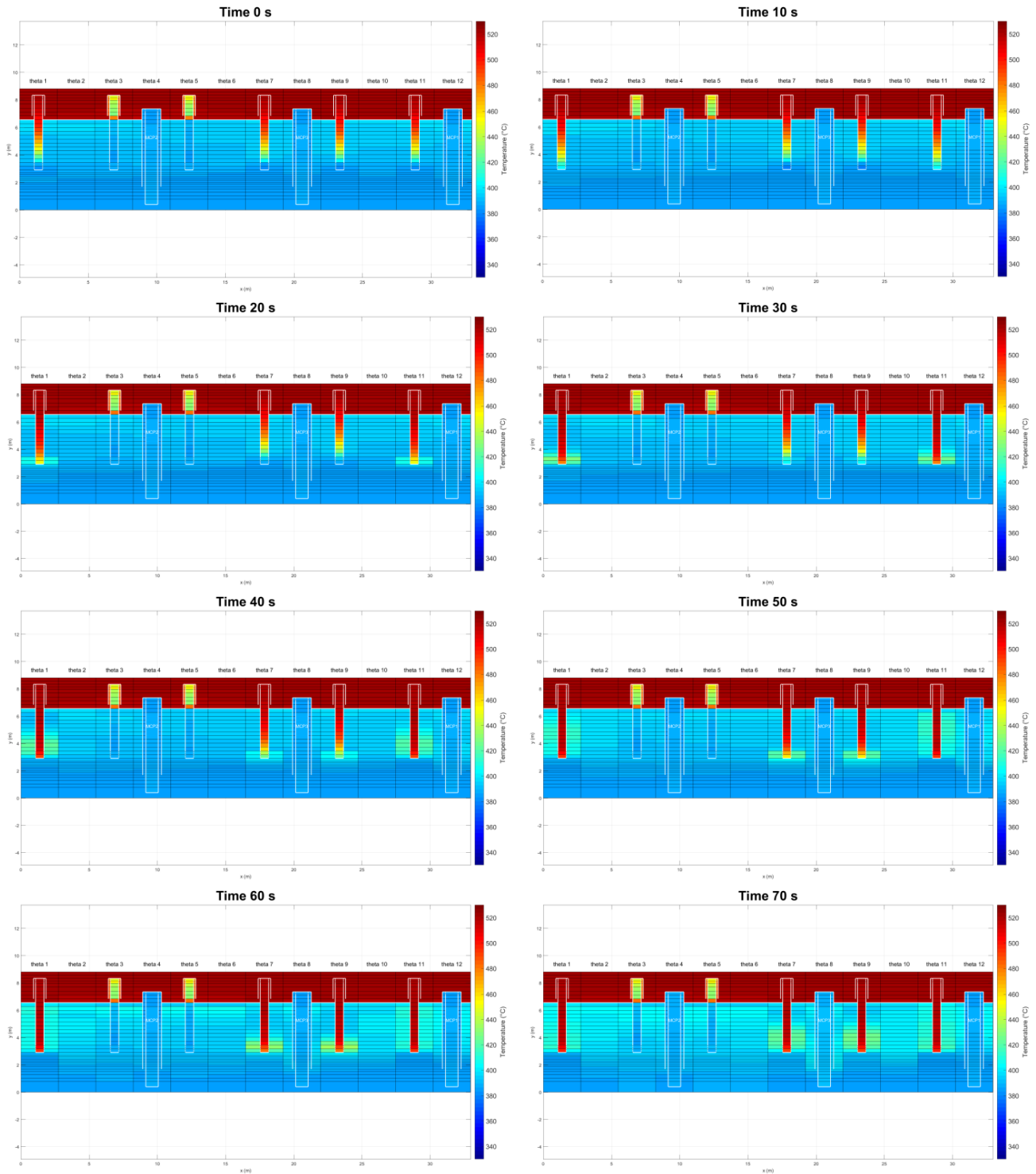
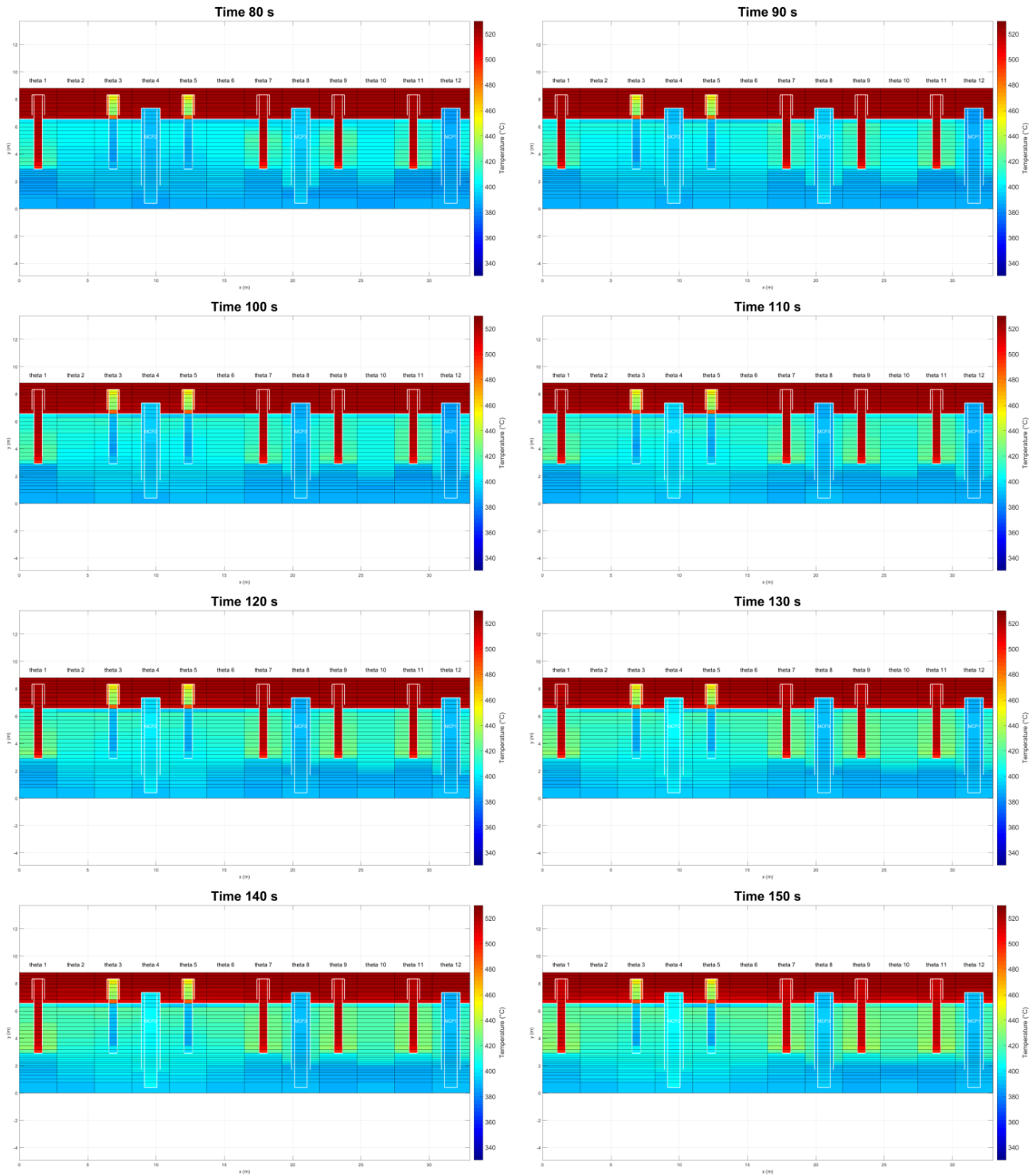


Fig. 5.12 – Blind results: IHXs power.







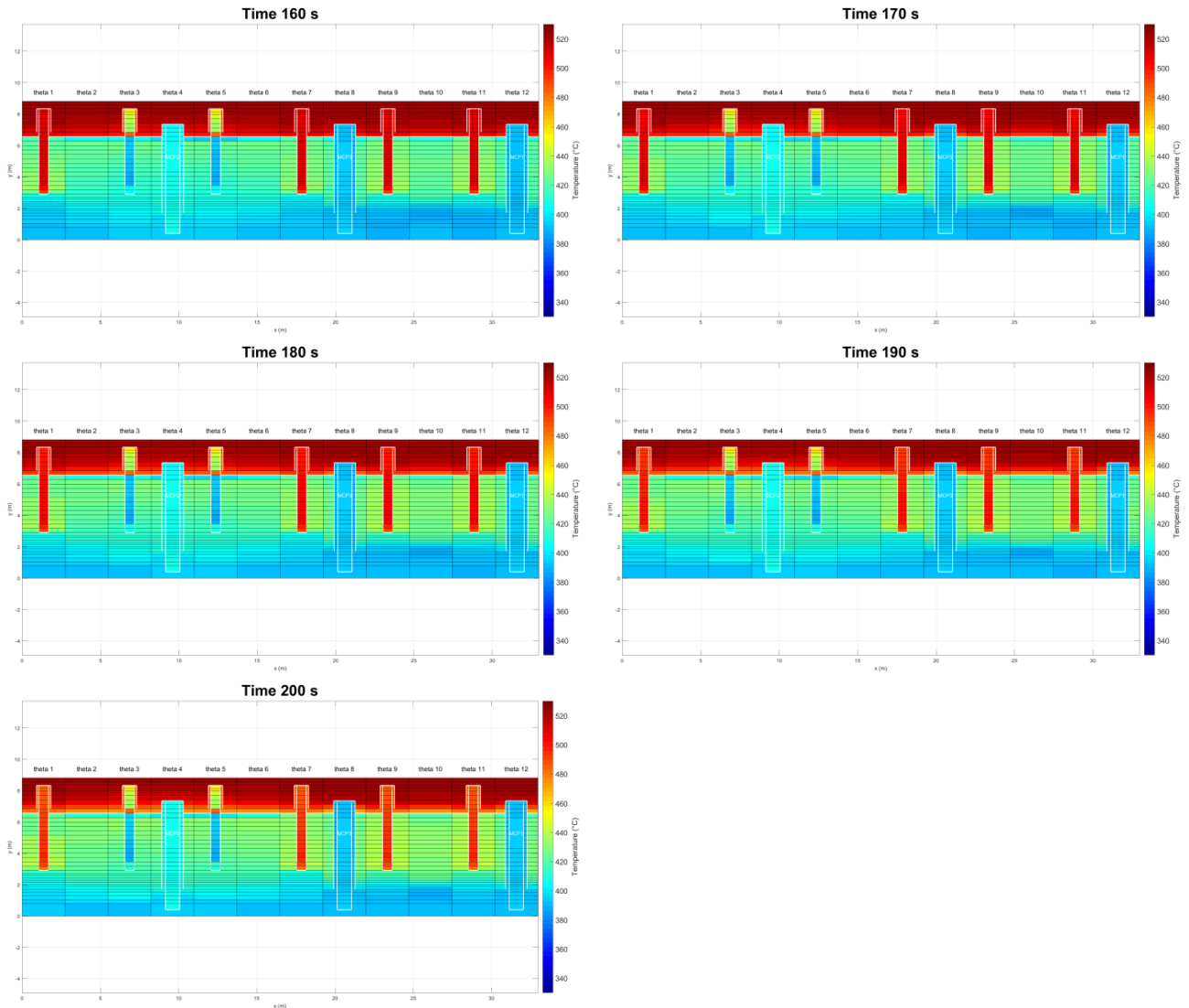
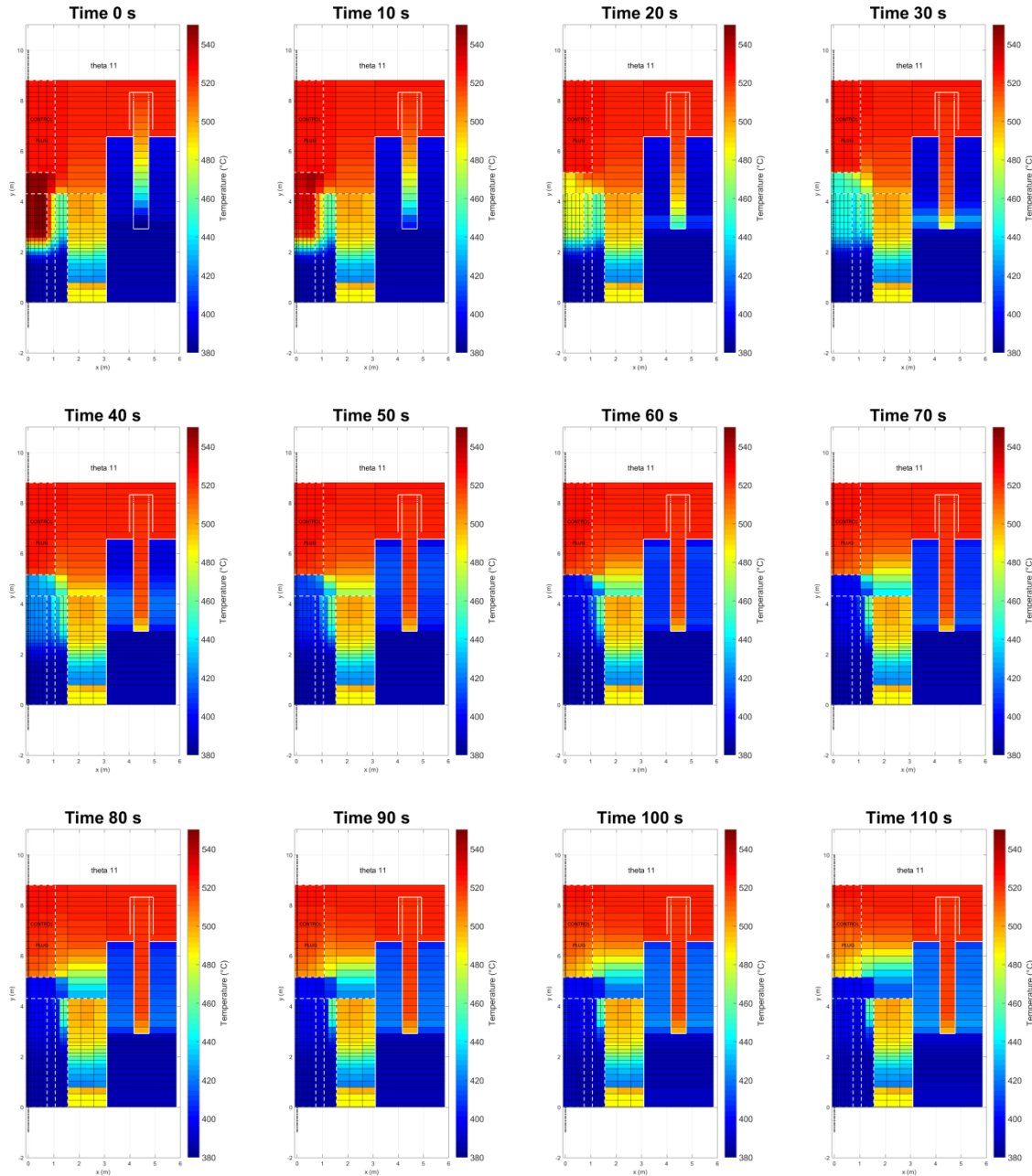


Fig. 5.13 – Blind results: screenshots of temperature trends, cylindrical slices through each MCPs and IHXs.





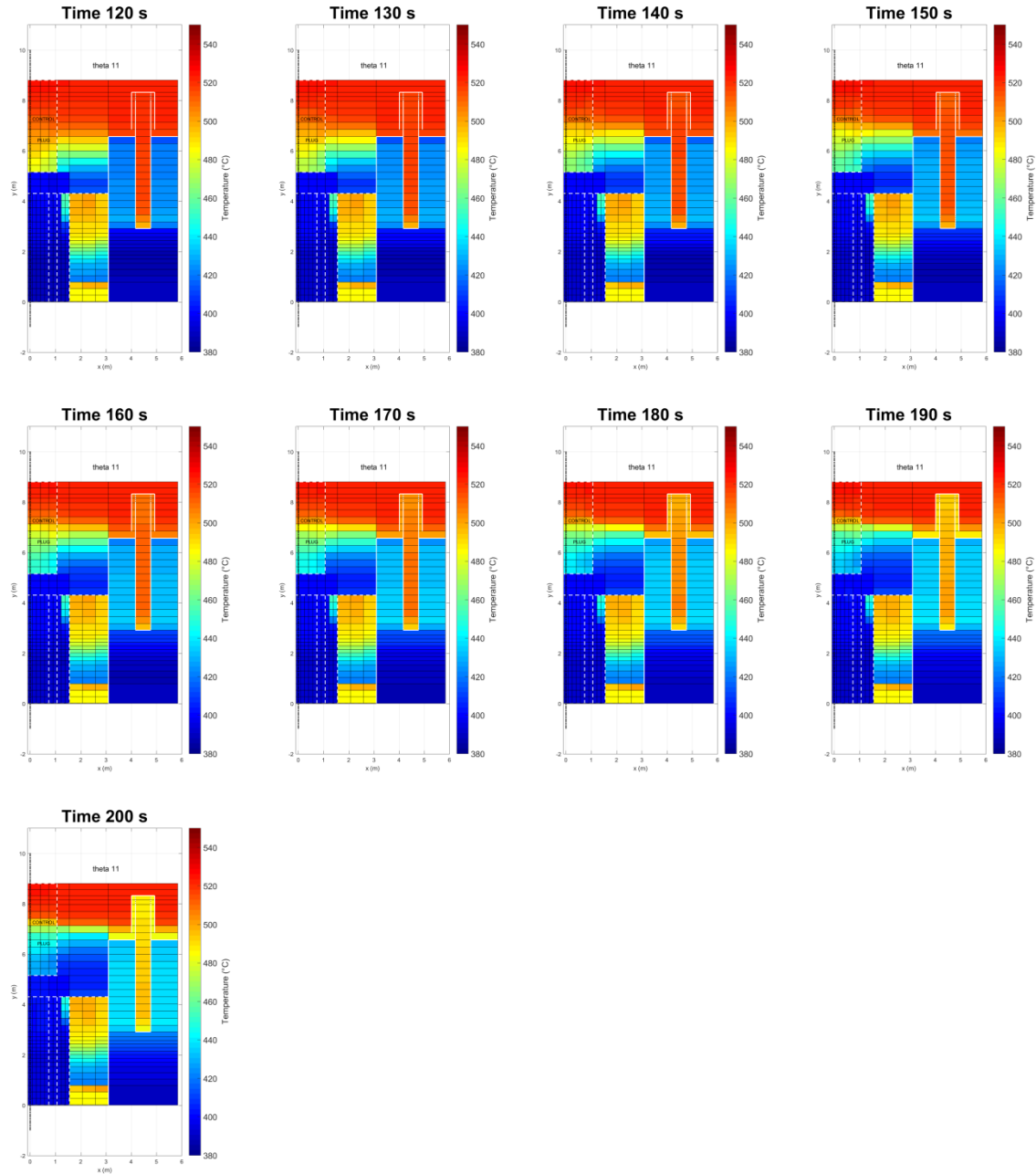



Fig. 5.14 – Blind results: screenshots of temperature trends, vertical slices from center (core region) to IHX 1 A.




 RICERCA SISTEMA ELETTRICO	<u>Title:</u> Development of BE numerical tools for LFR design and safety analysis – Part 2	<u>Distribution</u> PUBLIC	<u>Issue Date</u> 12.12.2017	<u>Pag.</u>
	<u>Project:</u> ADP ENEA-MSE PAR 2016	<u>Ref.</u> ADPFISS-LP2-144	Rev. 0	209 di 300


5.4 List of References

- [5.1] IAEA, *Benchmark Analysis of EBR-II Shutdown Heat Removal Tests*, TECDOC 1819, 2017.
- [5.2] A. Del Nevo, E. Martelli, **Validation of a Three-Dimensional Model of EBR-II and Assessment of RELAP5-3D Based on SHRT-17 Test**, Nuc. Tech. Vol. 193, N. 1, Jan. 2016.
- [5.3] M. Adorni, A. Del Nevo, F. D'Auria, and O. Mazzantini, *A Procedure to Address the Fuel Rod Failures during LB-LOCA Transient in Atucha-2 NPP*, Science and Technology of Nuclear Installations, vol. 2011, Article ID 929358, 11 pages, 2011. doi:10.1155/2011/929358.
- [5.4] B. Grosjean, S. li, *PHENIX Dissymmetrical Test Benchmark*, 2015
- [5.5] IAEA, *Benchmark analyses on the control rod withdrawal tests performed during the phénix end-of-life experiments*, TECDOC 1742, 2014.
- [5.6] IAEA, *Benchmark analyses on the natural circulation test performed during the PHENIX End-Of-Life experiments*, TECDOC 1703, 2013.
- [5.7] INL, The RELAP5-3D© Code Development Team, *RELAP5-3D® Code Manual Volume II: User's Guide and Input Requirements*, INL/MIS-15-36723, Revision 4.3, October 2015.
- [5.8] C.B. Davis, *Evaluation of the Use of Existing RELAP5-3D Models to Represent the Actinide Burner Test Reactor*, INL/EXT-07-12228, February 2007.
- [5.9] INL, The RELAP5-3D© Code Development Team, *RELAP5-3D© Code Manual Volume IV: Models and Correlations*, INL/MIS-15-36723, Revision 4.3, October 2015.



 RICERCA SISTEMA ELETTRICO	<u>Title:</u> Development of BE numerical tools for LFR design and safety analysis – Part 2 <u>Project:</u> ADP ENEA-MSE PAR 2016	<u>Distribution</u> PUBLIC	<u>Issue Date</u> 12.12.2017	<u>Pag.</u> 210 di 300
		<u>Ref.</u> ADPFISS-LP2-144	Rev. 0	



 RICERCA SISTEMA ELETTRICO	<u>Title:</u> Development of BE numerical tools for LFR design and safety analysis – Part 2	<u>Distribution</u> PUBLIC	<u>Issue Date</u> 12.12.2017	<u>Pag.</u> 211 di 300
	<u>Project:</u> ADP ENEA-MSE PAR 2016	<u>Ref.</u> ADPFISS-LP2-144	Rev. 0	


6 FUEL-COOLANT CHEMICAL INTERACTION

E. Macerata, M. Mariani, M. Cerini, S. Cervino, L. De Luca, M. Giola




POLITECNICO
MILANO 1863



 RICERCA SISTEMA ELETTRICO	<u>Title:</u> Development of BE numerical tools for LFR design and safety analysis – Part 2	<u>Distribution</u> PUBLIC	<u>Issue Date</u> 12.12.2017	<u>Pag.</u>
	<u>Project:</u> ADP ENEA-MSE PAR 2016	<u>Ref.</u> ADPFISS-LP2-144	Rev. 0	212 di 300

(Page intentionally left blank)



 RICERCA SISTEMA ELETTRICO	<u>Title:</u> Development of BE numerical tools for LFR design and safety analysis – Part 2	<u>Distribution</u> PUBLIC	<u>Issue Date</u> 12.12.2017	<u>Pag.</u>
	<u>Project:</u> ADP ENEA-MSE PAR 2016	<u>Ref.</u> ADPFISS-LP2-144	Rev. 0	213 di 300

6.1 Introduction

Within the development of GEN IV Lead-cooled Fast Reactors, the understanding of possible chemical interactions among fuel, cladding and coolant is still an open issue. The assessment of the chemical compatibility among the different components of the nuclear system is of paramount importance to be able to foresee the consequences of a cladding failure event both in nominal and accidental conditions.

In this perspective POLIMI has continued the theoretical work already started in the previous PAR projects concerning the development, validation and application of a DFT-GGA approach to estimate missing thermochemical parameters for compounds of interests in the development of LFRs. Beside the continuous update of the literature research in order to collect all the experimental data available, the computational activities focused on the estimation of data for ternary compounds and have contributed to further implement the ongoing thermochemical database.

The availability of such data could enable to go deeper in the study of such topic by means of thermodynamic analysis. With respect to the initially applied SOLGASMIX-PV code based on the minimization of the Gibbs free energy of the system under study, a well-consolidated method based on the same approach has been considered, i.e. CALPHAD (CALculation of PHase Diagrams) method. The possible applicability of CALPHAD method to this field by means of commercial software has been evaluated and main drawbacks or difficulties discussed.

Finally, the theoretical evaluations have been coupled with experimental activities aimed at studying chemical interactions among liquid lead and pellets of different oxides at different temperatures. Oxides of lanthanum, strontium and cerium have been chosen as main representatives of fission products.

6.2 Computational activities

6.2.1 Implementation of the thermochemical database


Even if very few experimental phase diagrams are available for ternary systems of interest for the present study, experimental findings of ternary compounds containing oxygen, lead and actinides or fission products have been found in Refs. [6.1][6.2].

Several DFT-GGA simulations have been performed by VASP in order to obtain the vibrational frequencies and the energetic quantities needed to calculate enthalpy of formation, entropy and heat capacity for a list of ternary oxides. In addition to PbUO_4 and Pb_3UO_6 belonging to the U-O-Pb system already considered in the past projects^[6.3], in the present work the following compounds have been studied: $\text{Pr}_2\text{Pb}_2\text{O}_7$, $\text{La}_2\text{Pb}_2\text{O}_7$, $\text{Eu}_2\text{Pb}_2\text{O}_7$ and SrPbO_3 . An attempt has been made also with the quaternary compound Ba_2PbUO_6 . Numerical results are here not reported since they are part of a paper in preparation.

The estimated formation enthalpies are all negative, thus indicating an exothermic formation reaction. In the case of SrPbO_3 , a formation enthalpy of $-920.83 \text{ kJ K}^{-1}$ was calculated in comparison with an experimental value of $-949.34 \text{ kJ K}^{-1}$, obtaining a deviation of about 3%.

Since in general the approach validation for ternary compounds is penalized by the availability of only few experimental data, the DFT-GGA values of heat capacity for the abovementioned compounds were compared with the values obtained by applying the Neumann-Kopp and Dulong-Petit laws. These empirical rules are often used to estimate heat capacity and its temperature dependence for mixed oxides. For the ternary/quaternary compounds here considered, the Cartesian graph reported in Fig. 6.1 clearly shows that the DFT-GGA values are in very good agreement with those derived with the Neumann-Kopp rule and differ from those obtained with the Dulong-Petit law with a deviation of about +2%.



 RICERCA SISTEMA ELETRICO	<u>Title:</u> Development of BE numerical tools for LFR design and safety analysis – Part 2	<u>Distribution</u> PUBLIC	<u>Issue Date</u> 12.12.2017	<u>Pag.</u>
	<u>Project:</u> ADP ENEA-MSE PAR 2016	<u>Ref.</u> ADPFISS-LP2-144	Rev. 0	214 di 300

6.2.2 Thermodynamic predictions by CALPHAD method

Thermodynamic computer simulations, along with extensive materials databases, are becoming increasingly important for material scientists and in different technological fields. The accuracy of thermodynamic predictions as well as the reliability of the thermodynamic database are crucial for the future development of computational thermodynamics.


Thermochemical equilibrium calculations provide the first approximation for the chemical composition of any system, as the properties of the system proceed towards the equilibrium with time. With simple systems of few species, detailed models taking into account chemical reaction kinetics, mass transport and physical properties of materials can be used to determine an accurate chemical composition. When handling large multicomponent multiphase systems, thermochemical equilibrium calculations are superior with regards to numerical efficiency^[6.4]. Thermochemical equilibrium calculations have been used in the calculation of phase diagrams, where extrapolation from experimental data has been used to calculate properties for chemical systems using thermodynamic principles. This thermodynamic modeling of phase equilibria has been termed the CALPHAD (CALculation of PHase Diagrams) method^[6.5], and in the past the production of various phase diagrams based on extrapolation of experimental data have been a major use of the method. These methods are based on the minimization of Gibbs energy. At constant temperature and pressure, the minimum of Gibbs energy corresponds to the thermodynamic equilibrium state of the system. Today, the thermochemical simulation methods based on the minimization of Gibbs energy are not limited to the calculation of phase diagrams. Increased computing power has made it possible to use thermodynamic equilibrium calculations even in multiphysics applications, where the equilibrium calculation may be run multiple times in serial or parallel fashion, so that even the complex chemistry of nuclear fuel has been modelled with this methodology^{[6.6], [6.7]}. Currently, the CALPHAD method is the only method that can be used efficiently with the required accuracy for practical applications in multi-component and multi-phase systems.

A thermodynamic equilibrium calculation needs thermodynamic data as its basis. The choice of species taken into account in an equilibrium calculation needs a proper knowledge of the chemistry of the system under consideration. The chemistry of the system of our interest, i.e. liquid lead and MOX fuel, is very complex, due to the steep temperature gradient^[6.8] as well as the formation of a multitude of fission products in the fuel^{[6.8], [6.9], [6.10]}. Even if the thermodynamic equilibrium calculation approach has been widely applied to various problems in numerous fields, it has some general limitations that are applicable to any system under thermodynamic consideration. In a real system several factors, such as inhomogeneity in temperature and pressure, kinetics or mass transport, could limit the assumption that the system is at equilibrium and so the distribution of the chemical species is that of a thermodynamic equilibrium state. In particular, in the conditions present in a nuclear reactor the effect of chemical kinetics could be assumed to be insignificant and the reference volume chosen so that temperature and pressure are sufficiently homogeneous. On the contrary, mass transport effects should not be ignored, since the severe temperature gradient and the formation of fission products within the fuel causes mass transport to occur between parts of fuel, affecting the local properties. However, the thermodynamic equilibrium state can be used as a basis for the estimation of the chemical state of the Pb-MOX system.

Chemical considerations on irradiated fuel

Concerning uranium oxide fuel, initially the fuel is chemically homogeneous, but with increasing burn-up the fission products form and separate into different phases^{[6.8], [6.11]}. The most abundant fission products are Zr, Nd, Ce, Sr, Ba, La, Pr, Y, Sm and Pm, as oxides soluble and insoluble in uranium oxide, Tc, Ru, Rh and Pd as metallic precipitates, and the volatile and gaseous Te, I, Cs, Kr and Xe, according to the classifications proposed by Olander and Kleykamp (Fig. 6.2). Moreover, as a consequence of fission, also the oxygen content of the fuel matrix changes as well as the partial pressure of oxygen over the fuel. Taking into account



 RICERCA SISTEMA ELETRICO	<u>Title:</u> Development of BE numerical tools for LFR design and safety analysis – Part 2	<u>Distribution</u> PUBLIC	<u>Issue Date</u> 12.12.2017	<u>Pag.</u>
	<u>Project:</u> ADP ENEA-MSE PAR 2016	<u>Ref.</u> ADPFISS-LP2-144	Rev. 0	215 di 300

the transport properties of FP within the fuel matrix and from the matrix to the gas gap, they can react with each other, with liberated oxygen, with cladding or, in case of defective fuel, with coolant that may enter the fuel rod. In absence of cracks in the fuel, fission products migrate axially and radially under the strong temperature gradients that enhance diffusion. While, when cracks begin to form, they become the primary route of migration from pellets to gas gap. The presence in the fuel cladding of a defect large enough allows diffusion of liquid lead into the fuel rod and of fission products in the coolant, changing also the inert atmosphere in the rod gap. Both transport processes and chemical reactions can occur. All these aspects have to be taken into consideration in order to establish which species consider in the calculation. For example we can neglect gaseous species of compounds with high vaporization temperature.

While a lot of detailed information was already acquired on these chemical aspects for reactors cooled by water, no comparable studies are available for reactors cooled by liquid lead.

Modeling chemical processes in nuclear fuel

Several efforts have been made over the years to apply the principles of thermodynamics to problems in nuclear fuel research. The principle of Gibbs free energy minimization has been already applied to nuclear fuel chemistry, as reported by Imoto et al. and Cordfunke et al.^{[6.12], [6.13]}. All these research works referred to water-cooled reactors and they all concluded that the lack or low reliability of thermodynamical data strongly limit such studies and may be responsible for the discrepancy observed with respect to the experimental evidencies.

Software and Databases


Besides the first free source SOLGASMIX^[6.14] and Lukas programs, thermodynamic calculations could be performed by means of a variety of commercial software packages, among which the most well-known are CaTCalc^[6.15], FactSage^[6.16], MatCalc^[6.17], MTDATA^[6.18], Pandat^[6.19] and Thermo-Calc^[6.20]. Although the features differ from one to another, all packages have a module for the calculation of binary and ternary phase diagrams, and some integrate the thermodynamic equilibrium calculations with the simulation of kinetic processes. Recently, some free CALPHAD software have been developed such as OpenCalphad^[6.21] and Gibbs, showing the same main features of the commercial software with some limitations.

The software packages need of a proper thermodynamic database, that can be commercial or user-specified databases. There are a few openly available multi-component databases and description of many binary and higher order systems, all in a format which can be read by the majority of CALPHAD software. CALPHAD-type databases are constructed from the assessments of binary, ternary and quaternary systems. Phase diagram and thermochemical data are taken into account for obtaining an optimized model parameter set to fit all types of data. One of the outstanding developments in the last decade is the possibility to apply first-principles calculations to estimate missing data and thus supplement laboratory experiments to a certain extent. Data from these computational methods are very valuable, especially if it is not possible to determine quantities experimentally. As compared to other computational approaches, these quantum-mechanically based methods have the advantage that no empirical assumption or fittings to experiment is required. Even though the most established first-principles method, density functional theory (DFT), makes assumptions for the exchange-correlation functional of the electrons, it is a decisive advantage that these approximations are independent of a particular material system under study. The synergistic work of scientists with expertise in CALPHAD simulations, first-principle calculations and experiments could be decisive to gain a higher predictive power of CALPHAD approaches.

6.3 Experimental activities

During this project year POLIMI has started an experimental campaign aimed at studying the chemical interaction between liquid lead and several compounds representative of the main fission products, in the



 RICERCA SISTEMA ELETRICO	<u>Title:</u> Development of BE numerical tools for LFR design and safety analysis – Part 2	<u>Distribution</u> PUBLIC	<u>Issue Date</u> 12.12.2017	<u>Pag.</u>
	<u>Project:</u> ADP ENEA-MSE PAR 2016	<u>Ref.</u> ADPFISS-LP2-144	Rev. 0	216 di 300

conditions experienced in the reactor during the nominal operation or under accidental maloperation. To the best of our knowledge, no interaction experiments are reported in the literature on FPs oxides in liquid lead. The only study available is reported by Vigier et al. about interaction between fresh MOX and molten lead-bismuth eutectic^[6,22]. In particular, different oxides were chosen for the experiments: lanthanum oxide (La₂O₃), cerium oxide (CeO₂), strontium oxide (SrO) and zirconium oxide (ZrO₂). Besides FPs oxides, also iron oxide (Fe₂O₃) and calcium oxide (CaO) were included to investigate their behaviour in contact with liquid lead.

For each compound different pellets were prepared under inert atmosphere inside a glove box filled with argon kept at constant oxygen level (no more than 0.1 ppm). First, powders were characterized by XRD and DSC, in order to be sure of their composition and then treated at about 130°C for 6 hours to eliminate humidity and trapped oxygen. Pellets were formed with the use of a manual press by applying a pressure lower than 100 bar for 4 minutes and extracted from the mould. Fig. 6.3 shows the manual press and the furnace used inside the glove box.


For lanthanum, strontium and iron oxides the pellets were formed and maintained their shape, while in the case of cerium, zirconium and calcium some problems were observed. CeO₂ pellets tend to split apart into parallel layers and so one of them was used in the experiments; whereas for ZrO₂ it was not possible to extract the pellet from the mould. Where possible, the pellet has been weighted and density has been calculated. In each experiment three glass test tubes are positioned in the graphite crucible, each containing about 4 g of lead and a FP oxide pellet. Lead consists of a piece of a lead wire with a 2 mm diameter and a purity of 99.9% provided by Alfa Aesar. Different experiments were performed in a furnace at temperatures ranging from 500 to 550°C for reaction times up to 7 hours. Fig. 6.4 shows some of the samples after the thermal treatment.

As can be seen from Fig. 6.4, the different samples exhibited a different behavior at a first visual analysis. After the thermal treatment in the case of the lanthanum oxide, the whole pellet was recovered and separated from solidified lead, while for cerium oxide only fragments of the pellet could be analyzed. At 550°C the pellet of SrO was found on the tube wall as it was blown up during the thermal treatment. Taking into account these first observations, the pellets characterization is in progress. In particular, the pellet or their fragments will be analyzed by means of XRD, in order to be able to identify new phases coming from the chemical reaction between initial lead and FP oxide. Interaction experiments up to 750°C have been already planned and further investigations on SrO-Pb system will be performed in order to explain what observed in the first experiments. Where possible and if it will be useful to gain new experimental findings, pellets will be analyzed by means of SEM-EDS after a suitable preparation that is still under optimization. Finally, to estimate a metal release from the pellet to Pb during the interaction, a portion of lead will be dissolved and analysed by ICP-MS.

6.4 Conclusions and future work

The work done by POLIMI during this year has contributed to acquire new thermodynamic data on ternary compounds of interest for the development of LFRs by means of DFT-based calculations. Such data are essential in order to implement a thermochemical database that will enable to go deeper in the analysis of the chemistry of the fuel-coolant system. Thanks to the progresses made in the computational thermodynamics, today it is possible to study thermodynamics of multi-component and multi-phase systems as well as other phenomena such as diffusion. In this perspective, POLIMI has investigated the CALPHAD method, at the moment the only one that can be used efficiently with the required accuracy for practical applications in multi-component and multi-phase systems. The review work has enabled to outline the potentialities of the CALPHAD method in the nuclear fuel research as well as the importance and scarce availability of reliable database and the development of several software able to integrate thermodynamic equilibrium calculations



 RICERCA SISTEMA ELETTRICO	<u>Title:</u> Development of BE numerical tools for LFR design and safety analysis – Part 2	<u>Distribution</u> PUBLIC	<u>Issue Date</u> 12.12.2017	<u>Pag.</u>
	<u>Project:</u> ADP ENEA-MSE PAR 2016	<u>Ref.</u> ADPFISS-LP2-144	Rev. 0	217 di 300

with kinetics or to be coupled with other software. The next step will be the investigation of the U-O-Pb and La-O-Pb systems by applying the CALPHAD method and exploiting the related thermochemical data estimated by DFT-GGA approach in the previous projects.

Finally, an experimental activity has been started aiming to observe the chemical reactivity between liquid lead and some oxides of fission products. Some interaction experiments were performed by varying the temperature and the reaction time. The characterization is still ongoing and the first resulting experimental findings will be used to optimize the experimental conditions adopted and, more in general, to better design the interaction experiments.



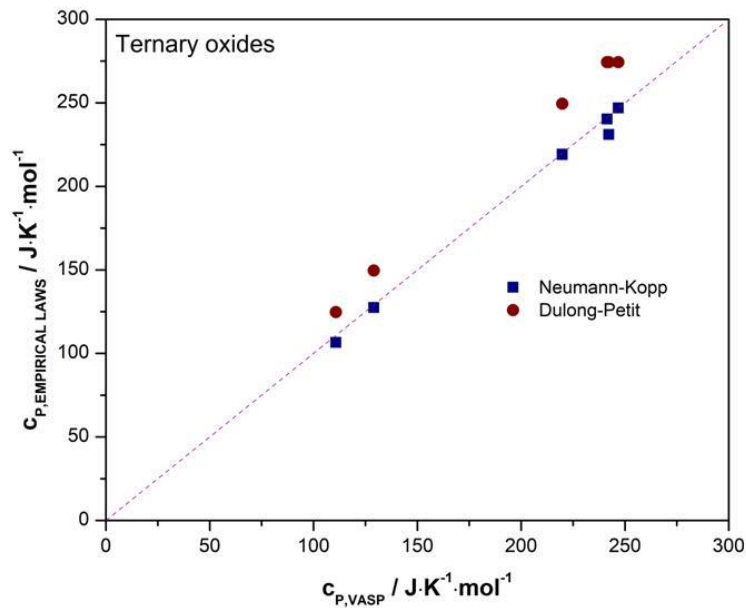


Fig. 6.1 – Comparison between the heat capacity value calculated from DFT-GGA simulations and the values obtained from the Neumann-Kopp and Dulong-Petit laws.

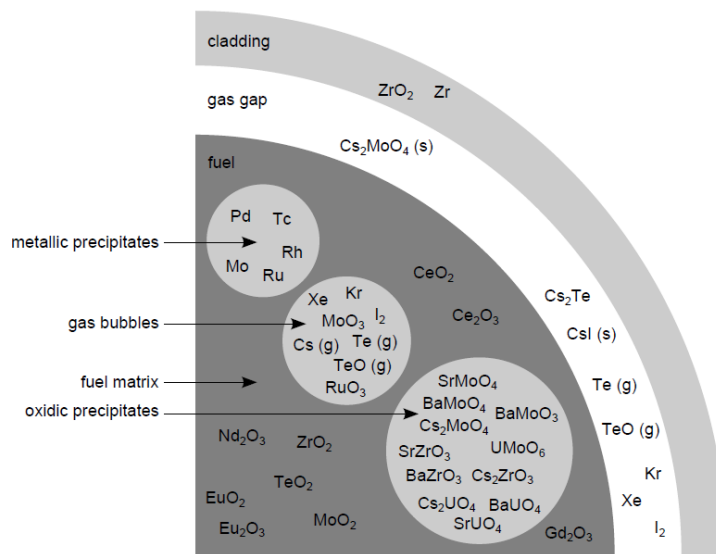


Fig. 6.2 – Schematical composition of irradiated fuel and species distribution.




 RICERCA SISTEMA ELETTRICO	<u>Title:</u> Development of BE numerical tools for LFR design and safety analysis – Part 2	<u>Distribution</u> PUBLIC	<u>Issue Date</u> 12.12.2017	<u>Pag.</u>
	<u>Project:</u> ADP ENEA-MSE PAR 2016	<u>Ref.</u> ADPFISS-LP2-144	Rev. 0	219 di 300



Fig. 6.3 – Manual press and furnace inside the glove box operating under inert atmosphere.

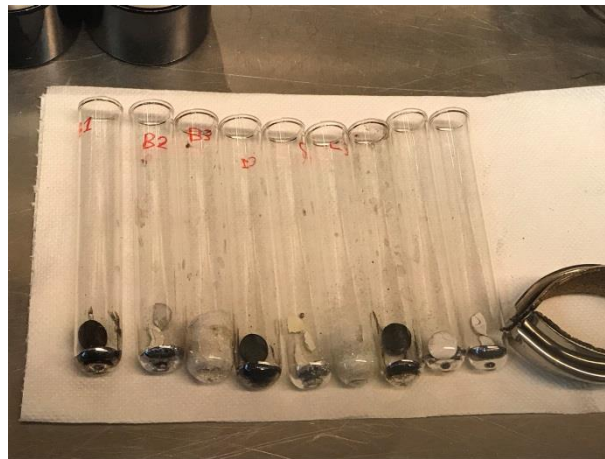



Fig. 6.4 – Some of the samples obtained from the interaction experiments.




 RICERCA SISTEMA ELETRICO	<u>Title:</u> Development of BE numerical tools for LFR design and safety analysis – Part 2	<u>Distribution</u> PUBLIC	<u>Issue Date</u> 12.12.2017	<u>Pag.</u>
	<u>Project:</u> ADP ENEA-MSE PAR 2016	<u>Ref.</u> ADPFISS-LP2-144	Rev. 0	220 di 300

6.5 List of References


- [6.1] Landolt-Bornstein Database, www.lb.chemie.uni-hamburg.de
- [6.2] ICSD Database, www.icsd.fiz-karlsruhe.de
- [6.3] E. Macerata, M. Mariani, M. Cerini, S.M. Cervino, M. Giola, **Studio delle interazioni tra combustibile, prodotti di fissione e refrigerante in sistemi LFR**, Rapporto ADPFISS – LP2 – 124 MSE-ENEA PAR2016.
- [6.4] Spencer PJ. A brief history of CALPHAD. Calphad. 2008; 32:1–8.
- [6.5] Saunders, N.; Miodownik, AP. CALPHAD (Calculation of phase diagrams): A comprehensive guide. Pergamon; Oxford: 1998.
- [6.6] M. S. Veshchunov, V. D. Ozrin, V. E. Shestak, V. I. Tarasov, R. Dubourg, and G. Nicaise. Development of the mechanistic code MFPR for modelling fission product release from irradiated UO₂ fuel. Nucl. Eng. Des., 236:179–200, 2006.
- [6.7] M. H. A. Piro, J. Banfield, K. Clarno, S. Simunovic, T. M. Besmann, B. J. Lewis, and W. T. Thompson. Coupled thermochemical, isotopic evolution and heat transfer simulations in highly irradiated UO₂ nuclear fuel. J. Nucl. Mater., 441:240–251, 2013.
- [6.8] D. R. Olander. Fundamental aspects of nuclear reactor fuel elements. Technical Report TID-26711-P1, Technical Information Centre, US Department of Energy, 1976. pp. 624.
- [6.9] H. Kleykamp. The chemical state of the fission products in oxide fuels. J. Nucl. Mater., 131:221–246, 1985.
- [6.10] B. J. Lewis, W. T. Thompson, and F. C. Iglesias. Fission product chemistry in oxide fuels, volume 2 of Comprehensive Nuclear Materials, pages 515–546. Elsevier, 2012. ISBN 978-0-08-056033-5.
- [6.11] M. H. Piro, T. M. Besmann, S. Simunovic, B. J. Lewis, and W. T. Thompson. Numerical verification of equilibrium thermodynamic computations in nuclear fuel performance codes. J. Nucl. Mater., 414:399–407, 2011.
- [6.12] S. Imoto. Chemical state of fission products in irradiated UO₂. J. Nucl. Mater., 140: 19–27, 1986.
- [6.13] E. H. P. Cordfunke and R. J. M. Konings. Chemical interactions in water-cooled nuclear fuel: a thermochemical approach. J. Nucl. Mater., 152:301–309, 1988.
- [6.14] Eriksson G. Thermodynamic studies of high-temperature equilibria. 12. SOLGASMIX, A computer-program for calculation of equilibrium compositions in multiphase systems. Chemica Scripta. 1975; 8:100–103.
- [6.15] Shobu K. CaTCalc: New thermodynamic equilibrium calculation software. Calphad. 2009; 33:279–287.
- [6.16] Bale CW, Bélisle E, Chartrand P, Deckerov SA, Eriksson G, Hack K, Jung I-H, Kang YB, Melançon J, Pelton AD, Robelin C, Petersen S. FactSage thermochemical software and databases - recent developments. Calphad. 2009; 33:295–311.
- [6.17] Kozeschnik E, Buchmayr B. MatCalc – A simulation tool for multicomponent thermodynamics, diffusion and phase transformation kinetics. Mathematical Modelling of Weld Phenomena. 2001; 5:349–361.
- [6.18] Davies RH, Dinsdale AT, Gisby JA, Robinson JAJ, Martin SM. MTDATA - Thermodynamic and Phase Equilibrium Software from the National Physical Laboratory. Calphad. 2002; 26:229–271.



 RICERCA SISTEMA ELETTRICO	<u>Title:</u> Development of BE numerical tools for LFR design and safety analysis – Part 2	<u>Distribution</u> PUBLIC	<u>Issue Date</u> 12.12.2017	<u>Pag.</u>
	<u>Project:</u> ADP ENEA-MSE PAR 2016	<u>Ref.</u> ADPFISS-LP2-144	Rev. 0	221 di 300


- [6.19] Cao W, Chen S-L, Zhang F, Wu K, Yang Y, Chang YA, Schmid-Fetzer R, Oates WA. PANDAT software with PanEngine, PanOptimizer and PanPrecipitation for multi-component phase diagram calculation and materials property simulation. Calphad. 2009; 33:328–342.
- [6.20] Shi P, Engström A, Sundman B, Ågren J. Thermodynamic calculations and kinetic simulations of some advanced materials. Materials Science Forum. 2011; 675-677:961–974.
- [6.21] OpenCalphad web page at <http://www.opencalphad.org>, visited 1 August 2016.
- [6.22] Vigier J-F., Popa K., Tyrpekl V., Gardeur S., Freis D., Somers J., Interaction study between MOX fuel and eutectic lead-bismuth coolant, J.Nucl.Mater., 467, 2015, pp. 840-847.



 RICERCA SISTEMA ELETTRICO	<u>Title:</u> Development of BE numerical tools for LFR design and safety analysis – Part 2	<u>Distribution</u> PUBLIC	<u>Issue Date</u> 12.12.2017	<u>Pag.</u> 222 di 300
	<u>Project:</u> ADP ENEA-MSE PAR 2016	<u>Ref.</u> ADPFISS-LP2-144	Rev. 0	

(Page intentionally left blank)




 RICERCA SISTEMA ELETTRICO	<u>Title:</u> Development of BE numerical tools for LFR design and safety analysis – Part 2	<u>Distribution</u> PUBLIC	<u>Issue Date</u> 12.12.2017	<u>Pag.</u>
	<u>Project:</u> ADP ENEA-MSE PAR 2016	<u>Ref.</u> ADPFISS-LP2-144	Rev. 0	223 di 300

7 DEVELOPMENT AND VALIDATION OF DECAY HEAT MODELS INTO THE FRENETIC CODE


D. Caron, R. Bonifetto, S. Dulla, P. Ravetto, L. Savoldi, R. Zanino



 RICERCA SISTEMA ELETTRICO	<u>Title:</u> Development of BE numerical tools for LFR design and safety analysis – Part 2	<u>Distribution</u> PUBLIC	<u>Issue Date</u> 12.12.2017	<u>Pag.</u> 224 di 300
	<u>Project:</u> ADP ENEA-MSE PAR 2016	<u>Ref.</u> ADPFISS-LP2-144	Rev. 0	

(Page intentionally left blank)



 RICERCA SISTEMA ELETTRICO	<u>Title:</u> Development of BE numerical tools for LFR design and safety analysis – Part 2	<u>Distribution</u> PUBLIC	<u>Issue Date</u> 12.12.2017	<u>Pag.</u>
	<u>Project:</u> ADP ENEA-MSE PAR 2016	<u>Ref.</u> ADPFISS-LP2-144	Rev. 0	225 di 300

At Politecnico di Torino, the NEMO research group has been involved in the development of the Fast REactor NEutronics/Thermal-hydraulicS (FRENETIC) code for the simulation of coupled neutronic/thermal-hydraulic transients in liquid-metal-cooled fast reactors with the core arranged in closed hexagonal subassemblies^[7.1]. The code has the objective to provide computationally efficient, approximate solutions suitable for core design and/or safety analyses at a level of detail that is more refined than that which can be offered by traditional systems analysis codes. The neutronic module of FRENETIC solves the multigroup neutron diffusion equations with delayed neutron precursors while the thermal-hydraulic module of FRENETIC solves the conservation of mass, momentum and energy equations of the coolant and the fuel pins.

The work carried out in 2016 continues the development^{[7.1]-[7.6]} and validation^{[7.7]-[7.10]} of this computational tool that first began in the year 2011. The work performed during this year activity is focused on the further development of the neutronic module by developing and implementing an adaptive time step selection algorithm for the quasi-static method.

7.1 Background and references

The FRENETIC code is composed of a neutronic module and a thermal-hydraulic module, which are coupled in order to provide a multiphysics (neutronic/thermal-hydraulic) description of a nuclear reactor core with hexagonal subassemblies. The neutronic module of FRENETIC solves the neutron and delayed neutron precursor balance equations in the multigroup diffusion theory approximation. The thermal-hydraulic module of FRENETIC solves the monodimensional (axial) mass, momentum and energy conservations laws of the coolant, together with the one-dimensional (axial or radial) heat conduction equation in the fuel pins, separately for each subassembly. The subassemblies are then thermally coupled to each other in the horizontal plane, resulting in a quasi-three-dimensional model.

7.1.1 Neutronic module


The neutronic module of the FRENETIC code solves an appropriate form of the time-dependent neutron transport equation and delayed neutron precursor balance equations, which may be written as

$$\left\{ \begin{array}{l} \frac{1}{v(E)} \frac{\partial}{\partial t} \phi(\mathbf{r}, E, \boldsymbol{\Omega}, t) = [(\mathcal{L} + \mathcal{M}_p)\phi](\mathbf{r}, E, \boldsymbol{\Omega}, t) + \sum_{i=1}^R \frac{\chi_i(\mathbf{r}, E)}{4\pi} \lambda_i c_i(\mathbf{r}, t) \\ \quad + S(\mathbf{r}, E, \boldsymbol{\Omega}, t), \\ \frac{\chi_i(\mathbf{r}, E)}{4\pi} \frac{\partial}{\partial t} c_i(\mathbf{r}, t) = [\mathcal{M}_i \phi](\mathbf{r}, E, \boldsymbol{\Omega}, t) - \frac{\chi_i(\mathbf{r}, E)}{4\pi} \lambda_i c_i(\mathbf{r}, t), \\ \quad i = 1, \dots, R, \end{array} \right. \quad (7.1)$$

and subject to appropriate initial and boundary conditions. In Eqs. (7.1), ϕ is the time-dependent angular neutron flux, $\lambda_i \chi_i / 4\pi$ is the time-dependent emissivity of delayed neutrons in precursor family i of a total of R precursor families, S is the independent angular neutron source rate density, v is the neutron velocity and \mathcal{L} , \mathcal{M}_p and \mathcal{M}_i represent the Boltzmann operator, the prompt fission operator and the delayed fission operator for neutron precursor family i , respectively. In the absence of an external source of neutrons, Eqs. (7.1) are modified by dividing the macroscopic cross section for fission neutron production by the effective multiplication eigenvalue, k_{eff} , in order to account for an initial condition that possibly is off-critical.

The neutron and delayed neutron precursor balance equations, Eqs. (7.1), are simplified further through the application of the multigroup approximation to the energy dependence and the diffusion theory approximation to the angular dependence^[7.11]. The resulting multigroup diffusion equations are solved by



 RICERCA SISTEMA ELETTTRICO	<u>Title:</u> Development of BE numerical tools for LFR design and safety analysis – Part 2	<u>Distribution</u> PUBLIC	<u>Issue Date</u> 12.12.2017	<u>Pag.</u>
	<u>Project:</u> ADP ENEA-MSE PAR 2016	<u>Ref.</u> ADPFISS-LP2-144	Rev. 0	226 di 300

means of a nodal discretisation in space^[7.4] and direct numerical, quasi-static and point-kinetic discretisations in time^[7.5].

In addition to the models for the spatial-temporal behaviour of the neutron flux, the neutronic module of the FRENETIC code includes models for the spatial-temporal behaviour of the photon flux^[7.6], allowing to account for the spatial-temporal effects of gamma heating that result from the prompt and delayed production of photons in neutron-nuclear reactions. The time-dependent photon transport equation and delayed photon precursor balance equations are can be written as

$$\left\{ \begin{array}{l} \frac{1}{v_\gamma} \frac{\partial}{\partial t} \phi_\gamma(\mathbf{r}, E_\gamma, \boldsymbol{\Omega}_\gamma, t) = [\mathcal{L}_\gamma \phi_\gamma](\mathbf{r}, E_\gamma, \boldsymbol{\Omega}_\gamma, t) + [\mathcal{P}_{\gamma p} \phi](\mathbf{r}, E_\gamma, \boldsymbol{\Omega}_\gamma, t) \\ \quad + \sum_{i=1}^{R_\gamma} \frac{\zeta_i(\mathbf{r}, E)}{4\pi} \lambda_i g_i(\mathbf{r}, t) + S_\gamma(\mathbf{r}, E_\gamma, \boldsymbol{\Omega}_\gamma, t), \\ \frac{\zeta_i(\mathbf{r}, E_\gamma)}{4\pi} \frac{\partial}{\partial t} g_i(\mathbf{r}, t) = [\mathcal{P}_{\gamma i} \phi](\mathbf{r}, E_\gamma, \boldsymbol{\Omega}_\gamma, t) - \frac{\zeta_i(\mathbf{r}, E_\gamma)}{4\pi} \lambda_{\gamma i} g_i(\mathbf{r}, t), \\ \quad i = 1, \dots, R_\gamma, \end{array} \right. \quad (7.2)$$

subject to appropriate initial and boundary conditions. In Eqs. (7.2), ϕ_γ is the time-dependent angular photon flux, $\lambda_{\gamma i} \zeta_i g_i / 4\pi$ is the time-dependent emissivity of delayed photons in precursor family i of a total of R_γ precursor families, S_γ represents a possible independent external source of photons, v_γ is the photon velocity, \mathcal{L}_γ is the Boltzmann operator and $\mathcal{P}_{\gamma p}$ and $\mathcal{P}_{\gamma i}$ are the prompt and delayed neutron-induced photon production operators, respectively. The coupling of the neutron and delayed neutron precursor balance equations, Eqs. (7.1), and the photon and delayed photon precursor balance equations, Eqs. (7.2), occurs through the neutron-induced photon production terms.

The photon and delayed photon precursor balance equations, Eqs. (7.2), are simplified further (similarly to the case of neutrons) through the application of the multigroup approximation to the energy dependence and the diffusion theory approximation to the angular dependence. Therefore, the coupled systems of neutron and delayed neutron precursor balance equations and photon and delayed photon precursor balance equations, Eqs. (7.1) and Eqs. (7.2), respectively, can be solved using the numerical methods developed previously for the neutronics equations.

Knowledge of the time-dependent evolution of the neutron and photon fluxes on the phase space allows to compute the spatial-temporal distribution of the power density through the expression


$$p(\mathbf{r}, t) = [(\mathcal{E} + \mathcal{K})\phi](\mathbf{r}, t) + [\mathcal{K}_\gamma \phi_\gamma](\mathbf{r}, t), \quad (7.3)$$

where $\mathcal{E}\phi$ is the power density generated by fission, $\mathcal{K}\phi$ is the power density generated in neutron-nuclear interactions other than fission and $\mathcal{K}_\gamma \phi_\gamma$ is the power density generated in photon-nuclear interactions. The definition for the power provided in Eq. (7.3) implicitly accounts for delayed effects both of neutrons and of photons as a result of each being accompanied by a model for delayed emissions.

7.1.2 Thermal-hydraulic module

The thermal-hydraulic module of the FRENETIC code solves the time-dependent mass, momentum and energy conservation equations for the fuel and the coolant in each subassembly^[7.11]. For the coolant, the full set of conservation equations are considered^[7.12]



 RICERCA SISTEMA ELETRICO	<u>Title:</u> Development of BE numerical tools for LFR design and safety analysis – Part 2	<u>Distribution</u> PUBLIC	<u>Issue Date</u> 12.12.2017	<u>Pag.</u>
	<u>Project:</u> ADP ENEA-MSE PAR 2016	<u>Ref.</u> ADPFISS-LP2-144	Rev. 0	227 di 300

$$\begin{cases} \frac{D}{Dt} \rho_c(\mathbf{r}, t) = -\rho_c(\mathbf{r}, t) \nabla \cdot \mathbf{u}(\mathbf{r}, t) \\ \rho_c(\mathbf{r}, t) \frac{D}{Dt} \mathbf{u}(\mathbf{r}, t) = \nabla \cdot \hat{\boldsymbol{\sigma}}(\mathbf{r}, t) + \rho_c(\mathbf{r}, t) \mathbf{f}(\mathbf{r}, t) \\ \rho_c(\mathbf{r}, t) \frac{D}{Dt} e_c(\mathbf{r}, t) = \hat{\boldsymbol{\sigma}}(\mathbf{r}, t) : \nabla \mathbf{u}(\mathbf{r}, t) - \nabla \cdot \mathbf{q}_c(\mathbf{r}, t) + Q_c(\mathbf{r}, t) \end{cases} \quad (7.4)$$

where ρ_c is the mass density, \mathbf{u} is the velocity of the coolant and e_c is the internal energy per unit mass, $\hat{\boldsymbol{\sigma}}$ is the stress tensor of the coolant, \mathbf{f} is the applied external force per unit mass of the coolant, \mathbf{q}_c is the conduction heat flux and Q_c is the external heat source per unit volume, which includes heat transfer effects between the fuel and the coolant as well as between the channel walls and the coolant.

Under the hypothesis of immobile structures, the fuel is described by the heat conduction equation

$$\rho_f(\mathbf{r}, t) \frac{\partial}{\partial t} e_f(\mathbf{r}, t) = -\nabla \cdot \mathbf{q}_f(\mathbf{r}, t) + Q_f(\mathbf{r}, t) \quad (7.5)$$

where ρ_f is the mass density, e_f is the internal energy per unit mass, \mathbf{q}_f is the conduction heat flux and Q_f is the external source of thermal energy per unit time per unit volume, which includes heat transfer effects between the fuel and the coolant in addition to energy production due to fission. The system of equations for the coolant, Eqs. (7.4), is closed by assuming that the fluid obeys the hypotheses of Navier-Stokes and both Eqs. (7.4) and (7.5) make use of the Fourier hypothesis, with the assistance of the standard thermodynamic relations. Each of Eqs. (7.4) and (7.5) is rendered complete by imposing proper initial and boundary conditions, the specifics of which depend on the problem under consideration.


With the inclusion of appropriate heat transfer correlations, as well as relationships for the relevant thermophysical properties of the materials under consideration, Eq. (7.4) in one-dimensional form (along the channel axis) and Eq. (7.5) are solved simultaneously for a given channel by the finite element method in space and the theta method in time. As a result, single, average values of the fuel and coolant temperatures, coolant velocity and pressure are computed at each axial node of each channel. The individual one-dimensional channels are then thermally coupled to their adjacent neighbours in the two-dimensional horizontal plane, resulting in a three-dimensional, full-core model. In transient conditions, the inter-channel coupling is explicit with respect to the time.

7.1.3 Modules coupling and feedback models

The coupling between the two modules of the FRENETIC code is achieved by providing the spatial distribution of the fuel and coolant temperatures as output from the thermal-hydraulic module and input to the neutronic module while the spatial distribution of the power density is output from the neutronic module and input to the thermal-hydraulic module. As each module may operate on a different computational domain and/or computational mesh, further elaboration of the distributions by the receiving module is typically required. In the neutronic module, the received fuel and coolant temperatures are spatially averaged on the volume of the computational node and attributed to the entire homogeneous volume. In the thermal-hydraulic module, the received linear power distribution is localised in the appropriate region.

With the auxiliary of an appropriate temperature-dependent model for the macroscopic cross sections, this approach to the coupling allows to account for the relevant feedback effects on each of the neutronic and the thermal-hydraulic models; that is, on the macroscopic cross sections in the neutronic equations and on the



 RICERCA SISTEMA ELETTRICO	<u>Title:</u> Development of BE numerical tools for LFR design and safety analysis – Part 2	<u>Distribution</u> PUBLIC	<u>Issue Date</u> 12.12.2017	<u>Pag.</u>
	<u>Project:</u> ADP ENEA-MSE PAR 2016	<u>Ref.</u> ADPFISS-LP2-144	Rev. 0	228 di 300

heat source in the thermal-hydraulic equations. In the cross section model implemented in FRENETIC, each macroscopic cross section for each reaction in each energy group of each homogeneous material is assumed to be characterised by two state variables, the fuel temperature T_f and the coolant temperature T_c , resulting in a temperature-dependence of the form $\Sigma_{xg}^m(T_f, T_c)$ for reaction x in group g of homogeneous material m . In order to preserve generality, the temperature dependence may be read in tabular form, in which case the appropriate value of the macroscopic cross section for a given material is obtained through bivariate linear interpolation with respect to the fuel and the coolant temperatures that characterise the computational volume in which the material is present. Thus, the number of discrete evaluations of the macroscopic cross section that are necessary to properly describe its temperature dependence, as well as the manner in which the temperature dependence is generated, are both left as modelling parameters.

The algorithm according to which the coupling is performed differs between steady-state and transient analyses, as seen in Fig. 7.1 and in Fig. 7.2, respectively. In steady-state computations, the steady-state neutron and photon balance equations (Eqs. (7.1) and (7.2) where all the time derivatives are set equal to zero) and the steady-state thermal-hydraulics equations (Eqs. (7.4) and (7.5), with all time derivatives set equal to zero) are solved by fixed-point iteration until tolerances imposed on the variation of the power distribution and on the variation of the temperature distribution between successive iterations are simultaneously satisfied. In transient computations, the two sets of equations are solved in parallel and at each time step selected for the coupling, the power and the temperature distributions are exchanged without iteration, resulting in a coupling scheme which is explicit in time.

7.2 Body of the report concerning the ongoing activities

The neutronic module of the FRENETIC code employs a coarse mesh nodal method to solve the multigroup neutron diffusion equations both for direct and adjoint problems, as well as direct numerical, quasi-static and point kinetics solvers for dynamics problems. In this year activity, an automatic adaptive time-step selection methodology for the time steps of the quasi-static method has been developed and studied, allowing an accurate and efficient temporal integration of the balance equations for the neutron flux via the quasi-static method. The content presented in this paragraph has been published in Ref. [7.13].


7.2.1 Introduction

The quasi-static method for the solution of the neutron and delayed neutron precursor balance equations, Eqs. (7.1), is based on the factorisation of the neutron flux into the product of a time-dependent amplitude function T and a time- and phase-space-dependent shape function ψ as

$$\phi(\mathbf{r}, E, \boldsymbol{\Omega}, t) = T(t)\psi(\mathbf{r}, E, \boldsymbol{\Omega}, t), \quad (7.6)$$

which is rendered unique through the inclusion of an initial condition on the amplitude function and the application of a normalisation criterion on the shape function. Thanks to the factorisation, the unknowns of the problem, T and ψ , may be solved separately on their corresponding time scales. Substitution of the factorisation, Eq. (7.6), in the neutron and delayed neutron precursor balance equations, Eqs. (7.1), and projection on a time-independent, phase-space-dependent weight function leads to the system of equations to be solved for the amplitude



	<u>Title:</u> Development of BE numerical tools for LFR design and safety analysis – Part 2	<u>Distribution</u> PUBLIC	<u>Issue Date</u> 12.12.2017	<u>Pag.</u>
	<u>Project:</u> ADP ENEA-MSE PAR 2016	<u>Ref.</u> ADPFISS-LP2-144	Rev. 0	229 di 300

$$\left\{ \begin{array}{l} \frac{d}{dt}T(t) = \frac{\rho(t) - \tilde{\beta}(t)}{\Lambda(t)}T(t) + \sum_{i=1}^R \lambda_i \tilde{c}_i(t) + \tilde{s}(t) \\ \frac{d}{dt}\tilde{c}_i(t) = \frac{\tilde{\beta}_i(t)}{\Lambda(t)}T(t) - \lambda_i \tilde{c}_i(t), \quad i = 1, \dots, R, \end{array} \right. \quad (7.7)$$

where the integral kinetics parameters include: the effective neutron generation time Λ , the effective delayed neutron fraction of delayed neutron precursor family i , $\tilde{\beta}_i$, and the dynamic reactivity ρ . Instead, substitution of the factorisation, Eq. (7.6), into the neutron and delayed neutron precursor balance equations, Eqs. (7.1), and application of the product rule of differentiation leads to the system of equations to be solved for the shape

$$\left\{ \begin{array}{l} \frac{1}{v(E)} \frac{\partial}{\partial t} \psi(\mathbf{r}, E, \boldsymbol{\Omega}, t) = \left[\left(\mathcal{L} - \frac{1}{vT} \frac{dT}{dt} + \mathcal{M}_p \right) \psi \right](\mathbf{r}, E, \boldsymbol{\Omega}, t) \\ \quad + \frac{1}{T(t)} \sum_{i=1}^R \frac{\chi_i(\mathbf{r}, E)}{4\pi} \lambda_i c_i(\mathbf{r}, t) + \frac{1}{T(t)} S(\mathbf{r}, E, \boldsymbol{\Omega}, t), \\ \frac{\chi_i(\mathbf{r}, E)}{4\pi} \frac{\partial}{\partial t} c_i(\mathbf{r}, t) = T(t) [\mathcal{M}_i \psi](\mathbf{r}, E, \boldsymbol{\Omega}, t) - \frac{\chi_i(\mathbf{r}, E)}{4\pi} \lambda_i c_i(\mathbf{r}, t), \\ \quad i = 1, \dots, R, \end{array} \right. \quad (7.8)$$

The quasi-static method foresees that the amplitude equations are solved on the amplitude time steps, Δt_T (consistent with the neutron effective generation time), using integral kinetics parameters that are updated on the reactivity time steps, $\Delta t_\rho \geq \Delta t_T$, which are computed using a shape that is updated on the shape time steps, $\Delta t_\psi \geq \Delta t_\rho$. The neutron flux at any time is formulated through the factorisation, Eq. (7.6). The correct application of the quasi-static method is related to the appropriate selection of the time steps employed in the algorithm, as the time steps have direct consequences both on the accuracy of the computed solution and on the efficiency of the method. Consequently, an adaptive time step selection algorithm is a natural complement of the quasi-static approach to integration.

7.2.2 Adaptive selection of the shape time steps

The methodology for the adaptive selection of the shape time steps utilises an approach similar to the ones adopted in the numerical integration of ordinary differential equations^{[7.14], [7.15], [7.16]}. In the application to the quasi-static method, an important consideration regards the individuation and the proper characterisation of the error of the shape.


7.2.2.1 Fundamentals of adaptive step size control

Adaptive step size control for the numerical integration of initial value problems is based on the estimation and on the control of the local error (or, alternatively, the local truncation error) introduced by the numerical method. Consider the initial value Cauchy problem in the independent variable t , to be solved numerically. It can be demonstrated that the local error of a numerical method of order q is^[7.14]

$$e(t, h) = \Theta(t)h^{q+1} + \mathcal{O}(h^{q+2}), \quad (7.9)$$

where Θ is the norm of the principal error function and h is the step size. In general, it is not possible to provide an exact expression for the local error; consequently, an appropriate bound must be estimated. By



	<u>Title:</u> Development of BE numerical tools for LFR design and safety analysis – Part 2	<u>Distribution</u> PUBLIC	<u>Issue Date</u> 12.12.2017	<u>Pag.</u>
	<u>Project:</u> ADP ENEA-MSE PAR 2016	<u>Ref.</u> ADPFISS-LP2-144	Rev. 0	230 di 300

assuming that all step sizes used in the integration algorithm satisfy the requirements of consistency of the numerical method and by neglecting higher order terms, the local error may be estimated by

$$\hat{e}_n = \hat{\Theta}_{n-1} h_{n-1}^{q+1}, \quad (7.10)$$

where the circumflex indicates an estimated quantity and the subscript n denotes a discrete point at which the solution is computed. The indexing is such that the subscript of the time step corresponds to the point of departure, $h_n = t_{n+1} - t_n$, while a time-dependent quantity shares the index of the time at which it is evaluated, $\hat{e}_n = \hat{e}(t_n)$.

Under the assumption that, asymptotically, the norm of the principal error function is constant between successive steps, Eq. (7.10) leads to the standard automatic step size selection algorithm^{[7.14], [7.15], [7.16]}

$$\frac{h_n}{h_{n-1}} = \left(\frac{1}{\hat{r}_n} \right)^{1/(q+1)}, \quad (7.11)$$

where $\hat{r}_n \equiv \hat{e}_n / \varepsilon$ is the excess local error and ε is the tolerance on the local error. That is, the next step size is chosen to be exactly the value for which the resulting excess local error is foreseen to be equal to unity ($\hat{r}_{n+1} = 1$). The step size relationship in Eq. (7.11) is capable of automatically adjusting the step size on the basis of the behaviour of the solution and on the basis of the value of \hat{r}_n : when $\hat{r}_n < 1$, implying that a larger step size could be used in the integration algorithm without exceeding the specified tolerance, the second member of Eq. (7.11) is greater than one and the proposed step size is expanded with respect to the previous value; when $\hat{r}_n > 1$, implying that a smaller step size is required to achieve the requested tolerance, the second member of Eq. (7.11) is less than one and the proposed step size is contracted with respect to the previous value.

7.2.2.2 Estimates of the local error of the shape


The definition of the excess local error in the case of a time- and phase-space-dependent function f may be generalised according to

$$\hat{r}_n \equiv \frac{\left\| \hat{\Theta}(\mathbf{r}, E, \boldsymbol{\Omega}, t_{n-1}) \Delta t_{\psi, n-1}^{q+1} \right\|_{L^p}}{\varepsilon_f^{abs} + \varepsilon_f^{rel} \left\| \tilde{f}(\mathbf{r}, E, \boldsymbol{\Omega}, \tilde{t}) \right\|_{L^p}}, \quad (7.12)$$

where the principal error function $\hat{\Theta}$ is now time- and phase-space-dependent, \tilde{f} is a value of f (that possibly has undergone some form of further elaboration) evaluated on the interval $\tilde{t} \in [t_{n-1}; t_n]$ and ε_f^{abs} and ε_f^{rel} are the tolerances on the absolute local error and on the relative local error, respectively. The symbol $\|\cdot\|_{L^p}$ represents the L^p norm of the argument computed on the phase space.

Mathematics-based estimate. A purely mathematical approach to the estimate of the error of the shape involves the development of an analytical expression for the local error in the case of the implicit Euler method, which is the traditional method employed to integrate the shape in the quasi-static approach, followed by the development of an appropriate approximation for that expression. The reference shape at any time is considered to be the one obtained by the formal integration of the shape in time. The approximate shape is the one obtained by the solution of the shape equations according to the implicit Euler method. The



 RICERCA SISTEMA ELETTRICO	<u>Title:</u> Development of BE numerical tools for LFR design and safety analysis – Part 2	<u>Distribution</u> PUBLIC	<u>Issue Date</u> 12.12.2017	<u>Pag.</u>
	<u>Project:</u> ADP ENEA-MSE PAR 2016	<u>Ref.</u> ADPFISS-LP2-144	Rev. 0	231 di 300

local error is defined as the difference between the reference solution and the approximate solution, each evaluated at the end of the time step and under the assumption that the solution at the beginning of the time step is known exactly for both. Consequently, the local error in the mathematics-based estimate is

$$e(t_n, \Delta t_{\psi, n-1}) = \left\| -\frac{\Delta t_{\psi, n-1}^2}{2} \left[\frac{\partial^2}{\partial t^2} \psi(\mathbf{r}, E, \boldsymbol{\Omega}, t) \right]_{t=t_{n-1}} \right\|_{L^p} + \mathcal{O}(\Delta t_{\psi, n-1}^3). \quad (7.13)$$

By analogy to Eq. (7.9) and Eq. (7.10), the upper bound of the principal error function is given by

$$\hat{\Theta}(\mathbf{r}, E, \boldsymbol{\Omega}, t_{n-1}) = -\frac{1}{2} \left[\frac{\partial^2}{\partial t^2} \psi(\mathbf{r}, E, \boldsymbol{\Omega}, t) \right]_{t=t_{n-1}}, \quad (7.14)$$

with the second temporal derivative of the shape given by the first temporal derivative of the second member of the first of Eqs. (7.8), after multiplying by the velocity. The corresponding estimate of the excess local error of the solution is given by Eq. (7.12) with $\hat{\Theta}$ as specified in Eq. (7.14), $f=\psi$ and $q=1$.

Physics-based estimate. An alternative approach is based on physical intuition by recalling that the quasi-static approach is valid only on intervals of time over which the variation of the shape is small. Therefore, an appropriate quantity to be regulated is the amount by which the shape varies on the shape time step, which can be considered to be equivalent to regulating the deviation of the quasi-static solution from the point-kinetic solution. However, it may be the case that a weighted variation of the shape is a more relevant quantity to monitor rather than the shape alone, as in the quasi-static method, the separation of flux into the product of the amplitude and the shape is accompanied by the projection onto a phase-space-dependent weight function. The interpretation offered above allows to develop an estimate of the error of the shape in a manner analogous to the previous case: the reference shape is considered to be that obtained from the integration according to the quasi-static approach while the approximate shape is considered to be that obtained from the integration according to the point-kinetic approach, which is equal to the shape at the beginning of the shape time step. Introduction of a time-independent, phase-space-dependent weight function and application of the same definition as before, the local error in the physics-based estimate is


$$e(t_n, \Delta t_{\psi, n-1}) = \left\| -w(\mathbf{r}, E, \boldsymbol{\Omega}) \Delta t_{\psi, n-1} \left[\frac{\partial}{\partial t} \psi(\mathbf{r}, E, \boldsymbol{\Omega}, t) \right]_{t=t_{n-1}} \right\|_{L^p} + \mathcal{O}(\Delta t_{\psi, n-1}^2). \quad (7.15)$$

By analogy to Eq. (7.9) and Eq. (7.10), the upper bound of the principal error function is given by

$$\hat{\Theta}(\mathbf{r}, E, \boldsymbol{\Omega}, t_{n-1}) = -w(\mathbf{r}, E, \boldsymbol{\Omega}) \left[\frac{\partial}{\partial t} \psi(\mathbf{r}, E, \boldsymbol{\Omega}, t) \right]_{t=t_{n-1}}, \quad (7.16)$$

with the first temporal derivative of the shape given by the second member of the first of Eqs. (7.8), after multiplying by the velocity. The corresponding estimate of the excess local error of the solution is given by Eq. (7.12) with $\hat{\Theta}$ as specified in Eq. (7.16), $f=w\psi$ and $q=0$. The weight function present in the physics-based



 RICERCA SISTEMA ELETTICO	<u>Title:</u> Development of BE numerical tools for LFR design and safety analysis – Part 2	<u>Distribution</u> PUBLIC	<u>Issue Date</u> 12.12.2017	<u>Pag.</u>
	<u>Project:</u> ADP ENEA-MSE PAR 2016	<u>Ref.</u> ADPFISS-LP2-144	Rev. 0	232 di 300

estimate is arbitrary and its inclusion is not essential to the definition of the error metric; however, there exist motivations for choosing the weight function to be consistent with the weight function of the scalar products utilised to compute the integral parameters of the quasi-static formulation.

7.2.2.3 Control algorithm for the shape time steps

The step size selection strategy, Eq. (7.11), pertains to nominal conditions of the integration when the asymptotic model applies. However, other considerations are necessary in order to provide a complete description of the general requirements of an adaptive integration scheme, most of which pertain to operation outside of the asymptotic regime. These include, but are not limited to, the selection of the initial step size, the formulation of appropriate restart strategies, additional measures of stability for the nominal step size controller and limitations imposed by the equation solver in implicit methods. The complete procedure for the selection of the shape time step is summarised in Fig. 7.3 and reference can be made to [7.13]. The additional logic required in the case of the non-linear improved quasi-static method is not shown.

7.2.3 Adaptive selection of the reactivity time steps

In order for the reactivity time steps to sufficiently resolve the evolution of the integral kinetics parameters on the shape time step, an adaptive approach to the selection of the reactivity time steps may be required. In the quasi-static approach, it is common for the adjoint-weighted integral reaction rates per unit amplitude to be characterised by a quadratic evolution on the shape time step as a result of the assumption that the operators and the shape are linear functions of time on the shape time step. Thus, the numerator and the denominator of a generic integral parameter each acquire the form

$$h(\tau) = H_0 + H_1\tau + H_2\tau^2, \quad (7.17)$$

for $\tau \equiv (t-t_n)/\Delta t_{\psi,n} \in [0;1]$, which represents the dimensionless time relative to the beginning of the shape time step.

Consider the task of integrating the amplitude equations across the shape time step, which may be carried out using an unspecified number of reactivity time steps. Each reactivity time step is to be characterised by a set of constant integral kinetics parameters that represent accurately the behaviour of their variable counterparts on the entire reactivity time step. Starting from a generic time τ_p , the objective is to identify an interval $\delta \equiv \Delta t/\Delta t_{\psi,n}$ over which an integral parameter does not deviate by more than a specified tolerance ε_p with respect to its mean value on the interval $[\tau_p, \tau_p + \delta]$. This criterion imposed on the integral parameter can be formally written as


$$\frac{(\overline{\delta h^2})^{1/2}}{|\bar{h}|} < \varepsilon_p, \quad (7.18)$$

with the mean value

$$\bar{h} \equiv \frac{1}{\delta} \int_{\tau_p}^{\tau_p + \delta} d\tau' h(\tau'), \quad (7.19)$$

and the quadratic mean



 RICERCA SISTEMA ELETTRICO	<u>Title:</u> Development of BE numerical tools for LFR design and safety analysis – Part 2	<u>Distribution</u> PUBLIC	<u>Issue Date</u> 12.12.2017	<u>Pag.</u>
	<u>Project:</u> ADP ENEA-MSE PAR 2016	<u>Ref.</u> ADPFISS-LP2-144	Rev. 0	233 di 300

$$\overline{\delta h^2} \equiv \frac{1}{\delta} \int_{\tau_\rho}^{\tau_\rho + \delta} d\tau' [h(\tau') - \bar{h}]^2. \quad (7.20)$$

Substitution of the second degree polynomial that represents the behaviour of the numerator or the denominator of a generic integral kinetics parameter on the shape time step, Eq. (7.17), into the definitions of the mean value and the quadratic mean, Eq. (7.19) and Eq. (7.20), respectively, integration and substitution of the results of the integration into the criterion applied to the variation allowed of the numerator or the denominator of the integral kinetics parameter on the reactivity time step, Eq. (7.18), followed by squaring both members and grouping like terms, leads to a fourth degree polynomial in δ

$$\begin{aligned} & \left[-\varepsilon_\rho^2 (H_0 + H_1\tau_\rho + H_2\tau_\rho^2)^2 \right] + \left[-2\varepsilon_\rho^2 (H_0 + H_1\tau_\rho + H_2\tau_\rho^2) \left(\frac{1}{2}H_1 + H_2\tau_\rho \right) \right] \delta \\ & + \left[-2\varepsilon_\rho^2 (H_0 + H_1\tau_\rho + H_2\tau_\rho^2) \left(\frac{1}{3}H_2 \right) + \frac{1}{3} (1 - 3\varepsilon_\rho^2) \left(\frac{1}{2}H_1 + H_2\tau_\rho \right)^2 \right] \delta^2 \\ & + \left[(1 - 2\varepsilon_\rho^2) \left(\frac{1}{2}H_1 + H_2\tau_\rho \right) \left(\frac{1}{3}H_2 \right) \right] \delta^3 + \left[\frac{1}{5} (4 - 5\varepsilon_\rho^2) \left(\frac{1}{3}H_2 \right)^2 \right] \delta^4 < 0. \end{aligned} \quad (7.21)$$

The zeros of the inequality, $\delta_{h,k}$, $k=1, \dots, 4$, represent the intervals of time over which the criterion described in Eq. (7.18) is respected. Only the real positive solutions are physically significant and, in the interest of caution, only the minimum real positive solution is retained if multiple real positive solutions exist. The value of the reactivity time step employed in the actual integration of the amplitude equations is the minimum real positive solution that results from the application of the criterion, Eq. (7.18), individually to each of the integral kinetics parameters.


Additional logic is required in order to prevent the restitution of an unreasonably small time step from the inequality of Eq. (7.21) when $|h|$ is small in magnitude. The approach adopted involves the estimation of the reactivity time step for which the absolute variation of the amplitude does not exceed the tolerance imposed on the integral kinetics parameters and to utilise this value as the minimum acceptable reactivity time step. The idea is justified by the fact that in the general solution of the amplitude equations, the integral kinetics parameters appear as arguments to exponential functions; therefore, to restrict the relative variation of the amplitude is more stringent than to restrict the relative variation of the integral kinetics parameters themselves.

The complete procedure for the selection of the reactivity time step is summarized in Fig. 7.4. Although not written, it is assumed that the reactivity time step is subject to an additional limitation in order not to exceed the end of the shape time step.

7.2.4 Representative results

Results are presented for the application of the adaptive time step selection methodologies to two representative transients. The first is a point-like transient in which the methodology for the reactivity time steps is studied, while the second is a spatial-spectral transient in which the methodology for the shape time steps is analyzed.



 RICERCA SISTEMA ELETTRICO	<u>Title:</u> Development of BE numerical tools for LFR design and safety analysis – Part 2	<u>Distribution</u> PUBLIC	<u>Issue Date</u> 12.12.2017	<u>Pag.</u>
	<u>Project:</u> ADP ENEA-MSE PAR 2016	<u>Ref.</u> ADPFISS-LP2-144	Rev. 0	234 di 300

7.2.4.1 Point-like transient

The first transient is a purely point-like transient, designed specifically to study the adaptive time step selection algorithm for the reactivity time steps. The system under consideration is an infinite medium reactor characterised by one group of neutrons and one delayed neutron precursor family with the neutron lifetime $l_{\infty}=10^{-5}$ s, the delayed neutron fraction $\beta=700$ pcm and the delayed neutron precursor decay constant $\lambda=0.1$ s⁻¹. The reactor, which is initially critical, is subject to a linear perturbation of the multiplication eigenvalue of the form $k_{\infty}(t)=1+at$ for $t\in[0;\infty)$, with $a=700$ pcm·s⁻¹.

Results are presented in Tab. 7.1, which provides the amplitude at various times as a function of the tolerance imposed on the maximum allowed variation of each of the integral kinetics parameters with respect to their mean value on the reactivity time step. The reference solution for this problem is obtained by the analytical method of Smets^[7.17]. As is to be expected for a method that is based on the hypothesis of constant integral kinetics parameters but applied to a problem in which this hypothesis is not verified, it is observed that the solution of the amplitude equations converges to the analytical value as the tolerance on the allowed variation is reduced, thereby rendering the constant values of the integral kinetics parameters to be increasingly more characteristic of the entire reactivity time step to which they are applied.


In Tab. 7.2, the corresponding number of reactivity time steps is presented for the results reported in Tab. 7.1. As the tolerance is reduced, the number of reactivity time steps increases, following approximately $N_p \propto \varepsilon_p^{-1}$, which is the behaviour expected in the case of integral kinetics parameters whose numerators and denominators are linear functions of time. In all cases, the number of reactivity time steps required in equal intervals of time is always the greatest at the beginning of the transient and decreases as the time evolves. Notwithstanding the linearity of the perturbation, the effective integral kinetics parameters vary non-linearly as a result of being the ratio of two linear functions and smaller reactivity time steps are required early in the transient to represent the non-asymptotic behaviour.

7.2.4.2 Spatial transient

The second transient involves the continuous insertion of reactivity over a finite interval of time, after which it is maintained constant. The system under consideration is that of the benchmark source situation number six proposed by Ref. [7.18] and consists of a thermal reactor in slab geometry divided into three homogeneous regions and initially symmetric with respect to the centreline of the system, as shown in Fig. 7.5. The two materials are characterised by two group diffusion theory parameters and six delayed neutron precursor families. The boundary conditions are zero flux on the external surfaces and the initial conditions are those of criticality with the delayed neutron precursors in equilibrium with the flux. In the initial configuration, the system is characterised by an effective neutron generation time $\lambda_0=21.48$ μ s and an effective delayed neutron fraction $\beta_{eff,0}=750.0$ pcm. The transient, which differs slightly from that described in the benchmark specification, is initiated by linearly increasing the removal cross section of the lower energy group of region 1 by 3 % in 1 s, after which the configuration is maintained constant; after 1 s, the perturbation is reversed in the same manner by which it is incurred so that the system is returned to its initial configuration.

In order to obtain a reference solution, the problem is solved first by direct numerical integration using constant time steps on a fine discretisation of the time domain. Then, the problem is solved with the predictor-corrector quasi-static method employing the adaptive time step selection algorithms. In the calculations, the tolerance imposed on the iteration error of the flux equations (from which the shape is obtained) is set at 10^{-9} on the relative L^2 norm of the flux between successive iterations. Only the relative error test is applied in the quantification of the excess local error of the shape of the flux ($\varepsilon_f^{abs}=0$). Nominally, the safety factor utilised in the selection of the shape time step is $\theta=0.95$; the maximum absolute reactivity time step is unrestrained and the maximum absolute shape time step is $\Delta t_{v,max}=10$ s. Results are presented in



 RICERCA SISTEMA ELETTRICO	<u>Title:</u> Development of BE numerical tools for LFR design and safety analysis – Part 2	<u>Distribution</u> PUBLIC	<u>Issue Date</u> 12.12.2017	<u>Pag.</u>
	<u>Project:</u> ADP ENEA-MSE PAR 2016	<u>Ref.</u> ADPFISS-LP2-144	Rev. 0	235 di 300

Tab. 7.3, which indicates the total power as a function of time, of the quantity regulated and of the tolerance imposed on the variation of the error metric on the shape time step. The reference solution is that obtained by direct numerical integration of the flux and precursor balance equations. Regardless of the quantity regulated, each solution approaches the reference result as the tolerance is decreased.

In Tab. 7.4, the cumulative number of shape time steps required to arrive at the time indicated is shown. The relationship between the number of shape time steps and the tolerance on the variation of the shape more or less follows the ideal behaviour $N_{\psi} \propto \varepsilon_{\psi}^{-q}$, except in the presence of artificial limitations. In all cases, the occasional rejected shape step occurs predominantly during the phase of the transient that follows the approach to the nominal shape step size from the starting shape step size and the indications are that these step rejections could be avoided with the use of a lower safety factor. However, for higher values of the tolerances, more spurious rejections of shape time step occur also during asymptotic conditions. The rejections do not occur on the first shape time step, which implies that the procedure for the selection of the initial shape time step is cautious. Similarly, the number of rejected shape steps in succession is often only one, but never exceeds two, which indicates that the technique to estimate the order outside of the asymptotic region is appropriate.

The behaviours of the error estimates and of the shape step size are shown in Fig. 7.6. At the beginning of each phase of the transient, the excess local error begins at approximately one half of an order of magnitude less than unity, which is a result of the method by which the first shape time step is selected, after which the excess local error approaches and remains near the safety factor. This behaviour occurs until the shape step size adjustment is limited either by the maximum expansion factor or by the maximum absolute shape time step, in which case the excess local error decreases in time. Correspondingly, the shape time step contracts and expands smoothly, adjusting the contraction or expansion factor to the current conditions of the transient. On larger time scales, the shape time step continuously increases to its maximum permitted value, after which it remains constant. When the shape time step is limited, either by a maximum expansion factor or by a maximum absolute value, the excess local error decreases.

7.2.5 Conclusions and future work on time step adaptiveness


The numerical scheme for time step adaptiveness in the frame of neutronics quasi-static calculations have been successfully implemented into the FRENETIC code and tested, verifying its capabilities. The present multiphysics coupling of FRENETIC approach foresees a data exchange between the neutronic and thermal-hydraulic module at fixed time intervals, given as input at the beginning of the simulation. Therefore, further development of this work must include the modification of the coupling approach to allow for time step adaptiveness in the data exchange between modules, in order to fully exploit the benefit of the quasi-static approach in the neutronic calculations.

7.3 Role of the activity, general goals and future development

7.3.1 Role of the activity and general goals

The objective of the FRENETIC code project at Politecnico di Torino, as stated from the very beginning of its development work, is to provide a computational tool that “fills the gap” between the results that can be obtained by a system code, where the reactor code is typically described with zero- or one-dimensional models, and the results of very refined Monte Carlo neutronic simulations or CFD analysis of the single fuel element, which are usually computationally very intensive. The FRENETIC code is to be seen as a computationally efficient tool for the generation of approximate solutions suitable for core design and/or safety analyses.



 RICERCA SISTEMA ELETTRICO	<u>Title:</u> Development of BE numerical tools for LFR design and safety analysis – Part 2	<u>Distribution</u> PUBLIC	<u>Issue Date</u> 12.12.2017	<u>Pag.</u>
	<u>Project:</u> ADP ENEA-MSE PAR 2016	<u>Ref.</u> ADPFISS-LP2-144	Rev. 0	236 di 300

Through its ability to provide multidimensional analyses of the neutronic and thermal-hydraulic behaviour of the full core of a liquid-metal-cooled fast reactor, the FRENETIC code is capable to account for phase-space-dependent evolution of the distributions of neutronic and thermal-hydraulic quantities and thus allows a more comprehensive understanding of the consequences of a particular transient, giving the ability to know whether some arbitrary initiating event leads to a spatial/localized phenomena or not. As a consequence, the FRENETIC code can be used as a design support code for parametric analysis of liquid-metal cooled fast reactors and transient simulations. In this role, the FRENETIC code can be fruitfully interfaced with other codes of different complexities and level of detail in the frame of the LFR code platform envisaged by ENEA, since the information on the evolution of the distributions of the neutronic and thermal-hydraulic quantities can be of use for the identification of the limits of application of more simplified models adopted in system codes.


7.3.2 Future development

The continued development of the FRENETIC code aims the implementation of the physical models that have been identified as relevant for the behaviour of LFR, in order to expand the code simulation capabilities.

In the last couple of years, the validation activity carried out on the EBR-II^[7.10] core allowed to identify the need for the implementation of a model accounting for the photon production and corresponding heat deposition. This activity still needs further validation, especially for what regards the photon nuclear data to be used as input. Additional R&D activity is requested in the frame of the optimization of the quasi-statics, since its time adaptiveness is currently working for the neutronic module and needs to be coupled to the thermal-hydraulic module without losing its efficiency.

One of the main aspect currently requiring additional R&D work is the modelling of the thermal dilation of the core structures, as this mechanism of feedback is known to be of importance in liquid-metal-cooled fast reactors. Moreover, the modelling of the bypass flow distribution between fuel elements is of great importance, as it is necessary in order to assess the temperature field of the fuel elements encasing and therefore their thermomechanical behaviour. These aspects will be the focus of future R&D activities.



 RICERCA SISTEMA ELETTRICO	<u>Title:</u> Development of BE numerical tools for LFR design and safety analysis – Part 2	<u>Distribution</u> PUBLIC	<u>Issue Date</u> 12.12.2017	<u>Pag.</u> 237 di 300
	<u>Project:</u> ADP ENEA-MSE PAR 2016	<u>Ref.</u> ADPFISS-LP2-144	Rev. 0	


	reference	$\epsilon_p=10^{-5}$	$\epsilon_p=10^{-6}$	$\epsilon_p=10^{-7}$	$\epsilon_p=10^{-8}$
t [s]	T(t)/T(0) [-]	T(t)/T(0) [-]	T(t)/T(0) [-]	T(t)/T(0) [-]	T(t)/T(0) [-]
0.000	1.00000	1.00000	1.00000	1.00000	1.00000
0.001	1.00028	1.00029	1.00028	1.00028	1.00028
0.010	1.00858	1.00858	1.00858	1.00858	1.00858
0.100	1.10887	1.10888	1.10887	1.10887	1.10887
0.200	1.24786	1.24787	1.24786	1.24786	1.24786
0.300	1.42806	1.42809	1.42807	1.42806	1.42806
0.400	1.67042	1.67046	1.67042	1.67042	1.67042
0.500	2.01254	2.01261	2.01255	2.01255	2.01254
0.600	2.52922	2.52935	2.52923	2.52922	2.52922
0.700	3.39159	3.39186	3.39162	3.39160	3.39159
0.800	5.08633	5.08700	5.08639	5.08633	5.08633
0.900	9.62994	9.63240	9.63018	9.62996	9.62994
1.000	35.8596	35.8844	35.8621	35.8598	35.8596

Tab. 7.1 – Amplitudes, relative to the initial value, as a function of the time and of the tolerance on the maximum allowed variation of the integral kinetics parameters with respect to their mean value on the reactivity time step for the point-like transient [7.13].

time [s]	$\epsilon_p=10^{-5}$		$\epsilon_p=10^{-6}$		$\epsilon_p=10^{-7}$		$\epsilon_p=10^{-8}$	
	N_p	(ΔN_p)	N_p	(ΔN_p)	N_p	(ΔN_p)	N_p	(ΔN_p)
0.000	0	(0)	0	(0)	0	(0)	0	(0)
0.001	67	(67)	640	(640)	6367	(6367)	63640	(63640)
0.010	6368	(6301)	63641	(63001)	636367	(630000)	6363641	(6300001)
0.100	72838	(66470)	728341	(664700)	7283358	(6646991)	72833548	(66469907)
0.200	92848	(20010)	928436	(200095)	9284302	(2000944)	92842984	(20009436)
0.300	104553	(11705)	1045484	(117048)	10454779	(1170477)	104547754	(11704770)
0.400	112858	(8305)	1128531	(83047)	11285246	(830467)	112852421	(8304667)
0.500	119300	(6442)	1192947	(64416)	11929406	(644160)	119294021	(6441600)
0.600	124564	(5264)	1245579	(52632)	12455723	(526317)	124557191	(5263170)
0.700	129014	(4450)	1290079	(44500)	12900718	(444995)	129007138	(4449947)
0.800	132869	(3855)	1328627	(38548)	13286190	(385472)	132861858	(3854720)
0.900	136270	(3401)	1362629	(34002)	13626201	(340011)	136261962	(3400104)
1.000	139312	(3042)	1393044	(30415)	13930351	(304150)	139303459	(3041497)

Tab. 7.2 – Number of reactivity time steps as a function of the time and of the tolerance on the maximum allowed variation of the integral kinetics parameters with respect to their mean value on the reactivity time step for the point-like transient [7.13]; N_p : cumulative number of reactivity time steps; ΔN_p : differential number of reactivity time steps.




 RICERCA SISTEMA ELETTRICO	<u>Title:</u> Development of BE numerical tools for LFR design and safety analysis – Part 2	<u>Distribution</u> PUBLIC	<u>Issue Date</u> 12.12.2017	<u>Pag.</u> 238 di 300
	<u>Project:</u> ADP ENEA-MSE PAR 2016	<u>Ref.</u> ADPFISS-LP2-144	Rev. 0	

regulation of mathematical quantity					
	reference	$\varepsilon_{\psi}=10^{-3}$	$\varepsilon_{\psi}=10^{-4}$	$\varepsilon_{\psi}=10^{-5}$	$\varepsilon_{\psi}=10^{-6}$
t [s]	p(t)/p(0) [-]	p(t)/p(0) [-]	p(t)/p(0) [-]	p(t)/p(0) [-]	p(t)/p(0) [-]
0.0	1.00000	1.00000	1.00000	1.00000	1.00000
1.0	0.65904	0.65902	0.65904	0.65904	0.65904
2.0	0.63088	0.63085	0.63088	0.63088	0.63088
3.0	0.86221	0.86218	0.86221	0.86221	0.86221
4.0	0.88634	0.88628	0.88633	0.88634	0.88634
10.0	NA	0.92096	0.92098	0.92099	0.92099
100.0	NA	0.95077	0.95078	0.95079	0.95079
1000.0	NA	0.95192	0.95193	0.95193	0.95193

regulation of physical quantity					
	reference	$\varepsilon_{\psi}=10^{-3}$	$\varepsilon_{\psi}=10^{-4}$	$\varepsilon_{\psi}=10^{-5}$	$\varepsilon_{\psi}=10^{-6}$
t [s]	p(t)/p(0) [-]	p(t)/p(0) [-]	p(t)/p(0) [-]	p(t)/p(0) [-]	p(t)/p(0) [-]
0.0	1.00000	1.00000	1.00000	1.00000	1.00000
1.0	0.65904	0.65887	0.65903	0.65904	0.65904
2.0	0.63088	0.63072	0.63087	0.63088	0.63088
3.0	0.86221	0.86193	0.86220	0.86221	0.86221
4.0	0.88634	0.88471	0.88626	0.88634	0.88634
10.0	NA	0.92052	0.92094	0.92098	0.92099
100.0	NA	0.95067	0.95077	0.95078	0.95079
1000.0	NA	0.95182	0.95192	0.95193	0.95193

Tab. 7.3 – Total power, relative to the initial value, as a function of time, of the quantity regulated and of the tolerance imposed on the variation of the error metric on the shape time step for the spatial transient [7.13]; NA: reference solution not computed for the entire duration of the transient.



 RICERCA SISTEMA ELETTRICO	<u>Title:</u> Development of BE numerical tools for LFR design and safety analysis – Part 2	<u>Distribution</u> PUBLIC	<u>Issue Date</u> 12.12.2017	<u>Pag.</u> 239 di 300
	<u>Project:</u> ADP ENEA-MSE PAR 2016	<u>Ref.</u> ADPFISS-LP2-144	Rev. 0	

regulation of mathematical quantity								
time [s]	$\varepsilon_\psi=10^{-3}$		$\varepsilon_\psi=10^{-4}$		$\varepsilon_\psi=10^{-5}$		$\varepsilon_\psi=10^{-6}$	
	N_ψ	(N_ψ^R)	N_ψ	(N_ψ^R)	N_ψ	(N_ψ^R)	N_ψ	(N_ψ^R)
0.0	0	(0)	0	(0)	0	(0)	0	(0)
1.0	22	(4)	57	(3)	167	(3)	515	(5)
2.0	29	(4)	72	(6)	206	(7)	627	(9)
3.0	50	(20)	129	(9)	377	(9)	1158	(10)
4.0	58	(21)	150	(12)	434	(11)	1326	(12)
10.0	65	(21)	168	(12)	489	(11)	1499	(12)
100.0	79	(21)	198	(12)	574	(11)	1759	(12)
1000.0	170	(21)	289	(12)	674	(11)	1924	(12)


regulation of physical quantity								
time [s]	$\varepsilon_\psi=10^{-3}$		$\varepsilon_\psi=10^{-4}$		$\varepsilon_\psi=10^{-5}$		$\varepsilon_\psi=10^{-6}$	
	N_ψ	(N_ψ^R)	N_ψ	(N_ψ^R)	N_ψ	(N_ψ^R)	N_ψ	(N_ψ^R)
0.0	0	(0)	0	(0)	0	(0)	0	(0)
1.0	9	(0)	50	(1)	456	(4)	4523	(7)
2.0	11	(0)	55	(1)	496	(4)	4903	(7)
3.0	19	(4)	95	(11)	875	(5)	8674	(11)
4.0	20	(4)	99	(11)	904	(5)	8940	(11)
10.0	22	(4)	105	(11)	944	(5)	9329	(11)
100.0	31	(4)	116	(11)	987	(5)	9723	(11)
1000.0	122	(4)	207	(11)	1078	(5)	9866	(11)

Tab. 7.4 – . Number of shape time steps as a function of time, of the quantity regulated and of the tolerance imposed on the variation of the error metric on the shape time step for the spatial transient [7.13]; N_ψ : cumulative number of shape time steps; N_ψ^R : cumulative number of rejected shape time steps.

- 1: **require:** initialisation of power and temperature distributions
- 2: **while** convergence not realised **do**
- 3: exchange power and temperature distributions
- 4: evaluate macroscopic cross sections according to temperature distribution
- 5: { solve neutron balance equations
 { solve mass, momentum and energy balance equations
- 6: construct power distribution
- 7: compare solutions to those of the previous iteration
- 8: **end while**
- 9: **return**

Fig. 7.1 – FRENETIC steady-state solution algorithm.



 RICERCA SISTEMA ELETTRICO	<u>Title:</u> Development of BE numerical tools for LFR design and safety analysis – Part 2	<u>Distribution</u> PUBLIC	<u>Issue Date</u> 12.12.2017	<u>Pag.</u>
	<u>Project:</u> ADP ENEA-MSE PAR 2016	<u>Ref.</u> ADPFISS-LP2-144	Rev. 0	240 di 300


- 1: **require:** solution of steady-state problem, $t = 0$
- 2: **while** $t < t_{end}$ **do** $\{t_{end}$: simulation end time $\}$
- 3: exchange power and temperature distributions
- 4: evaluate macroscopic cross sections according to temperature distribution
- at t
- 5: $\left\{ \begin{array}{l} \text{integrate neutron and precursor balance equations to } t + \Delta t_c \\ \text{integrate mass, momentum and energy balance equations to } t + \Delta t_c \end{array} \right.$
- 6: construct power distribution at $t + \Delta t_c$
- 7: $t = t + \Delta t_c$ $\{\Delta t_c$: time step for coupling $\}$
- 8: **end while**
- 9: **return**

Fig. 7.2 – FRENETIC transient solution algorithm.

- 1: **require:** $n \geq 1$, $m \geq 0$ and $\Delta t_{\psi, n-1}^{(m)} > 0$
- 2: $\{\text{calculation of the proposed contraction or expansion factor}\}$
- 3: **if** $\hat{r}_n^{(m)} < 1$ **then** $\{\text{solution accepted}\}$
- 4: $\hat{f}_n = \left(\theta / \hat{r}_n^{(m)}\right)^{1/(q+1)}$
- 5: **else** $\{\text{solution rejected}\}$
- 6: **if** $m == 0$ **then** $\{\text{first rejection of solution}\}$
- 7: $\hat{f}_n = \left(\theta / \hat{r}_n^{(m)}\right)^{1/(q+1)}$
- 8: **else** $\{\text{successive rejections of solution}\}$
- 9: $\hat{q}^* = \log \left(\hat{r}_n^{(m)} / \hat{r}_n^{(m-1)}\right) / \log \left(\Delta t_{\psi, n-1}^{(m)} / \Delta t_{\psi, n-1}^{(m-1)}\right) - 1$
- 10: $\hat{q} = \min \left[\max \left[\hat{q}_{min}, \hat{q}^*\right], \hat{q}_{max}\right]$
- 11: $\hat{f}_n = \left(\theta / \hat{r}_n^{(m)}\right)^{1/(\hat{q}+1)}$
- 12: **end if**
- 13: $m = m + 1$
- 14: **end if**
- 15: $\{\text{limitation of the contraction or expansion factor}\}$
- 16: $f_n = \min \left[\max \left[f_{min}, \hat{f}_n\right], f_{max}\right]$
- 17: $\{\text{calculation and limitation of the time step}\}$
- 18: $\Delta t_{\psi, n} = \min \left[\max \left[\Delta t_{\psi, min}, f_n \Delta t_{\psi, n-1}^{(m)}\right], \Delta t_{\psi, max}\right]$
- 19: **return** $\Delta t_{\psi, n}$

Fig. 7.3 – Algorithm for shape time step selection [7.13].



 RICERCA SISTEMA ELETTRICO	<u>Title:</u> Development of BE numerical tools for LFR design and safety analysis – Part 2	<u>Distribution</u> PUBLIC	<u>Issue Date</u> 12.12.2017	<u>Pag.</u>
	<u>Project:</u> ADP ENEA-MSE PAR 2016	<u>Ref.</u> ADPFISS-LP2-144	Rev. 0	241 di 300

- 1: **require:** $\Delta t_\psi > 0$
- 2: {calculation of the time step for the individual integral kinetics parameters}
- 3: **for** all h **do** { h : numerator or denominator of an integral kinetics parameter}
- 4: compute $\delta_{h,k}$, $k = 1, \dots, 4$
- 5: $\delta_h = \min_k [\{\delta_{h,k}\} \mid \delta_{h,k} \in \mathbb{R}^+]$
- 6: **end for**
- 7: {calculation of the lower bound of the time step}
- 8: compute δ_T
- 9: {limitation of the minimum proposed ideal time step}
- 10: $\delta = \max [\delta_T, \min_h [\{\delta_h\}]]$
- 11: {calculation and limitation of the time step}
- 12: $\Delta t_\rho = \min [\max [\Delta t_{\rho,min}, \delta \Delta t_\psi], \Delta t_{\rho,max}]$
- 13: **return** Δt_ρ

Fig. 7.4 – Algorithm for reactivity time step selection.



Fig. 7.5 – Geometry of the system considered for the spatial transient [7.13].



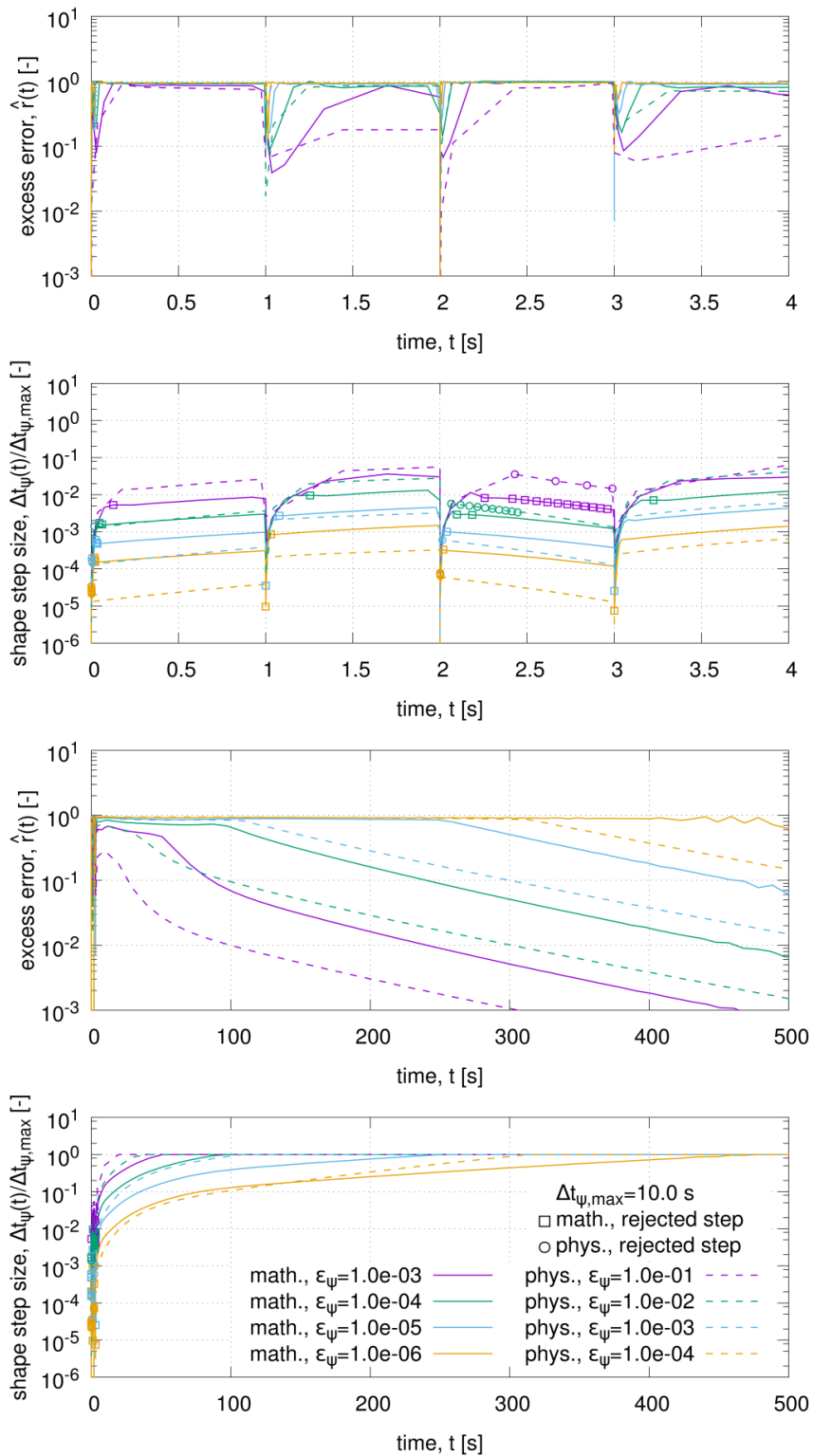



Fig. 7.6 – Error estimate and shape step size as a function of time, of the quantity regulated and of the tolerance for the continuous insertion of reactivity transient [7.13].




 RICERCA SISTEMA ELETTRICO	<u>Title:</u> Development of BE numerical tools for LFR design and safety analysis – Part 2	<u>Distribution</u> PUBLIC	<u>Issue Date</u> 12.12.2017	<u>Pag.</u>
	<u>Project:</u> ADP ENEA-MSE PAR 2016	<u>Ref.</u> ADPFISS-LP2-144	Rev. 0	243 di 300

7.4 List of References


- [7.1] R. Bonifetto, S. Dulla, P. Ravetto, L. Savoldi Richard and R. Zanino, “A full-core coupled neutronic/thermal-hydraulic code for the modeling of lead-cooled nuclear fast reactors,” *Nuclear Engineering and Design*, **261**, pp. 85-94, 2013.
- [7.2] R. Bonifetto, S. Dulla, P. Ravetto, L. Savoldi Richard and R. Zanino, “Progress in multi-physics modeling of innovative lead-cooled fast reactors,” *Transactions of Fusion Science and Technology*, **61**, pp. 293-297, 2012.
- [7.3] R. Bonifetto, S. Dulla, P. Ravetto, L. Savoldi Richard and R. Zanino, “Full-core coupled neutronic/thermal-hydraulic model of innovative lead-cooled fast reactors,” *Transactions of the American Nuclear Society*, **106**, pp. 630-632, 2012.
- [7.4] R. Bonifetto, D. Caron, S. Dulla, P. Ravetto, L. Savoldi Richard and R. Zanino, “Extension of the FRENETIC code capabilities to the three-dimensional coupled dynamic simulation of LFR,” Presented at the *16th International Conference on Emerging Nuclear Energy Systems (ICENES)*, Madrid, 26-30 May 2013, 2013.
- [7.5] D. Caron, S. Dulla and P. Ravetto, “New aspects in the implementation of the quasi-static method for the solution of neutron diffusion problems in the framework of a nodal method,” *Annals of Nuclear Energy*, **87**, pp. 34-48, 2016.
- [7.6] D. Caron, S. Dulla, P. Ravetto, L. Savoldi and R. Zanino, “Models and methods for the representation of decay and photon heat in spatial kinetics calculations,” *Proceedings of PHYSOR 2016: Unifying theory and experiments in the 21st century*, Sun Valley ID, 1-5 May 2016, pp. 2416-2425, 2016.
- [7.7] R. Zanino, R. Bonifetto, A. Ciampichetti, I. Di Piazza, L. Savoldi Richard and M. Tarantino, “First validation of the FRENETIC code thermal-hydraulic model against the ENEA integral circulation experiment,” *Transactions of the American Nuclear Society*, **107**, pp. 1395-1398, 2012.
- [7.8] R. Zanino, R. Bonifetto, A. Del Nevo, E. Martelli and L. Savoldi Richard, “Thermal-hydraulic code-to-code benchmark in a simplified EBR-II geometry,” *Transactions of the American Nuclear Society*, **109**, pp. 1759-1761, 2013.
- [7.9] R. Zanino, R. Bonifetto, A. Del Nevo and L. Savoldi, “Benchmark and preliminary validation of the thermal-hydraulic module of the FRENETIC code against EBR-II data,” *Proceedings of the International Topical Meeting on Advances in Thermal Hydraulics (ATH)*, Reno NV, 15-19 June 2014, pp. 173-187, 2014.
- [7.10] D. Caron, R. Bonifetto, S. Dulla, V. Mascolino, P. Ravetto, L. Savoldi, D. Valerio and R. Zanino, “Full-core coupled neutronic/thermal-hydraulic modelling of the EBR-II SHRT-45R transient,” *International Journal of Energy Research*, **In press**, 2016.
- [7.11] A. Henry, *Nuclear-reactor analysis*, MIT Press, Cambridge MA, 1975.
- [7.12] N. Todreas and M. Kazimi, *Nuclear systems*, Hemisphere, New York NY, 1990.
- [7.13] D. Caron, S. Dulla and P. Ravetto, “Adaptive time step selection in the quasi-static methods of nuclear reactor dynamics,” *Annals of Nuclear Energy*, **105**, pp. 266-281, 2017.
- [7.14] C. W. Gear, *Numerical initial value problems in ordinary differential equations*, Prentice-Hall, Englewood Cliffs NJ, 1971.
- [7.15] E. Hairer, S. P. Nørsett and G. Wanner, *Solving ordinary differential equations I: Nonstiff problems*, Springer, Berlin, 1987.



 RICERCA SISTEMA ELETTRICO	<u>Title:</u> Development of BE numerical tools for LFR design and safety analysis – Part 2	<u>Distribution</u> PUBLIC	<u>Issue Date</u> 12.12.2017	<u>Pag.</u>
	<u>Project:</u> ADP ENEA-MSE PAR 2016	<u>Ref.</u> ADPFISS-LP2-144	Rev. 0	244 di 300

- [7.16] E. Hairer and G. Wanner, *Solving ordinary differential equations II: Stiff and differential-algebraic problems*, Springer, Berlin, 1991.
- [7.17] H. B. Smets, “Exact solution of the reactor kinetics equations for linear, exponential, or reciprocal reactivity dependence on time,” *Mémoires de la Classe des sciences, Académie royale de Belgique, Collection in 8, 5^o*, **45**(3), 1959.
- [7.18] Benchmark Problem Committee, “Argonne Code Center: Benchmark problem book,” Technical report n. ANL-7416, Supplement 1, Argonne National Laboratory, Argonne IL, 1972.



 RICERCA SISTEMA ELETTRICO	<u>Title:</u> Development of BE numerical tools for LFR design and safety analysis – Part 2	<u>Distribution</u> PUBLIC	<u>Issue Date</u> 12.12.2017	<u>Pag.</u> 245 di 300
	<u>Project:</u> ADP ENEA-MSE PAR 2016	<u>Ref.</u> ADPFISS-LP2-144	Rev. 0	


8 DEVELOPMENT OF MULTI-PHYSIC CODE FOR LEAD-COOLED FAST REACTOR

A. Cammi, S. Lorenzi




POLITECNICO
MILANO 1863



 RICERCA SISTEMA ELETTRICO	<u>Title:</u> Development of BE numerical tools for LFR design and safety analysis – Part 2	<u>Distribution</u> PUBLIC	<u>Issue Date</u> 12.12.2017	<u>Pag.</u> 246 di 300
	<u>Project:</u> ADP ENEA-MSE PAR 2016	<u>Ref.</u> ADPFISS-LP2-144	Rev. 0	

(Page intentionally left blank)



 RICERCA SISTEMA ELETRICO	<u>Title:</u> Development of BE numerical tools for LFR design and safety analysis – Part 2	<u>Distribution</u> PUBLIC	<u>Issue Date</u> 12.12.2017	<u>Pag.</u>
	<u>Project:</u> ADP ENEA-MSE PAR 2016	<u>Ref.</u> ADPFISS-LP2-144	Rev. 0	247 di 300

8.1 Background and references

The activity is related to the development of a multi-physics code for Lead-cooled Fast Reactor (LFR). The multi-physics approach allows evaluating a wide set of core parameters (e.g., temperature field, velocity field, and neutron fluxes) with a unique simulation tools^{[8.1], [8.2], [8.3]}. This advantage may be valuable for core designing, when verifying the satisfaction of the operational constraints.

In particular, we present a multi-physics model for a lead fast reactor core-average channel, implemented in the general purpose finite-element software COMSOL Multiphysics, focusing on the coupling approach among the neutronic, the thermal-elastic and the fluid-dynamic phenomena

8.1.1 Multiphysics modelling

The LFR technology's severe design limits, along with a relatively low operational experience on heavy liquid metal cooled reactors, require dedicated tools of analysis to study the steady state and the transient behaviour of these GIF-IV systems. In this context, the Multi-Physics Modelling (MPM) approach is a promising tool for analysing the “reactor system”, both in operative and accidental conditions.

Traditionally, nuclear reactor analysis is performed by coupling neutron kinetics and thermal-hydraulic codes^{[8.4], [8.5]}. These coupled code techniques are often based on the operator-splitting technique, in which the single physics is solved by an independent, specialized code (e.g., the neutron kinetics code) and the solution is delivered as input for the other code (e.g., the thermal-hydraulics one) (Fig. 8.1). Due to the fact that these techniques usually are non-iterative, the nonlinearities due to the coupling are not resolved in a time step, possibly reducing the overall accuracy^[8.6]. On the other hand, this approach is still attractive due to the legacy of the mono-disciplinary code development. In this regards, it is interesting to notice that the Validation and Verification (V&V) performed on the single code cannot be transposed *tout-court* to the coupled system, the latter requiring a separate V&V procedure for the coupled simulations.


An alternative technique – used in this activity – is the implicit approach, which consists in solving in the same simulation environment the set of non-linear and time-dependent coupled partial differential equations of the different physics (neutronics, heat transfer, fluid dynamics, thermal-elasticity, etc.) in order to converge the nonlinearities at every time step and obtaining a tightly coupled solution^[8.6]. The implicit/tightly coupled solution can be achieved by two main family of techniques, the iterative and the fully-coupled ones. The former involves the iteration of the separate physics (Fig. 8.2) equation until convergence over the time step is reached (e.g., employing Picard iteration or Newton's method). The fully coupled techniques (Fig. 8.3) require the solution of a large monolithic matrix representing all the physics involved in the systems (e.g., using Jacobian-Free Newton-Krylov method). Both the approaches allow for higher-order coupling between the different physics, and make possible to perform solver iteration up to a desired degree of accuracy.

8.2 Body of the report concerning the ongoing activities

In this Section, the implicit multi-physics approach is adopted to study the behaviour of an LFR single-channel representative of the active-core average conditions (from now on referred to as core-average channel). Reference is made to the European Lead-cooled System (ELSY)^[8.7], developed in the frame of the EU-FP6-ELSY project.

The present work is focused on the coupling among neutronics, fluid dynamics, heat transfer, and thermal expansions. The multi-group neutron diffusion model, the CFD model, and the linear elasticity model are



 RICERCA SISTEMA ELETTRICO	<u>Title:</u> Development of BE numerical tools for LFR design and safety analysis – Part 2	<u>Distribution</u> PUBLIC	<u>Issue Date</u> 12.12.2017	<u>Pag.</u>
	<u>Project:</u> ADP ENEA-MSE PAR 2016	<u>Ref.</u> ADPFISS-LP2-144	Rev. 0	248 di 300

implemented in the same computational environment offered by the general purpose finite-element software COMSOL Multiphysics^[8,8]. For the CFD and the solid mechanics treatment, the models available in COMSOL are employed. On the other hand, for the neutronic treatment, a purpose-made six-group diffusion model is developed. This model is proved against the Monte Carlo code SERPENT^[8,9].

The proposed Multi-Physics (MP) model is adopted to investigate both the steady state conditions of the ELSY core-average channel, and two transients: an insertion of reactivity and a perturbed inlet lead temperature transient. Such transients are simulated both taking into account and neglecting the thermal expansion effects. Through these studies, the importance of thermal expansion effects is caught. It is also shown that the presented MP model represents a suitable simulation tool for a preliminary investigation of the LFR transient behaviour.

The Section is organised as follows. Sect. 8.2.1 describes how the different models are implemented in the MPM approach. The validation of the neutronic model is detailed in Sect. 8.2.2. In Sect 8.2.3, the results obtained by the present MP model are shown in terms of steady-state spatial distribution of some quantities of interest, and two case studies are presented to exemplify the MPM capabilities for simulating the transient behavior.

8.2.1 Multi-physics modelling approach.

In this section, the MP scheme of analysis is presented by describing the different equations adopted for neutronics, fluid dynamics, and heat transfer, and solved in the same simulation environment. Thermal expansion effects are included in such scheme via the equations of solid mechanics and combining them with the other physics, by means of the “moving mesh” technique.


System description

The single-channel layout chosen for the present study is based on the ELSY reactor with the Open Square Fuel Assembly (OSFA) design^{[8,7], [8,10]}. The core is arranged in 162 fuel assemblies, having fuel pins disposed in a square array, and surrounded by reflector assemblies. Such reactor features a core thermal power of about 1500 MWth. The inlet temperature of the lead, at nominal condition, is set equal to 400 °C, in order to avoid solidification. The outlet temperature of the lead, at nominal condition, is set to 480 °C in order to limit the corrosion of the structural and cladding materials that becomes significant at temperatures higher than 550 °C. The active-core diameter is equal to 4.65 m, and the active height is equal to 0.90 m. The proposed MP model is a two-dimensional axial-symmetric representation ($r; z$) of a single-channel, limited to the active height. Reference is made to the core average conditions at Beginning Of Life (BOL). Tab. 8.1 gives the main parameters of the presented model. Fig. 8.4a shows a transversal cross section of the analysed fuel pin. Fig. 8.4b represents the longitudinal ($r; z$) view of the modelled geometry (for clarity, the aspect ratio of the image is not preserved). An inactive channel length, below the active height, is adopted to allow for a complete lead flow development in order to avoid inaccurate estimation of the heat transfer between the lead and the cladding in the first centimeters of the active height. The evaluation of the effects related to the core radial expansion cannot be intrinsically caught by single channel analysis. The adoption of artificial corrective factors to take into account this effect is out of the scope of the present work.

Neutronics

The multi-group diffusion theory is employed in the neutronic model of the ELSY single-channel^[8,11]. Integrating over a set of six energy intervals (see Tab. 8.2) the continuous neutron diffusion equation, along with the balance equations for eight groups of precursors, the following set of partial differential equations is obtained:



 RICERCA SISTEMA ELETRICO	<u>Title:</u> Development of BE numerical tools for LFR design and safety analysis – Part 2	<u>Distribution</u> PUBLIC	<u>Issue Date</u> 12.12.2017	<u>Pag.</u>
	<u>Project:</u> ADP ENEA-MSE PAR 2016	<u>Ref.</u> ADPFISS-LP2-144	Rev. 0	249 di 300

$$\frac{1}{v_g} \frac{\partial \phi_g}{\partial t} = \nabla \cdot D_g \nabla \phi_g - \Sigma_{a,g} \phi_g - \sum_{g' \neq g} \Sigma_{s,gg'} \phi_{g'} + \sum_{g' \neq g} \Sigma_{s,g'g} \phi_{g'} + (1 - \beta) \chi_{p,g} \sum_{g'} (v \Sigma_f)_{g'} \phi_{g'} + \sum_i \chi_{d,g} \lambda_i c_i \quad (8.1)$$

$$\frac{\partial c_j}{\partial t} = -\lambda_j c_j + \beta_j \sum_g (v \Sigma_f)_g \phi_g \quad (8.2)$$

All the group constants are given in the COMSOL model as input. In the fuel, the dependency of the macroscopic neutron cross-sections on the local temperature and density is taken into account by means of the following equation:

$$\Sigma(T, \rho) = \left(\frac{\rho}{\rho_0} \right) \left[\Sigma_0 + \alpha \cdot \log \left(\frac{T}{T_0} \right) \right] \quad (8.3)$$

For the lead cross-sections, the above functional form is reduced to

$$\Sigma(T, \rho) = \left(\frac{\rho}{\rho_0} \right) \Sigma_0 \quad (8.4)$$

neglecting the Doppler broadening effects. For the sake of simplicity, the cross-sections are kept constant in the cladding, spring, plug, and thermal insulator domains. The functional forms of Eqs. (8.3) and (8.4) allow for the heterogeneity of temperature and density fields inside the core channel, in this way the thermal-hydraulic feedbacks on reactivity are caught. The accuracy of such simple approach will be assessed in Sect. 8.2.2.

Fluid dynamics and heat transfer

The model of the fluid flow (liquid lead) is based on the incompressible form of the Reynolds-Averaged Navier-Stokes (RANS) equations, considering in particular the standard k - ε turbulence model described by the following equations:

$$\nabla \cdot \mathbf{v} = 0 \quad (8.5)$$

$$\rho \frac{\partial \mathbf{v}}{\partial t} + \rho (\mathbf{v} \cdot \nabla) \mathbf{v} = \nabla \cdot \left[-p \mathbf{I} + (\eta + \eta_t) \left(\nabla \mathbf{v} + (\nabla \mathbf{v})^T - \frac{2}{3} k \mathbf{I} \right) \right] \quad (8.6)$$

$$\rho \frac{\partial k}{\partial t} + \rho (\mathbf{v} \cdot \nabla) k = \nabla \cdot \left[\left(\eta + \frac{\eta_t}{\sigma_k} \right) \nabla k \right] - \rho \varepsilon + \eta_t [\nabla \mathbf{v} : (\nabla \mathbf{v} + (\nabla \mathbf{v})^T)] \quad (8.7)$$


$$\rho \frac{\partial \varepsilon}{\partial t} + \rho (\mathbf{v} \cdot \nabla) \varepsilon = \nabla \cdot \left[\left(\eta + \frac{\eta_t}{\sigma_\varepsilon} \right) \nabla \varepsilon \right] - \frac{C_{\varepsilon 2} \rho \varepsilon^2}{k} + \frac{C_{\varepsilon 1} \eta_t \varepsilon}{k} [\nabla \mathbf{v} : (\nabla \mathbf{v} + (\nabla \mathbf{v})^T)] \quad (8.8)$$

The empirical constants are given as $C_{\varepsilon 1} = 1.44$, $C_{\varepsilon 2} = 1.92$, $C_\mu = 0.09$, $\sigma_k = 1.0$, $\sigma_\varepsilon = 1.3$.

The heat transfer model within the lead domain is described as follows:

$$\rho C_p \frac{\partial T}{\partial t} + \nabla \cdot [-(K + K_t) \nabla T] = \rho C_p \mathbf{v} \cdot \nabla T \quad (8.9)$$



 RICERCA SISTEMA ELETTRICO	<u>Title:</u> Development of BE numerical tools for LFR design and safety analysis – Part 2	<u>Distribution</u> PUBLIC	<u>Issue Date</u> 12.12.2017	<u>Pag.</u>
	<u>Project:</u> ADP ENEA-MSE PAR 2016	<u>Ref.</u> ADPFISS-LP2-144	Rev. 0	250 di 300

The turbulent thermal conductivity K_t is given by

$$K_t = \frac{C_p \eta_t}{Pr_t} \quad (8.10)$$

The turbulent Prandtl number Pr_t is calculated using the extended Kays-Crawford model^[8,12]:

$$Pr_t = \left[\frac{1}{2Pr_{t\infty}} + \frac{0.3}{\sqrt{Pr_{t\infty}}} \frac{C_p \eta_t}{K} - \left(0.3 \frac{C_p \eta_t}{K} \right)^2 (1 - e^{-K/0.3 C_p \eta_t Pr_{t\infty}}) \right]^{-1} \quad (8.11)$$

where

$$Pr_{t\infty} = 0.85 + \frac{100K}{C_p \eta (Re_\infty)^{0.888}} \quad (8.12)$$

and Re_∞ is set to $1.1 \cdot 10^5$.

As to the heat transfer modelling in the cladding, thermal insulator and plug materials, the following energy balance equation is adopted:

$$\rho C_p \frac{\partial T}{\partial t} = \nabla \cdot (K \nabla T) \quad (8.13)$$

with the corresponding values for the thermal conductivity, the density and the specific heat. Eq. (8.14) is adopted in the fuel domain:

$$\rho C_p \frac{\partial T}{\partial t} + \nabla \cdot (-K \nabla T) = Q \quad (8.14)$$

The volumetric heat source Q is explicitly computed, by means of the calculated neutron fluxes:

$$Q_f = \sum_g E_{f,g} \cdot \Sigma_{f,g} \cdot \phi_g \quad (8.15)$$


where $\Sigma_{f,g}$ are the macroscopic fission cross-sections, and E_f is the value of the average energy released per fission. The heat is considered to be released instantaneously and locally (i.e., disregarding gamma transport and delayed nuclear decay).

The heat transfer model takes into account the heat conduction and the radiative contribution across the helium gap between the fuel and the cladding. The radiative heat transfer is modelled by means of a heat flux from the fuel outer surface to the cladding inner surface as follows:

$$q(z)'' = \sigma_B \frac{1}{(1/\varepsilon_{fuel}) + (1/\varepsilon_{cladding}) - 1} [T_{fuel}^4(z) - T_{cladding}^4(z)] \quad (8.16)$$

where ε_{fuel} and $\varepsilon_{cladding}$ are the emissivities of the outer fuel surface and of the inner cladding surface, respectively. These values are kept constant during the simulations ($\varepsilon_{fuel} = 0.95$ and $\varepsilon_{cladding} = 0.5$).



 RICERCA SISTEMA ELETTRICO	<u>Title:</u> Development of BE numerical tools for LFR design and safety analysis – Part 2	<u>Distribution</u> PUBLIC	<u>Issue Date</u> 12.12.2017	<u>Pag.</u>
	<u>Project:</u> ADP ENEA-MSE PAR 2016	<u>Ref.</u> ADPFISS-LP2-144	Rev. 0	251 di 300

It is worth noting that the radiative contribution is computed locally at each node of the mesh at the outer boundary of the fuel and at the inner boundary of the cladding.

In order to speed up and simplify the calculations, effective and constant values of the thermo-physical properties C_p and K are adopted for the considered materials (Helium, MOX, UO₂, T91 steel and lead). It is noteworthy that the local value of temperature and density are adopted to compute the macroscopic cross-sections in order to intrinsically catch the thermal-hydraulic feedbacks on reactivity .

Solid mechanics and moving mesh

In order to take into account the fuel and cladding thermal expansion effects, the following equations of linear elasticity are introduced into the MP model:

$$\rho \frac{\partial^2 \mathbf{u}}{\partial t^2} = \nabla \cdot \boldsymbol{\sigma} \quad (8.17)$$

$$\boldsymbol{\epsilon} = \frac{1}{2} [\nabla \mathbf{u} + (\nabla \mathbf{u})^T] \quad (8.18)$$

$$\boldsymbol{\sigma} = \mathbf{C} : \left(\boldsymbol{\epsilon} - \alpha_{th} (T - T_{ref}) \right) \quad (8.19)$$


The coefficient of thermal expansion, as well as the Young modulus and the Poisson coefficient are kept constant with the temperature in order to simplify the problem solution. The Poisson coefficient and the Young modulus are used to derive the stiffness tensor \mathbf{C} under the isotropic material hypothesis. The column of fuel pellets is modelled as a unique continuous structure. Cracking, irradiation induced and other mechanical (e.g., creep) effects are neglected. The evaluation of such phenomena is beyond the scope of this work, which is focused on the intrinsic computation of the coupled effects involving the thermal expansion. The spring between the plug and the upper thermal insulator is simply modelled as a solid cylinder with a suitable Young modulus modified to reproduce the spring mechanical properties. For the sake of simplicity, the gravitational force is neglected.

The “moving mesh” technique offered by COMSOL allows deforming the mesh of the simulated domain. In the present work, the thermal-mechanical deformations are used to redefine the geometry, at each solver iteration. In this way, the different physics are influenced by the displacement field of the fuel and the cladding. Hence, the coupled effects due to thermal expansion (e.g., gap thermal resistance reduction, fuel expansion feedbacks on neutronics) are explicitly considered. Due to axial expansion of the fuel and the cladding, the two domains undergo high relative displacement during transients. This leads to a continuous change of the mesh boundary nodes facing each other across the gap. Such phenomenon gives rise to a computational concern for the radiative heat transfer model. To handle this issue, a boundary mapping is performed between the nodes of the fuel outer surface and the nodes of the cladding inner surface. In this way, at each time step, each node of the fuel outer boundary always interacts with the closest node belonging to the cladding inner boundary.

Boundary conditions

Below, the used boundary conditions are dealt with. Fig. 8.5a summarizes the main boundary conditions applied for the neutronic model. The present model is limited to a core single-channel. As a consequence, the choice of the neutronic boundary conditions is a relevant issue. The albedo boundary conditions are judged to be a suitable compromise between accuracy of the spatial characterization of the neutron fluxes and computational requirements. Albedo boundary conditions are imposed at the upper, lower and radial boundaries of the COMSOL model domain, namely:



	<u>Title:</u> Development of BE numerical tools for LFR design and safety analysis – Part 2	<u>Distribution</u> PUBLIC	<u>Issue Date</u> 12.12.2017	<u>Pag.</u>
	<u>Project:</u> ADP ENEA-MSE PAR 2016	<u>Ref.</u> ADPFISS-LP2-144	Rev. 0	252 di 300

$$\mathbf{n} \cdot (D_g \nabla \phi_g) = -\gamma_z \phi_g \quad (8.20)$$

$$\mathbf{n} \cdot (D_g \nabla \phi_g) = -\gamma_r \phi_g \quad (8.21)$$

Fig. 8.5b summarizes the main boundary conditions applied for the thermal-fluid dynamic model. A condition of thermal insulation is applied to the lower boundary of the lower thermal insulator and to the upper boundary of the steel plug. Symmetry conditions are considered at the outer radius of the fluid domain, accounting for the surrounding channel. At the lower boundary, the lead inlet velocity and temperature are imposed (T_{in} ; \mathbf{v}_{in}). In order to allow for a proper flow development below the active height, an inactive entrance channel 30 cm long is considered in the model. At the upper boundary of the fluid domain, the outlet boundary condition is applied, imposing the outlet pressure (p_{out}) and no viscous stress. The boundary condition at the interface between cladding and molten lead is treated by means of the standard wall function approach available in COMSOL^[8.8].

As far as the solid mechanics model is concerned, a condition of no axial displacement is applied to the lower boundaries of the lower thermal insulator and of the cladding domain. No radial displacement of the mesh is allowed at the outer radius of the channel. Within the lead domain, at the upper boundary, the moving mesh is forced to follow the cladding axial thermal expansion.

Numerical solution


The set of partial differential equations described above has been simultaneously solved by means of the “general-purpose” finite element software COMSOL Multiphysics. The geometry is meshed so as to achieve a good compromise between numerical accuracy and computational requirements. In particular, as shown in Fig. 8.6, a mapped mesh is judged suitable for the cladding and lead domains. A progressive mesh refinement near the wall is adopted in the lead domain (in green), while the fuel (in red) is meshed with triangular elements. The adopted elements are Lagrangian and quadratic-order. In order to reduce the computational cost of the simulation, the segregated solver is adopted. Tab. 8.3 shows the variables belonging to the different segregated groups. Segregated groups 1 to 4 are solved using the MULTifrontal Massively Parallel Sparse direct Solver (MUMPS). The equations of the RANS $k - \epsilon$ turbulence treatment are solved by means of the PARallel sparse Direct and multi-recursive Iterative linear SOLver (PARDISO). Transient analyses are treated with the implicit second order Backward Differentiation Formula (BDF) time integration method.

Neutronic input generation with SERPENT

The group constants (D_g , ν_g , β_i , $\nu \Sigma_{f,g}$, $\Sigma_{a,g}$, $\Sigma_{s,gg'}$, $\chi_{p,g}$, $\chi_{d,g}$) are calculated by means of the Monte Carlo neutron transport code SERPENT, using the nuclear data library JEFF 3.1 [8.13]. SERPENT is a three-dimensional continuous energy Monte Carlo neutron transport code, with group constant generation capabilities. The results presented in the following are obtained after runs of 250 million active neutron histories. Simulations consist in 500 active cycles of $5 \cdot 10^5$ neutrons subdivided in 32 parallel tasks. Fifty inactive cycles are adopted to allow for the convergence of the fission source distribution. Results related to reactivities are obtained by means of the k (multiplication factor) implicit estimate. Detectors with collision estimate of neutron flux are adopted to obtain the axial flux profiles.

As far as the SERPENT model is concerned, an infinite lattice of pins is simulated on the transversal (x ; y) plane. Infinite lead reflectors are adopted above the steel plug and below the lower thermal insulator.



 RICERCA SISTEMA ELETRICO	<u>Title:</u> Development of BE numerical tools for LFR design and safety analysis – Part 2	<u>Distribution</u> PUBLIC	<u>Issue Date</u> 12.12.2017	<u>Pag.</u>
	<u>Project:</u> ADP ENEA-MSE PAR 2016	<u>Ref.</u> ADPFISS-LP2-144	Rev. 0	253 di 300

The γ_z coefficient of Eq. (8.20) is calculated so as to have the same k_{eff} in both COMSOL and SERPENT models at nominal conditions. Then, the γ_r coefficient of Eq. (8.21) is set to allow for the radial leakage term and calculated so as to bring the system critical.

Tab. 8.4 gives the isotopic composition of the input materials.

An ad-hoc Octave^[8.14] procedure is developed for the conversion of the neutronic input for the different materials (i.e., fuel, lead, cladding, insulators and spring) from the SERPENT output to a COMSOL readable format. The procedure automatically produces a set of temperature and density dependent cross-sections and diffusion coefficients, according to Eqs. (8.3) and (8.4). The other neutronic parameters (i.e., ν_g , β_i , $\chi_{p,g}$, $\chi_{d,g}$), which are calculated at nominal conditions, are kept constant during the simulations.

8.2.2 Verification of the multi-physics neutronic model

Verification of the macroscopic cross-sections functional form

In the following, a brief discussion about the suitability of functional forms of Eqs. (8.3) and (8.4) is presented. For this purpose, the deterministic ECCO cell code^[8.15] is employed to evaluate the macroscopic cross-sections over a wide range of fuel and lead temperatures and densities. Subsequently, the data are compared with the macroscopic cross-sections calculated according to the Eq. (8.3). The choice of a deterministic code for this particular analysis is mainly due to its low computational requirements and the absence of statistical scattering of the points in the following comparisons.

Fig. 8.7a shows the fuel macroscopic capture cross-sections versus temperature, for the energy group 3. This group is chosen as the most representative because almost 40% of the neutrons belong to the energy range between 0.82 MeV and 67.38 keV, in nominal conditions. The macroscopic cross-sections of the other energy groups exhibit a similar behaviour and are not shown for brevity. For such analysis the fuel density is kept constant at nominal value (10.46 g/cm³). The α coefficient of Eq. (8.3) is calculated as follows:

$$\alpha = \frac{\Sigma_2 - \Sigma_1}{\log(T_2/T_1)} \quad (8.22)$$


where T_1 is 900 K, T_2 is 1500 K, Σ_1 and Σ_2 are the macroscopic cross-sections evaluated at these temperatures. As it can be seen in Fig. 8.7a, the logarithmic approximation well estimates the evaluated cross-sections over a wide range of temperatures.

Fig. 8.7b shows the fuel macroscopic capture cross-sections versus the fuel density, for the energy group 3. For such analysis the fuel temperature is kept at 1200 K. As shown in Fig. 8.7b, Eq. (8.3) well predicts the cross-sections dependence on the ratio ρ/ρ_0 .

In Sect. 8.2.1, it was mentioned that the functional form expressed by Eq. (8.4) is adopted for the calculation of the macroscopic cross-sections in the lead domain. Fig. 8.8a and Fig. 8.8b show the lead macroscopic capture cross-sections versus the lead temperature and density, respectively, for the energy group 3. As it can be deduced by comparing the two figures, the effect forced by the temperature variation is one order of magnitude lower than the one caused by the density variation. It is worth mentioning that the density range employed in Fig. 8.8b is calculated from the temperature range considered in Fig. 8.8a, according to the lead thermal expansion coefficient:

$$\rho = \rho_0 [1 - \beta_{\text{lead}}(T - T_0)] \quad (8.23)$$



 RICERCA SISTEMA ELETRICO	<u>Title:</u> Development of BE numerical tools for LFR design and safety analysis – Part 2	<u>Distribution</u> PUBLIC	<u>Issue Date</u> 12.12.2017	<u>Pag.</u>
	<u>Project:</u> ADP ENEA-MSE PAR 2016	<u>Ref.</u> ADPFISS-LP2-144	Rev. 0	254 di 300

The use of approximation expressed by Eq. (8.4) is acceptable for the lead domain, according to the purpose of the work.

Verification of the adopted neutron diffusion model

After assessing the cross-section functional dependence, the overall multi-group diffusion model implemented in COMSOL is assessed against the SERPENT code by comparing, for several cases, the multiplication factor k_{eff} . For this comparison, the albedo γ_r coefficient in COMSOL is set equal to zero, in order to simulate an infinite lattice of pins, as in SERPENT. The γ_z coefficient is kept constant and calculated in order to have the same k_{eff} both in SERPENT and COMSOL codes at nominal conditions. Within the COMSOL environment, the eigenvalue solver is employed to estimate the k_{eff} . The analysed cases can be summarized as follows:

- Fuel temperature ranging from 900 K to 1800 K, the other material properties and the geometry are kept at nominal condition.
- Fuel axial expansion varying from -0.5% to +1% of the nominal active length², the other material properties are kept at nominal condition.
- Lead density variation from -2% to +1% of the nominal density³, the other material properties and the geometry are kept at nominal condition.

For this study, two nuclear data libraries are adopted, namely: JEFF 3.1^[8.13] and ENDFb VII^[8.16]. The set of group constants employed as input in the COMSOL model is generated by means of a SERPENT run at nominal conditions with both libraries.


Fig. 8.9 shows the k_{eff} of the infinite lattice of pins predicted by COMSOL and SERPENT versus the fuel temperature. COMSOL results are presented in solid and dashed lines, while SERPENT results are depicted with bullets with an error bar of ± 2 standard deviations. As it can be seen in Fig. 8.9, the COMSOL neutronic model results have a good agreement with the Monte Carlo predictions. Despite the difference between the absolute k_{eff} estimates given by the two libraries, the trend of the curves is similar. Fig. 8.10a and Fig. 8.10b show the predicted k_{eff} versus the fuel axial expansion and the lead density variation, respectively. In these cases, the differences between COMSOL and SERPENT are greater than the previous case, but still acceptable for the preliminary evaluation of the coupled effects involving thermal-mechanical expansion in the fuel pin. For brevity, only results obtained employing the nuclear data library is JEFF 3.1 are shown in the following. Fig. 8.11a and Fig. 8.11b show the total neutron fluxes calculated by the two codes versus the z-coordinate and their relative difference, respectively. As it can be seen in Fig. 8.11a, the flux profiles appear in good agreement. Fig. 8.11b shows that the difference between the flux computed by the COMSOL model and the SERPENT code is higher than the statistical uncertainty of the Monte Carlo run. The error in the COMSOL estimation is higher nearby the upper and lower interfaces. However, the maximum error is lower than 4%.

In conclusion, the adoption of the six-group diffusion approach in the MP model appears to be a reasonable approximation for analysing the ELSY single-channel.

² These values correspond approximately to a fuel temperature ranging from 750 K to 2100 K.

³ These values correspond approximately to a lead temperature ranging from 600 K to 900 K.



 RICERCA SISTEMA ELETTRICO	<u>Title:</u> Development of BE numerical tools for LFR design and safety analysis – Part 2	<u>Distribution</u> PUBLIC	<u>Issue Date</u> 12.12.2017	<u>Pag.</u>
	<u>Project:</u> ADP ENEA-MSE PAR 2016	<u>Ref.</u> ADPFISS-LP2-144	Rev. 0	255 di 300

8.2.3 Results and discussion

Steady state behaviour of the system

In this Section, the capability of the proposed MP model to evaluate, in the same computational environment, the most relevant variables of the coupled physics is exploited to analyse the nominal steady-state behaviour of the system.

Fig. 8.12a shows the spatial description of temperature field. The maximum fuel temperature is reached quite above the mid of the active height. The fuel temperature profile reflects the axial shape of the neutron flux. Nevertheless, a certain asymmetry in the temperature field is due to the heat transfer with the lead, whose temperature grows along the channel length. Fig. 8.12b shows the cladding outer temperature and lead bulk temperature versus the z-coordinate, at nominal power conditions, useful for a preliminary verification of the respect of the temperature constraint (about 550 °C). The maximum difference between the cladding outer surface temperature and the lead bulk temperature, of about 15 °C, is reached at the mid active height, where the neutron flux features its maximum value.

Fig. 8.13a shows results from the fluid-dynamic analysis, specifically, the velocity field in the lead domain. It can be noticed that the employed inactive inlet channel allows for the complete hydro-dynamic development of the fluid flow. It is worth recalling that the model is focused on the active height, and the modelling of the whole channel (e.g., lower plenum, diagrid, etc.) is beyond the aim of this work. The modelled inactive channel is only accounted for the proper lead flow development, in order to avoid an inaccurate estimation of the heat transfer between the lead and the cladding, within the first centimeters of the active height. The lead velocity at the wall is not zero in Fig. 8.13a, due to the wall function treatment available in COMSOL.

In Fig. 8.13b, the effects of the thermal expansions of fuel and cladding, leading axially to a different gap reduction, are clearly visible. The gap thermal resistance undergoes a sensible variation along the axial coordinate, being lower at the mid-height, where the power generation is higher. This is typically neglected when simulations are performed by means of the conventional coupling of neutronic and thermo-hydraulic codes^[8,17]. Such figure presents an example of the potentialities provided by the fully-coupling between neutronics and thermal-elasticity.


Transient behaviour of the system

In this sub-section, two scenarios are considered as examples of the MPM potential to investigate the reactor transient behaviour, namely: an insertion of reactivity and a perturbed inlet lead temperature transient. For each of the two scenarios, transient analyses are performed both with and without thermal expansion effects. In the latter case, the displacement field is kept at nominal power conditions (i.e., not at room temperature conditions). This comparison allows appreciating the importance of the thermal expansion modelling in transient analyses.

Reactivity insertion

A step-wise insertion of reactivity (150 pcm) is simulated. Fig. 8.14a shows the system response to the reactivity insertion in terms of total pin power. The solid line represents the simulation without considering the thermal expansion effects, while the dashed line represents the simulation in the presence of these effects. An insertion of reactivity leads to a keff greater than one. As a consequence, the power begins to rise, as shown in Fig. 8.14a, with a prompt effect on the fuel temperature (Fig. 8.14b), whose increase corresponds to a negative feedback limiting the power to a maximum value, which is almost two times the nominal value. The negative temperature feedback is given by two major contributions: the Doppler effect, and the thermal expansion effect. The first contribution acts on the neutron cross-sections and is taken into account as discussed in Sect. 8.2. The thermal expansion feedback on neutronics is due to the reduction of the fuel-to-



 RICERCA SISTEMA ELETTRICO	<u>Title:</u> Development of BE numerical tools for LFR design and safety analysis – Part 2	<u>Distribution</u> PUBLIC	<u>Issue Date</u> 12.12.2017	<u>Pag.</u>
	<u>Project:</u> ADP ENEA-MSE PAR 2016	<u>Ref.</u> ADPFISS-LP2-144	Rev. 0	256 di 300

coolant mass ratio and is intrinsically modelled by the moving mesh technique. When considered, the axial expansion of the fuel gives further negative feedback, by lowering the maximum peak and the stationary power level, and the fuel temperature. When comparing the two analyses (with and without thermal expansion), notwithstanding that the Doppler effect plays the major role in limiting the power rise, the thermal effects lead to a sensible difference of the end-of-transient power levels.

Fig. 8.15a shows the fuel column (fuel and thermal insulators) relative axial expansion compared to the nominal power conditions. As expected, thermal expansion promptly follows the temperature rise. Thermal expansion also leads to an average gap size reduction of about 10%, as shown in Fig. 8.15b, reducing the overall gap thermal resistance by a similar value (in the present work, the helium thermal conductivity is kept constant).

Fig. 8.16 shows the cladding outer surface temperature at different instants during the reactivity insertion transient. Such insertion of 150 pcm (about 0.4 β) gives rise to an increase of about 40 °C of the maximum cladding temperature in few seconds. This figure points out the potential of the MPM approach to describe in detail point-wise values of important quantities during transient analysis.

Perturbed inlet lead temperature

In this case study, the inlet lead temperature is raised by 20 °C in one second. Fig. 8.17a shows the system response to the transient in terms of total pin power. Initially, a positive reactivity is inserted by the hot lead entering the channel, as effect of the lower lead density, which increases the fuel-to-coolant mass ratio. This causes a rise in the power level. After few seconds, the increase of the fuel temperature (Fig. 8.17b) smoothly reduces the reactivity and stabilises the power level to a value lower than the initial one.


Also in this transient, the fuel thermal expansion effects are significant (see Fig. 8.17a and Fig. 8.17b): the final pin power level and the final fuel average temperature variations are reduced of about 0.2 kW (~ 50%) and 5 °C (~ 60%), respectively, when compared to the simulation without considering the thermal expansion effects. Fig. 8.18 shows the cladding outer surface temperature at different instants during the perturbed lead inlet temperature transient. The hotter coolant causes an increase of the cladding outer surface temperature at the beginning of the active height. The perturbation propagates along the z-axis with a delay related to the lead velocity (about 1.2 m/s) and the system thermal inertial. It is worth recalling that, in this work, the diagrid expansion is not simulated. This effect may play a significant role reducing the reactivity of the system^[8,10].

8.2.4 Nomenclature

Latin symbols

C	stiffness tensor, Pa	K_t	lead turbulent thermal conductivity, $W m^{-1} K^{-1}$
c_i	concentration of the i th precursor group, m^{-3}	K^{-1}	
C_p	specific heat, $J kg^{-1} K^{-1}$	n	surface normal unit vector, -
$C_{\varepsilon 1}$	$k - \varepsilon$ model empirical constant, -	p	fluid pressure, Pa
$C_{\varepsilon 2}$	$k - \varepsilon$ model empirical constant, -	p_{out}	outlet pressure, Pa
C_{μ}	$k - \varepsilon$ model empirical constant, -	Pr_t	turbulent Prandtl number, -
D	neutron diffusion coefficient, m	$Pr_{t\infty}$	maximum turbulent Prandtl number defined in Eq. (8.12), -
E_f	average energy released per fission, J	Q	volumetric heat source, $W m^{-3}$
I	identity matrix, -	$q(z)$	radiative heat flux, $W m^{-2}$
k	turbulent kinetic energy, $m^2 s^{-2}$	r	radial coordinate, m
k_{eff}	effective neutron multiplication factor, -	Re_{∞}	free stream Reynolds number used in Eq. (8.12), -
K	thermal conductivity, $W m^{-1} K^{-1}$	t	time, s



 RICERCA SISTEMA ELETTTRICO	<u>Title:</u> Development of BE numerical tools for LFR design and safety analysis – Part 2	<u>Distribution</u> PUBLIC	<u>Issue Date</u> 12.12.2017	<u>Pag.</u>
	<u>Project:</u> ADP ENEA-MSE PAR 2016	<u>Ref.</u> ADPFISS-LP2-144	Rev. 0	257 di 300

T	temperature, K
T_{cladding}	cladding inner surface temperature, K
T_{fuel}	fuel outer surface temperature, K
T_{in}	inlet lead temperature, K
T_{ref}	reference temperature used in Eq. (8.19), K
T_0	reference temperature used in Eqs. (8.3) and (8.23), K
T_1	generic temperature used in Eq. (8.22), K
T_2	generic temperature used in Eq. (8.22), K
u	displacement vector, m
v	velocity vector, m s^{-1}
v_g	neutron speed of the gth group, m s^{-1}
v_{in}	inlet lead velocity, m s^{-1}
x	Cartesian x-coordinate of the SERPENT model, m
y	Cartesian y-coordinate of the SERPENT model, m
z	axial coordinate, m

Greek symbols

α_{th}	linear thermal expansion coefficient, K^{-1}
α	coefficient used in Eq. (8.3), -
β	total delayed neutron fraction, -
β_i	delayed neutron fraction of the ith precursor group, -
$\beta_{\text{lead}}^{\text{K}^{-1}}$	volumetric lead thermal expansion coefficient, K^{-1}
γ_r	radial albedo coefficient used in Eq. (8.21), -
γ_z	axial albedo coefficient used in Eq. (8.20), -
ε	turbulent dissipation rate, $\text{m}^2 \text{s}^{-3}$
$\varepsilon_{\text{cladding}}$	cladding inner surface emissivity, -
$\varepsilon_{\text{fuel}}$	fuel outer surface emissivity, -
ϵ	strain tensor, -

η	lead dynamic viscosity, Pa s
η_t	lead eddy viscosity ($= \rho C_{\mu} K^2 / \varepsilon$), Pa s
λ_i	decay constant of the ith precursor group, s^{-1}
ν	average number of neutrons emitted per fission, -
ρ	density, kg m^{-3}
ρ_0	reference density used in Eqs. (8.3), (8.4), and (8.23), kg m^{-3}
σ	Cauchy stress tensor, Pa
σ_B	Stefan Boltzmann constant, $\text{W m}^{-2} \text{K}^{-4}$
σ_e	k – ε model empirical constant, -
σ_k	k – ε model empirical constant, -
Σ	macroscopic cross-section, m^{-1}
Σ_a	macroscopic absorption cross-section, m^{-1}
Σ_f	macroscopic fission cross-section, m^{-1}
$\Sigma_{s,gg'}$	macroscopic group transfer cross-section (from group g to g'), m^{-1}
$\Sigma_{s,g'g}$	macroscopic group transfer cross-section (from group g' to g), m^{-1}
Σ_0	reference macroscopic cross-section used in Eqs. (8.3) and (8.4), m^{-1}
Σ_1	generic macroscopic cross-section used in Eq. (8.22), m^{-1}
Σ_2	generic macroscopic cross-section used in Eq. (8.22), m^{-1}
ϕ	neutron flux, $\text{m}^{-2} \text{s}^{-1}$
$\chi_{d,g}$	fraction of delayed neutrons generated in the gth group, -
$\chi_{p,g}$	fraction of prompt neutrons generated in the gth group, -

Subscripts


g	g^{th} neutron energy group, -
---	---

8.3 Role of the activity, general goals and future development

The activity is the first step for the development of a multi-physics code for lead-cooled fast reactor aimed at supporting both the design choice and the verification of other numerical tools. This tool is meant to represent an additional tool to be used in combination with the classic system codes in order to give a deeper insight about the complex physical phenomena occurring in the reactor (and their mutual interactions). When the purpose is to consider multiple phenomena, the coupling between single-physics code is not the optimal way to solve the phenomena due to the explicit exchange of data. The latter does not allow resolving the non-linearities of the system, lowering the accuracy of the model (and in general the efficiency). The explicit coupling approach has also some limitation in taking advantage of the present computational resources, usually not being suitable for parallel computation.


Even if the model simulates a single-channel a LFR, it takes into account the main physical phenomena – and their couplings – occurring within the reactor during an accidental time scale (neutronics, thermal-hydraulics and thermo-mechanics). The work has been useful also in order to evaluate the modelling approach of the different physics and how to couple the different phenomena (e.g., the neutronics and the thermal elasticity).



 RICERCA SISTEMA ELETTRICO	<u>Title:</u> Development of BE numerical tools for LFR design and safety analysis – Part 2	<u>Distribution</u> PUBLIC	<u>Issue Date</u> 12.12.2017	<u>Pag.</u>
	<u>Project:</u> ADP ENEA-MSE PAR 2016	<u>Ref.</u> ADPFISS-LP2-144	Rev. 0	258 di 300

Near-term efforts will be made in selecting a development platform which can make possible an efficient use of the available computational resources (i.e., parallelization) and allows an easy modification of the modelling description in order to be adjusted on the specific modelling needs and for a multi-user development. On this regard, the OpenFOAM library seems to be a promising tool. OpenFOAM is an open source library for numerical simulation in continuum mechanics using Finite Volume Method. The toolkit is very flexible thanks to the object-oriented programming, allowing users to customize, extend and implement complex physical model^{[8,18], [8,19]}. OpenFOAM grants the parallelization of the developed solvers thanks to dedicated routines based on geometrical domain decomposition. Consequently, future developments will be devoted to develop a multi-physics platform in OpenFOAM, starting with simple geometry (e.g., a fuel pin, which modelling strategy has been investigated in this activity and will guide the implementation in OpenFOAM) but aiming at representing more complex geometry.



 RICERCA SISTEMA ELETTRICO	<u>Title:</u> Development of BE numerical tools for LFR design and safety analysis – Part 2	<u>Distribution</u> PUBLIC	<u>Issue Date</u> 12.12.2017	<u>Pag.</u> 259 di 300
	<u>Project:</u> ADP ENEA-MSE PAR 2016	<u>Ref.</u> ADPFISS-LP2-144	Rev. 0	

Average linear power	23.5 kW m ⁻¹
Inlet lead temperature	400 °C
Outlet lead temperature	480 °C
Inlet lead velocity	1.6 m s ⁻¹
Pu enrichment	17 vol:%
Fuel density	95 %TD
Fuel pin active height	900 mm
Fuel pellet hole diameter	2.0 mm
Fuel pellet outer diameter	9.0 mm
Cladding inner diameter	9.3 mm
Cladding outer diameter	10.5 mm
Pin-pitch	13.9 mm
UO2 thermal insulator height	20 mm
Spring height	50 mm
Upper plug height	50 mm
Inactive channel length	300 mm

Tab. 8.1 – Main parameters of the analysed core single-channel [8.10]

Group number	Upper boundary		Lower boundary	
1	20	MeV	2.23	MeV
2	2.23	MeV	0.82	MeV
3	0.82	MeV	67.38	keV
4	67.38	keV	16.03	keV
5	16.03	keV	0.75	keV
6	0.75	keV	0	keV

Tab. 8.2 – Energy structure adopted in multi-group neutron diffusion

Group		Variables
1	ϕ_1, \dots, ϕ_6	neutron fluxes
2	c_1, \dots, c_6	precursors density
3	T, \mathbf{u}	temp. and displacement
4	p, \mathbf{v}	pressure and velocity
5	k, ε	turbulence variables

Tab. 8.3 – Segregated groups employed in the numerical solution.

Fuel		T91	Steel	Lead	
Isotope	wt%	Isotope	wt%	Isotope	wt%
U-234	0.002	Si-nat	0.50	Pb-204	1.4
U-235	0.295	V-nat	0.25	Pb-206	24.1
U-238	72.479	Cr-nat	9.00	Pb-207	22.1
Pu-238	0.364	Mo-nat	1.00	Pb-208	52.4
Pu-239	8.839	Fe-nat	88.30		
Pu-240	4.197	Ni-nat	0.13	Thermal Insulator	
Pu-241	0.949	Mn-55	0.60	Isotope	wt%
Pu-242	1.197	Nb-93	0.10	U-238	88.32
O-16	11.678	C-nat	0.12	O-16	11.68

Tab. 8.4 – Isotopic composition of the SERPENT input materials.



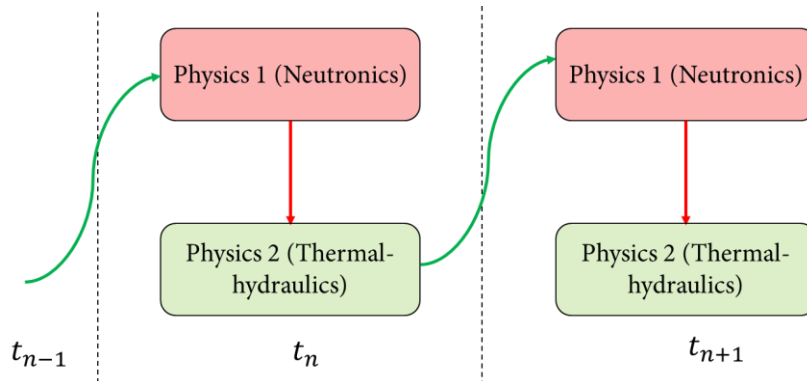


Fig. 8.1 – Explicit Operator Splitting approach in multi-physics modelling.

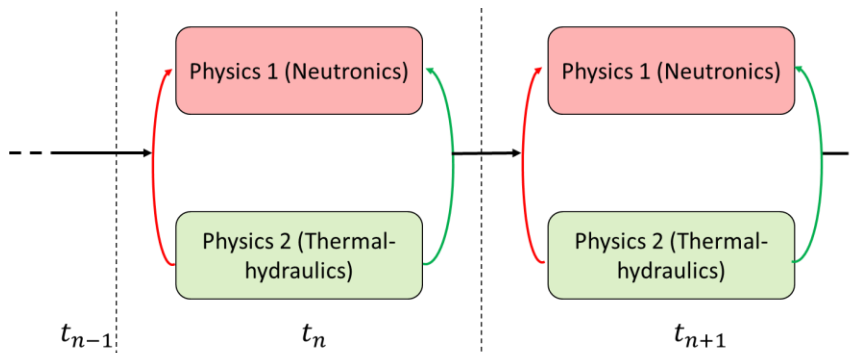


Fig. 8.2 – Implicit iterative approach in multi-physics modelling.

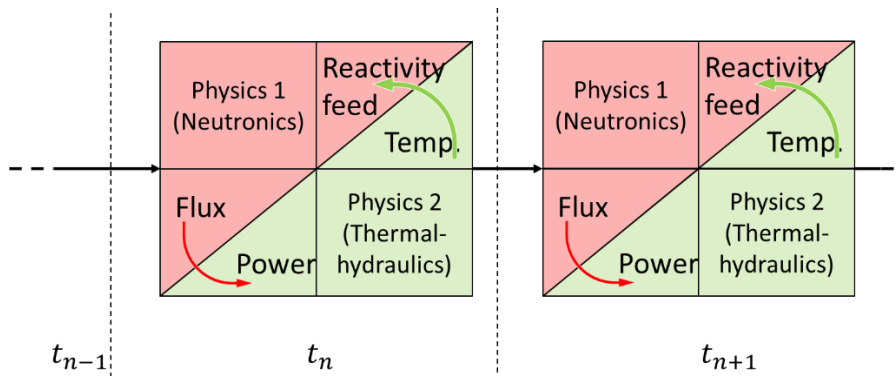


Fig. 8.3 – Implicit fully coupled (or monolithic) approach in multi-physics modelling.





Fig. 8.4 – (a) Analysed fuel pin and surrounding lead. Radial sizes at nominal conditions (room temperature), expressed in mm. (b) Longitudinal (r ; z) view of the modelled geometry.

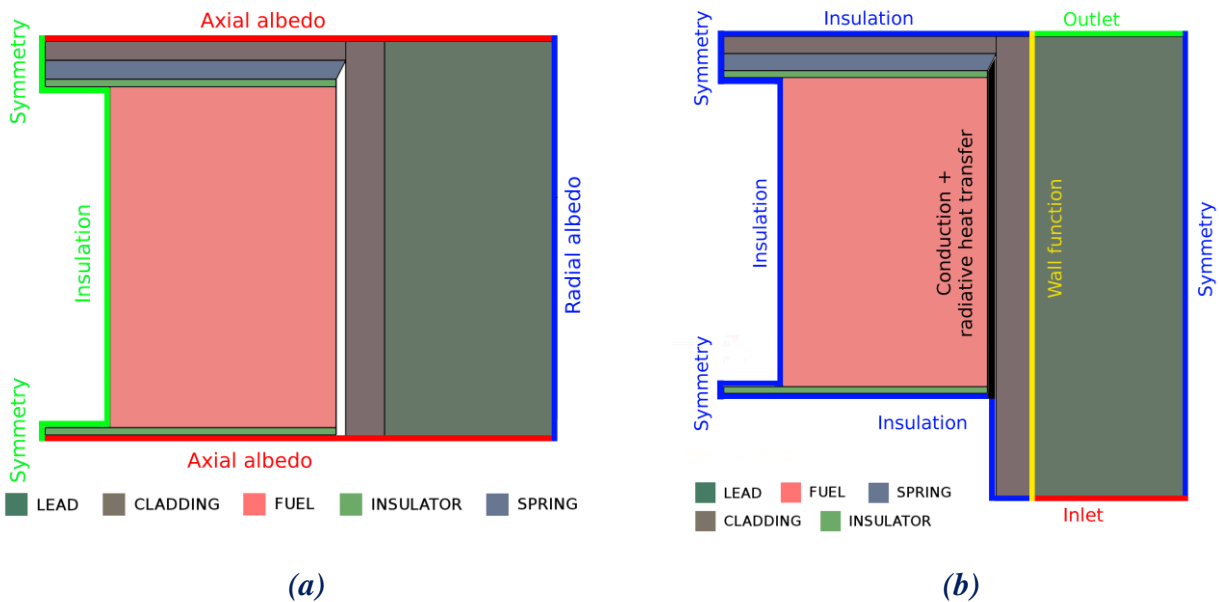


Fig. 8.5 – (a) Main boundary conditions applied for the neutronic model. (b) Main boundary conditions applied for the thermal-fluid dynamic model.

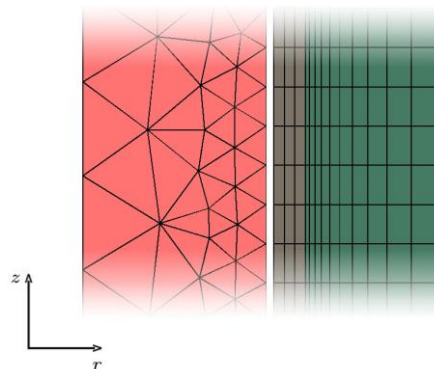


Fig. 8.6 – Meshed geometry.



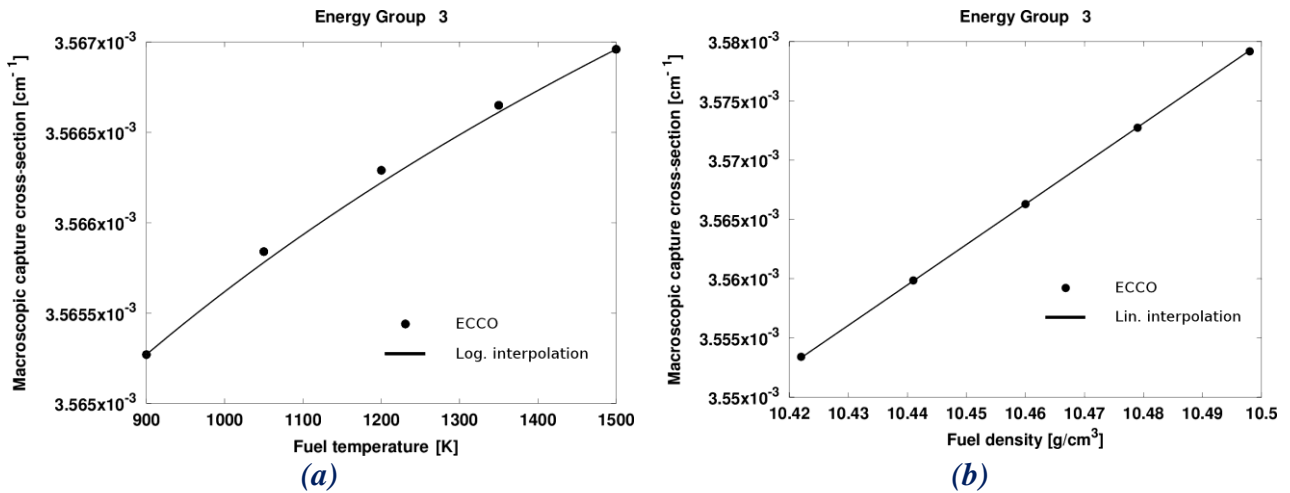


Fig. 8.7 – (a) Fuel macroscopic capture cross-section versus temperature of energy group 3. (b) Fuel macroscopic capture cross-section versus density of energy group 3.

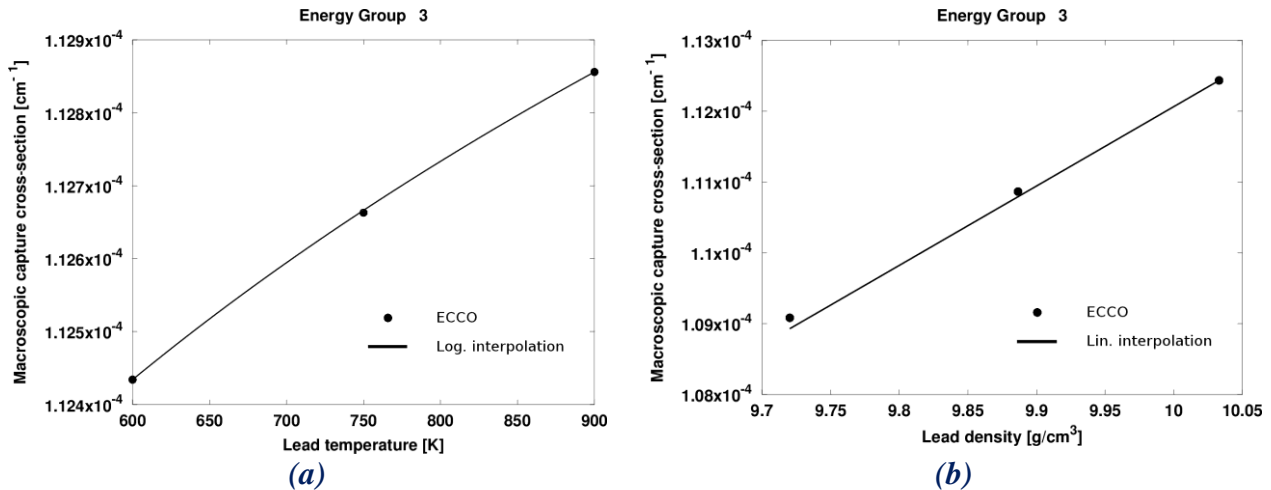


Fig. 8.8 – (a) Lead macroscopic capture cross-section versus temperature of energy group 3. (b) Lead macroscopic capture cross-section versus density of energy group 3.

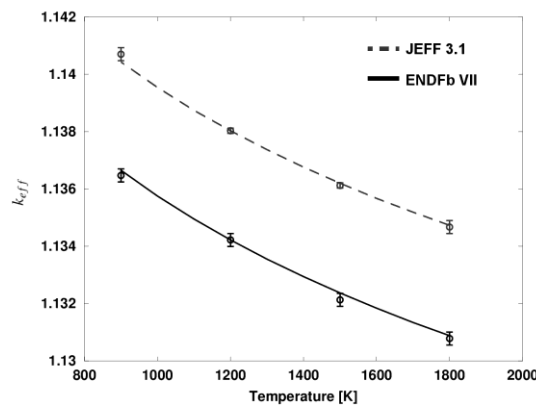
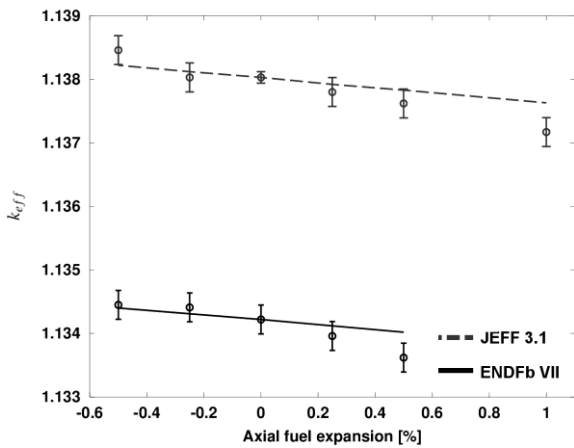
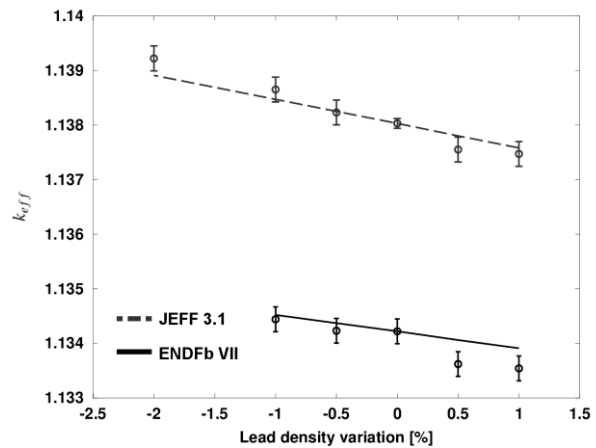


Fig. 8.9 – k_{eff} estimate versus fuel temperature. SERPENT: bullets, COMSOL: lines.



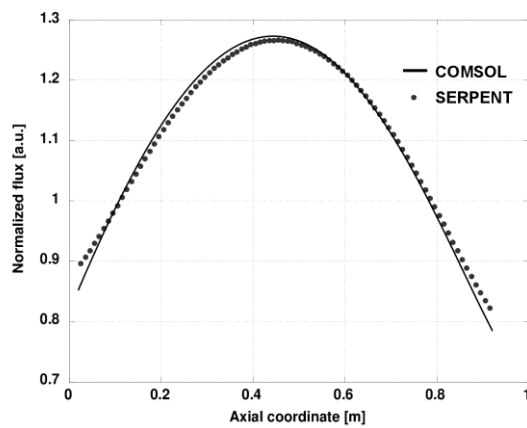


(a)

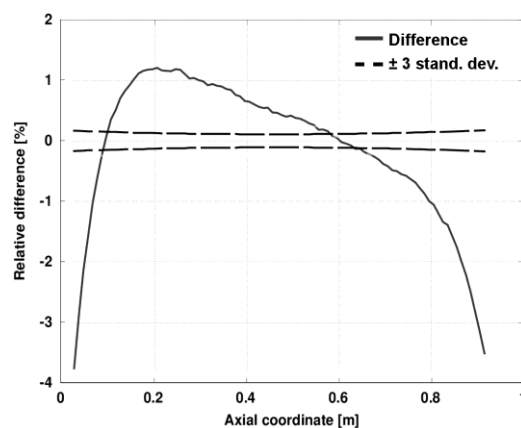


(b)

Fig. 8.10 – (a) k_{eff} estimate versus relative fuel axial expansion. SERPENT: bullets, COMSOL: lines. (b) k_{eff} estimate versus lead density variation. SERPENT: bullets, COMSOL: lines.



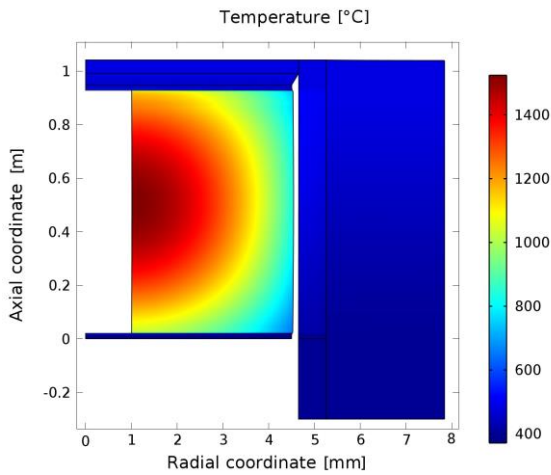
(a)



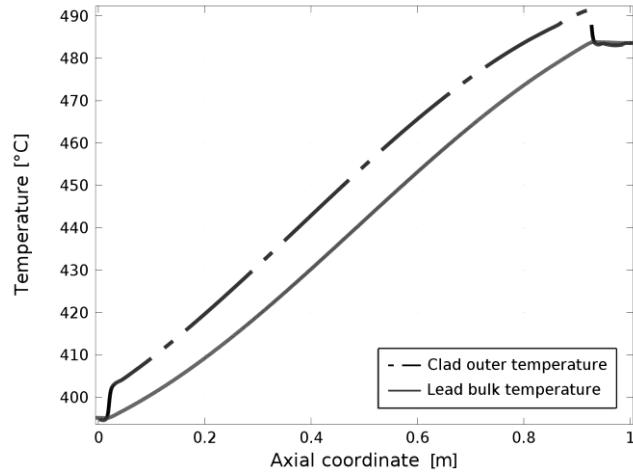
(b)

Fig. 8.11 – (a) Axial neutron flux profiles within the active height. SERPENT: bullets, COMSOL: lines. (b) Relative difference between axial neutron fluxes computed by COMSOL and SERPENT.



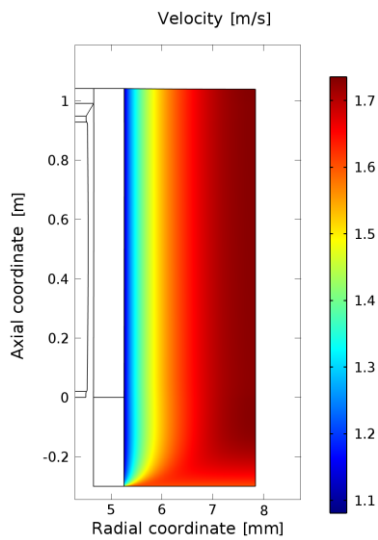


(a)

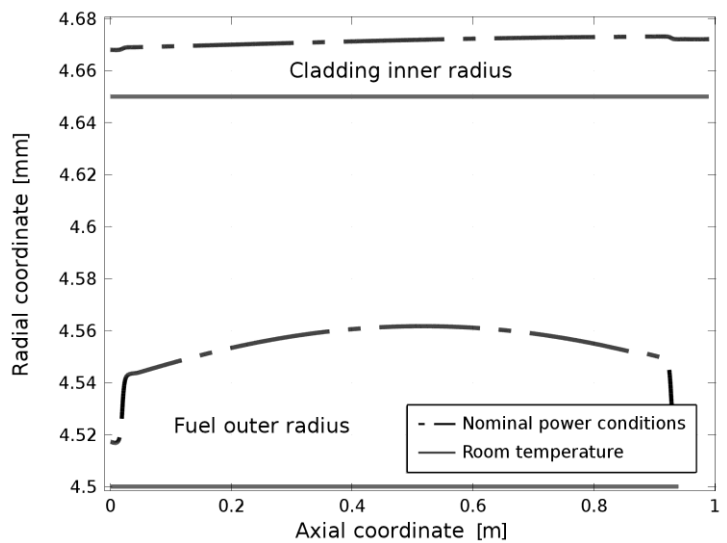


(b)

Fig. 8.12 – (a) Channel temperature field at nominal power conditions. (b) Cladding outer temperature and lead bulk temperature versus the z -coordinate, at nominal power conditions.

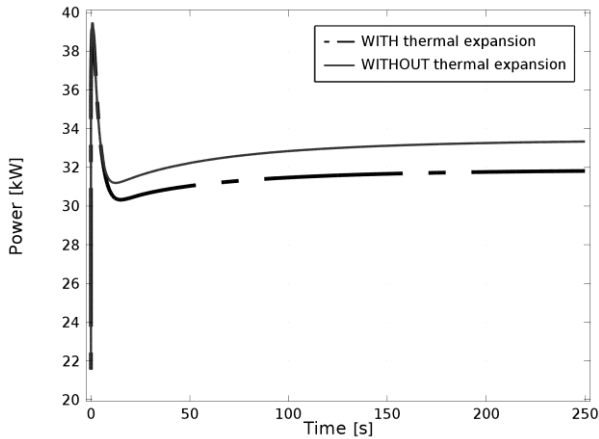


(a)

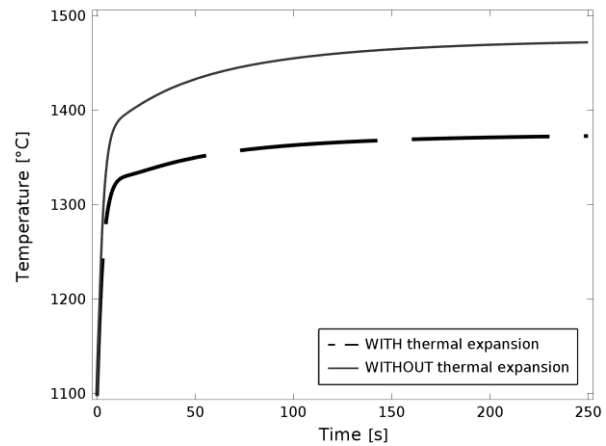


(b)

Fig. 8.13 – (a) Velocity field inside the fluid domain. (b) Outer fuel radius and inner cladding radius, as a function of the axial coordinate, at nominal power conditions and at room temperature conditions.

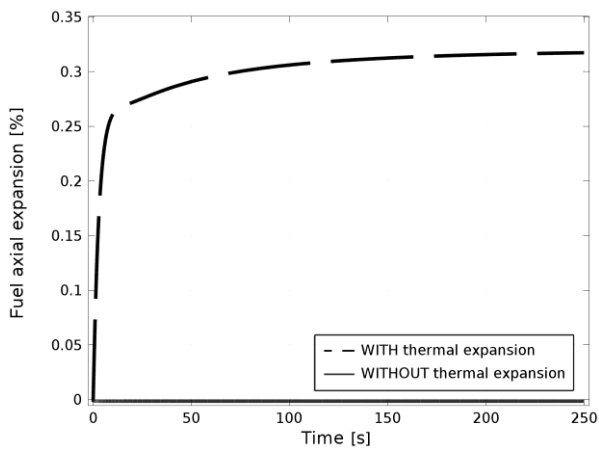


(a)

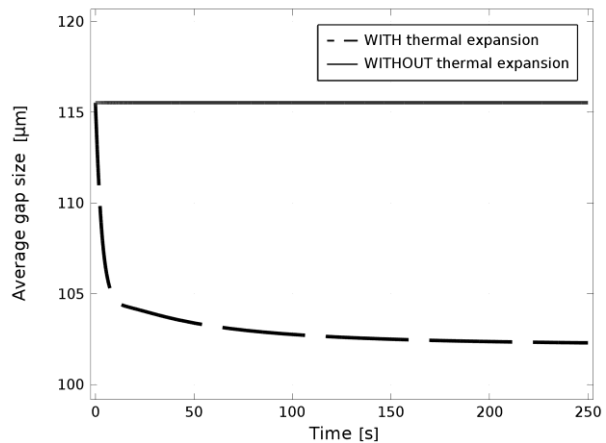


(b)

Fig. 8.14 – (a) Total pin power during the transient case study with a reactivity insertion of 150 pcm. (b) Average fuel temperature during the transient case study with a reactivity insertion of 150 pcm.



(a)



(b)

Fig. 8.15 – (a) Fuel axial expansion during the transient case study with a reactivity insertion of 150 pcm. (b) Average gap size during the transient case study with a reactivity insertion of 150 pcm.



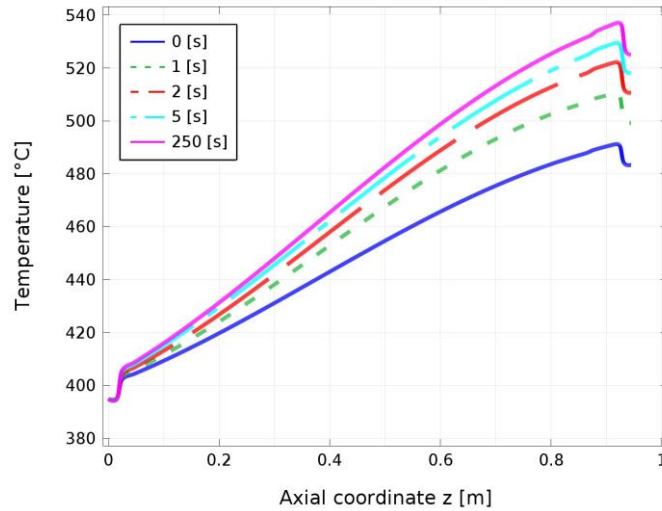
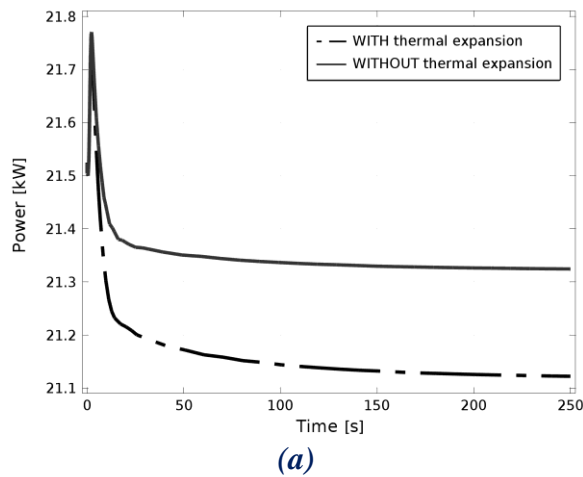
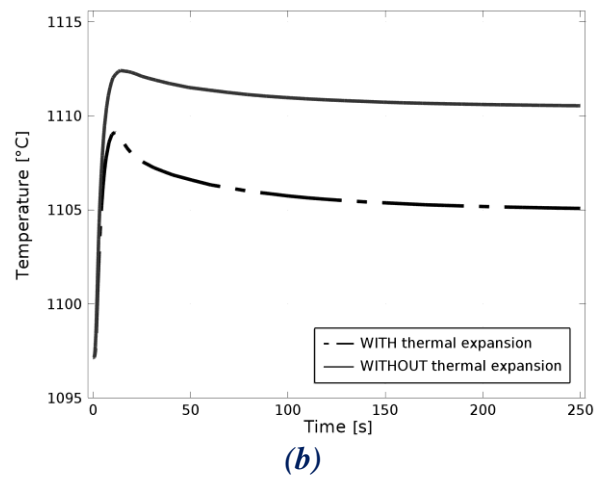


Fig. 8.16 – Axial profile of the cladding outer surface temperature during the transient case study with a reactivity insertion of 150 pcm.



(a)



(b)

Fig. 8.17 – (a) Total pin power during the transient case study with inlet lead temperature increase of 20 °C. (b) Average fuel temperature during the transient case study with inlet lead temperature increase of 20 °C.



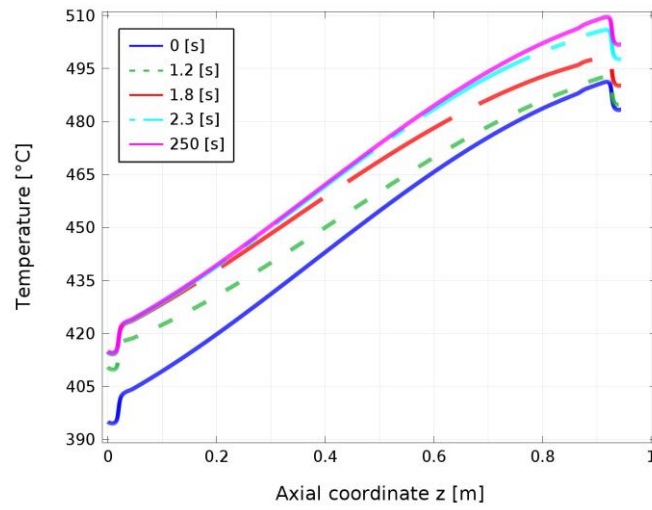



Fig. 8.18 – Axial profile of the cladding outer surface temperature during the transient case study with inlet lead temperature increase of 20 °C.




 RICERCA SISTEMA ELETRICO	<u>Title:</u> Development of BE numerical tools for LFR design and safety analysis – Part 2	<u>Distribution</u> PUBLIC	<u>Issue Date</u> 12.12.2017	<u>Pag.</u>
	<u>Project:</u> ADP ENEA-MSE PAR 2016	<u>Ref.</u> ADPFISS-LP2-144	Rev. 0	268 di 300

8.4 List of References

- [8.1] Cammi A, Di Marcello V, Luzzi L, Memoli V, Ricotti ME. A multi-physics modelling approach to the dynamics of Molten Salt Reactors. *Ann Nucl Energy* 2011;38. doi:10.1016/j.anucene.2011.01.037.
- [8.2] Aufiero M, Cammi A, Geoffroy O, Losa M, Luzzi L, Ricotti ME, et al. Development of an OpenFOAM model for the Molten Salt Fast Reactor transient analysis. *Chem Eng Sci* 2014;111:390–401. doi:10.1016/j.ces.2014.03.003.
- [8.3] Cammi A, Di Marcello V, Luzzi L, Memoli V. The multi-physics modelling approach oriented to safety analysis of innovative nuclear reactors. *Adv Energy Res* 2011;5:171–214.
- [8.4] Avramova MN, Ivanov KN. Verification, validation and uncertainty quantification in multi-physics modeling for nuclear reactor design and safety analysis. *Int J Heat Mass Transf* 1997;40:4191–6.
- [8.5] Salah AB, Hamidouche T, D’Auria F. Application of best estimate computational tools for safety accident analysis in nuclear plants. *Energy Convers New Res* 2008:143–59.
- [8.6] Mahadevan VS, Ragusa JC, Mousseau VA. A verification exercise in multiphysics simulations for coupled reactor physics calculations. *Prog Nucl Energy* 2012;55:12–32. doi:10.1016/j.pnucene.2011.10.013.
- [8.7] Alemberti A, Carlsson J, Malambu E, Orden A, Struwe D, Agostini P, et al. European lead fast reactor - ELSY. *Nucl Eng Des* 2011;241:3470–80. doi:10.1016/j.nucengdes.2011.03.029.
- [8.8] COMSOL. Comsol Multiphysics 4.2a, User’s Guide 2011.
- [8.9] SERPENT. No Title. PSG2/Serpent Monte Carlo React Phys Burn Calc Code 2011.
- [8.10] Sarotto M. ELSY core design static, dynamic and safety parameters with the open square FA. ELSY Core Des Static Dyn Saf Parameters with Open Sq FA 2009.
- [8.11] Duderstadt JJ, Hamilton LJ. *Nuclear Reactor Analysis*. New York: John Wiley and Sons; 1976.
- [8.12] Weigand B, Ferguson JR, Crawford ME. An extended Kays and Crawford turbulent Prandtl number model. *Int J Heat Mass Transf* 1997;40:4191–6.
- [8.13] Koning A. *The JEFF-3.1 Nuclear Data Library*. JEFF-31 Nucl Data Libr 2006.
- [8.14] Eaton JW, Bateman D, Hauberg S. *GNU Octave Manual Version 3*. GNU Octave Man Version 3 2008.
- [8.15] Rimpault G. Algorithmic features of the ECCO cell code for treating heterogeneous fast reactor subassemblies. *Int Top Meet React Phys Comput* 2005.
- [8.16] Chadwick MB, Obložinský P, Herman M, Greene NM, McKnight RD, Smith DL, et al. ENDF/B-VII.0: Next Generation Evaluated Nuclear Data Library for Nuclear Science and Technology. *Nucl Data Sheets* 2006;107:2931–3060. doi:10.1016/j.nds.2006.11.001.
- [8.17] Bandini G, Meloni P, Polidori M. Thermal-hydraulics analyses of ELSY lead fast reactor with open square core option. *Nucl Eng Des* 2011;241:1165–71. doi:10.1016/j.nucengdes.2010.04.034.
- [8.18] Weller HG, Tabor G, Jasak H, Fureby C. A tensorial approach to computational continuum mechanics using object-oriented techniques. *Comput Phys* 1998;12:620–31.
- [8.19] OpenFOAM. OpenFOAM 2016.




 RICERCA SISTEMA ELETTRICO	<u>Title:</u> Development of BE numerical tools for LFR design and safety analysis – Part 2	<u>Distribution</u> PUBLIC	<u>Issue Date</u> 12.12.2017	<u>Pag.</u>
	<u>Project:</u> ADP ENEA-MSE PAR 2016	<u>Ref.</u> ADPFISS-LP2-144	Rev. 0	269 di 300

9 VALIDATION OF **SIMMER** CODE AGAINST EXPERIMENTAL DATA


A. Pesetti, N. Forgione, A. Del Nevo



 RICERCA SISTEMA ELETTRICO	<u>Title:</u> Development of BE numerical tools for LFR design and safety analysis – Part 2 <u>Project:</u> ADP ENEA-MSE PAR 2016	<u>Distribution</u> PUBLIC	<u>Issue Date</u> 12.12.2017	<u>Pag.</u> 270 di 300
		<u>Ref.</u> ADPFISS-LP2-144	Rev. 0	

(Page intentionally left blank)



 RICERCA SISTEMA ELETTRICO	<u>Title:</u> Development of BE numerical tools for LFR design and safety analysis – Part 2	<u>Distribution</u> PUBLIC	<u>Issue Date</u> 12.12.2017	<u>Pag.</u>
	<u>Project:</u> ADP ENEA-MSE PAR 2016	<u>Ref.</u> ADPFISS-LP2-144	Rev. 0	271 di 300

9.1 Background and references

In the fission and fusion nuclear R&D, thermal-hydraulic and safety analyses are a fundamental issue in the development, design and licensing of nuclear power plants (NPPs). The investigation of the plant performance during accidental conditions has always been one of the main concern of nuclear safety. These analyses are fundamental to evaluate the possible consequences of a postulated accident and to support the design of components in order to assure their structural integrity, or in the worst case, to avoid jeopardizing the entire system.

Concerning the Gen. IV LFR plants and the WCLL-BB for the fusion DEMO reactor, one of the major safety problems is the interaction between water and metal alloy following a water tube rupture. Both systems use a heavy metal alloy (lead and lead-bismuth as primary coolant and lead-lithium as a neutron multiplier, respectively) and water (secondary or primary coolant, respectively). This interaction, called "Coolant-Coolant Interaction" (CCI), leads the system into a multi-phase and non-thermal equilibrium condition with possibility of vapor explosion and pressurization, and in the case of PbLi/water interaction with the exothermic chemical reaction and hydrogen production.

An experimental campaign was performed in ENEA C.R. Brasimone to provide experimental data by LIFUS5/Mod2 facility for investigating the LBE/water interaction, developing and validating physical modelling and for improving and qualifying computer codes in relevant conditions for SGTR event. LIFUS5/Mod2 is a separate effect test facility re-constructed on the basis of the operating experience on LIFUS5^{[9.1]-[9.3]}.

This report describes the LIFUS5/Mod2 facility, the implemented instrumentation, the test matrix and the post-test activity performed by UNIPI using SIMMER-III code. In particular, a series of 4 tests, performed at a pressure of 40 bar, were analysed. The experimental results were published in ENEA reports^{[9.4]-[9.8]}.

The post-test analysis was performed by the axial-symmetric SIMMER-III code. It is up to eight velocity field, multi-component, multiphase, Eulerian fluid-dynamics code coupled with a space and energy dependent neutron kinetics model^{[9.9], [9.10]}. The code was originally developed to deal with Core Disruptive Analysis (CDA) in Liquid Metal Fast Reactors (LMFRs) and over the years its range of applications was extended including issues related to advanced fast reactors, steam explosion and fuel coolant interaction phenomena. The capability of the SIMMER-III code to reproduce the phenomenology of the LBE-water interaction was studied and highlighted by previous activities performed at ENEA-Brasimone in collaboration with University of Pisa^{[9.1]-[9.3]}.


9.2 Body of the report concerning the ongoing activities

9.2.1 LIFUS5/Mod2 facility

LIFUS5/Mod2 facility, see Fig. 9.1, was designed to operate with heavy liquid metals, such as: lithium-lead alloy, lead-bismuth eutectic alloy and pure lead. The operation of the test facility has the objectives of 1) investigates relevant phenomena connected with the safety of HLM fast reactor designs and 2) develops and validates numerical models for simulation codes used in safety analysis.

LIFUS5/Mod2 consists of four main components: a reaction vessel (S1), where HLM/water interaction occurs, a water tank (S2) pressurized by means of a gas cylinder connected on the top, a dump tank (S3), where the water and HLM are transported as consequence of their interaction (disconnected for the experimental campaign) and a liquid metal storage tank (S4). The main features of the components characterizing LIFUS5/Mod2 facility are summarized in Tab. 9.1.



 RICERCA SISTEMA ELETTRICO	<u>Title:</u> Development of BE numerical tools for LFR design and safety analysis – Part 2	<u>Distribution</u> PUBLIC	<u>Issue Date</u> 12.12.2017	<u>Pag.</u>
	<u>Project:</u> ADP ENEA-MSE PAR 2016	<u>Ref.</u> ADPFISS-LP2-144	Rev. 0	272 di 300

The test section is configured in order to have an axial-symmetric geometry. With this configuration, the phenomena related to HLM/water interaction take place inside the vessel reducing, as far as possible, the perturbations due to structures inside the vessel.

The main vessel S1 (Fig. 9.1) is about 100 L, and it is partially filled with LBE. It is closed by the top flange sealed by a Garlock HELICOFLEX. During the experimental campaign the vessel S1 is closed and isolated, thus the dump tank is disconnected.

Internally, S1 can be divided in an upper cylindrical part and a lower hemispherical part. The main diameter is 420 mm and the overall height is 780 mm.

Inside the S1 vessel a support frame is placed (Fig. 9.2, Fig. 9.3 and Fig. 9.4), on which 68 thermocouples are installed. The frame, welded on the top flange, has an overall length of 590 mm. It is immersed into the LBE melt when the reaction tank S1 is closed.

The structure has four horizontal cruciform levels supporting thermocouples, highlighted by red dots in Fig. 9.3. The lower cruciform support, Level 1, is the nearest to the injection orifice and it has a vacuum (the central thermocouple is absent) in the central position, see Fig. 9.4, to avoid the anticipated impact with the water jet. The second level, as the higher ones, presents the frame reaching the axis of symmetry of the structure, see dotted circle in Fig. 9.4. Therefore, it constitutes an obstacle that fragments the water jet flowing upwards into the LBE melt.

The thermocouples set in the centre of the horizontal support structure is coaxial with the reaction tank S1 and the injection orifice. Each one of the four horizontal branches constituting a cruciform support, referred to as level, hosts four thermocouples, see Fig. 9.3.


The thermocouples nearest to the central one are considered belonging to the first ring, the outer ones to the fourth ring, see Fig. 9.3.

The water injection line, based on a ½" sch 80 pipeline, enters from the bottom of the vessel S1 in central position and protrudes internally 120 mm, see Fig. 9.2 and Fig. 9.3. At the top of the injection line the orifice, having a diameter of 4 mm, and its protective cap are mounted, see element “B” and “A” in Fig. 9.5, respectively. The cap is broken by the pressurization of the injection line at the beginning of the injection phase. The rupture occurs at a well-defined position by means of a circumferential notch “C” realised by machine tool. Therefore, the injection system shall be substituted at the end of each test.

The water line connects the tank S2 with the interaction vessel S1 and the vacuum pump. In the middle a discharge valve is installed, for draining the water at the end of the tests and removing steam formation during the conditioning heating phase.

As shown in Fig. 9.1, the water flows from S2 towards the valve V14, then the Coriolis flowmeter and finally through valve V4, before it enters in S1. The water line is also connected with the vacuum pump through the valve V3. Before the injection occurs, the vacuum pump is activated to remove the gas in the injection line. In this way, the line between the injection valve V14 and V3 is filled by low pressure air when the water injection starts. Therefore, the injected high pressure water expands and evaporates flowing toward the vessel S1.



 RICERCA SISTEMA ELETRICO	<u>Title:</u> Development of BE numerical tools for LFR design and safety analysis – Part 2	<u>Distribution</u> PUBLIC	<u>Issue Date</u> 12.12.2017	<u>Pag.</u>
	<u>Project:</u> ADP ENEA-MSE PAR 2016	<u>Ref.</u> ADPFISS-LP2-144	Rev. 0	273 di 300

Along the path of the water, two-phase flow occurs. The evaporation magnitude affects significantly the pressure drops in the injection line, which alter the amount of water injected in S1 and consequently its pressurization kinetics.

The water tank S2 is a 4 inch sch. 160 pipe, closed at the edges with proper welded plugs. The system has a volume of 15 L (plus those in the near level meter). It is connected on the top with the gas line, which is used for setting and keeping the pressure of the water according with the test specifications. The vessel S2 is connected by means of two lateral flanges on a magnetic level measurement device. The connections are one on the upper part of S2, where moisture of argon gas and vapour phase are present, and the other on the lower part.

A dump tank S3 (see Fig. 9.6) is part of LIFUS5/Mod2 facility. It can be connected by means of a 3" line to the top flange of S1. The volume is equal to 2 m³ and the design pressure is 1 MPa. It represents a safety volume used to collect the vapour and the gas generated by the interaction between the LBE and water. The tank S3 is disconnected during the experimental campaign.

The LBE in S1 is filled and drained just before and after each test, respectively. It is stored in the liquid metal storage tank S4 (see Fig. 9.6), which is connected to the bottom of the main vessel S1 using the same penetration of the water injection system. Indeed, LBE flows inside the injection line in the annular duct with respect to the water, as highlighted by circle in Fig. 9.2.

9.2.2 Instrumentation, control and data acquisition systems

The instrumentation, control and data acquisition systems of LIFUS5/Mod2 facility, see Fig. 9.6 and Fig. 9.7, were upgraded for improving the level of details of the parameters involved in the phenomena of interest, as well as for providing to code developers/users more reliable definition of the initial and boundary conditions.


Three types of measurements were planned in the facility and utilized for the acquisition, control and regulation systems.

The instrumentation for the interaction vessel (S1) is composed by: 68 low time constant thermocouples (TC), for temperature acquisition, installed on the support structure inside the vessel S1, providing measures at different radial, azimuthal and axial positions; 5 fast pressure transducers, one on the top of the vessel and four on the vessel wall at different elevations; 6 high temperature strain gauges installed on the reaction vessel, five of which on the internal wall at different heights and one externally.

The instrumentation for the water injection system is composed by: 1 level measurement gauge, mounted on the water tank support, having maximum resolution of 20-25 g in the experimental campaign conditions; 2 fast pressure transducers, placed on the bottom of the water tank and on the water injection line downstream the valve V4; 3 thermocouples, one of which in the dome of the water tank, the second one in the water side of S2 and the third one downstream the injection valve, near valve V3; 1 Coriolis flowmeter placed on the water line between the valves V14 and V4, to provide an accurate measurement of the mass flow of the water injected.

Besides the instrumentation of the acquisition system, the control and regulation systems, see Fig. 9.8, provide also some data to the acquisition system by means of: 1 absolute pressure transducer on the top flange of S1; 2 thermocouples on the vessel wall of S1; 3 absolute pressure transducers installed in the gas zone of S2 tank and in the gas line close to the gas cylinder.



 RICERCA SISTEMA ELETTRICO	<u>Title:</u> Development of BE numerical tools for LFR design and safety analysis – Part 2	<u>Distribution</u> PUBLIC	<u>Issue Date</u> 12.12.2017	<u>Pag.</u>
	<u>Project:</u> ADP ENEA-MSE PAR 2016	<u>Ref.</u> ADPFISS-LP2-144	Rev. 0	274 di 300

9.2.3 Test matrix

The experimental campaign is constituted by four tests, characterized by the pressure of the water tank S2 set at 40 bar, as reported in Tab. 9.2. The test matrix definition foresees the variation of three parameters: temperature of the injected water, gas argon to LBE volume ratio in S1 and total amount of injected water, i.e. the opening time of the injection valve. The water injection is carried out by the opening of the valve V14, that is adopted coherently with the past studies carried out at C.R. Brasimone^{[9.1]-[9.3]}.

The LBE temperature, injection line penetration in S1 and the injection orifice diameter are constant in all tests of the experimental campaign.

The main outcomes of the experimental campaign are the generation of detailed and reliable experimental data, the knowledge improvement of physical behaviour and phenomena, the investigation of the dynamic effects of energy release on the structures and the enlargement of the database for code validation. The test section details, the exact experimental boundary conditions and the pressure and temperature time trends measured during the first series of transients are published by specific ENEA reports^{[9.4]-[9.8]}.

9.2.4 SIMMER-III model

The SIMMER-III code can deal with safety analysis problems in advanced fast reactors and constitutes one of the few codes able to simulate the coolant-coolant interaction (CCI), taking into account the water evaporation occurring during the penetration into liquid metals.


The developed SIMMER-III geometrical domain of the LIFUS5/Mod2 facility is shown in left side of Fig. 9.9, the main components of which are connected by dotted arrows to the real ones depicted in the overall sketch in the right of the same figure. The geometrical domain is obtained by 23 radial and 88 axial subdivisions. The LBE is represented in red, the water in blue, the argon (cover gas) and air (injection line) in white and the non-calculation regions in light green. Rotating the 2D SIMMER-III domain along the axis of symmetry (blue dot-dashed line) the whole volumetric model is obtained, in which every cell is a toroidal volume with rectangular section.

The reaction vessel S1 was positioned in the upper part and coaxially to the model. The injection line is horizontally installed and cannot be coherently modelled in an axisymmetric domain. Therefore, to conserve the cylindrical shape of the injection tube, it was positioned vertically and coaxially with the entire model. The injection tube length is about 4 m. This value has been conserved in vertical direction and due to the water density, in experimental conditions, the simplification performed entails almost 0.4 bar of gravity pressure losses in the SIMMER-III model that do not occur in the experimental conditions. This simplification has been considered acceptable due to the considerably higher water pressure, i.e. 40 bar. The vertical injection line (½" of diameter) penetrates 120 mm into the vessel S1, at the top of this line the orifice with diameter of 4 mm is set. On the left of Fig. 9.9, the positions of the valve V14, V4 and the 2 inch tube, where the Coriolis flowmeter is set, are shown. In Fig. 9.9, the injection line is filled by water up to V14. The depicted SIMMER-III model is out of scale, because each axis has a specific scale factor.

The pressure time trends measured in the S2 dome is imposed as computational boundary condition of the simulations.

The SIMMER-III model shown in Fig. 9.9 depict the starting instant ($t = 0$ s) of the calculation, when the water begins to flow through the injection valve. At the top of injector, the injection orifice is kept closed for the lapse of time experimentally measured to achieve the cap rupture. The interruption of the water injection is simulated, as it occurs during the whole campaign, by the valve V4 closure, which isolates the vessel S1 from the pressurized water tank S2.



 RICERCA SISTEMA ELETRICO	<u>Title:</u> Development of BE numerical tools for LFR design and safety analysis – Part 2	<u>Distribution</u> PUBLIC	<u>Issue Date</u> 12.12.2017	<u>Pag.</u>
	<u>Project:</u> ADP ENEA-MSE PAR 2016	<u>Ref.</u> ADPFISS-LP2-144	Rev. 0	275 di 300

The injection line is implemented in the SIMMER-III model delimited by non-calculation regions. It implies that the fluid-structure coupling does not occur and consequently the pressure drops along the injection line are not directly computed by the code. In such a simplified configuration the single phase pressure drops are modelled by concentrated pressure drops simulated by means of Reynolds independent orifice coefficients set at cell junctions. This approximation does not allow the two phase pressure drops prediction directly by the code in the injection line.

Aiming to evaluate the influence of the evaporation occurring along the injection line, the tests were also simulated by SIMMER-III model having the injection line completely filled by water, as shown in Fig. 9.10. As presented in the following, such an approximation reduces the code prediction capability.

9.2.5 SIMMER-III results

The numerical results obtained by the SIMMER-III code for tests T#1, T#2, T#3 and T#4 are shown hereafter. Because of a low pressurization of the reaction tank S1 occurred during the execution of the first test^[9.5] the measured data are not compared with the computed ones in the present work. This test was repeated^[9.6], named T#1 in this study, at the end of the high pressure experimental campaign and the injection time chosen was almost equal to that adopted in test T#4^[9.8].

The experimental and calculated pressure time trends presented in the figures shown hereafter are differentiated by colours. The experimental pressure time trend in the dome of the water tank S2 is azure, its value has been imposed in the numerical simulations on the basis of the experimental data. The experimental pressure time trends in the reaction vessel S1 and injection line are green and grey, respectively, and the calculated values are depicted red and blue, respectively.

The integral value of the injected water mass is estimated on the basis of the level meter and remaining water in the injection line measurements. The Coriolis flowmeter working in two-phase flow conditions does not provide reliable data.


9.2.6 Test T#1

Test T#1 (named A1.2_1 in Ref. [9.6]) is numerically simulated with the SIMMER-III model shown in Fig. 9.9. It constitutes the reference test. The experimental and calculated pressure time trends are depicted in Fig. 9.11. Further calculation boundary conditions, not mentioned before, are summarized in Tab. 9.3.

The pressure time trends computed by the SIMMER-III code over-predict the measured data. The opening of the injection orifice occurs approximately 0.25 s after the water injection start. At this instant the computed pressure in the injection line overestimates the calculated one of almost 12 bar (blue and grey line respectively in Fig. 9.11). This is due to the lower pressure drops simulated along the injection line of the model. It also entails a calculated pressure time trend in S1 (red line in Fig. 9.11) with a higher slope than the measured one (green line). The kinetics of the pressure transient results therefore accelerated and the SIMMER-III code predicts the pressure plateau almost 1 s earlier.

The Tests T#1 and T#4 were performed imposing similar boundary and initial conditions. However, comparing Fig. 9.11 and Fig. 9.21, the experimental pressure time trends measured into the reaction tank (green lines) differ by almost 10 bar at about 1.5 s after the injection starting. The calculated data of such tests (red lines), instead, show pressurization time trends in agreement between them and the observable differences are attributed to the different pressure trends imposed in the dome of the water tank S2 and instant of the cap rupture.



 RICERCA SISTEMA ELETTRICO	<u>Title:</u> Development of BE numerical tools for LFR design and safety analysis – Part 2	<u>Distribution</u> PUBLIC	<u>Issue Date</u> 12.12.2017	<u>Pag.</u>
	<u>Project:</u> ADP ENEA-MSE PAR 2016	<u>Ref.</u> ADPFISS-LP2-144	Rev. 0	276 di 300

The numerical results obtained adopting the SIMMER-III model having the injection line filled by water (see Fig. 9.10), that means injecting water from the orifice, are shown in Fig. 9.12. It is possible to note, in comparison with Fig. 9.11, the complete loss of the pressurization data in the injection line (blue trend) and a higher overestimation of pressure time trends in the reaction tank S1 (red line). Therefore, it justifies the modelling of the low pressure air region in the injection line to improve the prediction capability of the code.

The SIMMER-III code predicts a water mass injected into S1 during the experiment equal to about 0.36 kg. This value is reasonably in agreement with that experimentally estimated of 0.42 kg^[9.6]. The higher numerical pressurization of S1, indeed, reduces the water entered in the reaction tank, therefore the obtained numerical result is coherent with the experimental one.

The analysis performed by the post processor BFCAL^[9.11] of the SIMMER-III code is focused on the investigation of the energy exchanges in the LBE and cover gas regions inside S1. The investigation of the vapour bubble formation and growth in the reaction tank is performed and shown in Fig. 9.13. The LBE void fraction equal to 1 is depicted in red and the blue cells indicate that LBE is substituted by other components that are, in this analysis, the cover gas of the reaction tank and the water injected from S1 bottom. The instant in which the vapour bubble enters in the cover gas region entails the loss of meaning of the cover gas compression work computed by the BFCAL postprocessor. Because of this tool takes into account only the initial cover gas volume and the addition of another gas is not taken into account by the BFCAL algorithm. As shown in Fig. 9.13, the vapour bubble reaches the cover gas almost 0.5 s after the start of the simulation, which is almost 0.25 s after the water injection start.

The instant in which the rupture of the vapour bubble occurs (entering into the cover gas) could be more precisely identified, as shown in Fig. 9.14, by the observation of the water kinetic energy time trend in the cover gas region (red line) becoming higher than zero. In the same figure, also the water kinetic energy trend in the LBE region is depicted (blue line). It starts to increase from zero at the cap rupture instant. The computed water kinetic energies have low values, having an order of magnitude of one Joule in the LBE and tenths of Joule in the cover gas region (Fig. 9.14).


9.2.7 Test T#2

The test T#2 (A1.3 in the ENEA report^[9.7]) injects water at lower temperature, 200°C. It is numerically simulated with the SIMMER-III model shown in Fig. 9.9. The experimental and calculated pressure time trends are depicted in Fig. 9.15. Further calculation boundary conditions, not mentioned before, are summarized in Tab. 9.4.

Analysing the SIMMER-III results, reported in Fig. 9.15, it can be seen that the code overestimates the pressures measured in S1 and injection line. In particular, it is possible to note that the computed pressure in the injection conduct, blue line, before the orifice opening, slightly overestimates the experimental data.

This difference is lower than in the tests T#1, T#3 and T#4 because of the lower water evaporation occurring in the test T#2 along the injection line, due to the lower water injection temperature: 200°C instead of 240°C. After the orifice opening, the blue line has a slope in agreement with the experimental grey one up to about $t = 0.6$ s, when the liquid water single-phase flow is established in the modelled injection line. At this instant the computed pressure in the injection line increases, becoming slightly lower than the pressure in the water tank dome. The calculated rapid passage from the two- to single-phase flow anticipates of about 0.4 s the same phenomenon experimentally observed. Such an abrupt flow regimes change entails a pressure peak of almost 43 bar.



 RICERCA SISTEMA ELETTRICO	<u>Title:</u> Development of BE numerical tools for LFR design and safety analysis – Part 2	<u>Distribution</u> PUBLIC	<u>Issue Date</u> 12.12.2017	<u>Pag.</u>
	<u>Project:</u> ADP ENEA-MSE PAR 2016	<u>Ref.</u> ADPFISS-LP2-144	Rev. 0	277 di 300

The pressure time trend calculated into the vessel S1, red line in Fig. 9.15, over-predicts the experimental data, as consequence of the higher pressure in the injection line. During the water injection transient, the measured pressure in the cover gas of the water tank S2 is not constant and decreases as shown by the azure line in Fig. 9.15.

The total water mass injected into the reaction vessel S1 has been computed by SIMMER-III code to be almost 0.4 kg, that is coherent with the value experimentally estimated^[9.7].

Fig. 9.16 shows the water injection and vapour bubble formation and growth. It is possible to note that the instant in which the bubble reaches the argon cover gas could be approximately estimated equal to 0.6 s after the calculation start and corresponding to almost 0.25 s after the water entrance into S1. These data are confirmed by the red line depicted in Fig. 9.17, where the water kinetic energy in the LBE (blue line) and cover gas regions (red line) are shown.

The water injected at 200°C entails lower water evaporation in S1 and consequently a higher water kinetic energy in comparison with the tests T#1, T#3 and T#4. The water kinetic energy in the LBE and cover gas regions reaches values almost equal to 7 and 2 J, respectively.

9.2.8 Test T#3

Test T#3 (A1.1 in the ENEA report^[9.4]) is performed increasing the cover gas fraction. Its volume has been set equal to 40% of the LBE volume. The calculated, employing SIMMER-III model of Fig. 9.9, and measured pressure time trends are shown in Fig. 9.18.

The higher free volume in S1, with respect to the other tests, yields a measured lower pressure value at the end of the transient, about 32 bar. Moreover, the slope of the pressure trend in S1 is almost the half of that measured in test T#4. Therefore, the increased cover gas slows down the kinetics of the transient and reduces the maximum pressure value reached in S1. Tab. 9.5 shows the numerical boundary and initial conditions of test T#3.


The calculated pressure time trends overestimate the experimental data in the first 3 s after the valve V14 opening, they are however qualitatively in agreement. The calculated pressure values are, instead, in good agreement with the experimental ones after the pressurization of the reaction vessel is reached, which occurs almost 2.5 s after the transient start.

At the instant of the orifice opening, the pressure computed in the injection line overestimates the measured one by almost 10 bar. The analogous difference in the test T#2 was almost a third, due to the lower water sub-cooling (240°C instead of 200°C) that entails a higher evaporation. Test T#3, thus, confirms the necessity to better take into account the two-phase flow pattern inside the injection line.

The overall computed water mass injected is almost 0.5 kg. This value is coherent with the other tests, because the higher cover gas allows that a higher quantity of water is injected in the reaction vessel. Instead, the experimentally estimated value^[9.4] is 0.38 kg.

Fig. 9.19 illustrates the LBE volume fraction during the water injection phase and the consequent vapour bubble formation. It is possible to observe that the vapour enters the cover gas at almost 0.7 s after the calculation start. This lapse of time is higher than that calculated in the other tests, because the higher cover gas volume defines a system having higher compressibility. Consequently, the water kinetic energy in the cover gas, see Fig. 9.20, has values higher than zero up to the end of the water injection ($t = 2$ s), instead the



 RICERCA SISTEMA ELETTRICO	<u>Title:</u> Development of BE numerical tools for LFR design and safety analysis – Part 2	<u>Distribution</u> PUBLIC	<u>Issue Date</u> 12.12.2017	<u>Pag.</u>
	<u>Project:</u> ADP ENEA-MSE PAR 2016	<u>Ref.</u> ADPFISS-LP2-144	Rev. 0	278 di 300

other tests show water kinetic energy in the cover gas decreasing earlier, see Fig. 9.14, Fig. 9.17 and Fig. 9.23.

Fig. 9.20 shows also that the higher cover gas volume entails a lower water kinetic energy in the LBE region (blue line) in comparison with the other tests.

9.2.9 Test T#4

Test T#4 (A1.4 in the ENEA report^[9,8]) has the same boundary and initial conditions of the test T#1, except only for the V4 closure instant, that was changed as shown in Tab. 9.2 and Tab. 9.6. It caused the complete closure of the valve V4 about 2.9 s after the valve V14 opening ($t = 0$ s). It occurred because the difference between the pressure measured in S1 and S2 becomes lower than 1 bar just before 3 s.

The calculated and experimental pressure time trends are shown in Fig. 9.21. The pressure transducer set in the injection line did not work properly and measured data near to 0 bar, as it is possible to see in Fig. 9.21, in which the grey line is depicted closely to the axis of the abscissas. However, it is reasonable to assume that, before the orifice opening, the pressure trends in the injection line is close to that measured during the test T#1 and T#3.

The numerical results obtained by the SIMMER-III code over-predict the experimental data during the phase of increasing pressure in S1, similarly to the other tests. The almost stationary pressure trends computed at the end of the transient are in good agreement with the measured data.

The calculated overall water mass injected during the transient is almost 0.37 kg. This value underestimates the measured data of 0.47 kg because of the faster S1 pressurization computed by SIMMER-III code.


As mentioned before, the test T#4 has the same injected water temperature and cover gas volume of the test T#1. Instead, the water injection start instant and the water tank (S2) pressurization are affected by experimental inevitable differences. Therefore, the first tenths of second of the water injection phase provides numerical results in terms of energetic analysis analogous to that obtained for the test T#1, as shown in Fig. 9.23.

The numerical simulation of the test T#4, see Fig. 9.21, coherently with the calculation results obtained for the other tests, shows that the pressure drops simulated along the injection line underestimate the measured trend.

The modelling of the injection line is at the basis of the pressure time trends overestimation, due to the underestimation of the two-phase pressure drops. Aiming to improve the obtained results, an application of the Lockhart-Martinelli multipliers is done and the obtained results are shown in Fig. 9.24. The calculated pressure time trend into the reaction vessel S1 shows a considerable slope reduction in comparison with Fig. 9.21 and the obtained results appear improved.

The adopted method is applied multiplying the implemented Reynolds independent orifice energy loss coefficients, calculated to take into account the single-phase friction pressure drops, by the Lockhart-Martinelli two-phase friction multiplier. It was evaluated on the basis of an average value of the quality parameter, equal to 0.3. It corresponds (assuming a unitary slip ratio) to friction multiplier that becomes too high when the quality in the channel decreases. Indeed, about 1.5 s after the water injection start, the single phase liquid flow occurs in the channel and the implemented L-M two-phase multiplier causes the underestimation of the S1 pressurisation. To reduce this inaccuracy, at almost 1.25 s after the valve V14 opening, the two-phase friction multiplier is set equal to 1. The obtained results are shown in Fig. 9.25 and



 RICERCA SISTEMA ELETTRICO	<u>Title:</u> Development of BE numerical tools for LFR design and safety analysis – Part 2	<u>Distribution</u> PUBLIC	<u>Issue Date</u> 12.12.2017	<u>Pag.</u>
	<u>Project:</u> ADP ENEA-MSE PAR 2016	<u>Ref.</u> ADPFISS-LP2-144	Rev. 0	279 di 300

appear to be in agreement with the experimental data, during the pressurization phase of the reaction vessel as well as at the end of the transient, when almost stationary pressure values are reached.

The temperature time trends are computed by the SIMMER-III code for all the tests of the experimental campaign. Hereafter the calculated and measured temperature trends of the corrected test T#4 (Fig. 9.25) are reported.

The measured temperatures are depicted by solid lines and the calculated results are represented by dotted lines. The temperature measured in the centre, first, second, third and fourth ring are depicted by red, green, blue, black and grey lines, respectively. In the legend of the following figures the information of the axial and radial position of the cell in which the shown temperature has been computed is provided by the two numbers between brackets, respectively.

Fig. 9.26 shows the measured and computed temperature at the first level of the support structure. The measured data show a moderate cooling effect only on the first ring, continuous green line. Instead, the numerical results show a higher cooling effect on the first and second ring, down to almost 200°C, during the first 0.5 s of the transient. Such an overestimation and anticipation of the cooling effect is due to the liquid-vapour water jet kinetics penetrating the molten LBE, predicted by the SIMMER-III code. It predicts a cold jet wider and faster to flow upwards than experimentally, so that it impacts earlier and with a higher cooling effect on the thermocouples of the first and second ring at the first level.

The mentioned difference is due to the fact that the SIMMER-III results are obtained adopting the default code settings, which appear not well suitable to take properly into account the expansion vapour kinetics in the LBE pool. The code predicts a faster formation of a larger vapour bubble than that experimentally measured, entailing a higher cooling effect. Moreover, the numerical results show that the vapour bubble can move upward after overcoming the LBE resistance, reducing its own wideness and Fig. 9.26 shows that the computed cooling effect on the first level disappears almost 0.5 s after the injection start.


Fig. 9.27 depicts the experimental and calculated temperature time trends in the second level of the support structure. The SIMMER-III code predicts the temperature in the central position of the cruciform support in reasonable agreement with the experimental data. Analogously to the previous figure, the code results anticipate the cooling effect on the thermocouple positioned in the centre of the level and also provide a delayed rewetting by LBE.

When the pressure in S1 tends to equalize that in the injection line, the amount of water injected decreases and consequently the temperature measured and calculated increases. SIMMER-III code computes the outer thermocouples, from the first to the fourth ring, cooled until 0.5 s after the injection start. Instead, the measured data show a cooling effect on the first thermocouples ring (green line) until almost 3 s after the transient start.

Fig. 9.28 and Fig. 9.29 show that the code overestimates the cooling effect in the central position of S1 at level 3 and 4. It is due to the absence, in the geometrical model, of the support structure and its four horizontal cruciform supports. Such a cruciform structure is not simulated in the geometrical model because its shape is not well reproduced by an axisymmetric model.

Thus, in the geometrical model, the jet of steam does not encounter obstacles along its upwards path and its cooling effect along the axis of S1 is constant at different height. Instead, the experimental configuration, see Fig. 9.4, entails that the injected water passes through the central opening of the first cruciform level and



 RICERCA SISTEMA ELETRICO	<u>Title:</u> Development of BE numerical tools for LFR design and safety analysis – Part 2	<u>Distribution</u> PUBLIC	<u>Issue Date</u> 12.12.2017	<u>Pag.</u>
	<u>Project:</u> ADP ENEA-MSE PAR 2016	<u>Ref.</u> ADPFISS-LP2-144	Rev. 0	280 di 300

impacts against the second and upper levels. The consequent jet fragmentation entails a reduced cooling effect on both the upwards levels, Fig. 9.28 and Fig. 9.29.

The temperature trends, computed by the SIMMER-III code, are generally also affected by the injection of water into the reaction tank S1 at higher pressure than during the experimental tests. It contributes to the anticipated cooling events at the four levels. The differences, shown in from Fig. 9.26 to Fig. 9.29, between the experimental and computed data are also due to water-LBE slip ratio modelled in the performed study by SIMMER-III default settings.

Moreover, the fragmentation of the water due to the horizontal cruciform structures is not simulated by the axisymmetric model. Therefore, the numerical analysis by means of a three-dimensional model (SIMMER-IV) appears to be suitable to reduce the described approximations.

9.2.10 Conclusions

The Department of Civil and Industrial Engineering (DICI) of University of Pisa performed the review of the experimental investigations on the vapour explosion phenomenon and the assessing of the consequent energy release. Moreover, central issue of the task is constituted by the post-test analysis of the experimental campaign performed on the LIFUS5/Mod2 facility at ENEA Brasimone R.C. The SIMMER-III was adopted aiming to identify the prediction code capabilities and limitations.

The experimental campaign is composed by a group of four test. The reference test is characterized by injecting water at 40 bar and 240°C into a pool of LBE at 400°C. The other tests are performed injecting water at lower temperature, implementing higher cover gas volume and changing the injection lapse of time, respectively. The injection is carried out by valve V14, positioned upstream the Coriolis flowmeter. It implies the presence of an extended low pressure air volume in the injection line.


The modelling of the LIFUS5/Mod2 facility by SIMMER-III code is performed accepting geometrical simplifications. Each group of tests is analysed by two models, with and without the implementation of the low pressure air region in the injection line. The model in which the supply line is completely filled by water provides higher pressurization time trends in the reaction tank as well as the lacking information of the pressurization in the injection line.

The SIMMER-III model, taking into account the vacuum region in the injection line, shows the presence of two-phase flow condition along the conduct during the first phase of the injection. The prediction of the two-phase pressure drops becomes a key issue to correctly predict the pressurization time trends in the reaction tank and in the injection line. A simplified application of the Lockhar-Martinelli (L-M) multipliers provides pressurization results in agreement with the experimental data (Test T#4).

The temperature time trends numerically simulated for each test show a general cooling anticipation and overestimation on the axis of the reaction vessel S1. This is due to the impossibility to model by an axisymmetric code the four horizontal cruciform supports that constitute an obstacle against which the water jet impacts and fragments. Moreover, the vapour evolution, expansion and buoyancy in the LBE pool is affected by the code default setting, which could be improved to better agree with the faced experimental conditions.

The injected mass flow rate is measured by Coriolis flowmeter and water level meter in S2, but the measured data show delayed acquired values in comparison to the injection start and also between them. The SIMMER-III code therefore could not be accurately validated on the basis of the available experimental data,



 RICERCA SISTEMA ELETTRICO	<u>Title:</u> Development of BE numerical tools for LFR design and safety analysis – Part 2	<u>Distribution</u> PUBLIC	<u>Issue Date</u> 12.12.2017	<u>Pag.</u>
	<u>Project:</u> ADP ENEA-MSE PAR 2016	<u>Ref.</u> ADPFISS-LP2-144	Rev. 0	281 di 300

but anyway it is able to provide consistent data of time dependent and integral value of the injected water flowrate.

9.3 Role of the activity, general goals and future development

DICI of Pisa University has a great experience on the use of SIMMER code, widely used and validated for the interaction between metal alloy and water in fission dedicated experimental facility (CIRCE-SGTR for MAXSIMA project^[9.13], LIFUS5/Mod2 for LEADER^[9.14] and THINS projects^[9.15]). SIMMER code is the only code capable of simulating the physical phenomena occurring during heavy metal liquid alloy and water interaction^[9.16]. It is a multi-dimensional (2-D and 3-D versions), multi-velocity field, multi-phase, multi-component, Eulerian, fluid-dynamic code coupled with a structure model and a space-time energy-dependent neutron kinetic model.


Recently, UNIPI has modified the source code to obtain a fusion version by implementing a chemical model for the exothermic reaction between PbLi and water^{[9.17], [9.18], [9.19]} enabling the evaluation of the energy and the hydrogen generation. Validation activity was concluded on LIFUS5 experimental campaign available in literature and is ongoing on experimental tests in LIFUS5/Mod3 for the EUROfusion project.

Nevertheless, the exclusive use of SIMMER code still remains prohibitive for the requested computational effort and the long calculation time (especially in its 3-D version).

Therefore, STH code should be applied to the portions of the system characterized by 1D components (i.e. pipes) meanwhile SIMMER code should be used to analyze a smaller part of the domain where 3D effects are significant and/or detailed flow information is demanded, and to model multi-phase and/or multi-component flow.

The feasibility study on coupling STH and SIMMER can be a future development of the work presented here and it will be investigated at UNIPI in PAR2017.



 RICERCA SISTEMA ELETTRICO	<u>Title:</u> Development of BE numerical tools for LFR design and safety analysis – Part 2	<u>Distribution</u> PUBLIC	<u>Issue Date</u> 12.12.2017	<u>Pag.</u>
	<u>Project:</u> ADP ENEA-MSE PAR 2016	<u>Ref.</u> ADPFISS-LP2-144	Rev. 0	282 di 300


SYSTEM S1		INTERACTION VESSEL
S1-1	Volume [m ³]	0.1
S1-2	Inner diameter [m]	0.42
S1-3	Height [m]	1.085
S1-4	Design pressure [bar]	200
S1-5	Design temperature [°C]	500
S1-6	Material	AISI 316
SYSTEM S2		WATER TANK
S2-1	Volume [m ³]	0.015
S2-2	Diameter	4 inch sch. 160
S2-3	Design pressure [bar]	200
S2-4	Design temperature [°C]	350
S2-5	Material	AISI 316
SYSTEM S3 [Disconnected]		DUMP TANK
S3-1	Volume [m ³]	2.0
S3-2	Inner diameter [m]	1
S3-3	Design pressure [bar]	10
S3-4	Design temperature [°C]	400
S3-5	Material	AISI 316

Tab. 9.1 – LIFUS5/Mod2 main features of components (from [9.4]).

#	E-BIC	T#1	T#2	T#3	T#4
1	Interaction system	S1	S1	S1	S1
2	LBE temperature [°C]	400	400	400	400
3	Water pressure [bar]	40	40	40	40
4	Water temperature [°C]	240	200	240	240
5	Argon volume/LBE volume [%]	30	30	40	30
6	Lasting time of the injection valve on [s]	2	2	2	3
7	Water injection penetration in S1 [mm]	120	120	120	120
8	Injector orifice diameter [mm]	4	4	4	4

Tab. 9.2 – Experimental campaign test matrix (from [9.4]).



 RICERCA SISTEMA ELETTRICO	<u>Title:</u> Development of BE numerical tools for LFR design and safety analysis – Part 2	<u>Distribution</u> PUBLIC	<u>Issue Date</u> 12.12.2017	<u>Pag.</u>
	<u>Project:</u> ADP ENEA-MSE PAR 2016	<u>Ref.</u> ADPFISS-LP2-144	Rev. 0	283 di 300

C-BIC	Value
V14 opening	0 s
Orifice opening	0.249 s
V4 closure	3 s or P(S2)-P(S1)<0 bar
S2 cover gas pressure	= experimental data

Tab. 9.3 – Computational-BIC of test T#1.

C-BIC	Value
V14 opening	0 s
Orifice opening	0.353 s
V4 closure	2 s or P(S2)-P(S1)<1bar
S2 cover gas pressure	= experimental data

Tab. 9.4 – Computational-BIC of test T#2.

C-BIC	Value
V14 opening	0 s
Orifice opening	0.329 s
V4 closure	2 s or P(S2)-P(S1)<1bar
S2 cover gas pressure	= experimental data

Tab. 9.5 – Computational-BIC of test T#3.

C-BIC	Value
V14 opening	0 s
Orifice opening	0.325 s
V4 closure	3 s or P(S2)-P(S1)<1bar
S2 cover gas pressure	= experimental data

Tab. 9.6 – Computational-BIC of test T#4.



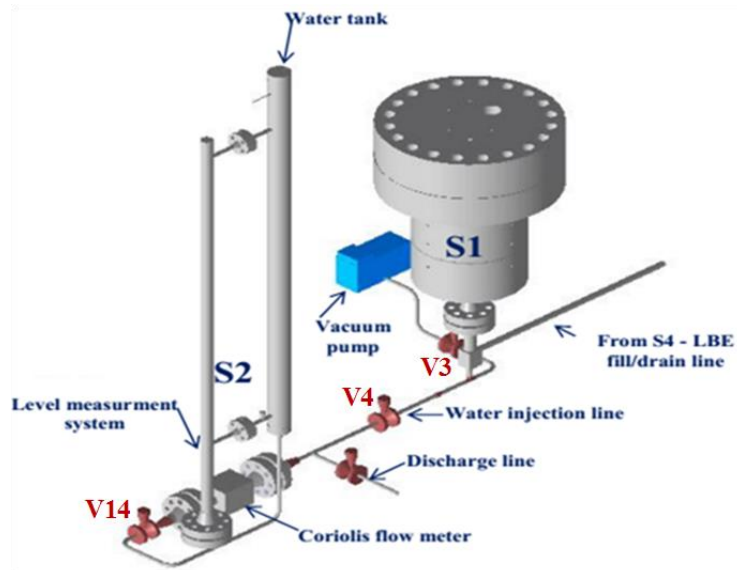


Fig. 9.1 – LIFUS5/Mod2 overall sketch (from [9.4]).

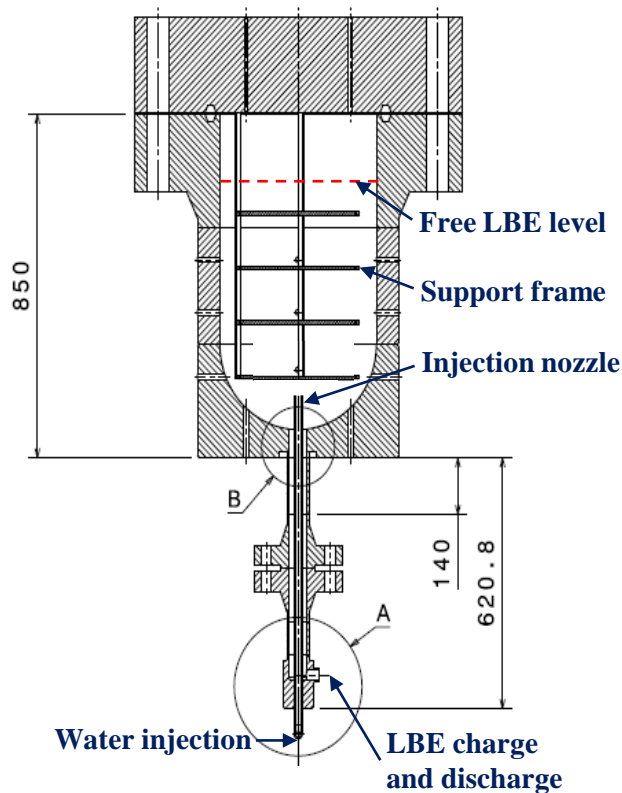


Fig. 9.2 – LIFUS5/Mod2 facility, S1 and injection system (from [9.4]).

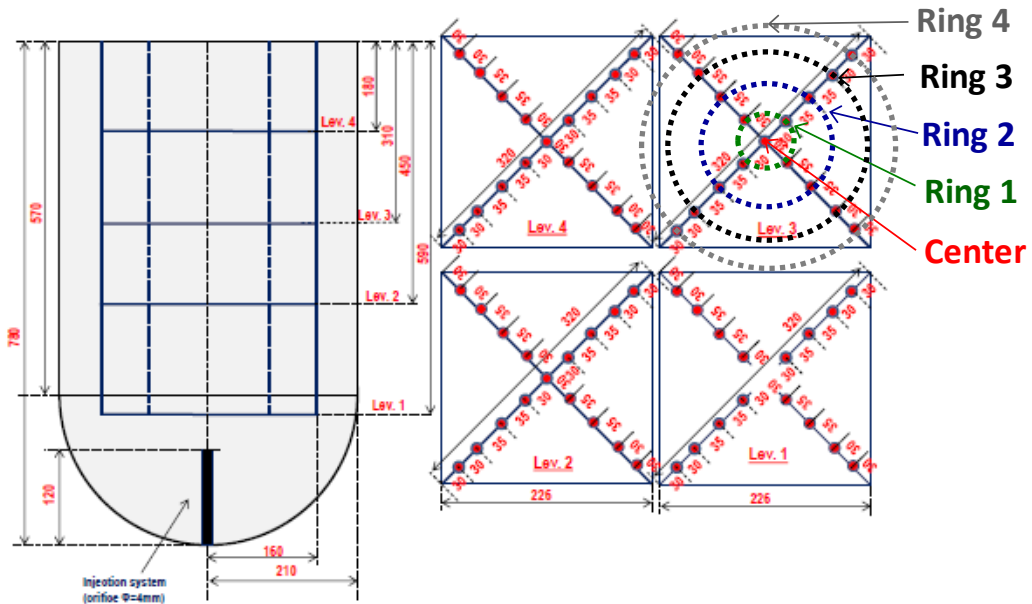


Fig. 9.3 – Support structure of the thermocouples in S1 (from [9.4]).

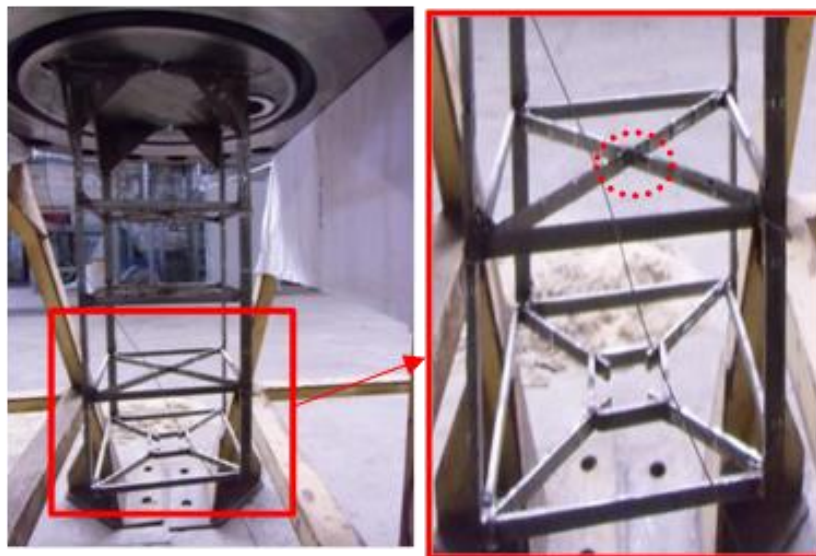


Fig. 9.4 – Detailed view of the TCs' support structure (from [9.4]).

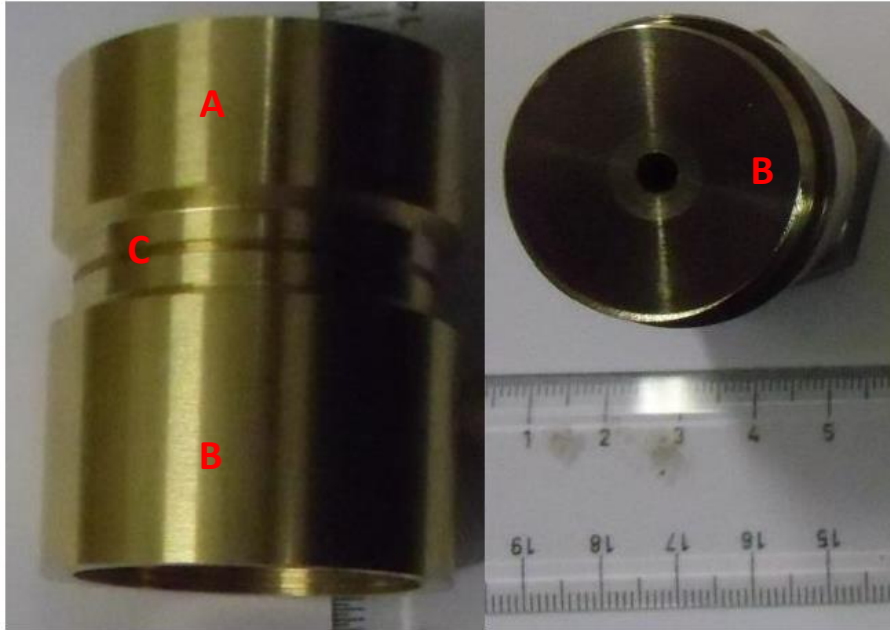


Fig. 9.5 – View of the protective cap “A” and injection orifice “B” (from [9.4]).

LIFUS5/Mod2
THINS configuration 2012

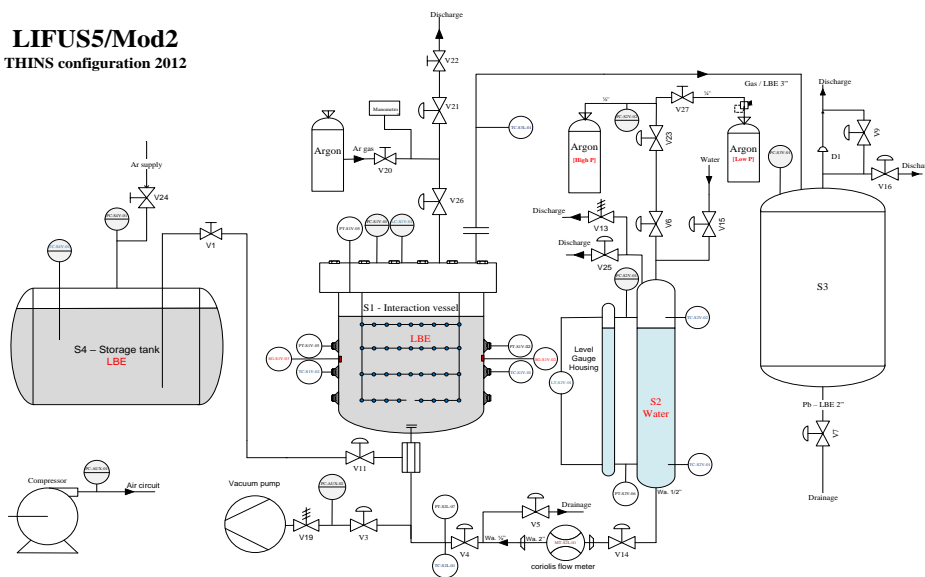


Fig. 9.6 – P&ID of LIFUS5/Mod2 facility, acquisition and control systems (from [9.4]).



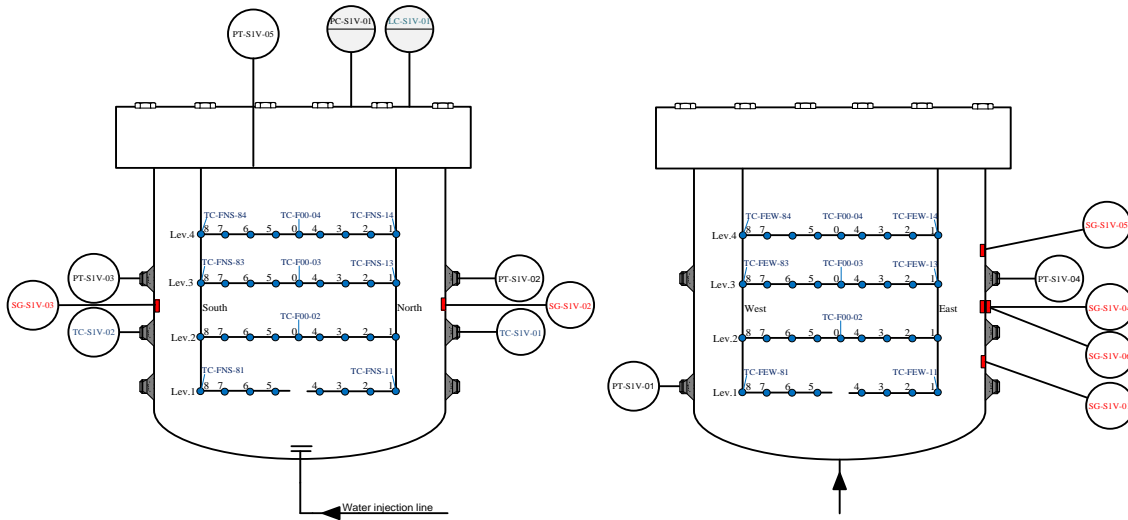


Fig. 9.7 – Implemented instrumentation on the support structure and reaction tank S1 (from [9.4]).

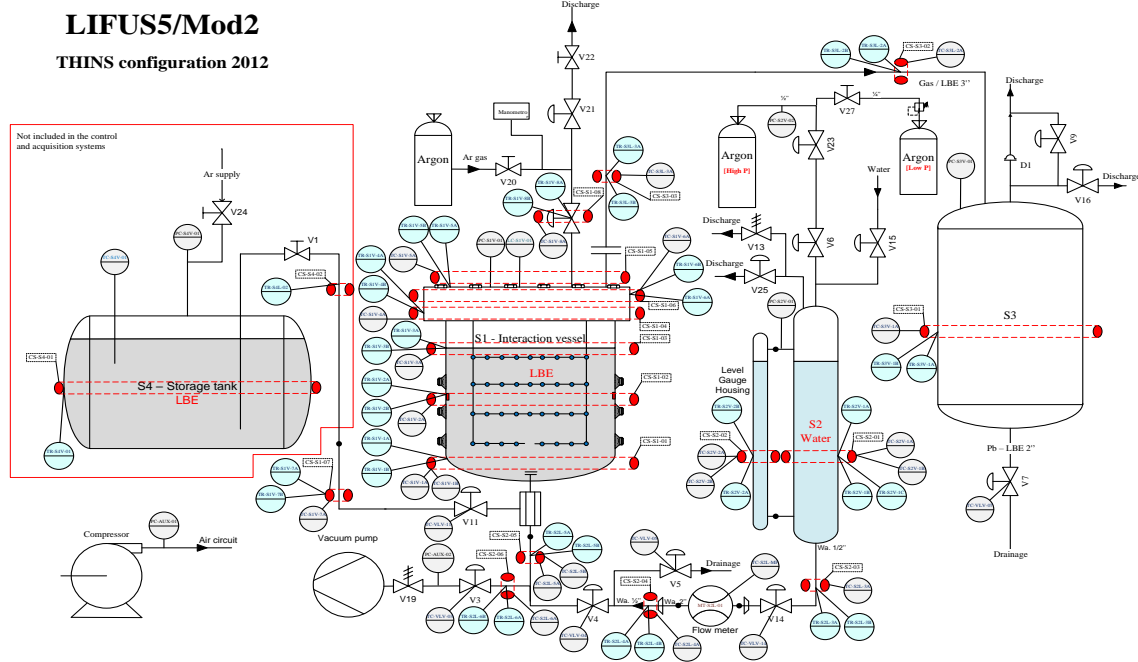


Fig. 9.8 – Control and regulation systems (from [9.4]).



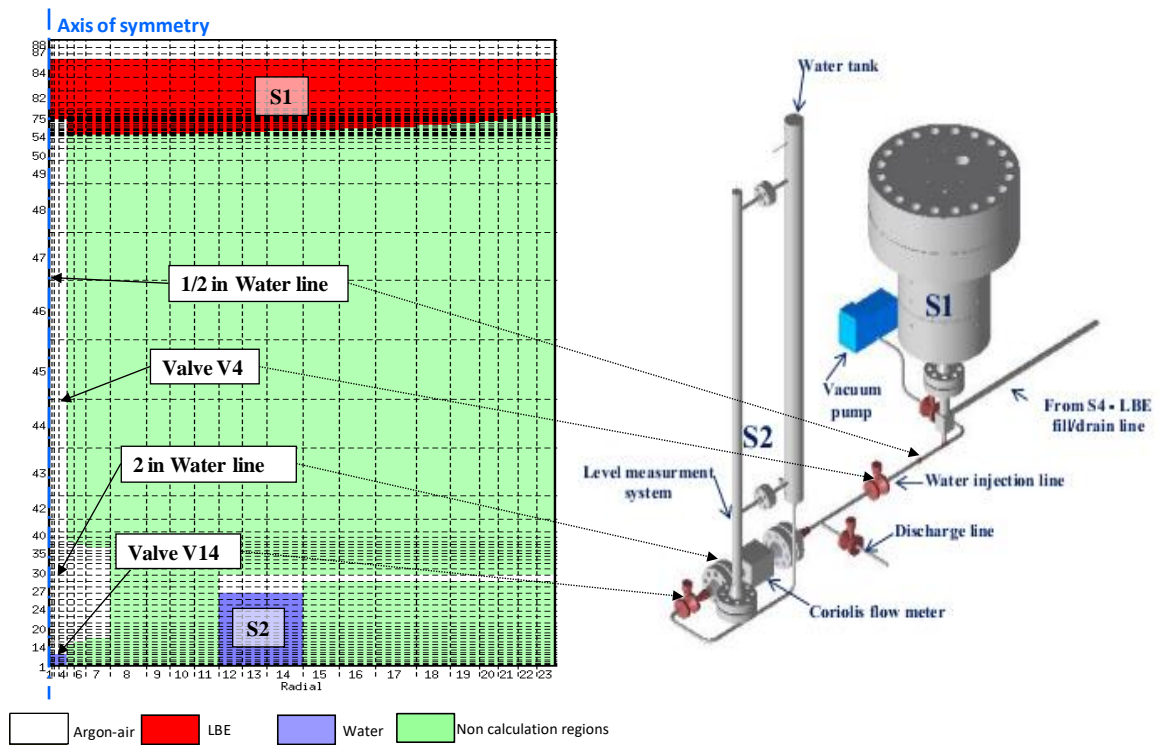


Fig. 9.9 – SIMMER-III geometrical model.

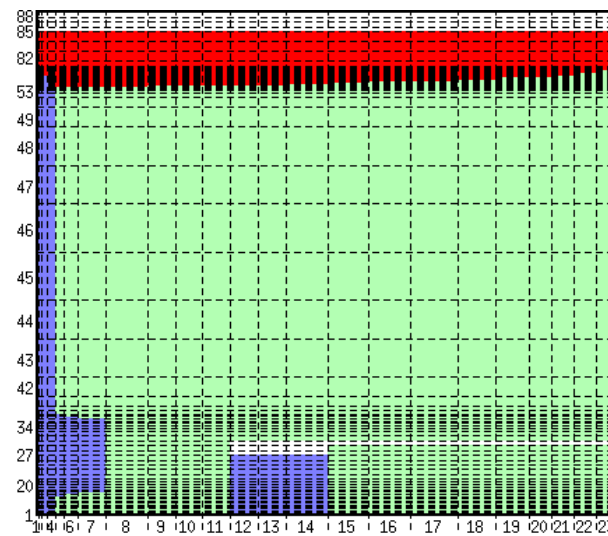


Fig. 9.10 – SIMMER-III geometrical model injecting water from the cap orifice.

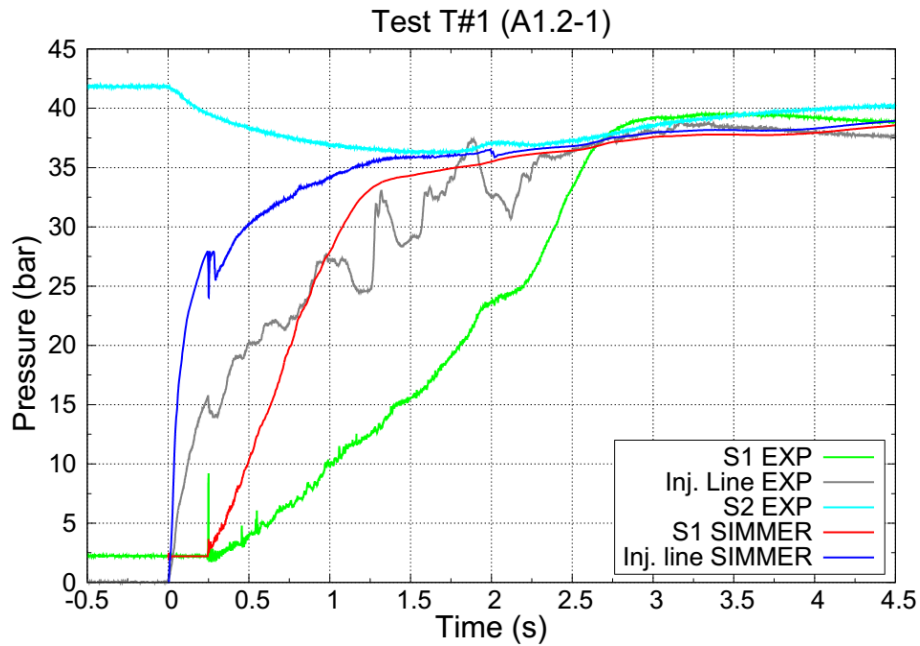


Fig. 9.11 – Calculated and experimental pressure time trends of the test T#1.

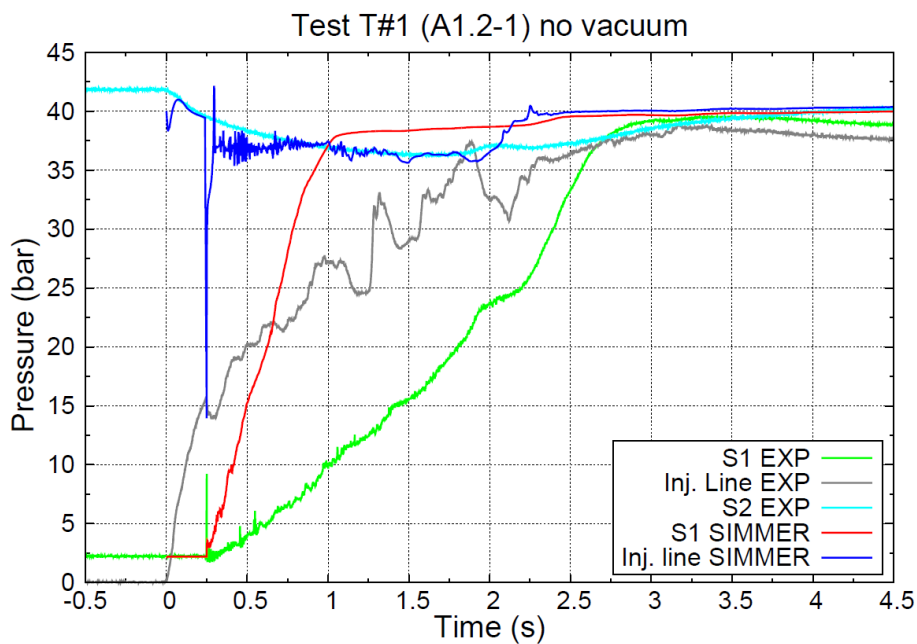


Fig. 9.12 – Calculated and experimental pressure time trends of the test T#1, without vacuum region in the injection line.



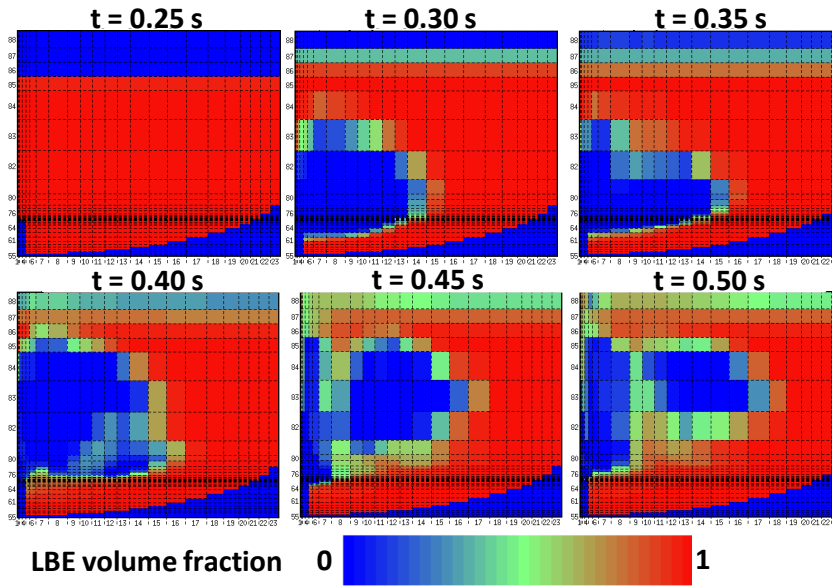


Fig. 9.13 – LBE volume fraction and vapour bubble evolution during the water interaction phase, calculated by SIMMER-III code.

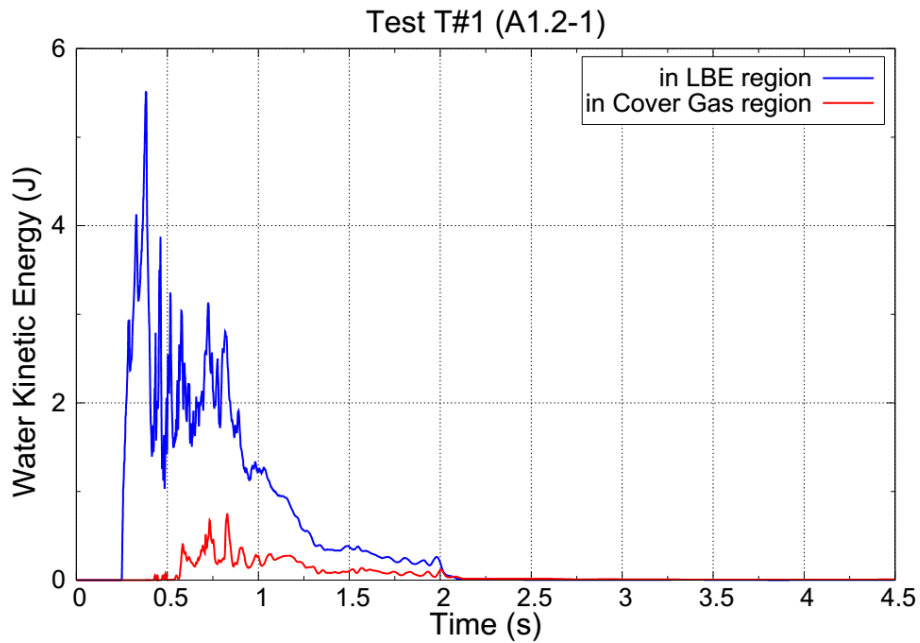


Fig. 9.14 – Water kinetic energy time trends in the cover gas and LBE regions, T#1.

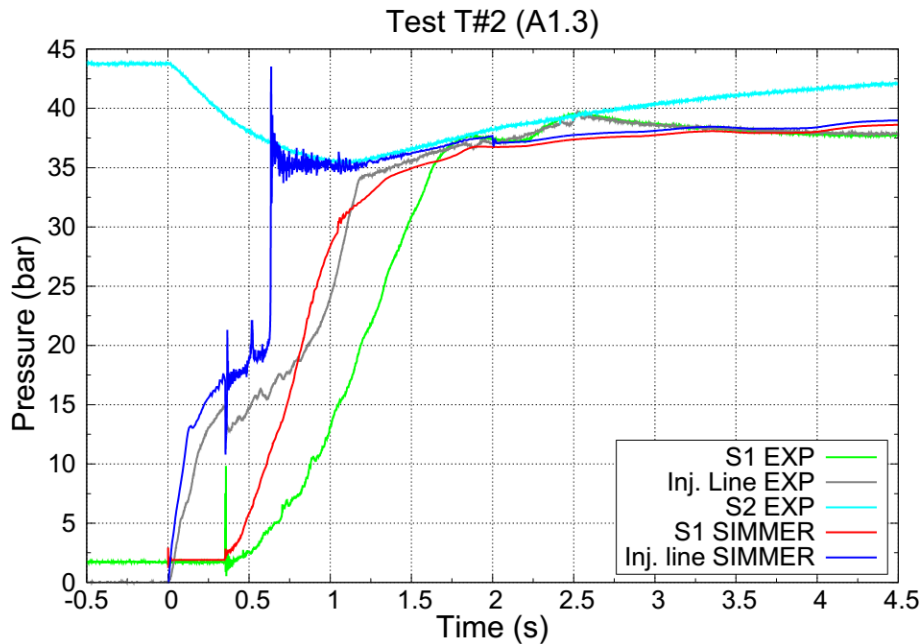


Fig. 9.15 – Calculated and experimental pressure time trends of the test T#2.

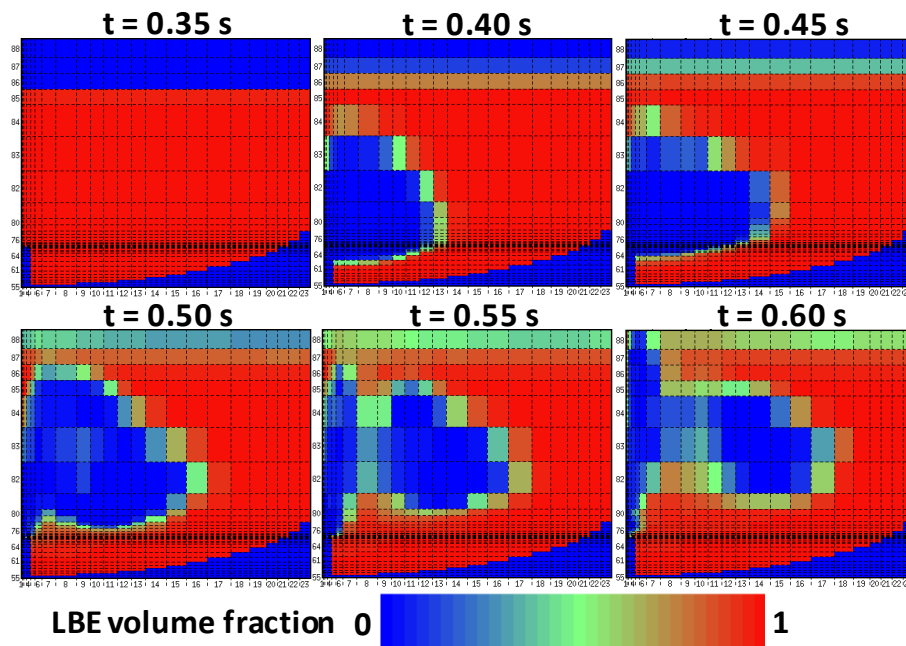


Fig. 9.16 – LBE volume fraction and vapour bubble evolution during the water interaction phase, calculated by SIMMER III code.



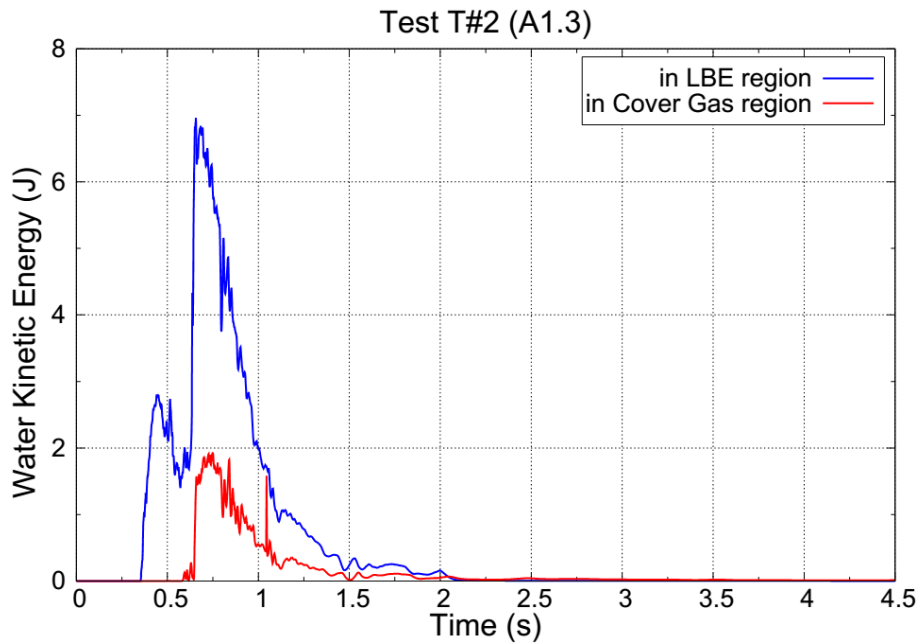


Fig. 9.17 – Water kinetic energy time trends in the cover gas and LBE regions, T#2.

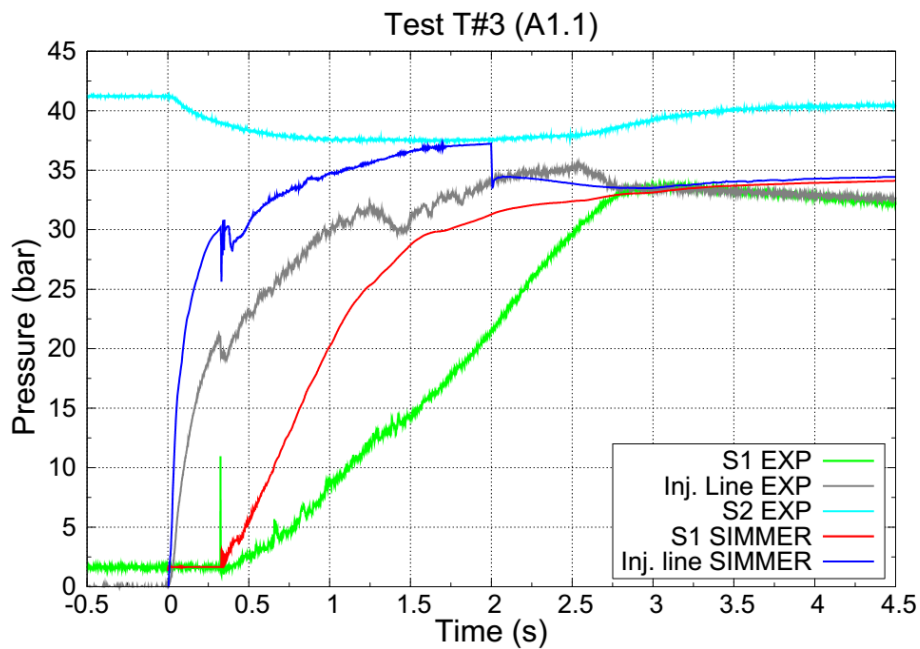


Fig. 9.18 – Calculated and experimental pressure time trends of the test T#3.



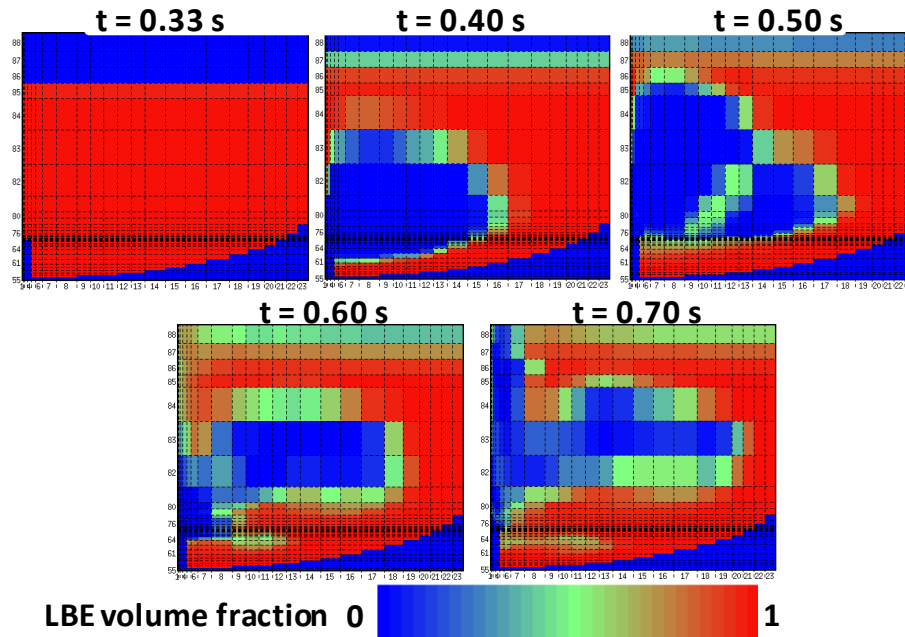


Fig. 9.19 – LBE volume fraction and vapour bubble evolution during the water interaction phase, calculated by SIMMER III code.

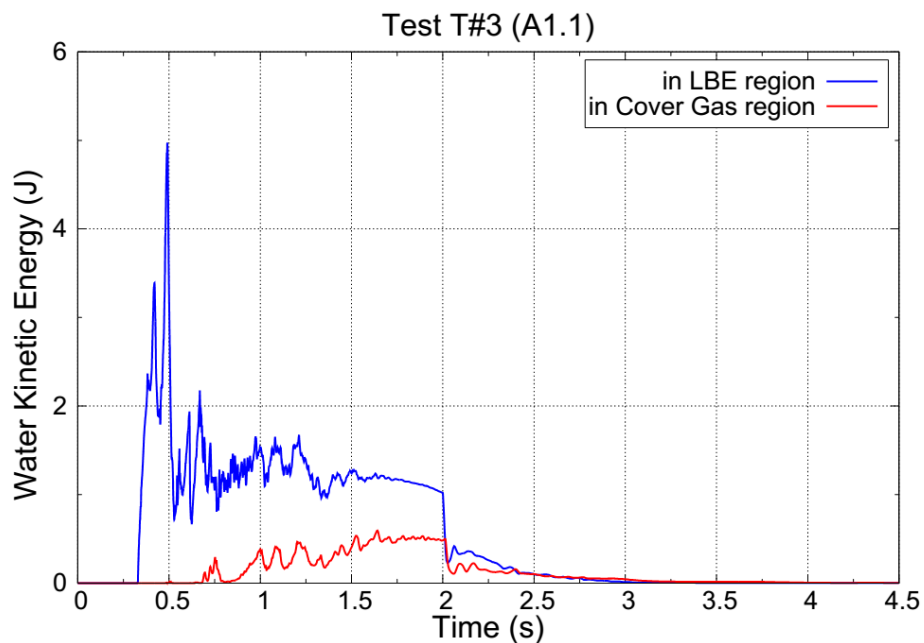


Fig. 9.20 – Water kinetic energy time trends in the cover gas and LBE regions, T#3.

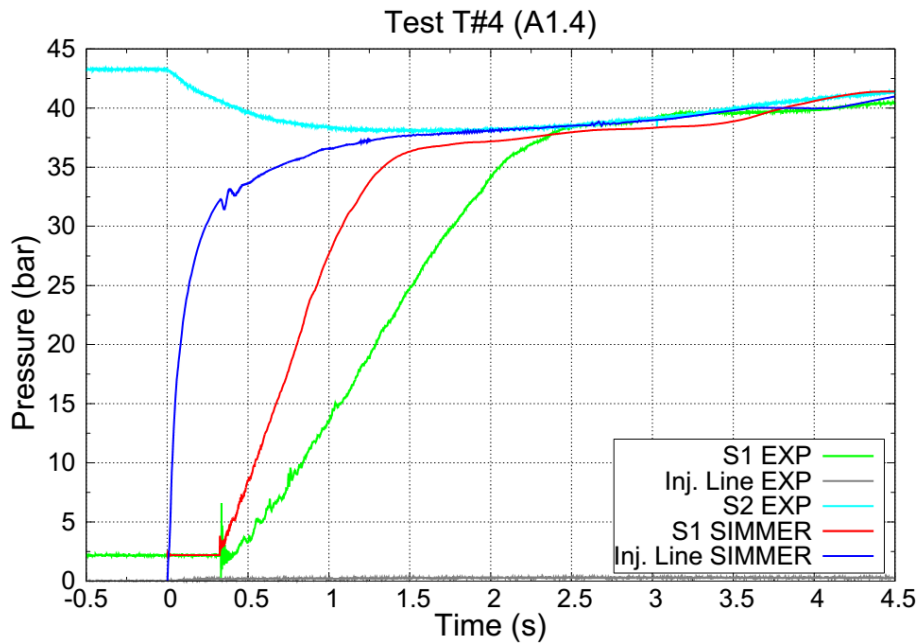


Fig. 9.21 – Calculated and experimental pressure time trends of the test T#4.

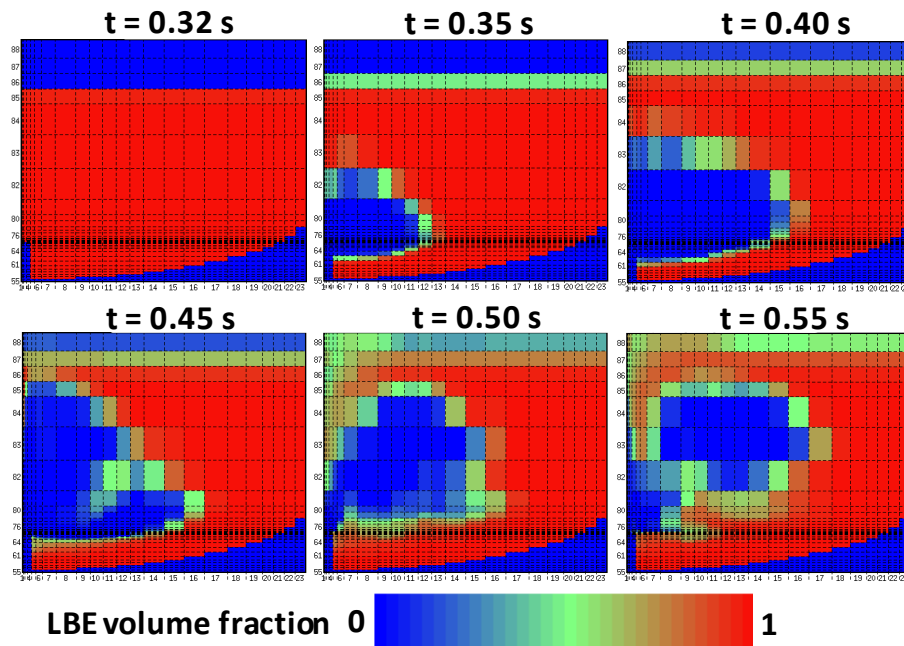


Fig. 9.22 – LBE volume fraction and vapour bubble evolution during the water interaction phase, calculated by SIMMER-III code.



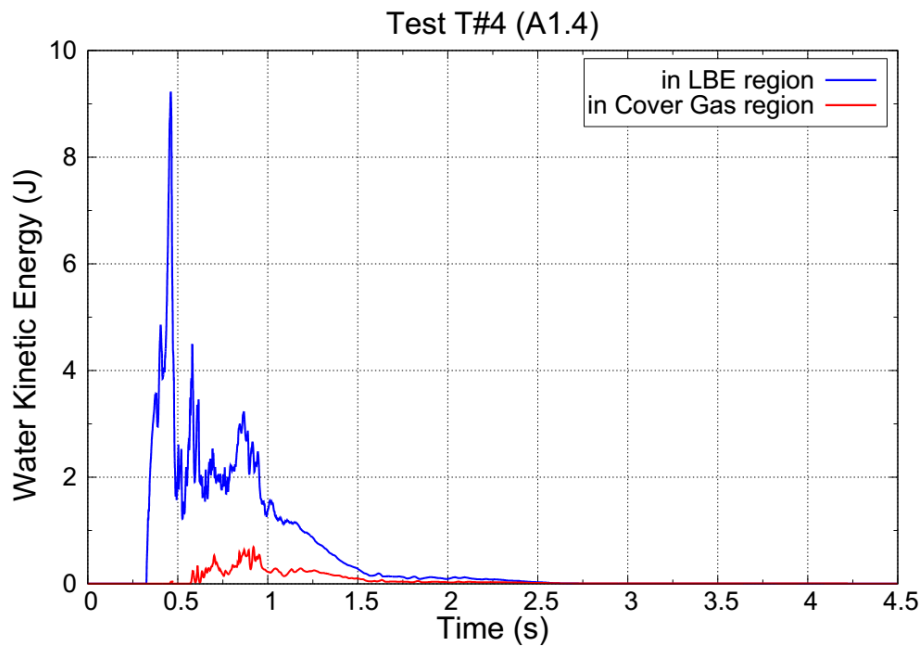


Fig. 9.23 – Water kinetic energy time trends in the cover gas and LBE regions, T#4.

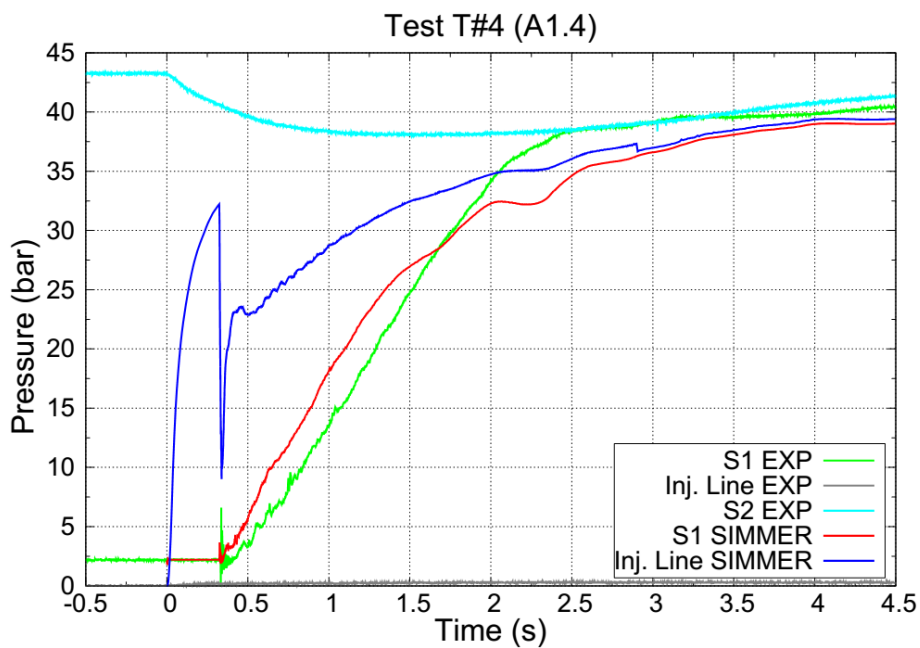


Fig. 9.24 – Calculated and experimental pressure time trends of the test T#4, with two-phase flow multiplier.



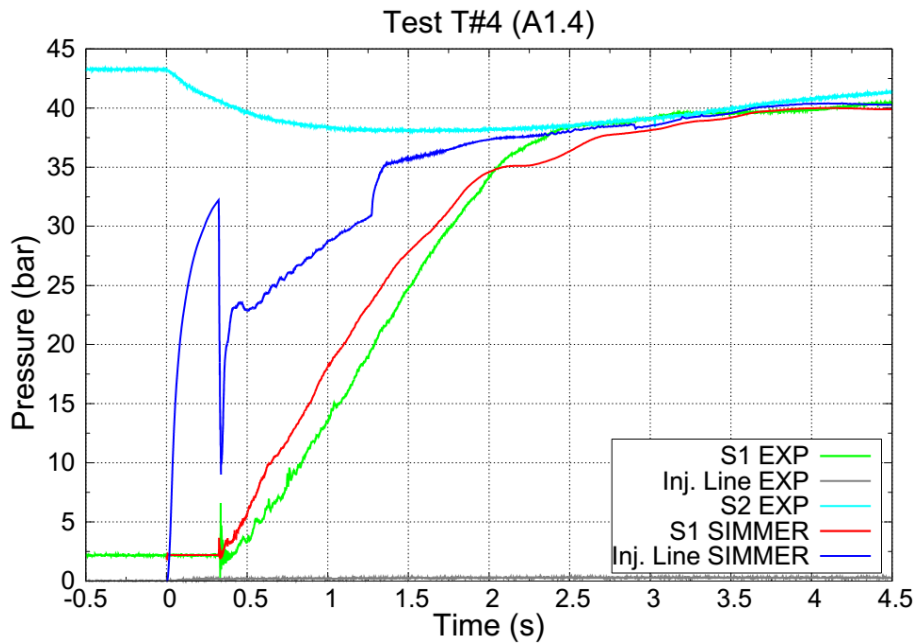


Fig. 9.25 – Calculated and experimental pressure time trends of the test T#4, with modified two-phase flow multiplier.

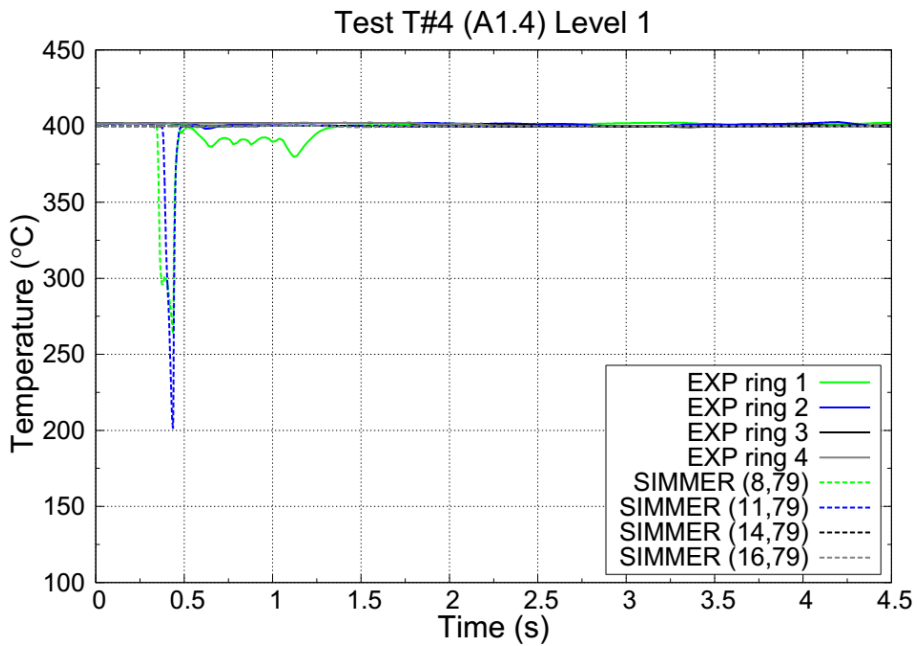


Fig. 9.26 – Experimental and calculated temperature time trends in the Level 1 of the test T#4.



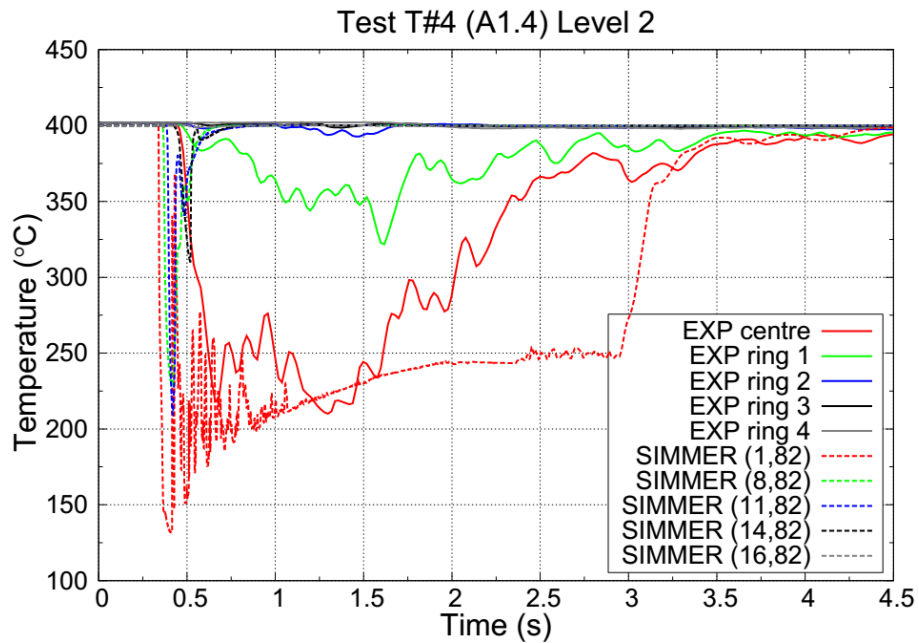


Fig. 9.27 – Experimental and calculated temperature time trends in the Level 2 of the test T#4.

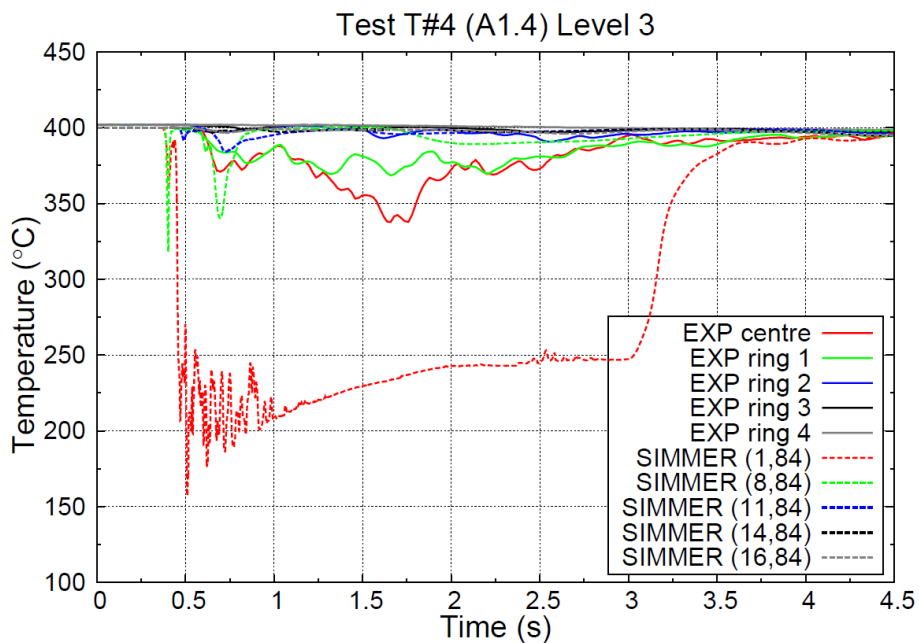


Fig. 9.28 – Experimental and calculated temperature time trends in the Level 3 of the test T#4.



Test T#4 (A1.4) Level 4

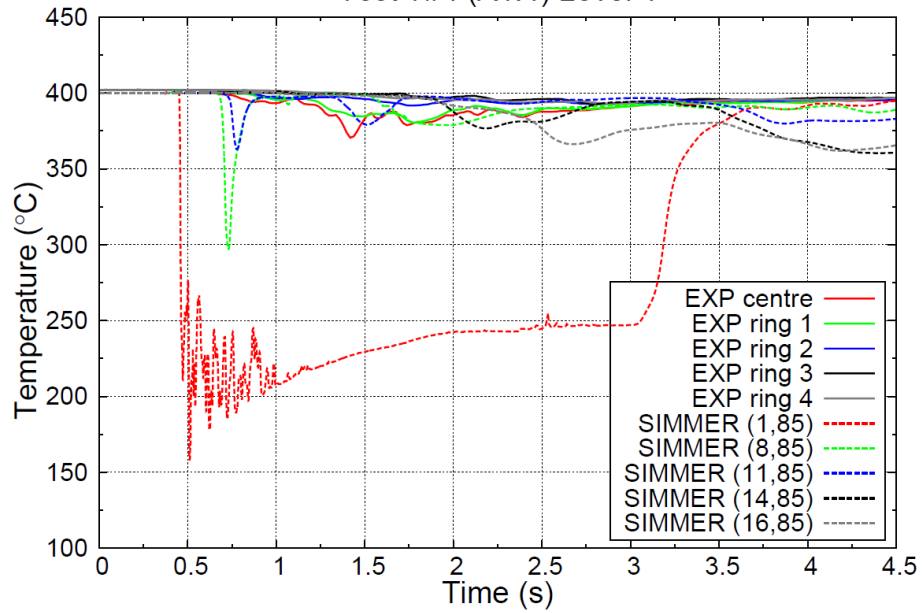



Fig. 9.29 – Experimental and calculated temperature time trends in the Level 4 of the test T#4.




 RICERCA SISTEMA ELETTRICO	<u>Title:</u> Development of BE numerical tools for LFR design and safety analysis – Part 2	<u>Distribution</u> PUBLIC	<u>Issue Date</u> 12.12.2017	<u>Pag.</u>
	<u>Project:</u> ADP ENEA-MSE PAR 2016	<u>Ref.</u> ADPFISS-LP2-144	Rev. 0	299 di 300

9.4 List of References

- [9.1] Ciampichetti, A., et al., *LBE-water interaction in sub-critical reactors: First experimental and modelling results*, Journal of Nuclear Materials, 376, 418-423, 2008.
- [9.2] Ciampichetti, A., et al., *Experimental and computational investigation of LBE-water interaction in LIFUS 5 facility*, Nuclear Engineering and Design, 239, 2468-2478, 2009.
- [9.3] Ciampichetti, A., et al., *LBE-water interaction in LIFUS 5 facility under different operating conditions*, Journal of Nuclear Materials, 415, 449-459, 2011.
- [9.4] Del Nevo, A., et al., 2013. *LIFUS5/MOD2 FACILITY – TEST A1.1 EDTAR, FP7 EC THINS - Task 4.1.2*, ENEA Technical report L5-T-R-040 Rev. 0, 2 July 2013.
- [9.5] Del Nevo, A., et al., *LIFUS5/MOD2 FACILITY – TEST A1.2 EDTAR, FP7 EC THINS - Task 4.1.2*, ENEA Technical report L5-T-R-039 Rev. 0, 2 August 2013.
- [9.6] Del Nevo, A., et al., *LIFUS5/MOD2 FACILITY – TEST A1.2_1 EDTAR, FP7 EC THINS - Task 4.1.2*, ENEA Technical report L5-T-R-045 Rev. 0, 19 August 2013.
- [9.7] Del Nevo, A., et al., *LIFUS5/MOD2 FACILITY – TEST A1.3 EDTAR, FP7 EC THINS - Task 4.1.2*, ENEA Technical report L5-T-R-041 Rev. 0, 8 August 2013.
- [9.8] Del Nevo, A., et al., *LIFUS5/MOD2 FACILITY – TEST A1.4 EDTAR, FP7 EC THINS - Task 4.1.2*, ENEA Technical report L5-T-R-044 Rev. 0, 10 August 2013.
- [9.9] Tobita, Y., et al., *The development of SIMMER III, an advanced computer program for LMFR safety analysis*. In: Proceeding of the IAEA/NEA Technical Meeting on Use of Computational Fluid Dynamics (CFD) Codes for Safety Analysis Reactors System Including Containment, November 11-14, Pisa, Italy, 2002.
- [9.10] Kondo, S., et al., *SIMMER III: a computer program for LMFR core disruptive accident analysis*, O-arai Engineering Centre, Japan Nuclear Cycle Development Institute, Research Document JNC TN 9400 2003-071, 2003.
- [9.11] AA.VV., *bfcsl (Ver.4.5) manual*, May 2012.
- [9.12] *Input Requirements*, January 2003.
- [9.13] Pesetti, A., Forgiione, N., Tarantino M., *Test section design for SGTR experimental investigation in CIRCE facility for HLMRS supported by SIMMER-III code*, Proc. of the 24th International Conference on Nuclear Engineering (ICONE24), Charlotte, NC, USA, June 26-30 2016.
- [9.14] Del Nevo, A., et al., *Experimental and Numerical Investigations of Interaction between Heavy Liquid Metal and Water for supporting the Safety of LFR Gen. IV Reactor Design*, Proc. of the 16th Int. Topical Meeting on Nuclear Reactor Thermal Hydraulics (NURETH-16), Log Number: 13807 Hyatt Regency Chicago, Chicago, IL, USA, Aug. 30-Sept. 4, 2015.
- [9.15] Pesetti, A., Del Nevo, A., Forgiione, N., *Experimental investigation and SIMMER-III code modelling of LBE–water interaction in LIFUS5/Mod2 facility*, Nuclear Eng. Des. 290 (2015) 119-126, <https://doi.org/10.1016/j.nucengdes.2014.11.016>.
- [9.16] AA.VV., *SIMMER-III: A Computer Program for LMFR Core Disruptive Accident Analysis – Version 3.A Model Summary and Program Description Code*, JNC TN 9400 2003-071, August 2003.



 RICERCA SISTEMA ELETTRICO	<u>Title:</u> Development of BE numerical tools for LFR design and safety analysis – Part 2	<u>Distribution</u> PUBLIC	<u>Issue Date</u> 12.12.2017	<u>Pag.</u>
	<u>Project:</u> ADP ENEA-MSE PAR 2016	<u>Ref.</u> ADPFISS-LP2-144	Rev. 0	300 di 300

- [9.17] Eboli, M., Forgione, N., Del Nevo, A., *Implementation of the chemical PbLi/water reaction in the SIMMER code*, Fusion Eng. Des. 109-111 (2016) 468-473, <https://doi.org/10.1016/j.fusengdes.2016.02.080>.
- [9.18] Eboli, M., Forgione, N., Del Nevo, A., *PbLi Water chemical interaction model – implementation in SIMMER-III Ver. 3F code*, DM-N-R-197, February 2016.
- [9.19] Eboli, M., Del Nevo, A., Forgione, N., M. T. Porfiri, *Post-test analyses of LIFUS5 Test#3 experiment*, Fusion Eng. Des. 124 (2017) 856-860, <https://doi.org/10.1016/j.fusengdes.2017.03.046>.

